Wireless Communications and Mobile Computing

Artificial Intelligence for Wireless Communications and Control Networks

Lead Guest Editor: Junjuan Xia
Guest Editors: Zhao Junhui and Panagiotis D. Diamantoulakis

Artificial Intelligence for Wireless Communications and Control Networks

Wireless Communications and Mobile Computing

Artificial Intelligence for Wireless Communications and Control Networks

Lead Guest Editor: Junjuan Xia
Guest Editors: Zhao Junhui and Panagiotis D. Diamantoulakis

Contents

Contents

Hindawi
Wireless Communications and Mobile Computing
Volume 2023, Article ID 9897273, 1 page
https://doi.org/10.1155/2023/9897273

Retraction

Retracted: Urban Ecological Monitoring and Prediction Based on Deep Learning

Wireless Communications and Mobile Computing

Received 18 July 2023; Accepted 18 July 2023; Published 19 July 2023

This article has been retracted by Hindawi following an investigation undertaken by the publisher [1]. This investigation has uncovered evidence of one or more of the following indicators of systematic manipulation of the publication process:

(1) Discrepancies in scope
(2) Discrepancies in the description of the research reported
(3) Discrepancies between the availability of data and the research described
(4) Inappropriate citations
(5) Incoherent, meaningless and/or irrelevant content included in the article
(6) Peer-review manipulation

The presence of these indicators undermines our confidence in the integrity of the article's content and we cannot, therefore, vouch for its reliability. Please note that this notice is intended solely to alert readers that the content of this article is unreliable. We have not investigated whether authors were aware of or involved in the systematic manipulation of the publication process.

Wiley and Hindawi regrets that the usual quality checks did not identify these issues before publication and have since put additional measures in place to safeguard research integrity.

We wish to credit our own Research Integrity and Research Publishing teams and anonymous and named external researchers and research integrity experts for contributing to this investigation.

The corresponding author, as the representative of all authors, has been given the opportunity to register their agreement or disagreement to this retraction. We have kept a record of any response received.

References

[1] J. H. Yang and C. P. Chan, "Urban Ecological Monitoring and Prediction Based on Deep Learning," *Wireless Communications and Mobile Computing*, vol. 2022, Article ID 1973777, 6 pages, 2022.

Hindawi
Wireless Communications and Mobile Computing
Volume 2023, Article ID 9823659, 1 page
https://doi.org/10.1155/2023/9823659

Retraction

Retracted: Wireless Control Industrial Robot Processing Irradiation System Based on Artificial Intelligence Technology

Wireless Communications and Mobile Computing

Received 18 July 2023; Accepted 18 July 2023; Published 19 July 2023

This article has been retracted by Hindawi following an investigation undertaken by the publisher [1]. This investigation has uncovered evidence of one or more of the following indicators of systematic manipulation of the publication process:

(1) Discrepancies in scope
(2) Discrepancies in the description of the research reported
(3) Discrepancies between the availability of data and the research described
(4) Inappropriate citations
(5) Incoherent, meaningless and/or irrelevant content included in the article
(6) Peer-review manipulation

The presence of these indicators undermines our confidence in the integrity of the article's content and we cannot, therefore, vouch for its reliability. Please note that this notice is intended solely to alert readers that the content of this article is unreliable. We have not investigated whether authors were aware of or involved in the systematic manipulation of the publication process.

Wiley and Hindawi regrets that the usual quality checks did not identify these issues before publication and have since put additional measures in place to safeguard research integrity.

We wish to credit our own Research Integrity and Research Publishing teams and anonymous and named external researchers and research integrity experts for contributing to this investigation.

The corresponding author, as the representative of all authors, has been given the opportunity to register their agreement or disagreement to this retraction. We have kept a record of any response received.

References

[1] L. Zhao, Q. Li, and G. Ding, "Wireless Control Industrial Robot Processing Irradiation System Based on Artificial Intelligence Technology," *Wireless Communications and Mobile Computing*, vol. 2022, Article ID 7068596, 8 pages, 2022.

Hindawi
Wireless Communications and Mobile Computing
Volume 2022, Article ID 6722848, 13 pages
https://doi.org/10.1155/2022/6722848

Research Article

Intelligent Time Allocation for Wireless Power Transfer in Wireless-Powered Mobile Edge Computing

Xiaogang Dong,[1,2] **Zheng Wan**,[1] **Changshou Deng**,[2] **Wenying Wen**,[1] **and Yuxuan Luo**[1]

[1]*School of Information Management, Jiangxi University of Finance and Economics, Nanchang 330013, China*
[2]*School of Computer and Big Data Science, Jiujiang University, Jiujiang 332005, China*

Correspondence should be addressed to Zheng Wan; wanzheng97@163.com

Received 31 March 2022; Revised 30 June 2022; Accepted 11 July 2022; Published 24 August 2022

Academic Editor: Zhao Junhui

Wireless-powered mobile edge computing is a new network computing paradigm that combines with the advantages of wireless power transfer and mobile edge computing. When the harvest-then-offload protocol is adopted in this network, the time of wireless power transfer has a significant impact on system performance. If the time is too short, the user cannot harvest enough energy. If it is too long, the user will not have enough time to complete the task offloading. Both result in many of user tasks being discarded. To address this problem, DEWPT, a differential evolution-based optimization scheme for wireless power transfer time, is proposed in this paper. DEWPT is designed with a hybrid mutation operator and a perturbation-based binomial crossover operator. The hybrid mutation operator combines the benefits of two mutation operators with distinct characteristics, so that DEWPT not only has a strong exploration ability but also can quickly converge. Meanwhile, the perturbation-based binomial crossover operator improves DEWPT's ability to exploit local space. These two improvements effectively enhance DEWPT's optimization performance, which is beneficial to find the optimal time for wireless power transfer. Furthermore, to improve the optimization efficiency, micro-population is introduced into DEWPT. Finally, the computation completion ratio maximization model is used to validate the performance of DEWPT in the wireless-powered mobile edge computing network with multiple edge servers. Numerical results show that the computation offloading scheme integrating with DEWPT can achieve a higher computation completion rate than three benchmark schemes, and is competitive in complexity. This demonstrates that DEWPT is an effective time allocation scheme for wireless power transfer.

1. Introduction

In recent years, the rapid development of Internet of Things (IoT) technology has spawned numerous new intelligent applications [1], such as virtual and augmented reality [2], unmanned driving [3], intelligent video analysis [4], and intelligent industrial production lines [5]. These applications are often computation-intensive and time-sensitive and have a very high demand for the computation capacity of wireless devices (WDs). However, WDs usually only have low computation power due to volume and manufacturing cost constraints [6]. In addition, the lifetime of WDs is very finite because of the battery capacity limitation. Therefore, the stable and sustainable operation cannot be maintained. Under the goal of service first, the two performance limitations have become the bottleneck that must be broken through to improve the quality of IoT services.

Mobile edge computing (MEC) [7, 8] and wireless power transfer (WPT), as two promising technologies, have attracted widespread concern in many fields. In the MEC architecture, the computation-intensive tasks of WDs can be offloaded to MEC servers deployed at the network edge for execution, which can effectively expand the computing power of WDs. Meanwhile, WPT can continuously charge the battery of WDs. It provides a solution to prolong the lifetime of WDs. Combining the advantages of MEC and WPT results in a

new computing paradigm, wireless-powered MEC (WP-MEC). WP-MEC has become a potential solution to solve the above bottlenecks of IoT. Due to this significant advantage of WP-MEC, the optimization design and application of WP-MEC have got a lot of attention in recent years. However, the majority of existing works only focus on the task offloading decision-making.

The allocation of WPT time is a crucial factor affecting the performance of WP-MEC when the harvest-then-offload protocol is employed. How to achieve the optimal allocation of WPT time is a problem worth of studying for the WP-MEC. The existing works usually adopt traditional optimization methods (such as bisection search) or mathematical programming methods (such as Lagrangian duality) to deal with the allocation of WPT time. However, these methods are only suitable for the simple network scenarios. In complex real network scenarios (such as the network with massive connections), they are either difficult to implement or achieve satisfactory optimization performance.

Based on the above shortcomings of the existing works, we focus on the allocation of WPT time for WP-MEC in this paper, aiming to achieve the optimal allocation of WPT time. To this end, a differential evolution-based optimization scheme for the WPT time allocation is proposed. The contributions of this paper are summarized as follows.

(i) A novel differential evolution algorithm is developed to optimize the time allocation for WPT in a WP-MEC with multiple edge servers, in which a hybrid mutation operator and a perturbation based binomial crossover operator are designed. The hybrid mutation operator combines the advantages of two mutation operators with distinct characteristics. The perturbation-based binomial crossover operator enhances search ability of the algorithm in the local space through a random perturbation

(ii) To improve the efficiency of the algorithm, a micro-population scheme is introduced into the algorithm. The scheme selects an appropriate population size based on trade-off between performance and efficiency. Therefore, it can guarantee the efficiency of finding a better WPT time without performance loss

(iii) A new task offloading scheme is constructed by integrating the algorithm into the computation completion rate maximization model. Extensive experiments are conducted to evaluate the performance of our proposed algorithm

The rest of this paper is organized as follows. The related works are discussed in Section 2. Section 3 presents the network model and problem formulation. The proposed scheme is described in Section 4, and the simulation results are given in Section 5. Finally, Section 6 concludes this work.

2. Related Works

Over the past few years, many existing works have studied the optimal design of WP-MEC from various perspectives. According to the optimization design objectives, these works can be divided into the following four categories.

2.1. Maximization of Computation Rate. Bi and Zhang [6] considered a multiuser WP-MEC system, where the user task offloading mode is binary mode. The authors designed a joint optimization scheme for WPT time, user computation mode, local CPU frequency, computation time, and offloading communication time, aiming to maximize computation rate. Huang et al. [9] extended the work of [6]. Deep reinforcement learning was introduced. It primarily addressed the issue of real-time selection of user computing mode in wireless channel time-varying scenarios. Zhou et al. [10] considered an unmanned aerial vehicle- (UAV-) enabled WP-MEC system. The computation rate maximization problem was investigated for both partial and binary computation offloading modes in this work. The two-stage algorithm and the three-stage alternative algorithm were designed for the two offloading modes, respectively. Simulation results showed that the two algorithms outperformed benchmark algorithms in terms of performance, converge rate, and computation complexity. However, it was assumed that users can simultaneously perform energy harvesting, local computing, and computation offloading.

For the WPT time, the bisection search algorithm was used in [6, 9] to find the optimal time of WPT while the work [10] directly assumes that the entire time frame is used for the WPT.

2.2. Maximization of Computation Efficiency. Zhou and Hu [11] studied the computation efficiency maximization problem of wireless-powered MEC networks under both partial and binary computation offloading modes. Different from other existing works, this work designed solution schemes for time division multiple access and nonorthogonal multiple access. Ji and Guo [12] considered a WP-MEC system including two users. It should be noted that this work only considered the offloading computation of user tasks. Based on the consideration of "doubly near-far" effect, the author devised a user cooperation scheme of task offloading to maximize the energy efficiency (the ratio of the user throughput to energy).

In these two works, the time allocation of WPT was optimized by the mathematical programming methods, such as Lagrangian method, Newton iteration method, and subgradient algorithm. Clearly, these methods are only suitable for the scenarios with a small user scale.

2.3. Minimization of Energy Consumption. The total energy consumption minimization problem of the wireless access point (WAP) was formulated in [13]. Subsequently, an optimal resource allocation scheme was developed for a practical scenario where latency-limited computation was required. Similar to [12], Hu et al. [14] also studied a two user WP-MEC system. However, the optimization objective was minimization of the WAP total transmission energy. The author first illustrated that the optimization is equivalent to a min-max problem. Next, a two-phase optimization method was devised to solve it. Wang et al. [15] investigated a multiple-user WP-MEC system. In their work, apart from the special scenarios where the channel state information and the task

state information are completely known, the author further studied the optimization scheme under the more practical application scenarios and proposed a sliding-window based online resource allocation scheme by integrating with the sequential optimization.

Similarly, these works either used the mathematical programming methods or assumed that the entire time frame is used for WPT.

2.4. Maximization of Computation Completion Ratio. The concept of computation completion ratio (CCR) [16] was first introduced for the optimization design of WP-MEC. CCR is a vital metric, which can effectively indicate the computing performance of WP-MEC. Meanwhile, the WP-MEC with multiple edge devices was considered in their work. Under this network configuration, the author proposed the CCR maximization scheduling scheme, which is termed as CoCoRaM. CoCoRaM achieved a higher CCR through joint optimizing the WPT time allocation and computation scheduling.

In the CoCoRaM, the approximate optimal time allocation of WPT was obtained by constructing a set of candidate times. The number of candidate times in the set is greater than the number of users. That is, as the user scale increases, the number of candidate times will grow.

Although the optimization design of WP-MEC system has been extensively studied in the previously mentioned works, there are still some issues that require further investigation, for example, the optimal time allocation of WPT. Despite bisection search, methods based on mathematical derivation and approximation method have been used to find the optimal time allocation of WPT. However, these methods either require analytical knowledge of model and complex computations or can only be applied to specific network scenarios. Therefore, an effective optimization scheme for the time allocation of WPT still deserved further research.

Some main notations used in this paper are summarized in Table 1.

Table 1: Summary of some main notations.

Notation	Definition
N	Number of users
Q	Number of MEC servers
U	Set of users
S	Set of MEC servers
D_i	Task size of the ith user
T	Time frame duration
E^h	Harvested RF energy
E^o	Energy of task offloading
E^l	Energy of local computing
ϕ_i	CPU cycles of processing one bit data
CCR	Computation completion ratio
$f^{\max}$	The upper of user CPU power
$f(\bullet)$	Fitness function
x	Decision matrix
$\boldsymbol{t}^l$	Local computing time vector
$\boldsymbol{f}$	Local computing CPU frequency
t^0	Offloading time vector
P	Power of ET
pop	Population of DE
NP	Population size
F	Scale factor
CR	Crossover probability
$pool$	Mutation operators pool
Λ_1, Λ_2	Control parameters
CBs	Computation bits
$\mathcal{F}(x)$	Probability density function

3. Network Model and Problem Formulation

This section will describe the network model, the local computing model, and the offloading computing model, respectively. A CCR maximization problem is then formulated.

3.1. WP-MEC Network with Multiple Edge Servers. As illustrated in Figure 1(a), a wireless-powered mobile edge computing network is investigated in this paper. It consists of a radio frequency (RF) energy transmitter (ET) with a single-antenna, N mobile wireless users, and Q wireless access points (WAP). Each WAP integrated with an MEC server provides the computing service to users. $\mathcal{U} = \{u_1, \cdots, u_N\}$ represents the set of users, and the set of edge servers is denoted by $\mathcal{S} = \{s_1, \cdots, s_Q\}$. The ET broadcasts RF energy through WPT for all users. Each user can harvest the RF energy by a single-antenna energy receiver to charge its rechargeable battery. The network system employs the binary offloading rule. That is, by utilizing the harvested energy, users can complete their computing task at local or a chosen MEC server (i.e., offloading computing). Certainly, if the energy harvested by a user is not enough to complete its task locally or offload it to any MEC server, its task will be discarded. For one time frame with duration T, the harvest-then-offload protocol (HTOP) is used, and each user has a task of size D_i bits to accomplish. Therefore, local computing of users and RF energy harvesting from ET can be simultaneously executed while the energy harvesting and task offloading cannot be performed concurrently. The time division multiple access protocol is used to avoid the communication interference caused by multiple users offloading tasks to the same MEC server. Figure 1(b) gives an example of the time allocation between WPT and computing offloading of users. Due to the powerful computation power of the edge servers and the very small task results, the time of edge servers computing and sending results back can be safely ignored like in [6, 17, 18]. The amount of RF energy harvested by each user can be calculated by a linear energy harvesting as formula (1)

$$E_i^h = \mu P g_i \tau_0, \tag{1}$$

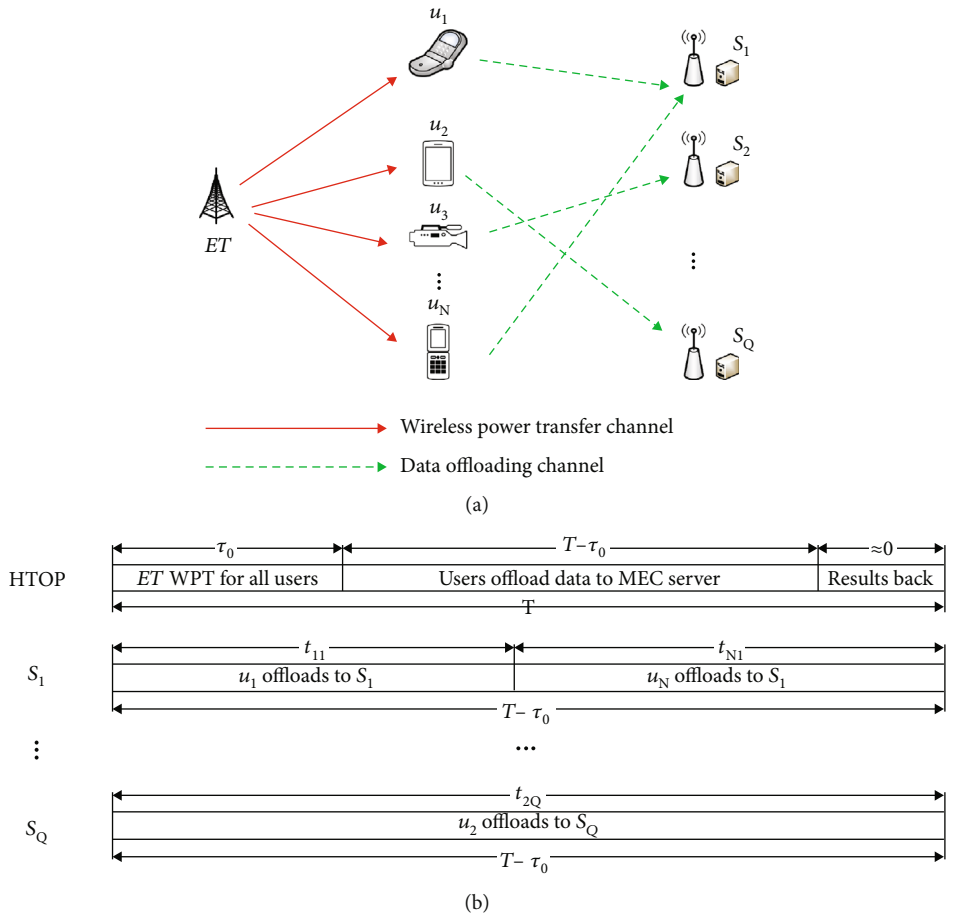

Figure 1: Network system. (a) WP-MEC network model. (b) Time allocation of HTOP.

where τ_0 is the time of WPT. The channel gain between ET and user u_i is denoted by g_i which remains constant in one time frame, and P is the energy transmission power of ET. μ denotes the energy harvesting coefficient.

3.1.1. Local computing model. If the user u_i performs its computation task locally, the relationship between CPU frequency and local computing time can be obtained by formula (2), and the energy consumption can be calculated by formula (3).

$$f_i t_i^l = D_i \phi_i, \tag{2}$$

$$E_i^l = k_i f_i^3 t_i^l, \tag{3}$$

where f_i denotes the CPU frequency, which can be adjusted between $(0, f^{\max}]$ by dynamic voltage and frequency scaling technique. t_i^l is the local computing time of u_i. ϕ_i represents the needing CPU cycles that u_i processes unit bit data. k_i is the computation energy efficiency coefficient of the processor's chip. The power consumption of the processor is modelled as $k_i f_i^3$ [6]. According to the constraint of energy, E_i^l cannot exceed E_i^h, i.e., $E_i^l \le E_i^h$.

3.1.2. Offloading computing model. When u_j offloads task to MEC server s_k for remote executing, the time of task uploading t_{jk}^o and the energy consumption E_{jk}^o can be obtained by formulas (4) and (5)

$$t_{jk}^o = \frac{D_j}{W \log_2\left(1 + \left(P_{jk} h_{jk} / \sigma^2\right)\right)}, \tag{4}$$

$$E_{jk}^o = P_{jk} t_{jk}^o, \tag{5}$$

where W is the transmission bandwidth. P_{jk} and h_{jk} are the transmission power and channel gain between u_j and s_k, respectively. σ^2 is the noise power. Likewise, E_{jk}^o must meet the energy constraint, i.e., $E_{jk}^o \le E_j^h$.

3.2. CCR Maximization Problem. As described in related work (Section 2), computation rate, computation efficiency, energy consumption, and computation complete ratio (CCR) are four common optimization objectives for the WP-MEC. Computation efficiency and energy consumption are only effective when all user tasks are guaranteed to be completed. Furthermore, the computation rate and the CCR are essentially equivalent when the user task information is a priori. But, as the ratio of processed computation data to the required computation data of all users, CCR can more directly reflect the optimization performance of

the scheme. Thus, maximization CCR is selected as the optimization objective in this paper. According to the binary offloading rule, each user has $(1+Q)$ options for task execution, i.e., local and Q MEC servers. A variate x_{ik} $(k \in [0, Q])$ is used to indicate the choice of user task execution. If u_i performs its task at the kth option, $x_{ik} = 1$. Otherwise, $x_{ik} = 0$. Note that $k = 0$ denotes local computing. So, the maximization problem of CCR is as formula (6)

$$\begin{aligned} \underset{\tau_0, \mathbf{x}, \mathbf{t^l}, \mathbf{f}, \mathbf{t^o}}{Max} \quad & CCR = \frac{\sum_{i=1}^{N} x_{i0} D_i + \sum_{k=1}^{Q} \sum_{j=1}^{N} x_{jk} D_j}{\sum_{i=1}^{N} D_i}, \\ \text{s.t. :} \quad & \\ & C1 : \tau_0 \le T, \\ & C2 : f_1 \in [0, f^{\max}], \forall i \in [1, N], \\ & C3 : 0 \le t_i^l \le t, \forall i \in [1, N], \\ & C4 : 0 \le t_{jk}^o \le T - \tau_0, \forall j \in [1, N] \forall k \in [1, Q], \\ & C5 : \sum_{j=1}^{N} t_{jk} \le T - \tau_0, \\ & C6 : E_i^l \le E_i^h, E_{jk}^o \le E_j^h, i, j \in [1, N], k \in [1, Q], \\ & C7 : x_{ik} \in \{0, 1\}, \forall j \in [1, N], \forall k \in [0, Q], \end{aligned} \tag{6}$$

where τ_0 is a float variate. $\boldsymbol{x} = \{x_{ik} | i \in [1, N], k \in [0, \mathrm{Q}]\}$ is an integer matrix. $\boldsymbol{t}^l = \{t_i^l | i \in [1, N]\}$, $\boldsymbol{f} = \{f_i | i \in [1, N]\}$, and $\boldsymbol{t}^o = \{t_{jk}^o | j \in [1, N], k \in [1, Q]\}$ are three float vectors. Obviously, the maximization problem is a mixed integer nonlinear programming problem that is NP-hard and difficult to solve by the traditional optimization methods.

4. The Proposed Scheme of WPT Time

This section will first analyze the nested optimization structure of the optimization problem, i.e., formula (6). Then, a WPT time allocation algorithm based on the differential evolution algorithm is proposed. In this algorithm, a hybrid mutation operator and a perturbation-based binomial crossover operator are designed for achieving the optimal allocation of WPT time, and the micropopulation is introduced to improve the optimization efficiency.

4.1. Analysis of Optimization Problem. According to the feature of the WP-MEC system, all energy consumed by users comes from the RF energy harvested by them. In one time frame, WPT time τ_0 is the only factor that affects the amount of energy harvested by the user when other factors are fixed. Furthermore, the user offloading operation should be completed within $(T - \tau_0)$. Based on these, the following conclusions can be drawn.

(i) The WPT time τ_0 is a crucial decision factor. Too short τ_0, the users cannot harvest enough energy. Too long τ_0, the users have less time for task offloading

(ii) Given a τ_0, different decision matrices $\boldsymbol{x}$ will significantly affect the offloading performance. Thus, it is only makes sense to evaluate whether the τ_0 is optimal based on the optimal decision matrix $\boldsymbol{x}^*$ and resource allocation. Meanwhile, the resource allocations (i.e., $\mathbf{t^l}, \mathbf{f}, \mathbf{t^o}$) are closely related to the decision matrix $\boldsymbol{x}$

According to these analyses, optimization problem (6) is essentially a nested optimization problem that can be divided into two layers, i.e., the inner layer and outer layer (see Figure 2). The inner layer determines the optimal decision matrix $\boldsymbol{x}$ for a given WPT time, as well as the corresponding resource allocation. The outer layer optimizes the WPT time. The solution of the inner layer serves as the basis for evaluating the solution of the outer layer. The work of [16] modelled optimization problem of the inner layer as a generalized assignment problem (GAP) and designed the generalized assignment problem-based computation scheduling (GAP-CS) algorithm for finding the optimal decision matrix $\boldsymbol{x}^*$ and the corresponding resource allocation under the given WPT time.

In this work, the outer optimization problem is focused. To design an optimization scheme for WPT time, we must understand the relationship between WPT time and CCR which is the optimization objective of this work. Since the required computation data of all users is a priori, here, we simplify CCR to computation bits (CBs), the molecular part of formula (6), and observe their relationship through a sampling experiment. Assume that the CBs are a function of WPT time τ_0 as formula (7). The sampling experiment adopts an iterative search method to obtain the optimal decision matrix $\boldsymbol{x}^*$ and the corresponding resource allocation. The observation results are given in Figure 3.

$$\mathrm{CBs} = f(\tau_0), \tau_0 \in [0, T]. \tag{7}$$

From the results of Figure 3, it can be seen that the function curve obviously has multiple extreme points (see green oval mark). This shows that CBs are a nonmonotonic multimodal function of WPT time. Equivalently, CCR is a nonmonotonic multimodal function of WPT time. Therefore, the optimization of WPT is difficult to solve by the traditional search methods directly, such as bisection search.

4.2. The Allocation of WPT Time Based on DE. Differential evolution (DE), which is a heuristic evolution algorithm, was proposed by Store and Price [19]. A population pop with NP individuals is maintained, and each individual of pop denotes a solution to the optimization problem. The pop is initialled by a random way, and then, mutation (8), crossover (9), and selection operators are performed to update the pop generation by generation [20]. The widely used mutation and crossover operators [21] are as formulas

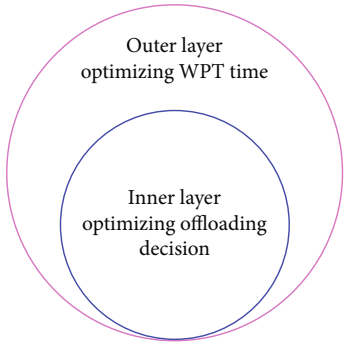

Figure 2: Nested optimization.

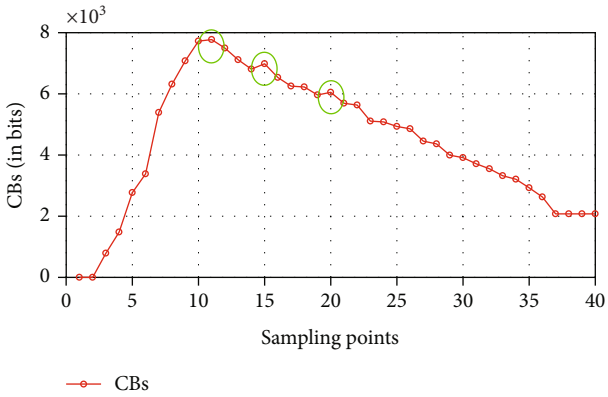

Figure 3: Results of sampling experiment.

(8) and (9)

$$V_i^g = X_{r1}^g + F \cdot \left(X_{r2}^g - X_{r3}^g\right), \tag{8}$$

$$U_{i,j}^g = \begin{cases} V_{i,j}^g, & \text{if } rand \le CR \text{ or } j = J, \\ X_{i,j}^g, & \text{otherwise,} \end{cases} \tag{9}$$

where $i \in [1, NP]$ is the index of individual. $r1, r2, r3 (r1 \neq r2 \neq r3 \neq i)$ are generated in $[1, NP]$ by a random manner. g is the index of generation. V, U represent the mutation individual and trial individual, respectively. $j = 1, 2, \cdots, D$, and D is the number of gene in an individual. F and CR are scale factor and crossover probability, respectively. $J \in [1, D]$ is a uniformly distributed random number. $f(\cdot)$ is the fitness function.

Due to the powerful optimization performance, DE has been successfully applied in many of fields [22–24]. Inspired by these successful applications, a novel DE algorithm is designed for optimization the allocation of WPT time in this work. Next, the detailed designs of this algorithm will be given.

4.2.1. Hybrid mutation operator. In the DE algorithm community, there are many of mutation operators [21]. Some of them have outstanding global searching capability, which is conducive to find the global optimal solution, say, DE/rand/1, as formula (8). Others of them have excellent local searching capability and can speed up the convergence of the algorithm, say, DE/best/1, as formula (10)

$$V_i^g = X_{best}^g + F \cdot \left(X_{r1}^g - X_{r2}^g\right), \tag{10}$$

where best is the index of the optimal individual in the gth generation. The other parameters are same as formula (8).

For a given real-world optimization problem, it is not easy to choose the best one among different mutation operators. On the other hand, in order to improve quality of WP-MEC service, finding the optimal WPT time should not only meet the requirement of high precision but also enhance the real-time performance as much as possible.

Based on the above analysis, a new hybrid mutation operator is designed. The main idea of the hybrid mutation operator includes three key points.

(i) A pool of mutation operators *pool* is constructed, which consists of a mutation operator with outstanding global search performance (DE/rand/1) and a mutation operator with a fast convergence rate (DE/best/1)

(ii) A random number q is generated in each iteration according to a uniform distribution u. The probability density function $\mathcal{F}(x)$ of u is formula (11), where a is the lower bound, and b is the upper bound, respectively

$$\mathcal{F}(x) = \begin{cases} \dfrac{1}{b-a}, & a \le x \le b, \\ 0, & \text{otherwise} \end{cases} \tag{11}$$

(iii) A fixed threshold θ is set in the algorithm's initial stage. In each generation, if q is greater than θ, the algorithm selects DE/rand/1 from *pool* to perform mutation. Otherwise, the DE/best/1 is selected from *pool* for mutation operation

The hybrid mutation operator can effectively improve the global search ability and accelerate the convergence rate of DE when solving the WPT time allocation problem. The detailed pseudocode of the hybrid mutation is given in Algorithm 1.

4.2.2. Perturbation-based binomial crossover. The crossover operator plays a crucial role in DE algorithm. Its major contribution is to improve the DE's exploitation performance. The binomial crossover operator, formula (9), has the characteristics of simple structure and easy implementation. However, there is still room for performance improvement, particularly when it comes to real-world applications. To further improve the exploitation performance of DE and enhance the efficiency of searching optimal WPT time in WP-MEC system, a perturbation-based binomial crossover

Input: *pool*, θ and the target individual
Output: mutation individual
1: generate a random number q by the uniform distribution u with the probability density function $\mathcal{F}(x)$
2: **if** $q < \theta$ **then**
3: select DE/rand/1 from *pool*, perform mutation to produce the mutation individual
4: **else**
5: select DE/best/1 from *pool*, perform mutation to produce the mutation individual
6: **return** mutation individual

Algorithm 1: Hybrid mutation operator.

Input: the set of users $\mathcal{U}$, the set of MEC servers S. The set of WP-MEC parameters para. The algorithm parameters: NP, F, CR, $maxIter$, $\Lambda_1 = \Lambda_2 = 0.1$.
Output: the optimal CCR∗
1: generate the initial population *pop* in a random way.
2: execute GAP-CS with para and each individual of *pop* to produce the decision matrix x.
3: $iter = 1$
4: **while** iter ≤ maxIter **do**
5: **for** $i = 1$ to NP
6: select $r1, r2, r3$ from $[1, NP]/i$ in random way
7: execute the hybrid mutation operator to produce v_i via Algorithm 1
8: execute the perturbation-based binomial crossover to produce u_i by formula (12)
9: execute GAP-CS with u_i and para to produce decision matrix x and resource allocation $\boldsymbol{t}^l, \boldsymbol{f}, \boldsymbol{t}^o$
10: calculate CCR by formula (6)
11: execute selection operator, and update the optimal CCR∗
12: **return** the optimal CCR∗

Algorithm 2: DEWPT.

as formula (12) is designed.

$$U_{i,j}^{g} = \begin{cases} V_{i,j}^{g} + \Lambda_1^* (-1)^{I_{\text{rnd}}}, & \text{if } rand < CR, \\ X_{i,j}^{g} + \Lambda_2^* (-1)^{I_{\text{rnd}}}, & \text{otherwise,} \end{cases} \tag{12}$$

where Λ_1 and Λ_2 are two fixed control parameters and the I_{rnd} is a random integer. The other notations are same as formula (9).

The main idea behind the perturbation-based binomial crossover is to improve the exploitation of the space around the target and mutant individuals through a random perturbation. In the actual implementation process, the perturbation range can be controlled by adjusting the sizes of Λ_1 and Λ_2. The values of Λ_1 and Λ_2 can be same or different according to the actual needs.

4.2.3. Micro-population for DE. The population size has a significant effect on the overall performance of DE algorithm [25]. When the population size is large, DE requires high computation cost and occupies a large amount of memory [26]. This makes DE difficult to apply to some application scenarios with small memory and high real-time requirements. Therefore, micro-population (no more than 10 individuals)-based DE algorithms have received high attention in recent years [27–29]. Furthermore, micro-population can meet the two goals of high efficiency and low computation cost of WP-MEC network optimization.

In view of the above analysis, we design a micro-population scheme for the DE algorithm to solve the WPT time allocation problem in this work. In order to obtain the optimal population size, we used several groups of population size less than 10 for pre-experiment (to save space, the pre-experiment process is omitted). Through verification and analysis, we found that DE has a higher probability of obtaining a better WPT time allocation when the population size is set to 6. Therefore, we set the population size of the proposed DE algorithm to 6.

Integrating the three aspects of design, we construct the solving framework for optimization problem (6), which is termed as DEWPT. In DEWPT, GAP-CS is used to solve the inner optimization problem. The pseudocode structure of DEWPT is described as Algorithm 2.

5. Simulation Results

In this section, we provide extensive simulations to evaluate the performance of our proposed scheme. The Reyleigh

Table 2: Parameter setting.

Parameters	Notations	Value
The duration of time frame	T	$0.3\,s$
Transmission bandwidth	W	$1.45\,MHz$
The ET power of broadcasting RF energy	P	$3\,w$
The energy harvesting coefficient	μ	0.51
The upper of user CPU power	$f^{\max}$	$0.5\,GHz$
The computation energy efficiency coefficient	k_i	10^{-28}
The CPU cycles of user processing one bit data (in cycles/bit)	ϕ_i	800
The transmission power of user offloading	p_{ik}	$0.12\,w$
The scope of user task size (in kb)	D_i	[50,150]
The scale factor of DE	F	0.5
The crossover probability of DE	CR	0.5
Population size of DE	NP	6

fading channel model is used in all simulations. Moreover, Table 2 gives the configuration of other parameters. Noted that each plotted point in all figures represents the average results of 20 group of user tasks.

Furthermore, the following three schemes are used as benchmark schemes for comparison.

(i) CoCoRaM: CoCoRaM is an approximation algorithm proposed in [16], which optimizes the WPT time by constructing a candidate set of WPT times, and the optimal offloading decision is got by GAP-CS

(ii) LCO: the WPT time is set to the time frame T. All users either perform their tasks locally or discard them and cannot offload them

(iii) COO: all users cannot perform tasks locally and either offload them to a selected edge device or drop them. The optimal WPT time and the optimal offloading decision are got by CoCoRaM and GAP-CS, respectively

5.1. The Impact of WP-MEC Size. In this group of simulations, we will investigate and compare the impact of network size on the optimization performance of four schemes by varying the number of users and MEC servers.

First, we validate the impact of changes in the number of users. Therefore, in this simulation, the number of users is increased from 10 to 90 with the step size of 10, and the number of edge servers is fixed to 5. Figure 4 gives the results of this simulation.

Figure 4(a) shows the comparison of CCR achieved by DEWPT, CoCoRaM, COO, and LCO. From the experimental results, it can be found that the CCR obtained by each scheme decreases with the increase of the number of users. The CCR achieved by DEWPT is the highest among the four schemes compared. Figure 4(b) gives the gains of DEWPT to CoCoRaM. It shows that the CCR gains of DEWPT to CoCoRaM grow with increasing in the number of users. The maximal gain is achieved when the number of users is 70, which is near 3.5%. When the number of users exceeds 70, the CCR gain decreases, but still achieves a gain of at least 2%. The computation capacity of WP-MEC is limited because the number of MEC server is fixed. When the number of users reaches 70, the computation load of offloading users approaches the maximum computation capacity of WP-MEC, and so, the CCR can no longer grow. Therefore, the CCR decreases when the number of users exceeds 70. However, DEWPT outperforms its main competitor, CoCoRaM, in all cases. This shows that DEWPT can find the better WPT time because the same method is used for the inner layer optimization. In addition, Figures 4(c) and 4(d) show the CCR gains of DEWPT to CCO and LCO, respectively. Clearly, DEWPT achieved significant gains to CCO and LCO, with maximum gains approaching 35% and 28%, respectively.

Next, we validate the impact of changes in the number of MEC servers. Hence, in this simulation, the number of edge servers is increased from 4 to 9 with the step size of 1, and the number of users is fixed to 50. Figure 5 gives the results of this simulation.

Figure 5(a) shows that the CCR achieved by DEWPT, CoCoRaM, and COO keep growing with increasing in the number of edge servers. Among them, DEWPT outperforms CoCoRaM and COO. The CCR achieved by LCO does not change. This is expected, as LCO performance is not affected by changing the number of edge servers. Figures 5(b)–5(d) show the gains of DEWPT to the other three competitors, respectively. Clearly, DEWPT has significant positive gains for all three competitors. Likewise, DEWPT is superior to the major competitor CoCoRaM in all cases. It shows that DEWPT can find the better WPT time.

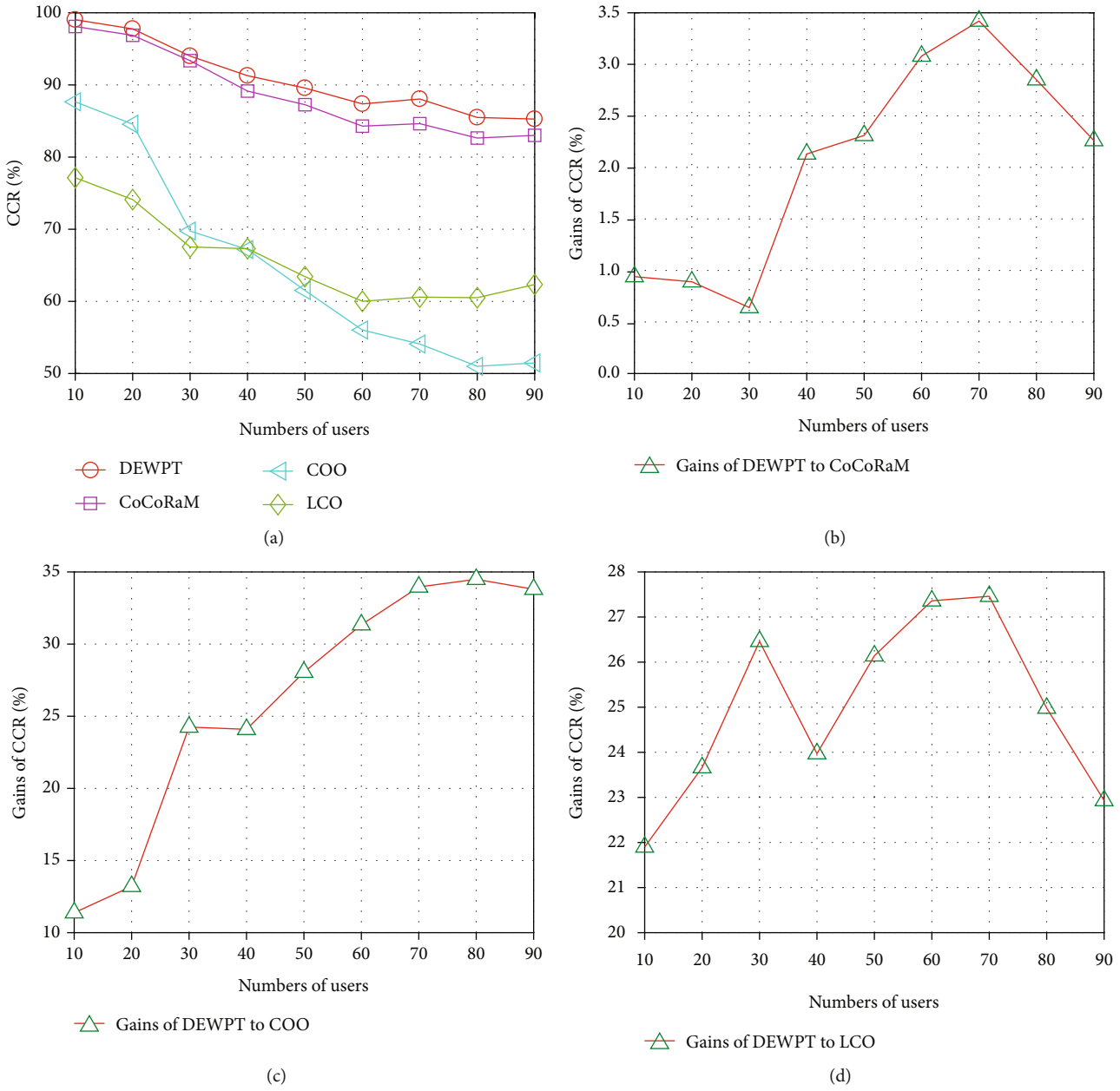

Figure 4: The impact of user scale size. (a) CCR comparison. (b) Gains of DEWPT to CoCoRaM. (c) Gains of DEWPT to COO. (d) Gains of DEWPT to LCO.

Based on these simulation results and analysis, it can be concluded that DEWPT has a better optimization performance than CoCoRaM, COO, and LCO.

5.2. Complexity Comparison. In this simulation, we will compare the computation complexity of DEWPT and its major competitor, CoCoRaM. For this purpose, we conduct the simulation under three user configurations (70 users, 80 users, and 90 users) and 5 edge servers. Figure 6 gives the results. The orange, purple, and green curves show the changes in CCR obtained by DEWPT with evolution iterations. The corresponding rectangle represents the CCR obtained by CoCoRaM.

As can be seen from Figure 6, the CCR achieved by CoCoRaM under three user configurations are 84.63%, 83.01%, and 82.64%, respectively. According to the analysis of [16], the size of candidate WPT times set of CoCoRaM is $N + \mathrm{Log}_{(1+\beta)}(T/\Delta t) + 3$. Therefore, the numbers of the candidate WPT time are higher than 70, 80, and 90 under three user configurations. That is, the numbers of WPT time evaluations are greater than 70, 80, and 90, respectively. However, under three user configurations, the CCR obtained by DEWPT exceeds that of CoCoRaM at the 4th, 5th, and 5th iteration, respectively. Because the population size of DEWPT is set to 6, the number of WPT time evaluations

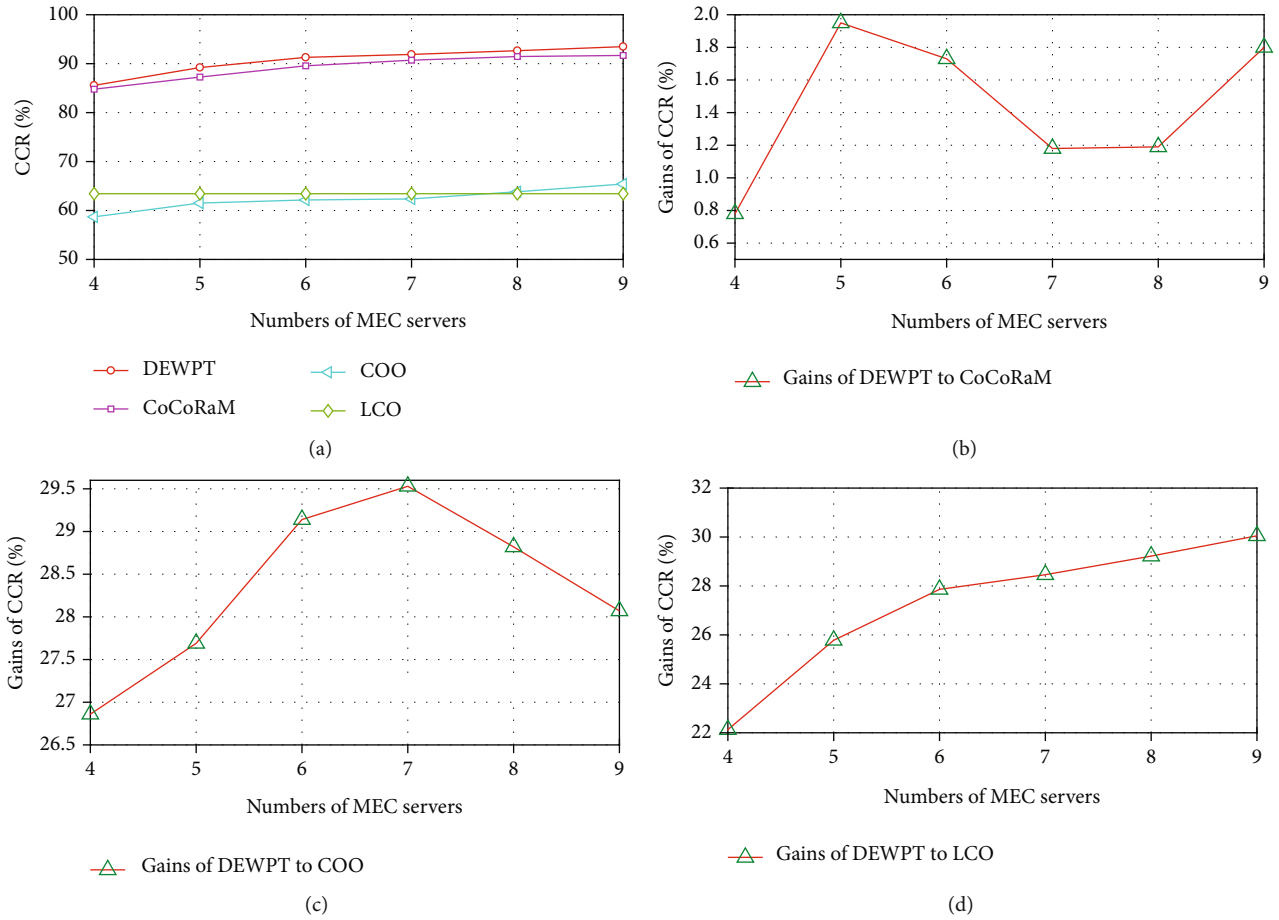

Figure 5: The impact of MEC server scale. (a) CCR comparison. (b) Gains of DEWPT to CoCoRaM. (c) Gains of DEWPT to COO. (d) Gains of DEWPT to LCO.

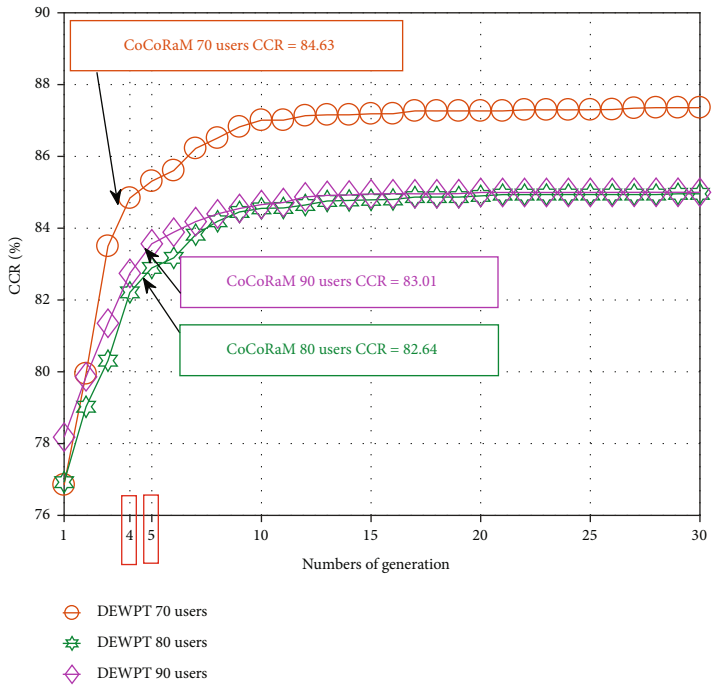

Figure 6: Complexity comparison.

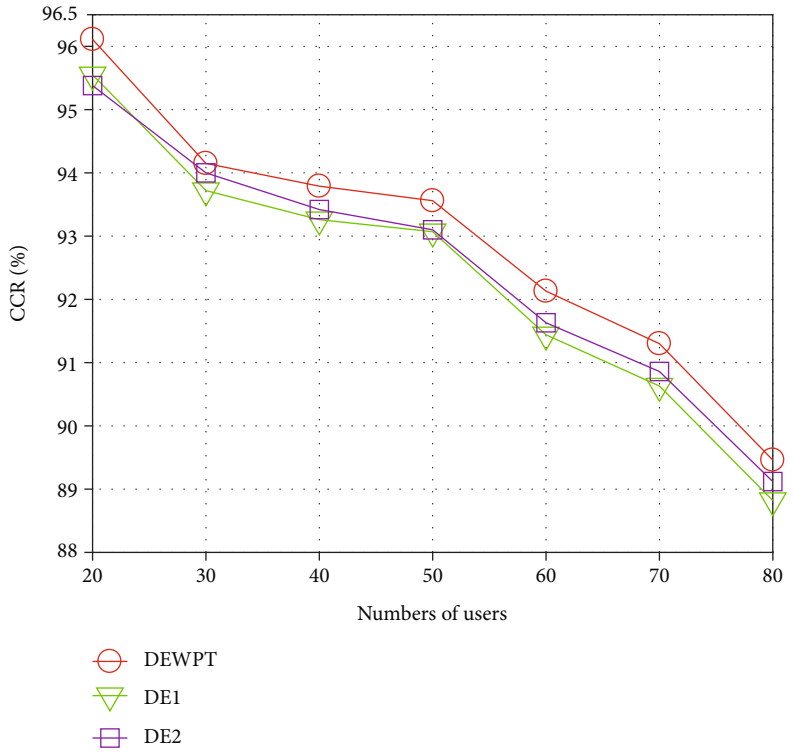

Figure 7: Comparison with the other DE algorithm.

is the product of the population size and the number of iterations, i.e., 24, 30 and 30, respectively. Obviously, DEWPT is much lower than CoCoRaM in terms of the number of WPT time evaluations, only about 1/3.

Thus, it can be concluded that DEWPT outperforms CoCoRaM in terms of the complexity.

5.3. Comparison with Other DE Algorithm. In this simulation, we will compare the DEWPT with the two DE algorithms which are termed as DE1 and DE2. The population size of three algorithms is all set to the same small population, i.e., $NP = 6$. In addition, the number of edge servers is set to 5, and the number of users increases from 20 to 80 with the step size of 10. DE1 only uses the mutation operator DE/rand/1 while DE2 only uses the mutation DE/best/1. At the same time, the traditional binomial crossover operator is used in them. Figure 7 gives the results of this simulation.

From Figure 7, it can be seen that DEWPT achieved a better CCR than DE1 and DE2 under different user numbers. The maximal gain is about 1% under different user numbers, because the optimal decision matrix can theoretically be obtained through the GAP-CS based on dynamic programming. Therefore, although the gain is small, it has shown that DEWPT can find a better WPT time than the other two DE algorithms. Hence, this proves that the hybrid mutation operator and the perturbation-based binomial crossover improve the optimization performance of DEWPT, and DEWPT is a better optimization algorithm for WPT time.

6. Conclusions

In this work, we studied the time allocation problem for WPT in WP-MEC network. A novel differential evolution-based optimization algorithm for WPT is developed, in which the hybrid mutation operator, perturbation-based binomial crossover operator, and the micro-population were designed to improve the algorithm's optimization performance. Then, the overall solving framework DEWPT for the maximization problem of computation completion ratio was constructed by integrating the algorithm. Finally, extensive numerical simulations showed that DEWPT can achieve a higher computation completion ratio than the other three benchmark schemes. This proved that the proposed algorithm can find the better WPT time, and it is an effective optimization scheme of WPT time for WP-MEC network.

A promising future research work is to design a priority-based user offloading order and jointly optimize WPT time allocation and offloading decision. Moreover, extending the work of this paper to more complex scenarios, such as intelligent reflecting surface-aided WP-MEC and nonorthogonal multiple access-assisted WP-MEC systems, is also a work worth studying.

Data Availability

The result data used to support the findings of this work are included within the article.

Disclosure

Part of this paper has been published by the 2022 International Conference on Computer Communications and Networks (ICCCN 2022).

Conflicts of Interest

The authors declare that they have no conflicts of interest.

Acknowledgments

This work is supported by the National Natural Science Foundation of China (nos. 61961021 and 61961022), the Science and Technology Foundation of Jiangxi Province (nos. 20202BABL202019 and 20202BABL202036), and the Science and Technology Project of Jiangxi Education Department (no. GJJ180251).

References

[1] J. Zhao, L. Yang, M. Xia, and M. Motani, "Unified analysis of coordinated multipoint transmissions in mmWave cellular networks," *IEEE Internet of Things Journal*, vol. 9, no. 14, pp. 12166–12180, 2022.

[2] M. Ma, L. C. Jain, and P. Anderson, "Future trends of virtual, augmented reality, and games for health," in *Virtual, Augmented Reality and Serious Games for Healthcare 1*, pp. 1–6, Springer, 2014.

[3] X. Zhang, H. Gao, M. Guo, G. Li, Y. Liu, and D. Li, "A study on key technologies of unmanned driving," *CAAI Transactions on Intelligence Technology*, vol. 1, no. 1, pp. 4–13, 2016.

[4] H. Liu, S. Chen, and N. Kubota, "Intelligent video systems and analytics: a survey," *IEEE Transactions on Industrial Informatics*, vol. 9, no. 3, pp. 1222–1233, 2013.

[5] N. D. Sarier, "Efficient biometric-based identity management on the blockchain for smart industrial applications," *Pervasive and Mobile Computing*, vol. 71, article 101322, 2021.

[6] S. Bi and Y. J. Zhang, "Computation rate maximization for wireless powered mobile-edge computing with binary computation offloading," *IEEE Transactions on Wireless Communications*, vol. 17, no. 6, pp. 4177–4190, 2018.

[7] M. Patel, B. Naughton, C. Chan, N. Sprecher, S. Abeta, and A. Neal, "Mobile-edge computing introductory technical white paper," *White paper, mobile-edge computing (MEC) industry initiative*, vol. 29, pp. 854–864, 2014.

[8] S. Shahzadi, M. Iqbal, T. Dagiuklas, and Z. U. Qayyum, "Multi-access edge computing: open issues, challenges and future perspectives," *Journal of Cloud Computing*, vol. 6, no. 1, pp. 1–13, 2017.

[9] L. Huang, S. Bi, and Y.-J. A. Zhang, "Deep reinforcement learning for online computation offloading in wireless powered mobile-edge computing networks," *IEEE Transactions on Mobile Computing*, vol. 19, no. 11, pp. 2581–2593, 2019.

[10] F. Zhou, Y. Wu, R. Q. Hu, and Y. Qian, "Computation rate maximization in UAV-enabled wireless-powered mobile-edge computing systems," *IEEE Journal on Selected Areas in Communications*, vol. 36, no. 9, pp. 1927–1941, 2018.

[11] F. Zhou and R. Q. Hu, "Computation efficiency maximization in wireless-powered mobile edge computing networks," *IEEE Transactions on Wireless Communications*, vol. 19, no. 5, pp. 3170–3184, 2020.

[12] L. Ji and S. Guo, "Energy-efficient cooperative resource allocation in wireless powered mobile edge computing," *IEEE Internet of Things Journal*, vol. 6, no. 3, pp. 4744–4754, 2019.

[13] F. Wang, J. Xu, X. Wang, and S. Cui, "Joint offloading and computing optimization in wireless powered mobile-edge computing systems," *IEEE Transactions on Wireless Communications*, vol. 17, no. 3, pp. 1784–1797, 2018.

[14] X. Hu, K.-K. Wong, and K. Yang, "Wireless powered cooperation-assisted mobile edge computing," *IEEE Transactions on Wireless Communications*, vol. 17, no. 4, pp. 2375–2388, 2018.

[15] F. Wang, H. Xing, and J. Xu, "Real-time resource allocation for wireless powered multiuser mobile edge computing with energy and task causality," *IEEE Transactions on Communications*, vol. 68, no. 11, pp. 7140–7155, 2020.

[16] T. Zhu, J. Li, Z. Cai, Y. Li, and H. Gao, "Computation scheduling for wireless powered mobile edge computing networks," in *IEEE INFOCOM 2020-IEEE Conference on Computer Communications*, pp. 596–605, Toronto, ON, Canada, 2020.

[17] J. Zhao, X. Sun, Q. Li, and X. Ma, "Edge caching and computation management for real-time Internet of vehicles: an online and distributed approach," *IEEE Transactions on Intelligent Transportation Systems*, vol. 22, no. 4, pp. 2183–2197, 2021.

[18] S. Bi, L. Huang, and Y. J. A. Zhang, "Lyapunov-guided deep reinforcement learning for stable online computation offloading in mobile-edge computing networks," *IEEE Transactions on Wireless Communications*, vol. 20, no. 11, pp. 7519–7537, 2021.

[19] R. Storn and K. V. Price, "Differential evolution - a simple and efficient heuristic for global optimization over continuous spaces," *Journal of Global Optimization*, vol. 11, no. 4, pp. 341–359, 1997.

[20] Y. Zhang, D. Gong, X. Gao, T. Tian, and X. Y. Sun, "Binary differential evolution with self-learning for multi-objective feature selection," *Information Sciences*, vol. 507, pp. 67–85, 2020.

[21] Y. Wang, Z. Cai, and Q. Zhang, "Differential evolution with composite trial vector generation strategies and control parameters," *IEEE Transactions on Evolutionary Computation*, vol. 15, no. 1, pp. 55–66, 2011.

[22] Y. Wang, C. Chen, P. Huang, and K. Wang, "A new differential evolution algorithm for joint mining decision and resource allocation in a MEC-enabled wireless blockchain network," *Computers & Industrial Engineering*, vol. 155, article 107186, 2021.

[23] Y. Wang, H. Liu, H. Long, Z. Zhang, and S. Yang, "Differential evolution with a new encoding mechanism for optimizing wind farm layout," *IEEE Transactions on Industrial Informatics*, vol. 14, no. 3, pp. 1040–1054, 2018.

[24] S. Zhou, L. Xing, X. Zheng, N. du, L. Wang, and Q. Zhang, "A self-adaptive differential evolution algorithm for scheduling a single batch-processing machine with arbitrary job sizes and release times," *IEEE Transactions on Cybernetics*, vol. 51, no. 3, pp. 1430–1442, 2021.

[25] H. Salehinejad, S. Rahnamayan, and H. R. Tizhoosh, "Micro-differential evolution: diversity enhancement and a comparative study," *Applied Soft Computing*, vol. 52, pp. 812–833, 2017.

[26] H. Salehinejad, S. Rahnamayan, and H. R. Tizhoosh, "Exploration enhancement in ensemble micro-differential evolution,"

in *IEEE Congress on Evolutionary Computation, CEC 2016*, pp. 63–70, Vancouver, BC, Canada, 2016.

[27] C. Brown, Y. Jin, M. Leach, and M. Hodgson, "JADE: adaptive differential evolution with a small population," *Soft Computing*, vol. 20, no. 10, pp. 4111–4120, 2016.

[28] Y. E. Yildiz and A. O. Topal, "Large scale continuous global optimization based on micro differential evolution with local directional search," *Information Sciences*, vol. 477, pp. 533–544, 2019.

[29] M. A. Sotelo-Figueroa, H. J. P. Soberanes, J. M. Carpio, H. J. Fraire Huacuja, L. C. Reyes, and J. A. Soria Alcaraz, "Evolving Bin Packing Heuristic Using Micro-Differential Evolution with Indirect Representation," in *Recent Advances on Hybrid Intelligent Systems, ser. Studies in Computational Intelligence*, vol. 451, pp. 349–359, Springer, 2013.

Hindawi
Wireless Communications and Mobile Computing
Volume 2022, Article ID 3393079, 8 pages
https://doi.org/10.1155/2022/3393079

Research Article

Correlation Analysis between Atmospheric Environment and Public Sentiment Based on Multiple Regression Model

Lei Duan

Luohe Medical College, Henan Province Engineering Research Center of Nutrition and Health, Luohe Henan 462000, China

Correspondence should be addressed to Lei Duan; 5032@lhmc.edu.cn

Received 17 February 2022; Accepted 11 April 2022; Published 1 July 2022

Academic Editor: Junjuan Xia

In recent years, with the gradual improvement of the public's demands for ecological and environmental services, changes in environmental quality, especially atmospheric environmental quality, have been highly concerned by the public. Public environmental emotions belong to psychological space information. How to quantify the changes in public environmental emotions caused by changes in environmental quality, comprehensively analyze the atmospheric physical and chemical factors that have a key impact on public environmental emotions, and achieve quantifiable and predictable public environmental emotions are difficult points of current research in the field of public environment. Based on the public participation perception method, this paper proposes a public environmental sentiment prediction model based on the analysis of the relationship between atmospheric environment and public environmental sentiment by using the collected public environmental satisfaction data. Taking the data of a city as an example, using atmospheric environmental factors and public environmental satisfaction, a multiple regression model (OLS) was established, and PM2.5, PM10, temperature (TMP), and humidity (HUM) were used as key factors to conduct Pearson correlation analysis with public environmental satisfaction. The results showed that PM2.5 and PM10 showed a strong negative correlation with public environmental satisfaction (-0.82 and -0.67), while TMP and HUM showed a weak positive correlation with public environmental satisfaction (0.3 and 0.19). Therefore, reducing the concentration of PM2.5 and PM10 in the city has a positive effect on improving public environmental satisfaction.

1. Introduction

In recent years, with the continuous acceleration of China's industrialization process, the utilization of resources and productivity has been significantly improved. However, the resulting ecological and environmental problems have become increasingly prominent, making people's normal living environment constantly disturbed [1]. People's physical and mental health has been affected to varying degrees through the continuous interference of various comprehensive ecological and environmental problems for a long time [2]. As a result, deteriorating environmental issues have now become a pain point for the public. Environmental issues have also become the social issues that the public is most concerned about, and they also affect people's psychological feelings and behavioral changes to the environment all the time [3, 4]. If we want to do in-depth research on environmental issues, we must start from the perception of the public after being affected by the environment.

The so-called perception is the response process of external information by people's feeling, attention, and perception. It mainly describes the consciousness and feeling reaction in the human brain after the objective affairs pass through the human sensory organs [5, 6]. Only with perception can people form the premise of understanding the external environment. Perception is also an important reference to guide individual behavior or social group behavior [7]. When a person is under a certain environmental area, the sensory organs will obtain the corresponding sensory information through the environment in which the person is located and then process the perceived sensory information in the mind and then give the specific evaluation of environmental protection management, environmental quality, and environmental behavior [8, 9].

Under the influence of the ecological environment, the conscious feeling and image formed by the human's perceptual organs after processing and analyzing the corresponding environmental feeling information in the brain is the environmental perception [10]. And due to certain differences in the subject of the perception object, the content of perception is also different. People have been exposed to constantly changing ecological environment areas for a long time so that people's perception of their own environmental areas is also accurate and changing at any time. Environmental awareness is the basic psychological guidance for people's environmental awareness and behavior [11, 12]. Whether the correct environmental awareness behavior can be formed depends on whether the environmental awareness behavior executor has the correct environmental awareness [13].

Environmental emotional relationship analysis is mainly to analyze the relationship between the main variables that affect environmental emotional changes and environmental emotions, which is basically the same as the general relationship analysis method [14]. Relational analysis refers to a method of using two or more random variables with the same characteristics (same level) to perform statistics and analysis by relying on their dependencies [15].

At home and abroad, the current research on relational analysis is mostly divided into static relational analysis and dynamic relational analysis. As the dominant factor of social emotion, public environmental emotion is a difficult problem in the current public environment field to realize the prediction of public environmental emotion. Most scholars at home and abroad are predicting some factors of air quality itself [16, 17]. For example, some scholars have pointed out that the air pollution level in Macau often exceeds the level recommended by the World Health Organization as the main problem. In order to make people take preventive measures and avoid high pollutants, further health risks under exposure, statistical models based on linear multiple regression (MR) and classification and regression tree (CART) analysis were built to predict the NO_2, PM10, PM2.5, and O_3 concentrations on the second day. Some scholars have used weather research and forecast models together with the Chemistry/Data Assimilation Research Testbed (WRFChem/DART) chemical weather forecast/data assimilation system and multicomponent data assimilation to study the improvement of air quality forecasts in eastern China. Some scholars have used a simplified Lagrangian particle dispersion modeling system and a Bayesian and multiplicative correction optimization (Bayesian-RAT) method to evaluate the mixing ratio prediction of PM10 and PM2.5, thereby evaluating the atmospheric particulate matter (PM) concentration prediction regional scale. Some scholars use Box-Jenkins' modeling theory to establish an ARIMA model that conforms to the changes in PM2.5 concentration in the study area to predict the PM2.5 concentration value in the next four days [18, 19].

Existing forecasts for atmospheric environmental factors appear to be too single, often using models to learn the value of a single time series variable, and there are few related studies on building public environmental sentiment prediction models using model ideas under deep learning [20, 21]. This paper studies the thinking and participatory perception method based on social perception computing, uses the public environmental sentiment data collected by the platform to measure the public's subjective environmental satisfaction, and establishes a multiple regression model and related analysis model to analyze the relationship between public environmental satisfaction and atmospheric environment in order to compare the influence of various atmospheric environmental factors on public environmental sentiment.

2. Method and Theory

2.1. Data Source. This paper will take Baiyin City as an example to comprehensively analyze the relationship between atmospheric environmental factors and public environmental satisfaction in the city and use the analysis results as the data and theoretical basis to build a public environmental sentiment prediction model, which will help the government to manage environmental problems and improve the regional human-land relations. This paper uses a questionnaire survey to collect data. In the early stage, the public environment perception data was scored directly by users (percentage system). This paper collects data on "public environmental satisfaction" from thousands of local citizens, with a total of 40,000 pieces of data, with a time span of one year [22]. Comprehensive analysis shows that there are different age groups, different genders, different educational levels, and different occupations among the users who submit the data, and the data is locally representative. The atmospheric environmental data in this chapter includes air pollution indicators and meteorological indicators, which correspond to public environmental satisfaction in time and have the same sample size, totaling 40,000 items. The atmospheric pollutants in the atmospheric environment data include AQI, PM2.5, PM10, SO_2, NO_2, O_3, and CO, which are derived from the hourly data of atmospheric pollutant concentrations at urban detection sites. The meteorological factor data includes FEELST, temperature (TMP), humidity (HUM), and wind speed (WINDSP), and these data are all from the China Weather Network.

2.2. Research Methods. In this study, the multiple linear regression model was used to initially screen the atmospheric environmental factors, and then, the Pearson correlation analysis was used to analyze the correlation between the screening results and public satisfaction.

2.2.1. Reverse Elimination Rule for Multiple Regression. The main idea of ordinary least squares (OLS) is to use the parameter estimation of linear regression and use the square sum of the difference between the actual sample value and the OLS estimation as the main reference parameter estimation value (by minimizing the square of the error to find the best variable match for the data). A method similar to the reverse elimination principle of the OLS model is principal component analysis (PCA). An excellent model should cover as much information as possible with as few features as

Table 1: Human comfort index and FEELST comparison table.

Human comfort index	Body temperature (degree Celsius)	Comfort level
0-20	<4	Extremely uncomfortable
20-40	2-8	Very uncomfortable
41-50	8-13	Uncomfortable
51-60	13-18	Comfortable
61-70	18-23	Comfortable
71-75	23-29	Comfortable
76-80	29-35	Comfortable
81-85	35-41	Very comfortable
85-100	>41	Extremely comfortable

possible. The way PCA learns from data is unsupervised learning. Therefore, the response variable in the data does not participate in the construction of the guiding principal components. PCA cannot guarantee a good interpretation of the direction of the predictor variables, and there are limitations in the extraction of the main variables. OLS is an alternative to supervised PCA. It uses multiple principal components as a new variable set and performs least squares regression on this basis. Therefore, the corresponding variables play the role of adjusting the parameters of the principal components, which can eliminate the drawbacks of the PCA method.

The process of constructing a multiple regression model using OLS is as follows. (1) Suppose there is a regression model, as shown in

$$Y = \beta_0 + \beta_1 X_1 + \cdots + \beta_n X_n + \varepsilon. \tag{1}$$

Assuming that the data in the sample has K groups of data: (t), $x_1(t), \cdots, x_n(t)$, the least squares method is used to calculate the regression coefficient between each group of data variables and is recorded as $?_i$, and the estimated value of the regression coefficient is recorded as b_0, $b_1, \cdots, b_n$; the calculation process of the square of the error is shown in

$$\sum_{t=1}^{k} \left(Y_{(t)} - b_0 x_1(t) - \cdots - b_n x_n \right)^2. \tag{2}$$

The input of the OLS model consists of four parts, which are the dependent variable, the independent variable, the missing item, and the constant item. For the construction of the multiple regression model, the first two parts are considered first. The first is the dependent variable, which acts as the response variable in the multiple regression, and the input data in the regression model assumed above is an array of length K. The second is the independent variable, which acts as the regressor in the regression model and in the OLS model. In the beginning, it is not assumed that the multiple regression model has a constant term, so the assumed regression model is shown in

$$Y = \beta_0 + \beta_1 X_1 + \cdots + \beta_n X_n + \varepsilon. \tag{3}$$

In the research data, the value of $X_0(t)$ is set to 1 for all $t = 1, \cdots, k$, whereby the input of the independent variable becomes $K \times (n+1)$ sets of data. In stepwise regression under linear conditions, the data samples are analyzed to determine which combinations of independent variables can be used to explain the largest variance in the dependent variable data, and then, the data combinations of these independent variables are retained. The principle of reverse elimination is used in the research method. First, all variables (air pollution indicators and public environmental satisfaction, meteorological indicators and public environmental satisfaction) are put into the model, respectively. We delete the independent variable with the largest difference from the threshold and finally check whether the multiple regression model contains an effective explanation for the variance of the dependent variable. To sum up, in the process of eliminating the independent variables, it will be carried out iteratively until no parameters meet the elimination conditions, and the remaining independent variable combination has the maximum explanatory power for the dependent variable.

2.2.2. Pearson Correlation Coefficient. Pearson correlation coefficient (Pearson correlation coefficient) is a linear correlation coefficient, which can analyze two or more elements with correlation characteristics. Considering that it can reflect the degree of linear correlation between atmospheric environmental factors and public environmental satisfaction, the value of the correlation degree is usually expressed by r or p, also known as the "correlation coefficient." In the Pearson correlation coefficient, the correlation coefficient between variables is expressed as the covariance between the studied variables divided by the standard deviation. For example, variable one is X, variable two is Y, and the Pearson correlation coefficient between the two variables is shown in

$$r_{xy} = \frac{\sum (x - \bar{x})(y - \bar{y})}{N \bullet S_x S_y}. \tag{4}$$

The above formula defines the overall correlation coefficient of the two variables, N represents the total number of data samples, $\bar{x}$ and $\bar{y}$ represent the average value of the two variable data, and S_x and S_y represent the standard deviation of the two variable data samples, respectively. Described by the above formula, r in the calculation process of the Pearson correlation coefficient can also be regarded as the cosine value of the angle between the two sets of vectors (variable X and variable Y). The value of r is between -1 and +1. If $r > 0$, the two variables are positively correlated; that is, the greater the value of one variable, the greater the value of the other variable. If $r < 0$, the two variables are negative; that is, the larger the value of one variable, the smaller the value of the other variable, and the larger the absolute value

Table 2: Air pollution index OLS model results (1).

Dep. variable	Satisfaction		*R*-squared			0.482
Model	OLS		Adj. *R*-squared			0.497
Method	Least squares		*F*-statistic			5023
	coef	Std err	*t*	$P > \|t\|$	[0.025	0.975]
const	104.4234	0.131	448.053	0	100.957	101.898
PM2.5	-0.1356	0.232	-49.834	0.008	-0.189	-0.178
PM10	-0.1682	0.076	-35.55	0.007	-0.083	-0.063
NO_2	0.0632	0.025	13.215	0.220	0.017	0.015
SO_2	-0.0757	0.112	-12.096	0.189	-0.051	-0.029
O_3	-0.0459	0.017	-7.594	0.429	-0.053	-0.025
CO	-0.0163	0.111	-3.453	0.132	-0.012	-0.003

Table 3: Air pollution index OLS model results (2).

Dep. variable	Satisfaction		*R*-squared		0.778	
Model	OLS		Adj. *R*-squared		0.785	
Method	Least squares		*F*-statistic		6032	
	coef	Std err	*t*	$P > \|t\|$	[0.025	0.975]
const	101.4359	0.254	443.065	0	100.897	101.832
PM2.5	-0.197	0.005	-69.887	0.003	-0.189	-0.178
PM10	-0.0683	0.005	-15.41	0	-0.083	-0.062

Table 4: Meteorological indicators OLS model results (1).

Dep. variable	Satisfaction		*R*-squared			0.523
Model	OLS		Adj. *R*-squared			0.578
Method	Least squares		*F*-statistic			4428
	coef	Std err	*t*	$P > \|t\|$	[0.025	0.975]
const	98.6598	0.191	399.105	0	87.512	93.875
TMP	-0.162	0.008	-53.894	0.007	-0.278	-0.179
FEELST	-0.0789	0.002	-12.72	0.386	-0.085	-0.069
WINDSP	0.0139	0.002	10.467	0.258	0.029	0.039
HUM	-0.0457	0.005	-12.726	0.087	-0.059	-0.045

Table 5: Meteorological indicators OLS model results (2).

Dep. variable	Satisfaction		*R*-squared			0.697
Model	OLS		Adj. *R*-squared			0.723
Method	Least squares		*F*-statistic			4489
	coef	Std err	*t*	$P > \|t\|$	[0.025	0.975]
const	98.6598	0.191	399.105	0	87.512	93.875
TMP	-0.162	0.008	-53.894	0.003	-0.278	-0.179
HUM	-0.0457	0.005	-12.726	0.002	-0.059	-0.045

of *r*, the stronger the correlation. It should be noted that there is no causal relationship here. If $r = 0$, there is no linear correlation between the two variables, but other forms of correlation (such as curves) are possible.

3. Results and Analysis

AQI (Air Quality Index) describes the freshness or pollution of the air and the impact of air pollutants on human health. The comfort index of the human body is a common expression method of human comfort in daily life, and the final evaluation of the index depends on the body temperature (FEELST) (Table 1). The body temperature mainly depends on the three indicators of TMP, HUM, and WINDSP. TMP is the main indicator for judging the human body's perception of climate temperature, and HUM and WINDSP are auxiliary indicators.

3.1. Screening of Influencing Factors of Public Environmental Emotions. Taking air pollutant indicators and meteorological indicators as independent variables and public environmental satisfaction as a dependent variable, an OLS multiple regression model was constructed, and multiple regression analysis was performed on it. It can be seen from Table 2 the OLS model constructed by air pollution indicators and public environmental satisfaction; the model uses $P = 0.05$ as the judgment threshold for reverse elimination and determines the two air pollution indicators PM2.5 and PM10. Table 3 shows the OLS model for pure analysis of PM2.5 and PM10. The experimental results show that the degree of fit is significantly improved. Tables 2 and 3 finally identify the strong influencing factors in the air pollution indicators, which are PM2.5 and PM10, respectively.

Table 4 shows the OLS model constructed by meteorological indicators and public environmental satisfaction. The model also uses $P = 0.05$ as the judgment threshold for

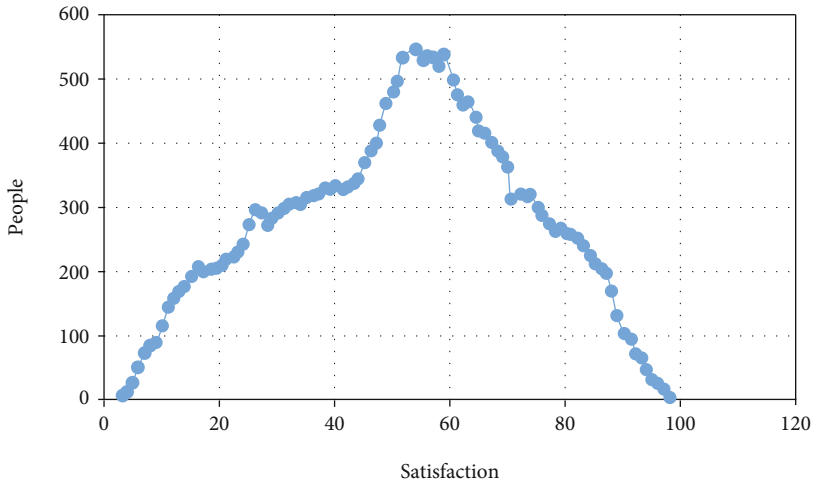

Figure 1: Distribution map of public environmental satisfaction.

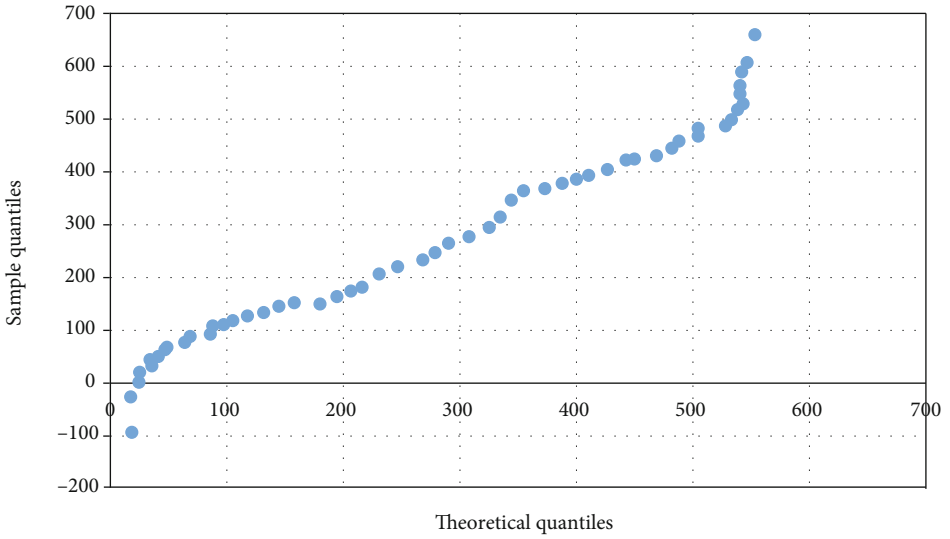

Figure 2: Normality test of public environmental satisfaction.

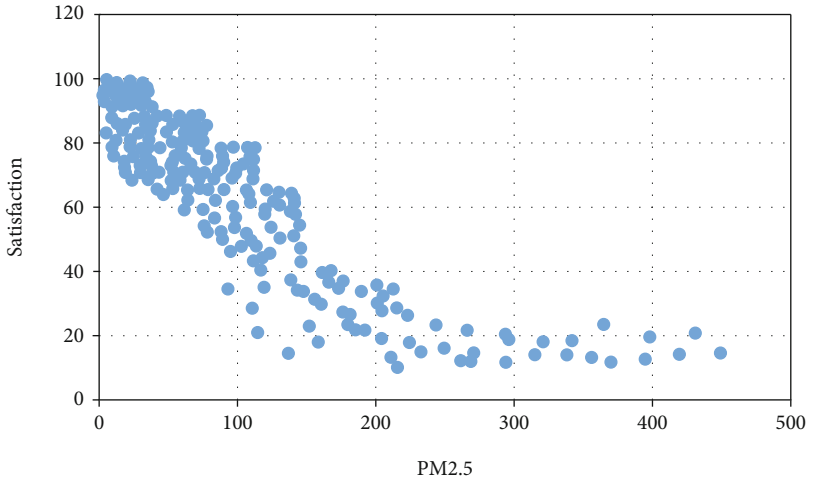

Figure 3: Correlation coefficient between PM2.5 and satisfaction.

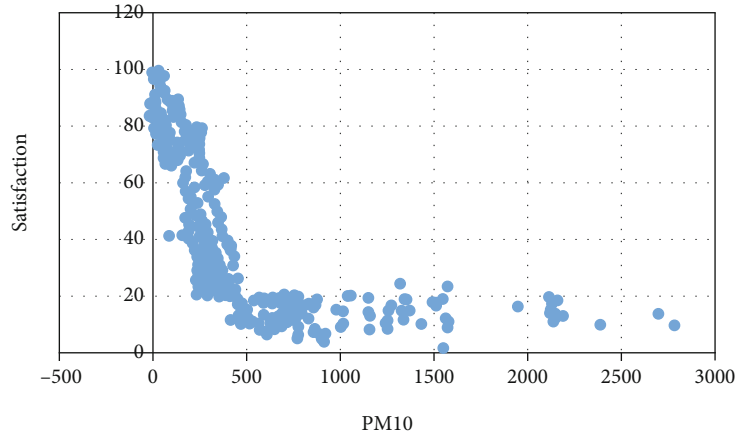

Figure 4: Correlation coefficient between PM10 and satisfaction.

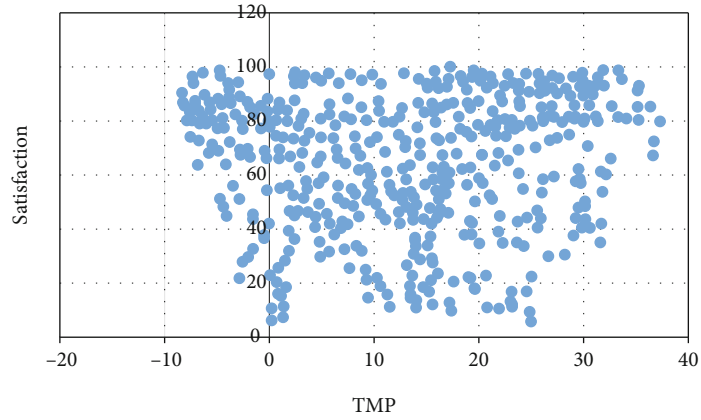

Figure 5: Correlation coefficient between TMP and satisfaction.

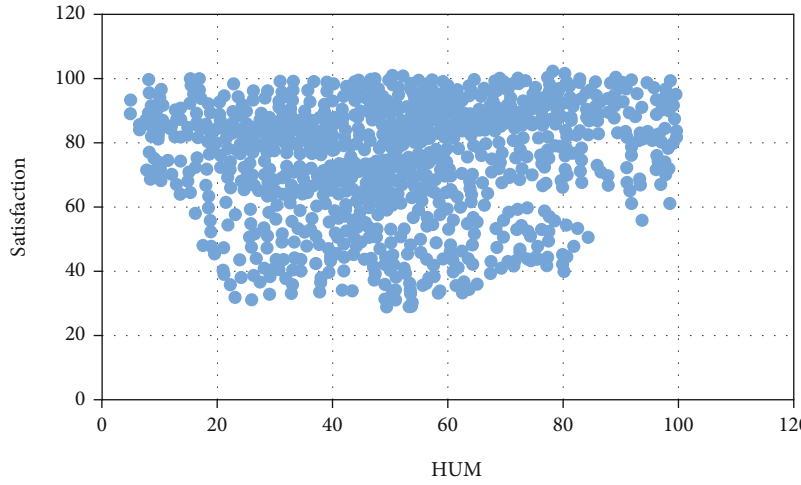

Figure 6: Correlation coefficient between HUM and satisfaction.

reverse elimination, and it is determined that the two meteorological indicators TMP and HUM have strong effects on public environmental satisfaction. For the explanatory power, the remaining indicators are eliminated. Table 5 shows the results of the OLS model that only contains TMP and HUM indicators. Compared with Table 4, the fitting accuracy of Table 5 is significantly improved. Finally, the strong influencing factors in the meteorological

indicators are determined, which are TMP and HUM, respectively. (2) Correlation analysis of factors influencing public environmental sentiment. Based on the analysis results of the OLS model, a Pearson correlation analysis will be carried out between air pollutant indicators, meteorological indicators, and public environmental satisfaction. According to its constraints, the premise of the correlation analysis is that the distribution of public environmental satisfaction conforms to a normal distribution. The distribution of public environmental satisfaction is shown in Figure 1. The abscissa in the figure is the score of public environmental satisfaction, and the ordinate is the choice. The number of people with a certain value of public environmental satisfaction value. In view of the data distribution in Figure 1, the normality test is carried out on the public environmental satisfaction data, and the test results are shown in Figure 2. Combining Figures 1 and 2, the distribution of public environmental satisfaction conforms to a normal distribution. Next, Pearson correlation analysis can be performed on public environmental satisfaction.

The analysis results of PM2.5 and PM10 are shown in Figures 3 and 4. In Figure 3, the correlation coefficient between PM2.5 and public environmental satisfaction has reached -0.82, which has a strong negative correlation. PM2.5 has the most direct harm to the human body and can cause damage to the respiratory system. The nose and throat cannot prevent PM2.5 fine particles. They can enter the body's bronchi, blood cells, and capillaries and finally spread to the entire blood circulatory system. Not only that, PM2.5 can also be used as a carrier to carry many harmful substances, such as bacteria, carcinogens, polycyclic aromatic hydrocarbons, and heavy metal particles. A large number of PM2.5 particles entering the lungs can block the local tissues of the lungs and affect the ventilation of local bronchial tubes. While PM2.5 has a huge impact on the public's body, it also has a corresponding impact on the public's "environmental satisfaction." When the body is uncomfortable due to PM2.5, the satisfaction will inevitably decrease. Therefore, there is a negative correlation between them.

As shown in Figure 4, the correlation coefficient between PM10 and public environmental satisfaction reaches -0.61, and the correlation coefficient is also relatively high. Different from PM2.5, PM10 is based on floating dust, which is a substance that can float in the atmosphere for a long time. Because pollutants float in the atmosphere for a long time, it is easy to form long-distance transmission, which leads to further expansion of the pollution range and becomes the atmosphere, a place where various substances in the environment undergo chemical reactions. Due to the relatively large particle size of PM10, PM10 particles are easily deposited, and the concentration near the ground is the highest, and the concentration will decrease correspondingly with the increase of altitude. Although PM10 can be directly inhaled into the respiratory tract, some of it can be blocked by the villi in the nasal cavity and some can be excreted through excretion. Compared with PM2.5, PM10 is relatively less harmful to human health, which indirectly proves that PM10 has less negative impact on public environmental satisfaction than PM2.5.

The analysis results of TMP and HUM are shown in Figures 5 and 6. The correlation coefficients between TMP (temperature), humidity (HUM), and public environmental satisfaction are 0.3 and 0.19, respectively, with a weak positive correlation, but this correlation relationships are not to be underestimated. From the perspective of TMP, generally lower temperature is conducive to the formation of better environmental emotions and improves the public's satisfaction with the current environment. However, at higher temperatures or when the temperature rises, the public's environmental emotional state is prone to fluctuations or exception. In summer, the public is often prone to irritability. When the situation is serious, it can be called "emotional heatstroke." It is a manifestation of emotional disturbance to summer weather. Most of them are caused by high TMP and HUM in regions due to long sunshine hours. At this time, their effect on the hypothalamus is significantly enhanced, affecting emotional regulation, so that emotions are easily out of control.

4. Conclusion

(1) This paper takes atmospheric environmental factors as the main object of research on the influencing factors of public environmental emotions and conducts experimental analysis on public environmental satisfaction from the perspectives of air pollution indicators and meteorological indicators. It is concluded that the public environmental satisfaction has a negative linear relationship with air pollution indicators and a positive linear relationship with meteorological indicators

(2) Among the air pollution indicators, PM2.5 and PM10 play a key role in the negative impact of the public's environmental satisfaction. Among the meteorological indicators, TMP and HUM play a key role in the positive impact of the public's environmental satisfaction. The public's environmental satisfaction obeys a normal distribution, indicating that most of the public's evaluation of the environment is moderate. The public environmental satisfaction has a strong negative correlation coefficient with PM2.5 and PM10, and the correlation coefficients are -0.82 and -0.67, respectively. Public environmental satisfaction has a weak positive correlation with both TMP and HUM, with correlation coefficients of 0.3 and 0.19, respectively

Data Availability

The figures and tables used to support the findings of this study are included in the article.

Conflicts of Interest

The author declares that there are no conflicts of interest.

Acknowledgments

This work was supported by the Employment and Entrepreneurship Research Projects in Henan Province "the impact of solution-focused brief therapy on the study habits, employment pressure, and mental health of students in financial difficulties in medical colleges" (JYB2019141).

References

[1] O. Weiss, G. Norden, P. Hilscher, and B. Vanreusel, "SKI tourism and environmental problems," *International Review for the Sociology of Sport*, vol. 33, no. 4, pp. 367–379, 1998.

[2] A. P. Vayda and B. J. McCay, "New directions in ecology and ecological anthropology," *Annual Review of Anthropology*, vol. 4, no. 1, pp. 293–306, 1975.

[3] E. Carmina, "Genetic and environmental aspect of polycystic ovary syndrome," *Journal of Endocrinological Investigation*, vol. 26, no. 11, pp. 1151–1159, 2003.

[4] D. Kaur, N. K. Bhardwaj, and R. K. Lohchab, "Environmental aspect of using chlorine dioxide to improve effluent and pulp quality during wheat straw bleaching," *Waste and Biomass Valorization*, vol. 10, no. 5, pp. 1231–1239, 2019.

[5] C. C. Chen, "Environmental impact assessment framework by integrating scientific analysis and subjective perception," *International Journal of Environmental Science & Technology*, vol. 6, no. 4, pp. 605–618, 2009.

[6] S. Phumsathan, "Environmental value orientation and environmental impact perception of visitors to Khao Yai National Park," *Kasetsart Journal of Social Sciences*, vol. 34, no. 3, pp. 534–542, 2013.

[7] J. C. Liu, P. J. Sheldon, and T. Var, "Resident perception of the environmental impacts of tourism," *Annals of Tourism Research*, vol. 14, no. 1, pp. 17–37, 1987.

[8] G. Cicia, T. Del Giudice, and I. Ramunno, "Environmental and health components in consumer perception of organic products: estimation of willingness to pay," *Journal of Food Products Marketing*, vol. 15, no. 3, pp. 324–336, 2009.

[9] F. Marincioni and F. Appiotti, "The Lyon-Turin high-speed rail: the public debate and perception of environmental risk in Susa valley, Italy," *Environmental Management*, vol. 43, no. 5, pp. 863–875, 2009.

[10] M. Anniko and W. Arnold, "Microtubule-associated proteins in adult human sensory organs," *Orl*, vol. 57, no. 2, pp. 78–81, 1995.

[11] D. L. Gadenne, J. Kennedy, and C. McKeiver, "An empirical study of environmental awareness and practices in SMEs," *Journal of Business Ethics*, vol. 84, no. 1, pp. 45–63, 2009.

[12] G. M. Perron, R. P. Côté, and J. F. Duffy, "Improving environmental awareness training in business," *Journal of Cleaner Production*, vol. 14, no. 6-7, pp. 551–562, 2006.

[13] Z. L. Liu, T. D. Anderson, and J. M. Cruz, "Consumer environmental awareness and competition in two-stage supply chains," *European Journal of Operational Research*, vol. 218, no. 3, pp. 602–613, 2012.

[14] R. Rodriguez-Ibeas, "Environmental product differentiation and environmental awareness," *Environmental and Resource Economics*, vol. 36, no. 2, pp. 237–254, 2007.

[15] J. Coleman, "Relational analysis: the study of social organizations with survey methods," *Human Organization*, vol. 17, no. 4, pp. 28–36, 1958.

[16] G. Corani, "Air quality prediction in Milan: feed-forward neural networks, pruned neural networks and lazy learning," *Ecological Modelling*, vol. 185, no. 2-4, article 513529, 2005.

[17] G. K. Kang, J. Z. Gao, S. Chiao, S. Lu, and G. Xie, "Air quality prediction: big data and machine learning approaches," *International Journal of Environmental Science and Development*, vol. 9, no. 1, pp. 8–16, 2018.

[18] S. Makridakis and M. Hibon, "ARMA models and the Box-Jenkins methodology," *Journal of Forecasting*, vol. 16, no. 3, pp. 147–163, 1997.

[19] Q. Zhang, T. Gao, X. Liu, and Y. Zheng, "Exploring the influencing factors of public environmental satisfaction based on socially aware computing," *Journal of Cleaner Production*, vol. 266, no. 6, article 121774, 2020.

[20] J. Sun, H. Yin, Y. Tian, J. Wu, L. Shen, and L. Chen, "Two-level multimodal fusion for sentiment analysis in public security," *Security and Communication Networks*, vol. 2021, Article ID 6662337, 10 pages, 2021.

[21] Y. Liu, D. Liu, and Y. Chen, "Research on sentiment tendency and evolution of public opinions in social networks of smart city," *Complexity*, vol. 2020, Article ID 9789431, 13 pages, 2020.

[22] L. Tu and Y. Zhao, "Air pollution and the public perception level and self-protection demand in three cities of China: fractional grey modelling analysis," *Journal of Mathematics*, vol. 2021, Article ID 4951714, 15 pages, 2021.

Hindawi
Wireless Communications and Mobile Computing
Volume 2022, Article ID 2605684, 7 pages
https://doi.org/10.1155/2022/2605684

WILEY | Hindawi

Research Article

Detecting IKEv1 Man-in-the-Middle Attack with Message-RTT Analysis

Yunxiao Sun,[1] **Bailing Wang**,[1] **Hongri Liu**,[1] **Yuliang Wei**,[1] **Di Wu**,[2] **and Jing Wang**[3]

[1]*Harbin Institute of Technology, 264209 Weihai, China*
[2]*School of Computer Science of Beijing University of Posts and Telecommunications, 100876 Beijing, China*
[3]*Information Research Center of Tsinghua University, 100084 Beijing, China*

Correspondence should be addressed to Bailing Wang; wbl@hit.edu.cn

Received 31 March 2022; Revised 18 May 2022; Accepted 23 May 2022; Published 14 June 2022

Academic Editor: Junjuan Xia

The IPSec has been a widely used VPN (virtual private network) protocol due to its security and convenience. The security of IPsec itself plays a fundamental role in the overall security of the application system. However, it can be found from the existing research that because of some insecurity issues in the application process, the IPsec protocol will suffer from the man-in-the-middle attack. In this paper, we constructed the first experiment environment of IKE (Internet Key Exchange) man-in-the-middle detecting, use normal distribution to detect the RTT (round-trip time), and get 90% of accuracy.

1. Introduction

IPsec is a secure network protocol suite that authenticates and encrypts network packets to allow safe encrypted communication between two computers over an Internet protocol network [1]. IPSec is a commonly used protocol for building VPN (virtual private network) tunnels that provide security for VPN negotiations and network access to random hosts. IKE (Internet Key Exchange) is a key management protocol that is used in conjunction with the IPSec protocol. It is a way of sharing encryption and authentication keys over an insecure channel. The IKE functions work in two stages: (1) creates an authenticated communication channel between peers by employing methods such as the Diffie-Hellman key exchange, which provides a shared key that is used to further encrypt IKE conversations; (2) the peers use the secure communication channel to negotiate security on behalf of other services such as IPSec. These methods result in the creation of two unidirectional channels, one inbound and the other outgoing.

Various security protocols have developed methods to protect against man-in-the-middle attacks over time. Asymmetric key agreement technology is used in all mainstream security protocols, including TLS, SSH, and IKE. The man-in-the-middle attacks can disrupt the key exchange process by replacing both parties' public keys. As a result, identity authentication is incorporated into security protocols. Different techniques of attacking the IPSec protocol have been documented in the literature [2–4], and man-in-the-middle attacks have always been a major threat source for security protocols [5]. Wireless networks, local area networks, and even wide-area networks are all vulnerable to man-in-the-middle attacks. Users may or may not have a clear perception when an attack happens.

The man-in-the-middle attack detection method is also distinct from methods used in typical intrusion detect systems [6]. Man-in-the-middle attacks have a better level of concealment than typical network attack methods like SQL injection and remote code execution. The network traffic was indistinguishable from normal traffic at the time of the attack. Man-in-the-middle attacks are impossible to protect against with firewalls and intrusion detection systems. Mirsky et al. [7] designed a man-in-the-middle attack detection algorithm named Vesper, which can identify man-in-the-middle attacks in LAN networks by measuring the RTT of echo packets. However, this method cannot detect attacks against specific application protocols and is difficult to apply to the WAN environment. According to current

research, the IKE protocol is widely used, but there are also various attacks against the protocol. If the user selects the preshared key authentication mode, when a man-in-the-middle attack occurs, neither the client nor the server can perceive the existence of the attack. Therefore, it has become an important task to study how to detect man-in-the-middle attacks in the IKE communication process. This paper provides a calculating approach based on RTT delay to detect whether there is a man-in-the-middle in the communication process to check and prevent the existence of man-in-the-middle attacks in the IPsec application process.

Our main contributions are as follows: (1) built the experimental environment for the IKE man-in-the-middle attack; (2) analyzed the statistical properties of RTT and concluded that RTT conforms to a normal distribution; (3) proposed a man-in-the-middle attack detection algorithm for IKE based on the confidential intervals of normal distribution, which achieved 90% accuracy rate; and (4) found the problem of unintentional leakage of the preshared key through case study. Compared with the existing methods, our proposed algorithm is nonintrusive to the system, only uses network traffic, and does not need to change the IPSec software source code and network topology. The algorithm has certain versatility and may be integrated into the intrusion detection system or applied to the man-in-the-middle attack detection of other security protocols.

2. Background Knowledge

The MITM attacker's ability is the Dolev-Yao model. The attacker can modify or delete message from the network. The middle-man model is based on the Dolev-Yao model. The main capabilities include the following:

(i) Familiar with modern cryptography. The attacker can decrypt the message with the right key

(ii) Familiar with the protocol and know the entities involved in the protocol

(iii) Has complete control over the network and can eavesdrop and intercept any messages transmitted in the system

In IKEv1, the main mode is an instantiation of the ISAKMP (Internet Security Association Key Management Protocol) identity protect exchange: the first two messages negotiate policy; the next two exchange Diffie-Hellman public values and ancillary data (e.g., nonces) necessary for the exchange; and the last two messages authenticate the Diffie-Hellman exchange. The authentication method negotiated as part of the initial ISAKMP exchange influences the composition of the payloads but not their purpose. The result of either main mode or aggressive mode is three groups of authenticated keying material shown in equations (1)–(4). The $N_i$and N_r are the nonces generated by the initiator and the responder separately. The x and y are the Diffie-Hellman public key of the peers, which are known as key exchange payload in the IKE message. The CKY_i and CKY_r are the SPI (Security Parameter Index) in the IKE message. The function PRF means pseudorandom function, which is used as the algorithm to derive key materials. SKEYID is the key seed, SKYEID_e is the key material used by ISAKMP SA to protect the confidentiality of its messages, SKYEID_a is the key material that ISAKMP SA uses to authenticate its messages, and SKYEID_d is the key material used to derive keys for non-ISAKMP SA.

$$\mathrm{SKEYID} = \mathrm{PRF}(pre\_shared\_key, N_i|N_r), \tag{1}$$

$$\mathrm{SKYEID\_}d = \mathrm{PRF}(\mathrm{SKEYID}, g^{xy}, \mathrm{CKY}_i|\mathrm{CKY}_r|0), \tag{2}$$

$$\mathrm{SKYEID\_}a = \mathrm{PRF}(\mathrm{SKEYID}, \mathrm{SKYEID\_}d, g^{xy}, \mathrm{CKY}_i|\mathrm{CKY}_r|1), \tag{3}$$

$$\mathrm{SKYEID\_}e = \mathrm{PRF}(\mathrm{SKEYID}, \mathrm{SKYEID\_}a, g^{xy}, \mathrm{CKY}_i|\mathrm{CKY}_r|2). \tag{4}$$

Because Diffie-Hellman is vulnerable to man-in-the-middle attacks, IKE introduced an identity authentication mechanism to prevent man-in-the-middle attacks during key exchange. IKEv1's identity authentication mechanism includes four types: two RSA-based methods, a digital signature-based method, and a preshared key-based method. The first three methods require the IPSec network administrator to issue a certificate for the user, and the user imports the certificate on their client device. The preshared key method requires the IPSec administrator to set a string password and send the string password to the user for configuration. The preshared key method is easy to operate and widely used. This type of authentication method is commonly used for VPN services for sale, and it is also used by many colleges and enterprises. Because users and network administrators do not have a deep understanding of the IPSec protocol, it is generally believed that the username and password used for login are required to be kept secret, and the preshared key does not need to be kept secret.

Through the analysis of the IKE key derivation process, when the man-in-the-middle attacker obtains the PSK, he can calculate the communication key with the client and the server, respectively, which shown in Figure 1.

The attacker controls the communication link between the initiator and the responder and can forward network packets and modify the content of the packets. In the message exchange process of the IKE protocol, the initiator first sends its SA proposal to the responder, and the responder selects the optimal combination of cryptographic algorithms from the SA proposal according to a certain security policy. At this stage, the attacker needs to parse the information necessary for the man-in-the-middle attack from the received message and forward the message without modifying the message content. In the second pair of messages, the initiator and the responder need to exchange the Diffie-Hellman public key and the nonce for the calculation of the key material. The attacker needs to generate two pair of Diffie-Hellman keys, including the public keys and the private keys, replace the initiator's public key ke_i with his own public key $\mathrm{fake\_ke}_i$, and replace the responder's public key ke_r with his own public key $\mathrm{fake\_ke}_r$. After the public key replacement is completed, the attacker can negotiate key material with the initiator and responder separately by

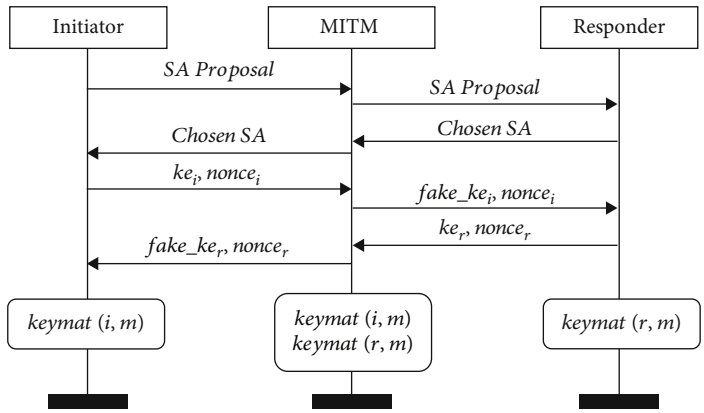

Figure 1: The man-in-the-middle attack of IKE.

the function keymat, thereby destroying the confidentiality and data integrity of the communication. Different from the traditional intrusion detection technology, man-in-the-middle attack detection does not have obvious characteristics. The network data message attacked by man-in-the-middle is the same as that under normal conditions in terms of length, contracting frequency, and so on. IPSec packets are encrypted; it is impossible to identify whether there is an intermediary in the link through the communication content. This brings challenges to man-in-the-middle attack detection.

Because the operation of Diffie-Hellman algorithm involves large number operation, the CPU time consumed cannot be masked by network jitter. Theoretically, when there is man-in-the-middle attack, on the client side, the round-trip time of the second pair of messages in IKE protocol will be significantly longer than that under normal circumstances. Therefore, this paper attempts to analyze the time consumed by each message interaction in the running process of IKE protocol to judge whether there are exceptions in the process of negotiation interaction.

3. The Problem Definition and Solution

3.1. MPRTT Definition. Protocol in C-S model, the client is the initiator, and the server is the responder. The message sequence of client denoted as $M_{cs} = \{m_{c1}, m_{c2}, \cdots, m_{cn}\}$, while the message sequence of server denoted as $M_{sc} = \{m_{s1}, m_{s2}, \cdots, m_{sn}\}$.

To start a new session, the client needs to do some initial operation including nonce generation, key generation, and cipher suite choice and then send out the first message m_{c1} over the network channel. The server will respond a message m_{s1} after processing the client's message.

Definition 1. A message pair means the initial message m_{cn} and its corresponding response message m_{sn}, donated as $MP_n = <m_{sn}, m_{cn}>$.

Definition 2. MPRTT_n denotes the time cost of processing the n-th message pair, and T_{cn} is the timestamp that client send the message m_{cn}, while T_{sn} is the timestamp that client receive the message m_{sn} from server. RTT is the round-trip time cost of a pair of messages. Then, $MPRTT_n = T_{sn} - T_{cn}$. The measurement method of MPRTT_n is shown in Figure 2.

The MPRTT_n represents the time spent by the client to process a pair of protocol messages, including fixed event delay and random event delay in the communication process. Fixed event delay is the sum of network channel transmission delay and protocol message processing delay in an ideal environment; random events include delays caused by events such as router queue cache, operating system cache, and operating system thread scheduling. In an ideal environment, the network channel transmission delay is recorded as $\mathrm{COST}_{\mathrm{chan}}$, the protocol message processing delay is recorded as $\mathrm{COST}_{\mathrm{proto}}$, and the delay caused by random events in the communication process is recorded as $\mathrm{COST}_{\mathrm{jitter}}$.

Definition 3. ΔRTT is the difference between the n-th message RTT and the RTT of the next message that means $\Delta\mathrm{RTT}_n = \mathrm{MPRTT}_{n+1} - \mathrm{MPRTT}_n$. For a certain system with IPSec device, ΔRTT is a variable with jitters, and it is a normal distribution. The ΔRTT with MITM attack is different from a normal system. The MITM detection problem can be transformed to a ΔRTT abnormal detection problem. Our approach of abnormal detection is based on the confidence interval of normal distribution.

3.2. ΔRTT Distribution. We studied the distribution of ΔRTT using statistic methods. The Grubbs method is to delete the outliners from the samples. There are three modes: left, right, and two-tailed. According to the experiments result, in two-tailed mode, the result is the best. Figure 3 shows the result after deleting the outliner data with Grubbs method. With the shape of Figure 3 and the quantile-quantile plot shown in Figure 4, we can assume that the ΔRTT is according with normal distribution.

3.3. ΔRTT Abnormal Detection. The main idea of detection algorithm is anomaly detection based on normal distribution confidence interval. The experimental data includes two parts: training set and test set. The training set has only

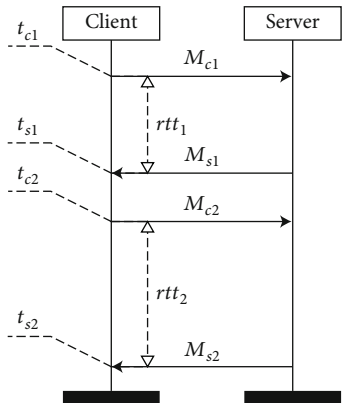

Figure 2: The measurement of MPRTT.

positive samples, that is, ΔRTT measurements under normal conditions. The anomaly detection algorithm is divided into three steps.

(1) Through the fitting of normal distribution, we can calculate the mean value μ and standard deviation σ of the samples

(2) Under a certain significance level α, calculate the confidence interval $[C_1, C_2]$

(3) For the ΔRTT value X measured in one IKE session, if $C_1 \leq X \leq C_1$, the X is normal and there is no man-in-the-middle attack. Otherwise, the X will be considered as abnormal, and there may exists a man-in-the-middle attacker over the channel

4. Experiments

4.1. Experiments Environment. The network topology of the experimental environment is shown in Figure 5. The IKE client runs on Windows 10 and macOS 10.15, respectively, using the built-in client software of the operating system. The IKE server runs on Alibaba cloud ECS, and the operating system is CentOS 7 2. The server software version is libreswan 1.39. The device *MITMBox* is the man-in-the-middle attacker, and the software is built based on several open-source software including DPDK, libgcrypt, and OpenSSL.

4.2. Data Sets. We implemented the attack program according to the IKE man-in-the-middle attack method mentioned in the paper of G. Wang et al. [8]. We implemented a IKEv1 MITM device; the device can forward the packet using DPDK. The result shows that with a known preshared key, we can break the Diffie-Hellman process in IKEv1 session and calculate a pair of keys between the initiator and responder. Then, we can break the secrecy and the authentication of ESP; packets transported in IPSec tunnel can be decrypted to plaintext.

We also implemented an automated tool to calculate the RTT of the IKE messages. The timestamp of a packet in *libpcap* is recorded in pcap frame header. In libnids, we use *nids_last_pcap_header* to get the pcap header, and *ts* in pcap header structure is the timestamp of current message, which is being processed in the callback function. The structure is defined in *nids.h* and *pcap.h*. The timestamp of each message is stored in an array, one array for M_{cs} and one for M_{sc}. The data measured for each IKE connection is taken as one sample, and the average value of three consecutive sampling results is taken as the RTT measurement result.

The automate tools support different operating systems. For Windows, we use *radialup* to connect IKE server. For macOS, we use *network-setup* to connect an IKE connection. And on Linux, we use *network-manager* to connect the IKE server. All the connect task can be managed with script programming language, such as shell and powershell. MPRTT measuring method is based on deep packet inspection. There are several open-source tools to capture packet during IKE session on client side. *tcpdump* or *dumpcap* are command line tools, and they are easy to make a automate packet capture engine, with the help of bash on Linux, or *powershell* on windows. The tools save the message in pcap format.

4.3. Experiment Results. The metrics utilized in classification tasks are used to evaluate our technique in this study. When an attack class is used as a positive class, for example, four different types of classification results are displayed below.

(i) True Positive (TP). There exists MITM attack and the classifier marked this sample as abnormal

(ii) False Positive (FP). There is no MITM attack and the classifier marked this sample as abnormal

(iii) True Negative (TN). There is no MITM attack and the classifier marked this sample as normal

(iv) False Negative (FN). There exists MITM attack and the classifier marked this sample as normal

We calculate performance measures using the following formulas based on the classification results provided above.

$$\begin{aligned} \text{Accuracy} &= \frac{\text{TP} + \text{TN}}{\text{TP} + \text{TN} + \text{FP} + \text{FN}}, \\ \text{Precision} &= \frac{\text{TP}}{\text{TP} + \text{FP}}, \\ \text{Recall} &= \frac{\text{TP}}{\text{TP} + \text{FN}}, \\ \text{F1} &= \frac{2 * \text{Precision} * \text{Recall}}{\text{Precision} + \text{Recall}}. \end{aligned} \tag{5}$$

In the experiment, we simulated 1000 normal sessions through an automated script. The measured data is used as the initial sample, and 10 training sets are obtained from the initial sample by random sampling without putting back. The sample size of each training set is 50. The 10 training sets are used to train the classifier, respectively. We measured the RTT of 5296 IKEv1 sessions as the testing set, including 4939 normal sessions and 357 sessions attacked by man-in-the-middle. The same test set is used to test the

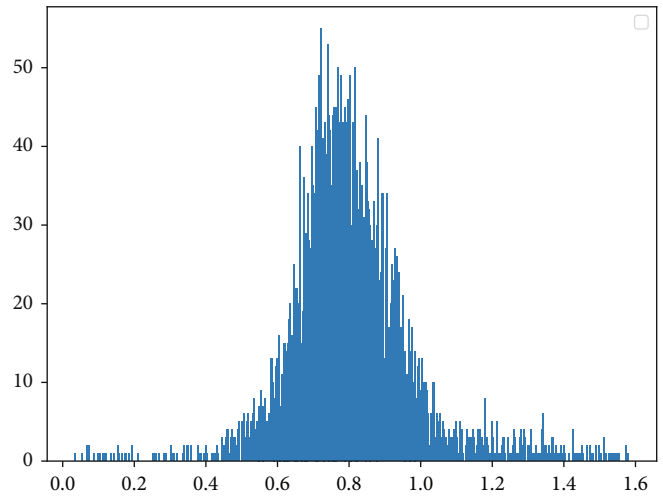

Figure 3: The frequency distribution histogram of RTT.

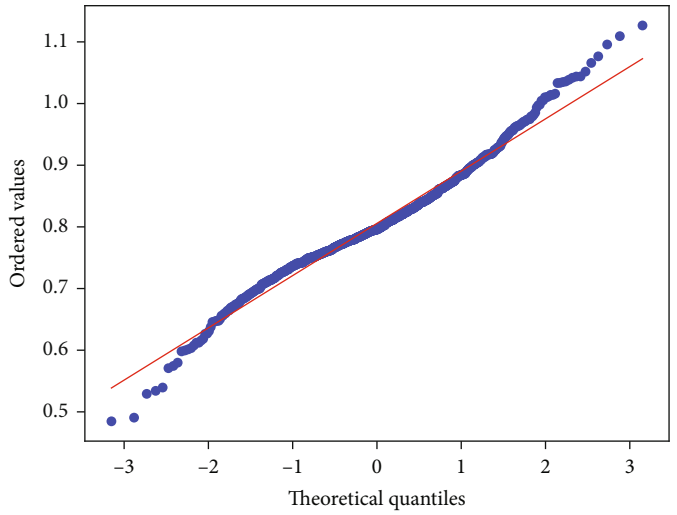

Figure 4: The quantile-quantile plot of RTT.

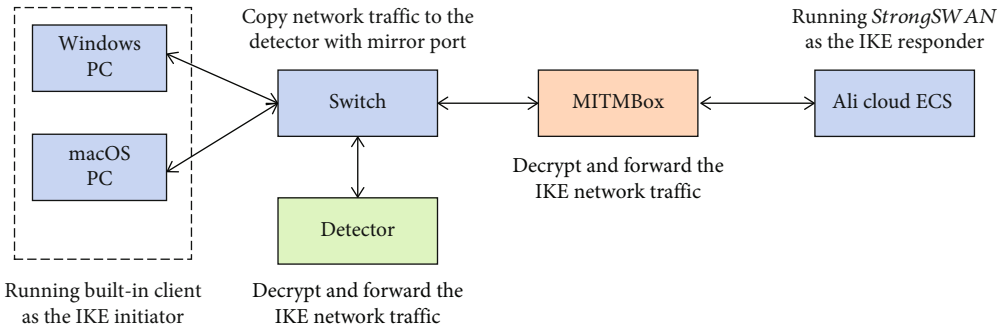

Figure 5: The network topology of the Experiment.

classification performance of 10 classifiers, to evaluate the stability of the algorithm. The significance level $\alpha = 0.01$. The experimental results are shown in Table 1.

The experimental results show that the anomaly detection algorithm based on normal distribution confidence interval can identify all man-in-the-middle attacks. At the same time, some normal sessions are identified as abnormal, and the false positive rate is about 9%. The standard deviation of F1 is 0.018. It shows that the classification algorithm is stable. By comparing the experimental data, we find that the gap between normal data and abnormal data is very large. In the normal session, the mean value of ΔRTT is

Table 1: The evaluation metrics of classification.

Round	Accuracy	Recall	Precision	F1
1	0.9335	1	0.9281	0.9627
2	0.9362	1	0.9311	0.9643
3	0.9261	1	0.9202	0.9584
4	0.8095	1	0.7941	0.8852
5	0.9175	1	0.9109	0.9534
6	0.9222	1	0.9159	0.9561
7	0.9261	1	0.9202	0.9584
8	0.9373	1	0.9322	0.9649
9	0.8999	1	0.8918	0.9428
10	0.8907	1	0.8818	0.9372

1.083, while in the attacked session, the mean value of ΔRTT is 48.509; therefore, recall can reach 1.

5. Case Study

The preshared key method is easy to operate and widely used. This type of authentication method is commonly used for VPN services for sale, and it is also used by many colleges and enterprises. Because users and network administrators do not have a deep understanding of the IPSec protocol, it is generally believed that the username and password used for login are required to be kept secret, and the preshared key does not need to be kept secret. Therefore, the entropy value of the preshared key of a large number of IPSec services is too low, and some are set as the website URL and some are set as the company name; passwords such as "123456" and "VPN" are also widely used. The built-in IPSec client of common operating system platforms is imperfect from the perspective of user experience. Usually, an administrator needs to write an instruction manual for the user. The user configures the IPSec client according to the manual. The general instruction manual will indicate PSK, and many instruction manuals are completely open without any access control, which leads to the leakage of PSK. By analyzing the interaction process of the IKE protocol, an attacker can conduct a man-in-the-middle attack on IPSec communication after mastering the PSK and can decrypt the data packet and tamper with the content of the data packet, destroying the confidentiality and authentication of the protocol.

To identify the situation of PSK usage in IPSec service, we use Google to search the public PSK. For university, we use the keyword "vpn psk inurl:edu" and analyzed the top 50 results. After removing duplicate pages, inaccessible pages, and pages not related to VPN, we got 34 websites. Among these websites, there are 26 of them have public the PSK on the web pages. Within the 34 results of Google search, 76% PSK has been published on the website. In the 26 known PSK, 69% of them has less than 10 characters, 50% of the PSK contain "vpn," 54% has some information associated with the organization, 46% of the PSK use uppercase or lowercase letters only, and 80% are in high risk of a dictionary attack.

Judging from the statistics of search results, we can infer that most network administrators do not have a thorough understanding of the IPSec protocol, which caused PSK leakage due to unconscious behavior. The PSK setting is too simple, making PSK vulnerable to dictionary attacks. The above survey reflects that there are still many security risks in the use of IPSec, which makes MITM attacks against IPSec easier to implement. In the current environment, it may be difficult to force many administrators to change their long-term behavior habits or force all IPSec users to upgrade the protocol. Therefore, it is very important to study how to detect MITM attacks against IPSec.

6. Conclusion

Since the birth of the IKE protocol, scholars have proposed a lot of improvement methods for its security. Ray et al. [9] proposed an elliptic curve cryptography (ECC) based and certificate less IKE protocol to avoid denial-of-service (DoS) attack. Yin and Wang [10] proposed an application-aware IPsec policy system on the existing IPsec/IKE infrastructure, in which a socket monitor running in the application context reports the socket activities to the application policy engine. With the application of IPsec in IoT (Internet of Things) [11–15], ICS (industrial control system) [16, 17], and other fields, its security should be paid more attention.

The related research work in this paper is a preliminary exploration of IPSec man-in-the-middle attack detection. It has been verified by experiments that during the IKE protocol interaction, the distribution of MPTTT conforms to the normal distribution, and when there is a man-in-the-middle attack during the protocol interaction, MPTTT will increase due to the addition of encryption calculations, which makes the distribution of the signal interval based on the normal distribution. Anomaly detection has become a method of IPSec man-in-the-middle attack detection. The experiments done in this paper are aimed at a specific DH-group scenario. In future research work, we will continue to study the changes in MPTTT in other scenarios. At the same time, because there is no public implementation method for IPSec man-in-the-middle attack, the research work of this paper can only be based on our own man-in-the-middle attack software. The software implementation method, hardware equipment, and optimization degree may have different effects on the experimental results. Therefore, improving the implementation method of man-in-the-middle attack equipment to make the equipment more universal is also one of our future research works.

Data Availability

The data used and/or analyzed in this study are available from the corresponding author upon request.

Conflicts of Interest

The authors declare that they have no conflicts of interest.

Acknowledgments

This work is supported in part by the "National Key R&D Program of China" (2021YFB2012400).

References

[1] S. Jahan, M. S. Rahman, and S. Saha, "Application specific tunneling protocol selection for virtual private networks," in *2017 International Conference on Networking, Systems and Security (NSysS)*, pp. 39–44.3, Dhaka, Bangladesh, 2017.

[2] D. Fang, P. Zeng, and W. Yang, "Attacking the IPsec standards when applied to IPv6 in confidentiality-only ESP tunnel mode," in *16th International Conference on Advanced Communication Technology*, pp. 401–405, PyeongChang, Korea, 2014.

[3] T. Mizrahi, "Time synchronization security using IPsec and MACsec," in *2011 IEEE International Symposium on Precision Clock Synchronization for Measurement, Control and Communication*, pp. 38–43, Munich, Germany, 2011.

[4] K. Bhargavan and G. Leurent, "Transcript collision attacks: breaking authentication in TLS IKE and SSH," in *Network and Distributed System Security Symposium–NDSS*, pp. 1–18, San Diego, California, USA, 2016.

[5] M. Conti, N. Dragoni, and V. Lesyk, "A survey of man in the middle attacks," *IEEE Communications Surveys & Tutorials*, vol. 18, no. 3, pp. 2027–2051, 2016.

[6] Z. Trabelsi and K. Shuaib, "NIS04-4: man in the middle intrusion detection," in *IEEE Globecom 2006*, pp. 1–6, San Francisco, California, USA, 2006.

[7] Y. Mirsky, N. Kalbo, Y. Elovici, and A. Shabtai, "Vesper: using echo analysis to detect man-in-the-middle attacks in LANs," *IEEE Transactions on Information Forensics and Security*, vol. 14, no. 6, 2019.

[8] G. Wang, Y. Sun, Q. He, G. Xin, and B. Wang, "A content auditing method of IPsec VPN," in *2018 IEEE Third International Conference on Data Science in Cyberspace (DSC) IEEE*, pp. 634–639, Guangzhou, China, 2018.

[9] S. Ray, R. Nandan, and G. P. Biswas, "ECC based IKE protocol design for internet applications," *Procedia Technology*, vol. 4, pp. 522–529, 2012.

[10] H. Yin and H. Wang, "Building an application-aware IPsec policy system," *IEEE/ACM Transactions on Networking*, vol. 15, no. 6, pp. 1502–1513, 2007.

[11] S. Raza, S. Duquennoy, J. Höglund, U. Roedig, and T. Voigt, "Secure communication for the Internet of Things—a comparison of link-layer security and IPsec for 6LoWPAN," *Security and Communication Networks*, vol. 7, no. 12, 2668 pages, 2014.

[12] S. Raza, T. Chung, S. Duquennoy, D. Yazar, T. Voigt, and U. Roedig, *Securing Internet of Things with Lightweight IPsec*, Swedish Institute of Computer Science, Kista, Sweden, 2010.

[13] M. Juma, A. A. Monem, and K. Shaalan, "Hybrid end-to-end VPN security approach for smart IoT objectsHybrid End-to-End VPN Security Approach for Smart IoT Objects," *Journal of Network and Computer Applications*, vol. 158, article 102598, 2020.

[14] M. B. M. Noor and W. H. Hassan, "Current research on Internet of Things (IoT) security: a surveyCurrent research on Internet of Things (IoT) security: A survey," *Computer Networks*, vol. 148, pp. 283–294, 2019.

[15] S. Siboni, A. Shabtai, N. O. Tippenhauer, J. Lee, and Y. Elovici, "Advanced security testbed framework for wearable IoT devices," *ACM Transactions on Internet Technology (TOIT)*, vol. 16, no. 4, article 26, pp. 1–25, 2016.

[16] T. D. Nguyen and M. A. Gondree, "Teaching industrial control system security using collaborative projects," in *Security of Industrial Control Systems and Cyber Physical Systems. CyberICS WOS-CPS 2016 2015*, A. Bécue, N. Cuppens-Boulahia, F. Cuppens, S. Katsikas, and C. Lambrinoudakis, Eds., vol. 9588 of Lecture notes in computer science, Springer, Cham, 2016.

[17] M. Nawrocki, T. C. Schmidt, and M. Wählisch, "Industrial control protocols in the Internet core: dismantling operational practices," *International Journal of Network Management*, vol. 32, no. 1, article e2158, 2022.

Hindawi
Wireless Communications and Mobile Computing
Volume 2022, Article ID 7252791, 11 pages
https://doi.org/10.1155/2022/7252791

Research Article

Node Replication Attack Detection in Distributed Wireless Sensor Networks

L. Sujihelen,[1] **Rajasekhar Boddu**,[2] **S. Murugaveni**,[3] **Ms. Arnika**,[4] **Anandakumar Haldorai**,[5] **Pundru Chandra Shaker Reddy**,[6] **Suili Feng**,[7] **and Jiayin Qin**[7]

[1]*Sathyabama Institute of Science and Technology, Chennai, India*
[2]*Department of Software Engineering, College of Computing and Informatics, Haramaya University, Dire Dawa, Ethiopia*
[3]*Department of ECE, SRM Institute of Science and Technology, India*
[4]*Department of Computer Science and Engineering, Faculty of Engineering and Technology, SRM Institute of Science and Technology NCR Campus, Modinagar, Ghaziabad, Uttar Pradesh, India*
[5]*Department of Computer Science and Engineering, Sri Eshwar College of Engineering, Coimbatore, Tamil Nadu, India*
[6]*Department of Computer Science and Engineering, CMR College of Engineering and Technology, Telangana, Hyderabad, India*
[7]*Computer, Electrical and Mathematical Sciences and Engineering Division, King Abdullah University of Science and Technology (KAUST), Thuwal 23955-6900, Saudi Arabia*

Correspondence should be addressed to Rajasekhar Boddu; rajsekhar.boddu@haramaya.edu.et

Received 25 February 2022; Revised 18 April 2022; Accepted 9 May 2022; Published 31 May 2022

Academic Editor: Junjuan Xia

Wireless sensor network (WSN) is an emerging technology used in emergency scenarios. There are a number of possible threats to WSNs because they use unsupervised IP addresses. Securing networks with unattended sensors is a real challenge nowadays. Sensor nodes lack power and storage, making them incompatible with normal security checks. It will be vital to make advancements in sensor network architecture and protocol design. There will be more vulnerability to attack if there is a lack of security. Especially, one key attack is node replication which induces the sensor node to acts as an original node, collecting data from the network and sending it to the attacker. In dynamic WSN, detecting an assault is difficult to find replica nodes. Therefore, this paper proposes a Strategic Security System (SSS) to discover replica nodes in static and dynamic distributed WSNs. It is mainly focused on enhancing detection accuracy, time delay, and communication overhead. The present system includes Single Stage Memory Random Walk with Network Division (SSRWND) and a Random-walk-based approach to detect clone attacks (RAWL). The proposed system has less memory and better detection accuracy.

1. Introduction

A real challenge in the present day is making the networks secure while dealing with unattended sensors. Sensor nodes are incompatible with routine security inspections due to their inherent power and storage limitations. Emerging innovations in designing the architecture of sensor networks and inventing new protocols will gain significant importance in the future. These advancements also invite new types of risks and attacks to affect the integrity of WSNs. It is important to detect and prevent node replication attacks in WSNs. Researchers' schemes for detecting threats and preventing them are presented in this study. The existing researchers have classified the detection schemes into two categories: static and mobile WSNs. Researchers have proposed various techniques for distributed wireless sensor networks.

Node replication attack is an active attack in WSN [1]. The replication attack is the root cause of many attacks in WSN. The replica node will behave like an original node and sense confidential data from the sensor networks [2, 3]. The overview of the replication attack is shown in Figure 1. The replicated node directs the target to attack.

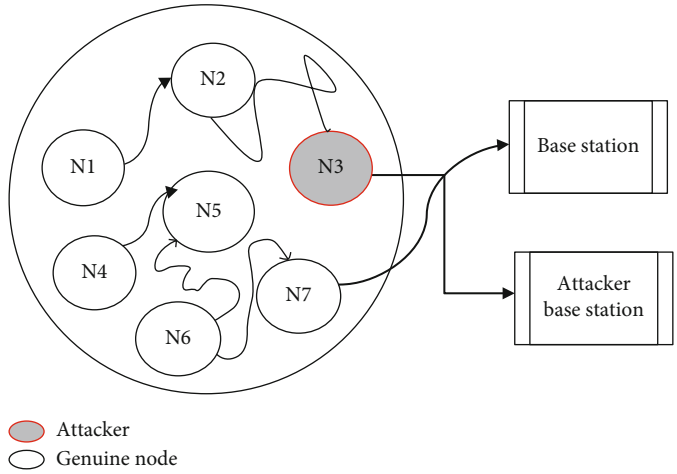

Figure 1: Overview of the replication attacks.

With a centralized approach, it is easy to detect node replication attacks. Monitor nodes send alarm messages when replicated nodes are present. There has been some analysis of detection schemes for centralized approaches.

The first solution for detecting a clone attack is based on a base station. The same node ID with a different location will identify the cloned node. The drawbacks are high communication costs and less detection accuracy. In addition to random key predistribution, the predistribution of keys is subject to certain conditions [4]. The node is assigned as a replicated node if it exceeds the threshold or criteria for key usage. The base station will count how many times it has been used. The drawback is an imbalance of message transfers. The SET approach is another method for analyzing and reporting clone detection [5]. This scheme divides the network into subsets. A separate leader is present for every subset. Base station information is sent to the subset leader. A clone node is found by performing intersection operations on each root. The base station performs the intersection computation.

A social fingerprint is computed by extracting neighborhood characteristics [6]. A fingerprint is attached to every message, and it verifies them accordingly. Using S-disjunct code, fingerprints are generated with less communication and computation overhead. There are highly sensitive sensors in the base station that allows fingerprint verification. The Bloom Method is used to detect node replication attacks [7]. This scheme consists of predistribution, election, and detection phases. All nodes are assigned a node ID in the predistribution phase. Cluster heads are elected during the election phase. Cluster heads construct bloom filters in the detection phase; then another cluster head verifies them. In the CSI approach, nodes sense and transmit information to neighbors [8].

There is a fixed threshold value assigned. A clone node is assigned to a sensor reading greater than its threshold value. In token-based clone detection, the token is transferred with location ID and node ID to another node before transferring the message. If the neighboring node is cloned, it can misbehave with the token message after receiving the token. The node authentication is done before transferring the communication. The limitation of this approach is less detection accuracy. Distributed techniques do not have a central monitoring authority. Yet the witness node is selected at random to receive the information. All neighbor nodes send signed copies of location claims when they broadcast their location. However, the security is enhanced despite the high communication cost. RM introduces LSM to reduce communication costs. Using LSM, the overall number of communications costs is reduced, but the energy consumed increases. RM or LSM cannot detect masked replication attacks.

Another approach to the location-based key protocol is improving detection accuracy based on a bilinear map [9]. The sensor retrieves the location-based key by its current position. The key computation is based on Elliptical Curve Cryptography (ECC). The SDC Scheme maps each node to a single cell with its location. Occasionally, the node's storage cell serves as its witness [10]. The node identities are mapped to the destination cells using a hash function as part of the P-MPC scheme. There are multiple cells with different probabilities associated with each node ID. It should be considered in the detection protocol that witness node selection is random and widely distributed. A uniform witness distribution is achieved by selecting nodes pseudorandomly. The main disadvantage of RED is how witness nodes are selected. This scheme cannot detect a masked replication attack [11]. An order-based protocol is discussed to limit the deployments on nodes. The installed nodes should establish communication with their neighbors [12]. There is a possibility that the replicated node has access to the old, deployed key, therefore failing to establish the keys. An active detection approach randomly selects several nodes and assigns them as witness node. The communication cost is high, and detection accuracy is high [13].

The paper [9] recommends that past nodes be selected using a Random Walk (RAWL) scheme to be the witnesses. The first step of RAWL involves broadcasting a signed location claim from every node. Subsequently, selected neighboring nodes receive the claim. Third, random nodes are chosen, and information is sent to initiate a random walk

through the network, and only those nodes that pass the walk will serve as witness nodes. Revoked replicas differ from their originals in the fourth step. TRAWL store's location claims within its table entries are significantly smaller than location claims. All passed nodes will remain witness nodes after they begin their random walk. The MRWS protocol will reduce the detection accuracy and detect replica nodes in large-scale sensor networks [14]. SSRWND protocol is the modification of RAWL and TRAWL. The communication cost and memory overhead are high for storing the node information in the Random Walk Table during a random walk in RAWL and TRAWL [15]. The SSRWND communication cost and detection accuracy are average. During the centralized approach of mobile WSNs, all mobile nodes are controlled by a monitor. The SPRT is used to detect mobile replication in a centralized approach. Low error rates are characteristic of this protocol. Since two nodes are at the same place simultaneously, replica nodes perform better than original nodes. The nodes checked for identical identities in the network are compared if the node pace is high.

An approach is discussed for detecting mobile replication using SPRT. Low error rates characterize this protocol. Because a replica node moves faster, the speed of the replica node is very high compared to the maximum node speed configured by the system. We check whether, in a network, identical identities have the same speed if the speed of the mobile node is high. This duplication of nodes will lead to nullity. By identifying replica nodes from the network, the hypothesis is accepted. In [16], the authors propose using both the time domain (TDD) and the space domain (SDD). All sensor nodes share a random number if they meet at any time. The same node is validated again if it runs into it by verifying the random number. A random number of bits is generated between two nodes in the range of each other. Each node's responsibility is to manage the table storing its ID and a random number. A comparison is made with the random number if it meets the node. If two random numbers are the same, each node will generate a new one. Replicas are also detected in cases where a node failed to meet earlier. The advantage of using XED is that replica nodes can be identified easily, but the drawback is that memory capacity is increased, and false replica detection results. There should be a limit on how many times a node can be visited in each interval if there is no replicating node.

Check the node ID and the time on a network with two replicas. It has two steps, offline and online: an EDD scheme. Before the sensor deployment, the network planner performs offline [17]. In this step, the parameters are calculated, including the duration to distinguish between the authentic node and the replica. Each node will perform the online step for each move. Every time interval, node replicas are encountered. In large-scale WSNs, efficient and distributed detection (EDD) cannot be applied. This scheme detects the UTLSE, which stores only a one-time location claim per replica of each witness node. Using the MTLSD protocol, nodes are assigned time-location claims. As opposed to protocol UTLSE, the MTLSD protocol has a greater detection chance [18].

Node replicator attacks in mobile wireless sensor networks can be detected using a distributed approach that does not require routing information. Node replication attack is a severe attack. The attack can be exceedingly injurious to many important functions of the sensor network, such as routing, resource allocation, and misbehavior detection. They exchange their time-location claims when they meet each other. Nodes will not transmit a witness's time location if they receive a neighbor. Even if a witness is not within the range, it will store the location claim. Instead of transmitting these claims, the witnesses carry them around the network. Data stored on local memory for every mobile node is verified with SDD-LC, exchanging information. In SDD-LWC, the information exchanged between nodes is common between their locally maintained tables. In SEDD [19], each node is monitored. Subnodes are monitored by each node at a set time interval, referred to as a monitor set. In addition to reducing storage overhead, the nodes monitored are monitored simultaneously. The article mentions another approach for exploiting mobile sensor networks to detect clone attacks. It has several advantages, including efficiency, avoiding synchronization, and revocation.

Another approach is to detect the replica node using the HIP/HOP method [20]. This method is the modification of the existing work [21]. In this scheme, the implied methodology divides the time into different rounds. The sensor nodes send their location claim to a neighbor node every round. The neighbor node will compare its history log for duplication. If the duplication occurs, then the location is verified. If there is a location conflict, the identified node will be assigned as a clone node [22]. The HIP verifies all the logs received and identifies the duplications. It has less storage requirement compared to the existing detection technique. In the HIP/HOP approach, the same technique will be challenging for global detection. Another approach is introduced to detect the replica node globally [23]. This approach is for detecting hybrid and global detection methods. The time slot is calculated as rounds. When the round is less, the detection accuracy is less [24, 25]. The existing system detection accuracy is very less, and the memory is very high. The proposed technique is the modification of SSRWND [15] and RAWL [9]. In the existing system, the network is divided into different regions. A node is selected for a random walk [19, 20]. The communication cost of selecting the node in each region is high in the existing system. Each node location claim, node ID, and signature are stored in a random walk. The drawback of RAWL and SSRWND is it occupies more memory to store the information of each node, such as node ID, signature, and location claim. If the duplication occurs in the random walk in the existing system, then the node-location ID is verified. If the location ID is different, the node is assigned as a replicated node. The major drawback in the existing system is that if the node ID and location ID are the same, it is assigned as a genuine node. If the genuine node is replicated, it is very difficult to identify in RAWL and SSRWND protocol. A SSS approach is proposed to overcome the issues in RAWL and SSRWND.

The Strategic Security System approach has three phases: prediction, detection, and isolation. If it predicts any node as

a clone node in the prediction phase, it is sent to the next phase. The detection phase verifies the node ID, packet loss, distance, energy level, and key. If any discriminants occur, that node is sent to the isolation phase. In the isolation phase, the node is isolated from the network connection. Compared with the existing methods, this method's detection probability is high, with less communication overhead and less memory capacity. Although there are the possibilities of launching both active and passive attacks in a WSN, it is vital to first cater to the active attacks to reduce the negative consequences and disastrous aftermaths of an attacker. In such an attempt, a shortlist of the area of the active and serious attacks is presented in this section. The proposed system focuses on the detection of node replication attacks. This section explains the different techniques already proposed by different researchers. If the random walk is not visited in any region in RAWL, this protocol fails to detect the replicated node. To overcome the existing techniques' issues, the SSS technique is proposed. The proposed technique is the modification of the RAWL and SSRWND. The detection accuracy, memory overhead, and communication overhead are reduced in the proposed technique. This article is arranged as an Introduction, proposed system, SSS approach, Results and Discussion, simulation results, Conclusions, and References.

2. Materials and Methods

This proposed SS method detects the replica node in the distributed static topology. It influences the modified SSRWND algorithm to detect node replication attacks. In distributed static topology, the nodes are randomly placed in the network, and the base station is placed at one of the edges of the topology area. Each node has to report the various conditions in the region of interest to the base station from time to time. The initiation of the network operation begins with the nodes being configured as the WSNs and the registration of each node in the WSN with the BS. At one time run, the SS is performed during the network initiation, initiated by the BS. After this, any random node can become or probe another node to become an SS-Manager. This node can either be at the SS-Predict or the SS-Detect mode, depending on the security threat level sensed by the neighboring nodes. The proposed system performs three distinct operations for security preservation. The entire proposed SS method architecture is given in Figure 2. Assume the node$\{a, b, c, d, e\}$ in the network. All the nodes should update the node ID andD_{ij}in the table at T's random time. The node$\{a\}$is duplicated, and node$\{e\}$did not update its information in the table. The node $\{a, e\}$ is selected and transferred to SS-Detect. SS-Detect phase can be initiated by a node that has predicted the presence of the malicious node or by the transition from the SS-Predict. This is a critical mode in which the predicted nodes (NodePM) undergo vigorous checking to identify maliciously or just let go as legitimate nodes.

As observed in Figure 2, the SS method is probed to act as a predictor of a replication attack (SS-Predict), a detector of the replication attack (SS-Detect), and isolation of the replication attacker node (SS-Isolate) at one point of time during network operation. A group of communication nodes generally operates in the manner assumed below:

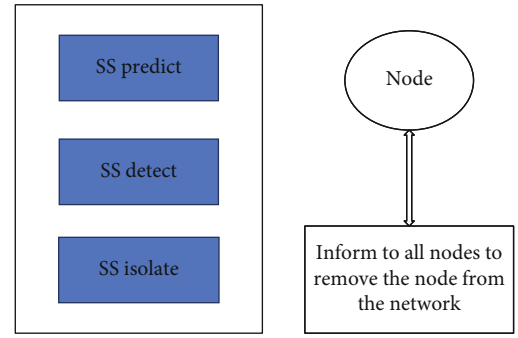

Figure 2: Architecture of SSS in a WSN.

A source sends a request to the destination to find the route to the destination.

A corresponding reply is obtained with the route to the destination.

The data are transmitted from the source to the destination along the route obtained.

A final acknowledgment of the receipt of the entire data is sent back to the source.

During these communication processes, a replicator can easily act as an internal node (a node in the network since the commencement of the network operation) and misuse/modify/reinforce larger attacks. Generally, a small attack, when successful, can be the source of the possibility of launching a chain of large attacks in a system. There is a constant need to launch random checks in a WSN system. Taking this issue as an important motive, the SS-Predict for a system is proposed. All nodes in a network with higher resources (bandwidth, energy, and processing capability) are shortlisted when a trigger is created. A node is decided to be the SS-Manager for that session and can act either as a predictor and/or a detector and/or an isolator.

2.1. Network Model. The network is divided into different regions. A base station is present on any side of the network. The network is divided into three areas. The SS-Manager was selected based on energy level and not SS-Manager from the three areas. The SS-Manager performs a random walk at a random time. During a random walk, all nodes update their information in a table. The SS-Manager is more secure. The SS-Manager performs three operations. The three operations of the proposed system are discussed below.

2.2. SS-Predict. SS-Predict is one of the operations of the proposed system in which a node in the network picks up the presence of malicious activity. A node that identifies the malicious activity is called SS-Manager. SS-Predicts follows two cases:

2.2.1. Case 1. SS-Manager verifies the table if any duplicate node ID is present. And also, the node does not update the information in the Random Walk Table (RWT), which is also shortlisted and sent to the SS-detect. The duplicate node ID, speed, battery level, and key will be selected in the

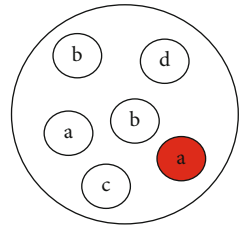

(a)

NID	D_{ij}
A	a–>b
B	b–>c
C	c–>d
D	d–>a
A	a–>b

(b)

Figure 3: (a) Network structure. (b) Random Walk Table.

existing system and checked for the replica. In the SS method, if the node does not update the details in RWT during the random walk, that node also checks for the replica. At a random time, t, each node updates its information as node ID (NID) and the distance between the neighbor nodes (Dij).

Assume the nodes$\{a, b, c, d, e\}$ in the network are shown in Figure 3(a). All the nodes should update the node ID andD_{ij}in the table at$T$'s random time. The node$\{a\}$is duplicated, and node$\{e\}$did not update its information in the table shown in Figure 3(b). The node$\{a, e\}$ is selected and transferred to SS-Detect.

2.2.2. Case 2. The neighbor nodes of the current node are assessed for the abnormal variation in the packet delivery ratio (M_1), packet loss ratio (M_2), and the delay metrics (M_3). The metrics M_1, M_2, and M_3 are measured using equations (1), (2), and (3), respectively.

$$M_1 = \frac{\text{PR}}{\text{PR} + \text{PL}}, \tag{1}$$

$$M_2 = \frac{\text{PL}}{\text{PR} + \text{PL}}, \tag{2}$$

$$M_3 = \frac{\text{Delay}}{\text{Current simulation time}}. \tag{3}$$

Each node is checked for variation in its recent metrics. $M_{1\text{avg}}$, $M_{2\text{avg}}$, $M_{2\text{avg}}$, and M_{avg} are the individual and total averages. The conditions in equations (4), (5), and (6) are tested for the prediction of a malicious node (NodePM). If any of the conditions are true, then the SS-Manager automatically transits into the SS-Detect mode, the next mode of operation in SS.

$$M_1 < < M_{1\text{avg}} \text{ and } M_1 > > M_{1\text{avg}}, \tag{4}$$

$$M_2 < < M_{2\text{avg}} \text{ and } M_2 > > M_{2\text{avg}}, \tag{5}$$

$$M_3 < < M_{3\text{avg}} \text{ and } M_3 > > M_{3\text{avg}}. \tag{6}$$

2.3. SS-Detect. SS-Detect phase can be initiated by a node that has predicted the presence of the malicious node or by the transition from the SS-Predict. This is a critical mode in which the predicted nodes (NodePM) undergo vigorous checking to identify maliciously or just let go as legitimate nodes. This checking process will use cryptographic methods to identify and distinguish the malicious node. The detected nodes will be labeled as "NodeDM" at the end of the SS-Detect mode. If the above metrics are not satisfied, the detection phase is used. Each node stores the neighbor node information such as node ID and distance between the node at a different time (dj, tj) and (dk, tk). If $dj > = dk$ at time $tj < tk$, then

$$\frac{dk - dj}{tk - tj} \neq [v \min, v \max], \quad \text{if } tj < tk, dj < \text{d}kdj. \tag{7}$$

The deviation is measured based upon the binary deviation array. If the deviation is greater than or equal to 1, it is assigned as a replicated node.

$$D = \begin{cases} 1, & d_j > dk \text{ or } d_j < dk, \\ 0, & d_j = dk. \end{cases} \tag{8}$$

2.4. SS-Isolate. The SS-Managers can only reach the isolated phase. However, any random node that cannot enter SS-Isolate mode will be genuine. If a node enters the SS-Isolate, the node is assigned as a replica node. The detected node information is sent to the neighbor node of the replica node, depending on the location and distance. Each node stores the neighbor information while deploying the node. If the node receives the neighbor node as a replica node, then the node removes the replica node from the neighbor list. If any node sends data to another node, the node should send data to the nearest node. If the nearest node is in the neighbor list, the data will be passed through that path. The operational flow of how the modes can be achieved in SS is shown in Figure 4.

3. Results and Discussion

Let us assume $\{a, b, c, d, e, f, g, h, i\}$ are the nodes, and two replica nodes $\{a, e\}$ are present in the network. At the random time (t), each node updates its node ID and distance in the RWT table. Suppose during random walk the node ID $\{a, b, c, d, e, f, g, h\}$ has entered the information in the RWT table. The node ID $\{a, e\}$ has been duplicated in the table, and the node ID $\{i\}$ has not been entered in the table.

```
Input:   Input all the nodes in each region
Output:  Filter the node has the same node id, node not updated in RWT table, Condition not satisfied nodes.
Description:
1.       Initialize the nodes
2.       if (Time=t) then
          UT[i]⊠— (NID[i], Dij[i]); //update node id and distance should be updated
3.       For (j=1;j<=I;j++)
          If(NID[k]=NID[j]) or ( !list[j][table])
             Send the node to SS-Detect
4.       For(i=1 to node)
          m1[i]=pr[i]/(pr[i]+pl[i])
          m2[i]=pl[i]/(pr[i]+pl[i]
          m3[i]=delay/current time
          If(m1[i] < m1avg && m1[i]>m1avg)
          If(m2[i]<m2avg && m2[i]>m2avg)
          If(m3[i]<m3avg && m3[i]>m3avg)
                SSS-Detect(node[i])
```

Algorithm 1: SS-Predict.

```
Input:   Filtered Node from SS-Predict
Output:  Detect the exact Attacker Node
Description:
    1.  If(node.dj>node.dk) then
          Assign A as 1
          Else
          Assign A as 0
    2.  If (Vi>vj), then //check the battery level for the nodes
          Assign A as 1
          Else
          Assign A as 0
    3.  If(node.A==1)
          SS-Isolate(node)
```

Algorithm 2: SS-Detect.

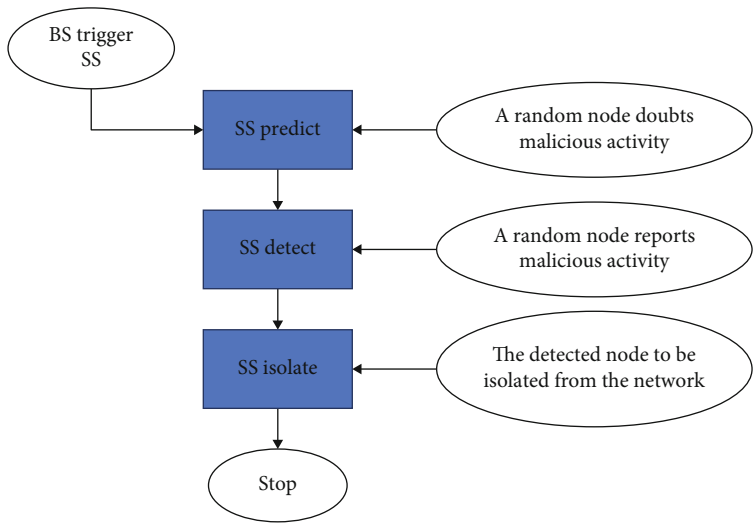

Figure 4: Working in SS modes.

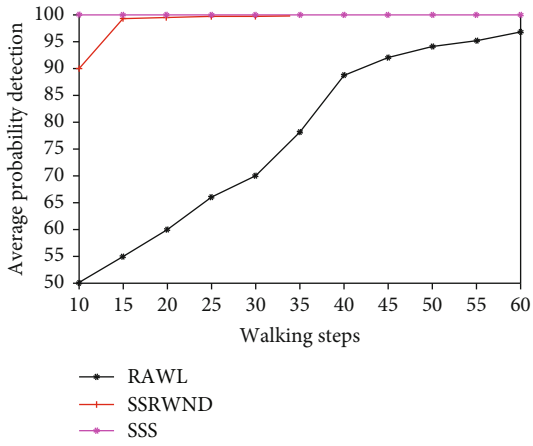

Figure 5: Detection ratio.

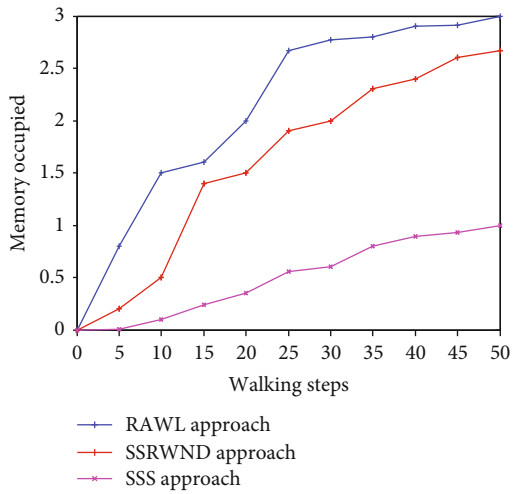

Figure 6: Memory overhead.

If there is any deviation in any metrics, the node is filtered. In predict phase, the node ID$\{a, e, i\}$ is filtered and transformed to the next phase. The next phase checks for the deviation in the distance and battery level. The replicated node is reported to all the nodes and isolated from the network. The probability of storing the distance information independently is $P(C2/(\sqrt{n}\log n))$ [RAWL]. Consider in $C1\sqrt{n}\log n$ step random walk; the distance claim stored is $P(C2/(\sqrt{n}\log n))$. If the distance claim is not updated in the table, then the probability is assigned as

$$P_{\text{no}} = \left(1 - \frac{C2}{\sqrt{n}\log n}\right) C1.\sqrt{n}\log n, \approx \frac{1}{e^{c1.c2}}. \quad (9)$$

$$P_{no} = 1 - \frac{1}{e^{c1.c2}}$$

Memory Cost per node is $O(C1.C2.\text{claim} + C1\sqrt{n}\log n$ .Entry). The table entry size in the SS technique is 2 bytes, 1 byte for node ID, and 1 byte for distance information.

Table 1: Detection probability.

	Walk step						
Methods	10	15	30	40	45	50	60
RAWL	50	60	70	88.7	91.9	94.0	96.7
SSRWND	90	99	99.7	100	100	100	100
SSS	100	100	100	100	100	100	100

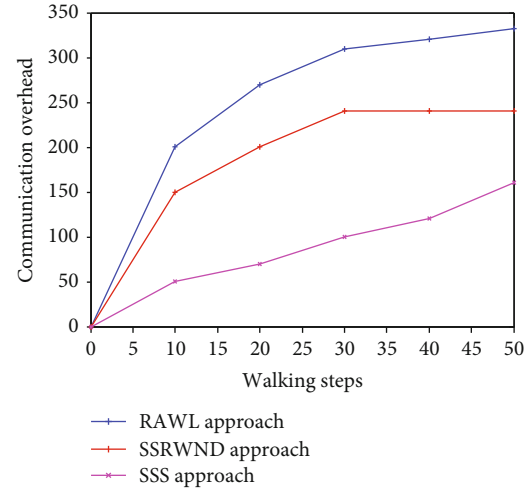

Figure 7: Communication overhead.

Table 2: Simulation parameters [26].

Parameter	Value
Channel type	Wireless channel
Simulation time	100 s
Number of nodes	50
MAC type	802.15.4
Traffic model	CBR
Simulation area	1100 × 700
Transmission range	250 m
Network interface type	WirelessPhy
Initial energy	10 J

The memory cost of storing the information in random walk occupies 40 bytes in RAWL and SSRWND. It is 20 times more in RAWL and SSRWND.

3.1. Security Analysis. The detection ratio is represented in equation (10).

$$\text{DR} = \frac{\text{Number}_{\text{Correctly identified attacks}}}{\text{Number}_{\text{Total attacks}}}. \quad (10)$$

Figure 5 shows the detection ratio of the SS over existing methods RAWL and SSRWND. Figure 6 shows that the SSS detection ratio is higher than RAWL and SSRWND. It detects the misbehavior node and checks for the cloned node. In a random walk, each node updates its claim and node ID in the RWT. If any conflicts occur, then the SSS-

Figure 8: NAM output of the flat topology.

Detect to be invoked. Each node should be verified with distance and packet delivery ratio in SSS-Detect. The filtered nodes from the SSS-Detect are assigned as clone node. In RAWL and SSRWND, if the random walk step increases, the detection rate is high. In SSS-Detect, if the random walk step is very less, it detects the 100% replicated node. If the random walk $r = 5$, the detection probability is shown in Table 1.

3.2. Memory Overhead. In SSS, the memory occupied for storing the information is 2 bytes. The existing system takes 40 bytes to store the information during a random walk. In the SSRWND approach, if the random walk is 5, it has 3 regions, and the walk step is 11. Then, the memory overhead is 1.8 KB to 4.94 KB. In the RAWL approach, if the random walk is 5 and 51 steps, the memory overhead should be 2.92 KB to 11.46 KB. If the random walk is 5 and 3 regions in the proposed approach, then the walk step is 5. The memory overhead is 0.33 KB to 1.04 KB, as shown in Figure 6.

3.3. Communication Overhead. The random walk$r = 3$, and the walk step is 5. The random walk should be in two regions and calculated as 3/2. The walking step is calculated as $2 * 16 = 32(C)$ and random walk as $3 * 5 = 15(A)$ for two regions. The total communication cost is calculated as $C + A(32 + 15 = 47)$. The communication cost is calculated and shown in Figure 7.

3.4. Simulation Analysis. NS-2 is used to perform simulations, and the simulation metrics are shown in Table 2 and Figure 8.

3.5. Packet Received. The total number of packets was received in an SSS plot against the existing protocols in Figures 4 and 5, respectively. The SSS checks the node ID and distance. The SSS performs better than the RAWL and SSRWND, as observed in Figure 9.

3.6. Packet Lost. SSS performs better in both packet delivery and packet lost, as shown in Figure 10, compared to their existing baseline protocols.

3.7. Delay. We varied the network size from 50 to 250 systems to evaluate network scalability and test the effects. It is compared with the current system and the proposed algorithm. The delay of the proposed system compared to the existing one will be very low if the node is 50, which is shown in Table 3, and the graph is shown in Figure 11.

3.8. Energy Consumption. Energy consumption improves the energy required to pass data packets, as shown in Table 4. It wastes energy by sending many unnecessary routing of data packets (including control packet data) without significantly increasing the transmission rate of data packets, as shown in Figure 12.

$$\text{Energy consumption (EC)} = \text{Initial energy} - \text{Current energy (J)}. \tag{11}$$

3.9. Analysis of Packet Delivery Ratio. It is the sum of the number of data packets that the destinations successfully received to the number of data packets that the source produces. Depending on time, the packet delivery ratio is given, where the number of nodes is m and the interval of time is s. Figure 13 indicates the pattern of PDR at various times. It has been shown in Figure 13 that the rate of packet loss decreases over time. The analysis shows that the proposed

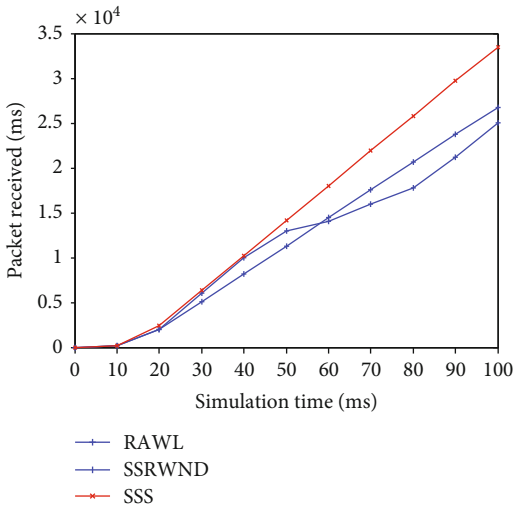

Figure 9: Packets received.

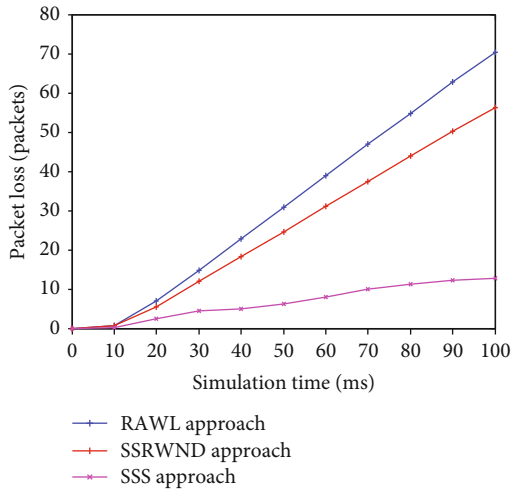

Figure 10: Packets Lost.

Table 3: Delay.

No. of nodes	50	100	150	200	250
Proposed algorithm	1	1.6	2	2.8	3
Existing algorithm	3	3.6	4	4.2	6

algorithm takes only a minimum number of nodes compared to the existing algorithm and less time to calculate it. With less time, PDR is increased, but more and more time is increasing. Figure 13 shows the analysis of the packet delivery ratio. For simulation, the number of nodes taken is 10, 20, 40, 60, 80, and 100. The packet delivery ratio is less compared with the existing system.

3.10. Analysis of Network Throughput. Network throughput is when packet orbits are successfully delivered over a network channel-
: throughput (bits/sec) = sum (number of successful packets) ∗ (average packet size))/total time sent in delivering that

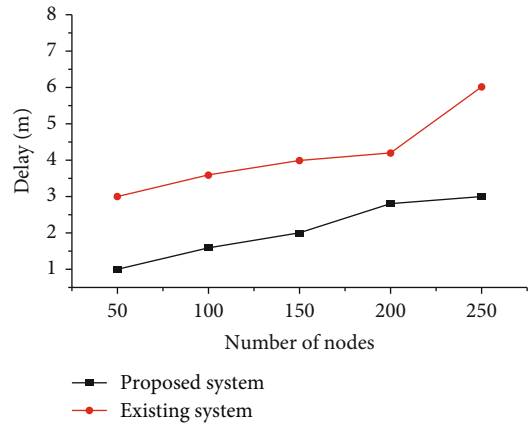

Figure 11: Delay

Table 4: Energy consumption.

No. of nodes	50	100	150	200	250
Proposed algorithm	380	400	600	920	1100
Existing algorithm	240	360	400	520	600

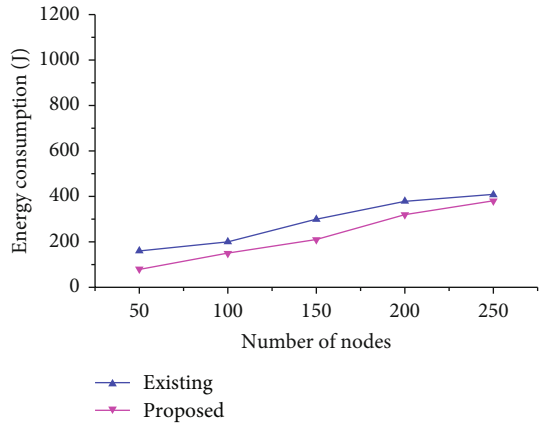

Figure 12: Energy consumption.

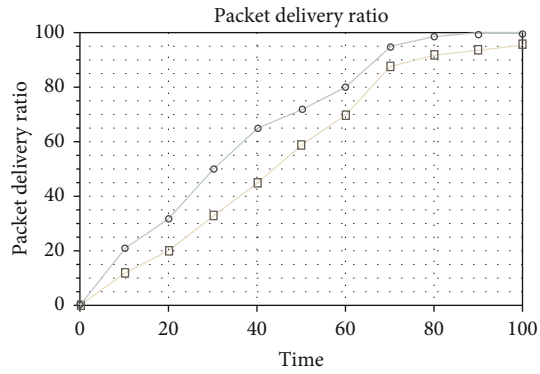

Figure 13: Analysis of packet delivery ratio

amount of data. The network throughput may be zero due to the jamming attack in certain cases. Let r be the transmission range and s be the time in secs. Mathematically, the network throughput can be expressed as the number of messages

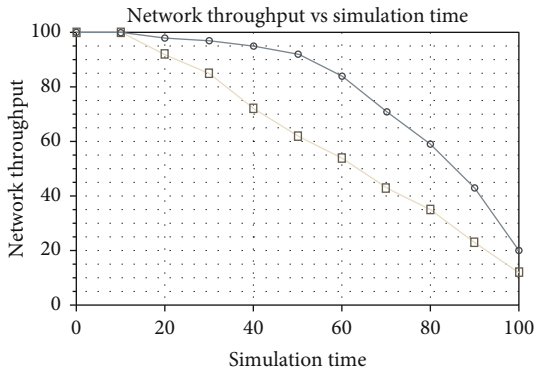

Figure 14: Analysis of network throughput.

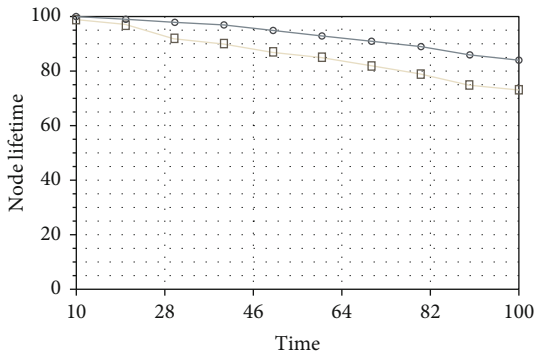

Figure 15: Analysis of node lifetime.

successfully transmitted per unit of time. And Figure 14 demonstrates the analysis of network throughput, which shows that the network throughput is high because the proposed algorithm does not use any extra information for dynamic updates compared to the existing technique. Figure 14 shows the analysis of network throughput. For simulation, the number of nodes taken is 10, 20, 40, 60, 80, and 100. The network throughput is less compared with the existing system.

3.11. Analysis of Node Lifetime. The lifetime of a node *Vx*, at time *t*, L*vxt*, is expressed as the ratio of the residual energy (Et) to the initial energy content of the node (Einit) and is expressed as a percentage value. In Figure 15, it is inferred that the node's lifetime in the proposed technique is longer than the lifetime of the node, which gives high stability among the nodes in the network and reduces overhead. The lifetime of the node should be stable. If the node is drained, it loses its energy; then, the node will be hidden and causes significant interference in the transmission.

Figure 15 shows the analysis of network throughput. For simulation the number of nodes taken is 10, 20, 40, 60, 80, and 100. The network throughput is less compared with the existing system. In the simulation, 100, 200, 500, 1500, and 2000 nodes are deployed in the network and verified. Initially, the number of malicious nodes is detected by verifying the Node-ID of the node that participates in the data transmission. To check the performance, the simulation is applied two times as the existing approach and the other one is with the proposed approach.

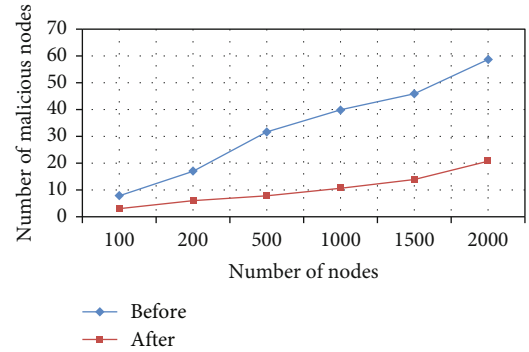

Figure 16: Controlled and uncontrolled malicious before and after applying the proposed system.

The result shown in Figure 16 illustrates the malicious behavior before and after applying the proposed system to the network. The number of malicious activities increases according to the number of nodes deployed in the network. From Figure 16, it is clear that severely malicious activity is found for more nodes, and for fewer nodes, less malicious activity is found. This controlled activity is deployed while verifying the node information itself. They are eliminated and do not reoccur during data transmission.

4. Conclusions

This paper presented a novel Strategic Security System (SSS), which performed three major operations such as prediction, detection, and isolation of replicators. The main advantages of this system are as follows: (i) there is no requirement for special nodes to act as an SS-Manager, and (ii) it consumes very petite additional resources from any security system. It is compatible with hierarchical topologies. From the simulation results, it can be concluded that this method serves to be one of the most efficient methods to eliminate the replicators from a network.

Data Availability

The data used to support the findings of this study are available from the corresponding author upon request.

Conflicts of Interest

The authors declare that they have no conflicts of interest.

Authors' Contributions

All authors have equal contribution.

References

[1] W. He, X. Liu, H. Nguyen, K. Nahrstedt, and T. Abdelzaher, "PDA: privacy-preserving data aggregation in wireless sensor networks," in *Proceedings of the IEEE 26th IEEE International Conference on Computer Communications (INFOCOM'07)*, pp. 2045–2053, Anchorage, Alaska, USA, 2007.

[2] B. Parno, A. Perrig, and V. Gligor, "Distributed detection of node replication attacks in sensor networks," in *2005 IEEE symposium on security and privacy (S&P'05)*, pp. 49–63, Oakland, CA, USA, 2005.

[3] W. T. Zhu, J. Zhou, R. H. Deng, and F. Bao, "Detecting node replication attacks in wireless sensor networks: a survey," *Journal of Network andComputer Applications*, vol. 35, no. 3, pp. 1022–1034, 2012.

[4] Y. Li, M. T. Thai, and W. Wu, *Wireless Sensor Networks and Applications*, Springer, New York, NY, USA, 2008.

[5] E. C. Ngai, J. Liu, and M. R. Lyu, "On the intruder detection for sinkhole attack in wireless sensor networks," in *IEEE international conference on communications, 2006. ICC'06*, vol. 8, pp. 3383–3389, Istanbul, Turkey, 2006.

[6] D. Gračanin, K. P. Adams, and M. Eltoweissy, "Data replication in collaborative sensor network systems," in *2006 IEEE International Performance Computing and Communications Conference*, p. 8, Maryland, USA, 2006.

[7] A. P. R. Da Silva, M. H. Martins, B. P. Rocha, A. A. Loureiro, L. B. Ruiz, and H. C. Wong, "Decentralized intrusion detection in wireless sensor networks," in *1st ACM international workshop on Quality of service & security in wireless and mobile networks*, pp. 16–23, ACM, 2005.

[8] S. Avancha, J. Undercoffer, A. Joshi, and J. Pinkston, "Security for wireless sensor networks," in *Wireless Sensor Networks*, pp. 253–275, Springer, US, 2004.

[9] A. S. K. Pathan, Ed., *Security of Self-Organizing Networks: MANET, WSN, WMN, VANET*, CRC press, 2010.

[10] A. S. K. Pathan, H. W. Lee, and C. S. Hong, "Security in wireless sensor networks: issues and challenges," in *Advanced communication technology, 2006. ICACT 2006*, vol. 2, p. 6, Phoenix Park, 2006.

[11] A. P. Renold, R. Poongothai, and R. Parthasarathy, "Performance analysis of LEACH with gray hole attack in wireless sensor networks," in *International Conference on Computer Communication and Informatics (ICCCI), 2012*, pp. 1–4, Coimbatore, India, 2012.

[12] J. Wang, G. Yang, Y. Sun, and S. Chen, "Sybil attack detection based on RSSI for wireless sensor network," in *2007 International Conference on Wireless Communications, Networking and Mobile Computing*, pp. 2684–2687, Shanghai, China, 2007.

[13] T. G. Lupu, "Main types of attacks in wireless sensor networks," in *WSEAS international conference. proceedings. recent advances in computer engineering*, Stevens Point, Wisconsin, USA, 2009.

[14] I. Krontiris, T. Giannetsos, and T. Dimitriou, "Launching a sinkhole attack in wireless sensor networks; the intruder side," in *2008 IEEE International Conference on Wireless and Mobile Computing, Networking and Communications*, pp. 526–531, Avignon, France, 2008.

[15] W. Z. Khan, M. Y. Aalsalem, and N. M. Saad, "Distributed clone detection in static wireless sensor networks: random walk with network division," *PLoS One*, vol. 10, no. 5, article e0123069, 2015.

[16] M. Y. Aalsalem, W. Z. Khan, N. M. Saad, M. S. Hossain, M. Atiquzzaman, and M. K. Khan, "A new random walk for replica detection in WSNs," *PLoS One*, vol. 11, no. 7, article e0158072, 2016.

[17] Y. Zeng, J. Cao, S. Zhang, S. Guo, and L. Xie, "Random-walk based approach to detect clone attacks in wireless sensor networks," *IEEE Journal on selected areas in communications*, vol. 28, no. 5, pp. 677–691, 2010.

[18] S. Lalar, S. Bhushan, and N. A. Surender, "Clone detection using fuzzy logic in static wireless sensor network," *International Journal of Vehicle Information and Communication Systems*, vol. 5, no. 3, pp. 334–353, 2020.

[19] M. Numan, F. Subhan, W. Z. Khan et al., "A systematic review on clone node detection in static wireless sensor networks," *IEEE Access*, vol. 8, pp. 65450–65461, 2020.

[20] M. Jamshidi, S. S. Poor, N. N. Qader, M. Esnaashari, and M. R. Meybodi, "A lightweight algorithm against replica node attack in mobile wireless sensor networks using learning agents," *IEIE Transactions on Smart Processing & Computing*, vol. 8, no. 1, pp. 58–70, 2019.

[21] M. Jamshidi, M. Esnaashari, A. M. Darwesh, and M. R. Meybodi, "Using time-location tags and watchdog nodes to defend against node replication attack in mobile wireless sensor networks," *International Journal of Wireless Information Networks*, vol. 27, no. 1, pp. 102–115, 2020.

[22] S. Anitha, P. Jayanthi, and V. Chandrasekaran, "An intelligent based healthcare security monitoring schemes for detection of node replication attack in wireless sensor networks," *Measurement*, vol. 167, p. 108272, 2021.

[23] L. Sujihelen and C. Jayakumar, "Inclusive elliptical curve cryptography (IECC) for wireless sensor network efficient operations," *Wireless Personal Communications*, vol. 99, no. 2, pp. 893–914, 2018.

[24] L. Sujihelen and C. Senthilsingh, "Detect the replica node in mobile wireless sensor networks," in *2021 5th International Conference on Intelligent Computing and Control Systems (ICICCS)*, Madurai, India, 2021.

[25] L. Sujihelen, M. Satyanarayana, and C. Senthilsingh, "Replica node detection in distributed wireless sensor networks," in *2021 5th International Conference on Trends in Electronics and Informatics (ICOEI)*, Tirunelveli, India, 2016.

[26] L. Sujihelen, C. Jayakumar, and C. Senthilsingh, "SEC approach for detecting node replication attacks in static wireless sensor networks," *Journal of Electrical Engineering and Technology*, vol. 13, no. 6, pp. 2447–2455, 2018.

Hindawi
Wireless Communications and Mobile Computing
Volume 2022, Article ID 6442778, 16 pages
https://doi.org/10.1155/2022/6442778

Research Article

A Prioritizing Interdiction Surface-Based Vulnerability Remediation Composite Metric for Industrial Control Systems

Zibo Wang,[1,2] Yaofang Zhang,[1,2] Zhiyao Liu,[3] Tongtong Li,[1,2] Yilu Chen,[1,2] Chen Yang,[4] Bailing Wang,[1,2,5] and Zhusong Liu[6,7]

[1]*School of Computer Science and Technology, Harbin Institute of Technology, Weihai 264209, China*
[2]*School of Cyber Science and Technology, Harbin Institute of Technology, Harbin 150001, China*
[3]*China Industrial Control Systems Cyber Emergency Response Team, Beijing 100040, China*
[4]*Institute of Software, Chinese Academy of Sciences, Beijing 100190, China*
[5]*Weihai Cyberguard Technologies Co. Ltd, Weihai 264209, China*
[6]*School of Computer Science and Technology, Anhui University of Technology, Anhui 243002, China*
[7]*School of Computer Science, Guangdong University of Technology, Guangzhou 510006, China*

Correspondence should be addressed to Chen Yang; yangchen@iscas.ac.cn and Bailing Wang; wbl@hit.edu.cn

Received 16 March 2022; Revised 25 April 2022; Accepted 30 April 2022; Published 29 May 2022

Academic Editor: Junjuan Xia

Recently, industrial control system (ICS) has gradually been a primary attack target. The main reason is that increasing vulnerabilities exposed provide opportunities for launching multistep and multihost attacks to breach security policies. To that end, vulnerability remediations are crucial for the ICS. However, there exist three problems to be tackled in a sound way. First of all, it is impractical to remove all vulnerabilities for preventing the multistep and multihost attacks in the consideration of the actual ICS demands. Secondly, ranking vulnerability remediations lacks a guidance. The last problem is that there is a lack of a metric for qualifying the security level after each remediation. In this paper, an ICS-oriented assessment methodology is proposed for the vulnerability remediations. It consists of three phases corresponding to the above problems, including (1) prioritizing Interdiction Surfaces, (2) ranking vulnerability remediations, and (3) calculating composite metrics. The Interdiction Surface describes a minimum set of vulnerabilities of which the complete removal may interdict all discovered attack paths in the system. Particularly, it innovates to take the urgent security demands of the ICS into account. Subsequently, ranking the vulnerability in the optimal Interdiction Surface is conducive to guide the remediations with the priority. A composite metric is ultimately given to assess the security level after vulnerability remediations. The effectiveness of the proposed methodology is validated in an ICS scenario which is similar to the real-world practice. Results show that the entire procedure is suitable for the context of the ICS. Simultaneously, the composite metric enhances both the comprehensiveness and the compatibility in contrast with attack path-based metrics. Hence, it overcomes the shortcomings when they are used in isolation.

1. Introduction

For the past few years, security incidents of the industrial control system (ICS) have shown an upward trend with the integrations of emerging technologies in development such as Cloud Computing and Internet of Tings (IoT) [1]. As a side effect of such technologies, more and more vulnerabilities in hardware, software, or policies are brought into the ICS, which allows attackers to gain unauthorized access to the system. However, sophisticated attackers are not satisfied to exploit single vulnerability any longer, and they instead launch multistep and multihost attacks with multiple vulnerabilities, posing a greater threat [2, 3].

Correspondingly, security analysts build the vulnerability-oriented model to be aware of possible exploitability behaviors from two aspects. One is for single vulnerability [4], and the other is for chained ones [5]. To have a deep insight on interactions among various

vulnerabilities, attack path- (AP-) based analysis is a typical approach for the ICS. It reveals potential risk dependencies among assets in the system, which is crucial for vulnerability remediations.

An initial idea of our work originates from urgent demands of security practitioners in the ICS about vulnerability remediations. They anticipate getting a security metric that is a quantitative measure of the security level after each remediation, which is of importance to assess the residual risks in the system. A variety of security metrics that play an importantly auxiliary role in the vulnerability remediations were proposed by previous relevant work [6]. Nevertheless, none of these existing isolated metrics are capable to directly be applied into the ICS, because it neglects the relevant demands whose descriptions are summarized briefly.

(D1) In order to prevent the attacks from the context of the ICS, interdicting all discovered APs is more feasible than removing all vulnerabilities in practice. Since a lack of a valid patch for the "0 Day" or a remote access is very common in the ICS, remediations for all vulnerabilities appear to be difficult compared to conventional information technology (IT) systems.

(D2) The disruption to the industrial process will be avoided if the multistep and multihost attacks are detected and eliminated in the early stage. In other words, each AP is interdicted as soon as possible so that the complete chain of vulnerabilities fails to form and reach the goal.

(D3) Remediations focus on as few vulnerabilities as possible, owning to the cost of vulnerability removals and limited budgets for the security maintenance. As we all know, the cost is constrained by the budgets, particularly for industrial manufacturers.

(D4) Most importantly, minimal impacts on the ICS components are ought to be taken into account while implementing the security measures mentioned above. After all, it means a considerable cost if the continuous operations of the ICS components such as the Programmable Logic Controller (PLC) and the Distributed Control System (DCS) are affected and even forced to shut down.

As a result, an ICS-oriented assessment methodology is proposed for the vulnerability remediations in our work. Firstly, a vulnerability-oriented attack graph (AG) is constructed. Then, we define an Interdiction Surface including vulnerabilities that may be remedied to eliminate APs in the consideration of the demands mentioned above, and the optimal one is selected by prioritizing. Subsequently, the vulnerabilities in the optimal Interdiction Surface are ranked, which determines the priority to be remedied. Finally, a specific calculation procedure is given for the composite metric of the system.

The contribution of this paper is summarized as follows.

(C1) The proposed concept, namely, Interdiction Surface, is more suitable for the context of the ICS because it caters to the demands of security practitioners. Simultaneously, it establishes a sound foundation for the vulnerability remediations in the further step.

(C2) The proposed composite metric overcomes the shortcomings of the existing metrics used in isolation, which fuses multiple well-known methods to enhance both the comprehensiveness and the compatibility of the AP-based metrics.

(C3) The proposed calculation procedure and each principle for prioritizing Interdiction Surface and ranking vulnerability remediations are explicit and easy to implement, which is conducive for the ICS practitioners to assess the security level after each remediation.

The rest of paper is organized as follows. In Section 2, the related work in the recent literature is reviewed. Section 3 provides some preliminaries to support relevant statements in our work. In Section 4, we describe the proposed methodology and elaborate it by a simple example. Section 5 demonstrates the experiment results in a case study close to the ICS in reality. Ultimately, we conclude the whole paper and provide the future research direction in Section 6.

2. Related Work

In the past two decades, the AP analysis has been attracting the growing interests from quantities of scholars and practitioners in the security vulnerability field. Among the researches on AP analysis, cut set-based methodologies are widespread to analyze critical APs for systems exposed to security threats. To assess threats, security metrics are imperative to measure the security. In this section, the related work is reviewed from the recently published research literature.

2.1. AP Analysis in the ICS. At present, the most mainstream model of the AP analysis is the AG. AG is a kind of formalized mathematical representation of how an attacker reaches final malicious goals by exploiting a set of vulnerabilities that constitute a multistep and multihost attack. Prioritizing APs is transformed to the discovery of critical nodes or edges in the AG for making sense of intrusion intentions, hardening systems, or mitigating risks [7–11]. From the perspective of AP-based applications in the ICS, typical analyzing approaches are estimating the node importance, i.e., the PageRank algorithm, and employing probabilistic graphical models, i.e., Markov Chain.

Nevertheless, performing the AP analysis for the ICS needs to make more effort on additional considerations of its scene characteristics. Stellios et al. modeled both the cyber connectivity and physical interactions to prioritize APs, no matter which AP is hidden or underestimated at risks [5]. Barrère et al. built AND/OR dependency graphs to identify a minimal number of the ICS components with overlapping security measures or critical missions [12, 13]. Considering the cost of remediations and security budgets for securing the IoT, Yiğit et al. leveraged a compact AG to construct a cost-effective protecting strategy applied to the large-scale environment [14]. Stergiopoulos et al. extracted graph series and utilized group clustering to analyze the risk of the entire network, concerning complexity and interactions of the complex networks in Industry 4.0 [15]. In our work, we likewise integrate the component impact into the proposed methodology as an ICS characteristic.

2.2. Cut Set-Based Methodologies. Cut set is a vital concept in the graph theory, which usually applies to security research fields such as network reliability and defense hardening. Identifying a cut set is a desirable means to prevent an attacker from reaching the final goal under the circumstance of appropriate security countermeasures, which is employed into the AP analysis.

There is no doubt that the cut set-based methodology appears in the context of the ICS to guarantee the system security as well. Incorporating the promising defense-in-depth principle, Mell et al. generated a colored AG that represents known vulnerability types in the ICS network [16]. And then, the problems of the shortest color path and the minimum color cut set were settled, exactly measuring both of the depth and the width and promoting the security posture. Ghazo and Kumar presented a discovering approach of critical-attack set for a supervisory control and data acquisition (SCADA) system based on the minimum-label cut set [17]. The minimum number of labels was obtained by a set of backward reachable strongly connected components. George and Thampi focused on the vulnerability-based assessment for edge devices of the IoT-assisted networks [18, 19]. A graphical model was formulated to isolate target devices from the attackers by a minimum cut set of vulnerabilities. In this regard, our research objective is similar.

In the point view of the game theory, an attacker looks forward to choosing the AP with the least amount of cost, whereas the optimal defensive investments allocated on the basis of the minimum cut sets may expand that cost. Such described scenario is an instance of problem called Interdiction Network [20–22]. Originally, the problem concerns on the interdiction between attackers and defenders. Attackers act as leaders to deteriorate the network performance by determining the best edge cut set [21] or k-critical ones [22]. In contrary, defenders act as followers to strengthen the targeted network. In our work, we introduce the analogous idea to define a concept named Interdiction Surface, which is customized for the ICS. The difference is that the defenders refer to interdicting all APs along with the vulnerability remediations.

2.3. Security Metrics. Security metrics for system-level security cover four aspects including system vulnerabilities, defense power, severity of attack or threat, and situations [23]. Our work focuses on the metrics of system vulnerabilities that can be further classified into individual-vulnerability-oriented ones such as metrics in the common vulnerability scoring system (CVSS, https://www.first.org/cvss/) and multiple-vulnerability-oriented ones such as the AP-based metrics.

Most of the existing metrics are aimed at the business process and internal network of enterprise IT system [24–26] rather than the ICS. But the security metrics in the ICS are essential for the AP analysis with a quantitative measure. The aforementioned literature regarding the ICS [12, 14] can be used to prove that point. In [12], the metric captures the security measure instances and is defined on a logical formulation transformed from the AND/OR graph. Afterwards, the variables in the formulation are assigned a compromise cost. In [14], the metric is the sum of the likelihoods of the APs, which guides the allocation of security budgets for the ICS. More generally, certain existing AP-based metrics are pointed out obvious drawbacks used in isolation, thus confusing security analysts to make wrong decisions, which is absolutely intolerable for the ICS [6]. Hence, a composite metric is proposed in our work to improve the deficiencies, especially for the security-level assessment.

3. Preliminary

In this section, we will briefly introduce a series of fundamental concepts to assist readers interested in the proposed approach. As building blocks, the basic terminologies and definitions are provided for further elaboration.

3.1. Vulnerability-Oriented Attack Graph. Since we seek to interdict as many APs as possible by removing vulnerabilities, vulnerability-oriented AG is adopted into the proposed approach. Its advantage is explicitly representing some vulnerabilities on a device, which makes it intuitive to figure out a chain of vulnerabilities to compromise a target system. The vulnerability-oriented AG is described as follows:

(i) Vulnerability-oriented AG: given a directed acyclic $\mathbf{AG} = (\mathbf{S}, \mathbf{E}, S_0, T)$, where $\mathbf{S} = \{S_i | i = 1, 2, \cdots, n\}$ is a set of nodes, $\mathbf{E} \subseteq \mathbf{S} \times \mathbf{S}$ is a set of edges that connect between pairs of nodes, S_0 is a source node, and T is a terminal node. The node in the AG represents an affected component running on a specific device, and the directed edge represents an exploitation of the vulnerability. Assume that S_0 is a compromising entry point of an attack, and T is a malicious goal that violates system

In fact, an attacker exploits each vulnerability with a varying difficulty level. Hence, vulnerabilities have different probabilities of being successfully exploited. In our work, we extract the empirical Exploitability Score (ES) from the CVSS to calculate Vulnerability Exploitability Probability. The definition is given as follows.

(ii) Vulnerability Exploitability Probability (VEP): the metrics of the ES consist of Attack Vector (AV), Attack Complexity (AC), Authentication (Au), and User Interaction (UI), where $\mathrm{ES} = 8.22 \times \mathrm{AV} \times \mathrm{AC} \times \mathrm{Au} \times \mathrm{UI}$. Exploitability probability EP is derived from the normalization of ES

3.2. Absorbing Markov Chain. Exploitation is a stochastic process in a multistep and multihost attack. Its probability of transition from one state to another is determined by the state of the current vulnerability. With the help of various privileges from vulnerabilities, an attacker may reach new state until realizing the final malicious goal. Therefore, such attack process is effectively described as an Absorbing Markov Chain. Some relevant terminologies and definitions are provided as follows:

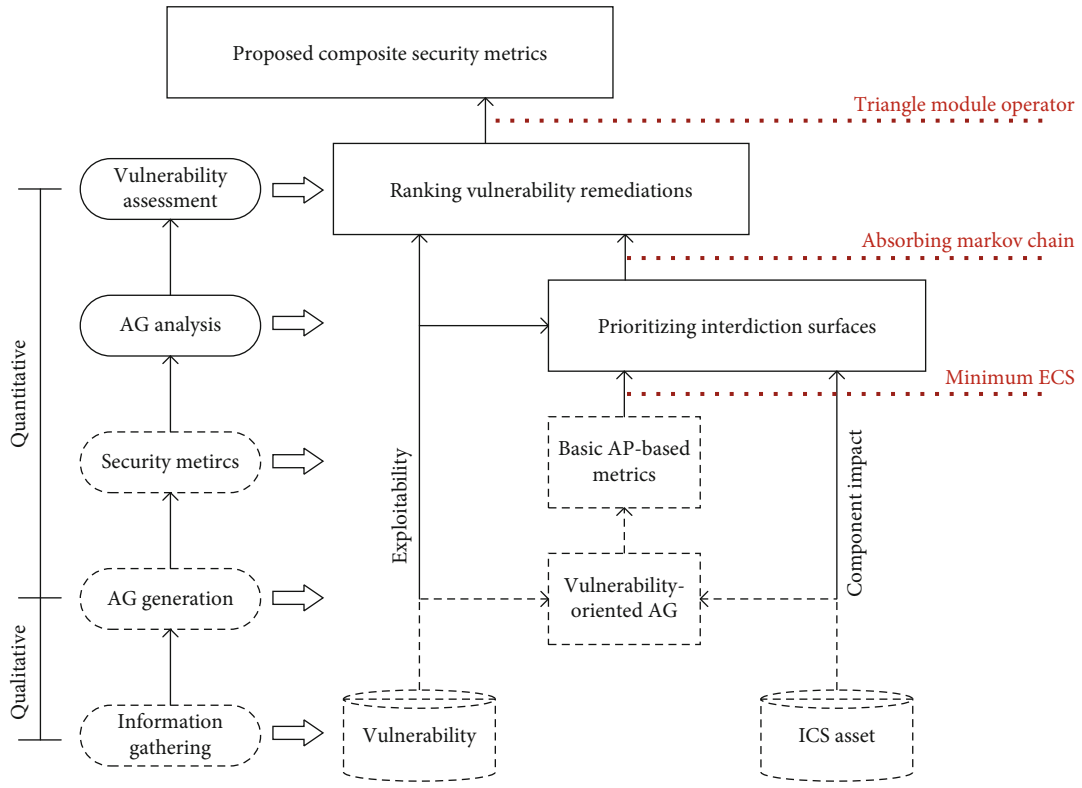

Figure 1: Overview of the proposed methodology.

(i) Markov Property: considering a discrete stochastic sequence including a finite number of states, $\mathbf{X} = \{x_1, x_2, \cdots, x_n\}$, if an equation $P(x_{i+1}|x_i, x_{i-1}, \cdots x_1) = P(x_{i+1}|x_i)$ is always satisfied where $P(x_{i+1}|x_i)$ denotes the probability of transition from x_{i+1} to x_i, it is defined as Markov Property. The sequence is called a Markov Chain

If there exist two states x_i and x_j in the Markov Chain $\mathbf{X}$, the transition probability $P(x_i|x_j)$ could be denoted as P_{ij} for short. Similarly, P_{ii} represents the probability of a transition to the state x_i itself.

(ii) Absorbing Markov Chain (AMC): if the state x_i can only transfer to itself and $P_{ii} = 1$, the state x_i is defined as an absorbing state. And other states of $\mathbf{X}$ could transfer to the absorbing state in finite times. Thus, the chain $\mathbf{X}$ is subsequently called AMC. Simultaneously, all transition probability for each state in the AMC should be added up to 1 [24]

3.3. Edge Cut Set. The cut set in the graph theory is classified into the node cut set and the edge cut set. The removal of nodes or edges in the set has an effect on the connectivity between certain nodes in a graph. According to the requirements of our work, the formal definitions on the edge cut set are overviewed.

(i) Edge cut set (ECS): given all nodes of a directed graph $\mathbf{G}$ are in a set $\mathbf{N}$, a cut divides $\mathbf{N}$ into two parts, $\mathbf{D}$ and $\bar{\mathbf{D}} = \mathbf{N} - \mathbf{D}$. The cut represents a set of edges, namely, ECS. Among them, each edge has a feature that one endpoint is in the set $\mathbf{D}$ and the other endpoint is in the set $\bar{\mathbf{D}}$

In other words, the definition indicates that collective removal of those edges from the graph G will disrupt node connectivity. Obviously, the ECS is not unique, since any set containing an ECS is also an ECS. To some extent, it is convenient for further analysis to reduce the number of the ECSs. Then, minimum ECS refers to as follows.

(ii) Minimum ECS: it is defined as an edge cut set satisfying that all strict subsets are not cut sets

3.4. Attack Path-Based Metrics. The AP-based metric may quantify the overall security of a system such as the network topology, vulnerabilities of services, weaknesses of protocols, as well as defense policies. It is roughly classified into two categories. One is intuitively obtained from the vulnerability-oriented AG, just as the following three typical metrics described [6, 23]:

(i) Number of APs: specifically, it is the number of complete paths in the vulnerability-oriented AG, defined as $\text{Num}_{\text{APs}} = |p_1, p_2, \cdots, p_n|$, where p_n denotes each AP. This metric is the total number of ways that an attacker leverages chained exploits

(ii) Shortest AP: this metric is the shortest length from an initial node to the same goal, defined as Len_{SAP}

$= \min[\text{len}(p_1), \text{len}(p_2), \cdots, \text{len}(p_n)]$, where $\text{len}(\cdot)$ denotes the length of each AP. It indicates that the minimum number of vulnerabilities is exploited to launch a multistep attack

(iii) Expectation of AP lengths: this metric is the arithmetic average of all AP lengths computed over the AG, which is defined as follows. It gives the expected effort of compromising a targeted system

$$\text{Exp}_{\text{APlen}} = \frac{\sum_{i=1}^{n} \text{len}(p_i)}{\text{Num}_{\text{APs}}} \quad (1)$$

By assigning values of expert experience on vulnerability, the other category metric takes account of the probability of AP. The cumulative probability of each exploit on the AP captures the likelihood to reach the final goal. Considering the AMC and the VEP, the following definition is given.

(iv) Probability of AP: given a vulnerability-oriented AG mapped into an AMC, P_{APMarkov} denotes the probability of an AP, which is defined as

$$P_{\text{APMarkov}} = \prod_{i=1}^{m} P_M(\text{EP}_i), \quad (2)$$

where m is the number of vulnerabilities included in the AP. $P_M(\text{EP}_i)$ denotes the transition probability of the AMC regarding the VEP whose specific calculation method is introduced in [24].

Despite the metrics mentioned in this subsection which provides referable results in security evaluation, they also could not meet a comprehensive demand, even misleading analysts, when utilized in isolation [6]. In the next section, we will discuss the shortcoming of these metrics in detail and present our novel metric for vulnerability remediations.

4. Proposed Methodology

As detailed ahead, the unique characteristics of the ICS such as the operational continuity and the limited budget for the security maintenance pose numerous obstacles for security analysts. In addition, it is impractical to eliminate all vulnerabilities in the ICS for the sake of techniques and costs. In terms of these two aspects, the proposed methodology intends to develop a novel security metric to provide a sound guidance for the vulnerability assessment, which is suitable for prioritized remediation requirements in the context of the ICS.

The overview of the proposed methodology is illustrated in Figure 1. We perform from a qualitative analysis to the quantitative one based on the AG modeling with information on the ICS assets and potential vulnerabilities. Interdicting APs with a fraction of vulnerabilities discovered for a given system is a conducive way instead of removing all vulnerabilities in the current security practice. For that reason, we optimize both the selection of vulnerability collection and the sequence of handling them, taking into consideration business impacts on ICS components and the efficiency of eliminating APs. Combined with a series of basic AP-based metrics, a composite metric is generated to improve the ability of capturing the security level in the wake of vulnerability remediations. The proposed methodology is divided into three phases as follows.

(P1) Prioritizing Interdiction Surfaces: in this phase, a concept "Interdiction Surface" is proposed to describe a collection including a relatively small number of vulnerabilities to be removed for the purpose of eliminating APs in the ICS. This concept is supported by the definition of the minimum ECS in the graph theory; however, the difference is that it considers the factor of business impacts on relevant ICS components. What is more, a specific calculation method is introduced to select an interdiction surface among plenty of similar results in a prioritizing manner.

(P2) Ranking vulnerability remediations: the primary goal of the phase is to rank each vulnerability which is a member of the optimal Interdiction Surface at present. The vulnerability-oriented AG of the given ICS is mapped into an AMC. Depending on two types of the typical AP-based metrics mentioned in the last section, each removal of the vulnerability is scored according to the contribution to eliminating as many APs as possible and decreasing the probability to accomplish a multistep attack. On the other side, it indicates less exploitable opportunities once the vulnerability is priority to be remedied.

(P3) Calculating composite security metrics: the ultimate goal of the phase is to quantify security level after removing a vulnerability selected in the P2. In order to avoid the drawbacks in single using of existing AP-based metrics mentioned in the previous literature, a composite metric is designed to assess security level in a holistic view. On the basis of Triangle Module Operator, we integrate the intermediate results which are in the first two phases together from three aspects, including the ranking level of each vulnerability in the prioritized interdiction surface, the transition probability, and the changes of the basic AP-based metrics before and after the removal of a specific vulnerability.

4.1. Prioritizing Interdiction Surfaces. Based on these four security demands of the ICS described in Introduction, we propose a concept called "Interdiction Surface" and then give an algorithm to prioritize such surfaces. Before the statements regarding the proposed methodology in this part, there are four targeted responses to the demands (D1~D4) with the help of the preliminaries in Section 3.

(R1) Recall that the minimum ECS is a set of edges whose collective removal ensures a graph divided into two parts. Incorporating the concept of the graph theory into the vulnerability-oriented AG, all APs are interdicted by removing a specific set whose members represent vulnerabilities to be remedied.

(R2) Each AP in our work is treated as a sequential chain of vulnerabilities. If the vulnerability located closely to the initial point of the entire chain is remedied, the AP could be interdicted as soon as possible. The shortest AP metric captures the phenomenon in a quantitative way.

Input: a vulnerability-oriented **AG**, a list of the VEPs, a list of impact value on the ICS components
Output: an optimal Interdiction Surface
1 get the edge set **E**, the node set **S**, the initial nodes S_0 and terminal node T from the **AG**
2 **for** an edge in the **Edo**
3 assign the Grade to each edge in the **S**
4 **End for**
5 initialize a set IS and then store each edge set with the same Grade into the set
6 initialize a set **RL**
7 **for** an edge in the **Edo**
8 store the relation of edges satisfying the Root-Leaf in the **RL**
9 **End for**
10 **for** a member in the IS**do**:
11 replace the root edge in **RL**with the leaf edge in the different grade to generate cut sets **P**
12 conduct the Minimized Testing for each new possible cut set in the **P**
13 **if** the possible cut set is the Minimum ECS **then**
14 add the possible cut set into the IS
15 **End if**
16 **End for**
17 assign the VEPs and the impact value to each edge and each node
18 calculate in Eq. (3) for each member in the IS
19 get the member with the minimum vale of the set of the calculation results
20 **Return**

Algorithm 1: Prioritizing Interdiction Surfaces.

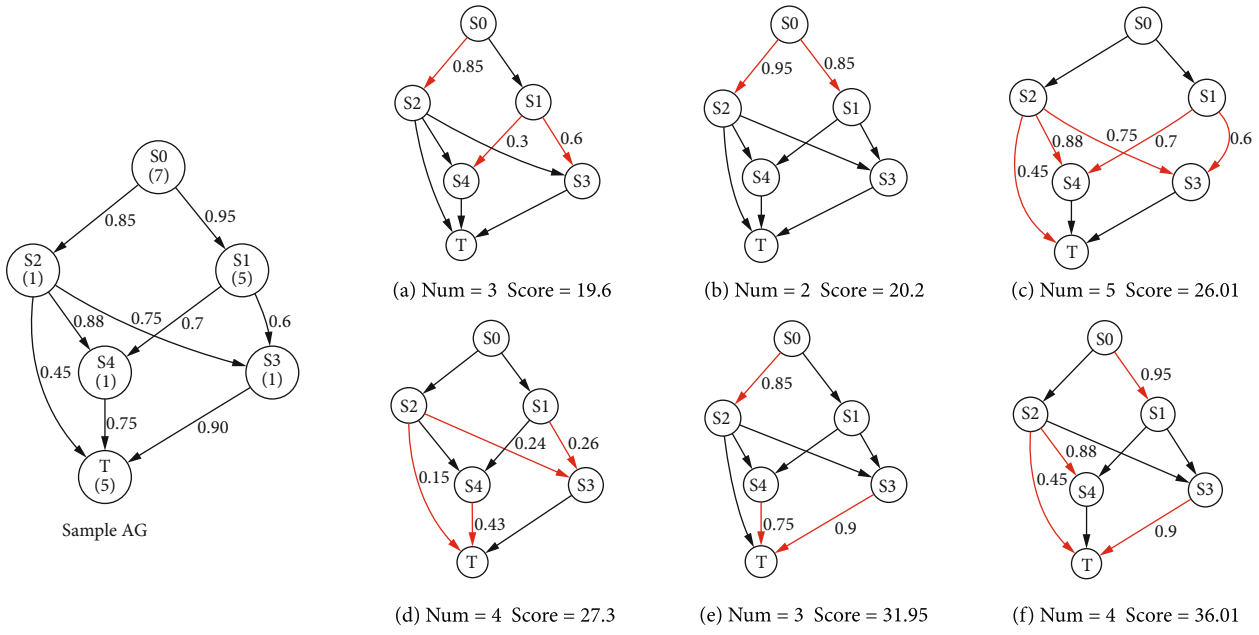

Figure 2: Illustration for prioritizing Interdiction Surface.

(R3) The set described in R1 is not unique. Meanwhile, each set has varying numbers of members. It is not a trivia to select a set with fewer but probably not the least members in the consideration of many factors offered in D3. It is essential to decide the size of the set referring to other metrics.

(R4) The impacts on the ICS components may also be quantified by multiple of means such as the expert knowledge in the ICS field, historical data on the industrial operation, and inspections from security analysts. The combination of the quantitative values and the VEP guarantees that impacts on the ICS merge into the process of the vulnerability assessment.

Accordingly, the Interdiction Surface is defined in accordance with these responses to the practical demands of the ICS, given as follows:

(i) Interdiction Surface: the virtual surface depicts a way to cut off all discovered APs, which consists of minimal set of vulnerabilities to be remedied. Its selection

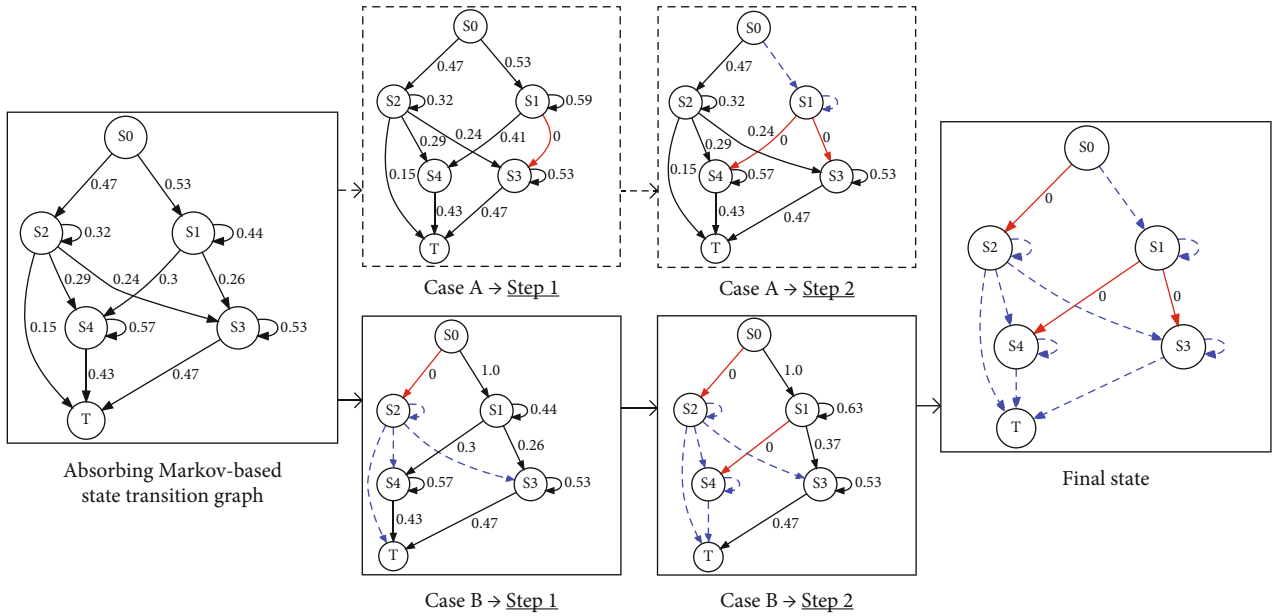

Figure 3: Illustration for removing the edges.

Table 1: AP metrics for case A.

AP-based metrics	Initial conditions	$S_1 \longrightarrow S_3$	$S_1 \longrightarrow S_4$	$S_0 \longrightarrow S_2$
Number of APs	5	4	3	0
Shortest AP	2	3	3	0
Expectation of AP lengths	2.8	3.75	3.667	0
Sum of probability of the eliminated APs	—	0.207	0.218	0.575

Table 2: AP metrics for case B.

AP-based metrics	Initial conditions	$S_0 \longrightarrow S_2$	$S_1 \longrightarrow S_4$	$S_1 \longrightarrow S_3$
Number of APs	5	2	1	0
Shortest AP	2	4	4	0
Expectation of AP lengths	2.8	4	4	0
Sum of probability of the eliminated APs	—	0.575	0.218	0.207

among the similar surfaces must comprehensively follow the principles including the shortest AP metric of a given vulnerability-oriented AG, fewer vulnerabilities, and the impacts on the ICS components, which is formulize as

$$\text{Score}_{\text{IS}} = \text{Cut}_{\text{num}} + \sum_{i \in \text{IS}} \text{Cut}_{\text{loc}}(i) + \sum_{i \in \text{IS}} \text{Com\_impact}(i), \quad (3)$$

where Cut_{num} denotes the number of vulnerabilities in the Interdiction Surface and $\text{Cut}_{\text{loc}}(i)$ denotes the length of the shortest AP between S_0 and each member of the Interdiction Surface. The impacts on the ICS components are denoted as

$$\text{Com\_impact}(i) = (\text{com\_impact}_S + \text{com\_impact}_T) \times \text{EP}_i, \quad (4)$$

where com_impact_S and com_impact_T denote the impacts on a pair of the ICS components regarding a vulnerability. Note that each edge in the AG represents a vulnerability, and the both endpoints of each edge represent the ICS components to support the business process or industrial operations. Hence, the removal of the vulnerability may have an impact on the ICS components in both core data exchanging and run monitoring.

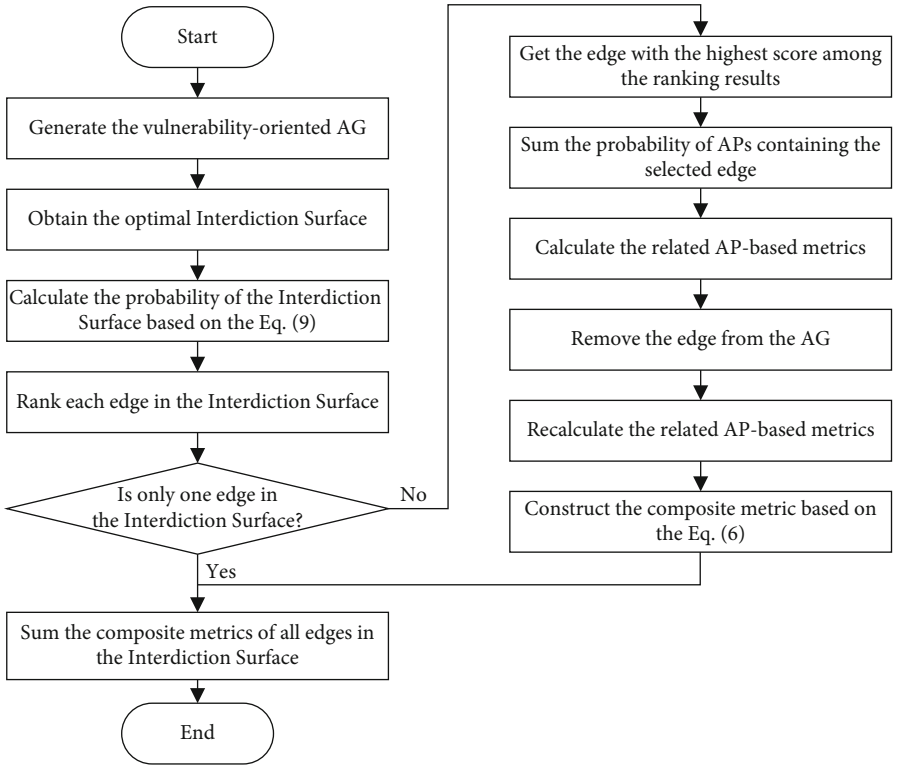

Figure 4: A flow chart for calculating the system security metric.

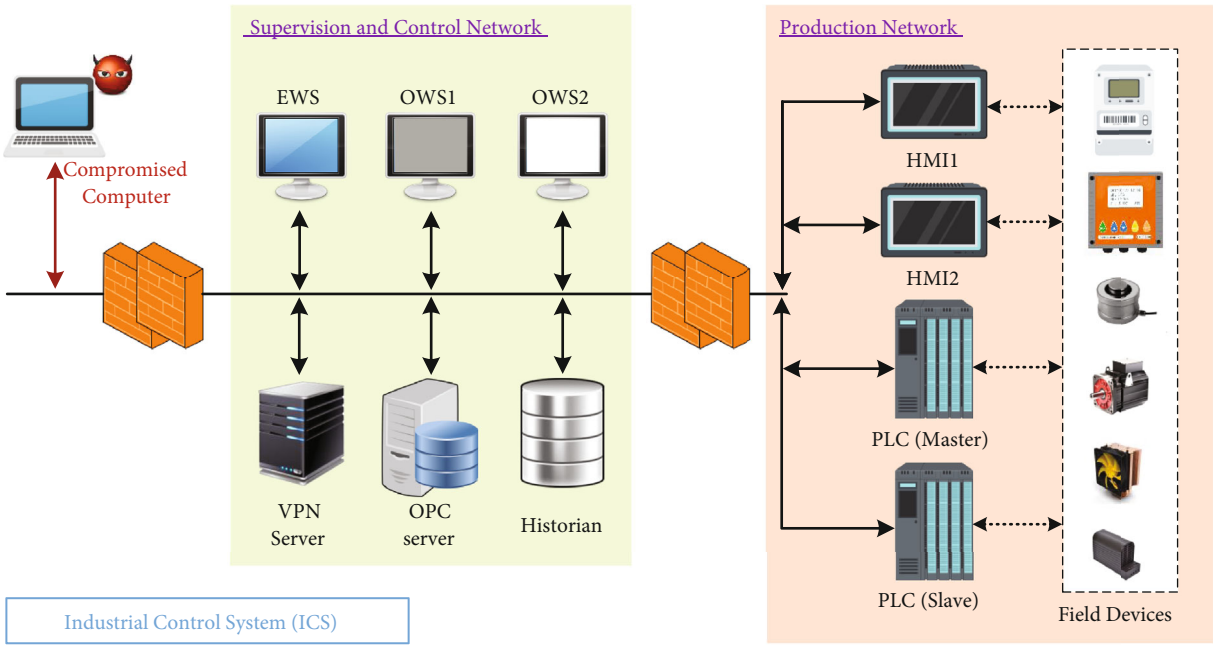

Figure 5: An ICS scenario.

The definition of the Interdiction Surface has a dependence on all minimum ECSs for a given vulnerability-oriented AG. In our work, we utilize the idea of the hierarchical approach in the literature [27] to obtain all minimum ECSs and then determine the prioritizing IS. There are some key concepts of the approach listed in advance.

By means of breadth-first search, each node in a directed acyclic graph is assigned a value called Grade with respect to the minimum number of edges traversed from a given initial node to the node. It is obvious that the sets of nodes with the same grades must be minimum cut sets. Besides, the minimum cut sets including nodes with the different grades is

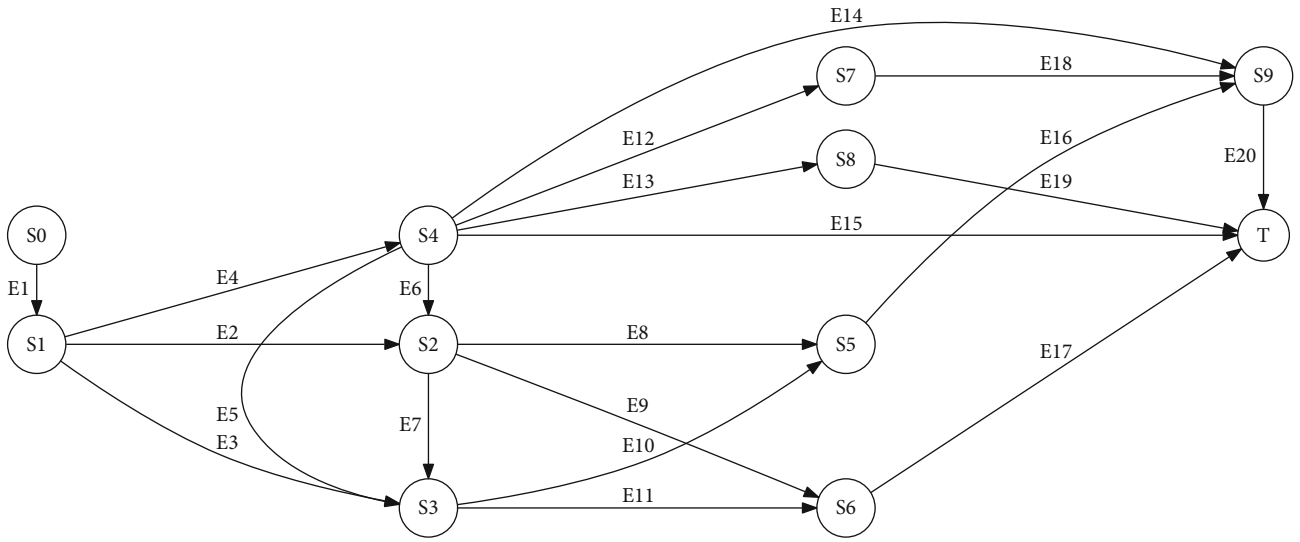

Figure 6: An AG for the ICS.

Table 3: Devices and affected components in the ICS.

Device name	Affected component	Node in AG	Access control	Component impact
Compromised computer	VPN Client	S0	S1	1000
VPN Server	Moxa EDR-G902	S1	S2, S3, S4	10
OPC Server	OPC UA .NET	S2	S3, S5, S6	1
Historian	SIMATIC Process Historian	S3	S5, S6	1
EWS	Windows SMBv3	S4	S2, S3, S7, S8, S9, T	1
OWS1	Siemens Control Center Server Application	S5	S9	1
OWS2	SIMATIC PCS 7	S6	T	1
HMI1	SIMATIC WinCC	S7	S9	9
HMI2	SIMATIC HMI Comfort Panels	S8	T	9
PLC master	SIMATIC S7-1500 CPU	S9	T	10
PLC slave	SIMATIC S7-1200 CPU	T	/	10

Table 4: Vulnerabilities in the ICS.

CVE No.	Edge in AG	ES
CVE-2020-14511	E1	3.9
CVE-2020-29457	E2, E6	0.8
CVE-2021-27395	E3, E5, E7	2.8
CVE-2020-0796	E4	3.9
CVE-2019-19292	E8, E10	2.8
CVE-2021-40359	E9, E11	3.9
CVE-2019-10916	E12	2.8
CVE-2019-6577	E13	2.3
CVE-2020-15782	E14, E16, E18	3.9
CVE-2021-37172	E15, E17, E19, E20	3.9

further explored by using a graphical relation of these nodes called Root-Leaf. On the basis of the grade of nodes, root nodes are taken place of leaf nodes to generate new possible cut sets until all the combinations are traversed. Finally, a minimized testing is conducted for the possible cut sets to ensure that the sets are minimum.

Note that the results in [27] are minimum node cut sets but directly not the minimum ECS in our work. Therefore, we improve the approach and integrate it with the calculation method in Equation (3) to form the proposed Algorithm 1 as follows.

A sample vulnerability-oriented AG is shown in Figure 2, which consists of six nodes and nine edges. S_0 and S_5 denote the source node and the terminal node, respectively, in the AG. The value in parenthesis of each node represents the impact component on the corresponding ICS component, and the value of each edge represents the VEP.

The optimal Interdiction Surface for the sample situation is the edge set $\{S_0 \longrightarrow S_2, S_1 \longrightarrow S_3, S_1 \longrightarrow S_4\}$ with $\text{score}_{\text{IS}} = 19.6$. There are twelve Interdiction Surfaces based on Algorithm 1, six of which are illustrated in Figure 2. The collection of the edges with the red color in each subgraph (a)–(f) denotes the Interdiction Surface. It is observed that the selection of Interdiction Surfaces is a comprehensive process

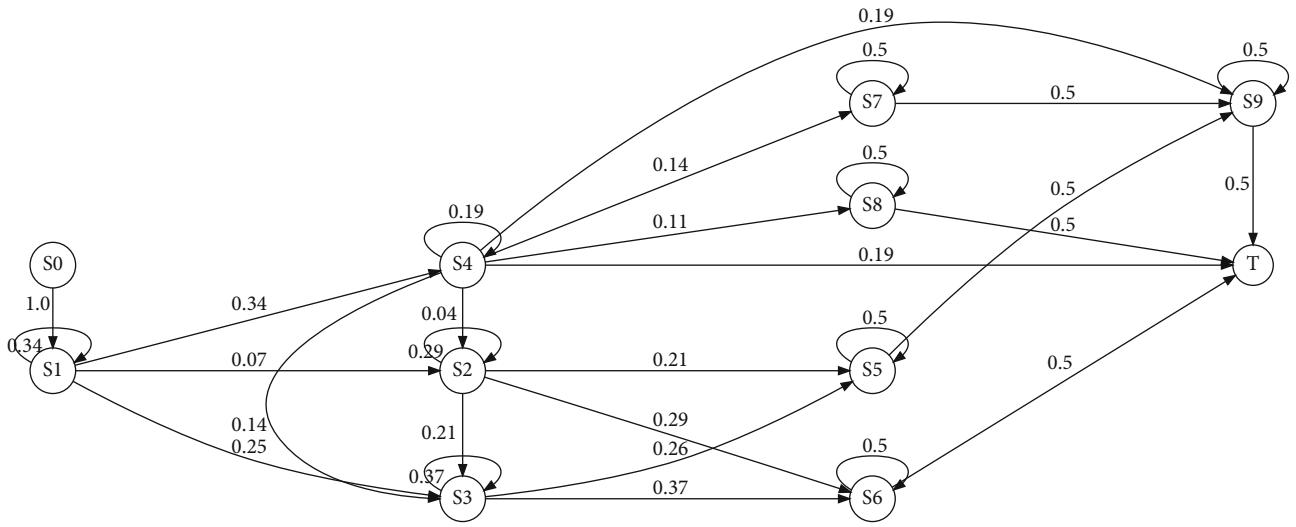

Figure 7: Absorbing Markov-based state transition AG.

Table 5: Top 10 probabilities of AP.

No.	AP	Probability of AP
1	E1, E4, E15	0.06513
2	E1, E3, E11, E17	0.04517
3	E1, E4, E14, E20	0.03256
4	E1, E4, E13, E19	0.01921
5	E1, E3, E10, E16, E20	0.01626
6	E1, E4, E12, E18, E20	0.01172
7	E1, E2, E9, E17	0.01041
8	E1, E4, E5, E11, E17	0.00862
9	E1, E2, E8, E16, E20	0.00375
10	E1, E4, E5, E10, E16, E20	0.00310

Table 6: Top 10 Interdiction Surfaces.

No.	Interdiction surface	Score in P1
1	E2, E4, E10, E11	26.75
2	E2, E3, E4	27.23
3	E4, E8, E9, E10, E11	31.88
4	E2, E4, E10, E17	36.75
5	E3, E4, E7, E8, E9	36.80
6	E4, E8, E10, E17	36.88
7	E2, E4, E11, E16	37.31
8	E4, E9, E11, E16	38.00
9	E4, E16, E17	43.00
10	E2, E4, E11, E20	46.31

without relying on single aspect in Equation (3). For instance, the results are differentiated, even if the number of members in each Interdiction Surface is the same.

4.2. Ranking Vulnerability Remediations. When security analysts have got the optimal Interdiction Surface which enables to eliminate all the APs in the current context of the ICS, a subsequent task is to decide which vulnerability is remedied first. Specifically, concerning on the vulnerabilities in the selected Interdiction Surface, it needs to provide a ranking list of the remediation. And a detailed schedule for the security maintenance is made to coordinate with plans of the industrial production.

In this phase, we employ a mix of more AP-based metrics to rank vulnerability remediations. The reason for the combination of the metrics is that it makes up for the shortcomings when each metric is used alone. For examples, the shortest AP reflects the least effort exerted by an attacker whereas it ignores multiple ways to reach the final goal that is captured by the number of APs. Moreover, the expectation of AP lengths indicates the average efforts made by attackers whereas it ignores the exploit likelihood which is captured by the probability of AP.

Let us proceed to analyze the motivating example. Assuming that only one vulnerability is remedied at a time, we attempt to answer how the sequence of removing each vulnerability in the selected Interdiction Surface has an influence on the AP-based metrics while interdicting all APs. First of all, all APs in the sample AG is mapped into multiple AMCs, forming an absorbing Markov-based state transition graph shown in Figure 3. Note that the value on each edge is relabeled as the transition probability. And then, two cases are illustrated that different sequences of removing edges may achieve the same aim of eliminating all APs in the AG. In this figure, a red solid line denotes a removal of one edge, and a blue dotted line denotes passively a disappearing edge, and the nodes it points to lose all connectivity with other nodes. Compared with these two cases, it is observed that the sequence of removing each edge results in the changes of the transition probability as well as the efficiency to eliminate the APs.

Furthermore, the changes of the AP-based metrics in these two cases are demonstrated in Tables 1 and 2 so as to quantify our discoveries. The first three basic AP-based metrics have the same trend in each case, whereas the rate of the changes is distinctly different. Taking the

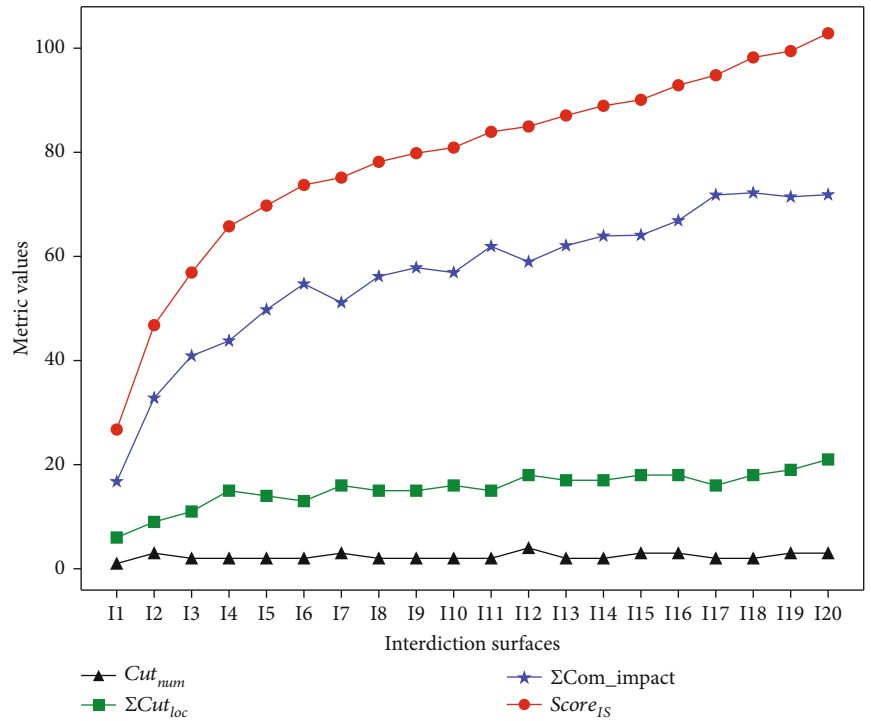

Figure 8: Prioritizing Interdiction Surface.

Table 7: 20 minimum cut sets chosen at random.

No.	Interdiction Surface
I1	E10, E11, E2, E4
I2	E17, E3, E4, E7, E8
I3	E20, E9, E11, E13, E15
I4	E20, E8, E9, E10, E11, E13, E15
I5	E17, E20, E10, E6, E13, E15
I6	E2, E19, E20, E11, E6, E15
I7	E3, E7, E8, E9, E5, E13, E15, E20
I8	E2, E19, E20, E10, E11, E6, E15
I9	E17, E2, E20, E6, E12, E13, E15
I10	E3, E20, E7, E9, E5, E12, E13, E15
I11	E2, E19, E20, E11, E6, E12, E15
I12	E6, E5, E12, E13, E14, E15, E16, E17
I13	E17, E2, E18, E10, E6, E13, E14, E15
I14	E16, E2, E19, E11, E6, E12, E14, E15
I15	E7, E8, E9, E11, E12, E15, E19, E20
I16	E8, E9, E10, E11, E14, E15, E18, E19
I17	E17, E3, E19, E7, E20, E5, E15
I18	E17, E3, E19, E7, E20, E6, E5, E15
I19	E3, E7, E8, E9, E5, E12, E15, E19, E20
I20	E3, E7, E8, E6, E5, E12, E14, E15, E17, E19

number of APs as an example, its value of each step decreases more in case B than that in case A, which means attackers may have less opportunities to reach their expected goal. In particular, we quantify the cumulative effect resulted from the removal of each edge by summing the probability of eliminated APs. Similarly, from the decrease of sum, it is more significant by removing the edge $S_0 \longrightarrow S_2$ in case B than removing the edge $S_1 \longrightarrow S_3$ in case A.

Therefore, two conclusions can be drawn, according to the analysis for the example. One is that it is effective to cope with the problem of this subsection for ranking the vulnerability remediations based on the combination of a series of the AP-based metrics. The other is that the quantifiable changes are able to assess the security level of the whole system. The latter will be described in the next subsection. The former conclusion concerning on a principle for ranking vulnerability remediations is formulized as

$$\text{Socre}_R(\text{Vul}) = 0.33 \times \left[\text{EP} + \text{Num}_{\text{SAP}}(\text{Vul}) + \sum_{i=1}^{k} P_{\text{E-APMarkov}}(i)\right] - \text{Exp}_{\text{APlen}}(\text{Vul}), \tag{5}$$

where $\text{Num}_{\text{SAP}}(\text{Vul})$ denotes the number of the shortest APs with respect to the vulnerability which represents an edge in the AG, k denotes the number of the eliminated APs once removing an edge, $P_{\text{E-APMarkov}}(i)$ denotes the probability of the ith eliminated AP, and $\text{Exp}_{\text{APlen}}(\text{Vul})$ denotes the expectation of AP lengths, and the AP contains the vulnerability. Except for the EP, the other terms in Equation (5) are normalized.

According to the Equation (5), the results are $\text{score}_R(S_0 \longrightarrow S_2) = 0.353$ and $\text{score}_R(S_1 \longrightarrow S_4) = 0.033$. Hence, the ranking result is $(S_0 \longrightarrow S_2) \gg (S_1 \longrightarrow S_4) \gg (S_1 \longrightarrow S_3)$ which is consistent with the previous analysis.

Table 8: Vulnerability remediation metric in each step.

No.	Edge in AG	Score in P2	Composite metric
1	E4	0.54	0.83
2	E11	0.308	072
3	E10	0.051	0.60
4	E2	—	—

4.3. Calculating Composite Security Metrics. At a high level, the security analysts are not satisfied with just ranking the vulnerability remediations. Meanwhile, they pay more attention to some security-relevant attributes the ICS possesses in reality. The attributes in our work concentrate on the AP-based metrics. However, more or less drawbacks exist in such metrics because of their one-sidedness, thus misleading the analysts to make the unreasonable decision. To address that, we propose a composite security metric in the situation of quantifying security level after each vulnerability remediation.

The other conclusion derived from the example is described as follows. Changes in the AP-based metrics are treated as benefits from the vulnerability remediations, which also turns to aggravate much burden on the multistep and multihost attacks. For instance, the decrease in the number of APs as well as the increase in both the expectation of AP lengths and the probability of APs may make the attacker take more and more effort associated with the time and costs until they could not afford and choose to give up the target. It means the system security level is enhanced as well. Apart from the benefits, the ranking results in the **P2** simultaneously affect the security level. The more appropriately vulnerabilities are ranked, the better the effect of preventing the ICS from the attacks can be attained.

To fuse these two aspects including the benefits and the ranking results, we introduce an approach called Triangle Module Operator into the proposed methodology to assess their combined effects on the security of the ICS. The approach has an advantage in fusing heterogeneous functions of different factors related to a system [28]. It strengthens and reconciles these factors to achieve a comprehensive evaluation, in which a single factor could not absolutely dominate in the result. As a result, the approach is suitable to balance the benefits and the ranking results within the composite metric.

The composite metric for a given vulnerability Vul is given as

$$\text{Com\_metric}(\text{Vul}) = \frac{\text{Ra} \times \text{Be}}{1 - \text{Ra} - \text{Be} + 2 \times \text{Ra} \times \text{Be}}, \quad (6)$$

where $\text{Vul} \in \text{IS}$, Ra denotes the ranking function, and Be denotes the benefit function. The ranking function is defined as

$$\text{Ra} = 1 - \frac{r(\text{Vul})}{\sum_{m \in \text{IS}} r(m)}, \quad (7)$$

where $r(\cdot)$ represents the ranking result for each member in the Interdiction Surface. The benefit function is defined as

$$\text{Be} = 0.25 \times \left(\sum P_{\text{APMarkov}} + P_{\text{IS}} + \text{EP} + \Delta M \right), \quad (8)$$

where $\sum P_{\text{APMarkov}}$ denotes the sum of the probability of APs and the APs contain the vul, and P_{IS} denotes the probability of the Interdiction Surface, which is defined as

$$P_{\text{IS}} = 1 - \prod_{m \in \text{IS}} [1 - \text{EP}(m)], \quad (9)$$

and ΔM represents the changes of three AP-based metrics, which is defined as

$$\Delta M = 0.33 \times (\Delta \text{Num}_{\text{APs}} + \Delta \text{Exp}_{\text{APlen}} - \Delta \text{Len}_{\text{SAP}}), \quad (10)$$

where $\Delta \text{Num}_{\text{APs}}$ denotes the changes of the number of APs, $\Delta \text{Exp}_{\text{APlen}}$ denotes the changes of the expectation of AP lengths, and $\Delta \text{Len}_{\text{SAP}}$ denotes the changes of the shortest AP. Note that the values of changes of three AP-based metric are normalized to adapt for the accumulated probability in Equation (8).

The main procedure for the composite metric calculation is shown in a flow chart (Figure 4). It combines the results obtained in the first two phases. The proposed system security metric for a given ICS is the sum of each composite metric calculated after each vulnerability remediation. After all APs are eliminated with the removal of the last edge in the selected Interdiction Surface, the ΔM cannot be calculated. Hence, the loop-out condition in Figure 4 is that there is only one edge in the Interdiction Surface.

According to Figure 4, the results of the motivating example are $\text{Com\_metric}(S_0 \longrightarrow S_2) = 0.67$ and $\text{Com\_metric}(S_1 \longrightarrow S_4) = 0.42$, respectively. The security-level value for the example system is the sum of these two values, 1.09.

5. Case Study

In this section, we validate the effectiveness of the proposed methodology with a complete and nearly realistic case. Initially, a hypothetical ICS scenario is introduced in Subsection 5.1. Then, a vulnerability-oriented AG is constructed in Subsection 5.2 to elaborate the representations of each node and each edge. In Subsection 5.3, each AP is mapped into the AMC to obtain an absorbing Markov-based state transition AG, and the probability of AP is calculated as well. Finally, the composite metric is analyzed to assess the security level in the situation of the vulnerability remediations in Subsection 5.4.

The proof-of-concept system is implemented in Python (version 3.8.10), running on an Ubuntu (version 20.04.1 LTS) Linux virtual machine assigned with the Quad-core CPUs and the 4 G RAM. All directed node-edge diagrams and all statistical figures are demonstrated, respectively, by the Graphviz (version 0.16) and the Matplotlib (version 2.2.5).

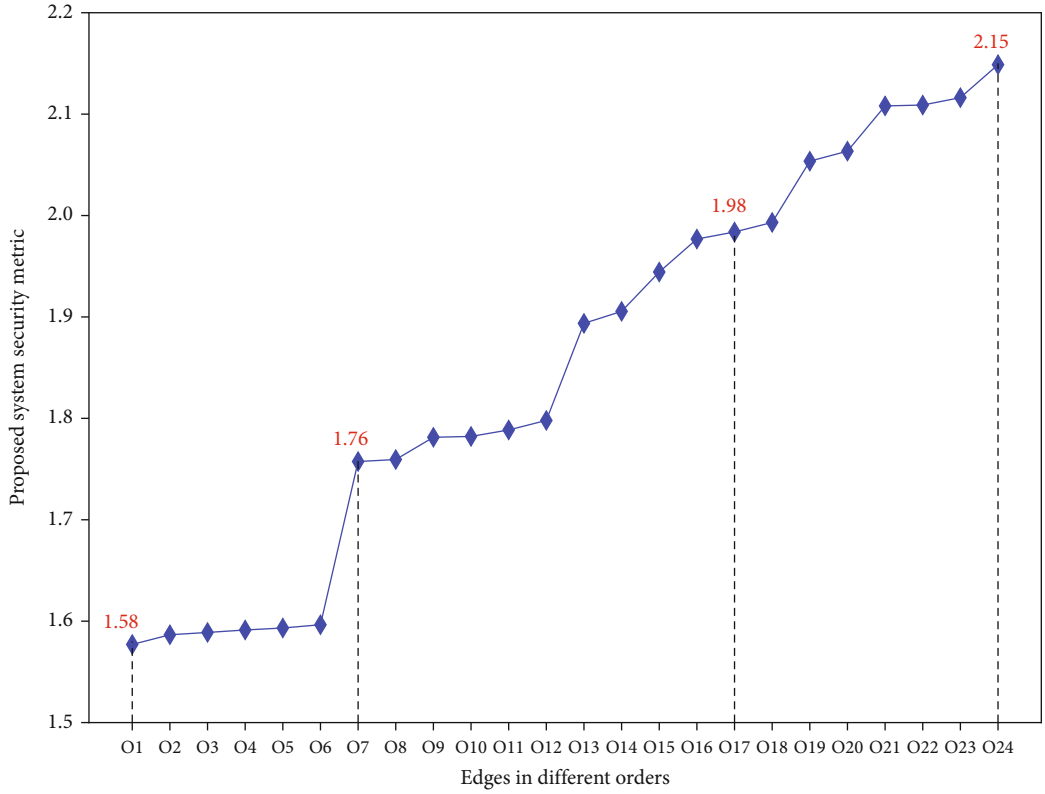

Figure 9: Proposed system security metric.

5.1. Hypothetical ICS Scenario. A hypothetical ICS scenario is illustrated in Figure 5, which is referred from the literature [29]. It shows a simplified SCADA system whose structure is in accordance with the real-world practice. The system is generally divided into three network domains. The network domain regarding the enterprise business process is omitted because it is out of our research scope. However, we assume that a compromised computer in that domain is a point of entry that is exploited by all possible multistep and multihost attacks targeting the physical process. The supervision and control network domain undertakes tasks such as an operating data acquisition and the remote monitoring on the industrial devices. Devices in this domain such as the engineering workstation (EWS) and the operation workstation (OWS) contain commercial-off-the-shell hardware and software whose known vulnerabilities could be always discovered. The production network domain is responsible for manipulating and regulating field devices by a series of networked and embedded ones such as the PLCs and the Human Machine Interface (HMI). Those devices gradually attracted the attention by attackers who aim to destroy the physical process. In this scenario, the PLCs have the master-slave architecture. We assume that the ultimate attack goal is the slave PLC.

5.2. Vulnerability-Oriented Attack Graph. A vulnerability-oriented AG for the ICS scenario is shown in Figure 6. The source node S_0 represents the compromised computer, and the terminal node T represents the slave PLC. The AG contains 11 nodes and 20 edges, which generates 16 APs terminated at the T. The construction approach for the AG is on the basis of our previously presented work [30] that focuses on an automatic planning-based AP discovery. In addition, the nodes in the graph are rearranged to demonstrate in a hierarchical way. It is convenient to test the Interdiction Surface while implementing Algorithm 1.

As listed in Table 3, the nodes in the AG represent the affected components on specific devices. Moreover, the access control relations among the components are given. The values in the last column represent the component impact, which are designated according to the response (R4) in Subsection 4.1. In particular, the impact value of the compromised computer is set to 1000 just for the purpose of the analysis. On one side, it avoids the ideal result that the Interdiction Surface only contains the edge E_1. On the other side, the optimal Interdiction Surface could be selected by properly adjusting the values of the component impact. It may be an effective way to reselect the vulnerability remediations owing to some special cases. For an example, industrial devices are unable to patch bugs in a continuous operation task.

The vulnerabilities from the National Vulnerability Database (NVD, https://nvd.nist.gov/) are assigned to the affected components disclosed in recent years. For simplicity, each component only includes one vulnerability. Each edge is related to one vulnerability encoded with a unique Common Vulnerabilities and Exposures (CVE) identification. The severity and the ES are directly searched in the CVSS by using the unique identification as an index. The information on the vulnerability is collected in Table 4.

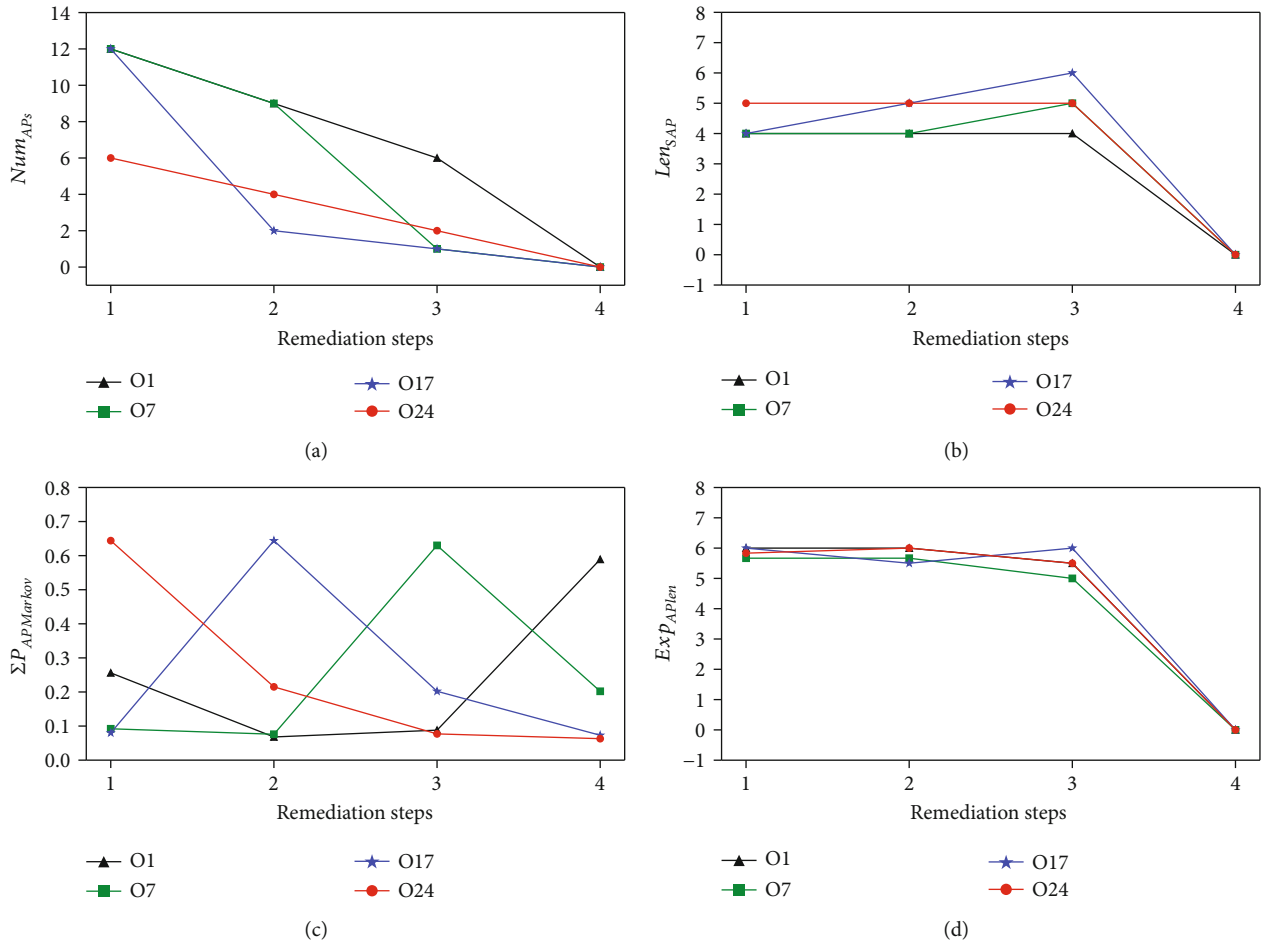

Figure 10: Existing security metric analysis.

Especially, two different edges correspond to the same vulnerability in the table because both endpoints of each edge represent the different affected components.

5.3. Absorbing Markov Chain. An absorbing Markov-based state transition AG is illustrated in Figure 7. Each AP in Figure 6 is mapped into the AMC. The value on each edge represents the transition probability whose initial value equals EP. Except for the source node and the terminal node, each node is added an edge pointing to itself, which represents a situation that means a failure of transition to the other state. And the initial value of the edge is set to 1. Given that all transition probability for each state in the AMC should be added up to 1, the value of each edge is recalculated as shown in Figure 7. Note that the edges pointing to themselves are only involved into the calculation on the AMC. In other words, such edges only have effects on the calculation of transition probability.

In Table 5, the top 10 probabilities of AP are listed among all APs. It is observed that the value of the probability has become quite small after multiplying all the transition probabilities for the edges of the AP, as the similar method presented in [10]. Subtle differences in numerical values between two APs make it difficult to compare, let alone to assess the security level for a given system based on the single metric. Unfortunately, the metric ignores the exploitability of each vulnerability in the situation of its remediation. Take the fifth AP and the eighth AP for instance. Excluding all other factors, the probability value of the fifth AP is almost twice as much as the one of the eighth AP. However, the eighth AP contains higher severity vulnerability than the fifth AP.

5.4. Proposed Composite Metric Analysis. A total of 215 Interdiction Surfaces are discovered for the ICS scenario. The top 20 of the results are listed in Table 6. It is obvious that the optimal Interdiction Surface is the set {E2, E4, E10, E11} with the lowest score in **P1**. The lower the score is, the smaller the impact on the ICS is. Meanwhile, the effect from the vulnerability remediations is relatively optimal. For instance, both the optimal Interdiction Surface and the tenth one contain the same number of the edges. The difference lies in the combination of the edges. E10 is involved into the optimal Interdiction Surface but E20 is into the tenth one. The devices connected to E10 are OPC Server and OWS2 in the supervision and control network. The vulnerability remediations have less influence on the physical process. However, the devices connected to E20 are the master

PLC and the slave PLC. These devices directly affect the physical process while remedying the vulnerability.

In order to further demonstrate the effectiveness of prioritizing the Interdiction Surfaces, the value of three terms in Equation (3) and the final result are shown in Figure 8. 20 horizontal axis points are listed in Table 7 representing the Interdiction Surfaces. We obtain a list with prioritizing all Interdiction Surface on the basis of their results. And then, one Interdiction Surface is taken out of each ten among the list until the total number of them reaches 20. It is observed that only the curve of the score_{IS} has a monotonically increasing trend, which means that none of three terms determines in isolation to get the optimal Interdiction Surface.

In Table 8, the ranking results of the edges in the optimal Interdiction Surface and the composite metric for each vulnerability are listed as follows. The value of the system security metric for the ICS scenario is the sum of the composite metric in each step, and its result is 2.15.

The composite metric is obtained for vulnerability remediations in the context of the ICS; however, it is ought to prove whether the metric can be taken place by the AP-based security ones in the literature [6, 23, 24] or not. Part of that point has been mentioned in Subsection 4.2 by a simple example. Some more intuitive comparisons between the proposed metric and the existing ones used in isolation are shown in Figures 9 and 10.

All permutations of the edges in the optimal Interdiction Surface are obtained, 24 sequences. The proposed system metric is calculated for each sequence. According to the value of the metric, each sequence is ranked and labeled as Oj where $j = 1, 2 \cdots, 24$. As illustrated in Figure 9, the sequence with the highest value is O24 whose sequence is $\text{E4} \gg \text{E11} \gg \text{E10} \gg \text{E2}$. The sequence corresponds to the result in Table 7. We select 4 sequences that are O1, O7, O17, and O24 so as to observe the changes of the existing AP-based metrics, as illustrated in Figure 10. The four selected sequences are intentionally assigned different initial edges, and the other three edges are in random order. The value of the remediation step on the horizontal axis points is the order of the edges in these four sequences.

Obviously, it is difficult to decide which sequence is optimal by the comparison of results from the four cases of Figure 10. Recall that the shortest AP and the expectation of AP should have the similar trend to assess the security level. However, the inconsistent conclusions for O7 and O17 are drawn between case (b) and case (d). The reason why the proposed metric is comparable is that the Triangle Module Operator plays a desirable role in reconciliation while fusing the ranking results and the benefits from the basic AP-based metrics. What is worse, the existing metrics lack consideration for the component impact so that they have no capability of the system-level assessment for the ICS scenario.

6. Conclusion

In this paper, we have proposed a composite metric for the vulnerability remediations in the ICS. The proposed metric integrates the urgent security demands into the novel definition called the Interdiction Surface including the vulnerabilities that are removed to eliminating all APs. Ranking the remediations for vulnerabilities is an effective way to decrease the probability to launch the multistep and multihost attacks as soon as possible. The composite metric overcomes the shortcomings of the existing ones used in isolation, which is more reasonable to assess the security level for the ICS. The entire procedure on the basis of the AP-based analysis is not only theoretical support but also practical to implement in reality.

Our future research direction is to improve the scalability for a large-scale environment of the ICS. Note that finding out all minimum ECSs in the AG is not trivial due to the fact that it is an NP-complete problem. More related algorithms on the fast enumeration of the ECSs will be introduced to the proposed methodology. In addition, parallel computing method based on hypergraph partitioning for the AG will be explored to calculate the composite metric at the same time so as to enhance the solving efficiency. And the AP reduction strategy is attempted to avoid invalid paths that are probably infeasible to reach the goal.

Data Availability

The data used to support the findings of this study are available from the corresponding author upon request.

Conflicts of Interest

All the authors hereby declare no conflicts of interest.

Acknowledgments

Our work is supported by the National Key R&D Program of China (2021YFB2012400).

References

[1] M. M. Ahmadian, M. Shajari, and M. A. Shafiee, "Industrial control system security taxonomic framework with application to a comprehensive incidents survey," *International Journal of Critical Infrastructure Protection*, vol. 29, article 100356, 2020.

[2] Z. C. Hu, X. Z. Yu, J. T. Shi, and L. Ye, "Abnormal event correlation and detection based on network big data analysis," *Computers, Materials & Continua*, vol. 69, no. 1, pp. 695–711, 2021.

[3] X. F. Wang, R. Ma, D. H. Tian, and X. J. Wang, "VCPEC: vulnerability correlation analysis based on privilege escalation and Coritivity theory," in *2020 the 10th International Conference on Communication and Network Security*, pp. 99–108, New York, NY, USA, 2020.

[4] A. Ur-Rehman, I. Gondal, J. Kamruzzaman, and A. Jolfaei, "Vulnerability modelling for hybrid industrial control system networks," *Journal of Grid Computing*, vol. 18, no. 4, pp. 863–878, 2020.

[5] I. Stellios, P. Kotzanikolaou, and C. Grigoriadis, "Assessing IoT enabled cyber-physical attack paths against critical systems," *Computers and Security*, vol. 107, article 102316, 2021.

[6] N. Idika and B. Bhargava, "Extending attack graph-based security metrics and aggregating their application," *IEEE Transactions on Dependable and Secure Computing*, vol. 9, no. 1, pp. 75–85, 2012.

[7] B. C. Che, L. Liu, and H. L. Zhang, "KNEMAG: key node estimation mechanism based on attack graph for IoT security," *Journal on Internet of Things*, vol. 2, no. 4, pp. 145–162, 2020.

[8] U. Garg, G. Sikka, and L. K. Awasthi, "Empirical analysis of attack graphs for mitigating critical paths and vulnerabilities," *Computers & Security*, vol. 77, pp. 349–359, 2018.

[9] X. G. Liu, "A network attack path prediction method using attack graph," *Journal of Ambient Intelligence and Humanized Computing*, pp. 1–8, 2020.

[10] K. Bi, D. Z. Han, G. C. Zhang, K. C. Li, and A. Castiglione, "K maximum probability attack paths generation algorithm for target nodes in networked systems," *International Journal of Information Security*, vol. 20, no. 4, pp. 535–551, 2021.

[11] H. Wang, Z. F. Chen, J. P. Zhao, X. Q. Di, and D. Liu, "A vulnerability assessment method in industrial Internet of Things based on attack graph and maximum flow," *IEEE Access*, vol. 6, pp. 8599–8609, 2018.

[12] M. Barrère, C. Hankin, N. Nicolaou, D. G. Eliades, and T. Parisini, "Measuring cyber-physical security in industrial control systems via minimum- effort attack strategies," *Journal of Information Security and Applications*, vol. 52, p. 102471, 2020.

[13] M. Barrère and C. Hankin, "Analysing mission-critical cyber-physical systems with AND/OR graphs and MaxSAT," *ACM Transactions on Cyber-Physical Systems*, vol. 5, no. 3, pp. 1–29, 2021.

[14] B. Yiğit, G. Gür, F. Alagöz, and B. Tellenbach, "Cost-aware securing of IoT systems using attack graphs," *Ad Hoc Networks*, vol. 86, pp. 23–35, 2019.

[15] G. Stergiopoulos, P. Dedousis, and D. Gritzalis, "Automatic analysis of attack graphs for risk mitigation and prioritization on large-scale and complex networks in Industry 4.0," *International Journal of Information Security*, vol. 21, no. 1, pp. 37–59, 2022.

[16] P. Mell, J. Shook, and R. Harang, "Measuring and improving the effectiveness of defense-in-depth postures," in *Proceedings of the 2nd Annual Industrial Control System Security Workshop on - ICSS '16*, pp. 15–22, Los Angeles, CA, USA, 2016.

[17] A. T. Al Ghazo and R. Kumar, "Identification of critical-attacks set in an attack-graph," in *2019 IEEE 10th annual ubiquitous computing, Electronics & Mobile Communication Conference (UEMCON)*, pp. 0716–0722, New York, NY, USA, 2019.

[18] G. George and S. M. Thampi, "Vulnerability-based risk assessment and mitigation strategies for edge devices in the Internet of Things," *Pervasive and Mobile Computing*, vol. 59, article 101068, 2019.

[19] G. George and S. M. Thampi, "Combinatorial analysis for securing IoT-assisted Industry 4.0 applications from vulnerability-based attacks," *IEEE Transactions on Industrial Informatics*, vol. 18, no. 1, pp. 3–15, 2022.

[20] G. Cybenko and G. F. Stocco, "Asymptotic behavior of attack graph games," in *Lecture Notes in Computer Science (including subseries Lecture Notes in Artificial Intelligence and Lecture Notes in Bioinformatics)*, pp. 104–112, Springer International Publishing, 2018.

[21] A. Ben Yaghlane, M. N. Azaiez, and M. Mrad, "System survivability in the context of interdiction networks," *Reliability Engineering and System Safety*, vol. 185, pp. 362–371, 2019.

[22] M. Mrad, U. S. Suryahatmaja, A. Ben Yaghlane, and M. N. Azaiez, "Optimalk cut-setsin attack/defense strategies on networks," *IEEE Access*, vol. 8, pp. 131165–131177, 2020.

[23] M. Pendleton, R. Garcia-Lebron, J. H. Cho, and S. Xu, "A survey on systems security metrics," *ACM Computing Surveys*, vol. 49, no. 4, 2017.

[24] H. Hu, Y. L. Liu, H. Q. Zhang, and Y. C. Zhang, "Security metric methods for network multistep attacks using AMC and big data correlation analysis," *Security and Communication Networks*, vol. 2018, 14 pages, 2018.

[25] C. Shan, B. Jiang, J. Xue, F. Guan, and N. Xiao, "An approach for internal network security metric based on attack probability," *Security and Communication Networks*, vol. 2018, Article ID 3652170, 11 pages, 2018.

[26] P. Mukherjee and C. Mazumdar, "'Security concern' as a metric for enterprise business processes," *IEEE Systems Journal*, vol. 13, no. 4, pp. 4015–4026, 2019.

[27] Y. C. Zhao, Y. B. Che, T. J. Lin et al., "Minimal cut sets-based reliability evaluation of the more electric aircraft power system," *Mathematical Problems in Engineering*, vol. 2018, Article ID 9461823, 11 pages, 2018.

[28] Y. N. Cao and M. Q. Wu, "RPL based on triangle module operator for AMI networks," *China Communications*, vol. 15, no. 5, pp. 162–172, 2018.

[29] A. Abou el Kalam, "Securing SCADA and critical industrial systems: from needs to security mechanisms," *International Journal of Critical Infrastructure Protection*, vol. 32, article 100394, 2021.

[30] Z. B. Wang, Y. F. Zhang, Z. Y. Liu, X. J. Wei, Y. L. Chen, and B. Wang, "An automatic planning-based attack path discovery approach from IT to OT networks," *Security and Communication Networks*, vol. 2021, Article ID 1444182, 18 pages, 2021.

Hindawi
Wireless Communications and Mobile Computing
Volume 2022, Article ID 1621445, 14 pages
https://doi.org/10.1155/2022/1621445

Research Article

Coordinated Optimization Control System of Big Data Intelligent Production Line

Shi He,[1] Guohua Cao,[1,2] Guoqing Ma,[1,3] Jingsong Duan,[1] and Jimeng Bai[1]

[1]*College of Mechanical and Electrical Engineering, Changchun University of Science and Technology, Changchun City, 130022 Jilin Province, China*
[2]*Chongqing Research Institute of Changchun University of Science and Technology, Chongqing City, 401135, China*
[3]*Wuhu HIT Robot Technology Research Institute Co., Ltd., Wuhu City, 241000 Anhui Province, China*

Correspondence should be addressed to Guohua Cao; caogh@cust.edu.cn

Received 19 February 2022; Revised 24 March 2022; Accepted 20 April 2022; Published 13 May 2022

Academic Editor: Junjuan Xia

A mature coordinated and optimized control system can bring timeliness and benefits to the production line. This paper firstly exemplifies the big data intelligent production line coordination control system model and algorithm. They, respectively, include the intelligent production line coordination control system model, the big data intelligent coordination control model, and the hardware key electrical control system model of the air conditioning assembly big data intelligent production line, taking the tea production line as an example. The parameters of the coordinated control model are identified by the algorithm and system design, which considers and adjusts the functional requirements of the system to maintain the stable operation of the software system and store and transmit efficiently. To achieve efficient fit between functional requirements and modules, it created a complete assembly automation production line that meets actual needs. Then, the experiment of big data intelligent coordination and optimization control system based on cement clinker production line is carried out, and the intelligent coordination control system of cement clinker is designed. Compared with the data, it can be seen that in the coordinated control mode, the fluctuation of the temperature and pressure of the main steam is smaller, which can make the entire power generation system operate safely and stably. Based on the fuzzy control of the waste heat boiler and steam turbine load coordination control requirements, the reasonable coordination control of the boiler system and the generator set is carried out through fuzzy control, and the optimization and adjustment are carried out. Finally, the comparison and analysis of fuzzy control and traditional control experiments are carried out, and a coordinated optimization system using fuzzy control is obtained. It requires less feeding material, consumes less energy in the production process, generates more power, and can increase the average income by 4.87%, which has a good practical application prospect.

1. Introduction

The intelligent production line under big data is composed of many complex components, generally including the control system, related process equipment, auxiliary equipment, and transmission system. The control methods of the control system include the feedback control method, open-loop control method, and open-loop control system controlled by a given amount. However, according to the actual needs of various types of production, the specific structure of the intelligent production line will have different changes. If it is classified according to the structure, it can generally be divided into automatic lines for special equipment, automatic lines for general equipment, and automatic lines with or without storage. With the rapid development of modern science and technology, the control technology in the production process has also been significantly improved. At present, in the production process of most enterprises, the distributed control system is generally used. The distributed control system is a new generation of instrument control

system based on the microprocessor, which adopts the design principles of decentralized control functions and centralized display operation, taking into account the separation and autonomy and comprehensive coordination. And then, the system has high requirements for the operator's technology and professionalism and relies on manual operation and processing, so the use of this system requires a large amount of work learning cost. In order to meet the increasing production demand, the existing control technology must be further optimized, so that the production efficiency of the entire production process can be significantly improved. Therefore, it is very necessary to conduct in-depth research on control technology, and the research results will provide great help and economic support for real production.

The innovation of this experiment is to use fuzzy control to design and optimize the coordination and optimization system of the intelligent production line to achieve a stable state, improve economic benefits, and control accuracy, which can be better applied in real life. The significance of this paper is to make the intelligent production line have better operation effect and precision control, stronger development adaptability, and higher practical significance.

2. Related Work

Yan et al. propose an optimized and coordinated model predictive control (MPC) scheme for a doubly fed induction generator (DFIG) with a DC-based converter system to improve the efficiency and dynamic performance of a DC grid. In this configuration, the stator and rotor of the DFIG are connected to the DC bus through voltage source converters, namely, the rotor-side converter (RSC) and the stator-side converter (SSC) [1]. Li et al. propose an optimal coordination method for electric vehicles (EVs) participating in frequency regulation (FR) under different power system operating states (PSOS). In the proposed method, the FR power of electric vehicles and generators is coordinated with different optimization objectives for a safe and economical operation of the power system [2]. Zhu et al. said that the efficient use of big data can improve the intelligence and automation of the manufacturing process, provide high-quality products and just-in-time production, increase productivity, and reduce costs. For example, by analyzing factory floor data, equipment monitoring data, and enterprise manufacturing databases, it can help store, explore, and make complex decisions about manufacturing systems [3]. Lade et al. believe that a smart production cell can be viewed as a large interconnected industrial system of materials, parts, machines, tools, inventory, and logistics that can relay data and communicate with each other. While the traditional focus has been on machine health and predictive maintenance, manufacturing has also begun to focus on analyzing data from the entire production line [4]. Liu et al. proposed the Mamdami fuzzy control logic to overcome the motion control of the multi-DOF TWIP robot and make its motion controlled smoothly. By introducing two additional degrees of freedom slider and swing configurations, the robot can maintain its vertical posture even when climbing and descending on slopes [5]. Xu et al. synthesized an adaptive fuzzy controller with a novel update law based on disturbance estimation and fuzzy approximation. The stability analysis of the closed-loop system is strictly established by the Lyapunov method. It verifies the performance of the proposed controller by simulation, obtaining faster convergence speed and higher accuracy [6]. However, these studies all have the problems of insufficient demonstration or unclear goals, which need to be further improved.

3. Big Data Intelligent Production Line Coordination Control System Model and Algorithm

3.1. An Intelligent Production Line Coordination Control System Model with a Tea Production Line as an Example. Before designing and developing the entire remote monitoring and control system, it is first necessary to clarify the user's requirements for the system and related functions [7]. In the process of tea production, users need to be able to monitor and control the real-time situation of the entire tea production line anytime, anywhere, so it is necessary to arrange relevant data sensors and remote communication devices on the tea production line [8]. In addition to viewing the situation through equipment in the plant, remote needs outside the plant also need to be met, so it is necessary to develop a client that can run on the Android system and can be used on mobile phones and tablets at the same time [9]. Among them, the two parts of the remote server and the remote database constitute the server unit, and the entire remote monitoring and control system is mainly composed of PLC, display screen, sensors, etc. After the PLC is put into operation, its working process is generally divided into three stages, namely, input sampling, user program execution, and output refresh. Completing the above three stages is called a scan cycle. During the whole operation period, the CPU of the programmable logic controller repeatedly executes the above three stages at a certain scanning speed. Its structure is shown in Figure 1.

According to the different usage environments of users, the following suggestions are put forward: In the case of maintaining the stable operation of the system, it is also necessary to ensure the safe operation of the production equipment in the factory building. Therefore, according to different user usage scenarios, different kinds of operation permissions are hereby assigned. It divides the system login mode into two types according to the user's use environment: one is the onsite mode, and the other is the remote mode. The advantage of this design is that when there are multiple users using the system at the same time, the priority operation authority of the system will be assigned to the user in live mode. At the same time, users in onsite mode have greater system authority to ensure the safety of onsite operations and avoid the risks brought by remote operations [10]. When the user is on site, he has better control over the entire production line, and remote operation has certain unknown risks. Therefore, the reasonable allocation of permissions is particularly important. Permission allocation under multiple users is shown in Figure 2.

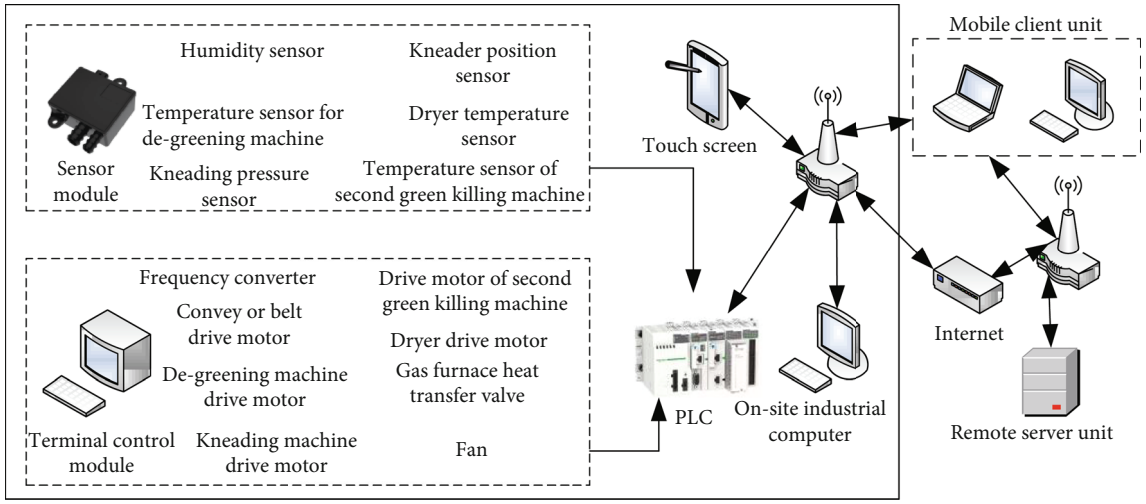

Figure 1: Frame design of the production line intelligent system.

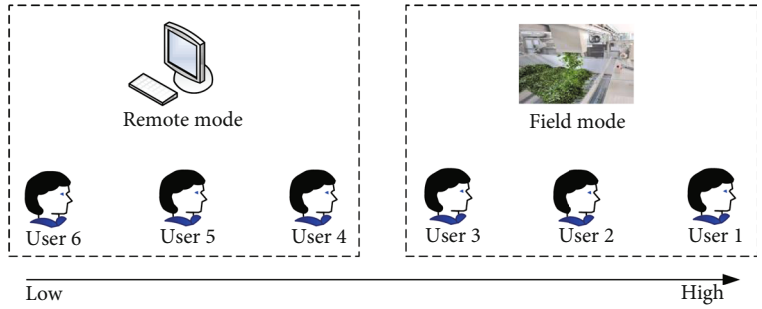

Figure 2: Priority design.

In the intelligent measurement and control system of the tea production line, the software system not only provides convenience and security to the production line but also the actual embodiment of the intelligent measurement and control system. The existence of the software system highlights the characteristics of its intelligence and informatization [11]. By using the relevant functions of the software system, users can timely and efficiently solve various difficult and miscellaneous diseases encountered in the tea production process. The software system not only reduces manpower expenditure but also significantly improves the work efficiency of the entire production line. At the same time, the software system can realize the monitoring, analysis, and transmission of data. For users, the software system can display data concisely and intuitively, store various data safely and stably, and quickly communicate and execute instructions issued by users [12]. In the Android-based intelligent measurement and control system, its software system is mainly composed of touch screen application, PLC, client program, remote server program, and onsite industrial computer-related programs, as shown in Figure 3.

In this intelligent measurement and control system, the most important and basic point is to maintain the stable operation of the software system, the various interfaces of the software system should be user-friendly, and the various data can be stored and transmitted stably and efficiently [13].

3.2. Big Data Intelligent Coordination Control Model. When designing and developing intelligent systems, since human subjective consciousness should be taken into consideration, the existing large-scale system profits cannot be fully applied [14]. The lack of relevant information will also have many adverse effects, so the existing reasonable method is based on the level of actual smart home coordination control. When establishing the overall model, it firstly studies and perfects each of the subsystems, so that the structure level of the entire system is clearer [15].

Let $A_i(s)$ and $B_i(s)$ be used as the state vector of the ith subsystem at time s in v_i-dimension and the control vector in u_i-dimension, respectively; at this time $i = 1, 2, \cdots, U$, we can get

$$A_i^N(s) = \left(a_{i1}(s), a_{i1}(s), \cdots, a_{iv_i}(s)\right), \tag{1}$$

$$B_i^N(s) = \left(b_{i1}(s), b_{i1}(s), \cdots, b_{iu_i}(s)\right). \tag{2}$$

The ith subsystem structure formula in this state can be calculated as follows:

$$A_i(s+1) = X_i(s)A_i(s) + Y_i(s)B_i(s) + Z_i(s)C_i(s) + W_i(s). \tag{3}$$

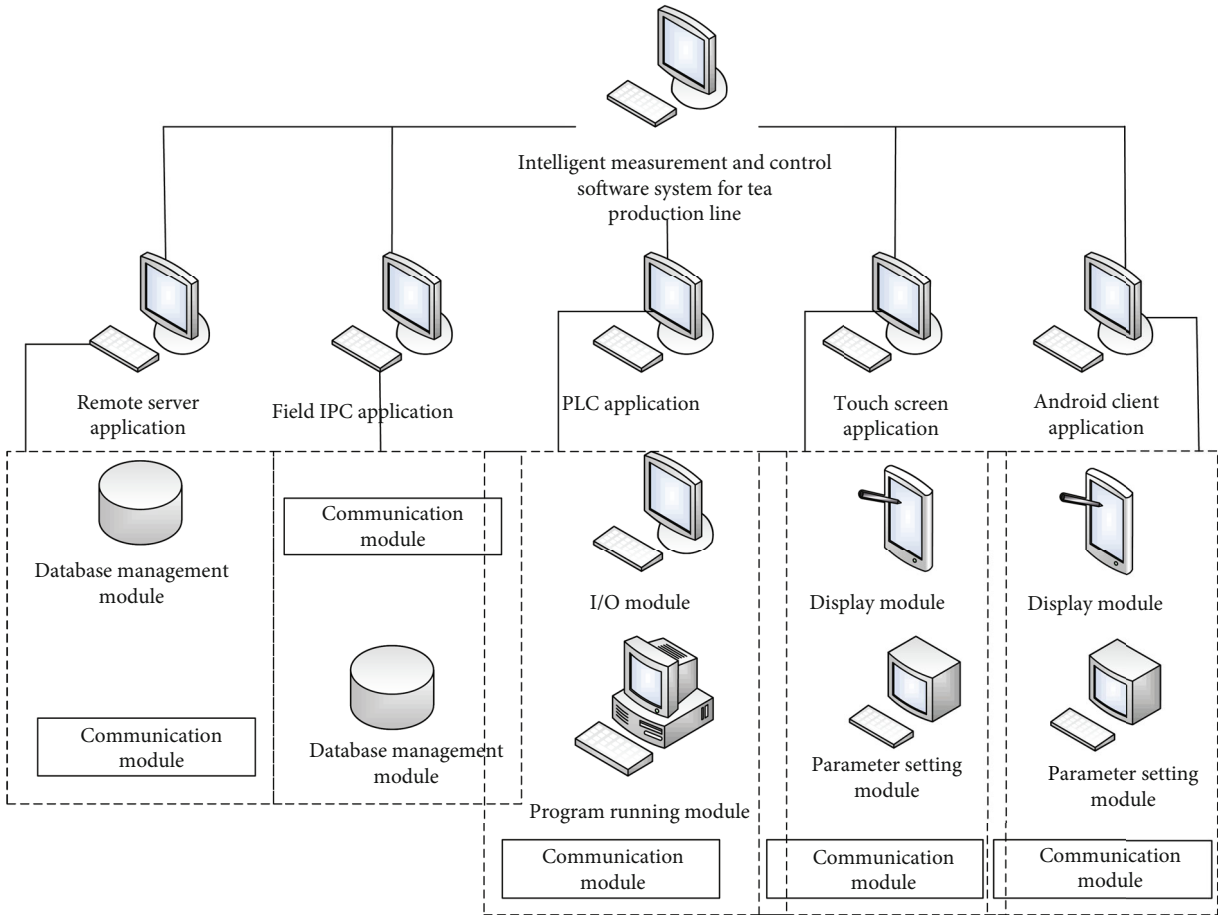

Figure 3: Overall structure of the software system.

The $C_i(s)$ in this formula is a h_i-dimensional associative vector; $X_i(s)$, $Y_i(s)$, and $Z_i(s)$ are used as time-varying system matrices for the corresponding time period; $W_i(s)$ is the random noise at this time; and E_{ik}, F_{ik} is set as a constant matrix; we can get

$$C_i(s+1) = \sum_{i}^{U}\{E_{ik}B_k(s) + F_{ik}A_k(s)\}, i = 1, 2, \cdots, U. \quad (4)$$

Let $D_i(s)$ be the p_i-dimensional output vector of the ith subsystem at time $2s$, then

$$D_i^N(s) = \left(d_{i1}(s), d_{i2}(s), \cdots, d_{ip_i}(s)\right), \quad (5)$$

$$D_i(s) = Q_i(s)A_i(s) + M_i(s), i = 1, 2, \cdots, U, \quad (6)$$

where $Q_i(s)$ is the time-varying parameter matrix and $M_i(s)$ is random noise. The complete model structure of the entire big data system can be expressed as follows:

$$A(s+1) = X(s)A(s) + Y(s)B(s) + Z(s) + C(s) + W(s), \quad (7)$$

$$D(s) = Q(s)A(s) + M(s), \quad (8)$$

$$A^N(s) = \left(A_1^N(s), A_2^N(s), \cdots, A_U^N(s)\right), \quad (9)$$

$$B^N(s) = \left(B_1^N(s), B_2^N(s), \cdots, B_U^N(s)\right), \quad (10)$$

$$D^N(s) = \left(D_1^N(s), D_2^N(s), \cdots, D_U^N(s)\right). \quad (11)$$

The dimensional state vector of this big data intelligent system v can be written as $v = \sum_{i=1}^{N} v_i$, u-dimensional control vector, u-dimensional state vector can be written as $u = \sum_{i=1}^{N} u_i$, and p-dimensional state vector can be written as $p = \sum_{i=1}^{N} p_i$; at this time, we can get

$$A_i(s+1) = X_i(s)A_i(s) + Y_i(s)B_i(s) + Z_i(s) \cdot \left[\sum_{k=1}^{N} E_{ik}B_i(s) + E_{ik}A_i(s)\right] + W_i(s), \quad (12)$$

$$A_i(s+1) = X_i(s)A_i(s) + Z_i(s)\sum_{k=1}^{N} E_{ik}A_i(s) + Y_i(s)B_i(s) + Z_i(s)\sum_{k=1}^{N} E_{ik}B_i(s) + W_i(s). \quad (13)$$

If order

$$\phi^N(s) = \left\{A_1^N(s), A_2^N(s), \cdots, A_U^N(s), B_1^N(s), B_2^N(s), \cdots, B_U^N(s)\right\}, \tag{14}$$

$$\lambda_i(s) = \left\{ \begin{array}{c} Z_i(s)F_x, Z_i(s)F_{i2}, \cdots, Z_i(s)F_{ii} + X_i(s), \cdots Z_i(s)F_{iU}, Z_i(s)F_x, \\ Z_i(s)F_{i2}, \cdots, Z_i(s)F_{ii} + Y_i(s), \cdots Z_i(s)F_{iU} \end{array} \right\}, i = 1, 2, \cdots, U, \tag{15}$$

then it can get

$$A_i(s+1) = \lambda_i(s)\phi(s) + W_i(s), i = 1, 2, \cdots, U. \tag{16}$$

At this point, $\lambda_i(s)$ can be described as a vector:

$$\lambda_i(s) = \left\{\varepsilon_{i1}^N(s), \varepsilon_{i2}^N(s)\varepsilon_{iv_i}^N(s)\right\}, i = 1, 2, \cdots, U. \tag{17}$$

For each state component a_{ik} in the ith subsystem:

$$a_{ik}(s+1) = \phi^N(s)\varepsilon_{ik}(s) + w_{ik}(s)\,; i = 1, 2, \cdots, U\,; k = 1, 2, \cdots, v. \tag{18}$$

If the parameters of the coordinated control model are identified, the parameters need to be predicted. Using the parameter estimation to generalize the gradient recursion algorithm, we can obtain

$$\widehat{\varepsilon}_{ik}(s) = \widehat{\varepsilon}_{ik}(s-1) + \left(\frac{1}{\|\phi(s)\|^2}\right)\phi(s) \cdot \left\{a_{ik}(s+1) - \phi^N(s)\widehat{\varepsilon}_{ik}(s-1)\right\}. \tag{19}$$

$\widehat{\varepsilon}_{ik}(s)$ is the parameter estimate. A sequence of parameter estimates is

$$\left\{\widehat{\varepsilon}_{ik}(1), \widehat{\varepsilon}_{ik}(2), \widehat{\varepsilon}_{ik}(V)\right\}\,; i = 1, 2, \cdots, U\,; k = 1, 2, \cdots, v. \tag{20}$$

The parameter prediction value can be obtained by using the corresponding algorithm to predict the unknown time-varying parameter:

$$\widehat{\varepsilon}_{ik}^*(V+1), \widehat{\varepsilon}_{ik}^*(V+2), \cdots, \widehat{\varepsilon}_{ik}^*(V+l)\,; i = 1, 2, \cdots, U\,; k = 1, 2, \cdots, v_i. \tag{21}$$

The l unknown in equation (21) represents the prediction step size. After the model is simplified, we set the control amount at the future time to $G(s)$; then, the adaptive prediction of the system state can continue, and the adaptive predictor can choose MATLAB:

$$\widehat{a}_{ik}(s+1) = \phi^N(s)\widehat{\varepsilon}_{ik}^*(s). \tag{22}$$

In the multistep forward prediction, when the time value is too large, the following can be derived:

$$\phi^N(s) = \left[A^N(s), B^N(s)\right], \tag{23}$$

$$\varepsilon_{ik}^N(s) = \left[x_{ik}^N(s), y_{ik}^N(s)\right]. \tag{24}$$

For the components of a given state, it is combined with the adaptive control algorithm. The types of adaptive control algorithms include the nonblind algorithm, blind algorithm, and semi-nonblind algorithm. We can get

$$B^{(ik)}(s) = B^{(ik)}(s) + \frac{\widehat{y}_{ik}^*(s)}{\|\widehat{y}_{ik}^*(s)\|^2} \cdot \left\{\widehat{a}_{ik}^*(s+1) - \widehat{x}_{ik}^N(s)a(s) - \widehat{y}_{ik}^N(s)B^{(ik)}(s-1)\right. \tag{25}$$

The corresponding value can be obtained using the adaptive control algorithm.

3.3. The Key Electrical Control System Model of the Hardware of the Air Conditioning Assembly Big Data Intelligent Production Line. The size of the PLC scale is mainly affected by the number of input points and output points. At the same time, the scale of PLC also needs to be adjusted according to actual needs for later expansion. Before starting the design of the system, it is necessary to determine the number of I/O points required, and at this time, it is necessary to consider the functional requirements of the system. And it also needs to take into account factors such as various unexpected situations after the system is completed and related equipment [16]. Therefore, in the early stage of system design, it is necessary for the system to have a certain excess space that can be reserved for later maintenance, upgrade, and expansion. The design margin of this space is at least 20.31%. According to the internal space of the control cabinet and the size of related components, the overall space is optimized and reduced as much as possible to ensure the integration of the entire system [17]. It analyzes the power of various electrical equipment to correctly select the appropriate power supply and draws the corresponding electrical schematics accordingly [18]. The function of the power filter is to obtain a power signal of a specific frequency by connecting the power filter to the power line or to eliminate the power signal of a specific frequency. Using this feature of the power filter, a square wave group or complex noise after passing through the power filter can be turned into a sine wave of a specific frequency. The system wiring diagram is drawn according to the final hardware selection [19]. The reasonable allocation of I/O addresses is mainly based on the final selection of input ports and output ports and controllers. This paper mainly describes the related design of the power system and its electrical control system [17]. In a complete automated production line, there are usually

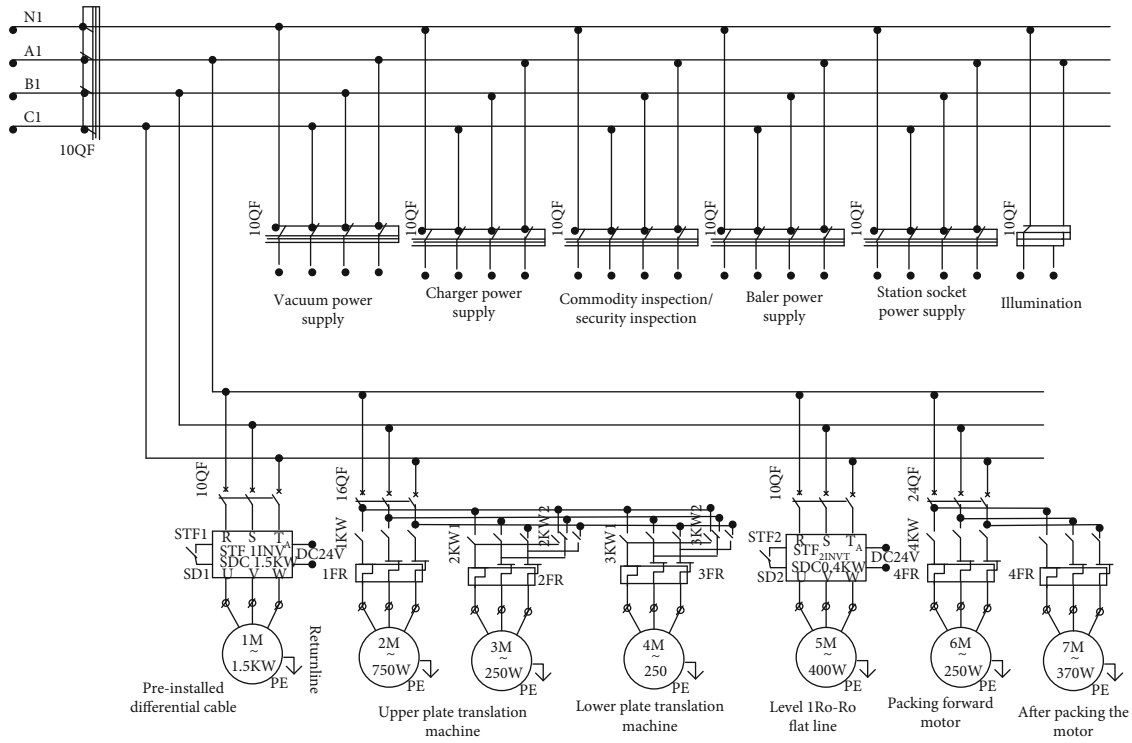

Figure 4: Main circuit power control of air conditioning electrical coordination control system.

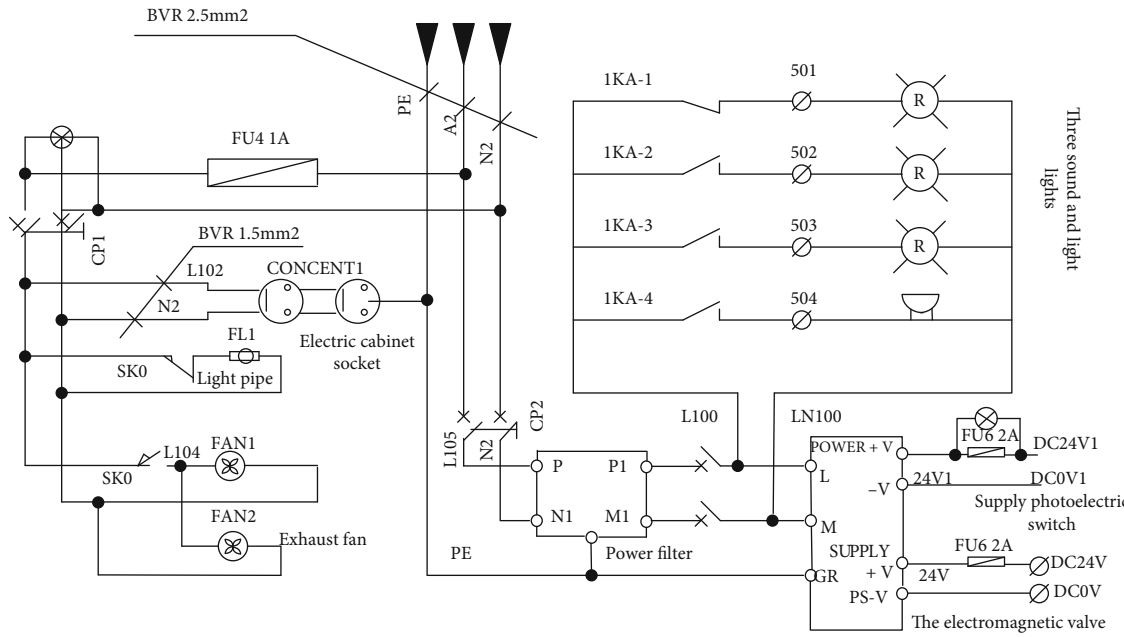

Figure 5: Main power control of air conditioning electrical coordination control system.

dozens of assembly stations, including drive motors, sensors, and automated workstations, and equipment such as low-voltage DC and high-voltage AC are generally designed in the same system. The complete development of the relevant design work of the system is mainly based on the required components and related requirements of the system.

In order to ensure the stable operation of the air conditioning assembly automation, a reasonable electrical diagram of the supply line in the store should be drawn before the development and design, as shown in Figure 4. In this supply line, it mainly supplies power to various motors, while the high-voltage power supply separately sets up dedicated high-voltage power supply sockets for automation equipment and workstations.

The electrical diagram of each electrical appliance in the control cabinet of the system is shown in Figure 5. In order

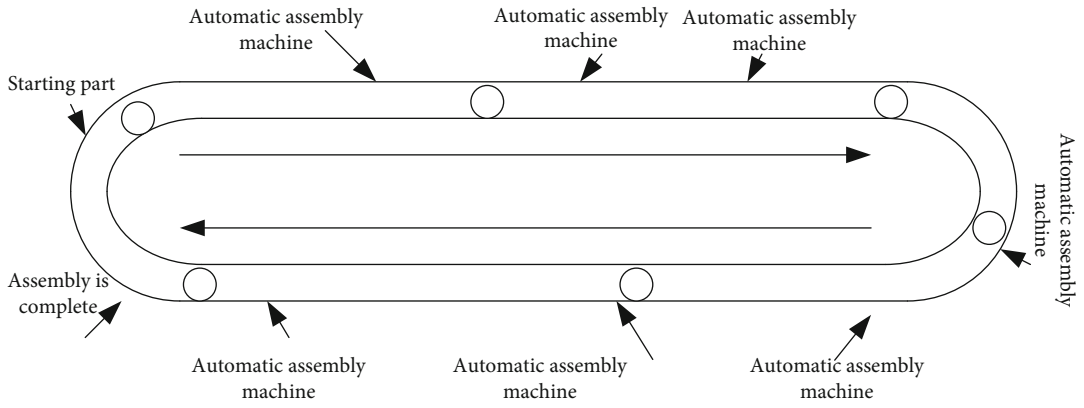

Figure 6: Circular automatic air conditioning assembly line.

to supply power to PLC, sensors, and other electrical appliances that require low-voltage power, the high-voltage power input in the entire system is converted into 24 V DC through the high-voltage conversion function of the switching power supply to ensure the stable operation of low-voltage electrical appliances. At the same time, in order to prevent the noise from adversely interfering with the electrical appliances, a power filter is preset in the bottom line to eliminate all kinds of noise. The function of the power filter is to obtain a power signal of a specific frequency by connecting the power filter to the power line or to eliminate the power signal of a specific frequency. Using this feature of the power filter, a square wave group or complex noise after passing through the power filter can be turned into a sine wave of a specific frequency.

In the working process of the system, the correct connection of the copper pipe joint of the pressure valve is mainly carried out by the positioning device to judge and determine the real-time position of the product. After the system detects the docking state of the joint and confirms that it is correct, the subsequent test procedure will be started. The purpose of this move is to ensure the perfect butt joint of the joint and make the pressure in the copper pipe quickly reach the corresponding pressure standard within the specified time, which is generally $0 \sim 5$ kPa. At the same time, when the whole system stops running, the pressure in the copper pipe is generally $0 \sim 25$ kPa. Through the corresponding sensor device, the system can monitor and collect data on the pressure in the copper pipe in real time. The main sensors in the air conditioning production line are pressure sensors, humidity sensors, temperature sensors, etc. When the product meets the inspection standard, the relevant device will release in real time and send the product to the next process; if the product does not meet the standard, an alarm procedure will be triggered and the product will be tested again. In order to ensure the reliability and safety of the wiring in the entire electrical system, the shielded wire is used as the signal wire for data acquisition, and the shielded wire needs to be separated from other electrical wires to avoid irrelevant interference. Figure 6 shows the layout structure of the annular assembly automated assembly line production line.

The modular design pushes the assembly automation production line to a more efficient and complete level. Under the blessing of modular design, each automatic assembly machine in the production line has the characteristics of interchangeability, so compared with the traditional special machine-specific assembly situation. The method can significantly reduce the related spare parts expenses of the assembling machine and also reduce the maintenance cost of the machine. Automated assembly equipment must be expanded and graded by several service centers. The upper control panel and module are used to operate the control measures of the secondary electronic computer distributed system. The module manipulates the actual operation control panel and checks the alarm system for common faults, making the entire control system more complete. In the development and design of the assembly automation production line, its functional requirements are given priority. The corresponding modules are developed based on functional requirements, which can achieve efficient fit between functional requirements and modules, thereby creating a complete assembly automation production line that meets actual requirements.

4. Experiment of Big Data Intelligent Coordination and Optimization Control System Based on Cement Clinker Production Line

4.1. Cement Clinker Intelligent Coordination Control System. The nonlinearity and complexity of the precalciner, the cyclone preheater, and the SP boiler will be more affected by the addition of the kiln tail waste heat boiler in the kiln tail system, making the overall uncertainty factors more. The cyclone preheater system is a hot air exchange and a dust collector. The material meets the hot air flow in a suspended state and is reheated. After the material is subjected to centrifugal force and collides with the cylinder wall, it enters the next stage preheater by its own weight. Among them, the relevant characteristics of the cyclone preheater are very easily changed by external factors, such as the amount of raw meal, heat dissipation, and raw meal and flue gas composition. And the characteristics of the cyclone preheater change dynamically, so the changes of its characteristics in each link are quite different. Since various factors in the process have high uncertainty and are difficult to express, it is also difficult to establish related mathematical

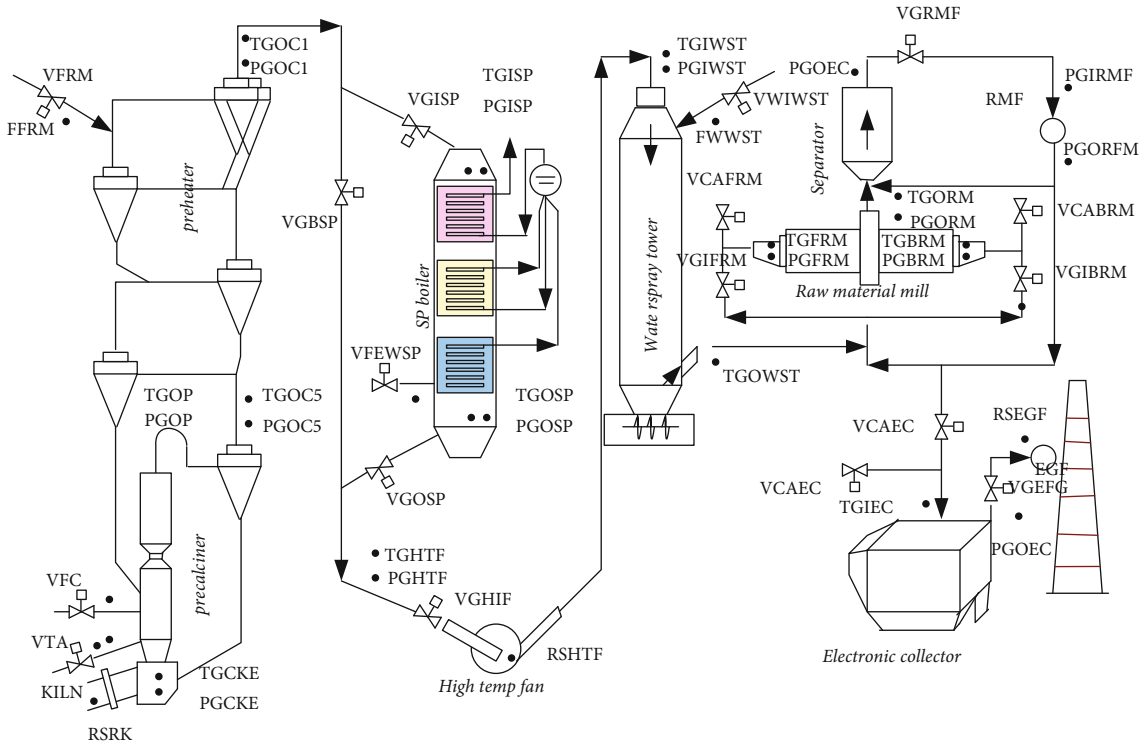

Figure 7: Control valves and measuring points of the coordinated control subsystem at the rear of the cement kiln.

models. If some uncertain factors in the process are ignored and a relevant mathematical model is established in a relatively ideal state, the results will be far from the actual situation, and the value and significance obtained will be extremely low. Therefore, the method of fuzzy control is adopted in this paper, and the control rules that need to be specifically expressed will be expressed in a fuzzy way in natural language. And it allows the controlled object to be controlled without establishing a mathematical model of the relevant controlled object. There are washing machines, air conditioners, microwave ovens, vacuum cleaners, cameras, and camcorders in household appliances; in the field of industrial control, there are water purification treatment, fermentation process, chemical reaction kettle, cement kiln, and so on. The exhaust gas discharged from the SP boiler should be reasonably controlled, especially the temperature of the exhaust gas should be controlled within a reasonable range, so as to meet the requirements of other equipment in the system such as high temperature fans and raw grinding systems. If the temperature of the waste gas is too high, the waste gas cannot be recycled; if the temperature is too low, the raw meal cannot be cooled by cold air and dried. In order to stably control the air temperature of the air inlet of the high temperature fan, a cold air valve is generally set up on the forehead of the high temperature fan. According to the change of the air temperature of the air inlet, it can be opened and closed appropriately to adjust the temperature of the exhaust gas. The raw meal input and the fuel input are also closely related, and it is necessary to coordinate the control of the two.

The coordinated control subsystem can mainly control SP boiler, raw meal mill, dust collector, and high-temperature fan. This subsystem participates in the relevant control, mainly in order to maintain the normal operation of the SP boiler and cement kiln system, while maintaining the relevant modifiable control parameters within a reasonable and standard range. The feed water of SP boiler comes from the low temperature economizer of the AQC boiler, and it absorbs heat again to generate superheated steam, which is mixed with the superheated steam of the AQC boiler and then goes to the steam turbine to generate power. The kiln tail control subsystem is mainly composed of seven parts. These seven parts mainly control the following objects: SP boiler feed water flow, coal feeder, raw meal feeder, high temperature fan speed, raw meal mill head cooling air valve, raw meal mill tail cooling air valve, flow through SP boiler gas flow, and humidification tower water spray. Figure 7 shows the location of the control valves and measuring points of the kiln tail control subsystem on the production line. It selects a certain field cement production line and conducts a 48-hour operation measurement without adding the fuzzy control system and adding the fuzzy control system. The relevant data were recorded and analyzed every 24 seconds. The actual operating conditions of the SP boiler in both cases are shown in Figure 8.

According to the relevant data in Figure 8, a detailed comparison of the temperature and pressure of the main steam in the two modes shows that compared with the temperature and pressure of the main steam in the traditional control mode, in the coordinated control mode, the temperature

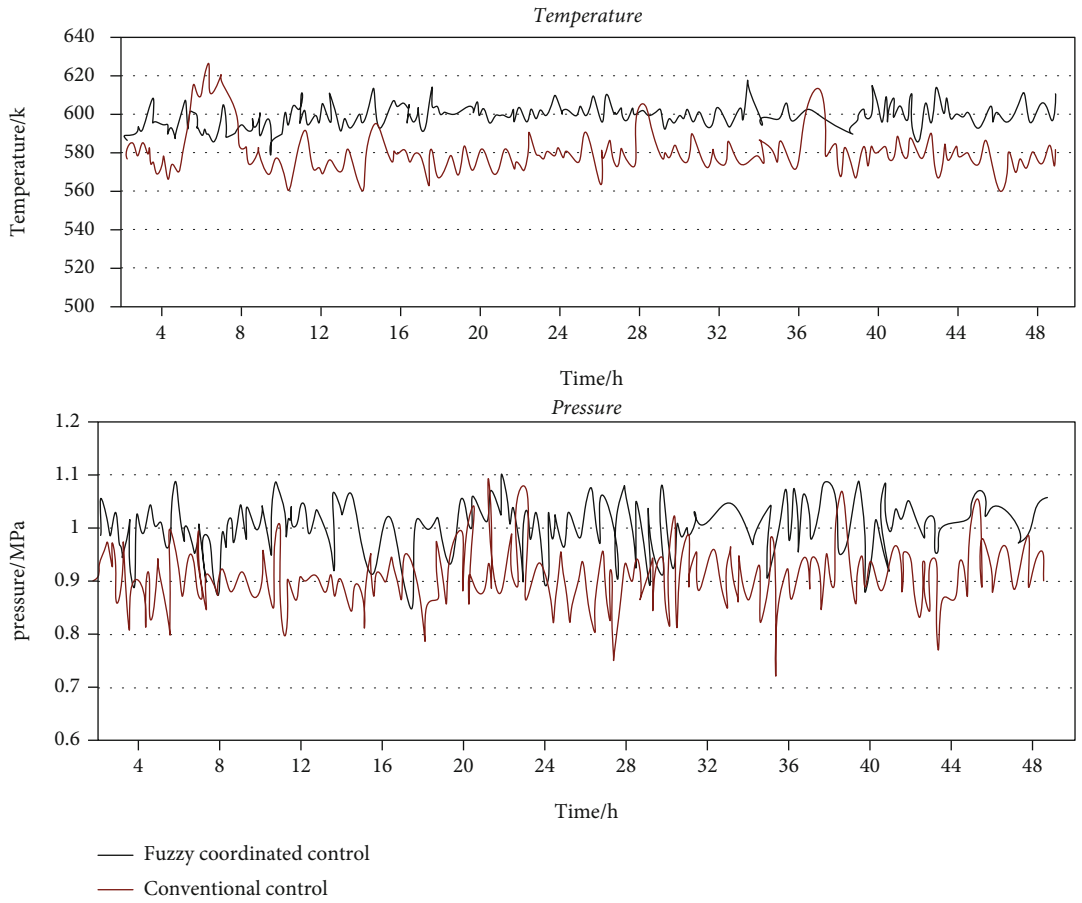

Figure 8: Comparison of main steam temperature and pressure of SP boiler based on fuzzy control and traditional mode.

and pressure of the main steam in the SP boiler are higher, and comparing the average temperature and pressure of the two, which is also the coordinated control mode, is significantly higher than the traditional control mode. The specific data and further analysis are given as follows: In the coordinated control mode, the average temperature of the main steam is 602.13 K, the peak temperature is 619.53 K, and the minimum temperature is 581.21 K. In the traditional control mode, the temperature of the main steam has obvious differences, which are 577.62 K, 629.88 K, and 560.48 K, respectively. Obviously, in the coordinated control mode, the temperature fluctuation of the main steam is significantly reduced, and its fluctuation range is 38.32 K; and the average temperature is increased, and the increase rate is 4.24%. The comparison of the main steam pressure of the two shows that in the coordinated control mode, the peak pressure is 1.09 MPa, the minimum pressure is 0.87 MPa, and the average pressure is 0.96 MPa; the corresponding pressure values of the main steam under the traditional control mode are 1.07 MPa, 0.71 MPa, and 0.88 MPa, respectively. It can be concluded that in the coordinated control mode, the fluctuation range of the pressure of the main steam is also objectively reduced to 0.22 MPa, and the increase rate of the average pressure is 9.09%. From the comparison and analysis of the above data, it can be seen that in the coordinated control mode, the fluctuation of the temperature and pressure of the main steam is smaller, and the amplitude change is also smaller.

4.2. Demand for Coordinated Control of Waste Heat Boiler and Steam Turbine Load Based on Fuzzy Control. The steam turbine generator set is driven by the exhaust gas in the cement kiln and the heat carried by it to generate electricity, which is the basic principle of the pure low-temperature waste heat power generation technology in cement production. The amount of power generation depends on many factors. If the flow rate and temperature of the waste gas in the cement kiln increase continuously, the power generation generated by the waste heat will also increase, and vice versa. At present, the cement production adopts the new dry process cement production technology, which will cause obvious fluctuations in the temperature of the exhaust gas in the entire cement kiln and will have a corresponding impact on the waste heat that can be used later. This will eventually lead to significant fluctuations in steam volume and steam temperature in the boiler, which will adversely affect the operation of the entire generator set. Therefore, in order to ensure the stable and reliable operation of the generator set, both the boiler system and the generator set should be coordinated and controlled, so as to adjust the fluctuation range as much as possible and increase the power generation.

Table 1: Deaerator and hot water well water level fuzzy control variables.

Variable	Basic domain	Quantitative universe	Fuzzy subset
Deaerator water level deviation value	(-999 mm, 999 mm)	(-5, 5)	{TH, SH, O, SL, TL}
Condenser water level deviation value	(-999 mm, 999 mm)	(-5, 5)	{TH, SH, O, SL, TL}
Condensate flow correction value	(-5 t/h, 5 t/h)	(-5, 5)	{TH, SF, O, SS, TS}
Condensate return flow correction value	(-5 t/h, 5 t/h)	(-5, 5)	{TH, SF, O, SS, TS}

Table 2: Deaerator water level deviation language variable assignment.

Water level deviation range (%)	Quantization level	TH	H	O	L	TL
≥-999	-5	0	0	0.1	0.6	0.9
(-999, -800)	-4	0	0	0.3	0	0.4
(-800, -600)	-3	0	0	0.2	1	0.7
(-600, -400)	-2	0	0	0	0.4	0
(-400, -200)	-1	0	0.2	0.8	0.2	1
(0, 200)	0	0	0.1	0	0.1	0
(200, 400)	1	0	0.4	0.2	0.3	0
(400, 600)	2	0.3	0.7	0	0	0
(600, 800)	3	0.6	0.9	0	0	0
(800, 1000)	4	0.7	0	0.9	0	0
>999	5	0.9	0.2	0	0	0

In order to reasonably coordinate the control of the boiler system and the generator set, the fuzzy control mode is used to optimize and adjust it. A fuzzy controller is established with a three-dimensional structure, in which there are three input variables, which are front pressure, boiler heat signal, and turbine power deviation. There is only one output variable, which is the correction value of the set value of the load regulator. According to the actual situation, the time t and the measured value N are reasonably selected, and the time and measured value selected by the controller are 60 s and 5 times, respectively. Through a detailed analysis of the thermal process and combined with relevant experience, the variables of the controller, its quantization level range, fuzzy subsets, etc. will be determined, as shown in Table 1.

The fuzzy relationship assignments are shown in Table 2.

The actual function of the fuzzy controller designed in this paper needs to be realized by software. Different operations of the control software can control the power of the steam turbine, the water level of the condenser, and the water level of the deaerator accurately. We select a cement plant for field simulation, and the data collected under traditional control mode and fuzzy control mode are shown in Figure 9.

It can be clearly seen that the coordinated control effect of the production line intelligent system based on fuzzy control is better. And the value of AQC boiler in the range of -50 to 50 is as high as 92.66%, while that of SP boiler is only 83.27%.

4.3. Comparative Analysis of Fuzzy Control and Traditional Control Experiments. The optimal operation of the pure low-temperature waste heat power generation system is to make full use of the waste heat of the waste gas produced by the new dry process cement production. Cement clinker production and waste heat power generation system is a complex physical and chemical process. It involves combustion, raw meal decomposition, clinker sintering, fluid mechanics, heat transfer, thermodynamics, environmental science, mechanical engineering, and other disciplines. It reduces the influence of the waste heat power generation system on the cement production process, avoids the large fluctuation of the main steam parameters, meets the long-term stable and efficient operation of the steam turbine, and increases the power generation per ton of clinker of the waste heat power generation system. The start-up of waste heat boilers and steam turbines is divided into two types: hot start and cold start. When the waste heat boiler has a short shutdown time and has a certain pressure and temperature, it can be started in a hot state. Because of its small heating and boosting range and a large allowable rate of change, the speed of heating and boosting is faster than that of cold startup, which shortens the startup time. Combined with the requirements of the thermal system and thermodynamic analysis, the optimal start-up method of the waste heat boiler under different thermal conditions is formulated. The main steam pressure is 0.5 MPa-1.0 MPa, and the temperature is between 468 K and 528 K, which can quickly open the waste heat boiler. It slowly opens the inlet baffle of the sedimentation chamber and closes the baffle of the small residual air flue gas channel, so that the amount of flue gas passing through the boiler is gradually increased, and the furnace temperature is kept rising slowly at a rate of 6 K/min. It adjusts the opening of the warm pipe steam exhaust valve according to the main steam pressure and temperature. When the pressure is higher than 0.8 MPa

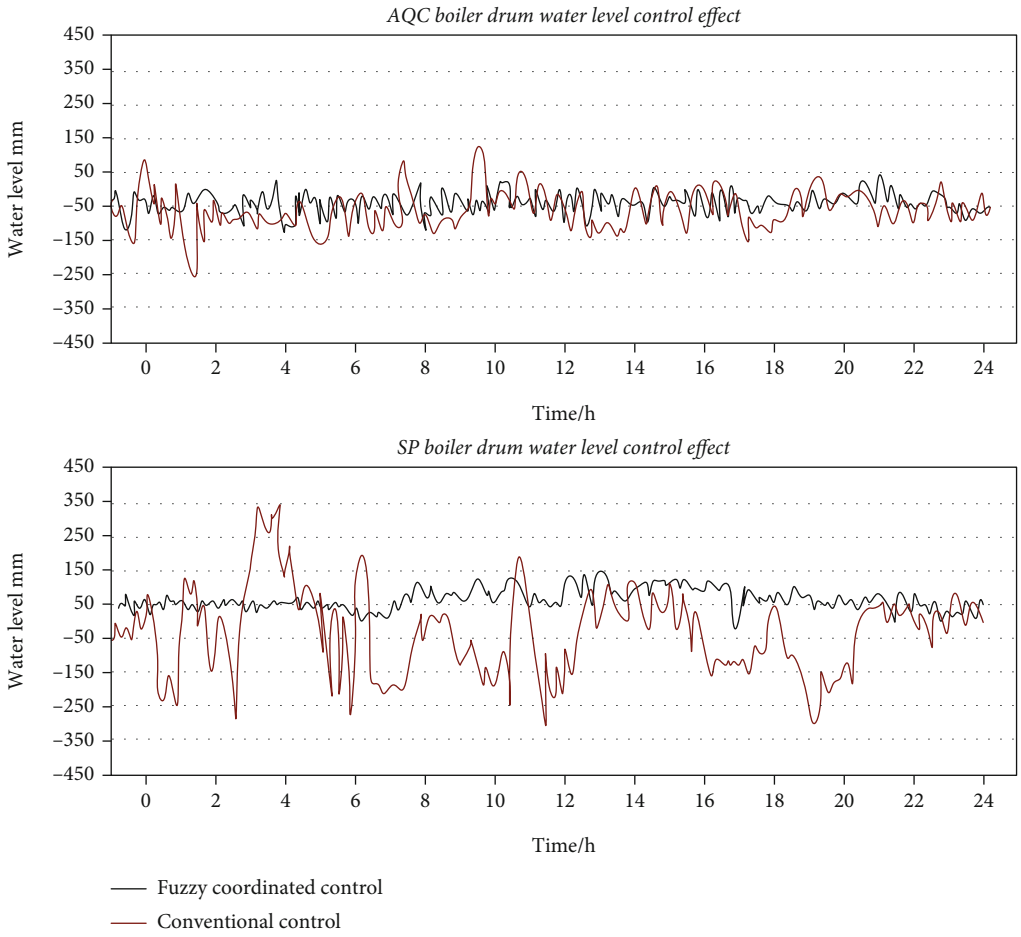

Figure 9: Drum water level distribution of AQC and SP boilers based on fuzzy control and traditional mode.

and the temperature is higher than 528 K, the steam exhaust valve of the heating pipe is fully opened to perform rapid heating; when the pressure is higher than 0.9 MPa and the temperature is higher than 568 K, the steam turbine can be started. The main steam pressure is lower than 0.5 MPa. When the temperature is lower than 468 K, it slowly opens the inlet baffle of the sedimentation chamber and closes the baffle of the small residual air flue gas channel, so that the amount of flue gas passing through the boiler increases gradually, keeping the furnace temperature rising slowly at a rate of 4 K/min; when the furnace temperature rises to 468 K, it can start quickly again. Figure 10 can be obtained.

In the production process of the cement kiln production line, after the exhaust gas is processed by the SP boiler, the flow and stability of the exhaust gas will tend to be relatively stable. Therefore, the start-stop status of the SP boiler depends on the production status of the cement kiln. When the cement kiln stops producing cement or its production status is not stable, the boiler will be shut down. When the raw material is put into the cement kiln or the waste heat power generation system stops running, the SP boiler will start up accordingly. For the analysis of the above two situations, before the raw materials are put into the cement kiln, the waste heat boiler needs to be operated under certain thermal conditions. The successful establishment of thermal

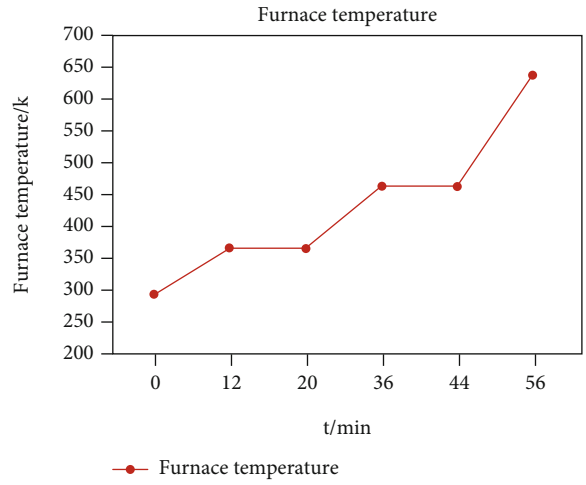

Figure 10: AQC boiler heating process.

conditions requires a certain period of time, during which time the exhaust gas will be discharged in large quantities. Therefore, it is necessary to recycle the waste gas before feeding. At this time, it is necessary to operate the SP boiler to recover the waste heat, so as to promote the steam turbine

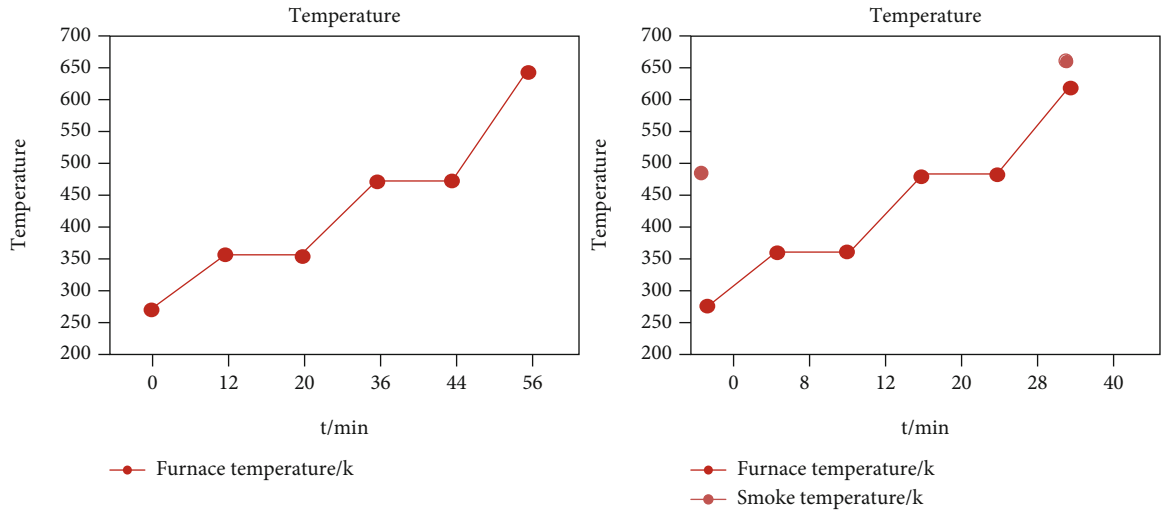

Figure 11: SP boiler heating process.

Table 3: 70-hour running data statistics.

	Statistical parameters	Traditional control	Fuzzy control
Clinker production	Raw meal feed amount (t)	11662.74	11680.43
	Clinker production (t)	7836.21	7877.49
	Coal supply (t)	996.47	923.52
	Production power consumption (kWh)	607142	600033
	Standard coal consumption per ton of clinker (kgce/t)	118.94	109.66
Waste heat power generation	Power generation (kWh)	293138	314675
	Power supply (kWh)	276542	297611
	Self-consumption rate (%)	7.66	7.64
	Power generation per ton of clinker (kWh/t)	38.94	40.02

to generate electricity. In the latter case, the waste heat boiler only needs to operate normally, as shown in Figure 11.

In order to rationally utilize the large amount of waste heat generated in the production process of cement kilns, a pure low-temperature waste heat power generation system is used to optimize the production process. While ensuring the stability of the entire production process and the fluctuation range of the main steam parameters, it can also maintain the stable and long-term power generation of the steam turbine. This further increases the power generation capacity of the waste heat power generation system. It should be noted that the waste heat boiler and steam turbine will work under two different operating conditions, which are hot start and cold start, respectively. If it is needed to work normally in a warm-start state, the conditions that need to be met are as follows: The waste heat boiler has a short shutdown time and can maintain a certain temperature and pressure in the furnace. Because under such conditions, the variation of temperature and pressure is very small, allowing larger changes to occur, and the rising rate of temperature and pressure is also significantly higher than that of cold start. According to the relevant knowledge and research of thermodynamics, this paper will analyze and determine the correct and reasonable selection of the start-up state of the waste heat boiler under different conditions. When the pressure range of the main steam is 0.5 MPa-1.0 MPa and the temperature range is 468 K-528 K, the boiler can be started quickly. When the pressure and temperature of the main steam reach 0.8 MPa and 528 K, respectively, the exhaust valve can be fully opened to make the warm pipe heat up quickly. When its pressure and temperature are 0.9 MPa and 528 K, respectively, turn on the steam turbine; and when the temperature and pressure drop to 0.5 MPa and 468 K, respectively, it gradually opens the baffle of the settling chamber and close the baffle of the flue gas channel to increase the amount of flue gas in the boiler. The actual test was carried out on the cement clinker production system and the waste heat power generation system, respectively, so that the two were continuously working for 48 hours under running and nonrunning conditions, and during the working process of the two, there is no situation of various kinds of stop working. The obtained data are shown in Table 3.

It can be seen from Table 3 that the coordinated optimization system using fuzzy control has less demand for feeding materials, less energy consumption in the production

process, more power generation, and the average income can be increased by 4.87%. This verifies the optimization effect of the coordinated control system of the cement clinker production line.

5. Discussion

Through the in-depth research and analysis of the cement clinker production system and the waste heat power generation system, this paper draws the law of the mutual influence between the two. And on this basis, we select the appropriate control parameters. Accordingly, this paper proposes relevant measures that enable coordinated control of the two systems. At the same time, under the guidance of fuzzy control theory and based on the proposed control strategy, it has carried out practical development of the coordinated optimal control system. In this paper, in order to reasonably control the water level of the steam drum of the waste heat boiler, a set of special and applicable water level control method is studied. There are three basic control methods for drum water level control: single-impulse control, double-impulse control, and triple-impulse control. There are many improvement methods, such as online self-tuning PID control, fuzzy method control, improved fuzzy three-impulse control, and predictive model control.

6. Conclusions

According to the coordinated optimization control system developed in this paper, the actual coordinated operation of the cement clinker production system and the waste heat power generation system is analyzed and researched, and the control methods of various processes of the latter are individually optimized. From all the data obtained, we select the best data to form the best control curve and method. Through the in-depth study of this paper, it can be concluded that under the guidance of the fuzzy control method, the developed coordinated optimal control system works well. It requires less materials and significantly reduces energy consumption, while the actual power generated by the power generation system increases, and the overall system yields an increase of 4.87%. It can be seen from the above research that the coordinated optimal control system has practical and effective utility.

Data Availability

No data were used to support this study.

Conflicts of Interest

The authors declare that there are no conflicts of interest regarding the publication of this article.

Acknowledgments

This article is one of the phased results of the national key research and development project "Data Intelligence Driven Real-time Operation Optimization Technology Research" (2020YFB1712202). This article is one of the phased achievements of the Jilin Province Science and Technology Development Project "Research on the Key Technology of Intelligent Grinding and Polishing of Complex Blade Robot Force Positions" (20190302122GX). This article is one of the phased achievements of the scientific research planning project of the Jilin Provincial Department of Education, "Research on the Force Position Parallel Grinding and Polishing Machining Mechanism and Motion Planning of Complex Blade Robots" (JJKH20200747KJ). This article is one of the phased achievements of the China Postdoctoral Science Foundation project "Aeronautical Blade Robot Force Position Parallel Grinding and Polishing Processing Mechanism and Motion Planning" (2021M692457).

References

[1] S. Yan, A. Zhang, H. Zhang, J. Wang, and B. Cai, "Optimized and coordinated model predictive control scheme for DFIGs with DC-based converter system," *Journal of Modern Power Systems and Clean Energy*, vol. 5, no. 4, pp. 620–630, 2017.

[2] C. Li, L. Zeng, B. Zhou et al., "An optimal coordinated method for EVs participating in frequency regulation under different power system operation states," *IEEE Access*, vol. 6, pp. 62756–62765, 2018.

[3] K. Zhu, S. Joshi, Q. G. Wang, and J. F. Y. Hsi, "Guest editorial special section on big data analytics in intelligent manufacturing," *IEEE Transactions on Industrial Informatics*, vol. 15, no. 4, pp. 2382–2385, 2019.

[4] P. Lade, R. Ghosh, and S. Srinivasan, "Manufacturing analytics and industrial internet of things," *IEEE Intelligent Systems*, vol. 32, no. 3, pp. 74–79, 2017.

[5] Y. Liu, X. Gao, and F. Dai, "Implementation of Mamdami fuzzy control on a multi-DOF two-wheel inverted pendulum robot," *Discrete & Continuous Dynamical Systems - S*, vol. 8, no. 6, pp. 1251–1266, 2015.

[6] B. Xu, F. Sun, Y. Pan, and B. Chen, "Disturbance observer based composite learning fuzzy control of nonlinear systems with unknown dead zone," *IEEE Transactions on Systems, Man, and Cybernetics: Systems*, vol. 47, no. 8, pp. 1–9, 2017.

[7] S. A. Abdul-Wahab, E. M. Hassan, K. S. Al-Jabri, and K. Yetilmezsoy, "Application of zeolite/kaolin combination for replacement of partial cement clinker to manufacture environmentally sustainable cement in Oman," *Environmental Engineering Research*, vol. 24, no. 2, pp. 246–253, 2019.

[8] T. G. Le, K. B. Yoon, and T. M. Jeong, "Degradation and reduction of small punch creep life of service-exposed Super304H steel," *Journal of Mechanical Science and Technology*, vol. 33, no. 11, pp. 5243–5250, 2019.

[9] T. Alam, "Fuzzy control based mobility framework for evaluating mobility models in MANET of smart devices," *Journal of Engineering and Applied Sciences*, vol. 12, no. 15, pp. 4526–4538, 2017.

[10] J. Bacik, F. Durovsky, P. Fedor, and D. Perdukova, "Autonomous flying with quadrocopter using fuzzy control and ArUco markers," *Intelligent Service Robotics*, vol. 10, no. 3, pp. 185–194, 2017.

[11] C. F. Juang, M. G. Lai, and W. T. Zeng, "Evolutionary fuzzy control and navigation for two wheeled robots cooperatively carrying an object in unknown environments," *IEEE Transactions on Cybernetics*, vol. 45, no. 9, pp. 1731–1743, 2015.

[12] S. Vrkalovic, T. A. Teban, and L. D. Borlea, "Stable Takagi-Sugeno fuzzy control designed by optimization," *International Journal of Artificial Intelligence*, vol. 15, no. 2, pp. 17–29, 2017.

[13] S. Saniuk and A. Saniuk, "Challenges of industry 4.0 for production enterprises functioning within cyber industry networks," *Production Engineering*, vol. 26, no. 4, pp. 212–216, 2018.

[14] S. Takahashi, Y. Shimizu, and Y. Mizutani, "Special issue on intelligent measurement for advanced production engineering," *International Journal of Automation Technology*, vol. 11, no. 5, pp. 681–681, 2017.

[15] Y. Yang, Z. Yuan, Z. Pi, W. Xia, C. Jiang, and K. Guo, "Construction and implementation of intelligent transparent automobile factories," *China Mechanical Engineering*, vol. 29, no. 23, pp. 2867–2874, 2018.

[16] T. M. Godinho, C. Costa, and J. L. Oliveira, "Intelligent generator of big data medical imaging repositories," *IET Software*, vol. 11, no. 3, pp. 100–104, 2017.

[17] E. Robinson, H. Balakrishnan, M. Abramson, and S. Kolitz, "Optimized stochastic coordinated planning of asynchronous air and space assets," *Journal of Aerospace Computing, Information, and Communication*, vol. 14, no. 1, pp. 10–25, 2017.

[18] Y. Guo, Q. Wu, H. Gao, X. Chen, J. Ostergaard, and H. Xin, "MPC-based coordinated voltage regulation for distribution networks with distributed generation and energy storage system," *IEEE Transactions on Sustainable Energy*, vol. 10, no. 4, pp. 1731–1739, 2019.

[19] Y. Han, K. Zhang, H. Li, E. A. A. Coelho, and J. M. Guerrero, "MAS-based distributed coordinated control and optimization in microgrid and microgrid clusters: a comprehensive overview," *IEEE Transactions on Power Electronics*, vol. 33, no. 8, pp. 6488–6508, 2018.

Hindawi
Wireless Communications and Mobile Computing
Volume 2022, Article ID 3501003, 12 pages
https://doi.org/10.1155/2022/3501003

Research Article

Design and Implementation of Smart Tourism Service Platform from the Perspective of Artificial Intelligence

Qi Li and Yi Zhang

Department of Tourism and Health Care, Hebei Institute of International Business and Economics, Qinhuangdao 066000, Hebei, China

Correspondence should be addressed to Yi Zhang; zhangyi@hbiibe.edu.cn

Received 14 February 2022; Revised 18 March 2022; Accepted 7 April 2022; Published 12 May 2022

Academic Editor: Junjuan Xia

With the advancement of science and technology and the further improvement of people's living standards, tourism has become a hot topic in today's society. This paper is aimed at studying the development of a smart tourism service platform using artificial intelligence recognition technology and automatic program design. This paper proposes functions such as online ticket booking through the design of intelligent access control in scenic spots (combined with intelligent voice, face recognition, and other technologies), scenic miniprograms, and WeChat public accounts. Tourists can collect tickets automatically through the intelligent assistant designed by the intelligent service system. This allows tourists to consult and interact with intelligent machine assistants, reducing human-to-human contact during travel, thereby reducing the probability of epidemic infection (mainly spread by coughing or sneezing, close contact with sick people, touching contaminated surfaces, etc.). Finally, the smart tourism service platform is promoted, and an online questionnaire survey is conducted on 2,000 tourists who use the service platform to understand the actual use of the system. The results of the questionnaire survey showed that among the 2,000 tourists' evaluations, 55.15% were satisfied with the system, 41.5% were very satisfied, 3.1% felt average, 0.25% felt dissatisfied, and 0% were very dissatisfied. At the same time, a large number of positive evaluation words were received in the feedback results of tourists, which shows that the smart service system designed in this paper is very popular with tourists. Meanwhile, a great deal of positive evaluation words were received in the feedback results of tourists (such as full of technology, special convenience, and special safety). This shows that the intelligent service system designed in this paper is very popular with tourists.

1. Introduction

With the advent of the economic era, the demand level of tourism consumers is gradually shifting from the level of experience dissemination to the level of undifferentiated that everyone can enjoy the same travel experience equally. The highlight of the experience economy lies in unique feelings. From this perspective, tourism is an important way for people to seek novelty, difference, wonder, beauty, and knowledge. The traditional way of mass travel ignores the interaction with tourism consumers, so it cannot provide tourism consumers with a unique and differentiated experience. Smart tourism overcomes the contradiction of popularized and standardized services. That is, while satisfying the tourists to enjoy the same experience products, it can also satisfy the personalized experience effect of the tourists. With the increase of urban population, people's thinking has also changed. In addition to meeting the basic living needs of clothing, food, housing, and transportation, people have begun to have more requirements for tourism, vacation, recreation, and other aspects [1]. However, the epidemic has had a great impact on the tourism industry in the past two years, and traditional travel methods are no longer suitable.

Academia representatives said that smart tourism refers to the provision of smart tourism services for tourists through Internet devices on mobile devices combined with

current Internet technology, and timely access to jobs and travel plans [2]. Smart tourism means that tourism enterprises and scenic spots are based on high-tech information technology, provide high-quality services, make full use of social resources, and meet the growth of tourism consumers' personalized needs. Leading industry representatives believe that smart tourism refers to tourism. With the help of a new generation of information network technology and the infrastructure of the tourism industry, the entire tourism system will be able to obtain and use relevant tourism information in a timely manner to realize intelligent service, management, and marketing, which is a new trend in the development of the tourism market [3, 4]. In fact, smart tourism is the effect of intelligent identification, which is necessary for mobile terminals to actively identify, receive, and feedback travel information in real time, and refers to the convenient use of various travel methods [5, 6].

Artificial intelligence is AI, and its realization of the concept of intelligence will have a self-evident impact on the relationship between computer science and intelligence [7]. The most concentrated expressions are intelligent algorithms and intelligent information processing. Computer science is the fundamental driving force behind the realization of intelligence. The relationship between neuroscience and intelligence can be divided into two levels: system structure level and operating mechanism level. The most concentrated expression is intellectual behavior and intellectual cognition, which as a way to achieve machine intelligence. As far as human intelligence is concerned, the overall structure of neurons is the condition that produces human intelligence. The constant interaction and stimulation between neurons leads to infinite sensory cognition and provides a good model for intelligent cognition.

It is a very good idea to use AI to combine various intelligent identification technologies, intelligent control programs, etc., to design a smart tourism service system. At present, many fields have begun to combine AI for intelligent services. Designing a smart tourism service system through AI can facilitate the management of scenic spots and facilitate tourists' sightseeing. During the epidemic, it can reduce personnel contact and better prevent and control the epidemic. It can be said that the realization of the intelligent service system has particularly important value and significance.

The innovations of this paper are as follows: (1) This paper analyzes the problems existing in the current form of tourism services and the methods that need to be improved. (2) This paper designs a multiservice platform such as a smart travel mobile APP that combines AI, WeChat public account, and small programs. (3) This paper conducts a questionnaire survey on the designed smart tourism service platform to understand the actual use effect of the system. (4) The smart tourism service platform in this paper combines smart access control, multinetwork terminals such as mobile APP, applet, and portal website, and smart technologies such as 3DVR.

2. Related Work

Regarding the research and design of smart tourism, many scholars have explored this. Naseri et al. expounded the innovation of smart tourism public service mechanism based on neural network. The construction of smart scenic spots not only needs to pay attention to the investment of basic hardware equipment but also needs to understand the needs and goals of tourists from the perspective of tourists and constantly innovate soft services (soft services refer to those services that are intangible and inseparable, including information services, management consulting, and health care services). Smart tourism is still lacking in the world, but it focuses on sustainable development, deep participation in tourism, deep connection between tourists and destinations, and the overall development impact of tourism economy and society and explores the overall evolution from tourism to smart tourism. Traditional tourism management concepts and models can no longer meet people's travel needs. The use of big data has promoted the development of tourism to a certain extent and solved the problem of tourism management [8]. Smart tourism is a real-time tourism service that utilizes cloud computing, network, and mobile internet platforms [9]. Zhou analyzed the cultural orientation of smart tourism systems in traditional villages. To protect the traditional village landscape, it is necessary to respect the credibility of the village landscape and protect the form and image of the landscape. The key to building a cultural tourism brand is the construction of traditional village source culture. Exploring the new path of "culture + tourism + Internet" will determine the final realization of the rise of tourism in the central plains [10]. With the rapid development of the times, tourism has become one of the main pillar industries of our era. Under the trend of informatization, a new smart tourism model has begun to take shape, bringing more opportunities and challenges to the development of the entire tourism industry. Li analyzed the concept and definition of new smart tourism and also analyzed the shortcomings of new smart tourism. He summarized the application of smart tourism in all aspects of the industrial chain and also summarized a smart tourism model evaluation project, which provided specific theoretical support and scientific basis for the overall development of tourism [11]. Today, tourism plays an important role in urban development, and cities are vying for tourism upgrades. As a new strategy for tourism development, night tourism needs the attention of stakeholders. The two most important aspects of night tourism development are nighttime environment and atmosphere. The increase in night tours is inseparable from local intelligence. Berastagi is one of the most popular tourist destinations in Caro Agung, where nightlife destinations can be found. Veronica S aims to explore the development of the environment and atmosphere of Belastaki night tours based on local wisdom. Veronica et al.'s research uses descriptive qualitative techniques to analyze data collected through field observations and in-depth interviews. Research has shown that integrating local wisdom into the environment to create a nighttime atmosphere can establish a unique identity for nighttime tourism in small towns [12]. Demolinggo et al.'s research identifies the potential and tourism characteristics of Pentinsari Village and analyzes the current state of tourism in Pentinsari Village's local wisdom, Memayu Haunin Bawono. He also studies the implementation

process of this smart tourism in sustainable tourism management using "multi-methods" or mixed methods in particular. In addition to non-participatory observations in the Pentinsari tourist village, Demolinggo et al. conducted in-depth interviews using a detailed sampling method with a total of 72 respondents (tourists). Research by Demolinggo et al. found that tourism and local wisdom combined appear to reinforce each other. In other words, by harmonizing the environment, art, culture, local life, and local wisdom, it can become a tourism product. Demolinggo et al.'s research can be used as a sustainable tourism management model for local knowledge [13]. As a spiritual tourism destination, the Basilica of Masetti is managed based on the exploration and learning of local wisdom. From sanctuary to spiritual resort, Masetti focuses on developing strategies for developing temples. Surveys in Putra I are qualitative and descriptive surveys using observations, interviews, surveys, and document collection. The results of Putra I suggest that amenities such as road transport and additional services in the area are in the good category. The philosophies and attitudes of the community unanimously agreed to develop the management of the sacred area of the Masetti Temple into a spiritual tourism destination based on local wisdom [14]. Smart tourism is one of the government-funded alternative tourism that is aimed at shifting from mass tourism to a more personal and culturally sensitive approach to provide a more professional travel experience. Famous for its unique large cave shape, Goalawa Temple is home to thousands of bats and is a tourist attraction for domestic and foreign tourists. The purpose of the study of Wismayani et al. was to explore the potential of the Goalawa Temple area and to understand the general perception of Goalawa Temple as a spiritual tourism development based on local wisdom. Using both descriptive and qualitative analytical methods through observations, interviews, surveys, and collection of document data, they detail the potential of the Goalawa Temple area. The potential of the Goarawa Temple area is spiritual and cultural tourism, and the supporting facilities, roads, and additional services in the area have been done very well. Desapesingahan's views and attitudes towards the development of the Goarawa Temple area as a spiritual tourism destination are highly appreciated and positively evaluated [15]. Although the above research can promote the development of smart tourism to a certain extent, the solutions they designed are either too complicated or cost a lot of money, or the system reliability is not enough, so it is difficult to pass.

3. AI-Based Smart Tourism Service Method

3.1. Smart Tourism

(1) Current situation of tourism

As an activity or phenomenon, tourism has existed for thousands of years in history, and it is one of the most basic human activities in the development of human society to a certain stage. Tourism is deeply rooted in the hearts of the people and is well known to the public.

(1) *Inbound Tourism Situation*. Figure 1 shows the trend chart and growth rate of the number of domestic inbound tourists. The following data are all compiled from public information. From 2004 to 2018, the number of inbound tourists received by the country increased from 14.8 million to about 22 million, with an increase of about 7.2 million and an increase of about half of the number in 2014. In 2012, the country's inbound tourism market accelerated its recovery, from a negative growth rate of about 27% to a positive growth rate of 75%, with rapid development. In addition to the negative growth in the number of inbound tourists due to the financial crisis in 2008 and the new crown epidemic in 2019, the number of inbound tourists has continued to increase. This shows that the domestic tourism industry has a very strong ability to respond to emergencies [16].

It can be seen from Table 1 that in 2012, 13 million foreign tourists were received in China, and the growth rate was as high as 75%. The growth rate showed a downward trend, and the impact of the epidemic in 2019 began to show a negative growth. After the financial crisis in 2008 to 2012, the number of tourists from Hong Kong, Macao, and Taiwan reached 2.15 million, which is related to the various convenience strategies implemented by Hong Kong, Macao, and Taiwan after the financial crisis (for example, inbound tourists can shorten the issuance time and extend the visa extension).

Figure 2 shows the foreign exchange earnings of inbound tourism. As shown in Figure 2(a), the foreign exchange earnings of domestic inbound tourism in 2012 reached US$3 billion. From 2,000 to 2012, foreign currency earnings increased with the increase in inbound tourists. The foreign exchange income in 2008 was the lowest in recent years, and the foreign exchange income declined due to the impact of the 2008 financial crisis and the epidemic in the past two years. As shown in Figure 2, from 2012 to 2016, the foreign exchange income of domestic inbound tourism maintained a growth rate of more than 25%. This shows that the domestic tourism industry has achieved remarkable results in innovating development ideas, changing development methods, highlighting characteristics, producing high-quality products, and improving quality [17, 18].

(2) *Outbound Tourism and Domestic Tourism*. Outbound tourism began in the mid-1980s when it first produced families in the fast-growing Guangdong province. This kind of outbound travel is paid by foreign relatives and friends, and it is guaranteed to return on time. At that time, tourist destinations were limited to Hong Kong, Macao, and Taiwan. Since the early 1990s, the number of people who have left Hong Kong, Macau, and Taiwan to visit relatives has increased rapidly. From 1993 to 1997, the number of outbound tourists organized by travel agencies increased by an average of 300,000 person-times per year, with an average annual growth rate of 42%. There is still a big gap between the scale of China's outbound tourism and the scale of inbound tourism, and the development of outbound tourism is slow [19].

Since 1997, the domestic outbound tourism strategy has undergone major adjustments, from family travel to overseas travel at own expense, which also shows from the side that outbound tourism is becoming more and more popular. And because of the deepening of reform and opening up, China's outbound tourism has expanded from Singapore, Malaysia, Thailand to the Philippines, New Zealand, Egypt,

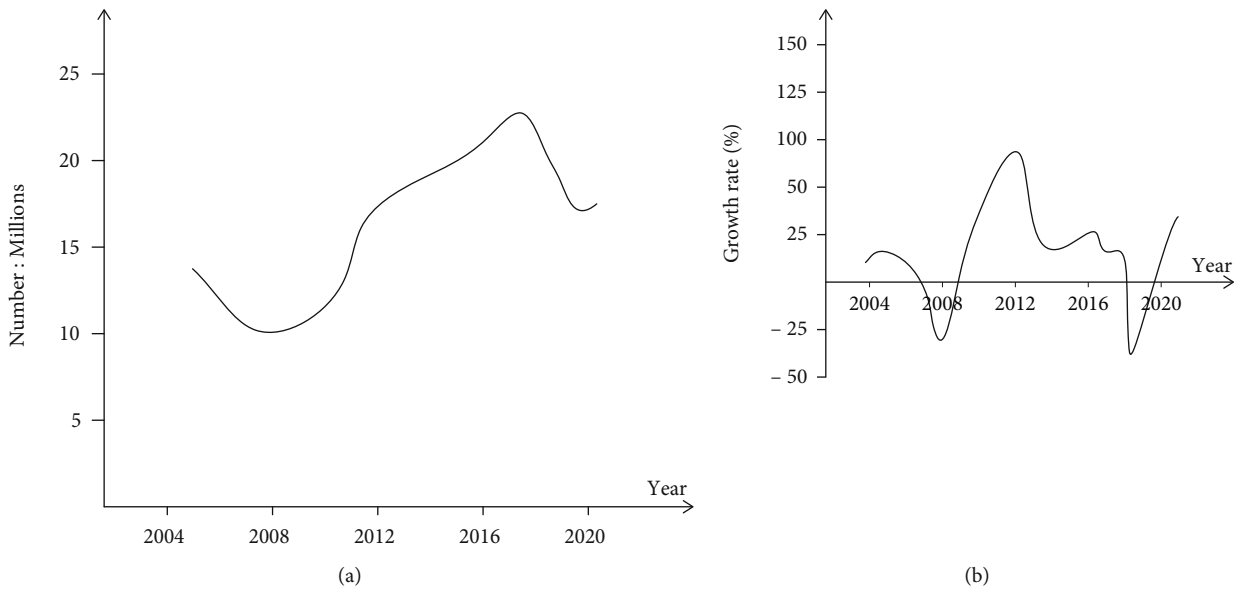

Figure 1: Inbound tourism situation. (a) The number of inbound tourists received in China. (b) The growth of the number of inbound tourists.

Table 1: Distribution of overseas tourists:thousand.

Year	Hong Kong, Macau, and Taiwan	Foreigner
2004	132	1348
2008	57	941
2012	215	1137
2016	361	1583
2020	121	1362

Germany, and other more than 30 countries and regions. In general, domestic travel to Hong Kong and Macau is becoming more and more mature, and border travel is gradually becoming more formalized. The three major elements of Chinese outbound travel, Hong Kong and Macao travel, border travel, and overseas travel, have initially formed a unified direction. In 2,000, the World Tourism Organization made a forecast for the development of world tourism in the first two decades of the 21st century. Due to its special political background and many historical reasons, Chinese outbound tourism refers to the travel activities of mainland Chinese citizens who cross national borders and cross specific borders to other countries or specific regions. Chinese outbound travel at their own expense has developed from outbound travel to visiting relatives [20].

Table 2 and Figure 3 show the statistics of domestic outbound tourism and domestic inland tourism. From 2004 to 2016, the number of domestic outbound tourists increased from 16.32 million to 32.06 million, a net increase of about 16 million. Especially from 2008 to 2012, the number of outbound tourists increased by more than 26 million, and the growth rate reached an astonishing 100%. At the same time, domestic tourism increased from 73.1512 million in 2004 to 148.752 million in 2016, with an average annual growth of 8.94%. The development of domestic tourism is relatively stable, and judging from the recent development, its development rate is generally between 4% and 5%. Since 2004, the average annual development rate of domestic tourism has been 6.54%.

As shown in Table 3, tourism is a part of the tertiary industry, and the development of tourism plays an important role in promoting the development of the tertiary industry. The tourism industry and other cultural tourism industries play a role in promoting the transformation of traditional industrial structure. The development of the cultural tourism industry can adjust the relationship between the secondary industry and the tertiary industry, and at the same time, it can also derive new categories from the traditional service industry and is conducive to the upgrading of the traditional service industry. The tourism industry and other cultural tourism industries can promote the integration and utilization of related industrial resources and the value-added benefits. For example, a book bar combined with a bookstore and a coffee shop can not only integrate the original market of bookstores and coffee shops but also drive the combination of the two to derive new consumption patterns.

(2) Smart Tourism Service Platform

Speaking of smart tourism, RFID technology has been used in some scenic spots in the United States as early as 2006, allowing tourists to carry portable smart devices to check in and check out, open doors, and purchase goods at hotels, which can be conveniently operated from time to time. Since 2009, some European countries have applied information technology to the tourism industry, established extensive tourism wireless networks, and built tourism management systems. Vehicle dispatching systems and portals in smart tourism can provide functions such as automatic navigation, safety monitoring, early warning, and emergency management. A mobile phone guide assistant was designed by a British company to help travelers provide travel services such as route planning, travel commentary, original scene

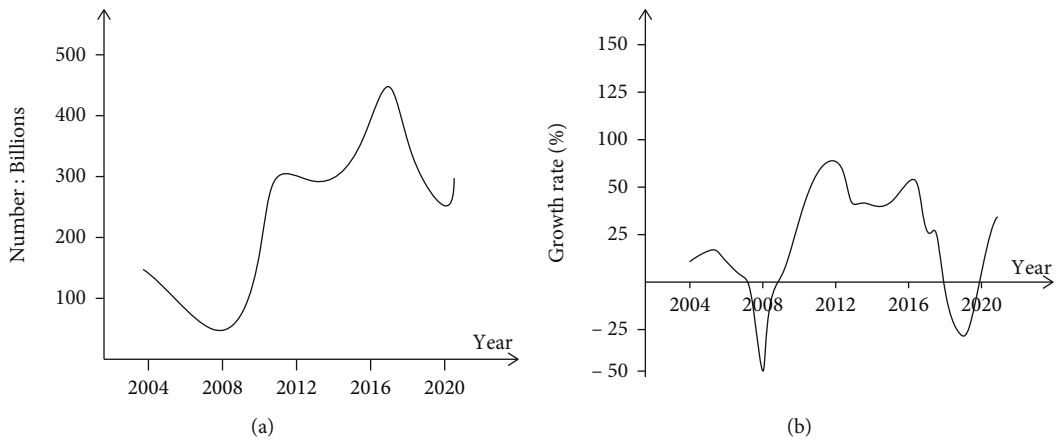

Figure 2: Inbound tourism revenue. (a) Foreign exchange income from inbound tourism. (b) Growth rate of foreign exchange income.

Table 2: Statistics on the number of domestic outbound tourism and domestic tourism:millions.

Year	Outbound tourism	Domestic tourism
2004	16.32	7315.12
2008	1.36	4212.45
2012	27.54	12453.5
2016	32.06	14875.2
2020	13.20	4215.49

reproduction, animation simulation, and video playback during the travel process [21, 22]. At present, smart tourism projects are also being launched with great fanfare in China. For example, the online virtual tourism system is currently used in the Forbidden City in Beijing. Before tourists travel, the system can project and restore the actual scene of the Forbidden City, making it easier for tourists to understand the scenic spot. Many Internet companies, such as Bao.com, Queer, and Ctrip, have developed many smart functions for convenient travel, such as the following: booking hotels, train tickets, air tickets, online ticket payment, and electronic navigation, which can greatly promote travel.

3.2. Artificial Intelligence. Artificial intelligence was formally proposed in the 1950s and 1960s. In 1950, a senior named Marvin Minsky (later known as the "Father of Artificial Intelligence"), along with his classmate Dunn Edmund, built the world's first neural network computer. This is also seen as a starting point for artificial intelligence. Artificial intelligence technologies include deep learning, data mining, and human-computer interaction based on big data. Among them, intelligent voice technology has always been a hot spot in the industry and has become the most widely used core representative in the industry. Intelligent speech technology is a system engineering, mainly including speech recognition, natural language understanding, dialogue management, natural language formation, speech synthesis, and other technologies. Among them, the processes of natural language understanding, dialogue management, and natural language generation, also known as intelligent dialogue systems, are the core technical difficulties of the entire intelligent voice dialogue process. In conclusion, there are two main directions of intelligent speech technology: speech recognition technology (ASR) and speech synthesis technology [23, 24].

Artificial intelligence is a branch of computer science that attempts to understand the essence of intelligence and produce a new type of intelligent machine that responds in a similar way to human intelligence. Research in this area includes robotics, language recognition, image recognition, natural language processing, and expert systems. Since the birth of artificial intelligence, the theory and technology have become more and more mature, and the application field has also continued to expand. It is conceivable that the technological products brought by artificial intelligence in the future will be the "containers" of human intelligence. Artificial intelligence can simulate the information process of human consciousness and thinking. Artificial intelligence is not human intelligence, but it can think like human beings and may surpass human intelligence.

3.3. Scheme Design. This paper proposes a system functional framework to meet the needs of tourists in scenic spots for "food, accommodation, travel, shopping and entertainment." According to different functions, the system can be divided into four layers, namely, platform layer, service layer, application layer, and user layer. The frame diagram is shown in Figure 4.

The user layer of the framework mainly includes mobile phone APP, WeChat public account and applet, and electronic tour guide certificate and roaming client; the application layer mainly includes VR scenic roaming applications, portal websites, and user monitoring systems; the service layer mainly includes Beidou positioning system, electronic map system, and data storage system; the platform layer mainly includes radio base stations, Beidou satellites, servers, and various base station equipment [25, 26].

The platform layer provides a good operating environment for the service layer and application layer above, ensuring that the system can run stably for a long time; the service layer is built on the platform layer to provide data services and operating environment for the application layer; the

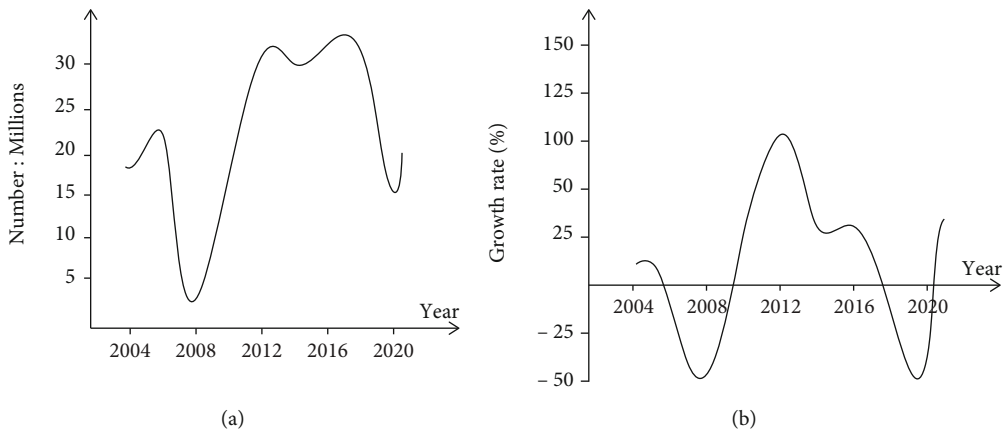

Figure 3: Outbound tourism situation. (a) Number of domestic outbound tourists. (b) Growth of domestic outbound tourists.

Table 3: Comparison of the growth of China's outbound tourism, GDP, and tertiary industry:billion.

Year	Outbound tourism	GDP	Tertiary industry
2004	221.37	1370000	453360
2008	151.02	3006700	567820
2012	564.07	5194700	752420
2016	671.63	7435850	845620
2020	261.08	10135670	1024520

application layer is mainly the specific implementation of each subsystem of the tourism platform; the user layer is mainly to allow users to use the digital functions of the scenic spot through various terminals.

The image processing difference algorithm designed by the system application layer is as follows:

$$d(u,v) = \sum_{i=1}^{m}\sum_{j=1}^{n}|S(i+u,j+v) - T(i,j)|, \quad (1)$$

where m and n represent the pixel size, (u, v) are the reference points, T is the reference template, and S is the test image.

The image processing equalization algorithm designed by the system application layer is as follows:

$$\text{Min}\bar{\sigma}^2 = \frac{1}{mn}\sum_{i=1}^{m}\sum_{j=1}^{n}(S(i+u,j+v) - T(i,j))^2. \quad (2)$$

In the formula, σ represents the error function algorithm.

$$\text{Min}\bar{D}(u,v) = \frac{1}{mn}\sum_{i=1}^{m}\sum_{j=1}^{n}|S(i+u,j+v) - T(i,j)|. \quad (3)$$

In the formula, $\bar{D}$ represents the mean value function algorithm.

$$\text{PDC}(u,v) = \sum_{i=1}^{m}\sum_{j=1}^{n}S(u,v). \quad (4)$$

In the formula, PDC table is the pixel difference.

The image processing normalization algorithm designed by the system application layer is as follows:

$$\sigma(u,v) = \frac{\sum_{i=1}^{m}\sum_{j=1}^{n}S(i+u,j+v)}{\sqrt{\sum_{i=1}^{m}\sum_{j=1}^{n}S(i+u,v+j)^2}\sqrt{\sum_{i=1}^{m}\sum_{j=1}^{n}T(i,j)^2}}. \quad (5)$$

Image detection absolute error method is as follows:

$$\varepsilon(u,v,m_k,n_k) = \left|S_{u,v}(m_k,n_k) - \bar{S}(u,v) - T(m,n) + \bar{T}\right|. \quad (6)$$

In the formula: $\bar{S}(u,v)$ represents the average range of the detected image.

Screening method for image detection is as follows:

$$I(u,v) = \left\{R\left|\min\left[\sum_{k=1}^{r}\varepsilon(u,v,m_k,n_k) \geq T_k\right]\right.\right\}. \quad (7)$$

In the formula, R represents the R-th detection, and ε represents the error with the detection template.

The processing method of system feature points is shown in Figure 5. Among them, V_1, V_2, V_3, and V_4 are the sum of squared differences in four different directions, respectively.

$$V_1 = \sum_{i=-k}^{k-1}\left(f_{c+i,r} - f_{c+i+1,r}\right)^2, \quad (8)$$

where (c, r) represents the center point and f represents the coordinate of the feature point.

$$V_2 = \sum_{i=-k}^{k-1}\left(f_{c,r+i} - f_{c,r+i+1}\right)^2, \quad (9)$$

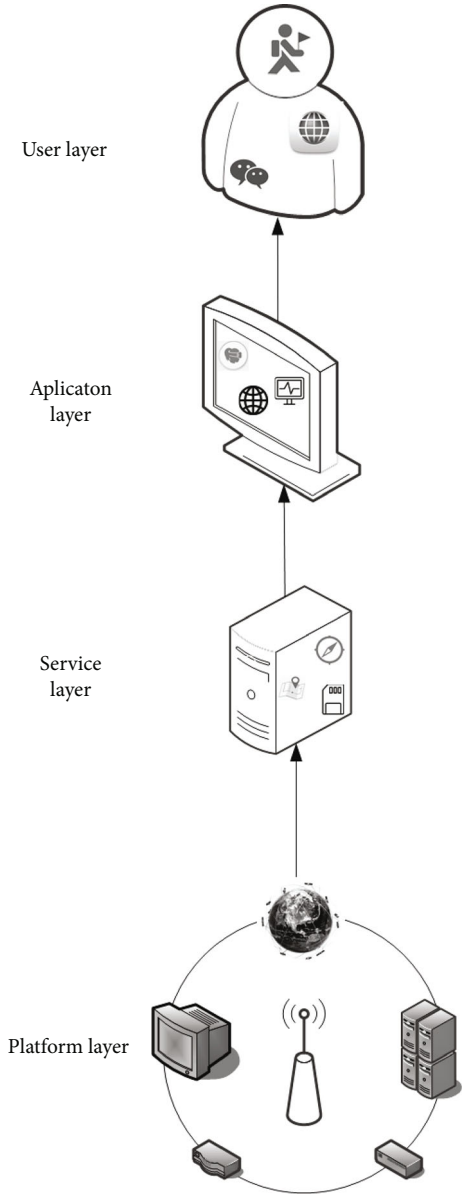

Figure 4: Overall framework of smart tourism.

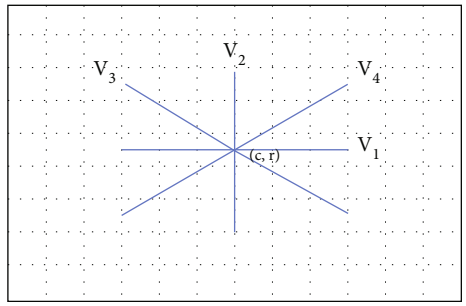

Figure 5: Detection of system image features.

$$V_3 = \sum_{i=-k}^{k-1} \left(f_{c+i,r+i} - f_{c+i+1,r+i+1}\right)^2, \tag{10}$$

$$V_4 = \sum_{i=-k}^{k-1} \left(f_{c+i,r-i} - f_{c+i+1,r-i-1}\right)^2. \tag{11}$$

In order to reduce the noise generated by the system detection process, the algorithm introduces the following function to set a detection range and reduce the amount of calculation.

$$G(x, y) = \frac{1}{2\pi\sigma^2} e^{-\left(x^2+y^2\right)/2\sigma^2}. \tag{12}$$

After the image point (x, y) changes according to the (u, v) direction, its image changes as follows:

$$E(u, v) = \sum_{x,y} G(x, y)[I(x + u, y + v) - I(x, y)]^2. \tag{13}$$

In the formula, $I(x, y)$ represents the detection corresponding point.

According to the above formula, it can be transformed into the following:

$$E(u, v) = \sum_{x,y} G(x, y)\left[I_x u + I_y v + O\left(u^2 + v^2\right)\right]^2, \tag{14}$$

where O represents the approximate point.

When the direction change is small, the image change can be considered as the average change, which can be calculated as follows:

$$E(u, v) = \sum_{x,y} G(x, y)\left\{\left[I_x, I_y\right]\begin{bmatrix} u \\ v \end{bmatrix}\right\}^2 = [u, v]M\begin{bmatrix} u \\ v \end{bmatrix}. \tag{15}$$

However, when the average change is relatively fast, the amount of calculation will be very large, so the eigenvalue R is introduced:

$$R = \det M - k\left(\tilde{M}\right)^2. \tag{16}$$

Use a fast detection algorithm for less feature points:

$$N = \sum_{i \forall P} |I(x) - I(p)| > \varepsilon_d. \tag{17}$$

Use a simple detection algorithm for feature points that are obvious:

$$\tau(p\,; x, y) = \begin{cases} 1 & \text{if } p(x) < p(y), \\ 0 & \text{otherwise}, \end{cases} \tag{18}$$

where p represents the range to be measured.

Table 4: Overall design framework of smart tourism.

Layer	Include	Estimated power consumption
User	Applets, Web, WeChat	1.5 W
APP	3dAR, Web portals, user positioning	3 W
Service	Position, Web, maps, 3D source	5 W
Basic	Beidou satellite, computer room, signal station	3KW

(a)

(b)

Figure 6: Positioning system desktop display.

For nd feature points to be tested, the feature set is as follows:

$$f_{nd}(p) = \sum_{1<n<nd} 2^{i-1}\tau(p; x_i, y_i). \tag{19}$$

The detection accuracy can be represented by e, and its formula is as follows:

$$e(H) = \frac{1}{N}\sum_{i=1}^{N}\sqrt{(x_{ci}-x_{ei})^2 + (y_{ci}-y_{ei})^2}. \tag{20}$$

In the formula, H represents the detection matrix, and N represents the corresponding detection point [26, 27].

4. AI Smart Tourism Platform Design

4.1. Design of the Model. The overall design framework is shown in Table 4. The service platform includes a tourist

Figure 7: 3D modeling software desktop.

Figure 8: VR scenic roaming scene.

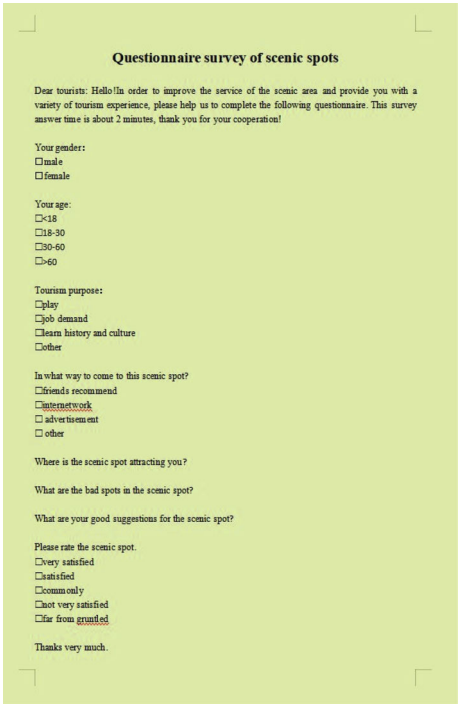

Questionnaire survey of scenic spots

Dear tourists: Hello!In order to improve the service of the scenic area and provide you with a variety of tourism experience, please help us to complete the following questionnaire. This survey answer time is about 2 minutes, thank you for your cooperation!

Your gender:
☐male
☐female

Your age:
☐<18
☐18-30
☐30-60
☐>60

Tourism purpose:
☐play
☐job demand
☐learn history and culture
☐other

In what way to come to this scenic spot?
☐friends recommend
☐internetwork
☐ advertisement
☐ other

Where is the scenic spot attracting you?

What are the bad spots in the scenic spot?

What are your good suggestions for the scenic spot?

Please rate the scenic spot.
☐very satisfied
☐satisfied
☐commonly
☐not very satisfied
☐far from gruntled

Thanks very much.

Figure 9: Questionnaire form.

positioning system, a three-dimensional scenic spot roaming system, a WeChat-based microexhibition system, a smart tourism information release portal website, and a background management system. These four systems cooperate with each other to better serve the smart tourist attractions, improve the service quality of the scenic spots, enhance the publicity effect of the scenic spot culture, and improve the travel experience of tourists.

The Beidou satellite positioning system is used in the positioning system of this paper, and the desktop display of visitor positioning is shown in Figure 6.

The 3D scene background building software used in this paper is 3D building, as shown in Figure 7.

The roaming effect of the 3D scene is shown in Figure 8:

4.2. Questionnaire Survey. In order to facilitate the understanding of the actual effect of the smart tourism service platform designed, this paper conducted a random questionnaire survey on the WeChat applet set up in a scenic spot, the WeChat public account, the portal website, and tourists visiting the scenic spot. A total of 2,000 questionnaires were selected in this paper. The content of the questionnaires included the gender and age of tourists, the purpose of tourists' travel, and the way to arrive at the scenic spot, as well as the evaluation and suggestion of the scenic spot, as shown in Figure 9.

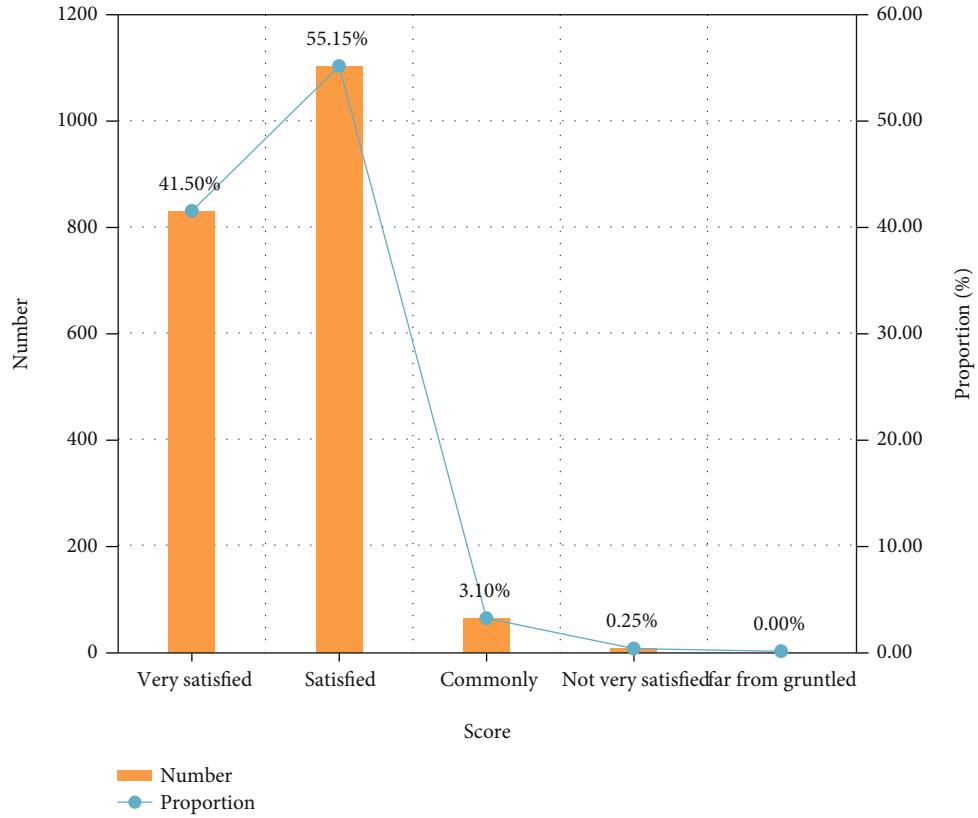

Figure 10: The results of the tourist survey of scenic spots.

4.3. Experimental Results. Finally, this paper summarizes all the obtained questionnaire results. Among the 2,000 questionnaires surveyed, 300 were filled out by tourists in scenic spots, 1,200 were from WeChat platform, and the other 500 were from other Internet platforms such as scenic portals and mini programs. All scores are shown in Figure 10. As can be seen from the figure, more than half of the survey results expressed satisfaction with the service of the scenic spot, 41.5% expressed great satisfaction, and a total of 96.65% were satisfied. This shows that the AI intelligent tourism service system designed in this paper has been recognized and loved by the majority of tourists. Some of them also expressed that they have a special sense of technology and are very convenient during travel and hope to be vigorously promoted. However, in this article, 3.1% of the tourists also said that they were in general, and 0.25% of the tourists said they were not satisfied. This part of tourists said that although VR roaming is very convenient to visit, the VR equipment will feel uncomfortable after wearing it for a long time. It has a relatively large radiation to the eyes, and the scene of VR roaming is not as good as actual viewing. This also shows that the design of this paper still needs to be improved.

5. Discussion

Under the background of the digital information age and the continuous development of personal computer hardware, the smart tourism platform proposed in this paper can bring people a new visual experience. It has broad market prospects and application prospects and will develop rapidly in the future. However, there are still many areas that need to be improved and perfected.

During the research period of this paper, since the tourism big data analysis platform of the scenic spot has not been substantially constructed, only the basic analysis platform of tourism big data has been developed according to its own data and technology. This platform has verified some functions of the smart tourism service platform based on big data, and more applications of big data in smart tourism services need to be further improved and improved. This paper does not have enough understanding of the relevant concepts, framework systems, technical systems, and related basic theories of "smart tourism," and the combination of basic theories and papers is still at a shallow level. This requires further systematic integration and exploration of tourism disciplines and information technology fields to strengthen theoretical research on the application of smart tourism in the field of rural tourism.

The prediction algorithm in this paper is not accurate enough, and it is necessary to further filter the input parameters to optimize the algorithm performance. A large amount of data in the virtual roaming subsystem model is useless for network transmission, resulting in problems such as long user delay and freezing; therefore, the modeling technology needs to be further optimized. In the construction of 3D scenes, the operation efficiency of the roaming system needs to be further improved, which requires optimizing the algorithm for recommending content to reduce the request time for content

recommendation services and improve the experience of tourists. In addition, the research method of the paper is relatively simple, most of which are analyzed and researched in a qualitative way, and there are few quantitative analysis methods, and the data statistics method of the questionnaire is also very simple.

Due to the limitations of the author's time, energy, and research funding, this article needs further market research. It analyzes the market development of customized travel demand and forecasts customized travel trends. The survey should be carried out all over the country, but this paper only selects the field survey of a certain scenic spot, so the conclusions of the survey may have certain limitations.

6. Conclusions

This paper first briefly describes the background of the topic selection in the abstract section and briefly introduces artificial intelligence and smart tourism services. Then, a detailed introduction and explanation are given in the introduction part, and then, an example analysis is carried out in the relevant work part to illustrate the current research status and shortcomings of smart tourism. Then, it proposes the significance of designing artificial intelligence smart tourism in this paper and then summarizes several innovations of this paper. It focuses on the introduction and explanation of smart tourism and artificial intelligence in the theoretical research part and then introduces the calculation method of the system image processing in the algorithm part. The experimental part first introduces the framework of the smart tourism service system designed in this paper and then shows the system desktop and 3D scenic scenes and other pictures. In the end, this paper selected 2,000 questionnaires through field investigation and online investigation of a scenic spot. The survey results show that the artificial intelligence smart tourism service platform designed in this paper is recognized and loved by the vast majority of tourists. The survey results show that 41.5% of them are very satisfied, and 96.65% are satisfied and very satisfied. The artificial intelligence smart tourism service platform designed in this paper has been recognized and loved by the vast majority of tourist.

Data Availability

No data were used to support this study.

Conflicts of Interest

The authors declare that there are no conflicts of interest regarding the publication of this article.

References

[1] M. Atiquzzaman, N. Yen, and Z. Xu, "Big data analytics for cyber-physical system in smart city," *International conference on Big Data Analytics for Cyber-Physical-Systems*, vol. 1303, 2021.

[2] G. Xiao, Q. Cheng, and C. Zhang, "Detecting travel modes using rule-based classification system and Gaussian process classifier," *IEEE Access*, vol. 7, pp. 116741–116752, 2019.

[3] M. Adil, M. A. Jan, S. Mastorakis et al., "Hash-MAC-DSDV: mutual authentication for intelligent IoT-based cyber-physical systems," *IEEE Internet of Things Journal*, 2022.

[4] M. Adil, H. Song, J. Ali et al., "EnhancedAODV: a robust three phase priority-based traffic load balancing scheme for Internet of Things," *IEEE Internet of Things Journal*, 2022.

[5] F. Zhu, C. Zhang, Z. Zheng, and A. Farouk, "Practical network coding technologies and softwarization in wireless networks," *IEEE Internet of Things Journal*, vol. 8, no. 7, pp. 5211–5218, 2021.

[6] A. Farouk, M. Zakaria, A. Megahed, and F. A. Omara, "A generalized architecture of quantum secure direct communication for _N_ disjointed users with authentication," *Scientific Reports*, vol. 5, no. 1, pp. 1–17, 2015.

[7] M. Adil, M. K. Khan, M. Jamjoom, and A. Farouk, "MHADBOR: AI-enabled administrative distance based opportunistic load balancing scheme for an agriculture internet of things network," *IEEE Micro*, vol. 42, no. 1, pp. 41–50, 2022.

[8] M. Naseri, M. A. Raji, M. R. Hantehzadeh, A. Farouk, A. Boochani, and S. Solaymani, "A scheme for secure quantum communication network with authentication using GHZ-like states and cluster states controlled teleportation," *Quantum Information Processing*, vol. 14, no. 11, pp. 4279–4295, 2015.

[9] S. Wang, "Innovation of tourism public service mechanism of wisdom tourism based on neural network," *Boletin Tecnico/Technical Bulletin*, vol. 55, no. 20, pp. 82–89, 2017.

[10] Z. Zhou, "Research on source culture orientation of wisdom tourism system in the traditional villages of the central plains," *Boletin Tecnico/Technical Bulletin*, vol. 55, no. 6, pp. 19–24, 2017.

[11] X. Li, "Research on the composition structure model of new wisdom tourism," *Agro Food Industry Hi Tech*, vol. 28, no. 1, pp. 1370–1374, 2017.

[12] S. Veronica, N. Ginting, and A. Marisa, "Local wisdom-based on development of the environment and atmosphere aspect of Berastagi night tourism," *International Journal of Architecture and Urbanism*, vol. 4, no. 2, pp. 144–155, 2020.

[13] R. H. Demolinggo, D. Damanik, K. Wiweka, and P. P. Adnyana, "Sustainable tourist villages management based on Javanese local wisdom 'Memayu Hayuning Bawono' best practice of Desa Wisata Pentingsari, Yogyakarta," *International Journal of Tourism & Hospitality Reviews*, vol. 7, no. 2, pp. 41–53, 2020.

[14] I. Putra, W. Maba, I. K. Widnyana, and A. A. K. Sudiana, "The management model of Masceti Pura Temple area in Bali as a spiritual tourism destination based on local wisdom," *International Journal of Research -GRANTHAALAYAH*, vol. 9, no. 2, pp. 291–298, 2021.

[15] P. Wismayani, I. A. Wiswasta, and I. K. Sumantra, "Development of Goa Lawah Temple as a spiritual tourism based on local wisdom," *International Journal of Contemporary Research and Review*, vol. 10, no. 2, pp. 21395–21400, 2019.

[16] J. W. Bi, Y. Liu, Z. P. Fan, and J. Zhang, "Wisdom of crowds: conducting importance-performance analysis (IPA) through online reviews," *Tourism Management*, vol. 70, pp. 460–478, 2019.

[17] I. Gst Ng Ag Gd Eka Teja Kusuma, N. Landra, and I. W. Widnyana, "Construction of Balinese local wisdom based on social model in the tourism sector in creating happiness to enhance

community satisfaction," *Asia Pacific Management and Business Application*, vol. 8, no. 1, pp. 53–64, 2019.

[18] R. Chatila, K. Firth-Butterflied, J. C. Havens, and K. Karachalios, "The IEEE global initiative for ethical considerations in artificial intelligence and autonomous systems [standards]," *IEEE Robotics & Automation Magazine*, vol. 24, no. 1, pp. 110–110, 2017.

[19] H. Lu, Y. Li, C. Min et al., "Brain intelligence: go beyond artificial intelligence," *Mobile Networks and Applications*, vol. 23, no. 7553, pp. 368–375, 2017.

[20] D. Hassabis, D. Kumaran, C. Summerfield, and M. Botvinick, "Neuroscience-inspired artificial intelligence," *Neuron*, vol. 95, no. 2, pp. 245–258, 2017.

[21] S. Makridakis, "The forthcoming artificial intelligence (AI) revolution: its impact on society and firms," *Futures*, vol. 90, pp. 46–60, 2017.

[22] R. Li, Z. Zhao, X. Zhou et al., "Intelligent 5G: when cellular networks meet artificial intelligence," *IEEE Wireless communications*, vol. 24, no. 5, pp. 175–183, 2017.

[23] S. D. Baum, "On the promotion of safe and socially beneficial artificial intelligence," *AI & SOCIETY*, vol. 32, no. 4, pp. 543–551, 2017.

[24] S. Price and P. A. Flach, "Computational support for academic peer review: a perspective from artificial intelligence," *Communications of the ACM*, vol. 60, no. 3, pp. 70–79, 2017.

[25] A. F. Chen, A. C. Zoga, and A. R. Vaccaro, "Point/counterpoint: artificial intelligence in healthcare," *Healthcare Transformation*, vol. 2, no. 2, pp. 84–92, 2017.

[26] M. Nasr, A. Mahmoud, M. Fawzy, and A. Radwan, "Artificial intelligence modeling of cadmium(II) biosorption using rice straw," *Applied Water Science*, vol. 7, no. 2, pp. 823–831, 2017.

[27] J. Lemley, S. Bazrafkan, and P. Corcoran, "Deep learning for consumer devices and services: pushing the limits for machine learning, artificial intelligence, and computer vision," *IEEE Consumer Electronics Magazine*, vol. 6, no. 2, pp. 48–56, 2017.

Hindawi
Wireless Communications and Mobile Computing
Volume 2023, Article ID 9823659, 1 page
https://doi.org/10.1155/2023/9823659

Retraction

Retracted: Wireless Control Industrial Robot Processing Irradiation System Based on Artificial Intelligence Technology

Wireless Communications and Mobile Computing

Received 18 July 2023; Accepted 18 July 2023; Published 19 July 2023

This article has been retracted by Hindawi following an investigation undertaken by the publisher [1]. This investigation has uncovered evidence of one or more of the following indicators of systematic manipulation of the publication process:

(1) Discrepancies in scope
(2) Discrepancies in the description of the research reported
(3) Discrepancies between the availability of data and the research described
(4) Inappropriate citations
(5) Incoherent, meaningless and/or irrelevant content included in the article
(6) Peer-review manipulation

The presence of these indicators undermines our confidence in the integrity of the article's content and we cannot, therefore, vouch for its reliability. Please note that this notice is intended solely to alert readers that the content of this article is unreliable. We have not investigated whether authors were aware of or involved in the systematic manipulation of the publication process.

Wiley and Hindawi regrets that the usual quality checks did not identify these issues before publication and have since put additional measures in place to safeguard research integrity.

We wish to credit our own Research Integrity and Research Publishing teams and anonymous and named external researchers and research integrity experts for contributing to this investigation.

The corresponding author, as the representative of all authors, has been given the opportunity to register their agreement or disagreement to this retraction. We have kept a record of any response received.

References

[1] L. Zhao, Q. Li, and G. Ding, "Wireless Control Industrial Robot Processing Irradiation System Based on Artificial Intelligence Technology," *Wireless Communications and Mobile Computing*, vol. 2022, Article ID 7068596, 8 pages, 2022.

Hindawi
Wireless Communications and Mobile Computing
Volume 2022, Article ID 7068596, 8 pages
https://doi.org/10.1155/2022/7068596

Research Article

Wireless Control Industrial Robot Processing Irradiation System Based on Artificial Intelligence Technology

Lijun Zhao,[1] Qingsheng Li ,[2] and Guanhua Ding[3]

[1]*Electrical and Electronic Engineering Department, Hebei Petroleum University of Technology, Chengde 067000, China*
[2]*Security Division, Hebei Petroleum University of Technology, Chengde 067000, China*
[3]*School of Electronic and Information Engineering, Beihang University, Beijing 100191, China*

Correspondence should be addressed to Qingsheng Li; liqingsheng@cdpc.edu.cn

Received 17 February 2022; Revised 16 March 2022; Accepted 1 April 2022; Published 9 May 2022

Academic Editor: Junjuan Xia

Radiation processing technology has been more and more widely used in light industry, chemical industry, food preservation, medical care, and other industries. Therefore, this paper designs a kind of wireless control system based on artificial intelligence technology γ radiation method, to strengthen the application of radiation processing equipment, and γ radiation monitoring can strengthen the radiation monitoring of its surrounding environment. The experimental results show that the C/Si atomic ratio of oxidized SiC fiber in air treated by this scheme is about 1.75, while the C/Si atomic ratio of SiC(Be) fiber treated by electron irradiation is close to 1 : 1.

1. Introduction

Food irradiation, with its unique technical advantages to reduce the loss of agricultural products and food, improves food quality, control food-borne diseases, etc., gained more and more attention from countries around the world. According to the statistical report published by the Food and Agriculture Organization (FAO) of the United Nations, the International Atomic Energy Agency (IAEA), and the World Health Organization (WHO), more than 40 countries around the world have approved more than 200 kinds of irradiated food, the total annual market sales amounted to about 400,000 tons, and food irradiation processing has been recommended by FAO, IAEA, and WHO as an international key promotion project [1, 2]. Food irradiation processing with radiation sources mainly γ-ray, electron beam two major types, of which China's cobalt source γ-ray is more widely used. But with the electron gas pedal beam energy and beam under the device to improve and perfect, electron beam irradiation in the processing capacity and economic efficiency has shown increasing advantages and in recent years has become the core equipment of the new irradiation processing device. Statistics from the irradiation industry associations show that China has built power 5 KW and above radiation processing with 83 electron gas pedals, with a total power of nearly 6469 KW, and another 8 high-power electron gas pedal device is under construction. Because the gas pedal has a high degree of automation, it can realize the online production and no radioactive waste sources generated and other advantages, while the electron beam energy can be adjusted through the acceleration voltage, the system is more convenient to control, and the line volume is flat, the product absorbed dose in uniform. Therefore, electron beam irradiation is expected to become the development direction of food irradiation processing [3]. The country in the "thirteenth five-year plan" period will increase the electron beam irradiation food application research support, the national development and reform commission also has to nonnuclear

power application as an opportunity to the electron beam radiation application of industrialization has given support. However, at present, most of the research results of food irradiation in China are concentrated in the processing application field of cobalt source γ-rays, and the basic research and application development of electron beam food irradiation are still quite weak, so the authors intend to make a review on the current research status and application characteristics of electron beam food irradiation in this field at home and abroad, in order to play a brick to lead the jade effect and promote the application of domestic electron beam food irradiation [4, 5]. The development of electron beam food irradiation applications in China is expected.

Electron beam irradiation has the following characteristics and advantages: (1) The equipment operation is highly controllable. The electron beam is generated by the electron gas pedal, its generation and disappearance is controlled by the power switch of the gas pedal, the size of the ionizing radiation energy is also adjusted by the accelerating voltage of the gas pedal, and the system control is relatively convenient. The electron beam energy is continuously adjustable within a certain range, the line volume is flat, and most of the devices under the beam use transmission devices, so that the absorbed dose of the product is uniform [6].

The accelerator is also equipped with ozone catalyst treatment device to achieve zero external ozone emission. Accelerator power that cut off the radiation source is safe and reliable and has no radioactive waste sources [7, 8].

The contributions of this paper are as follows:

The effect of traditional chemical fumigation insecticides on killing insect eggs is poor. Therefore, through appropriate dose of electron beam irradiation, this paper can not only kill 100% of insectivores and edible fungi but also kill other insect eggs in food and forest, which has the ability of killing in the whole period.

In order to make irradiation sterilization thorough and effective, we have designed a sterilization scheme for low-density food or food surface, which adopts electron beam sterilization. Irradiation does not need to remove product packaging, has no secondary pollution, has little impact on food quality and nutrition, and has good environmental protection performance.

This experiment shows that this scheme can effectively degrade the residues of pesticides and veterinary drugs, which is conducive to food safety.

2. Related Work

Research shows that E-beam food irradiation has unique technical characteristics and advantages in solving food safety problems, especially in preventing foodborne pathogenic microbial contamination in food, and in import and export quarantine, there is great potential for application [9, 10]. Due to the unique physical state and quality characteristics of cold and fresh animal-derived foods, the commonly used sterilization methods such as high-temperature and high-pressure sterilization and pasteurization can no longer help, while electron beam irradiation treatment is currently a better technology for sterilizing and preserving cold and fresh foods. [11] reported that the use of electron beam 0-3.85 kGy irradiation of boneless pork can effectively kill Escherichia coli and Salmonella in cold meat. Meanwhile, the quality and taste of carton packaged products after electron beam irradiation were not affected when stored under frozen or refrigerated conditions, but longer storage would affect the product gloss [12]. In [13], small packages of fresh pork were irradiated with 1 kGy low-dose electron beam, and the pork samples were inoculated with 103-104 g of Salmonella before irradiation, and the package gases were air vacuumed with 25% CO_2, 50% CO_2, and 72% CO_2 [14]. Electron beam irradiation of minced pork infected with four viruses was found to completely inactivate the viruses at 4.4-5.24 kGy. [15] studied the irradiation effect of electron beam irradiation on Listeria monocytogenes in minced pork and found that the sensitivity of each strain to electron beam varied and the sterilization D10 dose ranged from 0.372 to 0.447 kGy, for which he suggested the process dose of electron beam sterilization to be 4.5 kGy. [16] treated marinated chicken breast with electron beam and stored at 2°C for 8 weeks after irradiation at 2.9 kGy, the microbiological indexes met the requirements and had no effect on the quality. studied the resistance of a fungal spore to γ-rays and electron beam irradiation and showed that the sterilization effect of both was basically similar at the same absorbed dose. For the study of electron beam sterilization and preservation of cold and fresh animal-derived foods, scholars at home and abroad have also made useful exploration. For example, [5] investigated the effect of electron beam irradiation on the survival and repair of Escherichia coli at different pH. Blank et al. studied the sterilization effect of electron beam irradiation on cheese. [6] studied the effect of electron beam on the physical, physicochemical, and functional parameters of frozen stored liquid egg yolk [8–10].

E-beam irradiation has shown unique technical advantages and significant effects in killing microorganisms and pathogenic bacterial contamination in foods of plant origin. [7] used 10 kGy E-beam to irradiate eight spices, such as black pepper, onion powder, garlic powder, and white pepper, all of which were able to reduce the total bacterial content to less than 100 g without any significant effect on the quality. [8] studied wheat inoculated with spores of two strains of Tilletia controversa and T. tritici by 0-10.2 kGy E-beam irradiation, and the former bacteria were completely killed at a dose of 4.6-4.7 kGy. The doses of 4.6-4.7 kGy for the former strain and 10.2 kGy for the latter strain showed that a higher killing dose was required to kill the fungal spores as in the case of γ-rays. Studies on the processing quality of irradiated wheat showed that the E-beam irradiation treatment had no significant effect on its nutritional quality and processing characteristics, except for the reduction of surface gloss and water absorption of wheat. [9] irradiated brown rice, wheat, and mangold with E-beam and found that the total number of bacteria decreased to less than 100 g at 4 kGy irradiation and its viscosity was not affected, nor did it cause degradation of starch [10].

The above study shows that although the study of the effect of electron beam irradiation is not enough compared

with the study of the effect of γ-ray irradiation in terms of scope and depth, but it has a very good effect on foodborne microbial contamination and pathogenic bacteria, is an effective technical means to ensure food quality and safety, and in the dose range used has little effect on food quality and processing characteristics.

3. High-Energy Electron Accelerator

There are two main types of electron gas pedals used for irradiation processing, namely, electron linear gas pedals and high-voltage electron gas pedals, most of the irradiation gas pedals in the past belong to high-frequency, high-pressure type gas pedals, energy is mostly below 5 Mev. At present, directly used for irradiation of food, drugs, and medical devices, high-energy gas pedals are mainly microwave linear gas pedal and Loder gas pedal, the maximum output power of linear gas pedal has reached 15~25 kW, output/input ratio of about 10% to 20%. Most of the high-energy gas pedals produced in China are linear accelerators [15].

Therefore, these three types of gas pedals have their advantages and disadvantages, the structure of the standing wave gas pedal is the simplest and the smallest, and the return gas pedal is the second; the traveling wave and return gas pedal maximum beam power is relatively large and the standing wave gas pedal is slightly smaller; efficiency, the return gas pedal has the highest overall efficiency, small size, and simple structure, but the development time is short, and the application is just starting [5]. Therefore, in practical applications, the appropriate type can be selected according to its characteristics.

Russia, Japan, Belgium, France, and other countries are able to produce high-energy electron gas pedals [6]. Among them, Belgium IBA company strength is the strongest and its production of RHODOTRON type gas pedal high energy (10 MeV), high power, and advanced technology in the gas pedal for irradiated food and radiation disinfection in the world is leading.

In recent years, the domestic gas pedal research and development work is progressing rapidly, and on December 18, 2007, by the China Atomic Energy Research Institute of independent design and development of high-energy, high-power electron irradiation gas pedal 10 MeV/15 kW electron gas pedal irradiation demonstration project formally passed the acceptance [8].

4. Protection Requirements for Hardware Facilities

4.1. Radiation Safety Control Measures for Gamma Irradiation Processing Devices. Industrial γ-irradiated processing devices are used to irradiate products through γ-rays emitted by the decay of radionuclides to achieve certain purposes. At present, the γ sources of irradiators used in industry are mainly the nuclides 60Co, 137Cs, and so on. In the γ source used in industry, the γ source must be well controlled for protection. Before using γ source for industrial irradiation, the activity of γ source should be measured and calculated, and the correct safety measures should be taken according to the activity of the source. In the process of using γ source to irradiate industrial products, the source takes shielding measures in the process of using γ source to irradiate industrial products [5]. The open pool around the physical isolation must be set up (maintenance or auxiliary operations can be removed) to prevent the personnel concerned from inadvertently falling into the pool [6]. In the industrial irradiation of γ sources to reach the service life, to be replaced γ sources, and the decommissioning of γ sources for certain treatment. At present, the management of retired sources is confusing, for the end-of-life sources do not know how to deal with disposal caused a number of unused sources or waste sources out of control accidents [7]. To extend the service life of the source, it is necessary to submit to the audit and control department to check the sealing of the source, and only after passing can be used. Decommissioned sources can be returned to the business or disposed of as radioactive waste.

4.2. Radiation Safety Control Measures for Irradiation Sites. Irradiation sites are generally divided into control areas and supervision areas [8]. Control area is under normal conditions to control normal exposure or to prevent the spread of contamination, to prevent potential exposure type, to limit its extent, and to take special protective measures' type to make safety provisions of the area, not designated as a control area for the supervision of the area [5]. In the control area of the import and export, radiation danger warning signs must be set up, industrial irradiation γ sources used in the control area. In order to reduce the impact of direct and scattered radiation on the workplace outside the radiation room, the γ source storage channels to be labyrinthine and pays attention to ventilation. The air in the irradiation room irradiated by the strong source produces small amounts of harmful gases: ozone molecules and nitrogen oxides, where the amount of O_3 production is larger than that of NOx [9].

In order to prevent the effect of harmful gases on the staff, it is necessary to take good ventilation measures and centrifugal fans for air extraction. Means must be provided in the irradiation room and on the control console to stop, quickly interrupt, or terminate the operation of the irradiator at any moment and return the source to a fully shielded state, and there must be alarms and safety features in the irradiation room that can give visual and audible alarms when the source is out of control [6, 10]. In addition, for the site selection of γ irradiation processing device, the site of γ irradiation processing device should be selected from a stable site with good geological conditions, avoiding high-voltage transmission corridors and flammable and explosive sites according to the relevant national norms, and meeting the requirements of relevant national standards in the seismic protection zone. Comprehensive from the above requirements, collect hydrological, geological, meteorological, demographic, geographic ring mirror, seismic, and other information after the ring mirror impact assessment and after the regulatory approval to determine the plant site [5].

5. Manufacturing Solutions for This Article

5.1. Raw Materials. The PBeCS pioneer filament was synthesized in the laboratory [9], with a number average molecular weight of 2473, a molecular weight distribution of 3.36, and a softening point of 197°C.

5.2. Experimental Method

5.2.1. Electron Beam Irradiation of PBeCS Pioneer Filaments without Melting Treatment. Weigh the PBeCS pioneer wire in a fixed container, first vacuum, to achieve the required target vacuum, to the container into the gas containing oxygen and nitrogen and then continue to pump the vacuum, repeated 3 to 5 times to achieve the purpose of changing out the gas. Then, the gas is introduced and the flow ratio of $N_2 : O_2$ is controlled as 200 : 1, start to turn on the electron gas pedal (3.5 MeV), ensure that the electron flow is 1.5 mA (the dose rate is 0.63 kGy/s), irradiate continuously to the required irradiation dose (1.0, 1.5, and 2.0 MGy), reach the required irradiation dose, then turn off the gas pedal, stop irradiation, then remove the sample, weigh the mass, and calculate the mass loss rate.

5.2.2. Preparation of SiC(Be) Fibers. The PBeCS pioneer wire was weighed, placed inside the crucible, pressed with graphite at both ends, placed in a high-temperature tube furnace, protected by inert gas, at 500°C (heating rate 4°C/min), reacted for 2 h, then continued to heat up to 1250°C, reacted for 1 h, and naturally cooled to room temperature to obtain black SiC fibers.

5.3. Analytical Testing

5.3.1. Infrared Absorption Spectra. After the irradiated samples were made into KBr compacts, the infrared absorption spectra were measured by a Nicolet 6700 smart FTIR spectrometer. A simple semiquantitative analysis was performed according to the Lambert-Beer law. The ratio of the absorbance of different absorption peaks can be reduced to

$$\frac{A_1}{A_2} = \frac{K_1}{K_2} \times \frac{C_1}{C_2} = K\frac{C_1}{C_2}. \quad (1)$$

In this work, the degree of cross-linking reaction can be determined semiquantitatively by the change of Si-H, assuming the characteristic peak at 1250 cm^{-1} of Si–CH_3 as the internal standard in the calculation of the oxidation of the precursor PCS protofilament:

$$P_{\mathrm{Si-H}} = \frac{(A_{2100}/A_{1250})_g - (A_{2100}/A_{1250})_o}{(A_{2100}/A_{1250})_g} \times 100\%, \quad (2)$$

where A_{1250} is Si–CH_3 absorption peak intensity at 1250 cm^{-1}.

A_{2100} is the absorption peak intensity of Si-H at 2100 cm^{-1}; the subscript g represents green fiber; and the subscript o represents oxidation fiber.

5.3.2. Gel Content. The gel content was extracted in a continuous cycle of 15 times in a Soxhlet extractor with xylene as the solvent, and the mass change rate before and after extraction was calculated.

5.3.3. Elemental Analysis. The oxygen content of the fibers was tested by a LECO-60 combined meter (N/O/H); the elemental distribution on the diameter of the silicon carbide fibers was analyzed by an auger electron spectroscopy (AES) instrument of PHI 700 nanoscanning Osher system.

5.3.4. Microscopic Morphology Analysis. D8Discover diffractometer was used to analyze the phase of SiC fiber crop, and JEM-2100F scanning electron microscope was used to observe the surface morphology of silicon carbide fiber.

5.3.5. Determination of Mechanical Properties. The tensile strength of the fibers was measured by Model-YG001B electronic fiber strength meter with a specimen distance of 25 mm and a tensile rate of 2 mm/min.

6. Results and Discussion

6.1. Effect of Electron Irradiation on the Chemical Structure of PBeCS Pioneer Filaments. The infrared spectra of PBeCS precursor wires before and after irradiation are shown in Figure 1.

The main characteristic peaks of the FTIR spectra of each PBeCS pioneer filament sample are as follows: 3450 cm^{-1} and 1650 cm^{-1} are the O-H vibrations in H_2O, probably caused by the moisture absorption of the pioneer filament; 2950 cm^{-1} and 2900 cm^{-1} are the C-H stretching vibrations of methyl(-CH_3) and methylene(-CH_2 -); 2100 cm^{-1} is the characteristic stretching vibrations of Si-H; 1410 $cm^{-1}$is the C-H deformation vibrations of Si- CH_3; and 1360 cm^{-1} are the C-H vibrations of Si-. The C-H stretching vibration peaks of methyl(-CH_3) and methylene (-CH_2) are 2950 cm^{-1} and 2900 cm^{-1}; 2100 cm^{-1} is the characteristic stretching vibration peak of Si-H; 1410 cm^{-1} is the C-H deformation vibration peak of Si-; and 1360 cm^{-1} is the C-H out-of-plane vibration peak of Si—CH_2—Si. C-H is the out-of-plane vibration peak; 1250 cm^{-1} is the Si-deformation vibration peak; 1020 cm^{-1} is the Si-C-Si stretching vibration peak on Si—CH_2—Si; and 820 cm^{-1} is the Si-C stretching vibration peak.

The Si-H bond is a very active functional group, which can promote the cross-linking of PBeCS precursor filaments by consuming itself and increase the yield of porcelainization. The relative amounts of the Si-H reactive groups were characterized by $A_{\mathrm{Si-H}}/A_{Si-CH_3}$, as shown in Table 1, and the ASi-H/ASi-CH_3 decreased gradually with the increase of irradiation dose. Combined with Figure 1, it can be seen that with the increase of irradiation dose, a gradually enhanced Si-OH characteristic vibration peak appeared at 3680 cm^{-1}, while a gradually enhanced C=O stretching vibration peak also appeared at 1710 cm^{-1}.

This is mainly caused by the reaction between the C-H side chain and oxygen to form C=O double bonds [1]; the absorption peaks in the range of 1000-1100 cm^{-1} have a tendency to enhance and broaden to higher wave numbers,

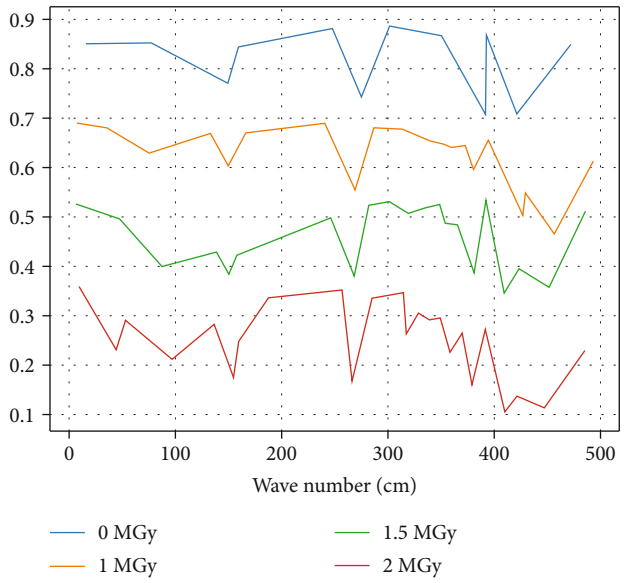

Figure 1: Infrared spectra of PBeCS pioneer filaments at different irradiation doses.

Table 1: Absorbance ratio of Si-H to Si-CH_3 in PBeCS pioneer filaments at different irradiation doses.

Irradiation dose/Mgy	A_{Si-H}/A_{Si-CH_3}
0	1.97
1	1.88
1.5	1.75
2	1.64

which is due to the close position of Si-O-Si and Si-CH_2-Si peaks, and appear to superimpose as one absorption peak, which also indicates the formation of Si-C-Si and Si-O-Si type bridging structures after irradiation.

6.2. Gel Content of Irradiated Products. During the cross-linking process of PBeCS pioneer filaments, the three-dimensional network structure begins to form, and the mass fraction of nonfusible material in the fiber, generally known as gel content, is mainly used to characterize the degree of nonfusion of the fiber [2], and the relationship between the gel content and oxygen content of PBeCS pioneer filaments and the irradiation dose is shown in Table 2. This indicates that the PBeCS precursor filaments do react with the oxygen in the mixed atmosphere under the electron beam irradiation, and the higher the irradiation dose, the higher the oxygen content.

When the irradiation dose was low, no gel content appeared, because only the oxidation reaction appeared and did not reach the irradiation dose required for the cross-linking reaction, with the dose further increased, the gel began to appear, and when the irradiation dose was 2.0 MGy, the gel content reached about 20%, and the fibers did not appear in the later sintering process, which indicates that after low dose irradiation by electron beam in oxygen-

Table 2: Effect of irradiation dose on PBeCS pioneer filaments.

Irradiation dose/ Mgy	Mass fraction of gel/%	Mass fraction of oxygen/%
0	0	0.76
1	0.1	3.54
1.5	0.7	4.98
2	19.8	5.97

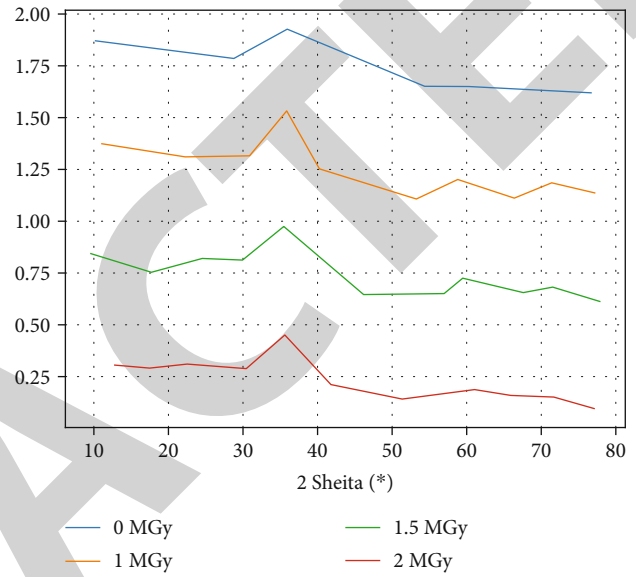

Figure 2: XRD patterns of beryllium-containing silicon carbide fibers with different irradiation doses.

containing atmosphere, it is possible to no melting treatment.

6.3. Microstructure and Mechanical Properties of SiC(Be) Fibers. The XRD patterns of the beryllium carbide containing fibers obtained by sintering the PBeCS pioneer filaments cross-linked with different irradiation doses at 1250°C under N_2 atmosphere are shown in Figure 2, where three sharp diffraction peaks, $\theta = 35.4°, 60.4°$, and $71.2°$, corresponding to the (111), (220), and (311) crystallographic planes of β-SiC, respectively, appear in the fiber diffraction patterns. 311) crystalline plane of β-SiC. From Figure 2, it can be seen that the intensity of the crystalline diffraction peak first increases with increasing irradiation dose and then tends to broaden and weaken. This is caused by the oxygen introduced during the irradiation process, which exists in the fiber as an amorphous phase SiC_xO_Y and its pyrolysis produces an amorphous SiO_2 that inhibits the grain growth. The higher the irradiation dose, the more oxygen is introduced, the more obvious the inhibition, and the worse the crystallinity.

When the PBeCS pioneer filaments treated with different irradiation doses were sintered under N_2 atmosphere, the crosslinking degree was too low at 1.0 and 1.5 MGy, and the merging of the silicon carbide fibers occurred as shown in Figure 3, and when the dose was continued to increase

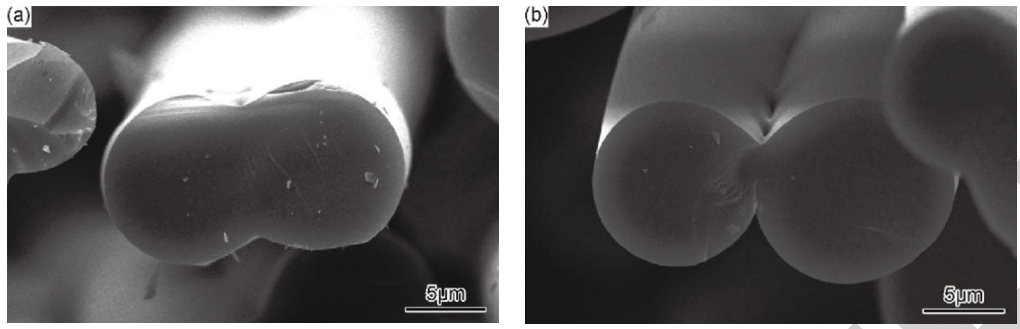

(a) (b)

Figure 3: SEM cross-sections of SiC(Be) fibers with different irradiation doses (a). 1.0 MGy. (b) 1.5 MGy.

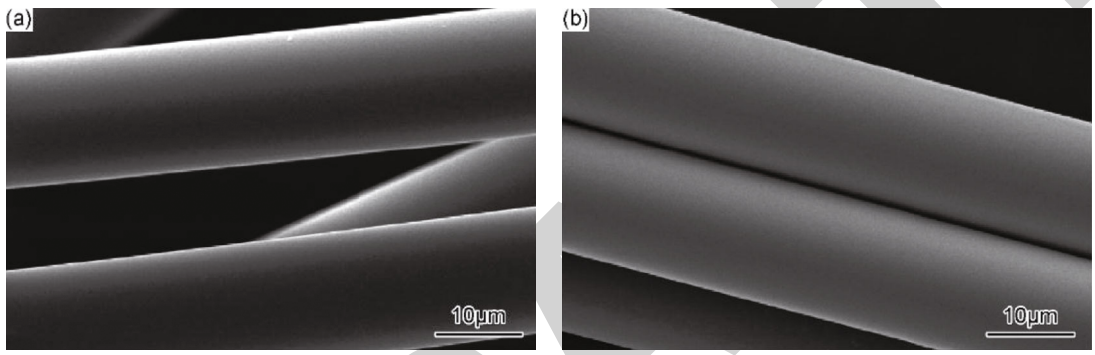

(a) (b)

Figure 4: SEM pictures of the surface of SiC(Be) fibers treated with air oxidation crosslinking and electron beam irradiation crosslinking. (a) Air oxidation crosslinking. (b) E-beam irradiation crosslinking.

Table 3: Mechanical properties of beryllium-containing silicon carbide fibers.

Curing method	Irradiation dose/Mgy	Tensile strength/Gpa	Tensile modulus/Gpa
Thermal oxidation curing in air	—	1.69	145
Electron beam irradiation	2	1.81	179

to 2.0 MGy, the gel content of the PBeCS pioneer filaments was relatively low (20%), but no merging occurred in the later sintering, and the synthesized fibers changed from the initial light yellow color to black as shown in Figure 4(b). The color of the synthesized fibers changed from light yellow to black at the beginning, as shown in Figure 4(b). The fibers cross-linked by irradiation at a dose of 2.0 MGy and air oxidation were tested for their mechanical properties, and the results are shown in Table 3, which shows that the strength of the fibers cross-linked by electron beam irradiation was significantly improved compared with those cross-linked by air oxidation.

Figure 4 shows the SEM photomicrographs of silicon carbide fibers cross-linked by air oxidation and irradiated at a dose of 2.0 MGy. From Figure 4, it can be found that the surface of the fibers was not damaged by the electron beam irradiation, and the fiber shape remained intact with a diameter of about 12-15 μm and a bright and dense surface. This further proves that electron beam irradiation has a good nonmelting effect on the pioneer filaments.

6.4. SiC(Be) Fiber Composition Analysis. The electron-irradiated and air-oxidized cross-linked fibers were sintered at 1250°C. The Si, C, and O content of the fibers was measured by AES (AES is difficult to test because the doped Be is a light element and its atomic fraction is less than 1%). As shown in Figures 5 and 6, the oxygen content of the electron irradiated fibers is 4.71% (atomic fraction, below), which is significantly lower than that of the air-oxidized cross-linked fibers (11.55%). The oxygen content of SiC fibers and its influence on the temperature resistance, creep resistance, and mechanical properties are important because the reaction of the oxygen-containing phase SiC_xO_Y in the fibers at high temperature results in the formation of SiO and CO gas, which leaves a large number of holes and defects in the fibers. This is because the reaction of the oxygen-containing phase 111 in the fiber at high temperature will form SiO and CO gas, which will leave a large number of holes and defects on the fiber, resulting in the destruction of the fiber structure and a rapid decrease in its tensile strength. At the same time, a large number of β-SiC

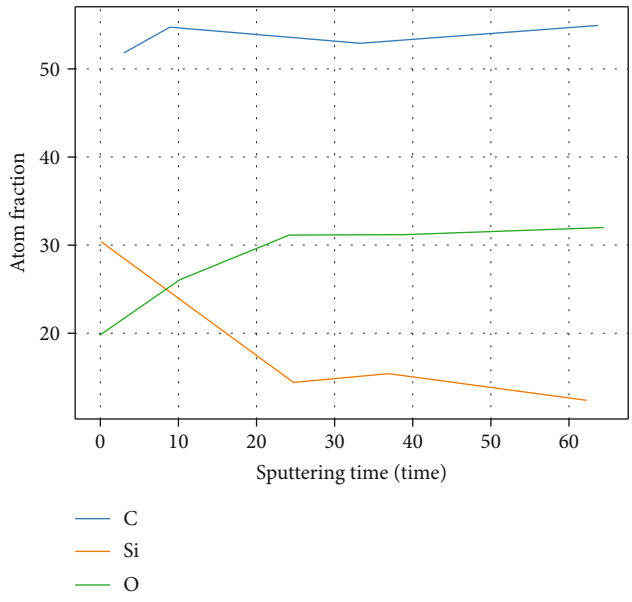

Figure 5: AES profile of SiC fibers cross-linked by air oxidation.

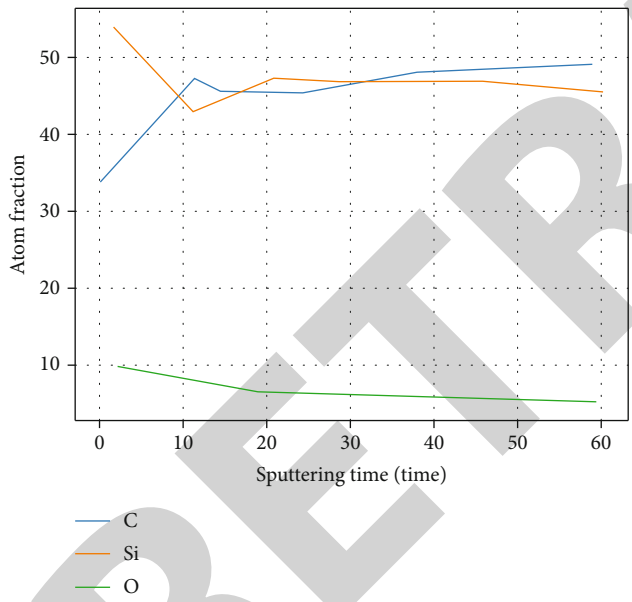

Figure 6: AES profile of electronically irradiated cross-linked SiC (Be) fibers.

microcrystals in the fiber are surrounded by SiC_xO_y, so that a large number of grain boundary phases will slip during the growth of fiber grains at high temperatures, resulting in lower creep resistance of the fiber [3, 4]. Therefore, reducing the oxygen content of fibers is a prerequisite for obtaining high-performance SiC fibers, and the use of electron irradiation crosslinking can significantly reduce the oxygen content of SiC fibers.

In addition, the C/Si atomic ratio of SiC fibers oxidized in air is about 1.75, while the C/Si ratio of SiC(Be) fibers treated by electron irradiation is close to the stoichiometric ratio of 1 : 1. For SiC fibers, the C/Si atomic ratio is another important index affecting their oxidation resistance, creep resistance, and mechanical properties. In SiC fibers, the presence of a large amount of excess C, which is sensitive to oxidizing atmosphere, reduces the oxidation resistance of the fibers, especially at high temperatures where the excess C will continue to oxidize and larger holes will appear on the fiber surface, which will promote the diffusion to the interior of the fibers and drastically reduce the fiber strength [15]. In addition, the distribution of excess C around the SiC grains will also limit the growth of β-SiC grains, while the carbon layer between the grain boundaries will promote grain boundary slip, resulting in fibers with low creep resistance [16].

Table 4: Parameters of chemical bonds in PBeCS pioneer filaments.

Chemical bond	Bond length/nm	Bond energy/(kj/mol^{-1})
Si—C	0.188	242.7-334.7
Si—H	0.147	320
C-H	0.107	415

6.5. Reaction Mechanism Speculation. In the PBeCS pioneer filament structure, the main chemical bonds are Si-C, Si-H, and C-H bonds, and the bond lengths and bond energies of these bonds are shown in Table 4, and the bond energy of Si-C bonds varies from 242.7 to 334.7 kJ/mol. The bond energy of Si-C bond varies in the range of 242.7 to 334.7 kJ/mol, and its specific value is related to the chemical environment around the C atom.

When the PBeCS pioneer filament is irradiated by electron beam, the high-energy electrons interact with the PBeCS pioneer filament and transfer the energy of the electrons through elastic collisions, in which the bond energy of Si-H (320 kJ/mol) is lower than that of C-H (415 kJ/mol), it is known that the H atom of Si-H bond is more active and can if the absorbed energy is sufficient, it is possible to get rid of the bond and become reactive particles or Si radicals, which react with oxygen to form Si-OH, which then undergoes dehydration condensation reaction to form Si-O-Si, and at the same time, as the bond energy of Si-C bond energy varies in the range of 242.7 to 334.7 kJ/mol, if the chemical environment around the C atom changes so that the Si-C bond energy is lower than that of Si-H (320 kJ/mol), then the Si-C bond will break, forming Si-CH_2-Si radicals, and the Si radicals will cross-link with Si-CH_2- to form Si-CH_2-Si.

7. Conclusions

The PBeCS pioneer filaments are irradiated by electron beam during irradiation to obtain nonmelting products by undergoing a series of chemical transformations. Irradiation in a low-oxygen atmosphere is mainly Si-H; Si-CH_3 reacts with O_2 to form Si-OH and C=O structured molecules, and then, Si-OH undergoes dehydration condensation to form Si-O-Si. Si-H reacts with Si- to form Si-CH_2-Si, and this structure is transformed into SiC fiber skeleton structure in later sintering.

Hindawi
Wireless Communications and Mobile Computing
Volume 2022, Article ID 3866143, 17 pages
https://doi.org/10.1155/2022/3866143

Research Article

ALBRL: Automatic Load-Balancing Architecture Based on Reinforcement Learning in Software-Defined Networking

Junyan Chen,[1,2] **Yong Wang**,[2] **Jiangtao Ou**,[3] **Chengyuan Fan**,[3] **Xiaoye Lu**,[2] **Cenhuishan Liao**,[2] **Xuefeng Huang**,[2] **and Hongmei Zhang**[1]

[1]*School of Information and Communication, Guilin University of Electronic Technology, Guilin 541004, China*
[2]*School of Computer Science and Information Security, Guilin University of Electronic Technology, Guilin 541004, China*
[3]*AI Sensing Technology, Chancheng District, Foshan 528000, China*

Correspondence should be addressed to Yong Wang; ywang@guet.edu.cn

Received 2 March 2022; Revised 26 March 2022; Accepted 11 April 2022; Published 2 May 2022

Academic Editor: Junjuan Xia

Due to the rapid development of network communication technology and the significant increase in network terminal equipment, the application of new network architecture software-defined networking (SDN) combined with reinforcement learning in network traffic scheduling has become an important focus of research. Because of network traffic transmission variability and complexity, the traditional reinforcement-learning algorithms in SDN face problems such as slow convergence rates and unbalanced loads. The problems seriously affect network performance, resulting in network link congestion and the low efficiency of inter-stream bandwidth allocation. This paper proposes an automatic load-balancing architecture based on reinforcement learning (ALBRL) in SDN. In this architecture, we design a load-balancing optimization model in high-load traffic scenarios and adapt the improved Deep Deterministic Policy Gradient (DDPG) algorithm to find a near-optimal path between network hosts. The proposed ALBRL uses the sampling method of updating the experience pool with the SumTree structure to improve the random extraction strategy of the empirical-playback mechanism in DDPG. It extracts a more meaningful experience for network updating with greater probability, which can effectively improve the convergence rate. The experiment results show that the proposed ALBRL has a faster training speed than existing reinforcement-learning algorithms and significantly improves network throughput.

1. Introduction

Due to the rapid development of network communication technology and the significant increase in network terminal equipment, service traffic in networks shows rapid growth. At the same time, these fast-growing service flows also bring new challenges to existing communication networks. The new-intelligent network architecture represented by software-defined networking (SDN) has led to an effective change in the Internet. In SDN, addressing network throughput is a substantial issue in traffic engineering (TE) [1–3]. Managing a large number of network devices and significant network traffic in high-load network conditions is complicated, and traffic forwarding decisions in complex SDN network situations have proven to be NP-hard issues [4].

Traditional routing-optimization schemes always forward traffic based on the open shortest path first (OSPF) [5], equal-cost multipath routing (ECMP) [6], or optimized heuristic algorithms [7]. The OSPF protocol routes all flow requests singularly to the shortest path. The ECMP protocol uses multiple links simultaneously to increase transmission bandwidth. However, based on fixed forwarding rules, these approaches are prone to link congestion, and they cannot meet the demands of the exponential growth of heavy traffic. Due to a lack of historical experience in data learning, heuristic algorithms can only establish models for fixed networks. It is challenging to determine network parameters when a network changes, and scalability is limited. In recent years, because of its robust learning algorithm and excellent performance, deep learning has been gradually applied to

computer networks. Many studies have used supervised learning methods in SDN to realize intelligent network management [8–14]. However, supervised learning requires a great many datasets for training, and slow decision-making in dynamic network scenarios also poses a problem. Compared with supervised learning, reinforcement learning (RL) is an online learning that can change its actions to obtain optimal rewards through continuous exploration, learning, and trial. Reinforcement learning opens a new way for solving complex network problems [15]. Some researchers have used traditional algorithms of reinforcement learning such as deep Q-learning network (DQN) [16–19], proximal policy optimization (PPO) [20], deep deterministic policy gradient (DDPG) [21–28], and twin delayed deep deterministic policy gradient (TD3) [29–31]. The DQN algorithm uses Q-tables to store value functions, but it leads to excessive memory overhead and sizeable computational complexity when the network size increases. The deterministic policy gradient algorithms such as DDPG and TD3 still encounter the problems of a slow convergence rate and of instability. They heavily affect network performance before convergence.

In this paper, we propose an automatic load-balancing architecture based on reinforcement learning (ALBRL) to solve the TE problem of SDN in terms of throughput. ALBRL adapts the improved DDPG algorithm to find the near-optimal path between network hosts by receiving information about the network links in the data plane. Subsequently, it generates an inter-link-weight matrix and creates the forwarding path flexibly using Dijkstra's algorithm. In this process, ALBRL evaluates the merit of the action by the link evaluation information at the next moment and updates the network based on the evaluation results. Compared with the DDPG algorithm, the proposed ALBRL uses a SumTree binary tree structure to update the experience pool sampling. The probability of sampling experiences with a more significant temporal-difference error (TD-error) and network load-balancing-rate factor becomes more prominent. ALBRL selects those more critical experiences to the network update, so the network parameters such as throughput can reach convergence values faster. The impact of the convergence of the reinforcement-learning model can be reduced when the network is changed.

The main contributions of our paper are as follows:

(1) An automatic load-balancing optimization algorithm in SDN based on an improved, DDPG, reinforcement-learning model is proposed, which uses a SumTree binary tree structure to optimize the extraction method of the empirical-playback mechanism in the traditional DDPG algorithm. It can effectively solve the problems of a long trial time and the unstable performance of SDN networks caused by the slow convergence rate of the DDPG algorithm

(2) A mathematical model for evaluating network load balancing in high-load traffic scenarios is proposed as the SDN network performance evaluation and is used as a reward for the ALBRL algorithm

(3) An experimental system using the proposed architecture is designed to verify the effectiveness of the ALBRL algorithm

The rest of this paper is organized as follows: Section 2 gives the related literature; Section 3 describes the general architecture of the network; Section 4 establishes the load-balancing optimization model; Section 5 describes the ALBRL algorithm; Section 6 verifies the algorithm through simulation experiments; and finally, our conclusion and future directions for work given in Section 7.

2. Related Research

The current network environment is characterized by its complexity, colossal data traffic, and diversified service requirements. A traffic scheduling strategy based on a traditional network cannot meet the needs of the existing network environment and cannot handle increasingly complex tasks. The advent of SDN with programmability has led an increasing number of researchers to combine machine learning algorithms with SDN to optimize network routing. There are many solutions to the problem of optimizing TE throughput in SDN networks using traditional methods. For example, the authors in [5–7] use traditional methods such as the OSPF algorithm, the EMCP algorithm, and ant-colony optimization algorithms to optimize the network. However, traditional machine learning algorithms cannot grasp the global network information from multiple dimensions and often cause network congestion.

The deep learning (DL) method can optimize network routing in multiple dimensions using historical experience. Some researchers have studied network traffic prediction methods for network load balancing and bandwidth optimization. Azzouni and Pujolle [8] and Novaes et al. [9] used the long- and short-term memory (LSTM) algorithm to predict traffic forwarding data between network hosts. However, the number of hosts in a virtual network is often much larger than the number of switches. Therefore, this method has a limited effect in optimizing the forwarding strategy of the switches. The authors in [10] use a gated recurrent unit neural network (GRU-NN) to achieve better accuracy in predicting network traffic. The authors in [11, 12] propose a routing strategy that employs the convolutional neural networks (CNN) to select routing paths according to the online network traffic. The authors in [13] propose an active controller selection algorithm to schedule packets between the switch and the controller. The authors in [14] use the predicted link-state value of the LSTM algorithm to optimize network load balancing. These methods based on supervised learning require a large number of data sets for training and face the problem of slow decision-making in dynamic network scenarios.

In this paper, we use RL-based methods to consider the optimization of TE throughput using historical experience. Compared with supervised learning, reinforcement learning is an online learning that can change its actions to obtain optimal rewards through continuous exploration, learning, and trial. The authors in [16] propose a Q-learning and

SDN intelligent routing (RSIR) algorithm. The authors in [17] propose a routing-optimization strategy based on deep RL (DRL-R). The authors in [18] propose a multicontroller route-planning algorithm based on DQN. These three methods show a better improvement of the network. Q-learning can generate paths between node pairs, which avoids relying on switch link information in traditional decision-making. However, Q-learning methods require a lot of time to train the Q-table between each host pair in large-scale networks. Therefore, they have significant requirements for the controller's performance. Chen et al. [19] propose an algorithm based on dueling double DQN to solve the TE problem. Compared with the OSPF and least load (LL) routing algorithms, it achieved higher performance in well-known network topologies such as fat-tree and NSFNet. However, the problem of its convergence rate is not considered. The authors in [20] propose a routing-optimization algorithm based on the PPO model. Because of the adoption of the strategy method, the prediction of routing strategy in PPO is more accurate than Q-Learning. However, because the PPO algorithm is an on-policy algorithm, the sample utilization rate of the model in training is low. In order to address the problems of PPO and DQN algorithms, some researchers have used the DDPG algorithm to optimize the SDN network. DDPG is a model-free, deterministic-strategy, gradient algorithm based on an actor-critical principle [21]. It uses the offline learning method and Q-network for training and takes samples from the replay buffer to minimize correlation between samples. The authors in [22] adapt the DDPG algorithm to find the optimal scheduling scheme for flows. The authors in [23, 24] present a QoS optimization algorithm based on DDPG that ultimately improves the load-balancing degree and throughput rate to ensure delay and packet-loss rate. The authors in [25] propose an intelligent traffic-sampling system based on DDPG that can maintain the load balance of multiple traffic analyzers. The authors in [26] propose an intelligence-driven experiential network architecture for automatic routing (EARS) to optimize a network intelligently. EARS adapts the DDPG algorithm to select the routing paths of elephant and mouse flow through different action strategies and obtain near-optimal routing decisions. The authors in [27] employ DQN and DDPG to build DRL-based routing, which has better performance than OSPF. The authors in [28] optimize DDPG and proposed a reliable and time-sensitive DDPG algorithm to find the optimal path of network stream and solve the problem of continuity. However, DDPG is usually not robust enough for hyperparameters and other fine tuning. One of the main reasons for failure is that the Q-function overestimates Q-values, resulting in the collapse of the policy due to the use of errors in the Q-function. TD3 uses double DQN to solve the overestimating action Q-value that is critical in DDPG [29]. The authors in [30, 31] use TD3 and pinning control theory to generate routing policies automatically, thus ensuring that the routing policy can dynamically adapt to changes in network traffic. Although the TD3 algorithm is better than DDPG in network performance, it also increases the complexity of the routing algorithm and the burden on the controller, which leads to sizeable computational complexity when the network size increases. In addition, deterministic policy gradient algorithms such as DDPG and TD3 face the problems of a slow convergence rate and instability. This will heavily affect network performance before convergence.

As we know, an algorithm based on reinforcement learning uses online learning, while the network is running and needs to retrain when the network traffic changes significantly. Our paper proposes an automatic load-balancing architecture based on the improved DDPG algorithm. It uses the SumTree structure to improve the experience-pool sampling method of DDPG, which can speed up the algorithm convergence rate. The ALBRL we propose can make routing decisions in a continuous action space and has a perfect convergence. When the network traffic changes significantly, it can quickly converge, reducing the network performance fluctuation caused by the convergence delay of the reinforcement-learning model.

3. Network Architecture

In this paper, we describe our designed network architecture based on deep reinforcement learning, as shown in Figure 1. Each plane of the specific network architecture is described as follows:

(1) Forwarding plane. The forwarding plane is made up of programmable forwarding devices (SDN switches) and hosts. The forwarding devices connect to the control plane with southbound interfaces and receive the policies delivered by the control plane, such as the OpenFlow flow table

(2) Control plane. The control plane consists of SDN controllers that connect the forwarding plane and the management plane. The control plane obtains the topology of the forwarding plane and distributes control policies through the southbound interfaces. Meanwhile, it provides data network resources to the management plane through the northbound interfaces. The controller function is divided into the following four modules:

(i) The topology-building module. This module periodically obtains network information from the forwarding plane and builds the network topology.

(ii) The link information-acquisition module. This module periodically obtains the network status information of the data plane through the south interface. It sends the state s_t and reward r_t to the RL agent according to the acquiring information from the forwarding plane.

(iii) The packet_in handling module. This module handles the packet_in message uploaded by the switch.

(iv) The flow-entry distribution module. The controller updates flow entries based on the action a_t and the

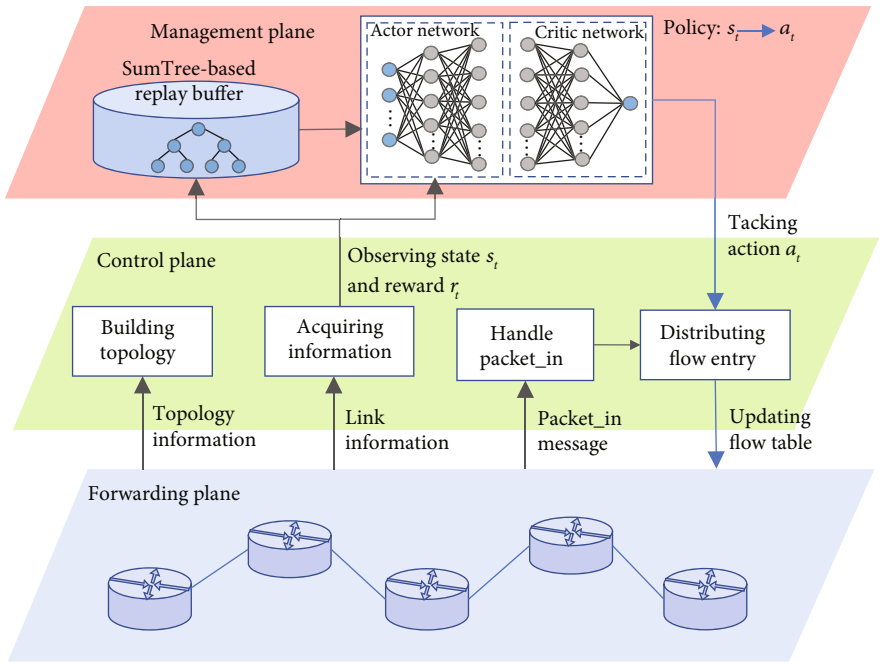

Figure 1: ALBRL network architecture. The architecture consists of the forwarding plane, the control plane, and the management plane.

packet_in message handling module and then actively issues flow entries.

(3) Management plane. The management plane runs a RL agent responsible for network load balancing. The agent adapts the DDPG algorithm, which uses SumTree-based replay buffers to find the near-optimal path between network hosts and generates link weights through the topology of the data obtained by the control plane and the network resource information of the forwarding plane. Then, the control plane updates flow entries based on link weight and send them to the forwarding plane.

4. Load-Balancing Optimization Model

This section describes the mathematical model for evaluating network load balancing in high-load traffic scenarios as the SDN network performance evaluation. We use $Graph = (V, E)$ to represent the undirected graph structure of the forwarding plane. We use M to denote the number of switches and N to denote the number of links. V is the set of all switches v, that is, $V = [v_1, v_2, \cdots, v_M]$. E is the set of all links e, that is, $E = [e_1, e_2, \cdots, e_N]$. A link e is defined by two connected forwarding nodes.

We use w_i to represent the weight value of the i-th link e_i, and we define W as the set of all link-weight values:

$$W = [w_1, w_2, w_3, \cdots, w_N]. \tag{1}$$

We use B to denote the set of link-bandwidth, as shown in Equation (2), where b_i represents the bandwidth of the link e_i:

$$B = [b_1, b_2, b_3, \cdots, b_N]. \tag{2}$$

We use U to describe the used-bandwidth set of all links, as shown in Equation (3), where u_i represents the used bandwidth of the link e_i:

$$U = [u_1, u_2, u_3, \cdots, u_N]. \tag{3}$$

It is critical to evaluate the performance of a network. This paper is concerned with the degree of load-balancing in the network. We sum the absolute value of the difference between the used bandwidth of each link and the average used bandwidth to describe the link-load-balancing factor φ:

$$\varphi = \sum_{i=1}^{N} |u_i - avg(U)|. \tag{4}$$

We define link utilization as the ratio of used bandwidth to link bandwidth, as shown in Equations (5) and (6), where r_i represents the link utilization rate of the link e_i.

$$R = [r_1, r_2, r_3, \cdots, r_N], \tag{5}$$

$$r_i = \frac{u_i}{b_i}. \tag{6}$$

In SDN, the load-balancing-rate factor ρ shows the relative utilization of the network links, which is calculated below:

$$\rho = \sum_{i=1}^{N} |r_i - avg(R)|. \tag{7}$$

Due to link bottlenecks in the forwarding path, forwarding packets of the same length may differ in network throughput [32]. Therefore, we define the network throughput as TP, shown in Equation (8), where H_i is the amount of traffic received by host i in the data plane and L_H is the number of hosts. The network throughput effectively measures the carrying capacity of the data plane:

$$TP = \sum_{i=1}^{L_H} H_i. \tag{8}$$

In this paper, our optimization objective is to maximize the network carrying capacity and minimize the link-load-balancing factor φ, as shown in Equation (9). Equation (10) represents the limiting condition for obtaining the optimization objective:

$$\max\ (TP - \varphi), \tag{9}$$

$$s.t. \begin{cases} 0 < w_i < 1 \\ u_i < b_i \end{cases}. \tag{10}$$

5. Automatic Load-Balancing Algorithm Based on Reinforcement Learning

This section describes the ALBRL routing-optimization algorithm and details the settings of the ALBRL parameters.

5.1. DDPG Algorithm. The RL model includes mainly the following components: the system environment, the RL agent, the reward, and the policy action. The RL agent continuously explores the surrounding environment through the learning scenario, a series of actions taken to transition from the initial state to the target state. Each step includes choosing and executing an action, changing the state, and acquiring a reward.

DDPG is a DRL algorithm based on deterministic policy gradient (DPG). It combines DQN and DPG into an actor-critic (AC) framework to realize efficient and stable continuous action control. During training, DDPG updates the policy through the off-policy method, selects the deterministic action, and maximizes the reward. DDPG stores the interactive information with the environment in the replay buffer and obtains the learning samples of the neural network by randomly sampling them through the empirical-playback mechanism.

The DDPG algorithm consists of the actor network, the critic network, and empirical-playback mechanism, as shown in Figure 2. The function of each component of DDPG is as follows:

(1) Actor network. The actor network adopts the deterministic policy function to output the policy action. It contains two neural networks: an actor online network for training and learning and an actor target network for preventing the correlation of training data. The actor online network selects the action a_t according to the state s_t and policy function μ and then interacts with the environment to get s_{t+1} and r_t. It uses the policy gradient to update the actor online network parameter θ^{μ}:

$$\nabla_{\theta^{\mu}} J = \frac{1}{N} \sum_i \nabla_a Q\left(s, a; \theta^Q\right)\Big|_{s=s_i, a=\mu(s_i)} \nabla_{\theta^{\mu}} \mu(s; \theta^{\mu})\Big|_{s_i}, \tag{11}$$

where N is the number of mini-batch samples.

The actor target network generates the optimal action a_{t+1} of the next state s_{t+1} randomly sampled from the experience pool. The network parameters $\theta^{\mu'}$ are periodically updated from θ^{μ}:

$$\theta^{\mu'} \longleftarrow \tau\theta^{\mu} + (1-\tau)\theta^{\mu'}, \tag{12}$$

where the target update rate τ is a hyperparameter that is much less than 1.

(2) Critic network. The critic network adopts Deep Q-learning function to estimate the policy action. It contains two neural networks: a critic online network and a critic target network. The critic online network is responsible for calculating the current Q value $Q(s_i, a_i; \theta^Q)$. It uses loss function L to update the critic online network parameter θ^Q, as shown in Equation (13), where y_i is the target Q value, as shown in Equation (14):

$$L = \frac{1}{N} \sum_i \left(y_i - Q\left(s_i, a_i; \theta^Q\right)\right)^2, \tag{13}$$

$$y_i = r_i + \gamma Q'\left(s_{i+1}, \mu'\left(s_{i+1}; \theta^{\mu'}\right); \theta^{Q'}\right). \tag{14}$$

In Equation (14), where γ is the reward discount factor, $\gamma \in [0, 1]$.

The critic target network uses Equation (14) to calculate the target Q value $Q'(s_{i+1}, a_{t+1}; \theta^{Q'})$. The network parameters $\theta^{Q'}$ are periodically updated from θ^Q:

$$\theta^{Q'} \longleftarrow \tau\theta^{Q} + (1-\tau)\theta^{Q'}, \tag{15}$$

where the target update rate τ is a hyperparameter that is much less than 1.

(3) Empirical-playback mechanism. The actor and critic networks process the transferred samples obtained during model training through the empirical-playback mechanism. They randomly extract a mini-batch of samples from the replay buffer each time for training the model. This paper adapts the priority empirical-playback mechanism based on the SumTree storage model to optimize the empirical-playback mechanism (see Section 5.2 for more details).

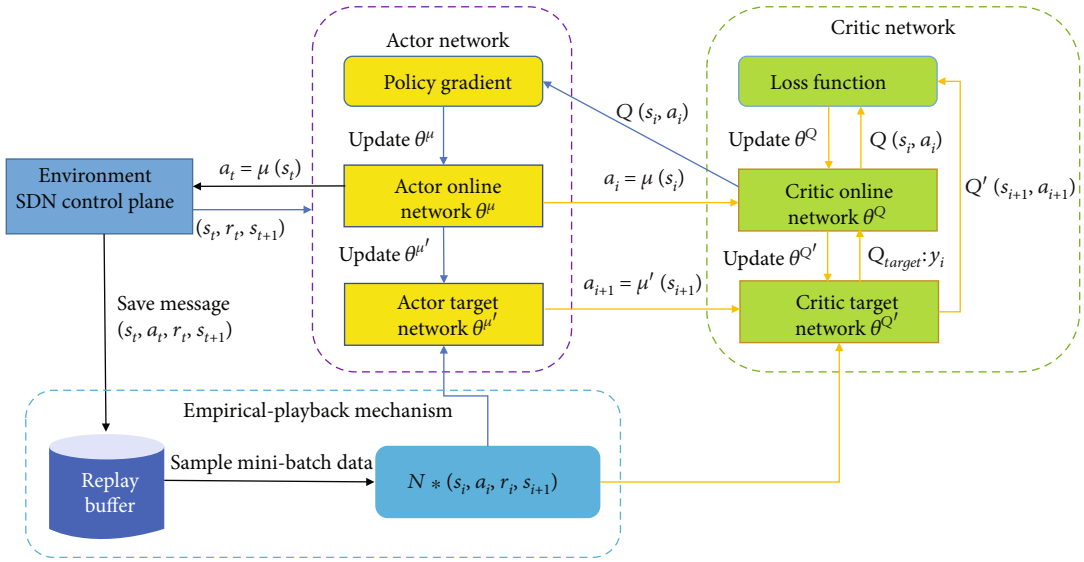

Figure 2: The DDPG framework. The framework consists of the actor network, the critic network, and empirical-playback mechanism.

5.2. The Improved DDPG Based on SumTree. In a real network scenario, the action space of the RL agent grows synchronously, increasing RL training time with the improvement in network scale. This puts the SDN network in the trial state of low performance for a long time before the model converges. Therefore, the learning convergence rate of the model is the key figure for measuring the model's performance. In addition, the network traffic state is random and diverse. When the network traffic fluctuates significantly, a model with good convergence performance can quickly restore the network to a stable convergence state.

A traditional DDPG algorithm processes the transfer samples obtained in model training through an empirical-playback mechanism. This mechanism randomly extracts a mini-batch of samples from the sample pool each time for training the model, causing the agent to be unable to distinguish the critical difference between different transferred samples. This leads to problems such as the low utilization of valuable samples, the coverage of some essential samples, and the reuse of samples. Therefore, it dramatically reduces the convergence rate of the model.

In our paper, we adapt the priority empirical-playback mechanism based on the SumTree storage model to optimize the empirical playback of DDPG. We use priority sampling to replace the original random sample, which increases the probability of significant reward experience extracting to speed up the agent learning the optimal strategy and improving the convergence rate of the model. The sample priority value p_i in the experience pool is mainly based on the TD-error δ_i of the value network and the network load-balancing-rate factor ρ:

$$p_i = |\delta_i| + \rho, \tag{16}$$

where ρ is shown in Equation (7), and δ_i is shown below:

$$\delta_i = r_i + \gamma Q'\left(s_{i+1}, a_{i+1}; \theta^{Q'}\right) - Q\left(s, a; \theta^{Q}\right). \tag{17}$$

The network load-balancing-rate factor ρ shows the relative utilization of network link. The TD-error δ_i indicates how far the value is from its next-step bootstrap estimate [33]. The larger the TD-error δ_i and the factor ρ, the higher the priority. The priority sample has a larger rising space of prediction accuracy, enhancing the model's effectiveness.

In the ALBRL we propose, the experience pool data is stored in the transition, including current state s_t, action a_t, reward value r_t, and updated state s_{t+1}. The transition uses the priority value p_i as the corresponding index. We store the priority value p_i in the SumTree leaf node. The parent node above the leaf node stores the sum of the priority values of the left and right child nodes, and the root node stores the sum of all leaf nodes, as shown in Figure 3. During data sampling, the SumTree model divides the sum of priority value p_i by the number of samples to obtain the number of intervals. Then, the model randomly selects a number in each interval. It starts from the root node of SumTree and searches downward according to specific rules. Finally, the model obtains the corresponding sample data through the priority value p_i conveyed by the previous search.

The data extraction steps of SumTree are as follows:

(1) Uniformly sample data in the root node, assuming that it is p

(2) Take the root node as the parent node, and traverse its child nodes

(3) If the left child node is more significant than p, take it as the parent node, and record its child nodes

(4) If the value of the left child node is less than p, subtract the value of the left child node from p, select the right child node as the parent node, and traverse its children

(5) Until the leaf node is traversed, the value of the leaf node is the priority. The corresponding transition can be found in the value stored in the leaf node

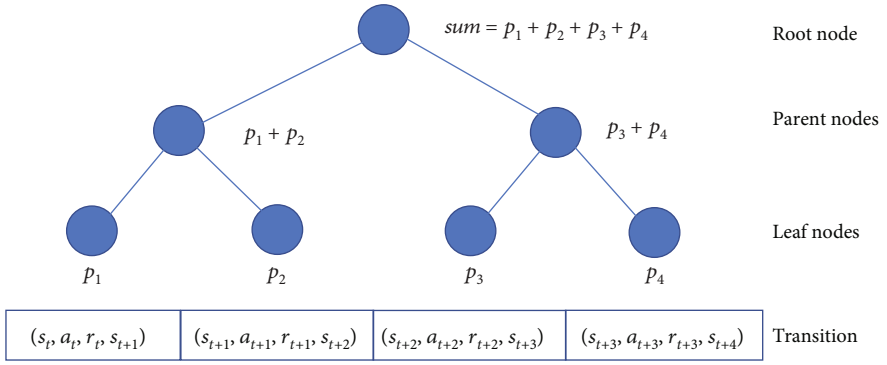

Figure 3: SumTree storage model.

According to the above data extraction method, the greater the priority value p_i, the greater is the probability of extracted data. The sampling probability and the importance-sampling weight are shown below:

$$P(i) = \frac{p_i}{\sum_j p_j}, \tag{18}$$

$$\omega_i = (N * P(i))^{-1} / \max_j (\omega_j). \tag{19}$$

We add the importance-sampling weight ω_i to update the actor online network parameter θ^μ:

$$\nabla_{\theta^\mu} J = \frac{1}{N} \sum_i \omega_i \left(\nabla_a Q\left(s, a; \theta^Q\right) \Big|_{s=s_i, a=\mu(s_i)} \nabla_{\theta^\mu} \mu\left(s; \theta^\mu\right) \Big|_{s_i} \right). \tag{20}$$

Regarding comparing the complexity of ALBRL and DDPG algorithms, since the SumTree-DDPG algorithm adopted by ALBRL is consistent with the DDPG algorithm in terms of the main body of the model, we focus on the complexity of the experience pool sampling. In the sampling process, the original DDPG uses unified random sampling to extract samples from the experience pool sequence, while ALBRL uses priority sampling based on the SumTree storage model. The difference between priority sampling and random sampling is the generation of the sampling sequence number. The random sampling method directly generates random numbers, and the time complexity is $O(1)$. In contrast, the priority sampling method we proposed stores the priority in a full binary tree structure, and we first need to find the leaf node as the sampling sequence number when sampling. Compared with the random sampling method, the time complexity of the priority sampling process is $O(log N)$, where N is the size of replay buffer [33]. In terms of space complexity, ALBRL needs to use one more binary tree structure, and the number of leaf nodes is equal to the size of the traditional experience pool. Therefore, the spatial complexity of ALBRL sampling is the same as DDPG, which is still $O(N)$. Compared with DDPG, the time complexity of ALBRL increases by $O(logN)$. Still, the ALBRL algorithm performance optimization is considerable, and it can reach the convergence state in less time.

5.3. The Network Load-Balancing Algorithm Based on ALBRL. The specific design of the state, action, and reward of the ALBRL model we propose in SDN is as follows:

(1) Reward. The reward r_t evaluates the pros and cons of traffic scheduling for the revenue obtained from the previous action. In the mathematical model described in Section 4, the optimization objective of the SDN load-balancing model is to maximize the network carrying capacity and minimize the link-load-balancing factor φ. We define the reward r_t as the optimization goal:

$$r_t = TP - \varphi. \tag{21}$$

(2) State. The state s_t is the network status information obtained from the environment. In our model, each state corresponds to a traffic matrix (flow request information in the network). We define $s_t = [D_t]$, where D_t represents the flow request matrix in the network at time t

(3) Action. The action a_t is the set of all link-weight values (as shown in Equation (1)) generated by the reinforcement-learning agent at time t according to the state s_t in the actor network.

The ALBRL agent interacts with the SDN environment through the abovementioned variables (state, action, and reward). First, the data plane's network status and performance indicators collected by the SDN controller can provide the state s_t for the ALBRL agent. Subsequently, ALBRL determines a set of link weights $a_t = [w_1, w_2, \cdots, w_N]$ according to the state s_t. The SDN controller uses the Dijkstra algorithm to generate a new flow path and to update the flow table according to the link weight. After the flow-table update, the reward r_t and the next state s_{t+1} are acquired through subsequent network measurement, optimizing

Input:
Reward discount factor γ, target update rate τ, target network parameter update frequency C, the number of mini-batch samples N, the number of iterations T.
Randomly initialize the actor-online-network parameter θ^{μ} and the critic-online-network parameter θ^{Q};
Initialize the actor target network μ' and the critic target network Q' with $\theta^{\mu'} \longleftarrow \theta^{\mu}$ and $\theta^{Q'} \longleftarrow \theta^{Q}$;
Initialize replay buffer B;
Initialize the data buffer of SumTree S, set the priority p_i of all leaf nodes to 0;
Initialize a random process $\mathcal{N}$ for action exploration;
Initialize state s_1 with n the collected information from the SDN controller and acquire its feature vector $\mu(s_1; \theta^{\mu})$;

1) **for** t =1, T **do**
2) Select the action weight $a_t = \mu(s_t) + \mathcal{N}$ according to the state s_t in the actor online network;
3) Deploy a_t on SDN controller;
4) Recalculate paths and issue the flow table;
5) Get the reward r_t, the new state s_{t+1}, and the terminate flag is_end_t from the SDN controller;
6) Store (s_t, a_t, r_t, s_{t+1}) in B;
7) Calculate the sample priority value: $p_i = |\delta_i| + \rho$;
8) Update all nodes of S;
8) Use the SumTree model to extract N samples from B;
10) Calculate the importance-sampling weight: $\omega_i = (N * P(i))^{-1} / \max_j(\omega_j)$;
11) Calculate the target Q value:
12) $$y_t = \begin{cases} r_t & \text{is\_}end_t \text{ is } true \\ r_t + \gamma Q'(s_{t+1}, \mu'(s_{t+1}; \theta^{\mu'}); \theta^{Q'}) & \text{is\_}end_t \text{ is } false. \end{cases}$$
13) Use loss function L to update the critic online network parameter θ^{Q}:
14) $L = 1/N \sum_i (y_i - Q(s_i, a_i; \theta^{Q}))^2$
15) Use the policy gradient to update the actor online network parameter θ^{μ}:
16) $\nabla_{\theta^{\mu}} J = 1/N \sum_i \omega_i (\nabla_a Q(s, a; \theta^{Q})|_{s=s_i, a=\mu(s_i)} \nabla_{\theta^{\mu}} \mu(s; \theta^{\mu})|_{s_i})$
17) **if** $t\%C = 0$ **then**
18) update the Critic-target-network and Actor-target-network parameters:
$\theta^{\mu'} \longleftarrow \tau\theta^{\mu} + (1-\tau)\theta^{\mu'}$
$\theta^{Q'} \longleftarrow \tau\theta^{Q} + (1-\tau)\theta^{Q'}$
19) **end if**
20) **end for**

Algorithm 1: ALBRL training algorithm.

network performance through iteration. We describe the ALBRL-training algorithm as shown in Algorithm 1.

6. Experiments and Analysis

In our experiments, the network simulation environments are the *Mininet* simulation, *Ryu* controller, and *OpenFlow 1.3* protocol. The computer is equipped with an AMD Ryzen 7 2400G CPU with a base frequency of 3.0 GHz, a 500GB SSD, and 32 GB RAM. In this paper, *Pytorch* was used to implement reinforcement-learning algorithms for SDN.

6.1. Experimental Setup. This experiment uses *iperf* to send packets and takes active flow-table distribution for issuing flow tables. The controller periodically computes the packet-forwarding policy and then sends it down to the corresponding switch through the southbound interface. Compared with passive flow-table distribution, active flow-table distribution can avoid the problem of the overloading or even the crashing of the controller due to a mismatch between the new path and the old flow table.

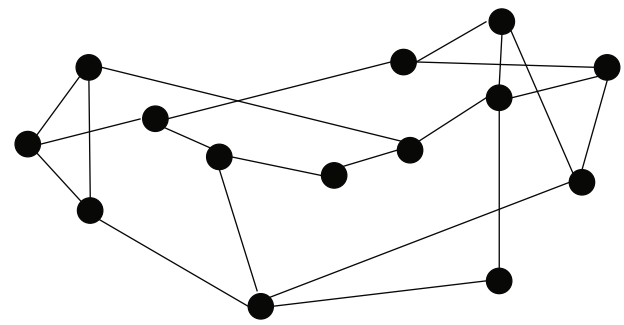

Figure 4: NSFNET topology. It consists of 14 switches with 21 links, all with a link bandwidth of 10 Mbps.

In our experiments, we used the National Science Foundation Network (NSFNet) as the experimental network topology, as shown in Figure 4. The topology consists of 14 switches with 21 links, all with a link bandwidth of 10 Mbps. Each switch connects to a host machine. This paper sets four different levels of traffic intensity for the NSFNet to simulate a realistic network situation, accounting for

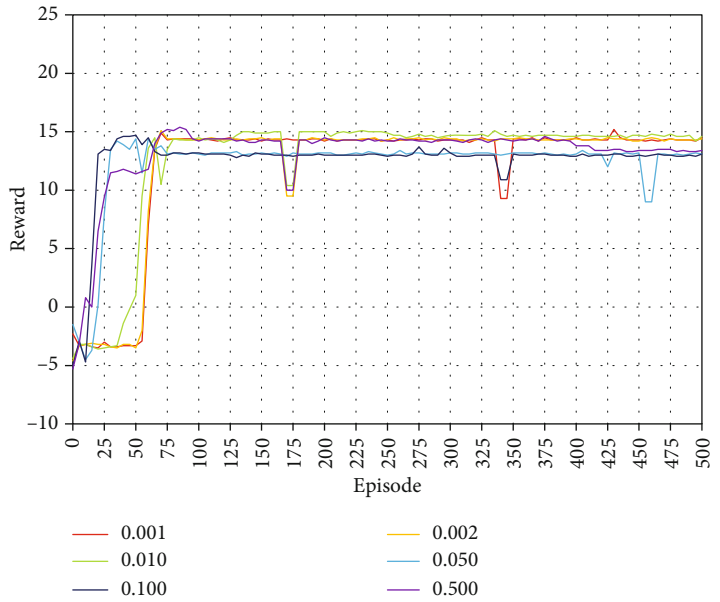

(a)

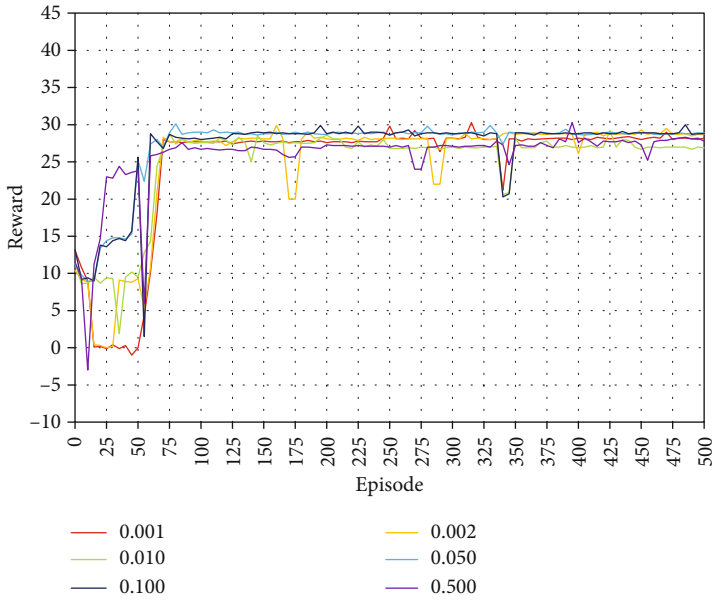

(b)

Figure 5: Continued.

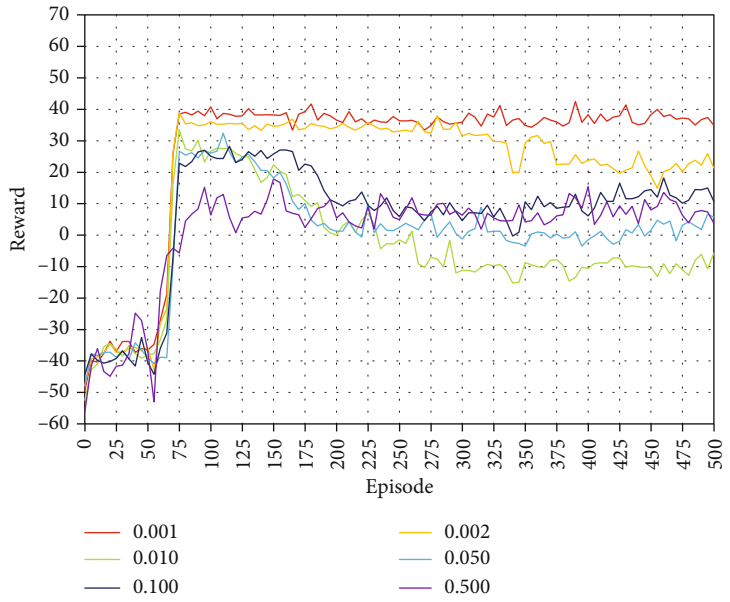

(c)

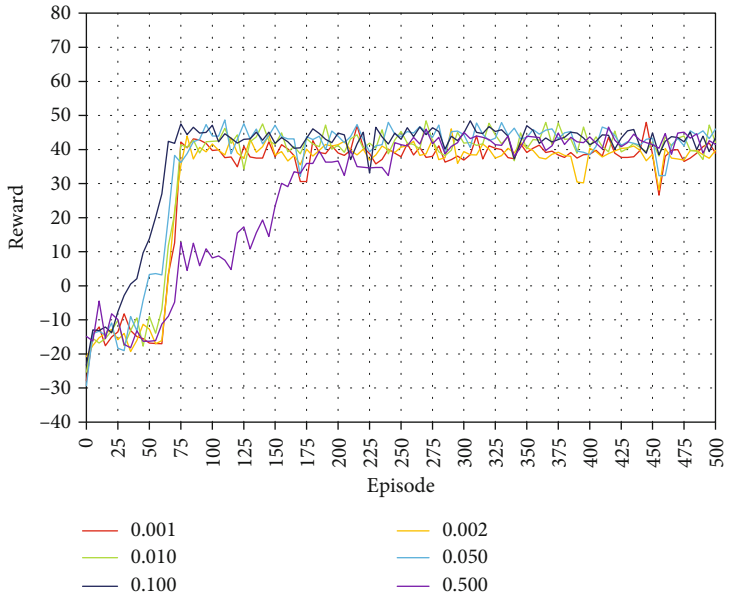

(d)

Figure 5: Effect of learning parameters: (a) traffic intensity is 25%; (b) traffic intensity is 50%; (c) traffic intensity is 75%; and (d) traffic intensity is 100%.

25%, 50%, 75%, and 100% of the entire network bandwidth, respectively. We use the gravity model [34] separately for each traffic intensity to randomly generate a traffic matrix for training.

In this section, we compare the convergence rate and network performance of ALBRL with the following algorithms:

(1) OSPF [5]: OSPF routes all flow requests singularly to the shortest path

(2) RSIR [16]: RSIR adapts the Q-learning algorithm to optimize the network in three dimensions: throughput, delay, and packet-loss rate. We only use throughput for optimization

(3) EARS [26]: EARS adapts the DDPG algorithm as the automatic routing decision algorithm to select the forwarding paths through action strategy and obtain near-optimal routing decisions

6.2. Parameter Setting. As an essential parameter in deep learning, the appropriate learning rate can quickly make the objective function converge to a local minimum. In the network, the actor learning rate is not involved in the RL

agent training process because the traffic is random, and there is no next state after each training. We change the critic-learning rate to observe the ABLRL convergence effect and determine the optimal value of the DRL critic-learning rate by the convergence rate and the maximum reward. The critic-learning rate was set to 0.001, 0.002, 0.01, 0.05, 0.1, and 0.5. The model's performance in the training environment was tested every five training steps in this experiment. The training results are shown in Figure 5.

Figure 5 shows that the reward curves obtained for different critic-learning rates are different. Moreover, the optimal critic-learning rate varies with varying intensities of traffic. The reward curve is best at a critic-learning rate of 0.1 when the traffic intensity is 25%. The highest reward value achieved is 15, as shown in Figure 5(a). When the traffic intensity is 50%, the reward curve is optimal at a critic-learning rate of 0.05, and the highest reward value achieved is 29, as shown in Figure 5(b). Although the reward curve at a critic-learning rate of 0.5 in this traffic intensity performed better than at 0.1 in the first 50 episodes, the reward convergence value of 27 was not as good as the reward convergence value at a critic-learning rate of 0.1. When the traffic intensity is 75%, the routing algorithm adjusts the link-weight values more frequently because some links have reached saturation. The reward convergence values are higher at lower critic-learning rates. The best reward curve at this flow intensity is with a critic-learning rate of 0.001, and the highest reward value achieved was 40, as shown in Figure 5(c). When the traffic intensity is 100%, most links are saturated, and so the maximum reward value reached by different critic-learning rates is the same. With a critic-learning rate of 0.1, the reward curve converges fastest. Thus, the best critic-learning rate is 0.1, and the highest reward value achieved is 45, as shown in Figure 5(d).

Based on the above results, in our experiments, the critic-learning rate of the parameter critic of ALBRL was set at a traffic intensity of 25%, 50%, 75%, and 100% with 0.1, 0.05, 0.001, and 0.1, respectively. Under these parameters, ALBRL can reach the convergence rate the fastest and most effectively.

Other hyperparameters set in the experiment are shown in Table 1.

Table 1: ALBRL training hyperparameters.

Hyperparameters	Value
Actor learning rate	0.001
Optimizer	Adam
Target update rate τ	0.01
Target network parameter update frequency C	1
Number of iterations T	500
Replay buffer B	32
Batch size N	8
Reward discount factor γ	0.99
Exploration noise	$\mathcal{N}(0,0.1)$

6.3. Algorithm Convergence Performance Comparison. After determining the critical learning rate, we compared the convergence performance of ALBRL and EARS algorithms under different traffic intensities. We trained 500 episodes for each traffic intensity and tested the model's performance in the training environment every five training steps. The experimental results are shown in Figure 6.

The reward value is used in reinforcement learning to measure the outcome of an action. The larger the reward value, the better the network performance is. When the traffic intensity is 25%, the ALBRL reward convergence value is the same as that of EARS, but the convergence rate of EARS is slightly faster, and the performance is somewhat better than that of ALBRL, as shown in Figure 6(a). When the traffic intensity is 50%, ALBRL converges at the same speed as EARS, but the ALBRL reward convergence value is higher than that of EARS, as shown in Figure 6(b). When the traffic intensity is 75%, the ALBRL reward convergence value is close to that of EARS, but the convergence rate is higher than that of EARS, which is improved by 47%, as shown in Figure 6(c). When the traffic intensity is 100%, the convergence value of the ALBRL reward is close to that of EARS, but the convergence rate is significantly higher than that of EARS, which is increased by nearly 70%. In addition, due to dynamic changes in network traffic, the reward value of EARS will fluctuate after convergence, while the reward value of ALBRL is more stable.

The results in Figure 6 show that the performance of ALBRL is close to that of EARS in a low-load network (traffic intensity less than 50%). Moreover, ALBRL can reach a convergence state faster than EARS in a high-load network (traffic intensity more than 50%), and after convergence, the reward value is more stable. Under low traffic intensity, the algorithm can reach the convergence state with more minor training episodes because of the lower traffic in the network. In the early stage of network operation, the priority value of the stored samples is close, and so the role of the priority-based empirical-playback mechanism is not apparent. Under high traffic intensity, the algorithm needs more training episodes to reach the convergence state. When the episode value is greater than 50, the priority values of stored samples begin to differ significantly. ALBRL causes the model to reach the convergence state quickly through the advantages of the priority playback mechanism in a high-load network.

6.4. Load-Balancing Performance Comparison. Throughput is an important indicator to measure the performance of load balancing. This paper tests the performance differences of four algorithms—ALBRL, EARS, RSIR, and OSPF—under different traffic intensities.

The throughput result of 25% traffic intensity is shown in Figure 7(a). The throughput of OSPF fluctuates significantly due to the dynamic change of network traffic. The throughput of RSIR is more stable than OSPF, but the values are lower than 40 Mbps. The performance of ALBRL and EARS is close, and the throughput value after convergence is 47 Mbps, which is better than that of OSPF and RSIR.

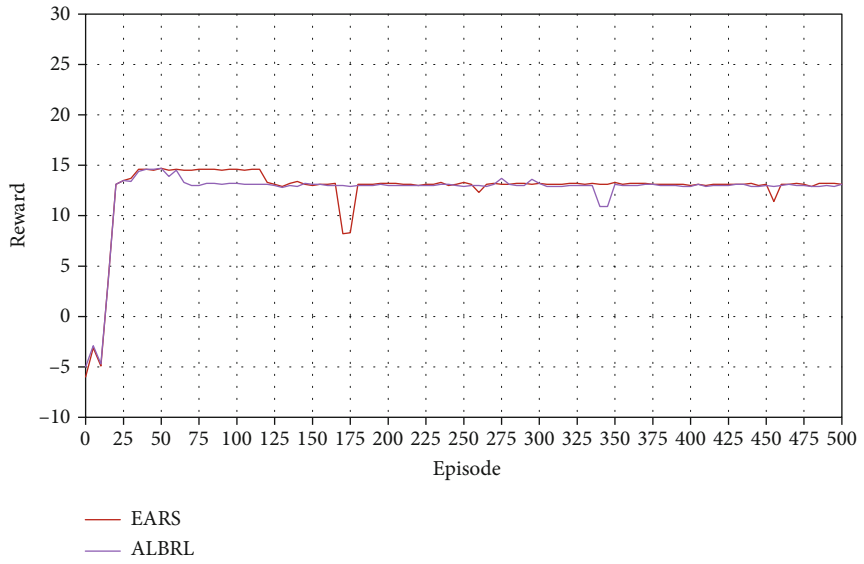

(a)

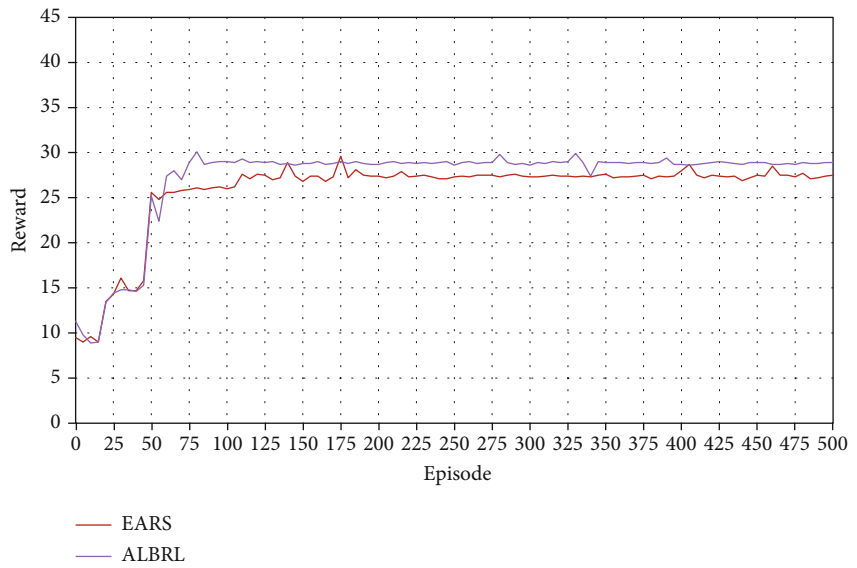

(b)

Figure 6: Continued.

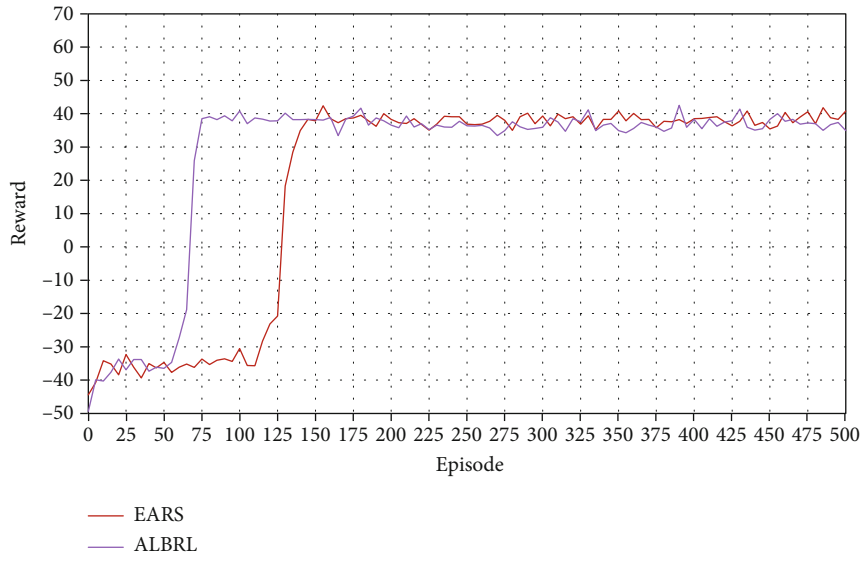

(c)

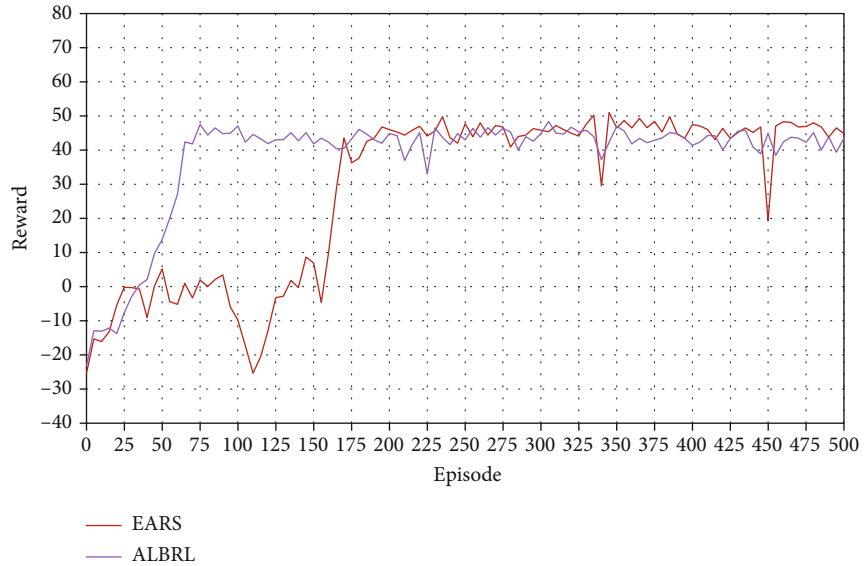

(d)

Figure 6: Convergence performance comparison: (a) traffic intensity is 25%; (b) traffic intensity is 50%; (c) traffic intensity is 75%; and (d) traffic intensity is 100%.

The throughput result of 50% traffic intensity is shown in Figure 7(b). The convergence rate of ALBRL is slightly higher than that of EARS, but the throughput during convergence is 87.5Mbps, which is higher than that of EARS. The throughput of OSPF and RSIR fluctuates wildly and is lower than that of ALBRL and EARS when they converge.

The throughput result of 75% traffic intensity is shown in Figure 7(c). The convergence throughput value of ALBRL is about 109 Mbps, which is close to EARS, but the convergence time is reduced by about 47%. The throughput of OSPF and RSIR are both lower than that of ALBRL and EARS when they converge.

The throughput result of 100% traffic intensity is shown in Figure 7(d). The convergence throughput of ALBRL is about 121 Mbps, which is lower than that of EARS, but the convergence time is reduced by about 36%. At the same time, there are two large fluctuations after the convergence of the EARS algorithm. The throughput of OSPF and RSIR is lower than that of ALBRL and EARS when they converge. Further, in the RSIR algorithm's later stage, severe congestion occurs on multiple links, resulting in a high packet-loss rate and a low total throughput value.

In a low-load network scenario, the network traffic does not reach the network forwarding bottleneck, and there is less congestion due to excessive traffic. Therefore, both ALBRL and the original DDPG algorithm can quickly reach the convergence state. The performance of ALBRL under low traffic intensity is close to EARS, but is better than OSPF and RSIR, as shown in Figures 7(a) and 7(b). However, when the network traffic scale exceeds the network forwarding

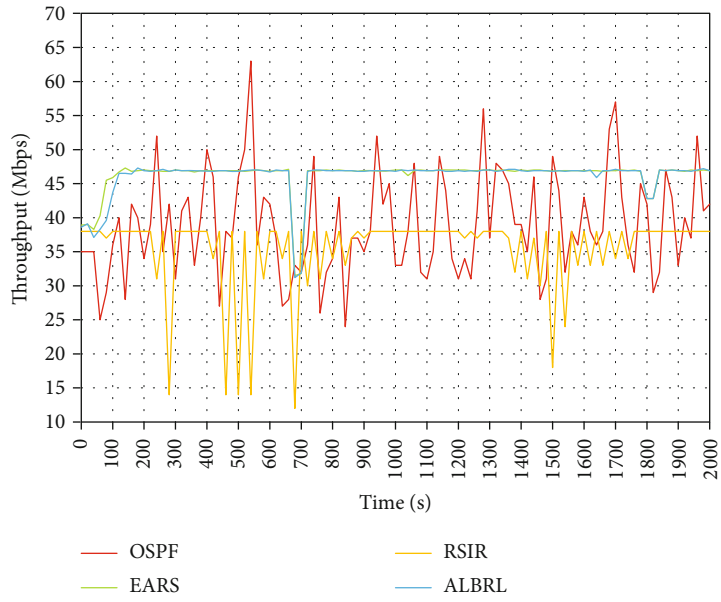

(a)

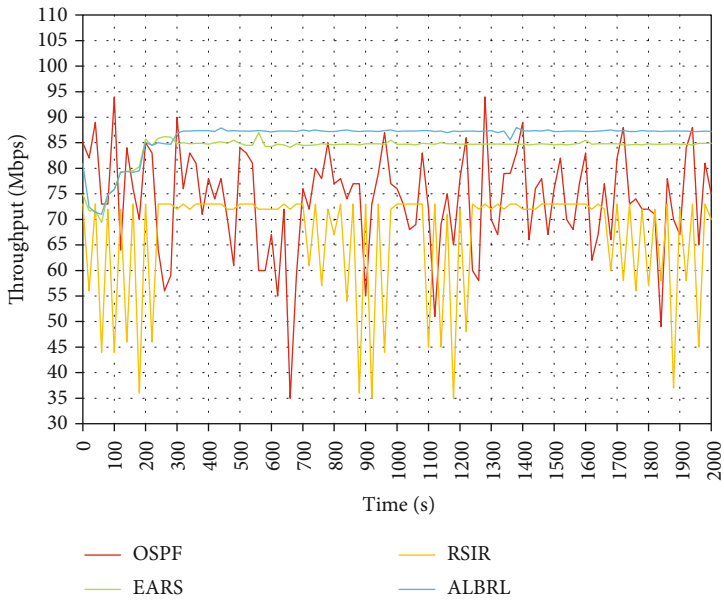

(b)

Figure 7: Continued.

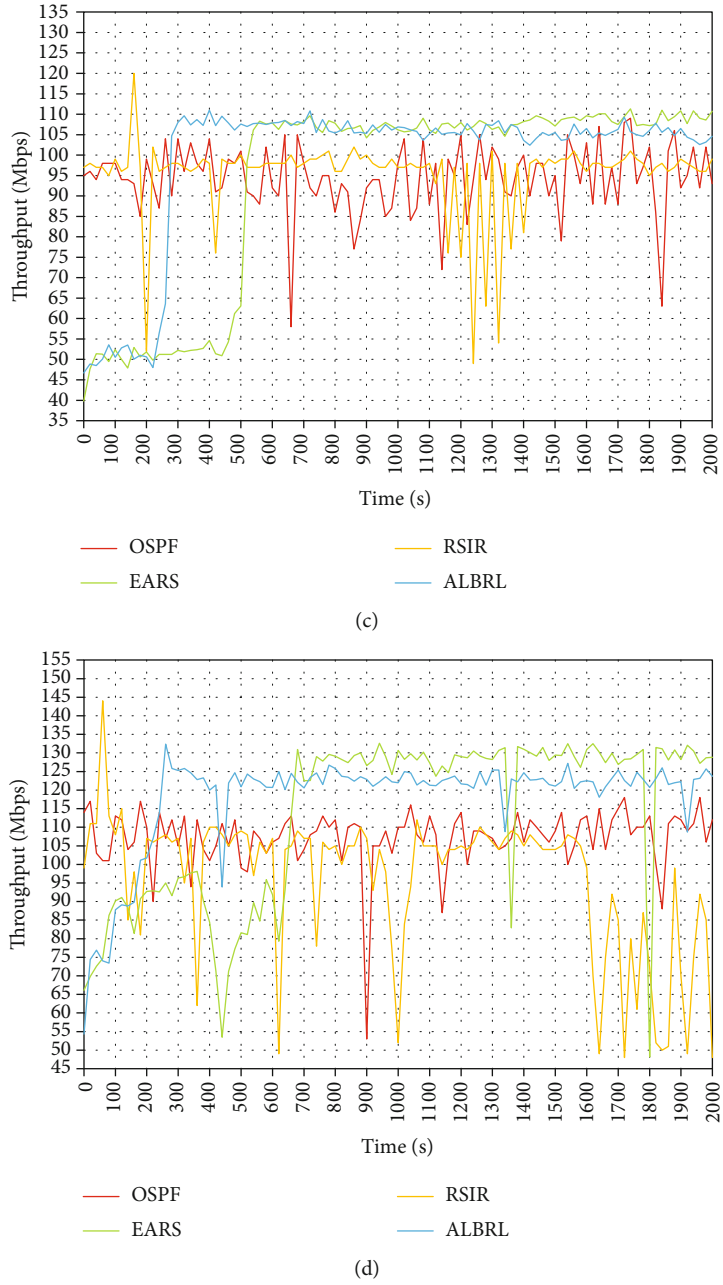

Figure 7: Overall throughput performance comparison: (a) traffic intensity is 25%; (b) traffic intensity is 50%; (c) traffic intensity is 75%; and (d) traffic intensity is 100%.

bottleneck in terms of reward convergence value since ALBRL can reuse those more valuable data, it can be closer to the optimal strategy than the other three algorithms. The experiments in Figure 7 show that the ALBRL algorithm can reach the convergence state faster than the other three algorithms, it is more stable, and it does not experience large fluctuations.

Our paper compares the four algorithms' average throughput rates with different traffic intensities in Figure 7, and the experimental results are shown in Figure 8.

Compared with EARS, ALBRL shows similar performance under low traffic intensity (less than 50%), but it is better than EARS under high traffic intensity (more than 50%). The throughput of ALBRL is 4~6% higher than that of EARS under high traffic intensity. Both ALBRL and EARS are based on the DDPG algorithm. Different from EARS, ALBRL uses the SumTree binary tree structure to optimize the extraction method of the experience pool of the traditional DDPG algorithm. Under low traffic intensity, the algorithm can reach the convergence state with more minor training episodes, and so the role of the priority-based, empirical-playback mechanism is not apparent. Under high traffic intensity, the algorithm needs more training episodes to reach the convergence state. When the episode value is greater than 50, the ALBRL extracts more meaningful

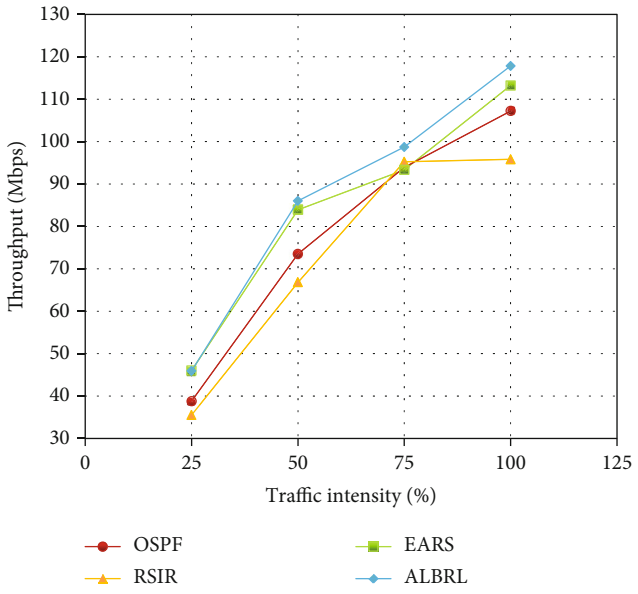

Figure 8: Model effective comparison.

experience for the network update with greater probability. Therefore, ALBRL can achieve convergence faster than EARS at a high traffic intensity.

Compared with RSIR, ALBRL is better in all traffic intensities. The throughput of ALBRL is 5~18% higher than that of RSIR. Each time the RSIR algorithm is trained, the Q table between each host pair needs to retrain for each instance of collected link information. However, the data between each host pair is irrelevant. Therefore, RSIR is likely to cause overload in the controller. At the same time, when RSIR outputs actions, due to the limitations of the value base, it can only output a single action when controlling routing, and it cannot realize fine control over the network as a whole. Thus, RSIR has multiple links with severe congestion in the later stages, resulting in high packet loss and large fluctuations in throughput. The ALBRL algorithm considers the entire network to create action vectors related to network routing for more refined control and thus for better optimization performance.

Compared with OSPF, the throughput of ALBRL is 10~14% higher than that of OSPF in all traffic intensities. OSPF is a static scheme based on fixed forwarding rules, which routes all flow requests singularly to the shortest path. Therefore, OSPF is prone to link congestion and cannot accommodate dynamic network environments.

Our experimental results show that ALBRL outperforms other algorithms under various traffic intensities. The ALBRL algorithm has a faster convergence rate and shows better performance and stability.

7. Conclusions and Future Work

This paper proposes an automatic load-balancing architecture based on an improved DDPG algorithm. The proposed ALBRL adapts the sampling method of updating the experience pool with the SumTree structure to improve the random extraction strategy of the empirical-playback mechanism in DDPG. It extracts more meaningful experiences for a network updating with greater probability, which can effectively improve the convergence rate. ALBRL can make routing decisions in a continuous action space and has a perfect convergence. The experimental comparison shows that the SDN routing algorithm based on ALBRL has a faster convergence rate and better performance and stability.

In the future, the specific measures on which we will focus are as follows: First, we will further enhance the convergence rate of deep reinforcement-learning algorithms by extending the existing single agent to multi-agent, and second, we will extend the network topology environment to test the load-balancing performance of the algorithm in large-scale networks.

Data Availability

The authors confirm that the data supporting the findings of this study are available within the article.

Conflicts of Interest

The authors declare that they have no conflicts of interest.

Acknowledgments

This work is supported by the National Natural Science Foundation of China (No.61861013), the major program of Natural Science Foundation of Guangxi (No.2020GXNSFDA238001), the Natural Science Foundation of Guangxi (No.2018GXNSFAA281318) and the Guangxi Project to Improve the Scientific Research Basic Ability of Middle Aged and Young Teachers (No.2020KY05033).

References

[1] J. Zhang, K. Xi, M. Luo, and H. J. Chao, "Dynamic hybrid routing: achieve load balancing for changing traffic demands," in *IEEE 22nd International Symposium of Quality of Service (IWQoS 2014)*, pp. 105–110, Hong Kong, China, May 2014.

[2] I. F. Akyildiz, A. Lee, P. Wang, M. Luo, and W. Chou, "Research challenges for traffic engineering in software defined networks," *IEEE Network*, vol. 30, no. 3, pp. 52–58, 2016.

[3] R. A. Ammal, P. C. Sajimon, and S. S. Vinodchandra, "Termite inspired algorithm for traffic engineering in hybrid software defined networks," *PeerJ Computer Science*, vol. 6, article e283, 2020.

[4] T. Hartman, A. Hassidim, H. Kaplan, D. Raz, and M. Segalov, "How to split a flow?," in *Proceedings IEEE INFOCOM*, pp. 828–836, Orlando, USA, March, 2012.

[5] A. Ali Khan, M. Zafrullah, M. Hussain, and A. Ahmad, "Performance analysis of OSPF and hybrid networks," in *International Symposium on Wireless Systems and Networks (ISWSN 2017)*, Lahore, Pakistan, Nov. 2017.

[6] M. Chiesa, G. Kindler, and M. Schapira, "Traffic engineering with equal-cost-multipath: an algorithmic perspective," *IEEE/ACM Transactions on Networking*, vol. 25, no. 2, pp. 779–792, 2017.

[7] M. Tanha, D. Sajjadi, R. Ruby, and J. Pan, "Traffic engineering enhancement by progressive migration to SDN," *IEEE Communications Letters*, vol. 22, no. 3, pp. 438–441, 2018.

[8] A. Azzouni and G. Pujolle, "NeuTM: a neural network-based framework for traffic matrix prediction in SDN," in *IEEE/IFIP International Conference on Network Operations and Management Symposium (NOMS 2018)*, Taipei, China, April 2018.

[9] M. P. Novaes, L. F. Carvalho, J. Lloret, and M. Proenca, "Long short-term memory and fuzzy logic for anomaly detection and mitigation in software-defined network environment," *IEEE Access*, vol. 8, pp. 83765–83781, 2020.

[10] S. A. Patil, L. A. Raj, and B. K. Singh, "Prediction of IoT traffic using the gated recurrent unit neural network- (GRU-NN-) based predictive model," *Security and Communication Networks*, vol. 2021, Article ID 1425732, 7 pages, 2021.

[11] B. Mao, F. Tang, Z. M. Fadlullah et al., "A novel non-supervised deep learning based network traffic control method for software defined wireless networks," *IEEE Wireless Communications*, vol. 25, no. 4, pp. 74–81, 2018.

[12] B. Mao, F. Tang, Z. M. Fadlullah, and N. Kato, "An intelligent route computation approach based on real-time deep learning strategy for software defined communication systems," *IEEE Transactions on Emerging Topics in Computing*, vol. 9, no. 3, pp. 1554–1565, 2021.

[13] H. Yu, K. Li, and H. Qi, "An active controller selection scheme for minimizing packet-in processing latency in SDN," *Security and Communication Networks*, vol. 2019, Article ID 1949343, 11 pages, 2019.

[14] J. Chen, Y. Wang, X. Huang, X. Xie, H. Zhang, and X. Lu, "ALBLP: adaptive load-balancing architecture based on link-state prediction in software-defined networking," *Wireless Communications and Mobile Computing*, vol. 2022, Article ID 8354150, 16 pages, 2022.

[15] D. K. Dake, G. S. Klogo, J. D. Gadze, and H. Nunoo-Mensah, "Traffic engineering in software-defined networks using reinforcement learning: a review," *International Journal of Advanced Computer Science and Applications*, vol. 12, no. 5, pp. 330–345, 2021.

[16] D. Velasco, O. Rendon, and N. Fonseca, "Intelligent routing based on reinforcement learning for software-defined networking," *IEEE Transactions on Network and Service Management*, vol. 18, no. 1, pp. 870–881, 2021.

[17] W. Liu, J. Cai, Q. Chen, and Y. Wang, "RL-R: deep reinforcement learning approach for intelligent routing in software-defined data-center networks," *Journal of Network and Computer Applications*, vol. 177, pp. 1–16, 2021.

[18] M. Manel, A. Kamel, and Y. Habib, "DQR: an efficient deep Q-based routing approach in multi-controller software defined WAN (SD-WAN)," *Journal of Interconnection Networks*, vol. 20, no. 4, pp. 2150002–2150026, 2020.

[19] Y. Chen, A. Rezapour, W. Tzeng, and S. Tsai, "RL-routing: an SDN routing algorithm based on deep reinforcement learning," *IEEE Transactions on Network Science and Engineering*, vol. 7, no. 4, pp. 3185–3199, 2020.

[20] X. Che, W. Kang, Y. Ouyang, K. Yang, and J. Li, "SDN routing optimization algorithm based on reinforcement learning," *Computer Engineering and Applications*, vol. 57, no. 12, pp. 93–98, 2021.

[21] T. P. Lillicrap, J. J. Hunt, A. Pritzel et al., "Continuous control with deep reinforcement learning," in *4th International Conference on Learning Representations (ICLR 2016)*, pp. 187–200, San Juan, Puerto Rico, May 2016.

[22] Z. Yao, Y. Wang, L. Meng, X. Qiu, and P. Yu, "DPG-based energy-efficient flow scheduling algorithm in software-defined data centers," *Wireless Communications and Mobile Computing*, vol. 2021, Article ID 6629852, 10 pages, 2021.

[23] J. Lan, C. Yu, Y. Hu, and Z. Li, "A SDN routing optimization mechanism based on deep reinforcement learning," *Journal of Electronics and Information Technology*, vol. 41, no. 11, pp. 2669–2674, 2019.

[24] J. Lan, X. Zhang, Y. Hu, and P. Sun, "Software-defined networking QoS optimization based on deep reinforcement learning," *Journal on Communications*, vol. 40, no. 12, pp. 60–67, 2019.

[25] S. Kim, S. Yoon, and H. Lim, "Deep reinforcement learning-based traffic sampling for multiple traffic analyzers on software-defined networks," *IEEE Access*, vol. 9, pp. 47815–47827, 2021.

[26] Y. Hu, Z. Li, J. Lan, J. Wu, and L. Yao, "EARS: intelligence-driven experiential network architecture for automatic routing in software-defined networking," *China Communications*, vol. 17, no. 2, pp. 149–162, 2020.

[27] W. Liu, J. Cai, Q. Chen, and Y. Wang, "DRL-R: deep reinforcement learning approach for intelligent routing in software-defined data-center networks," *Journal of Network and Computer Applications*, vol. 177, article 102865, 2021.

[28] M. Ibrar, L. Wang, G. Muntean, J. Chen, N. Shah, and A. Akbar, "IHSF: an intelligent solution for improved performance of reliable and time-sensitive flows in hybrid SDN-based FC IoT systems," *IEEE Internet of Things Journal*, vol. 8, no. 5, pp. 3130–3142, 2021.

[29] S. Fujimoto, H. Hoof, and D. Meger, "Addressing function approximation error in actor-critic methods," *35th International Conference on Machine Learning (ICML 2018)*, vol. 4, pp. 1587–1596, 2018.

[30] P. Sun, J. Lan, J. Shen, and Y. Hu, "An intelligent routing technology based on deep reinforcement learning," *Acta Electronica Sinica*, vol. 48, no. 11, pp. 2170–2177, 2020.

[31] P. Sun, J. Lan, J. Shen, and Y. Hu, "Pinning control-based routing policy generation using deep reinforcement learning," *Journal of Computer Research and Development*, vol. 58, no. 7, pp. 1563–1572, 2021.

[32] S. Ejaz, Z. Iqbal, P. Shah, B. H. Bukhari, A. Ali, and F. Aadil, "Traffic load balancing using software defined networking (SDN) controller as virtualized network function," *IEEE Access*, vol. 7, pp. 46646–46658, 2019.

[33] T. Schaul, J. Quan, L. Antonoglou, and D. Silver, "Prioritized experience replay," in *4th International Conference on Learning Representations (ICLR 2016)*, pp. 1–21, San Juan, Puerto Rico, May 2016.

[34] M. Roughan, "Simplifying the synthesis of internet traffic matrices," *ACM SIGCOMM Computer Communication Review*, vol. 35, no. 5, pp. 93–96, 2005.

Hindawi
Wireless Communications and Mobile Computing
Volume 2022, Article ID 6939868, 14 pages
https://doi.org/10.1155/2022/6939868

Research Article

A Novel Energy-Aware Routing in Wireless Sensor Network Using Clustering Based on Combination of Multiobjective Genetic and Cuckoo Search Algorithm

Xiuniao Zhao,[1] **Wentao Zhong**,[2] **and Yahya Dorostkar Navaei**[3]

[1]*College of Electronic Information Engineering, Gannan University of Science and Technology, Ganzhou, 341000 Jiangxi, China*
[2]*School of Information Engineering, Jiangxi University of Science and Technology, Ganzhou, 341000 Jiangxi, China*
[3]*Department of Computer and Technology Engineering, Qazvin Branch, Islamic Azad University, Qazvin, Iran*

Correspondence should be addressed to Yahya Dorostkar Navaei; y.dorostkar@qiau.ac.ir

Received 7 November 2021; Revised 9 December 2021; Accepted 30 March 2022; Published 19 April 2022

Academic Editor: Junjuan Xia

The development of various applications of wireless sensor networks has aroused great interest in using these types of networks in various fields. These networks, without infrastructure and self-organization, are easily deployed in most environments and collect information about environmental phenomena for analysis and proper response to accidents and send them to the basic centers. They do. Wireless sensor networks are made up of some sensor nodes that both act as sensors and act as relay nodes concerning to each other. On the other hand, the lack of infrastructure in these networks has limited resources so that the nodes of the battery are fed with limited energy. Due to the location of networks in difficult and impassable areas, it is not possible to recharge or replace the node battery. Therefore, saving energy consumption in this type of network is one of the most important challenges. Since the rate of energy consumption when sensing information and receiving data packets from another node is a fixed value, so sensor nodes have the highest energy consumption when sending data. Therefore, routing methods try to reduce energy consumption based on systematic approaches. One of the most promising solutions to reduce energy consumption in wireless sensor networks is to cluster the nodes and select the threaded node based on the data transfer parameters so that the average energy consumption in the nodes is reduced and the network lifetime is increased. Therefore, in this research, a new optimization approach using multiobjective genetic algorithm and cuckoo algorithm for clustering wireless sensor networks is presented. In this study, in order to select clustered nodes from a multiobjective genetic algorithms based on reducing intracluster distances and reducing energy consumption in cluster member nodes and near-optimal routing based on cuckoo optimization algorithm to transfer information between nodes have been used in the direction of the cavity. The implementation results show that considering the evolutionary capabilities of the multiobjective genetic algorithm and the cuckoo optimization algorithm, the proposed method in terms of energy consumption, efficiency, delivery rate, and packet transmission latency, compared to previous methods, has improved.

1. Introduction

Wireless sensor networks (WSNs) are networks made up of distributed microdevices with various sensing capabilities (called sensors) that are used to monitor the environment and send information to end users are used. WSN technologies were introduced more than 20 years ago and many projects have been proposed and implemented that have embraced this technology. Green computing was introduced in 2008 with the aim of reducing the use of limited resources and maximizing energy efficiency over the life of a system [1]. WSN usually includes a large number of sensors that are equipped with limited power sources but need to work for a long time without charging or replacing batteries. In order to prolong the life of the network and reduce energy consumption in the sensor nodes in the network, clustering techniques have been introduced to achieve efficient communication between sensors [1].

In clustering techniques, sensor nodes are combined in a network to form small separate clusters. Each cluster has a

leader known as a cluster head (CH) and the other nodes of a cluster are known as cluster members (CM). The selection of the head node is one of the main challenges that is considered the main problem of this research. Sensor nodes sense information from the environment and transmit it to the corresponding cluster head. Cluster heads, in turn, collect data from all sensor nodes in the cluster and, after aggregating the data and eliminating duplicate data, transfer it to the base station. Therefore, cluster nodes are responsible for organizing the network, collecting data, and transferring data from sensor nodes to the hole and remote base station, and their energy is consumed more than other nodes [2, 3]. Therefore, one of the requirements for selecting a threaded node is that the node with more residual energy be selected as a thread [4].

Data collection based on clustering approaches has several significant advantages over traditional designs. First, collecting data received from different sensor nodes in a cluster reduces the amount of data transmitted to the base station. Because duplicate data are lost due to the analysis of threaded nodes [5, 6]. Second, the sensor nodes in each cluster have the ability to send data directly to the node nodes, but since sending data over long distances requires more energy consumption, direct data transmission is avoided. Instead, transferring data to clustered nodes near sensor nodes in a cluster member consumes far less energy, so the need for energy across the network to transmit data is greatly reduced [7, 8]. Third, the rotation of the nodal nodes helps to ensure balanced energy consumption in the network, so as to prevent the hunger of certain nodes due to lack of energy. However, selecting the right threaded node with optimal capabilities while balancing power consumption and grid efficiency is a well-known NP-Hard problem in WSN [9].

NP-Hard problems cannot be solved by linear and polynomial methods and require the use of artificial intelligence, collective intelligence, or metaheuristic methods to find near-optimal solutions. In this regard, the use of heuristic and metaexploratory methods in the field of sensor node clustering and cluster head node selection in WSN, which seek to simultaneously improve conflicting goals in the network, has become common in recent research [10]. In [11], a genetic algorithm-based fuzzy optimized reclustering scheme to overcome the energy limitations and maximize network lifetime has been proposed. In [12], a routing protocol to maximize network lifetime has been developed, which is a combination of microgenetic algorithm with LEACH protocol. In [13], a clustering method using multiweight chicken swarm-based genetic algorithm for energy efficient clustering has been proposed. In [14], the OptiGACHS protocol has been proposed to improve cluster head (CH) selection by genetic algorithm using the criteria of distance, density, energy, and heterogeneous node's capability in the fitness function. In [15], an energy-aware routing protocol based on a multiobjective particle swarm optimization algorithm has been presented to improve quality of service (QoS) parameters. In [16], a statistical framework based on machine learning detection and unsupervised learning for effective signal retrieval has been introduced that can effectively approximate the distribution of unknown noise through a normalizing current. In this work, a low-complexity version of the framework is presented using an initial estimate to reduce the search space. In [17], a global heuristic search algorithm inspired by optimal heuristic underlying heuristic search is called the hyperaccelerated tree search (HATS) algorithm, which uses a deep neural network (DNN) to estimate the shortest path in a tree structure and speed up the underlying memory-bounded search algorithm. In [18], ubiquitous intelligent computing is proposed for mobile edge computing network (MEC) systems equipped with unmanned aerial vehicles (UAVs) using reinforcement learning and transfer learning algorithms to reduce latency and optimal energy consumption and the effect of jamming. In [19], in edge-edge computing networks, a system is designed to protect the physical layer through a deep reinforcement learning algorithm to reduce latency and energy consumption that used the Deep Q-Learning algorithm for automatic learning to optimize system performance. In [20], in a mobile edge computing network, federal learning has been used to outdated access points selection in order to reduce latency and energy consumption and increase system efficiency. In [21], a new framework for deep learning based on multioutput federally based IoT learning has been proposed called ME-FEEL, in which the main deep model uses multiple submodels with different depths and the final output has aggregated of the suboutputs. In this method, an output selection algorithm and bandwidth allocation based on a greedy approach is used to maximize the total number of outputs per communication cycle.

Therefore, in this research, a new optimization approach using multiobjective genetic algorithm (MOGA) and cuckoo search algorithm (CSA) for clustering wireless sensor networks is presented. In this study, in order to select clustered nodes from multiobjective genetic algorithm based on reducing intracluster distances and reducing energy consumption in cluster member nodes and near-optimal routing based on cuckoo optimization algorithm to transfer information between nodes, Eclipses have been used in the direction of the cavity. Considering the evolutionary capabilities of the multiobjective genetic algorithm and the cuckoo optimization algorithm, the proposed method is expected to improve in terms of energy consumption, efficiency, delivery rate, and packet transmission latency compared to previous methods.

In the previous methods, the selection of local cluster head nodes in each cluster using single-objective or multiobjective metaheuristic approaches has been presented. After selecting the cluster head nodes in order to transfer information from the sensor node to the sink, the cluster head node is done greedily. However, there may be a deadlock in the path between the cluster heads and due to the greedy approach, it gets stuck in the local optimal trap. Therefore, in the proposed method, in addition to selecting the optimal local cluster head nodes using a multiobjective genetic algorithm based on the quality of service parameters, the path between the sensor nodes to the sink among the cluster head nodes is based on the cuckoo search algorithm and its fitness

function that considers the criteria of the network. In the proposed method, in addition to finding local hops, the optimal global path is also found.

The main contribution of the article is summarized as follows:

(i) develop a forest environment monitoring scenario to prevent forest fires

(ii) using multiobjective genetic algorithm to select optimal cluster head in each cluster wireless sensor network

(iii) the trade-off between the quality of service parameters with respect to using the multiobjective fitness function

(iv) using cuckoo search algorithm to find the optimal global path among the optimal solutions

In the rest of the paper, in the second section, clustering methods based on swarm intelligence in the wireless sensor network will be examined. In the third section, the proposed method will be described in detail. In the fourth section, the test results and evaluation of the proposed method will be presented. In the fifth section, conclusions and future work will be presented.

2. Clustering Based on Swarm Intelligence

In this subsection, collective intelligence-based routing protocols for wireless sensor networks will be reviewed. The properties of these protocols will be highlighted according to the optimization mechanisms.

(i) Genetic Algorithm Based Energy Efficiency Clusters: Genetic Energy Consumption Algorithm (GABEEC) is used to extend network life using cycles. The genetic algorithm evaluates all chromosomes by calculating the fit function. The proportionality function has three parameters, including the distance at which the first node dies, the distance at which the last node dies, and the distance between the clusters. This is an attempt by the algorithm to reduce the lifespan by reducing the communication distance, but because of sending information about the remaining energy to the base station, it strengthens the communication at the head of the clusters. The Genetic Clustering Algorithm (GCA) uses two parameters to achieve a longer lifespan and the total transmission distance in a cluster and the number of network cluster heads [22, 23]. Genetic Algorithm-based Energy Efficient Clustering Hierarchy (GAECH) performs the genetic algorithm twice. Taking into account the available residual energy and the total cost of transmission, it improves the selection of the cluster head [4].

(ii) Ant Colony Optimization Protocols (ACO): Ant colony optimization is one of the bioinspiring mechanisms that routine optimization pathways. This protocol is dynamic and reliable and can provide data aggregation and aggregation routing structures. It also prevents network congestion and reduces power consumption and supports multipath data transmission to achieve reliable communication in wireless sensor networks. This protocol intends to maintain the maximum network life during data transmission in an efficient manner [5, 7]. The authors have proposed a cluster head selection algorithm using ant colony optimization to construct load-balanced clusters in the network. This algorithm considers the remaining energy of the node and the distance between nodes as the criterion for selecting the cluster head [9]. Another HACO-based clustering method organizes the energy efficient clustering protocol through local interactions between sensor nodes [10].

(iii) Particle Swarm Optimization (PSO): Particle swarm optimization is a subset of collective intelligence based on a population-based stochastic optimization method. The PSO applies the concept of social behaviors to flocks of birds or fish to real-world problems. This approach preserves local as well as global solutions and creates the best fit for a goal [24, 25]. PSO is also used to implement the information dissemination protocol in the article. The selection criteria for the head of the cluster based on the residual energy are the distance inside the cluster and the degree of the node [26]. The combined protocol of Harmony Search Algorithm (HSA) and PSO is also used to optimize clustering. This algorithm selects the hybrid head of the cluster with the proportionality function, which includes the residual energy of the nodes, the degree of the node, and the distance between the nodes. The HSA-PSO metaheuristic algorithm is used to select a constant number of cluster heads. In the case of a certain number of heads, it does not guarantee coverage of the entire network. Heads in HSAPSO use direct communication to transfer their data to the base station, which reduces its energy efficiency [26].

(iv) Clustering based on artificial bee colony optimization: ABC optimization is also used to form clusters in a wireless sensor network. Wireless Sensor Network Clustering Using the Artificial Bee Cloning Algorithm (WSNCABC) uses the artificial bee colony to calculate the eclipse fit using parameters such as node residual energy and distance from the base station to nodes. However, this algorithm suffers from the high cost of transferring data directly from the cluster to the base station [27–30]. Clustering protocol based on artificial bee colony (ABC-C) has been proposed in another study that improves the fit function. The residual energy, the distance from the node to the base station, and the quality

of the bond are considered parameters of the fit function. This algorithm selects the cluster head periodically [31]. The B-Sensor-C algorithm has been developed for event-based sensor networks. When an event occurs, the protocol forms clusters and selects the head. The most important node that confirms this event seems to be the head and others should follow it [32, 33].

(v) Energy-Aware Bee Colony Approach (EABCA) improves network performance with the fit function. For data delivery, multichannel communication between the head and the base station is required [34].

Table 1 shows a comparison of clustering methods based on collective intelligence in terms of important parameters in WSN clustering.

Table 1 is reproduced from Nabavi et al. (2021).

3. Preliminaries of the Proposed Method

As mentioned, in this study, in order to overcome the limited energy challenge in wireless sensor networks, we try to use a combination of two metaheuristic optimization algorithms for near-optimal routing. In the rest of this section, we will first introduce how these two algorithms work, and finally, in the next section, we will explain how to combine these two algorithms in order to create a routing method.

3.1. Genetic Algorithm. Genetic algorithm (GA) is one of the metaheuristic optimization algorithms inspired by the law of gene combination and generation. The algorithm starts with the initial population and continues the search to find a group of optimal chromosomes that may be possible solutions to the problem. Each chromosome is a string of genes that represent a specific solution that originates from the original population. The genetic algorithm, based on genetic laws and existing operators, repeatedly selects the most suitable solutions in the form of elite chromosomes and, in the next step, produces new chromosomes derived from selected chromosomes that are close to the optimal solutions. The initial population in the genetic algorithm is randomly selected and the coding of the chromosomes is varied based on different optimization problems. The initial population is evaluated in the first step based on the proportionality function, and to generate a new population, the selection operator takes action. The purpose of the selection operator is to select the optimal chromosomes that have the potential to become near-optimal solutions that these chromosomes use to produce populations in the next generation. The multiobjective proportionality function uses an expert approach in the Pareto space to balance the objectives of the problem and stores the Pareto front chromosomes in the reservoir of dominant solutions [35]. One common method for the operator is to select a roulette wheel in which each chromosome is assigned a portion of the wheel based on its merit and the value of the fit function, so for chromosomes for which the value of the fit function is greater. Naturally, there are more gaps and more chances to choose for the next population. Then, genetic algorithm operators, which include two crossover and mutation operators, combine chromosomes, and in some chromosomes, they change the values of one or more genes to produce values in the new generation of expert chromosomes. Produce a higher fit function. Genetic algorithm operators to diversify new populations are defined as follows [36]:

(1) Crossover operator: This operator combines two chromosomes based on a predefined parameter called Crossover probability and changes the values of both chromosomes. In the crossover operator, part of the first chromosome is replaced with part of the second chromosome based on the probability of crossover, and the new population produced accordingly will be a combination of both chromosomes

(2) The mutation operator randomly selects one or more genes from a chromosome and changes their values according to another predefined probability. The new chromosomes change slightly based on the crossover operator, which is applied to create diversity in the new population and to create chromosomes with higher proportion function values than the chromosomes of the previous generation

In each iteration of the genetic algorithm, the most appropriate chromosomes as an expert population are passed directly to the next generation of the population. Finally, the genetic algorithm is terminated based on some stop criteria, which may include a certain time to run the algorithm, a certain number of iterations, achieving a certain value of the proportionality function, achieving a certain amount of the objective function. And in other cases, at each step of the genetic algorithm, the chromosomes that pass to this stage are evaluated based on the fitness function to measure the degree of optimality and quality of the solution for each chromosome. The objectives used in the fit function may vary depending on the nature of the problem. In general, there are two main types of problems in the field of problem optimization, which are presented in the form of maximization and minimization problems. For maximization problems, the chromosomes with the highest value of the proportionality function are selected at each stage, and for inverse minimization problems, this equation is used [37].

3.2. Cuckoo Search Algorithm. Cuckoo Search Algorithm is a nature-inspired algorithm based on the reproduction of cuckoo birds. When using cuckoo search algorithms, it is important that potential solutions are associated with cuckoo bird eggs. Cuckoos lay their fertilized eggs in other cuckoos' nests, hoping that their eggs will be raised by other parents. There are times when cuckoos realize that the eggs in their nests do not belong to them, in which case the foreign eggs either come out of the nests or leave the whole nest. The cuckoo search optimization algorithm is based on the following three rules:

Table 1: Comparison of clustering methods based on swarm intelligence.

Base station location	Node establishment	Mobility	Heading the routing to base station	Rotate the head of the cluster	Approach	Clustering algorithm	Location	Protocol
Out of area	Random	Fixed	Straight	Each round	GA	Concentrated	Unconsciously	GABEEC
Center of the area	Random	Fixed	Straight	Each round	GA	Distributed	Unconsciously	GCA
Outside, corner, and center of the area	Random	Fixed	Straight	Each round	GA	Concentrated	Unconsciously	GAECH
Out of area	Random	Moving	Straight	Each round	ACO	Concentrated	Unconsciously	hACO
Out of area	Random	Fixed	Straight	Each round	ACO	Concentrated	Unconsciously	ANTCLUST
Within the area	Random	Fixed	Straight	Each round	PSO	Concentrated	Unconsciously	PSO
Within the area	Random	Fixed	Multistep	Each round	PSO	Concentrated	Unconsciously	PSO-SD
Within the area	Random	Semifixed	Straight	Each round	PSO	Concentrated	Unconsciously	HAS-PSO
Within the area	Random	Fixed	Straight	Each round	ABC	Concentrated	Unconsciously	WSNCABC
Within the area	Random	Fixed	Straight	Each round	ABC	Concentrated	Unconsciously	ABC-C
Out of area	Random	Moving	Multistep	Each round	ABC	Distributed	Unconsciously	Bee-Sensor-C
Center of the area	Random	Fixed	Multistep	Each round	ABC	Concentrated	Unconsciously	EABCA

(i) Each cuckoo randomly selects a nest and lays an egg

(ii) The best nests are passed on to the next generation with their quality eggs

(iii) For a certain number of nests, a host cuckoo can detect an external egg with a probability of pa∈ [0,1]. In this case, the host cuckoo can discard the egg or leave the nest and build a new location elsewhere

The last rule can be approximated by substituting the ratio of host nests to new nests (with new random solutions). The quality of fit of a solution can simply be commensurate with the value of the target performance. From an executive point of view, the representation of the initial population is such that each egg in a nest is shown as a solution and each cuckoo can lay only one egg (thus, a solution is shown). It is safe to say that there is no difference between an egg, a nest, or a cuckoo. The goal is to use a new and potentially better solution (cuckoo egg) to replace the worse bad solution in the nest [38].

The cuckoo search algorithm is very effective for general optimization problems because it maintains a balance between local random search and global random search. The balance between local and global random search is controlled by a pa∈ switch parameter [0,1]. Stochastic local and global searches are defined by relationships 1 and 2, respectively [38].

$$x_i^{t+1} = x_i^t + \alpha s \bigotimes H(p_a - \varepsilon) \bigotimes \left(x_j^t - x_k^t\right), \qquad x_i^{t+1} = x_i^t + \alpha L(s, \lambda). \tag{1}$$

In the above equations, x_i^t, x_j^t, and x_k^t are the current position for the eggs in a random permutation, the α factor is related to the positive step size in order to select the next nest, x_j^{t+1} is the position of the eggs in the next step, s is the step size, $\bigotimes$ is the internal multiplication of two matrices, H is the heavy-side function, p_a is the probability of switching between local and public search, ε is a fixed number with the same distribution, and $L(s, \lambda)$ is the Lévy distribution to define a random search step size used.

3.3. Methodology. In this paper, a combined method based on multiobjective genetic algorithm and cuckoo search has been presented. This method is based on a clustering approach in which the multiobjective genetic algorithm tries to find the optimal CH by evaluating the main network criteria such as the distance between CM in each cluster, the distance from the CH to the sink and the residual energy of CHs. Selecting the optimal CH can optimize energy consumption and other QoS objectives. The sensed data in the network is first transmitted by the CM to the CH and then sent to the sink through multihop routes between the CHs. Given that the multiobjective genetic algorithm tries to optimize local QoS objectives in each cluster, the final route between the CHs may be chosen based on greedy methods, in which it may not be global optimal. In this paper, to overcome this challenge, the cuckoo search algorithm has been used. In fact, the cuckoo search algorithm takes the routes between the CHs as input, and if the route specified between the CHs in the multiobjective genetic algorithm is not global optimal, this route will be discarded and a global optimal route between the CHs will be selected in the network. The global optimal route in the cuckoo search algorithm has been found to reduce the overall energy consumption in the network, increase the data delivery rate, and reduce the end-to-end latency. Figure 1 shows an overview of the proposed method in the form of a flowchart.

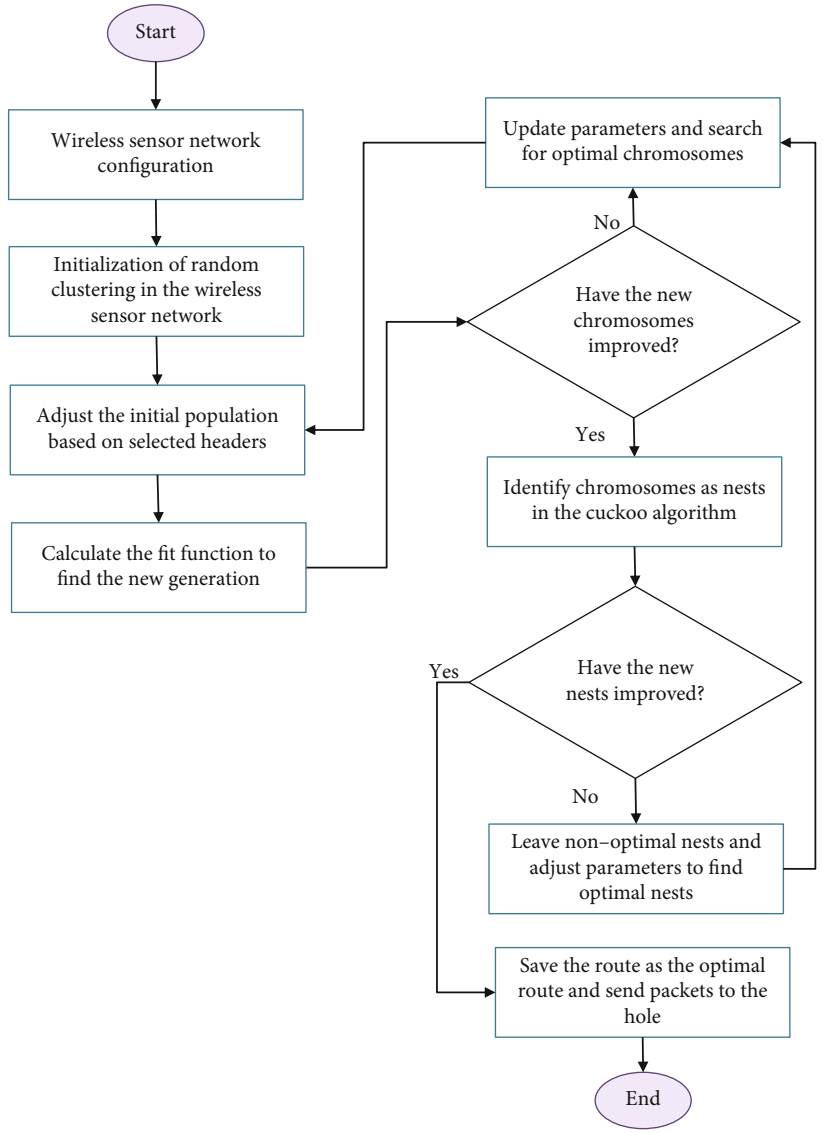

Figure 1: Flowchart of the proposed method.

According to the flowchart of the proposed method, this method has three general steps which are as follows:

(a) wireless sensor network configuration and initial clustering of nodes using partition clustering algorithm

(b) selection of optimal local header nodes using the main criteria by the multiobjective genetic algorithm

(c) determining the global optimal route with the aim of reducing energy consumption, increasing the data delivery rate, and reducing the end-to-end latency using the cuckoo search algorithm

Details of each of the main steps are provided below.

3.3.1. Network Model. In this section, the details of the proposed network are presented. The proposed wireless sensor network includes N sensor nodes and a fixed sink. Network settings are set according to the standard settings in other articles. Initially $C\,(C \subset N)$ random nodes are selected as the CHs. These nodes have been considered cluster centers in the proposed network. The other nodes in the network have connected to close CH based on the partitioning clustering method and initial clusters have formed. The distance between nodes in the network and CHs is measured by the Euclidean distance [23]. Each node has been assigned to the nearest CH and the nodes close to the sink have not been assigned to any cluster and have been connected directly to the sink. After the clusters have formed, each CH notifies the other nodes by a message. Once receiving this message, CMs of the cluster have sent a reply to the CH for confirmation. Thus, information about CMs and CHs has been stored in the routing table.

3.3.2. Cluster Head Selection Using MOGA. After the formation of initial random clusters and random selection of initial CHs, in the second step, the proposed MOGA method

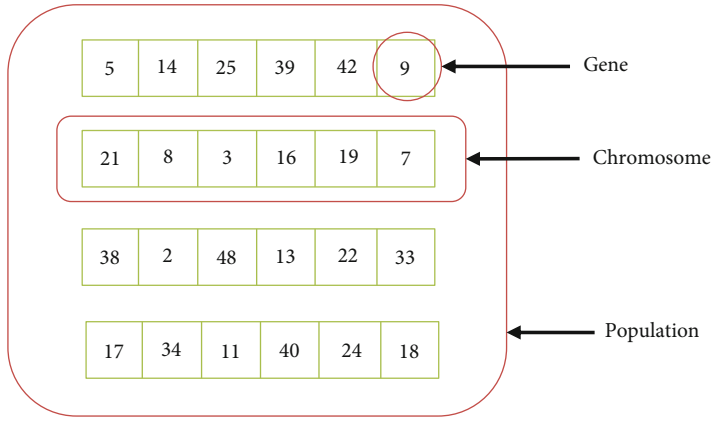

Figure 2: The view of initial population in the proposed method.

is used to find the optimal CHs. The initial population in the MOGA consists of random CHs that are found the optimal solution in exploration stages as local optimal CHs. The initial population and genetic operators are described as follows.

(1) Initial Population. Given that in this paper, the MOGA algorithm is used to find the optimal CHs in each cluster, each of the input chromosomes is considered a solution to this problem. Each gene on each chromosome represents a CH. Hence, the number of genes on each chromosome is equal to the number of clusters. Due to the fact that the number of clusters in the first stage is randomly selected, hence, the number of genes is adjusted according to the initial clusters. Figure 2 shows an overview of the initial population in MOGA.

As can be seen from Figure 2, the initial population in MOGA consists of chromosomes that have genes with random integer numbers. Each number in genes refers to the index of a node selected as the node. The selection of nodes in the initial stage is random and then changed by genetic operators in the exploration stage and will become optimal nodes to be selected as CH.

The following are important steps in MOGA:

Step 1. Initial random population production. The initial population size can be selected randomly depending on the number of clusters. The initial population is considered 100 chromosomes.

Step 2. Nondominant sorting. The values of the fitness function are calculated for the given objectives. For each chromosome to become a nondominant solution, it must not dominate any other chromosome. Each chromosome has ranked by fitness values [39]. After ranking the individuals based on the fitness function, the first half of the individuals are selected as the optimal chromosomes.

Step 3. Genetic operation. At this stage, two parents are randomly selected from the optimal individuals. From these two parents, two new children are born, called the "new generation." These offspring are produced using crossover and mutation operations.

In this paper, we use one-point crossover, where two parents (chromosomes) exchange part of their genes with each other at the point of intersection. Crossover rate is the probability that several genes from each parent will be selected for crossover operation.

Another method to produce offspring is mutation. Only one chromosome has been selected to mutate on it. In mutation, a bit is randomly placed in the parent. The mutation rate is the probability that several bits in the chromosomes will change.

Step 4. Select. Fitness values for each child generated by crossovers and mutation are calculated. Produced individuals gather after crossover and mutation with the original population. Again, sorting operations are performed on these individuals and their rankings are evaluated. When sorting is done, the number of individuals equal to initial population has been selected and others have been rejected.*(2) Fitness Function.* As mentioned, the fitness function parameters in the proposed method include the distance CH from other CMs, the distance from CH to the sink, and the amount of residual energy for CH. Therefore, the fitness function in the proposed method is to optimize these parameters to find the optimal CHs in order to reduce energy consumption, increase the data delivery rate, and reduce the end-to-end latency. For this purpose, a minimization function is used in the proposed method, which selects nodes as CH in each step of data transfer with the lowest average distance within the cluster, the minimum distance to the sink and the least energy consumed (maximum residual energy). Due to the fact that CHs are responsible for transferring packets from CMs to the sink, CHs are evaluated in each round and, if necessary, replaced with nodes that are more optimized. In this case, the cluster is updated and the CMs join the new CH. Finding such nodes causes the energy of some CHs not to run out sooner than other nodes and the energy consumption in the clusters and in the whole network is balanced. In relation 6, the proposed

fit function is shown [23].

$$D_{AVG_i} = \sqrt{\sum_{i=1}^{M}\sum_{j=1}^{N}\left|x_i - x_j\right|^2},$$

$$D_{sink_i} = \sqrt{\sum_{i=1}^{M}\left|x_i - x_s\right|^2}, \tag{2}$$

$$F1 = \min\left(\sum_{i=1}^{M} D_{AVG_i} + \sum_{i=1}^{M} D_{sink_i} - \sum_{i=1}^{M} E_{r_i}\right).$$

Subject to

$$\begin{aligned} &\sum_{\mathrm{i}=1}^{\mathrm{M}} \mathrm{E}_{\mathrm{r_i}} \le \mathrm{E}_{\mathrm{init_i}}, \\ &\sum_{\mathrm{i}=1}^{\mathrm{M}} \mathrm{DS}_{\mathrm{i}} \le \mathrm{D}_{\mathrm{i,f}}, \\ &\sum_{i=1}^{M} D_{AVG_i} \le \varepsilon, \\ &E_r > 0, D_{sink_i} \ge 0, D_{AVG_j} \ge 0, \end{aligned} \tag{3}$$

where x_i and x_j are the coordinates of nodes i and j, x_s is the coordinates of the sink, D_{AVG_i} is the mean distances within the cluster i, E_{r_i} is the residual energy of nodes i, N is the number of nodes, M is number of clusters, E_{init_i} is the primary energy of nodes i, f is the farthest node in each cluster from the sink, and ε is the cluster diameter. Due to the existing limitations, the residual energy of CH should not be more than its initial energy, the distance from CH to the sink should be less than the distance of the farthest node in the cluster from the sink, the average distances within the cluster should be less than or equal to the diameter of the cluster.

Given that the values of the input parameters to the proportionality function are not in the same range, it is necessary to normalize the data before evaluation. In the proposed method, the MIN-MAX normalization criterion is used [40]. Given the values of the fit function for each chromosome, the chromosome that is uncontrollable will eventually be obtained as the final solution of the MOGA algorithm. Based on this chromosome, CHs are selected and the route between these CHs to send data to the cavity is determined.

3.3.3. Cuckoo Search Algorithm to Find Global Optimal Route. In the previous section, the MOGA algorithm selected the best nodes as CH according to the network parameters. These nodes are the most suitable option in any cluster at any step of data transfer. Sending data from CM to the sink requires sending multihop steps, in which each hop is a CH. How to send data between CHs specifies the route between CM to the sink. Determining which CHs in the route between CM and sink improve objectives of network is an issue that creates a global optimal path. In this paper, the cuckoo search algorithm is used to solve this problem. The cuckoo search algorithm takes the possible routes between the CM and the sink as input. In this algorithm, each path is considered a nest. Due to its metaheuristic nature, this algorithm tries to find the best nest. The best route can optimize the network's objectives. In other words, data transfer in each step of the optimal route saves the total energy of the network, increases the data delivery rate, and reduces the end-to-end latency in the network. The routes between the CM and the sink are evaluated based on the fitness function in Equation 6 to find the global optimal route.

$$F2 = \min\left(\sum_{i=1}^{M} L_i + \sum_{i=1}^{M} E_t - \sum_{i=1}^{M} DR_i\right). \tag{4}$$

Subject to

$$\begin{aligned} &\sum_{i=1}^{n} L_i \ge L_{dir}, \\ &\sum_{\mathrm{i}=1}^{\mathrm{n}} \mathrm{E}_{\mathrm{t}} < \mathrm{E}_{\mathrm{dir}}, \\ &\sum_{i=1}^{n} DR_i > 0. \end{aligned} \tag{5}$$

In the above relation, F2 is defined as the fitness function of the cuckoo search algorithm, L_i is the end-to-end latency of CHs, E_t is the prediction of total consumed energy, DR_i is the data delivery rate in route i, L_{dir} is the latency of one-hop data transfer, and E_{dir} is the energy consumption of one-hop data transfer. The route with the least value of the fitness function F2 is selected as the optimal global route.

4. Implementing the Proposed Method

In this article, a forest monitoring scenario is used to prevent fires. The risk of forest fires is one of the problems that the environment always faced. Recently, in order to prevent forest fires and prevent the destruction of pastures, methods have been proposed for permanent monitoring of the forest using communication equipment. Wireless sensor network based on communication between sensors and aggregation of data from the environment in forest areas is one of the new technologies that has been proposed for monitoring the forest environment. In this type of monitoring program, you can go to the installation of thermal sensors and radiation sensors. In some cases, the use of animals as biological sensors has been suggested, but the problem with these reptiles is their slow nature, which makes them very difficult to track. Forest fires most often occur on the ground and are always spread regularly and usually depend on wind speed. To detect forest fires, thermal sensors can be used that periodically transmit ambient temperature data. Therefore, thermal sensors are used in the proposed network in this paper. These sensors are installed in the forest environment at random distances and periodically transmit the ambient

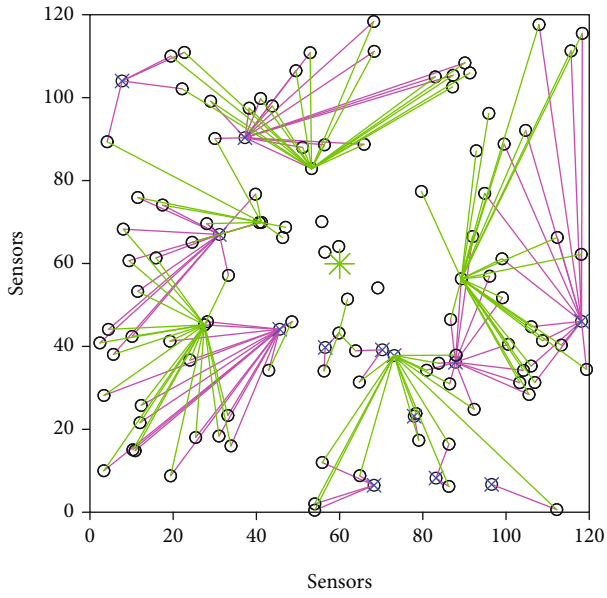

Figure 3: The replacement of new cluster headed nodes with previous headed nodes.

temperature to the hole. Of course, for better network efficiency, by setting a temperature threshold, information can be sent when the forest temperature exceeds the threshold. Since in this article the goal is to find the optimal path using multiobjective genetic algorithm and cuckoo search, we have used this sensing version to improve the service quality parameters in this method.

In order to implement the proposed method, we first configure the wireless sensor network based on the existing standard parameters. The proposed network is implemented in an environment of 100×100. In order to implement this scenario, the MATLAB software version 2020 and LEACH toolbox have been used. The proposed network has 100 sensor nodes and one hole. The hole node first gathers information about the locations of sensors in the network and selects several random cluster head nodes based on this information. Cluster nodes are randomly selected and sensor nodes join cluster nodes based on their distance to form clusters. After the first cluster formation and sending the data to the head node, information about the initial energy and distances within the cluster and the distance of the head node to the origin can be calculated.

Of course, some nodes around the hole may not be clustered according to their distance to the nearest node because their distance to the hole is less than their distance to the nearest node. These sensor nodes can communicate directly with the hole to transmit information.

This information is entered into the genetic algorithm as the primary chromosome and the implementation of the second step of the proposed method begins. At this stage of the proposed genetic algorithm, the initial population is evaluated according to the randomly selected thread nodes. In order to initially evaluate the input population to the proposed genetic algorithm, the proportionality function is applied to the initial population. Based on this, the proposed genetic algorithm measures the threaded nodes in terms of

Table 2: The output of cuckoo search algorithm to find quality routes.

This solution as a nest must be abandoned
5 6 7 19 20 29 55 62 63 65 72 79 100
****
This nest is selected by probability 0.51759
3 11 32 37 42 43 52 64 72 91 95
****
This solution as a nest must be abandoned
14 15 21 35 40 47 64 67 69 71 93 99 100
****
This nest is selected by probability 0.56215
11 32 37 40 43 52 55 64 65 70 75 86 90 91 95
****
This solution as a nest must be abandoned
14 15 21 35 40 47 64 67 69 71 93 99 100
****
This nest is selected by probability 0.88169
11 37 40 52 57 59 64 65 70 75 79 80 86 90 91 95
****

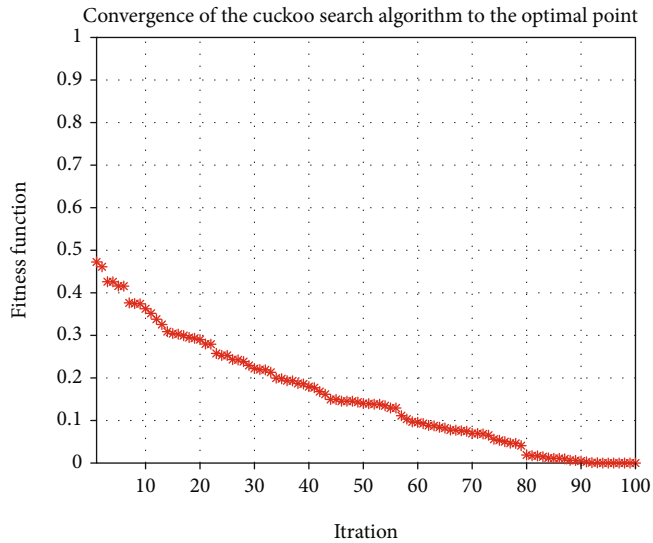

Figure 4: Convergence of the cuckoo search algorithm towards the optimal point.

residual energy, average intracluster distances, and distance from the hole. The values of the proportionality function are calculated for each of the head nodes in the initial population. In the meantime, some threaded nodes have good proportion function values, but some are weak, so in the

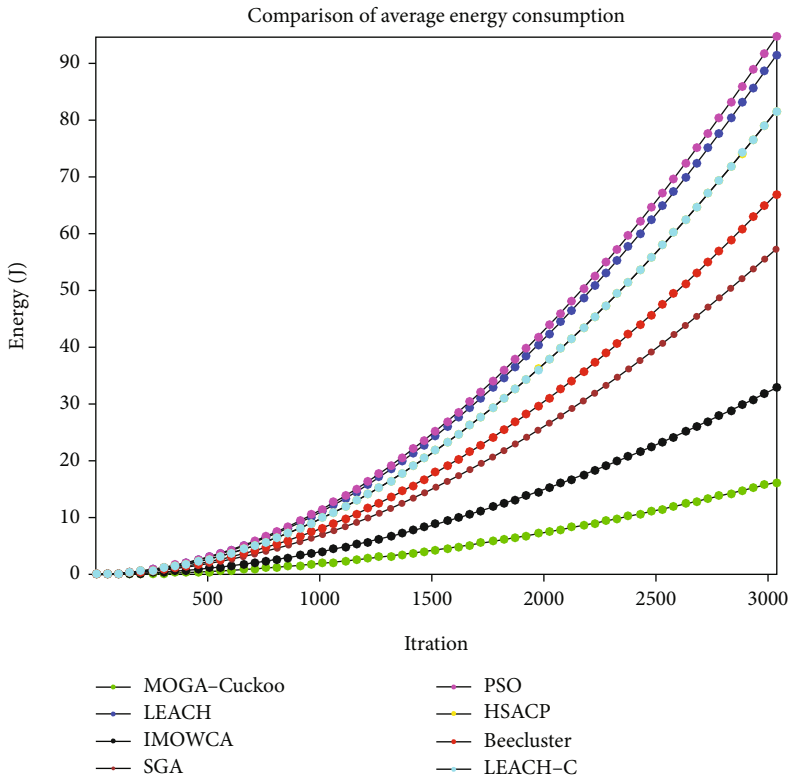

Figure 5: Comparison between the proposed method and previous methods in terms of energy consumption.

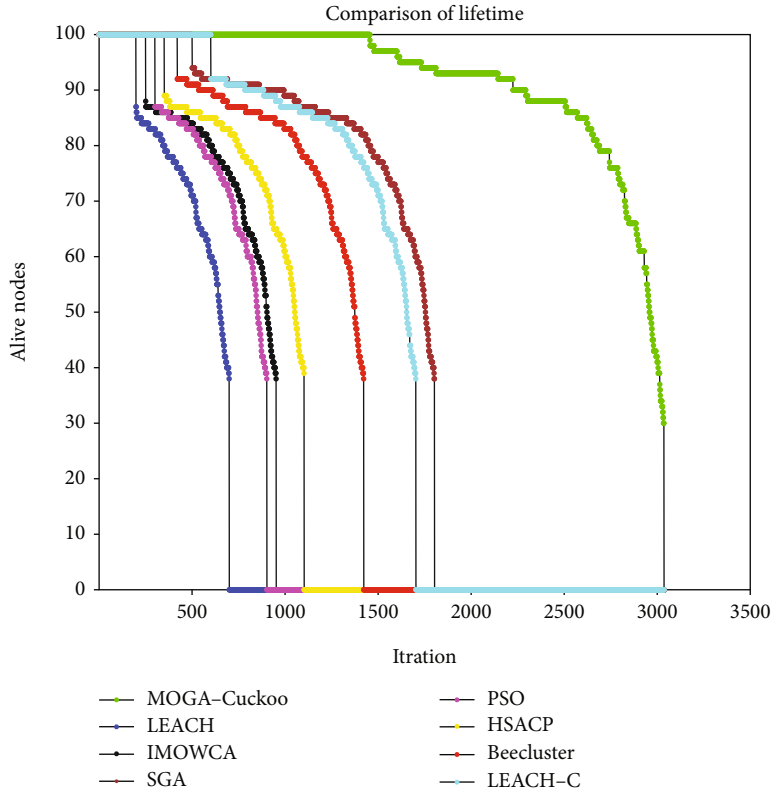

Figure 6: Comparison between the proposed method and previous methods in terms of network life.

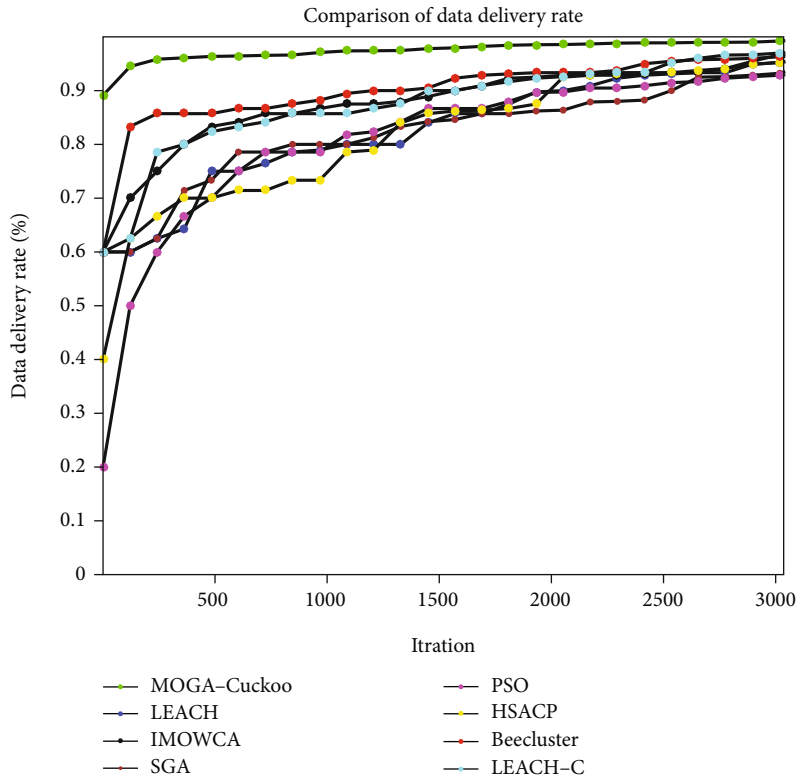

Figure 7: Comparison between the proposed method and previous methods in terms of data delivery rate.

next step, based on the fitting and mutation operators of a new population production, we will examine the proportional function values in the new population. The new population in the proposed method, like the original population, will be a combination of cluster head nodes that will replace the previous cluster head nodes, and based on this, the proportional function of this population will be remeasured. Proportion function values are then calculated for the new population. Also, the related clusters of some cluster head nodes that are located on undesirable chromosomes are disintegrated and serious clusters are formed with the clusters on the optimal chromosomes.

As shown in Figure 3, the previous threaded nodes are marked with a black × mark, the previous connections were marked with blue lines; now, the connections with the new cluster head nodes are marked with red lines. New cluster head nodes have been selected as the proposed solution for transferring information from sensor nodes and aggregating data and sending them to the hole node. However, due to the distances of the head nodes from the sink node, if a head node sees another head node in the direct path to the hole, send packets instead of direct transfer to the hole through the multistep transfer process between head nodes. It will be a hole until it reaches the node.

Now, the proposed method enters the third stage, in which the cuckoo search optimization algorithm examines the path quality based on the clues obtained from the genetic algorithm. The cuckoo search algorithm has the ability to find the optimal route in the whole network due to its global search capability. In fact, at this stage, the proposed method of the selected path assignment determines whether it is optimal for transmitting data packets, or there may be a more optimal path, and the genetic algorithm is stuck in a local optimal trap. Table 2 shows the output of the cuckoo search algorithm for the proposed paths by the genetic algorithm.

As shown in Table 2, the optimal routing in the proposed method is based on the cuckoo search algorithm. The cuckoo search algorithm, according to its proportionality function, examines the quality of the proposed paths by the genetic algorithm, and the paths that improve the network goals are returned with the value of their proportionality function. Figure 4 shows the convergence of the cuckoo search algorithm towards the optimal point.

As shown in Table 2, the optimal routing in the proposed method is based on the cuckoo search algorithm. The cuckoo search algorithm, according to its proportionality function, checks the quality of the proposed paths by the genetic algorithm, and the paths that improve the network goals are returned with the value of their proportionality function. The optimal route is selected and after reaching a dead end, it is detected by the cuckoo search algorithm. These paths have been selected as nonoptimal paths and need to reexamine the values of the fit function and update the routing table. Also, in Table 2, it can be seen that the optimal paths have been selected as the shortest route between the sensor node and the sink in the current network conditions and it has been confirmed after reviewing by cuckoo search algorithm that information has been transferred through this route. In this paper, the cuckoo search algorithm is used in order to find the optimal global path of the owl according to the global search property. The

optimal global path is determined based on the fit function in this algorithm. Hence, Figure 4 shows the convergence of the cuckoo search algorithm towards the optimal point.

As shown in Figure 4, since the fitness function in the cuckoo search algorithm is decreasing, this algorithm selects the optimal paths with the lowest value of the proportionality function as the globally optimal path. The parameters of the proportion function in the cuckoo search algorithm try to find the optimal path with the least energy loss, the least amount of latency, and the most data delivery rate. Hence, the lower the value of the fitness function, the more efficient the path found. According to Figure 4, it can be seen that the cuckoo search algorithm reduces the value of the target function in each step of data transfer to converge to the optimal point. Therefore, it can be said that using the cuckoo search algorithm to investigate the global optimization of the path whose steps have been selected by the multiobjective genetic algorithm in each cluster can help optimize the service quality parameters in the wireless sensor network. The network simulation continues until the energy of the wireless sensor nodes is terminated by the transmission of information. When the nodes within the network lose their energy, that area of the network that is covered by a particular node is disrupted and the so-called network hole occurs. In such cases, the other nodes are responsible for collecting data from that area of the network hole. This happens until other nodes are unable to collect data from the entire network environment. In this case, the life of the network ends.

4.1. Evaluation of the Proposed Method. The evaluation of the proposed method is done in order to evaluate the quality of the proposed method and to present the improvement created by the proposed method based on the initial problem proposed. To evaluate wireless sensor networks, various criteria have been introduced in the publications, which we will discuss in the proposed method of energy consumption, network life, and data delivery rate. Due to the importance of routing in wireless sensor networks in order to balance the energy consumption between nodes, in order to validate the proposed method to compare it with the previous methods in terms of energy consumption and other criteria. We evaluate. For this purpose, we compare the proposed method with the methods [41–43] in terms of the mentioned evaluation criteria. Figure 5 shows a comparison between the proposed method and previous methods in terms of average energy consumption in the network.

As shown in Figure 5, the average energy consumption is calculated for different methods. The lower the average energy consumption diagram, the more balanced the energy consumption at the sensor nodes in the network. This makes the network longer and the network available for a longer period time. In the proposed method, according to the selection of the optimal local cluster nodes in each cluster by the multi-objective genetic algorithm and the selection of the globally optimal path by the cuckoo search algorithm, the service quality parameters are optimized. As can be seen from Figure 5, the proposed method has a lower average energy consumption per 100 nodes than the previous methods. Figure 6 also compares the proposed method with previous methods in terms of the lifespan and death of the first node in the network.

As shown in Figure 6, network lifetime is calculated in different ways. Network lifetime is directly related to the energy consumption of wireless sensor nodes. In fact, the more balanced the power consumption of the sensor nodes in the network, the longer the network lifetime will be. Network lifetime in WSN applications is a very important criterion for evaluating the efficiency of routing methods. Therefore, in the proposed method, by selecting the optimal cluster head nodes and the optimal global path, we have tried to reduce the distance between the hops and reduce energy consumption in sending information. Therefore, the proposed method has been able to improve energy consumption in sensor nodes. Also, in the proposed method, the lifetime of the network is significantly increased. According to Figure 6, the proposed method has a longer lifetime than the previous methods and the first node in the proposed method dies much later than other methods, which shows the balance of energy consumption in the proposed method. Figure 7 also shows a comparison between the proposed method and previous methods in terms of delivery rate.

As shown in Figure 7, the proposed method has a higher delivery rate than the previous methods, which indicates the selection of the optimal route and avoidance of bottlenecks and the loss of the least amount of packets in the proposed method. According to the evaluation criteria in the wireless sensor network, the proposed method can be seen according to the use of multiobjective genetic algorithm in order to find the optimal head node in each step of information transfer and also to find the optimal global path using a cuckoo search algorithm. It has less energy, longer life, and a better delivery rate than other methods.

5. Conclusion and Discussion

Wireless sensor networks are one of the newest media for monitoring and controlling the environment, which is able to collect information from the environment and provide data for network applications without the need for infrastructure and in a self-organizing manner. Therefore, the great popularity of these networks has caused many challenges, one of the most important challenges is the imbalance of energy consumption in the network. Due to the energy limitations of sensor nodes, energy imbalances can overshadow all grid performance metrics. Therefore, in this research, a new optimization approach using multiobjective genetic algorithm and cuckoo algorithm for clustering wireless sensor networks is presented. In this research, in order to select clustered nodes from multiobjective genetic algorithm based on reducing intracluster distances and reducing energy consumption in cluster member nodes and near-optimal routing based on cuckoo optimization algorithm to transfer information between nodes, Eclipses have been used in the direction of the hole.

The problem of channel estimation is directly related to the number of messages and the complexity of the calculations performed to find the optimal path. In this paper, for

better network performance and less complex channel estimation, the temperature threshold is determined and when the forest temperature exceeds the threshold, information is sent from the sensors to the hole. In this case, the number of messages sent on the network will increase in a balanced way. Also, the energy consumption of the sensor nodes will be balanced and the energy of one node will not run out sooner than the others. To transfer information, it is necessary to send a routing package by the node to inform the nodes of the cluster about the status of the new node and send a confirmation message by the node. Due to the fact that the notification process of the new head occurs only in the event of a temperature rise and is local, the number of messages due to communication overhead will be low. Also, the computational overhead to find a new clue and the optimal path occurs in each round of data transfer when sensing the critical message, it is expected that the control of the control and computational overhead in the proposed method does not exceed a certain limit.

The results of the proposed method show that considering the evolutionary capabilities of the multiobjective genetic algorithm and the cuckoo optimization algorithm, the proposed method in terms of average energy consumption, delivery rate, and network life, compared to previous methods, has made significant improvements.

In order to provide suggestions for future work in the continuation of this article, we can use NSGA-II or NSGA-III algorithms to find the optimal local head-clusters. In these algorithms, according to the ranking of nondominant solutions, possible cluster head nodes can be sorted. In this ranking, the first node can be selected as the current cluster head node, and if the energy of the current cluster head node has decreased, the second node in the ranking as the most likely candidate for the cluster head node can be considered. In this case, the volume of calculations performed to find the optimal cluster head nodes in each cluster will be significantly reduced. If the second node in the ranking cannot achieve the proper fitness function, other nodes in the network can be evaluated.

Data Availability

The data used to support the findings of this study are derived from the simulation results.

Conflicts of Interest

The authors declare that they have no conflicts of interest.

References

[1] S. Misra and R. Kumar, "A literature survey on various clustering approaches in wireless sensor network," in *2016 2nd international conference on communication control and intelligent systems (CCIS)*, Mathura, India, 2016.

[2] S. Mudundi and H. H. Ali, "A new robust genetic algorithm for dynamic cluster formation in wireless sensor networks," in *Proceedings of Wireless and Optical Communications*, Montreal, Quebec, Canada, 2007.

[3] S. Einy, C. Oz, and Y. D. Navaei, "The anomaly- and signature-based IDS for network security using hybrid inference systems," *Mathematical Problems in Engineering*, vol. 2021, Article ID 6639714, 10 pages, 2021.

[4] B. Baranidharan and B. Santhi, "GAECH: genetic algorithm based energy efficient clustering hierarchy in wireless sensor networks," *Journal of Sensors*, vol. 2015, Article ID 715740, 8 pages, 2015.

[5] Y. Sun, W. Dong, and Y. Chen, "An improved routing algorithm based on ant colony optimization in wireless sensor networks," *IEEE Communications Letters*, vol. 21, no. 6, pp. 1317–1320, 2017.

[6] S. Einy, C. Oz, and Y. D. Navaei, "IoT cloud-based framework for face spoofing detection with deep multicolor feature learning model," *Journal of Sensors*, vol. 2021, Article ID 5047808, 18 pages, 2021.

[7] T. Gui, C. Ma, F. Wang, and D. E. Wilkins, "Survey on swarm intelligence based routing protocols for wireless sensor networks: an extensive study," in *2016 IEEE international conference on industrial technology (ICIT)*, Taipei, Taiwan, 2016.

[8] Y. A. Nanehkaran, Z. Licai, J. Chen et al., "Anomaly detection in heart disease using a density-based unsupervised approach," *Wireless Communications and Mobile Computing*, vol. 2022, Article ID 6913043, 14 pages, 2022.

[9] C. K. Ho and H. T. Ewe, "A hybrid ant colony optimization approach (hACO) for constructing load-balanced clusters," in *2005 IEEE congress on evolutionary computation*, Edinburgh, UK, 2005.

[10] J. Kamimura, N. Wakamiya, and M. Murata, "A distributed clustering method for energy-efficient data gathering in sensor networks," *International Journal of Wireless and Mobile Computing*, vol. 1, no. 2, pp. 113–120, 2006.

[11] M. K. Shahzad, S. M. R. Islam, M. Hossain, M. Abdullah-al-Wadud, A. Alamri, and M. Hussain, "GAFOR: genetic algorithm based fuzzy optimized re-clustering in wireless sensor networks," *Mathematics*, vol. 9, no. 1, p. 43, 2021.

[12] M. Radhika and P. Sivakumar, "Energy optimized micro genetic algorithm based LEACH protocol for WSN," *Wireless Networks*, vol. 27, no. 1, pp. 27–40, 2021.

[13] N. Ajmi, A. Helali, P. Lorenz, and R. Mghaieth, "MWCSGA—-multi weight chicken swarm based genetic algorithm for energy efficient clustered wireless sensor network," *Sensors*, vol. 21, no. 3, p. 791, 2021.

[14] A. S. Nandan, S. Singh, and L. K. Awasthi, "An efficient cluster head election based on optimized genetic algorithm for movable sinks in IoT enabled HWSNs," *Applied Soft Computing*, vol. 107, article 107318, 2021.

[15] Z. Peng, M. S. Jabloo, Y. D. Navaei et al., "An improved energy-aware routing protocol using multiobjective particular swarm optimization algorithm," *Wireless Communications and Mobile Computing*, vol. 2021, Article ID 6677961, 16 pages, 2021.

[16] K. He, L. He, L. Fan, Y. Deng, G. K. Karagiannidis, and A. Nallanathan, "Learning-based signal detection for MIMO systems with unknown noise statistics," *IEEE Transactions on Communications*, vol. 69, no. 5, pp. 3025–3038, 2021.

[17] K. H. Le He, L. Fan, X. Lei, A. Nallanathan, and G. K. Karagiannidis, "Towards optimally efficient tree search with deep learning," 2021, https://arxiv.org/abs/2101.02420.

[18] L. Chen, R. Zhao, K. He, Z. Zhao, and L. Fan, "Intelligent ubiquitous computing for future UAV-enabled MEC network systems," *Cluster Computing*, pp. 1–11, 2021.

[19] L. Chen and J. Xia, "Physical-layer security on mobile edge computing for emerging cyber physical systems," *Computer Communications*, vol. 99, pp. 1–12, 2022.

[20] X. Lai, "Outdated access point selection for mobile edge computing with cochannel interference," *IEEE Transaction on Vehicular Technology*, vol. 70, 2021.

[21] S. Tang, L. Chen, K. H. Xia, L. Fan, and A. Nallanathan, "Computational intelligence and deep learning for next-generation edge-enabled industrial IoT," 2021, https://arxiv.org/abs/2110.14937.

[22] S. Bayraklı and S. Z. Erdogan, "Genetic algorithm based energy efficient clusters (GABEEC) in wireless sensor networks," *Procedia Computer Science*, vol. 10, pp. 247–254, 2012.

[23] S. R. Nabavi, V. Ostovari Moghadam, M. Yahyaei Feriz Hendi, and A. Ghasemi, "Optimal selection of the cluster head in wireless sensor networks by combining the multiobjective genetic algorithm and the gravitational search algorithm," *Journal of Sensors*, vol. 2021, Article ID 2292580, 16 pages, 2021.

[24] S. Einy, C. Oz, and Y. D. Navaei, "Network intrusion detection system based on the combination of multiobjective particle swarm algorithm-based feature selection and fast-learning network," *Wireless Communications and Mobile Computing*, vol. 2021, Article ID 6648351, 12 pages, 2021.

[25] M. Azharuddin and P. K. Jana, "Particle swarm optimization for maximizing lifetime of wireless sensor networks," *Computers & Electrical Engineering*, vol. 51, pp. 26–42, 2016.

[26] B. Singh and D. K. Lobiyal, "A novel energy-aware cluster head selection based on particle swarm optimization for wireless sensor networks," *Human-centric Computing and Information Sciences*, vol. 2, no. 1, p. 13, 2012.

[27] S. Okdem, D. Karaboga, and C. Ozturk, "An application of wireless sensor network routing based on artificial bee colony algorithm," in *2011 IEEE Congress of Evolutionary Computation (CEC)*, New Orleans, LA, USA, 2011.

[28] Z. Peng, M. Rastgari, Y. D. Navaei et al., "TCDABCF: a trust-based community detection using artificial bee colony by feature fusion," *Mathematical Problems in Engineering*, vol. 2021, Article ID 6675759, 19 pages, 2021.

[29] S. Jamali and Y. D. Navaei, "A two-level product recommender for E-commerce sites by using sequential pattern analysis," *International Journal of Integrated Engineering*, vol. 8, no. 1, 2016.

[30] Y. D. Navaei and M. Afzali, "Dihedral product recommendation system for E-commerce using data mining applications," *International Journal of Computer & Information Technologies (IJOCIT)*, vol. 3, pp. 610–631, 2015.

[31] D. Karaboga, S. Okdem, and C. Ozturk, "Cluster based wireless sensor network routing using artificial bee colony algorithm," *Wireless Networks*, vol. 18, no. 7, pp. 847–860, 2012.

[32] X. Cai, Y. Duan, Y. He, J. Yang, and C. Li, "Bee-sensor-C: an energy-efficient and scalable multipath routing protocol for wireless sensor networks," *International Journal of Distributed Sensor Networks*, vol. 11, no. 3, Article ID 976127, 2015.

[33] Y. D. Navaei and M. Afzali, "A survey on product recommendation system in E-commerce," *International Journal of Computer & Information Technologies (IJOCIT)*, 2014.

[34] D. L. Zaheeruddin and A. Pathak, "Energy-aware bee colony approach to extend lifespan of wireless sensor network," *Engineering*, vol. 13, no. 1, pp. 29–46, 2017.

[35] A. Konak, D. W. Coit, and A. E. Smith, "Multi-objective optimization using genetic algorithms: a tutorial," *Reliability Engineering & System Safety*, vol. 91, no. 9, pp. 992–1007, 2006.

[36] P. Kuila and P. K. Jana, *Evolutionary computing approaches for clustering and routing in wireless sensor networks, in Sensor Technology: Concepts, Methodologies, Tools, and Applications*, IGI Global, 2020.

[37] I. Casas, J. Taheri, R. Ranjan, L. Wang, and A. Y. Zomaya, "GA-ETI: an enhanced genetic algorithm for the scheduling of scientific workflows in cloud environments," *Journal of computational science*, vol. 26, pp. 318–331, 2018.

[38] M. Mareli and B. Twala, "An adaptive Cuckoo search algorithm for optimisation," *Applied computing and informatics*, vol. 14, no. 2, pp. 107–115, 2018.

[39] S. E. Bouzid, Y. Seresstou, K. Raoof, M. N. Omri, M. Mbarki, and C. Dridi, "MOONGA: multi-objective optimization of wireless network approach based on genetic algorithm," *IEEE Access*, vol. 8, pp. 105793–105814, 2020.

[40] S. Patro and K. K. Sahu, "Normalization: a preprocessing stage," 2015, https://arxiv.org/abs/1503.06462.

[41] H. Ouchitachen, A. Hair, and N. Idrissi, "Improved multi-objective weighted clustering algorithm in wireless sensor network," *Egyptian Informatics Journal*, vol. 18, no. 1, pp. 45–54, 2017.

[42] P. S. Mann and S. Singh, "Improved artificial bee colony metaheuristic for energy-efficient clustering in wireless sensor networks," *Artificial Intelligence Review*, vol. 51, no. 3, pp. 329–354, 2019.

[43] Z. F. Ma and G. M. Li, "Improvement on LEACH-C protocol for wireless sensor network," *Artificial Intelligence Science and Technology: Proceedings of the 2016 International Conference (AIST2016)*, World Scientific, 2017.

Hindawi
Wireless Communications and Mobile Computing
Volume 2022, Article ID 8593474, 12 pages
https://doi.org/10.1155/2022/8593474

Research Article

Security Performance Analysis of Relay Networks Based on κ-μ Shadowed Channels with RHIs and CEEs

Jiangfeng Sun,[1] **Xiaohong Wang**,[2] **Yiwei Fang**,[3] **Xinji Tian**,[2] **Mingfu Zhu**,[1] **Jiangtao Ou**,[4] **and Chengyuan Fan**[4]

[1]*The College of Computer Science and Technology, Henan Polytechnic University, Jiaozuo 454003, China*
[2]*The College of Physics and Electronic Information Engineering, Henan Polytechnic University, Jiaozuo 454003, China*
[3]*Wuhan Maritime Communication Research Institute, Wuhan 430079, China*
[4]*AI Sensing Technology, Foshan 528000, China*

Correspondence should be addressed to Xiaohong Wang; wangxiaohonghpu@163.com

Received 13 January 2022; Revised 25 February 2022; Accepted 28 March 2022; Published 13 April 2022

Academic Editor: Zhao Junhui

This paper mainly describes the transmission reliability and physical layer security of multiantenna decode-and-forward relay networks over the κ-μ shadowed fading distribution. We consider the existence of residual hardware impairments (RHIs) and channel estimation errors (CEEs) at the same time. Firstly, we give the network model. On this basis, we analyze the reliability and security by deriving the exact expressions of outage probability (OP) and intercept probability (IP). To further verify and investigate the theoretical derivation, the approximate analysis of OP is obtained under the high signal-to-noise ratio. In addition, we also use an optimized antenna selection technology at the transmitter to improve the security performance. Finally, through the comparative study of theoretical simulation and Monte Carlo simulation results, the factors affecting network transmission and security are acquired. The interesting conclusion is that both RHIs and CEEs can increase OP and decrease IP; that is to say, the existence of RHIs and CEEs can reduce reliability and enhance security.

1. Introduction

With the widespread application of wireless communication technology, physical layer security (PLS) technology is highly concerned by scholars because it can take advantage of channel fading to improve antieavesdropping performance. The PLS was first proposed in [1]. Then, Yang et al. in [2] described that one of the dominating troubles faced by the 5G network is how to ensure the security of wireless data transmission. PLS have been generally studied in different system models, such as cooperative nonorthogonal multiple access (NOMA) systems [3], green communication systems based on relay selection [4], and multihop relay systems [5]. Moreover, Zhu and Yao in [6] also designed a cooperative beamforming scheme to enhance the PLS of cognitive radio networks. The authors of [7] investigated the reliability of quasistatic Rayleigh fading by deriving its outage probability (OP). The authors in [8] proposed a PLS project based on channel precompensation to improve the anti-interference of the polarization shift keying modulation system. Fan et al. in [9] used the relay selection to improve PLS when there are multiple users and multiple eavesdroppers.

In the actual communication process, interference from obstacles or other factors will be encountered inevitably, and the phenomenon that causes the power of the received signals to change with time and position is called channel fading. On account of the rapid development of communication networks, the researches on the transmission and security performances of various models under fading channels have been more and more favored by scholars. The authors in [10] studied the security of the fading channels when there was an eavesdropper in the system model. The authors of [11] explored the channel capacity of multiple-input

multiple-output (MIMO) systems under Rayleigh fading. Zhu et al. in [12] considered the full-duplex decode-and-forward (DF) system in the Rayleigh fading and gave the upper and lower bound expressions of its OP. New closed-form expressions of the strictly positive secrecy capacity (SPSC) and secure outage probability (SOP) over κ-μ fading channels were given in [13]. Badarneh et al. deduced the precise expression of the nth moment of the dual α-μ fading in [14]. And the performance was researched in terms of channel quality estimation index and average channel capacity (ACC). By deriving the precise expressions of average duration of fades (ADF) and probability density function (PDF) for dual Hoyt fading in [15], the authors investigated the statistical characteristics of the fading model of the narrow-band amplify and forward (AF) in this fading environment. In [16], the OP of double shadowed κ-μ fading was analyzed, and the effect of double shadowed on wireless fading channels was discussed. The authors of [17] derived the accurate expressions of PDF and cumulative distribution function (CDF) of amplitude and signal-to-noise ratio (SNR) of multicascade κ-μ fading channels and obtained the closed-form expressions of OP, average symbol error probability (ASEP), and ACC.

In wireless communication networks, cooperative relay technology can improve system reliability, energy efficiency, and system coverage, which has been studied extensively [18–24]. The authors in [18] researched the performance of the double-hop relay system. The application of a full-duplex AF relay system in vehicle-to-vehicle (V2V) was investigated in [19]. Majhi et al. of [20] deduced an accurate expression of the OP of orthogonal frequency division multiplexing (OFDM) relay system. The authors in [21] considered the selection of relay antenna in the V2V communication model using both physical-layer network coding and AF schemes in dual Nakagami-m channels. The OP of the two-way relay DF system under the packet fading channels was investigated in [22]. The authors in [23] studied the influence of the relay selection scheme and the number of relays on the outage performance of cognitive radio networks (CRN) by analyzing the OP. The authors of [24] analyzed the security of relay systems using AF under generalized-K fading.

Due to the time-varying characteristics of the communication state, radio frequency devices will be affected by many factors, such as phase noise and power amplifier nonlinearity. These irreparable hardware impairments (HIs) will distort the signals in transmission, so it is necessary to consider the HIs in a communication system. In addition to the above-mentioned HIs that will threaten the accurate transmission of the signal, the existence of CEEs is also one of the reasons for the mismatch between the expected signal and the actual transmission signal. To make the research more practical, many researchers have considered the influence of transceiver HIs and CEEs on the system during modeling and analysis [25–31], such as cognitive amplification and forwarding multirelay networks [25], beyond fifth-generation Internet of Things collaborative NOMA relay system [26], and ambient backscatter NOMA systems [27]. The authors of [28] described the performance of multiple relay systems when there were both transceiver HIs and CEEs. The authors in [29] studied the influence of RHIs and CEEs on cooperative NOMA systems by analyzing OP and the energy efficiency. The influences of the MIMO system with CEEs, RHIs, and imperfect successive interference cancellation effects on Nakagami-m fading were investigated in [30]. Li et al. of [31] researched the reliability and security performance of cooperative multirelay systems with RHIs and CEEs by deriving and analyzing the accurate expressions of OP and IP.

Through studying the existing fading channels, we found that the newly emerging κ-μ shadowed fading can characterize many fading channels by changing its parameters, such as Rice, Nakagami-m, Rayleigh, and κ-μ. The κ-μ shadowed fading was first proposed in [32]. Due to its composite characteristics, the channels can be applied to many scenarios. As shown in [33], a secure multicast scheme under κ-μ shadowed fading with multiple users and multiple eavesdroppers was studied. Sun et al. in [34] investigated the security performance of the single-input multiple-output relay communication architecture over the κ-μ shadowed distribution by deriving the precise and approximate expressions of SOP and SPSC. The closed-form expressions of the OP and the ASEP of the two-hop multiantenna wireless transmission system based on the AF relay node of the κ-μ shadowed fading system were deduced in [35]. Illi et al. in [36] researched the security of a dual-hop underwater communication system based on the κ-μ shadowed architecture. The authors in [37] studied the performance of the dual-hop autofocus communication network over the κ-μ shadowed fading.

References [10–17] mainly described the research of scholars on wireless fading channel in recent years, [18–24] were aimed at elaborating a widely used cooperative relay technology, [25–31] presented the performance of the system when scholars consider the existence of CEEs and HIs in different models in recent years, and [32–37] described the relevant researches on κ-μ shadowed fading channel in recent years. Synthesizing the above researches, to the author's knowledge, no scholars have studied the effects of RHIs and CEEs with DF under κ-μ shadowed fading. Therefore, we develop this work. First of all, we consider an eavesdropping model with DF relay and study the influence of CEEs and RHIs on the transmission performance and anti-interference ability of the network over κ-μ shadowed fading channels. In addition, to further verify and analyze the theoretical derivation, the high SNR approximate analysis of OP is obtained. Moreover, we also compared the ideal and non-ideal situations

The rest of this article is organized as follows. In Section 2, the statistical characteristics of the system model and the κ-μ shadowed fading are given, and the expressions of each parameter are analyzed when the RHIs and CEEs are considered simultaneously. In Section 3, the antenna selection scheme at the transmitter is given first; then, the precise expressions of OP and IP under ideal and nonideal situations are described. In Section 4, the approximate expressions of high SNR of OP under fixed value and varying function of channel estimation variance are derived. In Section 5, the numerical simulation results are discussed in detail. Section 6 summarizes the article, and the next section is the appendix.

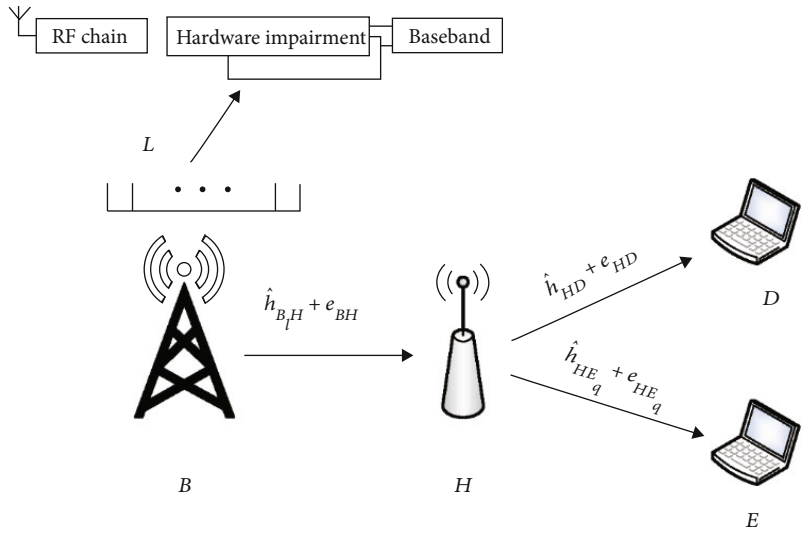

Figure 1: The system model.

2. System Model and Statistical Features

2.1. System Model. In Figure 1, we consider the classic Wyner wiretapping model. The model includes a transmitter (B), a relay (H), a receiver user (D), and an eavesdropper (E). The B is equipped with L antennas $\{B_1, B_1, \cdots, B_l, \cdots, B_L\}$, H and legitimate D have an antenna, and E has Q antennas $\{E_1, E_1, \cdots, E_q, \cdots, E_Q\}$. On account of the existence of the shadowed fading, all signals from the B can only be transmitted to H and cannot be directly sent to D or E. In addition, the information transmission mode at the relay is assumed to be DF.

As can be seen, the communication system of this model is divided into two time slots: (i) B sends the original signals to H; (ii) the H decodes the signals and forwards them to D. To improve the antieavesdropping ability, we have added artificial noise to the model. Since it is difficult to acquire the channel state information (CSI) of all nodes, the effective way to solve this problem is channel estimation which can be divided into three types, including reference signal-based estimation [38], blind estimation [39], and semiblind estimation [40]. The method used in this paper belongs to the first category that uses training sequences to estimate the CSI. According to the method in reference [41], the actual communication channel is expressed as

$$h_{XY} = \widehat{h}_{XY} + e_{XY}. \tag{1}$$

In (1), $XY \in \{B_lH; HD; HE_q\}$, $(1 \le l \le L, 1 \le q \le Q)$, h_{XY} is the channel coefficient, and $\widehat{h}_{XY}$ denotes the channel estimation of h_{XY}. $e_{XY} \sim CN(0, \sigma^2_{e_{XY}})$ represents the CEEs and $\sigma^2_{e_{XY}}$ denotes the estimated variance. We assume two typical conditions: (i) $\sigma^2_{e_{XY}} = M$, where M is a nonnegative value; (ii) $\sigma^2_{e_{XY}} = \Omega/(1 + \delta\rho\Omega)$, where $\Omega, \delta > 0$, and ρ represent the variance of the channel gain, the quality parameter of the CEEs, and the variance of the average SNR, respectively.

2.2. The First Transfer Process. During this course, the signals from B to H are represented as x_{B_lH}, and $E\{|x_{B_lH}|^2\} = 1$. We considered both RHIs and defective CSI, so the information at the H can be described as

$$y_{B_lH} = \left(\widehat{h}_{B_lH} + e_{B_lH}\right)\left(\sqrt{P_B}x_{B_lH} + \eta_{t,B_lH}\right) + \eta_{r,B_lH} + \nu_{B_lH}, \tag{2}$$

where $\widehat{h}_{B_lH}$ represents the channel from the antenna chosen by the B to H. The total transmit power is P, and τ is employed to represent the selected antenna power allocation factor, and $1 - \tau$ indicates the power allocation factor of the unchecked antenna. Here, we employ P_B to indicate the power of the B, then $P_B = \tau P$. x_{B_lH} is the valid signal from B to H, $E\{|x_{B_lH}|^2\} = 1$, and $\nu_{B_lH} \sim CN(0, \sigma^2_{B_lH})$ is the additive white Gaussian noise (AWGN). η_{t,B_lH} and η_{r,B_lH} are, respectively, expressed as the distortion noise caused by RHIs at the transmitting and the receiving terminal.

2.3. The Second Transfer Process. At H, the relay forwards the decoding of the signal to D and E. To improve the antieavesdropping ability, when H transmits information to D and E, the influence of artificial noise is also considered. In the actual communication system, due to the existence of CEEs at D, there will be some artificial noise and residual interference [42–44]. In summary, the information at D and E_q can be written as

$$y_{HD} = \left(\widehat{h}_{HD} + e_{HD}\right)\left(\sqrt{P_H}x_{HD} + \eta_{t,HD}\right) + \eta_{r,HD} + \nu_{HD}, \tag{3}$$

$$y_{HE_q} = \left(\widehat{h}_{HE_q} + e_{HE_q}\right)\left(\sqrt{P_H}x_{HE_q} + \eta_{t,HE_q}\right) + \eta_{r,HE_q} + \nu_{HE_q}, \tag{4}$$

where x_{HD} and x_{HE_q} represent the actual signals transmitted to D and E_q with $E\{|x_{HD}|^2\} = E\{|x_{HE_q}|^2\} = 1$. $x_{J_{HD}}$ and $x_{J_{HE_q}}$ are, respectively, denoted as the signals sent to D and E_q with artificial noise. And $E\{|x_{J_{HD}}|^2\} = E\{|x_{J_{HE_q}}|^2\} = 1$. $\xi_1 \in (0,1)$ and $\xi_2 \in (0,1)$ separately describe the factitious noise quantization coefficients at D and E_q. ν_{HD} and ν_{HE_q}, respectively, represent the composite AWGN with mean value 0 and variance σ^2_{HD} and $\sigma^2_{HE_q}$. P_S and P_J represent the transmit power of relay and factitious noise and $P_B = P_H = P_g$. $\eta_{t,HD}$ and $\eta_{r,HD}$ are, respectively, expressed as the distortion noise caused by RHIs during H to D communication. η_{t,HE_q} and η_{r,HE_q} are, respectively, expressed as the distortion noise caused by RHIs during H to E_q communication. As mentioned in [45], the distortion noise can be written as

$$\eta_t \sim CN\left(0, f_t^2 P_g\right), \eta_r \sim CN\left(0, f_r^2 P_g |h|^2\right). \tag{5}$$

The distortion noise was regarded as the product of η_t, η_r, and h. For an achievable channel h, the composite distortion power at the receiving terminal can be described as

$$E_{\eta_t,\eta_r}\left\{|h\eta_t + \eta_r|^2\right\} = P_g|h|^2\left(f_t^2 + f_r^2\right) = P_g\left|\widehat{h} + e\right|^2\left(f_t^2 + f_r^2\right). \tag{6}$$

From (6), we can get that power only rests with the p_g and the $|\widehat{h}_{XY}|^2$. Where $f_{XY} = \sqrt{f_{t,XY}^2 + f_{r,XY}^2}$, the messages at H, D, and E_q were described as

$$y_{B_lH} = \left(\widehat{h}_{B_lH} + e_{B_lH}\right)\left(\sqrt{P_B}x_{B_lH} + \eta_{B_lH}\right) + \nu_{B_lH}, \tag{7}$$

$$y_{HD} = \left(\widehat{h}_{HD} + e_{HD}\right)\left(\sqrt{P_H}x_{HD} + \sqrt{\xi_1 P_J}x_{J_{HD}} + \eta_{HD}\right) + \nu_{HD}, \tag{8}$$

$$y_{HE_q} = \left(\widehat{h}_{HE_q} + e_{HE_q}\right)\left(\sqrt{P_H}x_{HE_q} + \sqrt{\xi_2 P_J}x_{J_{HE_q}} + \eta_{HE_q}\right) + \nu_{HE_q}, \tag{9}$$

where the comprehensive distortion noises from RHIs at $B_l \longrightarrow H$, $H \longrightarrow D$, and $H \longrightarrow E_q$ are, respectively, expressed as $\eta_{B_lH} \sim CN(0, f^2_{B_lH}P_B)$, $\eta_{HD} \sim CN(0, f^2_{HD}P_H)$, and $\eta_{HE_q} \sim CN(0, f^2_{HE_q}P_H)$. Besides, $f_{B_lH} = \sqrt{f^2_{t,B_lH} + f^2_{r,B_lH}}$, $f_{HD} = \sqrt{f^2_{t,HD} + f^2_{r,HD}}$, and $f_{HE_q} = \sqrt{f^2_{t,HE_q} + f^2_{r,HE_q}}$.

The signal-to-interference-plus-noise ratios (SINRs) of $B_l \longrightarrow H$, $H \longrightarrow D$, and $H \longrightarrow E_q$ are given as

$$\gamma_{B_lH} = \frac{\rho_{B_lH}\left|\widehat{h}_{B_lH}\right|^2}{\rho_{B_lH}\left(\sigma^2_{e_{B_lH}} + \left|\widehat{h}_{B_lH}\right|^2 f^2_{B_lH} + \sigma^2_{e_{B_lH}} f^2_{B_lH}\right) + 1}, \tag{10}$$

$$\gamma_{HD} = \frac{\rho_{HD}\left|\widehat{h}_{HD}\right|^2}{\rho_{HD}\sigma^2_{e_{HD}} + \left(\xi_1 P_J/\sigma^2_{HD} + \rho_{HD}f^2_{HD}\right)\left(\left|\widehat{h}_{HD}\right|^2 + \sigma^2_{e_{HD}}\right) + 1}, \tag{11}$$

$$\gamma_{HE_q} = \frac{\rho_{HE_q}\left|\widehat{h}_{HE_q}\right|^2}{\rho_{HE_q}\sigma^2_{e_{HE_q}} + \left(\xi_2 P_J/\sigma^2_{HE_q} + \rho_{HE_q}f^2_{HE_q}\right)\left(\left|\widehat{h}_{HE_q}\right|^2 + \sigma^2_{e_{HE_q}}\right) + 1}, \tag{12}$$

where $\rho_{B_lH} = P_B/\sigma^2_{B_lH}$, $\rho_{HD} = P_H/\sigma^2_{HD}$, and $\rho_{HE_q} = P_H/\sigma^2_{HE_q}$.

2.4. Statistical Features. In the model, we consider the widely applied κ-μ shadowed fading, and the PDF of the channel gain has been given in [46] as

$$\begin{aligned} f_{|\widehat{h}_{XY}|^2}(x) = {} & \frac{{m_{XY}}^{m_{XY}}(1+\kappa_{XY})^{\mu_{XY}}{\mu_{XY}}^{\mu_{XY}}}{\Gamma(\mu_{XY})(m_{XY}+\kappa_{XY}\mu_{XY})^{m_{XY}}\psi_{XY}} \\ & \cdot \exp\left(-\frac{x(1+\kappa_{XY})\mu_{XY}}{\psi_{XY}}\right) \times \left(\frac{x}{\psi_{XY}}\right)^{\mu_{XY}-1} {}_1F_1 \\ & \cdot \left(m_{XY}; \mu_{XY}; \frac{\mu^2_{XY}\kappa_{XY}(1+\kappa_{XY})x}{\psi_{XY}(m_{XY}+\kappa_{XY}\mu_{XY})}\right). \end{aligned} \tag{13}$$

After some mathematical operations, the CDF expression of the channel gain can be obtained as

$$\begin{aligned} F_{|\widehat{h}_{XY}|^2}(x) = {} & \left(\frac{m_{XY}+\kappa_{XY}\mu_{XY}}{m_{XY}}\right)^{-m_{XY}} \frac{1}{\Gamma(\mu_{XY})}\sum_{i=1}^{\infty}\frac{(m_{XY})_i}{(\mu_{XY})_i i!} \\ & \cdot \left(\frac{m_{XY}\kappa_{XY}\mu_{XY}}{(m_{XY}+\kappa_{XY}\mu_{XY})m_{XY}}\right)^i \times (\mu_{XY}+i-1)! \\ & \cdot \left\{1 - \sum_{s=0}^{\mu_{XY}+i-1}\frac{x^s}{s!}\left[\frac{(1+\kappa_{XY})\mu_{XY}}{\psi_{XY}}\right]^s \right. \\ & \left. \cdot \exp\left(-\frac{(1+\kappa_{XY})\mu_{XY}}{\psi_{XY}}x\right)\right\}. \end{aligned} \tag{14}$$

The meanings of κ, m, and μ in (13) and (14) are all channel parameters, where m is the shaping parameter of Nakagami-m fading, and $\mu > 0$ is related to the number of received signal groups. $\kappa = d^2/2\mu\sigma^2$ is a positive number, d^2 represents the total power of the dominating constituent, and $2\mu\sigma^2$ is the total power of the scattered wave. $\psi = E\{|\widehat{h}_{XY}|^2\}$, and $|\widehat{h}_{XY}|$ indicates the amplitude of the channel. The capacity formula of the Shannon theorem is defined as

$$C = \frac{1}{2}\log_2\{1+\gamma\}. \tag{15}$$

According to (10) and (11), we can get the expression of the instantaneous channel capacity of $B \longrightarrow H$ and $H \longrightarrow D$

as

$$C_{BH} = \frac{1}{2}\log_2\left\{1 + \frac{\rho_{BH}\left|\widehat{h}_{BH}\right|^2}{\rho_{BH}\left(\sigma^2_{e_{BH}} + \left|\widehat{h}_{BH}\right|^2 f^2_{BH} + \sigma^2_{e_{BH}} f^2_{BH}\right) + 1}\right\}, \tag{16}$$

$$C_{HD} = \frac{1}{2}\log_2\left\{1 + \frac{\rho_{HD}\left|\widehat{h}_{HD}\right|^2}{\rho_{HD}\sigma^2_{e_{HD}} + \left(\xi_1 P_J/\sigma^2_{HD} + \rho_{HD} f^2_{HD}\right)\left(\left|\widehat{h}_{HD}\right|^2 + \sigma^2_{e_{HD}}\right) + 1}\right\}. \tag{17}$$

The eavesdropper employs multiple relay combining (MRC) algorithm to intercept legal information; the SINR at $H \longrightarrow E$ is

$$\gamma_{HE} = \sum_{q=1}^{Q} \gamma_{HE_q}. \tag{18}$$

The SINR of $H \longrightarrow E$ is expressed as

$$\gamma_{HE} = Q\gamma_{HE_q}. \tag{19}$$

So we can get the instantaneous capacity of $H \longrightarrow E$ as

$$C_{HE} = \frac{1}{2}\log_2\left\{1 + \frac{Q\rho_{HE_q}\left|\widehat{h}_{HE_q}\right|^2}{\rho_{HE_q}\sigma^2_{e_{HE_q}} + \left(\xi_2 P_J/\sigma^2_{HE_q} + \rho_{HE_q} f^2_{HE_q}\right)\left(\left|\widehat{h}_{HE_q}\right|^2 + \sigma^2_{e_{HE_q}}\right) + 1}\right\}. \tag{20}$$

3. Performance Analysis of Outage Probability (OP) and Intercept Probability (IP)

To improve the performance of the communication systems, we use the optimal transmit antenna selection (OTAS) strategy at the transmitter with multiple antennas and deduce the precise expressions of OP and IP to analyze its reliability and security.

3.1. OP Analysis. In this section, we discuss the transmission performance of multiantenna cooperative communication systems in the existence of RHIs and CEEs from the perspective of OP.

3.2. Outage Probability. The OP of the system model can be indicated as

$$P_{\text{out}} = \Pr\{C_{XY} < R_s\}, \tag{21}$$

where the target threshold is R_s.

Under the premise of CEEs and RHIs, using the OTAS protocol, the channel gain containing the estimation error can be obtained as

$$\left|\widehat{h}_{BH}\right| = \max_{1\le l\le L}\left\{\widehat{h}_{B_l H}\right\}. \tag{22}$$

The CDF of the channel gain during $B_l \longrightarrow H$ transmission is written as

$$\begin{aligned} F_{\left|\widehat{h}_{XY}\right|^2}(x) = \Bigg\{ & \left(\frac{m_{XY} + \kappa_{XY}\mu_{XY}}{m_{XY}}\right)^{-m_{XY}} \frac{1}{\Gamma(\mu_{XY})}\sum_{i=1}^{\infty}\frac{(m_{XY})_i}{(\mu_{XY})_i i!} \\ & \times (\mu_{XY} + i - 1)! \times \left(\frac{m_{XY}\kappa_{XY}\mu_{XY}}{(m_{XY} + \kappa_{XY}\mu_{XY})m_{XY}}\right)^i \\ & \cdot \left\{1 - \sum_{s=0}^{\mu_{XY}+i-1}\frac{x^s}{s!}\left[\frac{(1+\kappa_{XY})\mu_{XY}}{\psi_{XY}}\right]^s \right. \\ & \left. \cdot \exp\left(-\frac{(1+\kappa_{XY})\mu_{XY}}{\psi_{XY}}x\right)\right\}\Bigg\}^L. \end{aligned} \tag{23}$$

With the DF algorithm, the channel capacity in the information transmission of $B_l \longrightarrow H$ and $H \longrightarrow D$ is expressed as

$$C_H = \min\left(C_{BH}, C_{HD}\right). \tag{24}$$

Through the above analysis, in the following theorem, we will research the exact expression of the OP of the κ-μ shadowed fading with RHIs and CEEs.

Theorem 1. *For κ-μ shadowed fading, the accurate expressions of OP for two scenes are expressed as follows:*

(1) Nonideal condition (with RHIs and CEEs)

$$P^{ni}_{out} = I_1 + I_2 - I_1 I_2. \tag{25}$$

To ensure that OP is not zero, we set $1 - \Theta f^2_{BH} > 0$ and $\rho_{HD} - \Theta(\xi_1 P_J/\sigma^2_{HD} + f^2_{HD}\rho_{HD}) > 0$. I_1 and I_2 correspond to equations (35) and (36) in the appendix, respectively.

(2) Ideal condition ($f_{BH} = f_{HD} = 0$ and $\sigma^2_{e_{BH}} = \kappa^2_{e_{HD}} = 0$)

$$\begin{aligned} P^{id}_{out} = \Bigg\{ & \left(\frac{m_{BH} + \kappa_{BH}\mu_{BH}}{m_{BH}}\right)^{-m_{BH}} \frac{1}{\Gamma(\mu_{BH})}\sum_{i=1}^{\infty}\frac{(m_{BH})_i}{(\mu_{BH})_i i!} \\ & \cdot (\mu_{BH} + i - 1)!\left(\frac{m_{BH}\kappa_{BH}\mu_{BH}}{(m_{BH} + \kappa_{BH}\mu_{BH})m_{BH}}\right)^i \times \left\{1 - \sum_{s=0}^{\mu_{BH}+i-1}\frac{\varphi_3^s}{s!}\left[\frac{(1+\kappa_{BH})\mu_{BH}}{\psi_{BH}}\right]^s \right. \\ & \left. \cdot \exp\left(-\frac{(1+\kappa_{BH})\mu_{BH}}{\psi_{BH}}\varphi_3\right)\right\}\Bigg\}^L + \Bigg\{\left(\frac{m_{HD} + \kappa_{HD}\mu_{HD}}{m_{HD}}\right)^{-m_{HD}} \\ & \cdot \frac{1}{\Gamma(\mu_{HD})}\sum_{i=1}^{\infty}\frac{(m_{HD})_i}{(\mu_{HD})_i i!}(\mu_{HD} + i - 1)!\left(\frac{m_{HD}\kappa_{HD}\mu_{HD}}{(m_{HD} + \kappa_{HD}\mu_{HD})m_{HD}}\right)^i \\ & \times \left\{1 - \sum_{s=0}^{\mu_{HD}+i-1}\frac{\varphi_4^s}{s!}\left[\frac{(1+\kappa_{HD})\mu_{HD}}{\psi_{HD}}\right]^s \exp\left(-\frac{(1+\kappa_{HD})\mu_{HD}}{\psi_{HD}}\varphi_4\right)\right\}\Bigg\} \\ & - \Bigg\{\left(\frac{m_{BH} + \kappa_{BH}\mu_{BH}}{m_{BH}}\right)^{-m_{BH}} \frac{1}{\Gamma(\mu_{BH})}\sum_{i=1}^{\infty}\frac{(m_{BH})_i}{(\mu_{BH})_i i!}(\mu_{BH} + i - 1)! \\ & \cdot \left(\frac{m_{BH}\kappa_{BH}\mu_{BH}}{(m_{BH} + \kappa_{BH}\mu_{BH})m_{BH}}\right)^i \times \left\{1 - \sum_{s=0}^{\mu_{BH}+i-1}\frac{\varphi_3^s}{s!}\left[\frac{(1+\kappa_{BH})\mu_{BH}}{\psi_{BH}}\right]^s \right. \\ & \left. \cdot \exp\left(-\frac{(1+\kappa_{BH})\mu_{BH}}{\psi_{BH}}\varphi_3\right)\right\}^L \times \left\{\left(\frac{m_{HD} + \kappa_{HD}\mu_{HD}}{m_{HD}}\right)^{-m_{HD}} \right. \\ & \cdot \frac{1}{\Gamma(\mu_{HD})}\sum_{i=1}^{\infty}\frac{(m_{HD})_i}{(\mu_{HD})_i i!}(\mu_{HD} + i - 1)!\left(\frac{m_{HD}\kappa_{HD}\mu_{HD}}{(m_{HD} + \kappa_{HD}\mu_{HD})m_{HD}}\right)^i \\ & \left. \times \left\{1 - \sum_{s=0}^{\mu_{HD}+i-1}\frac{\varphi_4^s}{s!}\left[\frac{(1+\kappa_{HD})\mu_{HD}}{\psi_{HD}}\right]^s \exp\left(-\frac{(1+\kappa_{HD})\mu_{HD}}{\psi_{HD}}\varphi_4\right)\right\}\right\}, \end{aligned} \tag{26}$$

where $\varphi_3 = \Theta/\rho_{BH}$ and $\varphi_4 = \Theta/(\rho_{BH} - \Theta\xi_1 P_J/\sigma^2_{HD})$.

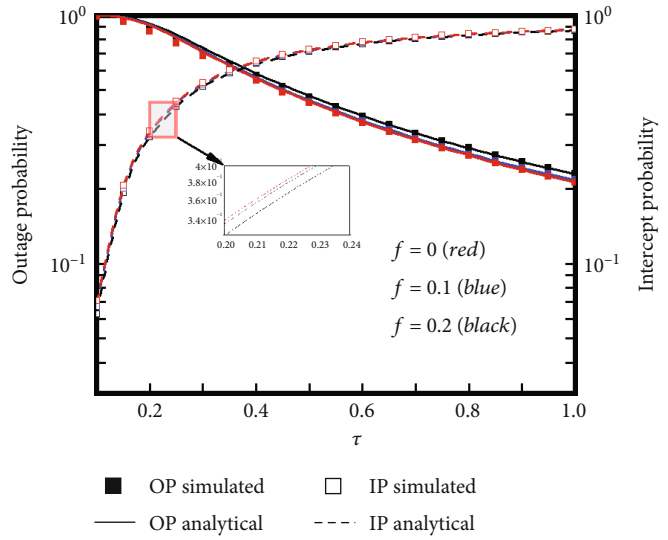

FIGURE 2: OP and IP versus τ for different f ($\{\xi_1, \xi_2\} = \{0.05, 0.95\}$, $P = 5$ dB, $\sigma_e^2 = 0.1$, $\kappa = 1$, $m = 2$, $\mu = 2$, $L = 2$, and $Q = 2$).

Proof. See Appendix A. □

3.3. IP Analysis. IP means the probability that the capacity of the eavesdropping channel is greater than R_S, which is written as

$$P_{\text{int}} = \Pr\{C_{HE} > R_s\}. \tag{27}$$

For the precise expressions of IP under the κ-μ shadowed fading, the two scenes will be given below.

3.4. Nonideal Condition. Substituting (20) into (27), we obtain

$$P_{\text{int},i.i.d}^{\text{ni}} = \Pr\left\{\frac{Q\rho_{HE_q}\left|\widehat{h}_{HE_q}\right|^2}{\rho_{HE_q}\sigma_{e_{HE_q}}^2 + \left(\xi_2 P_J/\sigma_{HE_q}^2 + \rho_{HE_q} f_{HE_q}^2\right)\left(\left|\widehat{h}_{HE_q}\right|^2 + \sigma_{e_{HE_q}}^2\right) + 1} > \Theta\right\} = 1 - F_{\left|\widehat{h}_{HE_q}\right|^2}(\varphi_5). \tag{28}$$

where $\varphi_5 = (\Xi[\sigma_{e_{HE_q}}^2(\rho_{HE_q} + \xi_2 P_J/\sigma_{HE_q}^2 + \rho_{HE_q} f_{HE_q}^2) + 1])/(\rho_{HE_q} - \Xi(\xi_2 P_J/\sigma_{HE_q}^2 + \rho_{HE_q} f_{HE_q}^2))$, $\Theta = 2^{2R_S} - 1$, and $\Xi = \Theta/Q$. Substituting (14) into (28), we can get the exact expression of OP as

$$P_{\text{int},i.i.d}^{\text{ni}} = 1 - \left(\frac{m_{HE_q} + \kappa_{HE_q}\mu_{HE_q}}{m_{HE_q}}\right)^{-m_{HE_q}} \frac{1}{\Gamma\left(\mu_{HE_q}\right)} \sum_{i=1}^{\infty} \frac{\left(m_{HE_q}\right)_i}{\left(\mu_{HE_q}\right)_i i!} \cdot \left(\frac{m_{HE_q}\kappa_{HE_q}\mu_{HE_q}}{\left(m_{HE_q} + \kappa_{HE_q}\mu_{HE_q}\right)m_{HE_q}}\right)^i \times \left(\mu_{HE_q} + i - 1\right)! \cdot \left\{1 - \sum_{s=0}^{\mu_{HE_q}+i-1} \frac{\varphi_5^s}{s!}\left[\frac{\left(1+\kappa_{HE_q}\right)\mu_{HE_q}}{\psi_{HE_q}}\right]^s \exp\left(-\frac{\left(1+\kappa_{HE_q}\right)\mu_{HE_q}}{\psi_{HE_q}}\varphi_5\right)\right\}. \tag{29}$$

where $\Xi < (\rho_{HE_q}\sigma_{HE_q}^2)/\xi_2 P_J$.

3.5. Ideal Condition. Similar to the derivation of (29), we obtain

$$P_{\text{int}}^{id} = 1 - \left(\frac{m_{HE_q} + \kappa_{HE_q}\mu_{HE_q}}{m_{HE_q}}\right)^{-m_{HE_q}} \frac{1}{\Gamma\left(\mu_{HE_q}\right)} \sum_{i=1}^{\infty} \frac{\left(m_{HE_q}\right)_i}{\left(\mu_{HE_q}\right)_i i!} \cdot \left(\frac{m_{HE_q}\kappa_{HE_q}\mu_{HE_q}}{\left(m_{HE_q} + \kappa_{HE_q}\mu_{HE_q}\right)m_{HE_q}}\right)^i \times \left(\mu_{HE_q} + i - 1\right)! \cdot \left\{1 - \sum_{s=0}^{\mu_{HE_q}+i-1} \frac{\varphi_6^s}{s!}\left[\frac{\left(1+\kappa_{HE_q}\right)\mu_{HE_q}}{\psi_{HE_q}}\right]^s \exp\left(-\frac{\left(1+\kappa_{HE_q}\right)\mu_{HE_q}}{\psi_{HE_q}}\varphi_6\right)\right\}, \tag{30}$$

where $\varphi_6 = \Xi/(\rho_{HE_q} - \Xi\xi_2 P_J/\sigma_{HE_q}^2)$, $\Theta = 2^{2R_S} - 1$, and $\Xi = \Theta/Q$ and we set $\Xi < (\rho_{HE_q}\sigma_{HE_q}^2)/\xi_2 P_J$.

4. Asymptotic Analysis

To further verify and investigate the theoretical derivation, we give the asymptotic analysis of the high SNR approximation of OP. It can be divided into the following two conditions: nonideal case and ideal case.

Theorem 2. *The precise expressions of the asymptotic analysis of the high SNR approximation of OP are as follows:*

(1) Nonideal case

When $\sigma_{e_{XY}}^2 = \Omega/(1 + \delta\rho\Omega)$, equation (42) can be obtained from Appendix B. When $\sigma_{e_{XY}}^2 = a$,

$$P_{out}^{\infty,ni2} = I_5 + I_6 - I_5 I_6, \tag{31}$$

where a is a constant, $1 - \Theta f_{BH}^2 > 0$, and $1 - \Theta\xi_1/2 - \Theta f_{HD}^2 > 0$.

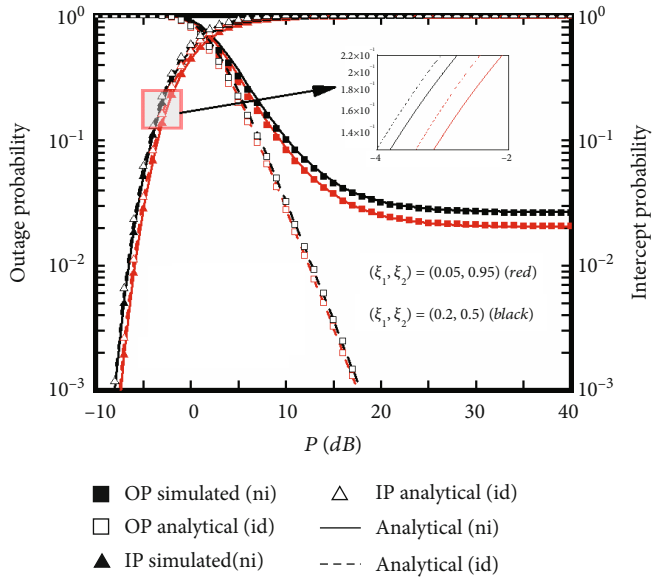

FIGURE 3: OP and IP versus P for different $\{\xi_1, \xi_2\}$ ($L = 2$, $\kappa = 1$, $m = 2$, $\mu = 2$, $\tau = 0.8$, and $Q = 2$).

(2) Ideal case

$$P_{out}^{\infty,id} = I_7 + I_8 - I_7 I_8. \tag{32}$$

Proof. See Appendix B. □

5. Numerical Analysis

In this section, we exhibit the comparison charts between theoretical derivations and Monte Carlo simulations in Figures 2–7. As can be seen from the graphs, the numerical results coincide well with the simulation, which confirms the validity of the deduced results. In the simulation, our parameters are set as follows: $\kappa_{XY} = \kappa$, $m_{XY} = m$, $\mu_{XY} = \mu$, $R_s = 0.5$, $P_B = P_H = P_g$, $P_J = P_B/2$, $\sigma^2_{e_{XY}} = \sigma_e^2$, $\sigma^2_{XY} = 1$, and $\psi_{XY} = 1$. It should be noted that although the theoretical formulas of IP and op contain infinite series, it will not affect the simulation results, because the theoretical formulas will converge when the number of cycles is greater than 45.

Figure 2 describes the variation of OP and IP with the power distribution factor τ and distortion noise f. It can be concluded that as τ increases, OP gradually becomes smaller, while IP continues to rise. And the increase of the distortion noise parameter will reduce the reliability and improve the antieavesdropping ability.

Figure 3 illustrates the changes of OP and IP with transmit power under different artificial quantization coefficients. Both ideal situations ($\sigma_e^2 = 0$, $f = 0$) and nonideal situations ($\sigma_e^2 = 0.1$, $f = 0.1$) are considered. It can be seen that as ξ_1 augments, OP gradually aggrandizes, and the reliability of the system decreases. And due to distortion, the value of OP under ideal conditions is always lower than that with RHIs. In addition, increasing the value of ξ_2 will raise the IP, which means that the security of the channel will be reduced.

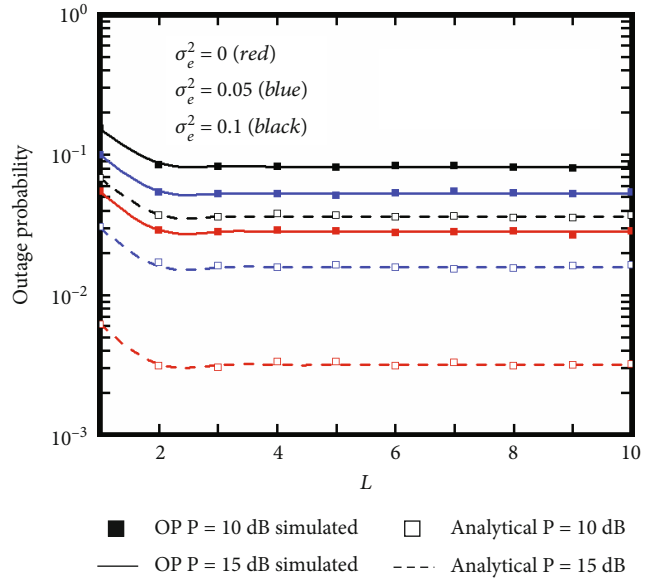

FIGURE 4: OP and IP versus L for different σ_e^2 and P ($\{\xi_1, \xi_2\} = \{0.05, 0.95\}$, $f = 0.1$, $\kappa = 1$, $m = 2$, $\mu = 2$, and $\tau = 0.8$).

Figure 4 plots the impact of different antenna numbers L and CEEs on OP. We clearly find that the increase of transmission power can enhance the transmission performance, while the augment of CEEs will impair the reliability. When the number of antennas is less than 4 dB, the OP decreases as the number of antennas adds. When L is greater than 4 dB, the OP changes less, which shows that the application of OTAS to improve the reliability of the system is more suitable when the number of antennas is small.

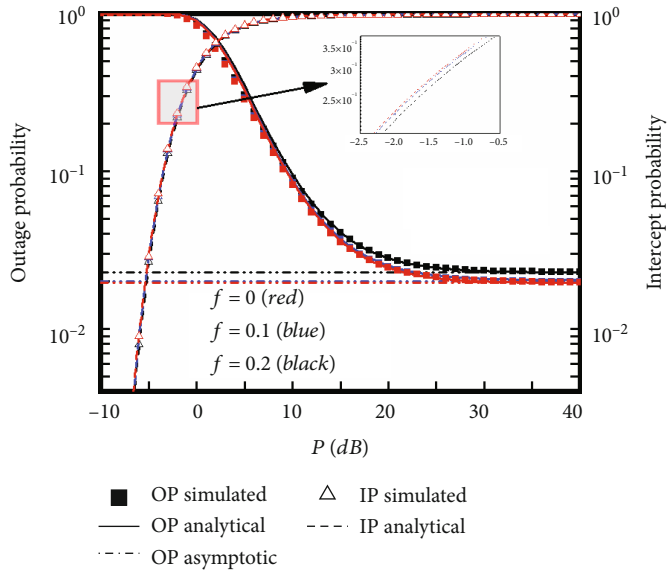

FIGURE 5: OP and IP versus P for different f ($\{\xi_1, \xi_2\} = \{0.05, 0.95\}$, $\tau = 0.8$, $\sigma_e^2 = 0.1$, $f = \{0, 0.1, 0.2\}$, $\kappa = 1$, $m = 2$, $\mu = 2$, $L = 2$, and $Q = 2$).

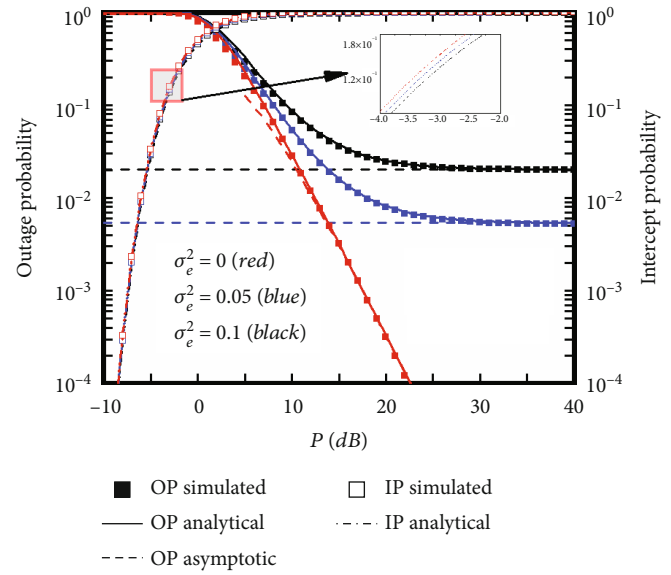

FIGURE 6: OP and IP versus P for different σ_e^2 ($\{\xi_1, \xi_2\} = \{0.05, 0.95\}$, $\tau = 0.8$, $L = 2$, $\kappa = 1$, $m = 2$, $\mu = 2$, $Q = 2$, and $f = 0.1$).

Figure 5 presents the variation of OP and IP with transmission power when RHIs and CEEs exist at the same time. The figure shows that with the increases of f, OP increases while IP decreases. The results illustrate that RHIs are detrimental to the reliability of the system. And OP has an error floor under nonideal conditions. In addition, there is an optimal transmission power, which can balance the security and reliability in the communication process.

Figure 6 illustrates the change of OP and IP with the transmit power under different CEE conditions. The approximate curves in Figure 6 are drawn based on (31) and (32). We can see that in nonideal situations, with the increase of σ_e^2, the reliability of the channel decreases and there exists an error floor. And the value of OP under the nonideal case is always greater than under the ideal case. In addition, compared with OP, CEEs have less impact on IP. This manifests that CEEs play an important role in the reliability but has little impact on the security.

Figure 7 plots the variation of OP under the conditions of different antenna numbers L and parameters μ. In this simulation, we set an ideal case ($\sigma_e^2 = 0$, $f = 0$) and a nonideal case ($\sigma_e^2 = 0.1$, $f = 0.1$). It can be concluded that due to the existence of fixed CEEs, there exists an error floor independent of transmission power under nonideal condition. And because of the existence of CEEs and RHIs, the nonideal situation of OP has been worse than the ideal situation. At the same time, we can see that the augment of L and μ can make the system more reliable.

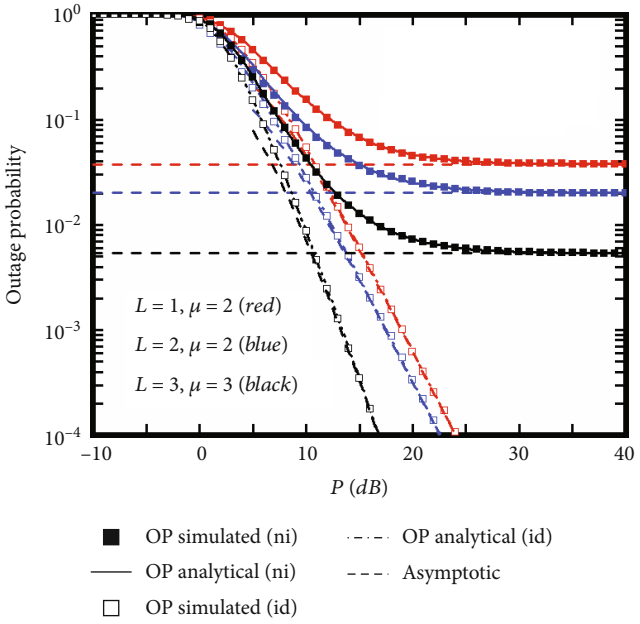

FIGURE 7: OP versus P for different L and μ ($\{\xi_1, \xi_2\} = \{0.05, 0.95\}$, $\tau = 0.8$, $\kappa = 1$, $m = 2$, $L = \{1, 2\}$, and $\mu = \{2, 3\}$).

6. Conclusion

This paper mainly studies the influence over the κ-μ shadowed fading when RHIs and CEEs exist simultaneously. Meanwhile, we used the multiantenna selection scheme on the transmitting terminal and discussed the multiantenna receiving technology on the eavesdropping transmitting terminal. In addition, we employed the DF method to transmit the destination signal and then verified the correctness of the derivation through simulation We discover that large f, large ξ, large σ_e^2, and small L can reduce the reliability. In addition, small ξ, large f, and large σ_e^2 can improve the anti-eavesdropping ability on the κ-μ shadowed network. Finally, it is concluded that RHIs and CEEs can reduce the reliability and enhance its security, because RHIs and CEEs often appear in the practical communication network. It is very meaningful to do performance analysis on this premise. As an extension of this work, we will study the scenario of multiple base stations and multiple receivers with different relay protocols.

Appendix

A. The Proof of Theorem 1

Combining (21) and (24), the expression of OP can be obtained as

$$\begin{aligned} P_{\text{out}} &= \Pr\left\{\min\left(C_{BH,}C_{HD}\right) < R_S\right\} = 1 - \Pr\left\{\min\left(C_{BH,}C_{HD}\right) > R_S\right\} \\ &= \Pr\left\{C_{BH} < R_S\right\} + \Pr\left\{C_{HD} < R_S\right\} \\ &\quad - \Pr\left\{C_{BH} < R_S\right\} \Pr\left\{C_{HD} < R_S\right\} = I_1 + I_2 - I_1 I_2. \end{aligned} \tag{33}$$

In the following process of solving the closed-form expressions of I_1 and I_2, we set $\Theta = 2^{2R_S} - 1$. Then, we substitute (16) into (33) and obtain

$$\begin{aligned} I_1 &= \Pr\left\{\frac{1}{2}\log_2\left(1 + \frac{\rho_{BH}\left|\widehat{h}_{BH}\right|^2}{\rho_{BH}\left(\sigma_{e_{BH}}^2 + \left|\widehat{h}_{BH}\right|^2 f_{BH}^2 + \sigma_{e_{BH}}^2 f_{BH}^2\right) + 1}\right) < R_S\right\} \\ &= \Pr\left\{\left|\widehat{h}_{BH}\right|^2 < \frac{\Theta\rho_{BH}\sigma_{e_{BH}}^2\left(1 + f_{BH}^2\right) + \Theta}{\rho_{BH}\left(1 - \Theta f_{BH}^2\right)}\right\}, \end{aligned} \tag{34}$$

where we set $\varphi_1 = (\Theta\rho_{BH}\sigma_{e_{BH}}^2(1 + f_{BH}^2) + \Theta)/(\rho_{BH}(1 - \Theta f_{BH}^2))$. Finally, substituting (23) into (34), we get the exact expression of I_1 as

$$\begin{aligned} I_1 = \Pr\left\{\left|\widehat{h}_{BH}\right|^2 < \varphi_1\right\} &= \left\{\left(\frac{m_{BH} + \kappa_{BH}\mu_{BH}}{m_{BH}}\right)^{-m_{BH}} \frac{1}{\Gamma(\mu_{BH})}\right. \\ &\cdot \sum_{i=1}^{\infty} \frac{(m_{BH})_i}{(\mu_{BH})_i i!}\left(\frac{m_{BH}\kappa_{BH}\mu_{BH}}{(m_{BH} + \kappa_{BH}\mu_{BH})m_{BH}}\right)^i \times (\mu_{BH} + i - 1)! \\ &\left.\cdot \left\{1 - \sum_{s=0}^{\mu_{BH}+i-1} \frac{\varphi_1^s}{s!}\left[\frac{(1 + \kappa_{BH})\mu_{BH}}{\psi_{BH}}\right]^s \exp\left(-\frac{(1 + \kappa_{BH})\mu_{BH}}{\psi_{BH}}\varphi_1\right)\right\}\right\}^L. \end{aligned} \tag{35}$$

Similar to the method of solving I_1, we substitute (24) into (33) to gain formula (36), and then, we combine (14) and (36) to get the exact expression of I_2 as

$$\begin{aligned} I_2 &= \Pr\left\{\frac{\rho_{HD}\left|\widehat{h}_{HD}\right|^2}{\rho_{HD}\sigma_{e_{HD}}^2 + \left(\xi_1 P_J/\sigma_{HD}^2 + \rho_{HD} f_{HD}^2\right)\left(\left|\widehat{h}_{HD}\right|^2 + \sigma_{e_{HD}}^2\right) + 1} < \Theta\right\} \\ &= \Pr\left\{\left|\widehat{h}_{HD}\right|^2 < \frac{\Theta\left[\sigma_{e_{HD}}^2\left(\rho_{HD} + \xi_1 P_J/\sigma_{HD}^2 + \rho_{HD} f_{HD}^2\right) + 1\right]}{\rho_{HD} - \Theta\left(\xi_1 P_J/\sigma_{HD}^2 + \rho_{HD} f_{HD}^2\right)}\right\}, \end{aligned} \tag{36}$$

where we set $\varphi_2 = (\Theta[\sigma_{e_{HD}}^2(\rho_{HD} + \xi_1 P_J/\sigma_{HD}^2 + \rho_{HD} f_{HD}^2) + 1])/(\rho_{HD} - \Theta(\xi_1 P_J/\sigma_{HD}^2 + \rho_{HD} f_{HD}^2))$. After further simplification, I_2 can be expressed as

$$\begin{aligned} I_2 = \Pr\left\{\left|\widehat{h}_{HD}\right|^2 < \varphi_2\right\} &= F_{\left|\widehat{h}_{HD}\right|^2}(\varphi_2) \\ &= \left\{\left(\frac{m_{HD} + \kappa_{HD}\mu_{HD}}{m_{HD}}\right)^{-m_{HD}} \frac{1}{\Gamma(\mu_{HD})} \sum_{i=1}^{\infty} \frac{(m_{HD})_i}{(\mu_{HD})_i i!}\right. \\ &\cdot \left(\frac{m_{HD}\kappa_{HD}\mu_{HD}}{(m_{HD} + \kappa_{HD}\mu_{HD})m_{HD}}\right)^i \times (\mu_{HD} + i - 1)! \\ &\left.\cdot \left\{1 - \sum_{s=0}^{\mu_{HD}+i-1} \frac{\varphi_2^s}{s!}\left[\frac{(1 + \kappa_{HD})\mu_{HD}}{\psi_{HD}}\right]^s \exp\left(-\frac{(1 + \kappa_{HD})\mu_{HD}}{\psi_{HD}}\varphi_2\right)\right\}\right\}. \end{aligned} \tag{37}$$

Substitute the obtained I_1 and I_2 into (33), and finally, acquire (25). Moreover, we can obtain the ideal expression of OP in (26) by setting $f_{BH} = f_{HD} = 0$ and $\sigma_{e_{BH}}^2 = \kappa_{e_{HD}}^2 = 0$.

B. The Proof of Theorem 2

B.1. Nonideal Situation

(1) When $\sigma_{e_{XY}}^2 = \Omega/(1+\delta\rho\Omega)$

When seeking the approximation of high SNR, we can employ a similar method to [47] to obtain the following expression for the CDF of the channel gain of the κ-μ shadowed fading as

$$F_{|\hat{h}_{XY}|^2}(x) = \left(\frac{m_{XY}+\kappa_{XY}\mu_{XY}}{m_{XY}}\right)^{-m_{XY}} \frac{1}{\Gamma(\mu_{XY})} \sum_{i=1}^{\infty} \frac{(m_{XY})_i}{(\mu_{XY})_i i!} \cdot \left(\frac{m_{XY}\kappa_{XY}\mu_{XY}}{(m_{XY}+\kappa_{XY}\mu_{XY})m_{XY}}\right)^{i} \times \frac{1}{(\mu_{XY}+i)} \cdot \left(\frac{(1+\kappa_{XY})\mu_{XY}}{\psi_{XY}}x\right)^{\mu_{XY}+i} \exp\left(-\frac{(1+\kappa_{XY})\mu_{XY}}{\psi_{XY}}x\right). \tag{38}$$

According to (38), we can get the approximate expression (39) of the CDF as

$$F_{|\hat{h}_{BH}|^2}^{\infty,\mathrm{ni}}(x) = \left\{\left(\frac{m_{BH}+\kappa_{BH}\mu_{BH}}{m_{BH}}\right)^{-m_{BH}} \frac{1}{\Gamma(\mu_{BH})} \cdot \sum_{i=1}^{\infty}\left(\frac{m_{BH}\kappa_{BH}\mu_{BH}}{(m_{BH}+\kappa_{BH}\mu_{BH})m_{BH}}\right)^{i} \times \frac{1}{(\mu_{BH}+i)}\frac{(m_{BH})_i}{(\mu_{BH})_i i!} \cdot \left(\frac{(1+\kappa_{BH})\mu_{BH}}{\psi_{BH}}x\right)^{\mu_{BH}+i} \exp\left(-\frac{(1+\kappa_{BH})\mu_{BH}}{\psi_{BH}}x\right)\right\}^{L}. \tag{39}$$

Similar to the method in Appendix A, the expressions of I_1 and I_2 can be written as

$$I_3 = F_{|\hat{h}_{BH}|^2}^{\infty,\mathrm{ni}}(\varphi_1) = \left\{\left(\frac{m_{BH}+\kappa_{BH}\mu_{BH}}{m_{BH}}\right)^{-m_{BH}} \frac{1}{\Gamma(\mu_{BH})}\sum_{i=1}^{\infty}\left(\frac{m_{BH}\kappa_{BH}\mu_{BH}}{(m_{BH}+\kappa_{BH}\mu_{BH})m_{BH}}\right)^{i} \cdot \times \frac{1}{(\mu_{BH}+i)}\frac{(m_{BH})_i}{(\mu_{BH})_i i!}\left(\frac{(1+\kappa_{BH})\mu_{BH}}{\psi_{BH}}\varphi_1\right)^{\mu_{BH}+i} \exp\left(-\frac{(1+\kappa_{BH})\mu_{BH}}{\psi_{BH}}\varphi_1\right)\right\}^{L}, \tag{40}$$

$$I_4 = F_{|\hat{h}_{HD}|^2}^{\infty,\mathrm{ni}}(\varphi_2) = \left(\frac{m_{HD}+\kappa_{HD}\mu_{HD}}{m_{HD}}\right)^{-m_{HD}} \frac{1}{\Gamma(\mu_{HD})}\sum_{i=1}^{\infty}\left(\frac{m_{HD}\kappa_{HD}\mu_{HD}}{(m_{HD}+\kappa_{HD}\mu_{HD})m_{HD}}\right)^{i} \cdot \times \frac{1}{(\mu_{HD}+i)}\frac{(m_{HD})_i}{(\mu_{HD})_i i!}\left(\frac{(1+\kappa_{HD})\mu_{HD}}{\psi_{HD}}\varphi_2\right)^{\mu_{HD}+i} \exp\left(-\frac{(1+\kappa_{HD})\mu_{HD}}{\psi_{HD}}\varphi_2\right). \tag{41}$$

In summary, we can get the approximate expression of OP at high SNR as

$$P_{\mathrm{out}}^{\infty,\mathrm{ni}1} = I_3 + I_4 - I_3 I_4. \tag{42}$$

(2) When $\sigma_{e_{XY}}^2 = a$ (a is a fixed value)

When we set $P_J = P_R/2$, the expressions of $B \longrightarrow H$ and $H \longrightarrow D$ channel capacity under high SNR are deduced as

$$C_{BH}^{\infty,\mathrm{ni}} = \frac{1}{2}\log_2\left(1 + \frac{\left|\hat{h}_{BH}\right|^2}{\sigma_{e_{BH}}^2 + f_{BH}^2\left(\left|\hat{h}_{BH}\right|^2 + \sigma_{e_{BH}}^2\right)}\right), \tag{43}$$

$$C_{HD}^{\infty,\mathrm{ni}} = \frac{1}{2}\log_2\left(1 + \frac{\left|\hat{h}_{HD}\right|^2}{\sigma_{e_{HD}}^2 + \left(\xi_1/2 + f_{HD}^2\right)\left(\left|\hat{h}_{HD}\right|^2 + \sigma_{e_{HD}}^2\right)}\right). \tag{44}$$

Combined with the method in Appendix A, the formula of OP at high SNR can be obtained as

$$\begin{aligned} P_{\mathrm{out}}^{\infty,\mathrm{ni}2} &= \Pr\left\{\min\left(C_{BH}^{\infty,\mathrm{ni}}, C_{HD}^{\infty,\mathrm{ni}}\right) < Rs\right\} = \Pr\left\{C_{BH}^{\infty,\mathrm{ni}} < Rs\right\} \\ &\quad + \Pr\left\{C_{HD}^{\infty,\mathrm{ni}} < Rs\right\} - \Pr\left\{C_{BH}^{\infty,\mathrm{ni}} < Rs\right\} \Pr\left\{C_{HD}^{\infty,\mathrm{ni}} < Rs\right\} \\ &= I_5 + I_6 - I_5 I_6, \end{aligned} \tag{45}$$

where I_5 and I_6 are, respectively, expressed as

$$I_5 = \Pr\left\{\left|\hat{h}_{BH}\right|^2 < \varphi_7\right\} = \left\{\left(\frac{m_{BH}+\kappa_{BH}\mu_{BH}}{m_{BH}}\right)^{-m_{BH}} \frac{1}{\Gamma(\mu_{BH})} \cdot \sum_{i=1}^{\infty}\left(\frac{m_{BH}\kappa_{BH}\mu_{BH}}{(m_{BH}+\kappa_{BH}\mu_{BH})m_{BH}}\right)^{i} \times (\mu_{BH}+i-1)!\frac{(m_{BH})_i}{(\mu_{BH})_i i!} \cdot \left\{1 - \sum_{s=0}^{\mu+i-1}\frac{\varphi_7^{\,s}}{s!}\left[\frac{(1+\kappa_{BH})\mu_{BH}}{\varphi_7}\right]^{s}\exp\left(-\frac{(1+\kappa_{BH})\mu_{BH}}{\varphi_7}\varphi_7\right)\right\}\right\}^{L}, \tag{46}$$

$$I_6 = \left(\frac{m_{HD}+\kappa_{HD}\mu_{HD}}{m_{HD}}\right)^{-m_{HD}} \frac{1}{\Gamma(\mu_{HD})}\sum_{i=1}^{\infty}\frac{(m_{HD})_i}{(\mu_{HD})_i i!}\left(\frac{m_{HD}\kappa_{HD}\mu_{HD}}{(m_{HD}+\kappa_{HD}\mu_{HD})m_{HD}}\right)^{i} \times (\mu_{HD}+i-1)!\left\{1 - \sum_{s=0}^{\mu_{HD}+i-1}\frac{\varphi_8^{\,s}}{s!}\left[\frac{(1+\kappa_{HD})\mu_{HD}}{\varphi_8}\right]^{s}\exp\left(-\frac{(1+\kappa_{HD})\mu_{HD}}{\varphi_8}\varphi_8\right)\right\}, \tag{47}$$

where $\varphi_7 = ((\Theta\sigma_{e_{BH}}^2(1+f_{BH}^2))/(1-\Theta f_{BH}^2))$, $\varphi_8 = ((\Theta\sigma_{e_{HD}}^2(1+\xi_1/2+f_{HD}^2))/(1-\Theta\xi_1/2-\Theta f_{HD}^2))$. By substituting the calculated I_5 and I_6 into (45), the precise expression (31) of the OP under high SNR can be obtained.

B.2. Ideal Situation. When $\sigma_{e_{XY}}^2 = \Omega_{XY}/(1+\delta\rho_{XY}\Omega_{XY})$, the high SNR of OP under ideal case can be approximated as

$$I_7 = \left\{\left(\frac{m_{BH}+\kappa_{BH}\mu_{BH}}{m_{BH}}\right)^{-m_{BH}} \frac{1}{\Gamma(\mu_{BH})}\sum_{i=1}^{\infty}\frac{(m_{BH})_i}{(\mu_{BH})_i i!}\left(\frac{m_{BH}\kappa_{BH}\mu_{BH}}{(m_{BH}+\kappa_{BH}\mu_{BH})m_{BH}}\right)^{i} \times \frac{1}{(\mu_{BH}+i)}\left(\frac{(1+\kappa_{BH})\mu_{BH}}{\psi_{BH}}\varphi_3\right)^{\mu_{BH}+i}\exp\left(-\frac{(1+\kappa_{BH})\mu_{BH}}{\psi_{BH}}\varphi_3\right)\right\}^{L}, \tag{48}$$

$$I_8 = \left(\frac{m_{HD}+\kappa_{HD}\mu_{HD}}{m_{HD}}\right)^{-m_{HD}} \frac{1}{\Gamma(\mu_{HD})}\sum_{i=1}^{\infty}\frac{(m_{HD})_i}{(\mu_{HD})_i i!} \cdot \left(\frac{m_{HD}\kappa_{HD}\mu_{HD}}{(m_{HD}+\kappa_{HD}\mu_{HD})m_{HD}}\right)^{i} \times \frac{1}{(\mu_{HD}+i)} \cdot \left(\frac{(1+\kappa_{HD})\mu_{HD}}{\psi_{HD}}\varphi_4\right)^{\mu_{HD}+i}\exp\left(-\frac{(1+\kappa_{HD})\mu_{HD}}{\psi_{HD}}\varphi_4\right), \tag{49}$$

$$P_{\text{out}}^{\infty,\text{id}} = I_7 + I_8 - I_7 I_8. \quad (50)$$

Data Availability

The data used to support the findings of this study are available from the corresponding author upon request.

Conflicts of Interest

The authors declare that there is no conflict of interest about the publication of this paper.

Acknowledgments

This work was supported in part by the Key Scientific Research Projects of Higher Education Institutions in Henan Province under Grant 20A510007 and in part by the Doctoral Fund of Henan Polytechnic University under Grant B2022-13.

References

[1] A. D. Wyner, "The wire-tap channel," *The Bell System Technical Journal*, vol. 54, no. 8, pp. 1355–1387, 1975.

[2] N. Yang, L. Wang, G. Geraci, M. Elkashlan, J. Yuan, and M. Di Renzo, "Safeguarding 5G wireless communication networks using physical layer security," *IEEE Communications Magazine*, vol. 53, no. 4, pp. 20–27, 2015.

[3] A. Li, "Enhancing the physical layer security of cooperative NOMA system," in *In 2019 IEEE 3rd information technology, networking, Electronic and Automation Control Conference (ITNEC)*, pp. 2194–2198, Chengdu, China, 2019.

[4] Y. Yao, "Adaptive relay selection with physical layer security for green communications," in *In 2020 IEEE/CIC International Conference on Communications in China (ICCC)*, pp. 1174–1178, Chongqing, China, 2020.

[5] J.-H. Lee, "Full-duplex relay for enhancing physical layer security in multi-hop relaying systems," *IEEE Communications Letters*, vol. 19, no. 4, pp. 525–528, 2015.

[6] F. Zhu and M. Yao, "Improving physical-layer security for CRNs using SINR-based cooperative beamforming," *IEEE Transactions on Vehicular Technology*, vol. 65, no. 3, pp. 1835–1841, 2016.

[7] J. Barros and M. R. D. Rodrigues, "Secrecy capacity of wireless channels," in *In 2006 IEEE International Symposium on Information Theory*, pp. 356–360, Seattle, WA, USA, 2006.

[8] L. Liang, D. Wei, and M. Li, "Wireless physical layer security based on channel pre-compensation for PolSK modulated systems," in *In 2017 IEEE 9th International Conference on Communication Software and Networks (ICCSN)*, pp. 357–361, Guangzhou, China, 2017.

[9] L. Fan, X. Lei, T. Q. Duong, M. Elkashlan, and G. K. Karagiannidis, "Secure multiuser communications in multiple amplify-and-forward relay networks," *IEEE Transactions on Communications*, vol. 62, no. 9, pp. 3299–3310, 2014.

[10] P. K. Gopala, L. Lai, and H. El Gamal, "On the secrecy capacity of fading channels," *IEEE Transactions on Information Theory*, vol. 54, no. 10, pp. 4687–4698, 2008.

[11] F. Benkhelifa, A. Tall, Z. Rezki, and M.-S. Alouini, "On the low SNR capacity of MIMO fading channels with imperfect channel state information," *IEEE Transactions on Communications*, vol. 62, no. 6, pp. 1921–1930, 2014.

[12] Y. Zhu, Y. Xin, and P.-Y. Kam, "Outage probability of Rician fading relay channels," *IEEE Transactions on Vehicular Technology*, vol. 57, no. 4, pp. 2648–2652, 2008.

[13] N. Bhargav, S. L. Cotton, and D. E. Simmons, "Secrecy capacity analysis over κ-μ fading channels: theory and applications," *IEEE Transactions on Communications*, vol. 64, no. 7, pp. 3011–3024, 2016.

[14] O. S. Badarneh, D. B. da Costa, M. Benjillali, and M.-S. Alouini, "Selection combining over double α-μ fading channels," *IEEE Transactions on Vehicular Technology*, vol. 69, no. 3, pp. 3444–3448, 2020.

[15] N. Hajri, N. Youssef, and M. Patzold, "A study on the statistical properties of double Hoyt fading channels," in *In 2009 6th International Symposium on Wireless Communication Systems*, pp. 201–205, Siena, Italy, 2009.

[16] R. Singh and M. Rawat, "Outage analysis of double shadowed κ-μ fading channels," in *In 2019 10th International Conference on Computing, Communication and Networking Technologies (ICCCNT)*, pp. 1–4, Kanpur, India, 2019.

[17] D. H. Tashman, W. Hamouda, and I. Dayoub, "Secrecy analysis over cascaded κ-μ fading channels with multiple eavesdroppers," *IEEE Transactions on Vehicular Technology*, vol. 69, no. 8, pp. 8433–8442, 2020.

[18] M. M. Harb and M. F. Al-Mistarihi, "Dual hop differential amplify-and-forward relaying with selection combining cooperative diversity over Nakagami-m fading channels," in *In 2016 8th IEEE International Conference on Communication Software and Networks (ICCSN*, pp. 225–228, Beijing, China, 2016.

[19] K. Eshteiwi, B. Sleim, and G. Kaddoum, "Full duplex of V2V cooperative relaying over cascaded Nakagami-m fading channels," in *In 2020 International symposium on networks, Computers and Communications (ISNCC)*, pp. 1–5, Montreal, QC, Canada, 2020.

[20] S. Majhi, P. Kumar, and Y. Nasser, "Outage performance of opportunistic of OFDM relaying over Rician fading channel," in *In 2016 23rd International Conference on Telecommunications (ICT)*, pp. 1–5, Thessaloniki, Greece, 2016.

[21] S. O. Ata and I. Altunbas, "Relay antenna selection for V2V communications using PLNC over cascaded fading channels," in *In 2015 International Wireless Communications and Mobile Computing Conference (IWCMC)*, pp. 1336–1340, Dubrovnik, Croatia, 2015.

[22] K. Hu, Q. Gao, Z. Wang, and W. Huang, "Outage performance of two-way decode-and-forward relaying over block fading channels," in *In 2017 IEEE 9th International Conference on Communication Software and Networks (ICCSN)*, pp. 51–55, Guangzhou, China, 2017.

[23] X. Zhang, Z. Yan, Y. Gao, and W. Wang, "On the study of outage performance for Cognitive Relay Networks (CRN) with the Nth best-relay selection in Rayleigh-fading channels," *IEEE Wireless Communications Letters*, vol. 2, no. 1, pp. 110–113, 2013.

[24] L. Wu, L. Yang, J. Chen, and M.-S. Alouini, "Physical layer security for cooperative relaying over Generalized-K fading channels," *IEEE Wireless Communications Letters*, vol. 7, no. 4, pp. 606–609, 2018.

[25] S. Solanki, P. K. Sharma, P. K. Upadhyay, D. B. da Costa, P. S. Bithas, and A. G. Kanatas, "Cognitive multi-relay networks

with RF hardware impairments and channel estimation errors," in *In GLOBECOM 2017 - 2017 IEEE Global Communications Conference*, pp. 1–6, Singapore, 2017.

[26] X. Li, Q. Wang, M. Liu et al., "Cooperative wireless-powered NOMA relaying for B5G IoT networks with hardware impairments and channel estimation errors," *IEEE Internet of Things Journal*, vol. 8, no. 7, pp. 5453–5467, 2021.

[27] X. Li, M. Zhao, M. Zeng et al., "Hardware impaired ambient backscatter NOMA systems: reliability and security," *IEEE Transactions on Communications*, vol. 69, no. 4, pp. 2723–2736, 2021.

[28] S. Solanki, P. K. Upadhyay, D. B. da Costa, P. S. Bithas, A. G. Kanatas, and U. S. Dias, "Joint impact of RF hardware impairments and channel estimation errors in spectrum sharing multiple-relay networks," *IEEE Transactions on Communications*, vol. 66, no. 9, pp. 3809–3824, 2018.

[29] X. Li, M. Liu, C. Deng et al., "Joint effects of residual hardware impairments and channel estimation errors on SWIPT assisted cooperative NOMA networks," *IEEE Access*, vol. 7, pp. 135499–135513, 2019.

[30] M. Toka and O. Kucur, "Performance of MRT/RAS MIMO-NOMA with residual hardware impairments," *IEEE Wireless Communications Letters*, vol. 10, no. 5, pp. 1071–1074, 2021.

[31] X. Li, M. Huang, C. Zhang et al., "Security and reliability performance analysis of cooperative multi-relay systems with nonlinear energy harvesters and hardware impairments," *IEEE Access*, vol. 7, pp. 102644–102661, 2019.

[32] J. F. Paris, "Statistical characterization of κ-μ shadowed fading," *IEEE Transactions on Vehicular Technology*, vol. 63, no. 2, pp. 518–526, 2014.

[33] A. S. M. Badrudduza, S. M. S. Shahriyer, M. K. Kundu, and S. Shabab, "Enhancement of secrecy multicast capacity over κ-μ shadowed fading channel," in *In 2019 IEEE International Conference on Telecommunications and Photonics (ICTP)*, pp. 1–4, Dhaka, Bangladesh, 2019.

[34] J. Sun, H. Bie, and X. Li, "Security performance analysis of SIMO relay systems over composite fading channels," *KSII Transactions on Internet and Information Systems*, vol. 14, no. 6, pp. 1–6, 2020.

[35] M. S. Aloqlah, I. E. Atawi, and M. F. Al-Mistarihi, "On the performance of fixed-gain amplify-and-forward dual-hop relay systems with beamforming under κ-μ shadowed fading," in *In 2015 IEEE 26th Annual International Symposium on Personal, Indoor, and Mobile Radio Communications (PIMRC*, pp. 814–818, Hong Kong, China, 2015.

[36] E. Illi, F. E. Bouanani, and F. Ayoub, "Performance analysis of dual-hop underwater communication system subject to κ-μ shadowed fading channel," in *In 2016 International Conference on Advanced Communication Systems and Information Security (ACOSIS)*, pp. 1–6, Marrakesh, Morocco, 2016.

[37] R. H. Shaik and R. K. Naidu, "Performance evaluation of dual-hop amplify-and-forward scheme over κ–μ shadowed fading channels," *Physical Communication*, vol. 33, pp. 206–214, 2019.

[38] S. Furrer and D. Dahlhaus, "Multiple-antenna signaling over fading channels with estimated channel state information: capacity analysis," *IEEE Transactions on Information Theory*, vol. 53, no. 6, pp. 2028–2043, 2007.

[39] C. W. R. Chiong, Y. Rong, and Y. Xiang, "Blind estimation of MIMO relay channels," in *2014 IEEE Workshop on Statistical Signal Processing (SSP)*, pp. 400–403, Gold Coast, QLD, Australia, 2014.

[40] N. Missaoui, I. Kammoun, and M. Siala, "Efficient user identification and semi-blind channel estimation for MU-MIMO systems," *IEEE Wireless Communications Letters*, vol. 6, no. 2, pp. 150–153, 2017.

[41] X. Li, J. Li, Y. Liu, Z. Ding, and A. Nallanathan, "Outage performance of cooperative NOMA networks with hardware impairments," in *In 2018 IEEE Global Communications Conference (GLOBECOM)*, pp. 1–6, Abu Dhabi, United Arab Emirates, 2018.

[42] X. Ding, T. Song, Y. Zou, X. Chen, and L. Hanzo, "Security-reliability tradeoff analysis of artificial noise aided two-way opportunistic relay selection," *IEEE Transactions on Vehicular Technology*, vol. 66, no. 5, pp. 3930–3941, 2017.

[43] F. Gabry, R. Thobaben, and M. Skoglund, "Outage performances for amplify-and-forward, decode-and-forward and cooperative jamming strategies for the wiretap channel," in *In 2011 IEEE Wireless Communications and Networking Conference*, pp. 1328–1333, Cancun, Mexico, 2011.

[44] L. Peng, G. Zang, Q. Zhou, Y. Gao, and C. Xi, "Security performance analysis for cooperative communication system under Nakagami-m fading channel," in *In 2017 IEEE 17th International Conference on Communication Technology (ICCT)*, pp. 187–192, Chengdu, China, 2017.

[45] E. Bjornson, M. Matthaiou, and M. Debbah, "A new look at dual-hop relaying: performance limits with hardware impairments," *IEEE Transactions on Communications*, vol. 61, no. 11, pp. 4512–4525, 2013.

[46] V. Kumar, B. Cardiff, S. Prakriya, and M. F. Flanagan, "Effective rate of downlink NOMA over κ-μ shadowed fading with integer fading parameters," in *In 2020 IEEE International Conference on Communications Workshops (ICC Workshops)*, pp. 1–7, Dublin, Ireland, 2020.

[47] J. Sun, H. Bie, X. Li, J. Zhang, G. Pan, and K. M. Rabie, "Secrecy performance analysis of SIMO systems over correlated κ-μ shadowed fading channels," *IEEE Access*, vol. 7, pp. 86090–86101, 2019.

Hindawi
Wireless Communications and Mobile Computing
Volume 2023, Article ID 9897273, 1 page
https://doi.org/10.1155/2023/9897273

Retraction

Retracted: Urban Ecological Monitoring and Prediction Based on Deep Learning

Wireless Communications and Mobile Computing

Received 18 July 2023; Accepted 18 July 2023; Published 19 July 2023

This article has been retracted by Hindawi following an investigation undertaken by the publisher [1]. This investigation has uncovered evidence of one or more of the following indicators of systematic manipulation of the publication process:

(1) Discrepancies in scope
(2) Discrepancies in the description of the research reported
(3) Discrepancies between the availability of data and the research described
(4) Inappropriate citations
(5) Incoherent, meaningless and/or irrelevant content included in the article
(6) Peer-review manipulation

The presence of these indicators undermines our confidence in the integrity of the article's content and we cannot, therefore, vouch for its reliability. Please note that this notice is intended solely to alert readers that the content of this article is unreliable. We have not investigated whether authors were aware of or involved in the systematic manipulation of the publication process.

Wiley and Hindawi regrets that the usual quality checks did not identify these issues before publication and have since put additional measures in place to safeguard research integrity.

We wish to credit our own Research Integrity and Research Publishing teams and anonymous and named external researchers and research integrity experts for contributing to this investigation.

The corresponding author, as the representative of all authors, has been given the opportunity to register their agreement or disagreement to this retraction. We have kept a record of any response received.

References

[1] J. H. Yang and C. P. Chan, "Urban Ecological Monitoring and Prediction Based on Deep Learning," *Wireless Communications and Mobile Computing*, vol. 2022, Article ID 1973777, 6 pages, 2022.

Hindawi
Wireless Communications and Mobile Computing
Volume 2022, Article ID 1973777, 6 pages
https://doi.org/10.1155/2022/1973777

Research Article

Urban Ecological Monitoring and Prediction Based on Deep Learning

Jun He Yang[1,2] **and Chia Pang Chan**[3,4]

[1]*Department of E-Sport Technology Management, Cheng Shiu University, No.840, Chengcing Rd., Niaosong Dist., Kaohsiung City 83347, Taiwan*
[2]*Super Micro Mass Research & Technology Center, Cheng Shiu University, No.840, Chengcing Rd., Niaosong Dist., Kaohsiung City 83347, Taiwan*
[3]*Department of Long Term Care of Management, College of Nursing, Chung Hwa Medical University, No. 89, Wenhua 1st Rende Dist., Tainan 717, Taiwan*
[4]*Guangdong-Taiwan College of Industrial Science & Technology, Dongguan University of Technology, No.251, Xueyuan Road, Dongzheng Community, Guancheng Sub-district, Dongguan, Guangdong, China*

Correspondence should be addressed to Chia Pang Chan; acechan@o365.hwai.edu.tw

Received 18 February 2022; Accepted 19 March 2022; Published 13 April 2022

Academic Editor: Junjuan Xia

Obtaining comprehensive and accurate air quality information is conducive to people's daily travel and living arrangements, especially to protect people's health from air pollutants. Due to the limited number of air quality monitoring stations and the lack of training samples, the generalisation performance of air quality estimation model is often not good enough. Therefore, we propose an urban air quality index (AQI) prediction and AQI level estimation method based on deep multi-task learning. We consider various urban big data information related to air quality (meteorology, transportation, enterprise self-test, POI, road network, etc.), and use machine learning methods such as deep learning and graph embedding learning to learn the representation of relevant information, and establish the relationship between these related representations and air quality. Experiments show that this scheme can estimate the level of urban air quality index joint prediction task and air quality index, and the model has generalisation performance.

1. Introduction

With industrial development and population expansion, various harmful substances are emitted into the air, causing air pollution. Having comprehensive and accurate information on air quality helps to protect the ecological environment and human health from the dangers of air pollution [1]. Many cities have set up air quality monitoring stations to monitor air quality in real time. However, the number of air quality monitoring stations is limited. It is not possible to know with certainty the air quality at locations where no air quality monitoring stations have been set up, and air quality monitoring stations cannot predict future air quality [2]. Therefore, estimating air quality in areas without monitoring stations and predicting future air quality at monitoring stations can provide comprehensive air quality information in space and time, helping people to rationalise their travel plans and assisting relevant organisations in making environmental decisions. Existing air quality estimation methods are based on urban data related to air quality (e.g., meteorological, road network, and POI) to establish the relationship between air quality in two areas, thus using the air quality in areas with monitoring stations to estimate the air quality in areas without monitoring stations [3]. However, existing air quality estimation methods do not adequately consider data related to air quality, and do not take into account information such as company self-measurement and the angle of relative location between areas. Secondly, existing work has defined and extracted features manually, which are often incomplete and take a lot of time to design and verify their validity [4]. Also, due to the limited number of monitoring sites and the lack of

training samples, the models often fail to achieve good generalisation performance [5].

To address these problems, this paper proposes a deep multi-task learning-based urban air quality prediction and estimation method, which integrates a variety of air quality-related urban big data information (meteorology, enterprise self-measurement, road network, POI, etc.), learns the representation of this related information through deep learning and machine learning methods such as graph embedding learning, and improves the generalisation performance of single-task models by combining air quality prediction and estimation tasks through multi-task learning [6].

2. Related Work

2.1. Air Quality Estimates. Existing air quality estimation methods include mainly physical dispersion simulation-based methods and statistical and data-driven methods.

Physical dispersion simulation-based methods estimate the distribution of pollutants by simulating the pattern of pollutant dispersion [7, 8]. Linear statistical model-based methods use linear models such as spatial interpolation or land-use regression combined with land-use related characteristics to estimate air quality. For example, the kriging-based air quality estimation method [9] uses a spatial interpolation method called fuzzy genetic linear member kriging to estimate the geospatial distribution of air quality. The land-use regression-based approach [10] uses a land-use regression model to establish the relationship between land-use related characteristics (e.g., land use, traffic patterns, and population density) and air quality.

As linear statistical models are unable to establish non-linear relationships between urban air quality and land-use related characteristics, non-linear statistical models are also widely used in air quality estimation [11]. Established methods based on non-linear statistical models include those based on supervised learning and those based on semi-supervised learning [12].

Methods based on supervised learning include those based on generalised additive models and those based on Gaussian process regression. For example, [13] used generalised additive models to establish the relationship between air quality and the relevant explanatory variables. [14] used Gaussian process regression to establish relationships between characteristics such as traffic flow, population density, temperature, and air quality. Such non-linear models also fail to achieve good estimation performance due to the limited number of training samples [15]. [16] proposed an air quality estimation method based on a collaborative training algorithm, which combines a variety of data such as meteorology, traffic flow, road network structure, and POI in cities, and uses conditional random fields and artificial neural networks to model the relationship between relevant features and urban air quality. [17] used unlabelled data to increase the number of training samples through the collaborative training algorithm; however, the collaborative training algorithm did not control the noise introduced during the iterative training process, and therefore, the model could not achieve better results.

2.2. Air Quality Forecasting Methodology. Existing air quality prediction methods are divided into those based on physical dispersion modelling and those based on statistical and data-driven methods.

Methods based on physical dispersion modelling predict the distribution of pollutants by simulating the pattern of pollutant dispersion, such as Gaussian models [18], dynamic street canyon models, and computational fluid dynamics [19], which mostly use functions related to meteorology, street geography, receptor location, traffic flow, and dispersion factors to simulate the dispersion of pollutants. However, such methods usually require empirical assumptions to be met and parameter settings are not generalisable.

Linear statistical modelling-based approaches use linear models to model the linear relationship between air quality over its own time series or with other characteristics to make predictions about future air quality. For example, [20] used an autoregressive sliding average model to model the trend in air pollutant concentrations over their own time series to predict future average air pollutant concentrations. For example, [12] used polynomial regression combined with meteorological data to predict daily maximum concentrations O_3 and [13] used kernel regression combined with meteorological data to predict daily maximum concentrations. [14] used artificial neural networks and linear regression to predict future air quality in NO_2 the area to be predicted by combining meteorological and historical air quality from the area to be predicted and from the surrounding air quality monitoring stations.

3. Learning of Regional Non-Temporal Information Representation Based on Graph Embedding Methods and Convolutional Neural Networks

The POI category and density of an area tend to reflect the land use and traffic patterns of the area, and are directly or indirectly related to the air quality of the area; for example, areas with factories tend to have poorer air quality, and areas with parks tend to have better air quality. Road network structure and traffic patterns are strongly correlated, with traffic-generated emissions being a source of urban air pollutants, and the road network structure to some extent reflecting the air quality of the region. The traditional method extracts relevant features such as road network and POI, simply counts the number of various types of POI contained in each area and the length of various types of road network as relevant features, ignoring the hierarchical information between different categories of POI/road network, and when there are more categories of POI, the statistical features extracted by the traditional method are rather sparse. The graph embedding method LINE is a method of embedding an information network into a low-dimensional vector space by representing each vertex in the network with a vector in the low-dimensional space. In this paper, the LINE method is used to embed the non-temporal information of each region into a low-dimensional vector by

combining the information network graph consisting of coordinates, road network, and non-temporal data such as POI of all regions to be estimated and regions to be predicted. In order to extract more non-temporal features relevant to AQI prediction and AQI class estimation, the low-dimensional vector of non-temporal information is further processed by a convolutional neural network to extract local features, and the output of the convolutional neural network is used as the final regional non-temporal information representation for subsequent AQI prediction and AQI class estimation tasks.

3.1. Learning Non-Temporal Information Representation of Regions Based on the Graph Embedding Method LINE

Definition 1. Area-region diagram. The region-area diagram $G_{dd} = (D \cup D, \varepsilon_{dd})$, representing the physical distance relationship between grid regions, is shown in Figure 1, where D denotes the set of grid regions, ε_{dd} denotes the set of edges between grid regions, and each grid region d_i and grid region d_j is separated by an edge e_{ij}, with edge weight w_{ij} defined as the physical distance between d_i and d_j.

Definition 2. Area-POI diagram. The region-POI diagram $G_{dp} = (D \cup P, \varepsilon_{dp})$, representing the distribution of POIs within a grid influence region, is shown in Figure 2, where D denotes the set of grid regions, p denotes the set of POI categories, and ε_{dp} denotes the set of edges of grid regions and POI categories. If the grid region d_i has POIs of category P_j within the grid influence region, an edge e_{ij} exists between grid region d_i and P_j POI categories; the edge weight w_{ij} is defined as the number of POIs of category P_j contained within the grid influence region of d_i.

Definition 3. Area-road network diagram. The region-road network diagram $G_{dr} = (D \cup \mathrm{RD}, \varepsilon_{dr})$ represents the distribution of road sections within the grid influence area, as shown in Figure 3, where D denotes the set of grid regions, RD denotes the set of road section categories, and ε_{dr} denotes the set of edges between grid regions and road section categories. If there are road sections of category r_j within the grid influence area of grid region d_i, there exists an edge e_{ij} between grid region d_i and road section category r_j, and the edge weight w_{ij} is defined as the total length of road sections of category r, contained within the grid influence area of d_i. According to the Chinese urban planning guidelines, this paper classifies urban roads into four classes as shown in Table 1.

For the three diagrams defined above, using the LINE method to learn the low-dimensional vector representation of all vertices in each diagram, the diagrams Gdd, Gdp, and Gdr correspond to the objective functions L(Gdd), L(Gdp), and L(Gdr), respectively, and the total objective

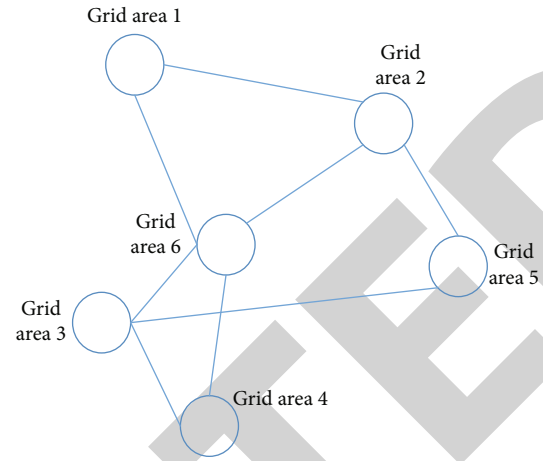

Figure 1: Area-region map.

function $L(G)$ as shown in the following equation.

$$
\begin{aligned}
L(G_{dd}) &= -\sum_{e_{ij} \in \varepsilon_{dd}} w_{ij} \log p(v_j|v_i), \\
L(G_{dp}) &= -\sum_{e_{ij} \in \varepsilon_{dp}} w_{ij} \log p(v_j|v_i), \\
L(G_{dr}) &= -\sum_{e_{ij} \in \varepsilon_{dr}} w_{ij} \log p(v_j|v_i), \\
L(G) &= L(G_{dd}) + L(G_{dp}) + L(G_{dr}).
\end{aligned} \tag{1}
$$

In the calculation reference formula of $p(v_j|v_i)$, by optimising the objective function $Z(g)$, the low-dimensional vector representation of all vertices in the graph can be obtained; that is, the low-dimensional vector representation $u^{d_i \in R^{\varphi}, R^{\varphi}}$ of non-temporal information of each region d_j can be obtained, which represents the vector space of φ, and the connection relationship of regional location, POI, and road network in the graph can be embedded into the low-dimensional vector, in order to extract more non-temporal information related to AQI prediction and AQI level estimation tasks.

3.2. AQI Forecasting Tasks. In this paper, multiple complex factors related to air quality are taken into account when predicting the AQI of a region to be predicted: historical meteorological, historical air quality, historical traffic, historical business self-measurement, and weather forecast data of the region to be predicted; non-temporal data such as coordinates, P0I, and road network of the region to be predicted; and historical meteorological and historical air quality data of the region of global influence. A graph embedding method and a CNN are used to learn the representation of this relevant non-temporal information, and a recurrent neural network is used to learn the representation of this relevant temporal information, and based on these relevant representations, the AQI of the area to be predicted at multiple times in the future [21–23].

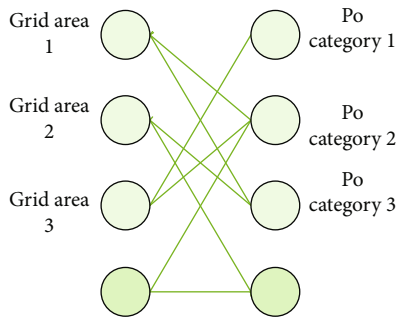

Figure 2: Area-POI diagram.

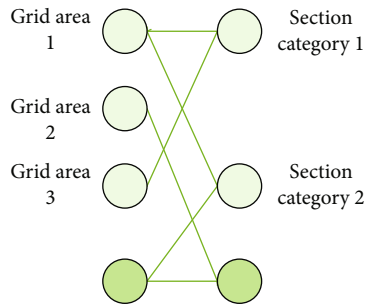

Figure 3: Regional-road network map.

Table 1: Classification of urban roads.

Road grade	Vehicle speed (km/h)	Road width (m)
1	60-80	40-70
2	40-60	30-60
3	30-40	20-40
4	0-30	16-30

The output LSTM is called the output LSTM, based on μ^{d_f}, $\mathbf{F\_h}^{d_f}$, $\mathbf{F\_h}_t^{d_f}$, $\mathbf{F\_c}_t^{d_f}$, $\mathbf{G\_h}^{g}$ and $\mathbf{G\_h}_t^{g}$. This paper uses a one-layer LSTM to predict d_f the AQI at z future moments. First, all the vectors in $\mathbf{F\_h}_t^{d_f}$ and $\mathbf{G\_h}_t^{g}$ are joined together to obtain μ^{d_f} a linear transformation $\mathbf{FALL\_h}_t^{d_f}$ and the output of the linear transformation is non-linearly processed by the tanh function to obtain $\mathbf{h}_t^{d_f}$ as shown in equation (2), as the initial hidden state information of the output LSTM.

$$\mathbf{h}_t^{d_f} = \tanh\left(W_h^{d_f}\mathbf{FALL\_h}_t^{d_f}\right). \tag{2}$$

Similarly, all the vectors in $\mathbf{F\_c}_t^{d_f}$ are concatenated to obtain $\mathbf{FALL\_c}_t^{d_f}$, and after a linear transformation and non-linear processing, $c_t^{d_f}$ is obtained as the initial memory cell information for the output LSTM.

When the input sequence of the input recurrent neural network is too long, the output LSTM is often not good enough when the output LSTM is initialized with only the output of the input recurrent neural network at the last moment, so in this paper, when using the output LSTM to predict the AQI at z future moments, an attention mechanism is introduced, and at each step of generating the sequence of AQI prediction values, the input recurrent each position of the input sequence of the neural network is searched, and the most relevant part of the output LSTM at the current moment is selected to calculate the context vector, and the AQI prediction value at the current moment is calculated based on this context vector. Let $\mathbf{h}_j$ denote the output of the output LSTM at moment y, and let $\mathrm{METL}\,\tilde{c}_j^{d_f}$ denote the context vector associated with the d_f long-term sequence of weather data at moment y for which the attention mechanism has been introduced, $\mathrm{METL}\,\tilde{c}_j^{d_f}$ as shown in the following equation.

$$\begin{aligned}
\mathrm{METL}\,\tilde{c}_j^{d_f} &= \sum_{n=1}^{l} \mathrm{METL_}\alpha_{jn}^{d_f}\,\mathrm{METL_}\mathbf{h}_n^{d_f},\\
\mathrm{METL_}\alpha_{jn}^{d_f} &= \exp\ \mathrm{score}h_j, \mathrm{METL_}hh_n^{d_f}\sum_{n'}\exp\left(\mathrm{score}\left(h_j, \mathrm{METL_}h_{n'}^{d_f}\right)\right),\\
\mathrm{score}\left(\mathbf{h}_j, \mathbf{METLhh}_n^{d_f}\right) &= \mathbf{h}_j^{\mathrm{T}}\mathbf{METL_h}_n^{d_f}.
\end{aligned} \tag{3}$$

where $\mathbf{METLhh}_n^{d_f}$ represents the hidden state output of the input recurrent neural network at moment n when a long-term sequence of d_f weather data is used as the input sequence of the input recurrent neural network, $\mathrm{METL\_}\alpha_{jn}^{d_f}$ represents the weight of $\mathrm{METL\_}hh_n^{d_f}$, score is a scoring function to calculate the correlation between the hidden state output of the input recurrent neural network at moment n and the output of the output LSTM at/moment, and $\mathrm{METL}\,\tilde{c}_j^{d_f}$ is the weighted sum of the hidden states of the input recurrent neural network at all moments.

Table 2: Comparison of classification results of different urban air quality estimation methods.

Urban air quality estimation method	MAP
U-Air	0.713 ± 0.008
Semi-EP (k=1)	0.674 ± 0.003
Semi-EP (k=2)	0.714 ± 0.002
Semi-EP (k=3)	0.732 ± 0.002
Semi-EP (k=4)	0.736 ± 0.004
DAFE	0.761 ± 0.003

4. Experimental Comparison of Relevant Urban Air Quality Estimation Methods

The results of the different urban regional air quality estimation methods are shown in Table 2. The results demonstrate that for the Semi-EP method, its average classification accuracy is highest at fc =3, which is consistent with the results of [15]. The results in Table 2 show that the performance of the proposed method is significantly better than that of U-Air and Semi-EP on the dataset used in this paper, which may

Table 3: Comparison results of different urban air quality prediction methods.

Method	MAE			
	1-6H	7-12H	13-24H	25-48H
FFA	20.59 ± 0.294	25.96 ± 0.258	34.75 ± 0.489	37.71 ± 0.534
DAFE	18.26 ± 0.485	21.65 ± 0.681	22.59 ± 0.717	24.52 ± 0.849

be due to the fact that, compared to U-Air and Semi-EP, features are defined and constructed manually and the proposed method uses graph embedding methods to classify the features. The non-temporal and temporal feature representations learned by the proposed method using graph embedding and deep neural networks are more representational [24, 25].

The FFA method uses a linear regressor to model the relationship between local characteristics such as historical air quality, current weather, and weather forecasts at the site to be predicted and the future air quality at the site to be predicted, and an artificial neural network to model the relationship between current weather and global characteristics such as historical air quality at neighbouring monitoring sites and the future air quality at the site to be predicted. The results of the two models are then integrated using a regression tree. For the classification of the global impact space, the same approach as for FFA is adopted. The results of the different AQI prediction methods are shown in Table 3. The results in Table 3 show that the mean absolute error of the proposed method is smaller than the mean absolute error of the FFA method. This may be due to the fact that the method proposed in this paper establishes a better non-linear relationship between the air quality of the site to be predicted and the local factors than the FFA method, and the change in the mean absolute error of the FFA method is greater than that of the method proposed in this paper as the distance between the time to be predicted and the current time increases. This may be due to the fact that the relevant feature representations learned by the proposed method using graph embedding and deep neural networks are more representational and take into account the previous AQI prediction when predicting the null AQI at a certain time, introducing more information.

5. Conclusions

This paper proposes a deep multi-task learning-based approach for urban AQI prediction and AQI class estimation. On the one hand, a variety of urban big data information related to air quality (meteorology, traffic, enterprise self-measurement, POI, road network, etc.) is considered, and machine learning methods such as deep learning and graph embedding learning are used to learn representations of relevant information and establish relationships between these relevant representations and air quality, so as to estimate AQI levels in areas without air quality monitoring stations and to estimate AQI levels in areas with air quality monitoring stations, AQI prediction for regions with air quality monitoring stations.

Data Availability

The experimental data used to support the findings of this study are available from the corresponding author upon request.

Conflicts of Interest

The authors declared that they have no conflicts of interest regarding this work.

References

[1] R. Janarthanan, P. Partheeban, K. Somasundaram, and P. N. Elamparithi, "A deep learning approach for prediction of air quality index in a metropolitan city," *Sustainable Cities and Society*, vol. 67, article 102720, 2021.

[2] S. Weichenthal, M. Hatzopoulou, and M. Brauer, "A picture tells a thousand…exposures: opportunities and challenges of deep learning image analyses in exposure science and environmental epidemiology," *Environment International*, vol. 122, pp. 3–10, 2019.

[3] Z. Han and A. Xu, "Ecological evolution path of smart education platform based on deep learning and image detection," *Microprocessors and Microsystems*, vol. 80, article 103343, 2021.

[4] X. Li, L. Peng, Y. Hu, J. Shao, and T. Chi, "Deep learning architecture for air quality predictions," *Environmental Science and Pollution Research*, vol. 23, no. 22, pp. 22408–22417, 2016.

[5] D. Qin, J. Yu, G. Zou, R. Yong, Q. Zhao, and B. Zhang, "A novel combined prediction scheme based on CNN and LSTM for urban PM2.5 concentration," *IEEE Access*, vol. 7, pp. 20050–20059, 2019.

[6] L. Liu and Y. Zhang, "Smart environment design planning for smart city based on deep learning," *Sustainable Energy Technologies and Assessments*, vol. 47, article 101425, 2021.

[7] A. Heydari, M. Majidi Nezhad, D. Astiaso Garcia, F. Keynia, and L. De Santoli, "Air pollution forecasting application based on deep learning model and optimization algorithm," *Clean Technologies and Environmental Policy*, vol. 24, 2021.

[8] A. Bekkar, B. Hssina, S. Douzi, and K. Douzi, "Air-pollution prediction in smart city, deep learning approach," *Journal of big Data*, vol. 8, no. 1, pp. 1–21, 2021.

[9] Y. Jiang, C. Li, L. Sun, D. Guo, Y. Zhang, and W. Wang, "A deep learning algorithm for multi-source data fusion to predict water quality of urban sewer networks," *Journal of Cleaner Production*, vol. 318, article 128533, 2021.

[10] Q. Yuan, H. Shen, T. Li et al., "Deep learning in environmental remote sensing: achievements and challenges," *Remote Sensing of Environment*, vol. 241, article 111716, 2020.

[11] S. Christin, É. Hervet, and N. Lecomte, "Applications for deep learning in ecology," *Methods in Ecology and Evolution*, vol. 10, no. 10, pp. 1632–1644, 2019.

Hindawi
Wireless Communications and Mobile Computing
Volume 2022, Article ID 6243729, 12 pages
https://doi.org/10.1155/2022/6243729

Research Article

The Curriculum System of Business English Majors in Higher Vocational Colleges from the Perspective of the Internet of Things Business Model

Pilan Wen

Qinghai Higher Vocational and Technical Institute, Haidong, 810700 Qinghai, China

Correspondence should be addressed to Pilan Wen; lelandjunior@mail.cu.edu.kg

Received 12 February 2022; Revised 4 March 2022; Accepted 24 March 2022; Published 12 April 2022

Academic Editor: Junjuan Xia

As the country pays more attention to higher vocational education, major higher vocational schools have begun to enroll in multiple majors, but many higher vocational schools do not have the admission requirements for business English majors. This paper is aimed at studying the business English curriculum system in higher vocational colleges from the perspective of the Internet of Things business model. This paper proposes a questionnaire survey analysis method based on the professional curriculum system of business English in higher vocational colleges. This algorithm is more pertinent than ordinary algorithms, and it is more explanatory for the research on the curriculum system of higher vocational business English. This method can more accurately explain the problems existing in the current higher vocational business English courses through detailed analysis of the course objectives, course implementation, and course evaluation. The experimental results of this paper show that the current curriculum system for business English majors in higher vocational colleges has problems in three aspects: curriculum objectives, curriculum implementation, and curriculum evaluation. 20% of the student group thinks that the curriculum system for business English majors has problems.

1. Introduction

The development history of domestic higher vocational education is short, and the level of development is low, so the curriculum model of higher vocational education has not formed a complete system. Part of the curriculum model is based on the introduction of foreign advanced models, and the other part is based on the domestic secondary vocational curriculum model, combined with the characteristics and connotations of higher education, to develop its own higher vocational curriculum model. At present, the mainstream curriculum modes of vocational education mainly include broad foundation, living module cluster curriculum mode, multi-integrated curriculum mode, and modular curriculum mode. In today's development of the Internet of Things, the business model based on the Internet of Things has also undergone great changes, which has a great impact on business English majors, especially for vocational colleges with low conditions [1, 2]. Therefore, it is necessary to study the curriculum system of business English in higher vocational colleges.

Only by attaching importance to education can we have a better future. Based on the research on the curriculum system of higher vocational business English majors, this paper has the following innovations: (1) this paper proposes a questionnaire survey analysis method based on the curriculum system of business English majors in higher vocational colleges. Different from ordinary data analysis methods, the algorithm in this paper is more aimed at the study of the professional curriculum system of higher vocational colleges, and a factor with a higher degree of generalization is added to measure the design effect of the curriculum. (2) Research on the curriculum system of business English majors in higher vocational colleges is based on the perspective of the business model of the Internet of Things. Many literatures are used in the application of the Internet of

Things in high-tech, and there are few applications in education. This article mentions the impact of IoT business models on business English majors.

2. Related Work

The development of modern education has developed to a relatively high stage, not only in the details of the classification of education but also in the comprehensiveness of education. Therefore, there are many studies on curriculum design in education. A two-year follow-up study of prepubertal girls aged 7-9 years by Alwis and others found that curriculum design needs to take into account the age factors of the school subject, and curriculum design for younger ages needs to be more careful [3]. The purpose of Tan-Sisman et al.'s study was to comparatively investigate the curriculum development process in Singapore and Turkey in terms of administrative structure and educational reform. The results show similarities and differences in the centralized approach, administrative units, and their tasks in Singapore and Turkey in terms of the administrative structure of curriculum development [4]. In Zambia, Kalungia and others conducted a study of the local training curriculum system for pharmacists. Their study found that pharmacy education in Zambia offers many career prospects in hospitals, communities, drug manufacturing, drug regulation, public health administration, and academic development [5]. There are many research directions for business models, most of which are based on formula strategies. Stubbs' research is based on interviews with 14 Australian companies to enrich the understanding of the characteristics of sustainable business models that align profit and social impact [6]. The purpose of the study by Cosenz is to explore how system dynamics modeling can provide methodological support for the design of business models to better communicate the business strategy and manage performance. Their research found that the methodological support provided by system dynamics for business model design can effectively improve business strategy communication and performance management by adopting a systematic and flexible perspective to identify and analyze the main causal relationships between key elements [7]. A systematic literature review based on business model ontology is presented by Nikou and Bouwman to lay the foundation for the development of these applications. The research shows that the existing literature mainly focuses on the service platform component of the business model and its potential technical challenges, while the nontechnical business model components such as value proposition, organization, and revenue model have not received the attention that is considered necessary [8]. Lombardi and Schwabe research, develop, and analyze business models based on sharing economy principles. In this model, energy storage operators offer their energy storage systems to different types of customers. Every customer uses ESS for their single-use case. Furthermore, they found that larger battery sizes in terms of power and capacity are profitable and lead to increased revenue streams [9]. The purpose of the study by Prendeville and others is to explore how the ecodesign dilemma contributes to the evolution of ecodesign in companies. Their research is based on the commercial Internet to explore the most efficient business models. They do this through an empirical study of the ecodesign decision-making process of individual companies [10]. Through related work, it can be found that the curriculum research on business English is more based on the school's curriculum and does not fully consider the needs of the student group. And under the Internet business model, there is no solution to the employment needs of students after graduation.

3. Professional Courses of Business English Courses

3.1. Business English. It has only been decades since the advent of business English, and the teaching of business English has only begun to develop in China for nearly 20 to 30 years. The development of practical business English courses is only in its infancy. However, with China's accession to the World Trade Organization (WTO) and the increasingly frequent commercial and trade exchanges with other countries in the world, the scope of activities has expanded, business English has become increasingly important, and the connotation of the concept of "business English" has become more and more abundant. "Business English" currently has various translations or corresponding terms such as "Foreign Trade English" in China. It is also called "International Business English." The word "International" is added to indicate that it is related to foreign business and trade. It can be seen that the course names are also extremely inconsistent. Due to the different backgrounds and motivations of business English learners, although "business English courses" under various names have common characteristics, they are often very different. Therefore, it can be said that there is currently no clear and consensus definition of "business English" [11, 12].

Because business English belongs to English for Special Purposes (ESP), the teaching of business English has its typical characteristics. By analyzing the needs of the market, schools, teachers, students, and other aspects, a real industry corpus, based on the real context, is used to cultivate students' ability to communicate effectively in English in a specific environment. The teaching of business English includes both theoretical teaching and practical teaching. In the practical teaching, there are both teaching of various practical courses for business English majors, and business English is used as a separate course in practical teaching [13, 14]. In this paper, the practical teaching of business English refers to the teaching of foreign trade negotiation courses by the teachers of the business English colleges of the higher vocational colleges studied by using the project teaching method. The project team formed by the students, under the guidance of teachers, prepares each work item in the foreign trade negotiation course textbook before the project, displays it during the project, and summarizes after the project.

3.2. Courses. Curriculum is the guarantee of professional development, the carrier of student training, and the most critical and direct stable factor affecting the improvement of students' quality. Vocational education curriculum is the overall

design and arrangement of the educational content, process, and standards by the organizer of vocational education. It is the blueprint and basic basis for various educational, teaching, practice, and practical activities of vocational education.

A major refers to a department in an institution of higher learning or an academic category in a secondary specialized school. There is still no complete consensus on how to build a major in a university. Specifically, professional construction, as an important part of cultivating senior professional talents, covers a wide range of contents, from the setting of disciplines and the introduction of teachers to teaching practice, practice opportunities, and student quality improvement. As for these contents, where efforts should be made depends on the society's requirements for talent quality and skills. For example, reforming and adjusting the professional direction, building high-quality teachers, expanding social cooperation, increasing practical projects and opportunities, promoting teaching, learning reward and punishment mechanisms, etc., are all methods that are of great benefit to the cultivation of higher vocational talents.

4. Questionnaire Survey Method Based on the Study of the Business English Professional Curriculum System

4.1. Cluster Analysis. The uses of clustering are very broad. In business, clustering can help market analysts to distinguish different consumer groups from the consumer database and summarize the consumption patterns or habits of each type of consumers. As a module in data mining, it can be used as a separate tool to discover some deep information distributed in the database and summarize the characteristics of each category. The methods of cluster analysis can be divided into hierarchical analysis and nonhierarchical analysis.

The analytic hierarchy process can be divided into two different methods: agglomeration type and branch type. The agglomeration type is to agglomerate similar samples one by one and finally aggregate them into several different categories. The branch type is the opposite. It starts to think that all the samples are of the same class and then divides them one by one and finally divides all the samples into several different classes. Here, we use an agglomerative clustering method to cluster the indicators.

Consider each of the m metrics as a category. For example, if there are indicators $\{A_1, A_2, \cdots A_m\}$ and r answer sheets, the indicators A_m are, respectively, represented by vectors in the dimension space, as shown in

$$A_m = \{a_{m1}, a_{m2}, \cdots a_{mr}\}^T. \tag{1}$$

Use D_{ij} to represent the distance between two classes, as in

$$D_{ij} = \left|A_i - A_j\right| = \sqrt{\sum_{a=1}^{r} \left(A_{ia} - A_{ja}\right)^2}. \tag{2}$$

The distance matrix is listed in Table 1.

Table 1: Distance matrix.

	A_1	A_2	…	A_m
A_1	1	D_{12}	…	D_{1m}
A_2		1	…	D_{2m}
…			1	…
A_m				1

Select the smallest distance in the distance matrix, and combine these two categories to form a new variable A_{m+1}, as shown in

$$A_{m+1} = \frac{1}{2r}\left(A_{i1} + A_{j1}, A_{i2} + A_{j2}, \cdots, A_{im} + A_{jm}\right). \tag{3}$$

Repeat step 2 until all indicators are merged into one category, and on this basis, the hierarchical structure of cluster analysis is shown in Figure 1. In Figure 1, the vertical axis represents the category of the samples and the horizontal axis represents the distance between the categories.

4.2. Principal Component Extraction. When we analyze and process the evaluation data, because there are too many indicators and there is a certain correlation between them, the information reflected by the observed data overlaps to a certain extent. And when the number of answer sheets is large, it becomes complicated to study the distribution law of answer sheets in high-dimensional space. Here, we apply principal component analysis to extract key indicators and replace more original variables with fewer comprehensive variables, and these comprehensive variables can reflect the information of the original variables as much as possible and are not related to each other. There are many factors considered in the questionnaire, so the extraction of principal components is considered. First enter the answer sheet value matrix, such as

$$X = \begin{bmatrix} X_{11} & \cdots & X_{1r} \\ \vdots & \ddots & \vdots \\ X_{m1} & \cdots & X_{mr} \end{bmatrix}. \tag{4}$$

For given m samples, find the correlation coefficient between samples. Each element in the correlation matrix is represented by the corresponding correlation coefficient, as shown in

$$S_j = \sqrt{\frac{1}{m-1}\sum_{i=1}^{m}\left(X_{ij} - \bar{X}_j\right)}, \quad j = 1, 2, \cdots, r, \tag{5}$$

where X_{ij} is shown in

$$\bar{X}_j = \frac{1}{m}\sum_{i=1}^{m} X_{ij}. \tag{6}$$

Then, calculate the sample correlation matrix; first assume

$$y_{ij} = \frac{X_{ij} - X_j}{S_j}, \tag{7}$$

$$Y = \left(y_{ij}\right)_{m\times r}. \tag{8}$$

Formula (9) can be obtained by calculation:

$$r_{ij} = \frac{1}{m-1}\sum_{i=1}^{m}\frac{\left(X_{ij} - X_j\right)}{S_j} * \frac{\left(X_{ik} - X_k\right)}{S_k}. \tag{9}$$

So we have to standardize the data array, as in

$$R = \left(r_{ij}\right)_{r\times r}. \tag{10}$$

According to the obtained eigenvectors, the principal components are shown in

$$y_m = a_{m1}x_1 + a_{m2}x_2 + \cdots + a_{mr}x_r. \tag{11}$$

Among the m principal components, the sum of the contribution rates of the previous q principal components is α, as shown in

$$\alpha = \frac{\sum_{i=1}^{q}\lambda_i}{\sum_{i=1}^{m}\lambda_i}, \tag{12}$$

where λ_i is the i-th principal component. When $\alpha > 85\%$, it can be considered that the principal components can represent all the information of the original data, so the q principal components selected in this article are shown in

$$Z_j = a_{1j}y_{j1} + \cdots + a_{rj}y_{jr}. \tag{13}$$

The selected first q principal component sample values are shown in

$$Z_{ij} = \sum_{i=1}^{r} y_{ij}a_{ij}. \tag{14}$$

By repeating this process, the principal component indicators that play a leading role, which are less than the original number of indicators, can be extracted from each type of indicators.

4.3. Rough Set Attribute Reduction Algorithm. The rough set attribute reduction algorithm only selects the conditions with high attribute importance to add to the reduction and does not consider the redundancy between the conditional attributes in the reduction. The reduction is often not necessary; that is, it contains redundant attributes. The rough set attribute reduction algorithm makes full use of the theoretical knowledge of rough sets. We can make assumptions like this: suppose to delete a certain set of attributes in the data and then judge the importance of this set of attributes by observing the decision set. When a group of attributes is deleted, the decision set does not change, and the importance of this group of attributes is not significant. However, when a certain group of attributes is deleted, the decision set has changed, and the group of attributes plays a great role [15].

The C set represents conditional attributes, and the division of U generated by R_C is defined as

$$\frac{U}{R_C} = \{C_1, C_2, \cdots, C_I\}. \tag{15}$$

For the knowledge system S, the D set represents the decision attribute; then, define a binary equivalence relation R_D of D, as shown in

$$xR_Dy \Leftrightarrow f_j(x) + f_j(y), \quad \forall d_j \in D. \tag{16}$$

Then, the division of U generated by R_D is defined as

$$\frac{U}{R_D} = \{D_1, D_2, \cdots, D_J\}. \tag{17}$$

Next, use $\mathrm{POS}_C(D)$ as the positive domain of the condition attribute set C of the decision attribute set D, as shown in

$$\mathrm{POS}_C(D) = \bigcap_{J=1}^{J} R_C\left(D_J\right). \tag{18}$$

Define γ to satisfy

$$\gamma_C(D) = \frac{\left|\mathrm{POS}_C(D)\right|}{|U|}. \tag{19}$$

Therefore, the importance of a certain attribute subset C_1 with respect to D is defined as

$$\sigma_{CD} = \gamma_C(D) - \gamma_{C-C_I}(D). \tag{20}$$

5. The Development of Business English from the Perspective of the Internet of Things Business Model

5.1. Introduction of Related Technologies

5.1.1. Internet of Things. The Internet of Things itself represents the development direction of the next generation of information technology, but the Internet of Things is not a new concept. Some remote automation control applications in the early last century can be regarded as the prototype of the Internet of Things application [16–18]. So far, there have been more and more research results on the theory of the Internet of Things in academia. The application field of the Internet of Things involves all aspects, and the application in infrastructure fields such as industry, agriculture, environment, transportation, logistics, and security has effectively promoted the intelligent development of these aspects,

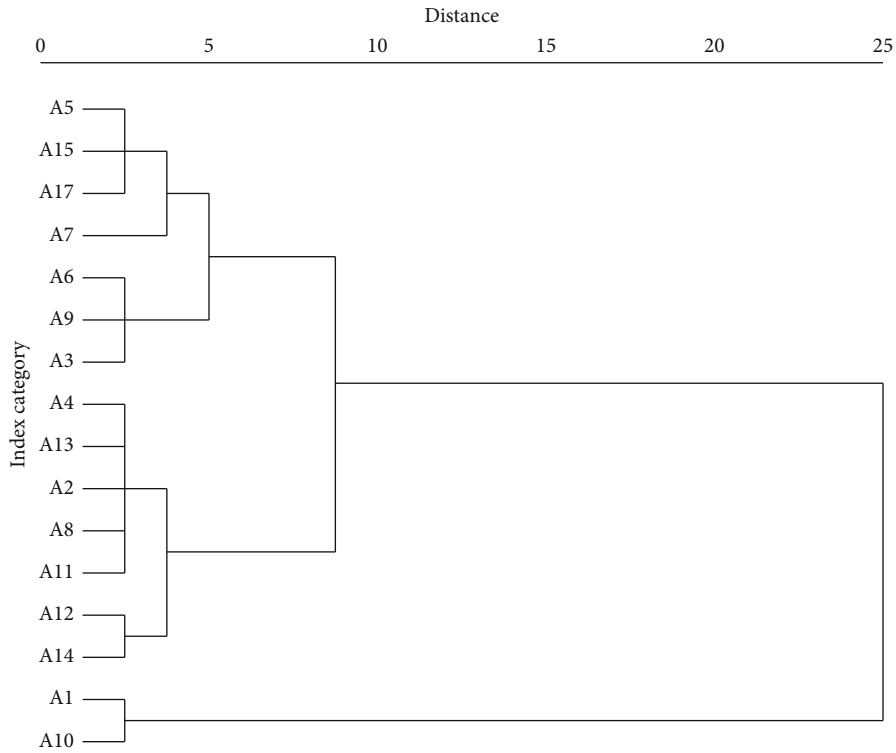

Figure 1: Results of cluster analysis of indicators by the shortest distance method.

making the limited resources more reasonable, thereby improving the efficiency and effectiveness of the industry. In short, the Internet of Things is a new type of information-based intelligent technology that connects various sensors with the Internet.

According to the definition of the Telecommunication Standardization Sector of the International Telecommunication Union, the Internet of Things (IoT) is an infrastructure that provides information transmission services [19, 20]. It provides interconnection services for interconnecting physical and virtual objects on a global scale based on existing communication technologies [21, 22]. According to the definition of ISO/IEC/JTC1WG10, the Internet of Things is an infrastructure that connects objects, people, systems, and information systems and can intelligently process and respond to information in the physical and virtual worlds. The content of the latter is an expansion of the former, but its core connotation is the same. That is to say, the Internet of Things is initiated and transmitted by things actively, transmits all kinds of perceived information in real time through the network, and uses computer technology to timely control the information of massive data, so as to achieve the Internet that communicates between people and things and things and things. Its development is shown in Figure 2.

In Figure 2, we can see that the development of the Internet of Things is inseparable from the development of the Internet. In the era of 2G and 3G, there is no concept of the Internet of Things. Even if there is, the network at that time is not enough to support the Internet of Everything. In the 4G era, the speed of the network has been very fast, and the concept of the Internet of Things has become more and more familiar to more and more people. Now, entering the 5G era, not only has the technology of the Internet of Things been greatly developed but also its network transmission protocol has reached global unity, which means that the Internet of Everything is no longer science fiction. Table 2 shows the bearer methods and applications of the Internet of Things.

5.1.2. Business Model. The term business model was first proposed in the 1950s. After entering this century, the business model began to be discussed more widely. On the one hand, most discussions on business models are not academic in nature; on the other hand, the views of industry practitioners are rarely adopted in academic research. This has also led to huge differences in the definition of the term business model among academics and industry practitioners. The definition of the business model can be roughly summarized as how one party in the market produces a certain commodity or service and provides it to another party in the market in order to obtain some form of return [23]. Although the definition of the business model has not yet reached a consensus in academia and industry, this paper summarizes and refines on the basis of consulting various different theories the common business model characteristic elements from different theories.

After comparing and analyzing the business model definitions from different perspectives as shown in Figure 3, this paper gives the business model definition from the network perspective of system integration. That is, the business model refers to, in order to maximize customer value, integrate

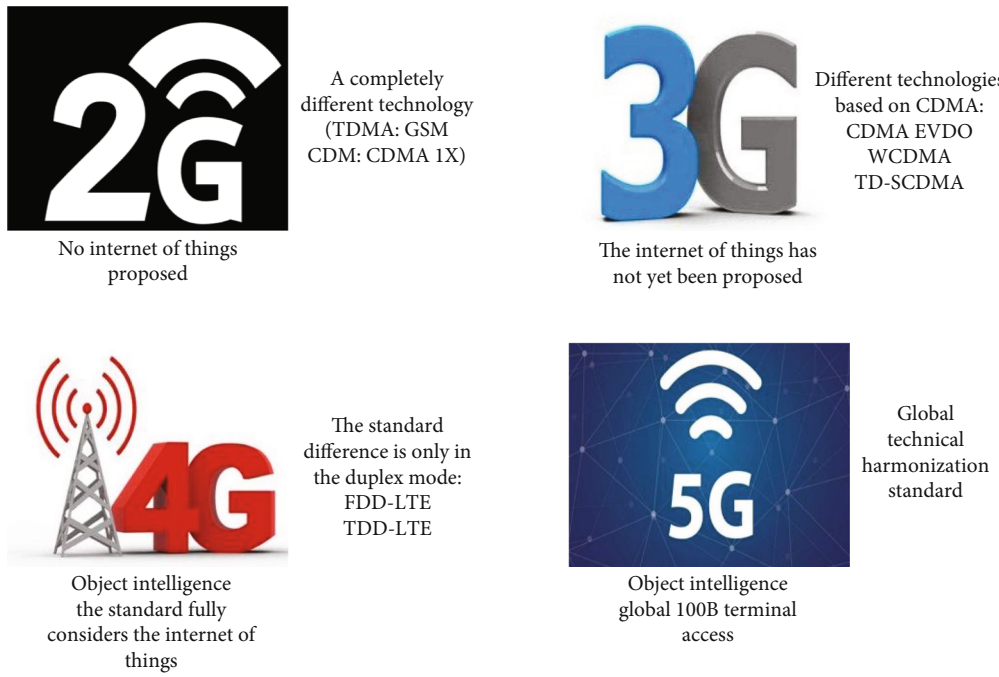

Figure 2: The development trend of the Internet of Things.

Table 2: Trends of Internet of Things bearing modes.

Market segmentation	Related applications	Application characteristics
3%	HD video	Ultrahigh ARPU value
12%	Video surveillance, medical care, smart city	High ARPU value
25%	Smart homes, smart buildings, Internet of vehicles, M2M nodes	Middle and low ARPU
60%	Public utilities, industry monitoring, wearables, device tracking, sensing	Low ARPU

various resources and capabilities inside and outside the organization, and form an efficient operation system with unique core competitiveness, an overall solution designed by an organization that ultimately realizes value in the form of products or services to achieve sustainable profit goals.

The business model is the process of realizing enterprise value. The business model carries the entire process of an enterprise from the initial idea or product prototype to the product entering the market and finally being purchased by consumers and generating profits. Studying the business model of the enterprise will help the enterprise to identify target customers, optimize the product structure, improve the utilization efficiency of enterprise resources, improve the service level of the enterprise, and optimize the combination of sales channels, create good customer relationships, optimize customer experience, reduce production costs, and optimize corporate organizational structure.

The research on the constituent elements of the business model plays an important role in the modeling of the business model, and the conceptual model of the business model can guide business model innovation in the corporate world. Therefore, it is necessary to conduct in-depth research on the constituent elements of the business model. Based on a large number of studies of relevant domestic and foreign literature, this paper summarizes the existing research results on the components of business models, as shown in Figure 4.

In Figure 4, from 1996 to 2012, the researches related to business models are selected for analysis each year. It can be found that the research on business models is more about e-commerce types and less about other types of enterprises.

Among them, Larcher et al. [24] proposed that the business model mainly contains four key elements. They are value proposition, key process, key resource, and profit model, and they can create and transmit value in the process of interaction.

The four-element theory of the business model is shown in Figure 5, which is mainly composed of the following four modules:

Customer value proposition: customer value proposition refers to the way a company generates value for customers and determines how far the company can develop in the future.

Profit model: the profit model refers to the way in which the enterprise can bring value to customers and at the same time realize its own profit.

Key resources: key resources refer to key resources such as technology, equipment, products, and personnel required to create value for customers.

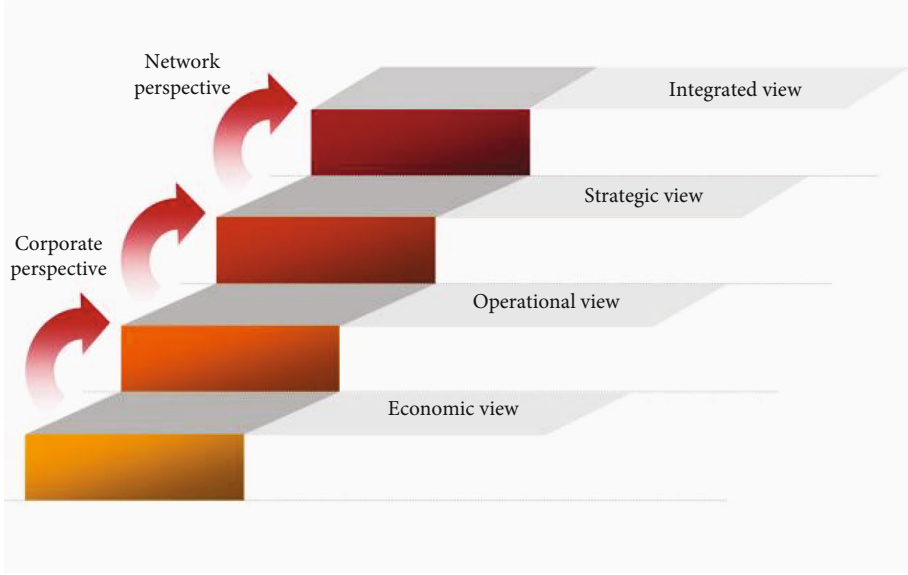

Figure 3: Business model definition development trajectory.

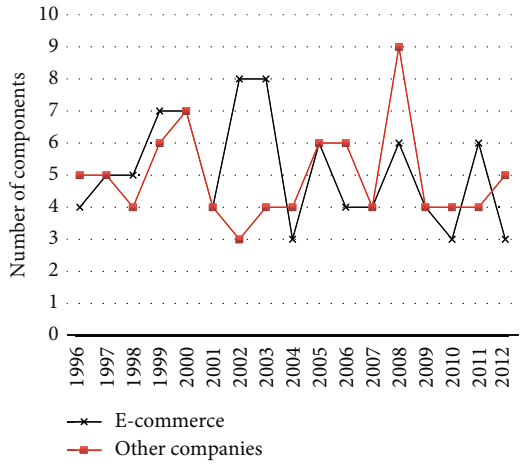

Figure 4: Elements of related research business models.

Key process: the key process refers to the safeguard measures and processes required by the enterprise to create value for customers, including a series of internal systems and processes within the enterprise, including research and development, production, sales, after-sales, performance appraisal, and system specifications.

Prendeville et al. [10] put forward the famous "smile curve" theory and used it as Acer's corporate development strategy. They proposed that if an enterprise wants to achieve long-term development in the fierce market competition, it must give up low value-added work and transfer its energy and resources to high value-added work. If the added value of the entire product life cycle is plotted, it looks like the mouth shape of a smile, so this theory is called the "smile curve" theory. Through the perspective of the "smile curve," enterprises can clearly know their own position in the value chain and then provide some references for the long-term development of enterprises [25].

As shown in Figure 6, observing the schematic diagram of the "smile curve" can be found: the middle of the curve is the manufacturing part, the value generated is relatively low, and it belongs to the low value-added area. On the left is the R&D and technology part, which generates relatively high value and belongs to the high value-added area. On the right is the sales and service segment, which generates relatively high value and is also classified as a high value-added area. It can be clearly seen from Figure 6 that if a company wants to expand its own value, it should try to extend in the direction of both ends of the "smile curve." That is, on the one hand, it extends to the left to expand its technological advantages, and on the other hand, it extends to the right to improve the experience brought by the service.

5.1.3. IoT Business Model. The formation and development of any IoT business model are closely related to external environmental factors including political, legal, economic, social, and technological factors. Among them, the policy and legal environment provides healthy and stable operating conditions for the business model. The economic environment provides capital and material guarantees for the operation of business models and is the source of profits. The social environment sets the direction for the development of business models to meet changing social needs. The technological environment is the fundamental driving force for the improvement and innovation of business models.

6. Higher Vocational Business English Course System

6.1. Survey on the Current Situation of the Business English Curriculum System in Higher Vocational Colleges. Only by clarifying the current situation of the business English curriculum system in higher vocational colleges can the improvement strategies of the higher vocational business English curriculum system be effectively proposed and

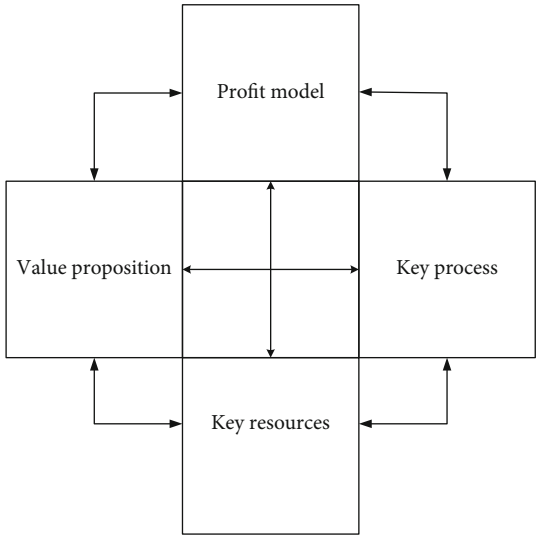

Figure 5: Four elements of a business model.

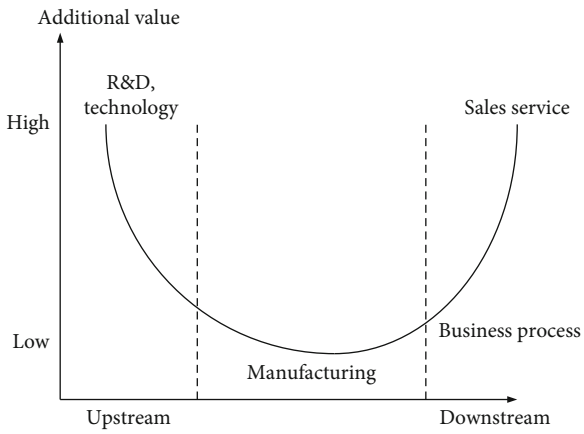

Figure 6: "Smile curve."

implemented from the perspective of the business model of the Internet of Things. Through the sample survey, we objectively understand the actual state of the business English curriculum system in higher vocational colleges and take the hotel management undergraduate curriculum system indicators from the perspective of the Internet of Things business model constructed in this paper as the expected state. The two are compared, and the ways and methods to improve the current situation of the business English curriculum system in higher vocational colleges are discussed through the perspective of the business model of the Internet of Things.

According to the above index system, through the questionnaire design, the designed questionnaire consists of four major parts, namely: personal basic information, course objectives, course implementation, and course evaluation, with a total of 15 questions. The question format is based on single choice. The specific composition of the questionnaire content is as follows.

The first part is basic personal information. A total of 3 questions are designed in this part, including the subject's major, batch type, and grade.

The second part is "course objectives." According to the index system constructed in this paper, four topics are designed in this part, mainly involving "knowledge and skill goals" and "emotion goals." Through these topics, try to understand the teaching results of "knowledge and skill goals" and "emotional goals" in higher vocational business English teaching.

The third part is "course implementation." According to the index system constructed in this paper, four topics are designed in this part, mainly involving "hardware conditions" and "software conditions." Through these questions, try to understand the construction and use of "hardware conditions" and "software conditions" in business English teaching in higher vocational colleges.

The fourth part is "course evaluation." According to the index system constructed in this paper, four topics are designed in this part, mainly involving "teaching evaluation" and "course evaluation." Through these questions, try to understand the design and implementation of "teaching evaluation" and "course evaluation" in higher vocational business English teaching.

The details are shown in Table 3.

Before obtaining primary research data by means of a questionnaire, a test is required. First, after the first draft of the questionnaire is completed, the expert group is asked to review it to determine whether the questionnaire has face validity and content validity. Cronbach's coefficient is a statistic that refers to the average of the half-half reliability coefficients obtained by all possible item division methods of the scale. It is the most commonly used reliability measurement method. Usually the value of the Cronbach coefficient is between 0 and 1. If the coefficient does not exceed 0.6, it is generally considered that the internal consistency reliability is insufficient; when it reaches 0.7-0.8, it means that the scale has considerable reliability, and when it reaches 0.8-0.9, it means that the reliability of the scale is very good. After verification, the overall coefficient of this student questionnaire is shown in Table 4. Therefore, through the test of the test results, the questionnaire has certain reliability and validity.

The methods of the questionnaire survey are the distribution of online questionnaires and the actual distribution of surveys. The subjects of the survey are the first-, second-, and third-year students from three higher vocational business English majors. A total of 400 questionnaires were distributed, all of which were recovered, the recovered questionnaires were screened roughly, blank answers and those with blank basic information were regarded as invalid questionnaires, 17 invalid questionnaires were excluded, and 383 valid questionnaires were finally obtained, with an effective rate of 95.75%, as shown in Figure 7.

6.2. Investigation Results

6.2.1. Analysis of the Current Situation of Curriculum Objectives. According to Figure 8, it can be seen that although colleges and universities pay more attention to the teaching of knowledge and skills, they are not perfect in the teaching of knowledge application and skills, and

Table 3: Questionnaire setting table.

Course objectives	Knowledge and skill objective A1	① excellent, ② good, ③ fair, ④ poor, ⑤ very bad
	Complete, basic system operation skills A2	① excellent, ② good, ③ fair, ④ poor, ⑤ very bad
	Harmonious communication between teachers and students A3	① excellent, ② good, ③ fair, ④ poor, ⑤ very bad
	Interested in learning and enterprising A4	① excellent, ② good, ③ fair, ④ poor, ⑤ very bad
Course implementation	Make full use of professional operating system B1	① excellent, ② good, ③ fair, ④ poor, ⑤ very bad
	Make full use of teaching laboratory B2	① excellent, ② good, ③ fair, ④ poor, ⑤ very bad
	Industry is deeply involved in B3 in terms of teaching resources	① excellent, ② good, ③ fair, ④ poor, ⑤ very bad
	Flexible use of teaching methods B4	① excellent, ② good, ③ fair, ④ poor, ⑤ very bad
Course evaluation	The teaching attitude is generous, the appearance is dignified, and he is a good teacher C1	① excellent, ② good, ③ fair, ④ poor, ⑤ very bad
	Teachers and students interact actively, and the atmosphere is active and orderly C2	① excellent, ② good, ③ fair, ④ poor, ⑤ very bad
	The quality of the teaching materials is high, and the lesson plans are well prepared C3	① excellent, ② good, ③ fair, ④ poor, ⑤ very bad
	Heuristic teaching, combining theory with practice C4	① excellent, ② good, ③ fair, ④ poor, ⑤ very bad
Basic information	School	A: school, B: school, C: school
	Professional	Fill in your major
	Grade	A: first grade, B: second grade, C: third grade

Table 4: Cronbach's coefficient of the test results of the student questionnaire.

Variable	Cronbach's alpha	Number of items
Overall reliability of the questionnaire	0.897	12
Course objectives	0.91	4
Course implementation	0.784	4
Course evaluation	0.69	4

more research needs to be done in practical teaching. Learning interest and enterprising spirit determine to a certain extent students' love for hotel management major. The degree of harmony between teachers and students affects the teaching effect in the classroom. Although it has paid attention to the cultivation of students' interest and initiative in learning and the maintenance of teacher-student relationship, there is still room for improvement. In terms of knowledge and skill transfer, the implementation effect of practical teaching and application ability training is not good. In terms of emotional goals, there is room for improvement in the enhancement of students' professional interest.

6.2.2. Analysis of the Current Situation of Curriculum Implementation. As can be seen from Figure 9, in the teaching process, teachers will teach the course content in combination with industry needs and hotspots of the times, but they are not fully integrated and the degree of integration is relatively shallow. Therefore, in the teaching process, in addition to the teaching materials as the center, more supplements should be supplemented by industry needs and frontier knowledge of disciplines. In the teaching process, the participation of teachers and talents in colleges and universities is not enough. Even if there are excellent industry personnel to teach courses in colleges and universities, they are limited to the sharing of industry experience and experience, and their participation in courses and teaching needs to be deepened. And in the teaching process, there are few types of teaching methods used, and the scope of application is not wide enough, which needs to be further strengthened. In terms of hardware conditions, the use of professional operating systems is not sufficient, and the construction and use of teaching laboratories need to be improved. In terms of software conditions, in the construction of teachers' team, the degree of industry participation is low, and the degree of integration between the teaching content of industry teachers and the teaching objectives of actual courses is low. The use of teachers' teaching methods needs to be improved.

6.2.3. Analysis of the Current Situation of Course Evaluation. As can be seen from Figure 10, in the teaching process, the problem of emphasizing theory over practice still exists, and it is not optimistic. And in the classroom, the teaching of professional content is the main method, and the proportion of training students' comprehensive quality is relatively low. In terms of course content, the degree of integration with industry needs and the updating of cutting-edge knowledge are insufficient. In terms of curriculum structure, insufficient attention is paid to the proportion of practical curriculum and the cultivation of students' comprehensive quality.

6.3. Countermeasures and Suggestions for the Higher Vocational Business English Course System Based on Analysis Results. In the aspect of goal expression, it should be clear, including not only the content to be learned but also the degree of learning that should be achieved. Clear

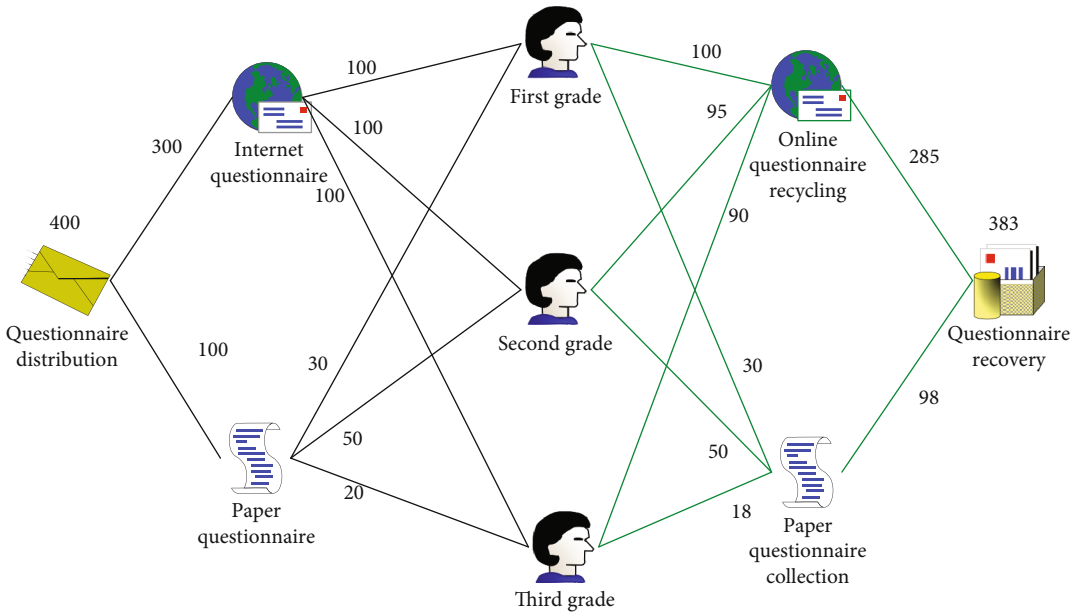

Figure 7: Schematic diagram of questionnaire distribution and recovery.

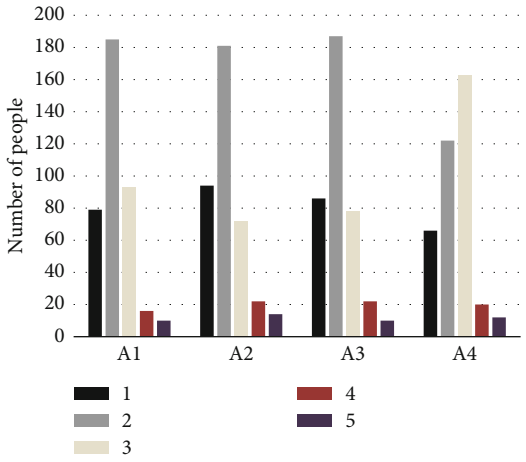

Figure 8: Analysis of the current situation of curriculum objectives.

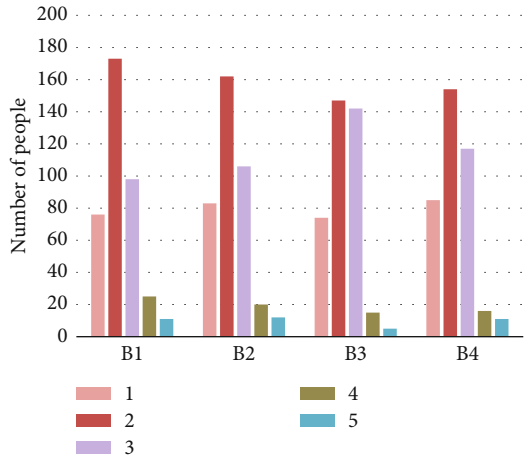

Figure 9: Analysis of the current situation of curriculum implementation.

and unambiguous presentation of course objectives is the foundation of effective teaching.

In the course of curriculum setting, while fully considering the subject standard, we should also consider the industry demand standard and combine the two effectively to ensure the scientific nature of the curriculum setting. Changing the matching mode of practical and theoretical courses creates more opportunities for applying theory to practice and then rise to theory and avoid the phenomenon of low efficiency of practical courses. While cultivating students' professional ability, they should also pay attention to their own development and improve their comprehensive ability.

During the implementation of the course, the construction of the teaching laboratory should be improved and the opportunities for use should be increased, so that students can fully practice and improve the learning effect of students. The industry's participation in college teaching should not be limited to excellent staff teaching work experience in colleges and universities, and the industry experience and knowledge acquired by the industry should be fully integrated into the course teaching. It should really effectively use a variety of teaching methods, not mere formality, and take the improvement of teaching effect as the test standard.

7. Conclusions

The development of technology will enrich people's lives, but the development of education is what really needs long-term development. In the context of global interconnection, business English majors have great employment opportunities and have developed by leaps and bounds. This article is based on the research on the curriculum system of business English majors in higher vocational colleges from the perspective of the business model of the Internet of Things. This article first introduces the background and

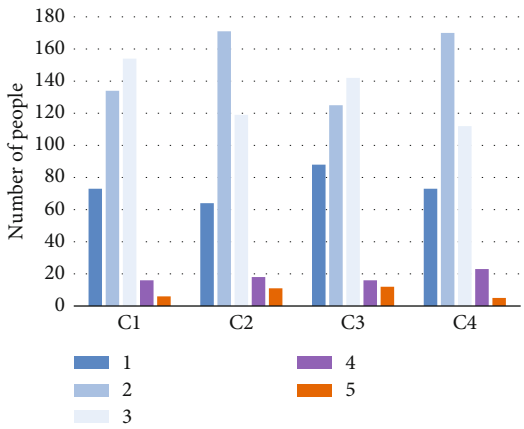

Figure 10: Analysis of the current situation of course evaluation.

significance of this article and then analyzes the domestic and foreign research on the business model of higher vocational education and the Internet of Things. After that, the important concepts of this article, business English, courses, etc. will be introduced. Then, the questionnaire analysis algorithm proposed in this paper is introduced in detail, combined with cluster analysis, principal component analysis, and rough set attribute reduction algorithm. Afterwards, it explains the business model of the Internet and analyzes it in conjunction with the business English major. Finally, the course design of business English is investigated and analyzed. The analysis results suggest that the current higher vocational business English education still needs to introduce talents and develop more practical courses. At the same time, this paper also has some shortcomings, mainly because the survey in this paper is only for the student group, and the follow-up research can add interviews and increase the investigation and analysis of teachers and school leaders.

Data Availability

The data that support the findings of this study are available from the corresponding author upon reasonable request.

Conflicts of Interest

The author declared no potential conflicts of interest with respect to the research, authorship, and/or publication of this article.

References

[1] T. Grubljesic, P. S. Coelho, and J. Jaklic, "The shift to socio-organizational drivers of business intelligence and analytics acceptance," *Journal of Organizational and End User Computing*, vol. 31, no. 2, pp. 37–64, 2019.

[2] Y. Sun, H. Song, A. J. Jara, and R. Bie, "Internet of things and big data analytics for smart and connected communities," *IEEE Access*, vol. 4, pp. 766–773, 2016.

[3] G. Alwis, C. Linden, S. Stenevi-Lundgren et al., "A school-curriculum-based exercise intervention program for two years in pre-pubertal girls does not influence hip structure," *Dynamic Medicine*, vol. 7, no. 1, pp. 1–8, 2008.

[4] G. Tan-Sisman and Y. Karsantk, "Curriculum development in Singapore and Turkey: reflections of administrative structure and educational reforms," *Bartın Üniversitesi Eğitim Fakültesi Dergisi*, vol. 10, no. 1, pp. 109–130, 2021.

[5] A. C. Kalungia, L. T. Muungo, S. Marshall, B. Apampa, C. May, and D. Munkombwe, "Training of pharmacists in Zambia: developments, curriculum structure and future perspectives," *Pharmacy Education*, vol. 19, no. 1, pp. 69–78, 2019.

[6] W. Stubbs and B. Characterising, "Characterising B Corps as a sustainable business model: an exploratory study of B Corps in Australia," *Journal of Cleaner Production*, vol. 144, pp. 299–312, 2017.

[7] F. Cosenz, "Supporting start-up business model design through system dynamics modelling," *Management Decision*, vol. 55, no. 1, pp. 57–80, 2017.

[8] S. Nikou and H. Bouwman, "Mobile health and wellness applications," *International Journal of E-Business Research (IJEBR)*, vol. 13, no. 1, pp. 1–24, 2017.

[9] P. Lombardi and F. Schwabe, "Sharing economy as a new business model for energy storage systems," *Applied Energy*, vol. 188, no. FEB.15, pp. 485–496, 2017.

[10] S. M. Prendeville, F. O'Connor, N. Bocken, and C. Bakker, "Uncovering ecodesign dilemmas: a path to business model innovation," *Journal of Cleaner Production*, vol. 143, no. FEB.1, pp. 1327–1339, 2017.

[11] X. Li, X. Liu, Y. Li et al., "Human activity recognition based on the inertial information and convolutional neural network," *Journal of Biomedical Engineering*, vol. 37, no. 4, pp. 596–601, 2020.

[12] R. Santhoshkumar, M. K. Geetha, and J. Arunnehru, "SVM-KNN based emotion recognition of human in video using HOG feature and KLT tracking algorithm," *International Journal of Pure and Applied Mathematics*, vol. 117, no. 15, pp. 621–634, 2017.

[13] X. M. Wang, Z. Liu, and W. B. Ni, "Motion measurement and recognition method of human arm based on MEMS sensors," *Journal of Chinese Inertial Technology*, vol. 25, no. 6, pp. 701–707, 2017.

[14] P. Wang, "Research on sports training action recognition based on deep learning," *Scientific Programming*, vol. 2021, Article ID 6878, 8 pages, 2021.

[15] S. Chaudhary and S. Murala, "Deep network for human action recognition using Weber motion," *Neurocomputing*, vol. 367, no. Nov.20, pp. 207–216, 2019.

[16] J. Gulczyńska, "Controversies around the system, organisation and curriculum structure of secondary school education in Poland, in the years 1944–1948," *Biuletyn Historii Wychowania*, vol. 38, no. 38, pp. 283–299, 2019.

[17] Z. Lv, Y. Han, A. K. Singh, G. Manogaran, and H. Lv, "Trustworthiness in industrial IoT systems based on artificial intelligence," *IEEE Transactions on Industrial Informatics*, vol. 17, no. 2, pp. 1496–1504, 2021.

[18] Z. Lv and A. K. Singh, "Big data analysis of Internet of things system," *ACM Transactions on Internet Technology*, vol. 21, no. 2, pp. 1–15, 2021.

[19] Z. Lv, R. Lou, J. Li, A. K. Singh, and H. Song, "Big data analytics for 6G-enabled massive Internet of things," *IEEE Internet of Things Journal*, vol. 8, no. 7, pp. 5350–5359, 2021.

[20] M. Adil, M. A. Jan, S. Mastorakis et al., "Hash-MAC-DSDV: mutual authentication for intelligent IoT-based cyber-physical systems," *IEEE Internet of Things Journal.*, 2021.

[21] H. Kim, "Exploring the concept and content structure of 'academic Korean' within the KSL curriculum," *Multicultural Education Studies*, vol. 13, no. 1, pp. 91–118, 2020.

[22] C. W. Yu and K. J. Yoon, "Exploring the improvement directions of the 2015 revised physical education curriculum document structure," *Journal of Korean Society for the Study of Physical Education*, vol. 24, no. 1, pp. 1–15, 2019.

[23] J. L. Suárez-Domínguez and S. Jiménez-García, "The MEIF curriculum reform and the disciplinary structure of the curricula at the Universidad Veracruzana," *Revista Educación*, vol. 43, no. 1, pp. 113–134, 2019.

[24] A. Larcher, G. De Naeyer, F. Turri et al., "The ERUS curriculum for robot-assisted partial nephrectomy: structure definition and pilot clinical validation," *European Urology Supplements*, vol. 18, no. 6, pp. e2617–e2619, 2019.

[25] L. Piscicelli, G. Ludden, and T. Cooper, "What makes a sustainable business model successful? An empirical comparison of two peer-to-peer goods-sharing platforms," *Journal of Cleaner Production*, vol. 172, pp. 4580–4591, 2018.

Hindawi
Wireless Communications and Mobile Computing
Volume 2022, Article ID 6855947, 11 pages
https://doi.org/10.1155/2022/6855947

Research Article

Equalization Network-Aided SCMA Codec Scheme with Deep Learning

Fang Jiang,[1,2] Xing Huang,[1] Shu-ping Jiang,[1] Yi Wang,[1,2] Yao-hua Xu ,[1,2] and Tian-yu Yin[1]

[1]*Key Laboratory of Intelligent Computing & Signal Processing (Anhui University), Ministry of Education, Hefei 230601, China*
[2]*Anhui Internet of Things Spectrum Sensing and Testing Engineering Technology Research Center, Hefei 230601, China*

Correspondence should be addressed to Yao-hua Xu; xyh@ahu.edu.cn

Received 18 September 2021; Revised 4 November 2021; Accepted 23 March 2022; Published 11 April 2022

Academic Editor: Junjuan Xia

With the rapid development of the Internet of Things, sparse code multiple access (SCMA), which aims to promote spectrum efficiency and support massive connectivity in the future beyond fifth- and sixth-generation massive machine-type communication (mMTC) scenarios, has been widely investigated. To improve the bit error rate (BER) performance of the SCMA system in the uplink Rayleigh fading channel, we propose a novel deep learning-based SCMA codec scheme. The proposed scheme consists of an equalization network-aided decoder network and a denoising autoencoder- (DAE-) based encoder network. At the decoder, an equalization network and a multiuser detection network constitute the decoder network. The equalization network, composed of two deep neural network (DNN) units, compensates for the phase shift of the signal through the fading channel, which improves the antifading capability of the system. At the encoder, a complete DAE is constructed, which introduces an extra noise layer at the input of the encoder that yields a robust encoder output representation, improving the antinoise capability of the system. We use an end-to-end training method to train the SCMA codec and optimize the parameters and structural model of the neural network. Simulation results show that our proposed scheme can reduce the detection time and improve the BER performance of the system in the uplink Rayleigh fading channel.

1. Introduction

With the widespread popularity of mobile intelligent devices and the rapid development of Internet of Things technology, there are new challenges to satisfying the customer quality of service (QoS), such as those associated with the massive connectivity of the number of terminal devices [1], communication network security [2], and complex channel environments [3]. To improve the spectrum efficiency and the number of connections under the massive machine-type communication (mMTC) scenarios of beyond fifth-generation/sixth-generation (B5G/6G) technologies, nonorthogonal multiple access (NOMA) plays an indispensable role in mobile communication systems.

NOMA was proposed for 5G wireless communications [4]. Sparse code multiple access (SCMA) [5] is a code domain multiplexing NOMA technology in NOMA schemes. In SCMA, the information bits of coding are directly mapped to the multidimensional complex grid nodes, which are called codeword maps. Thanks to the design of a multidimensional constellation and the combination of constellation rotation and the spread spectrum, codebooks for each user can be achieved. In addition, compared with the traditional code division multiple access (CDMA) [6] modulation and spread spectrum coding mode under the same number of time and frequency resources, the SCMA system transmits the user codewords in a nonorthogonal way on a time-frequency resource block. In this way, the reuse rate of resource blocks is greatly improved; thus, the system can be connected to multiple user devices.

An excellent SCMA communication system requires effective multiuser detection algorithms and optimal codebook design. The multiuser detection issue is also called decoding in the SCMA system. Using the message passing algorithm (MPA) [7] based on the Tanner graph is a general method to solve the decoding problem of SCMA, with the performance of the algorithm being close to that of maximum posterior probability decoding. However, the high

complexity index in the MPA operation and multiplication and the high hardware performance requirements render practical application of MPA difficult to achieve. To apply the SCMA system to practical engineering, it is necessary to study how to reduce the decoding complexity of SCMA [8–13], although some bit error rate (BER) performance is sacrificed in these schemes. This problem was also investigated in [14–17] to improve the BER performance of the system in terms of the BER performance of the Rayleigh fading channel. A suboptimal SCMA codebook design algorithm for an uplink Rayleigh fading channel was proposed [15], which reduces the multidimensional parent constellation design to a nonconvex optimization problem and expands two factors to achieve better coding gain. To further promote the application of SCMA systems in practical engineering, we study a whole codec scheme to address multiuser detection and optimal codebook design issues under a Rayleigh fading channel.

Due to the universality of artificial intelligence in various fields, recent studies have also begun to apply neural networks to communication systems [18–29]. For example, some studies were based on deep learning technology to deal with the signal detection problem of MIMO systems [22–24], and there were also studies using artificial intelligence (AI) technology in UAV networks [25–27]. In addition, new ways of thinking about communications as an end-to-end joint optimization of the communication system, which utilizes autoencoders to jointly learn transmitter and receiver implementations as well as signal encodings without any prior knowledge, were introduced in [30]. The application of this method for the physical layer to the SCMA system is realized in an SCMA scheme that proposes codeword generation and signal detection based on deep learning [31] and an intermediate density code division multiple access (MDMA) based on deep learning [32], the algorithm of which is represented by a new Tanner graph to achieve multiuser detection without iteration by adjusting the edge weights in the neural network. In [33], according to a new deep neural network (DNN) method for SCMA to reduce the computational complexity and improve the BER performance, the author proposes dense code multiple access based on deep learning. The SCMA decoder is designed as a classifier and detected by deep learning methods to reduce the detection complexity in [34]. These algorithms can achieve better BER performance than the traditional MPA multiuser detection method in the Gaussian channel, but the BER performance limitation problem in the uplink Rayleigh fading channel is still not solved.

This paper is aimed at solving the problem of poor BER performance of the SCMA system in the uplink Rayleigh fading channel and further promoting the use of the SCMA system in practical engineering. We propose an equalization network-aided SCMA codec scheme based on deep learning. By using multiple DNN units, we present the SCMA encoder, equalizer, and multiuser detection module, optimize both the encoding and decoding ends, and train in an end-to-end manner. In the decoder network, which is composed of equalization and multiuser detection subnets, the equalization subnet is used to learn the parameters of the Rayleigh fading channel and compensate for the signal because it is affected by the fading channel. Moreover, the SCMA encoder is constructed by several DNN units of the denoising autoencoder (DAE) structure, which is a codeword mapped to improve the robustness of the codebook generated by introducing an extra noise layer at the input end. We use an end-to-end approach to train and optimize the parameters and structural model of the neural network so that the neural network can converge quickly. Simulation results show that our proposed SCMA codec scheme can reduce the detection time of the receiver and improve the BER performance of the system in the uplink Rayleigh fading channel. We now summarize our major contribution as follows:

(1) Equalization network-aided SCMA decoder design: To enhance the multiuser detection performance in the Rayleigh fading channel, an equalization network-aided SCMA decoder is designed. Compared with the deep learning-aided SCMA (D-SCMA) decoder [31], the decoder is composed of three DNN units instead of a single DNN unit. An equalization network composed of two DNN units has also been added, and by learning the parameters of the Rayleigh channel and compensating for the signal, the BER performance and the training time performance can be more effectively improved

(2) Denoising autoencoder structure-based SCMA encoder design: To enhance the robustness of the codebook, we introduce an extra noise layer at the encoder input. In the training phase, adding an appropriate amount of noise to the source data can improve the antinoise performance of the neural network. Simulation results verify that the proposed encoder is superior to its counterparts

2. System Model

For the uplink SCMA system, we assume that the number of users in the SCMA system is J and the number of resource blocks is K. Due to the sparse structure of the system, the sparse code allocation for each user is extended to K resource blocks. The number of users $J > K$ such that the overload rate of the SCMA system is defined as $\lambda = J/K$. For example, the factor diagram matrix of the SCMA system is expressed as Equation (1). In light of the SCMA codebook design, $m = \log_2(M)$ bit data are sent each time, and the system encoder encodes them into a K-dimensional composite codeword where the sparse codeword has only N nonzero elements, with $N < < K$.

$$F = \begin{bmatrix} 1 & 0 & 1 & 0 & 1 & 0 \\ 0 & 1 & 1 & 0 & 0 & 1 \\ 1 & 0 & 0 & 1 & 0 & 1 \\ 0 & 1 & 0 & 1 & 1 & 0 \end{bmatrix}. \tag{1}$$

The complex codewords of 6 users are superimposed onto 4 resource blocks to realize the nonorthogonal superposition and transmission of signals. Each connection line between user j and resource block k can be seen as the coding mapping of each user on the resource block.

The codeword of user j can be written as $x_j = [x_{j1}, x_{j2}, \cdots, x_{jK}]^{\mathrm{T}}$, and the received signal y is expressed by the following formula:

$$y = \sum_{j=1}^{J} \mathrm{diag}(h_j) x_j + n, \tag{2}$$

where $h_j = [h_{j1}, h_{j2}, \cdots, h_{jK}]^{\mathrm{T}}$ is the channel gain between the user and the resource block and, in the Rayleigh fading channel, $h_j \sim CN(0, 1)$. diag $(\cdot)$ represents the logarithmic matrix, and the noise $n = (n_1, n_2, \cdots, n_K)^{\mathrm{T}}$ is the additive white Gaussian noise with a mean value of 0 and a variance of σ^2.

3. Proposed Scheme

In this section, we propose a codec scheme, namely, the equalization network-aided SCMA DAE system, referred to as EN-DAE-SCMA. The SCMA system structure of this scheme is shown in Figure 1, where the number of users is $J = 6$ and the number of time-frequency resource blocks is $K = 4$. Multiple DAEs are used to construct the encoding end of the system, with each DAE composed of DNN units. The user codebook is modulated by the DAE-based DNN units, where each DNN unit represents a codeword mapper, and then, the user codebook is connected to the resource block according to the original factor graph to obtain a complete SCMA codebook. The decoding end of the system consists of an equalization network and a multiuser detection network to decode each user's sent data.

The DNN contains many hidden layers that have stronger learning and training capabilities and mapping capabilities than single-layer neural networks. The calculation formula of the i-th neuron in each hidden layer can be expressed as follows:

$$z_i = f\left(\sum_{t=1}^{T} W_{t,i} \times v_t + b_i\right), \tag{3}$$

where z_i is the output data, v_t is the input data, $W_{t,i}$, b_i, and T are the weight, bias, and number of neurons, respectively, and $f(\cdot)$ represents the nonlinear activation function formula.

The main purpose of the EN-DAE-SCMA system is to reconstruct user data $s = [s_1, s_2, s_3, s_4, s_5, s_6]^{\mathrm{T}}$ through the designed encoding end and decoding end. After the user data are encoded, the received user signal is detected by the decoder through the fading channel and noise pollution, with the reconstructed user data being $\hat{s} = [\hat{s}_1, \hat{s}_2, \hat{s}_3, \hat{s}_4, \hat{s}_5, \hat{s}_6]^{\mathrm{T}}$, where $s \neq \hat{s}$. By optimization of the network to minimize the mean squared error between the reconstructed data and the original data, it can be expressed by the following formula:

$$\min_{\theta} (\|s - \hat{s}\| ; \theta), \tag{4}$$

where θ represents the set of weights and biases of the neural network of the entire system.

3.1. SCMA Encoder. To construct the encoding end of the EN-DAE-SCMA system, we make changes on the basis of the D-SCMA [20] encoder and introduce an extra noise layer at the input end. According to the factor graph, we use a DAE-based DNN unit to learn the mapping process for each edge connecting the user and the resource block to obtain the corresponding codeword. The DNN unit based on the DAE is called the SCMA codeword mapper. The structure of the codeword mapper is shown in Figure 2.

Since the input data transmitted by each user to the encoding end of the EN-DAE-SCMA system are expressed as r, r is the binary bit data, and there are m possible types of information, where $m = 2^b$, with b representing the number of bits per transmission, where $b = 2$. Binary input data are randomly generated and encoded into a one-hot vector, which is an M-dimensional vector s, where only one element is 1 and all the other elements are 0. The encoded one-hot vector is used as the input data of the encoding end. To make the codeword sparse, the user binary vector $S_j = (S_1, \cdots, S_{2K})^{\mathrm{T}}$ represents the SCMA mapping matrix corresponding to user j. The connection mode between the user and the resource block is determined by the SCMA factor matrix, which can be randomly generated according to the overload rate of the SCMA system.

Each DAE-based DNN unit autonomously learns the mapping process from a certain user to a certain resource block after receiving the user data and outputs a two-dimensional codeword that represents the real parts R and imaginary parts I of the complex codeword. Let $f_{kj}(s_j ; \theta_f)$ be the two-dimensional codeword mapped from resource k to user j, where s_j represents the original input data vector sent by user j to the neural network and θ_f represents the weight and bias of the EN-DAE-SCMA system encoder. The encoding end is based on a denoising autoencoder; that is, a noise layer is added after the input layer of each DNN unit. A certain proportion of noise is added to the input data to pollute the original user data s with noise. The data after passing through the noise layer can be expressed as follows:

$$\hat{s} = s + \varepsilon, \quad \varepsilon \sim N(0, \sigma^2 I). \tag{5}$$

After the data are polluted with noise, the two-dimensional codeword mapped from user j to resource k can be expressed as $f_{kj}(s_j ; \varepsilon ; \theta_f)$. The number of hidden layers of the codeword mapper of the encoder network is set to 3, i.e., $L = 3$, and each hidden layer contains 32 hidden nodes.

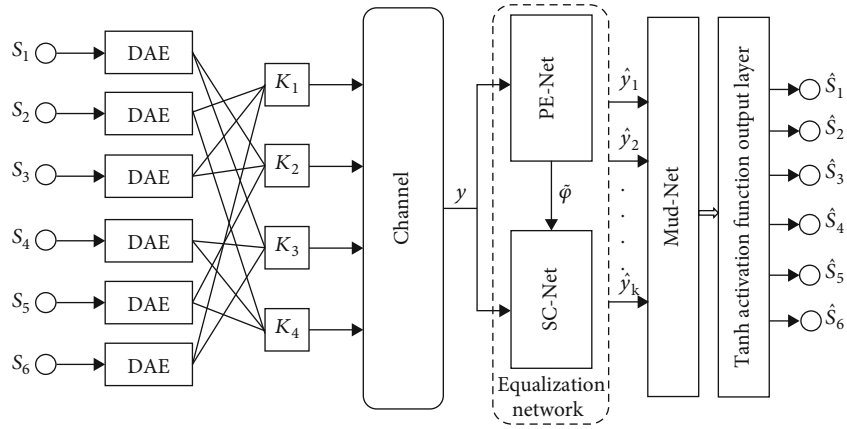

Figure 1: Equalization network-aided SCMA denoising autoencoder structure.

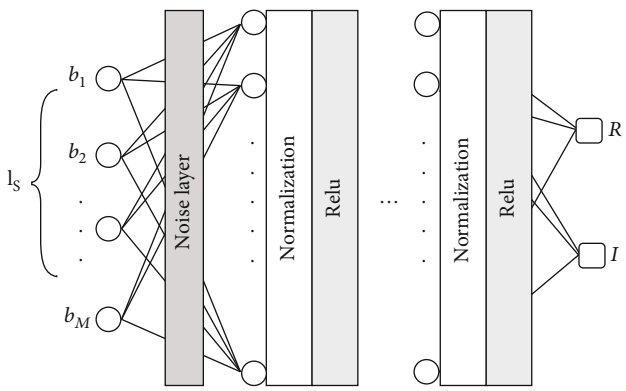

Figure 2: SCMA encoder structure.

The ReLU activation function is used in the hidden layer of the encoder network, and it can be expressed as follows:

$$f_{\text{Relu}}(x) = \max(0, x). \tag{6}$$

All the codewords sent on the same resource block are superimposed together and then transmitted by adding Gaussian white noise. Therefore, the data received on the resource block k are expressed as follows:

$$y_k = \sum_{j=1}^{J} h_{kj} f_{kj}(s_j; \varepsilon; \theta_f) + n_k, \tag{7}$$

where h_{kj} is the channel gain, each transmission is static, and n_k is the additive white Gaussian noise over the resource block k.

3.2. SCMA Decoder. The receiver decoder of the system consists of an equalization network and a multiuser detection network, in which the network architecture of the equalization network is inspired by the spatial transform network used in the field of computer vision (maintaining the spatial invariance of the input data). As shown in Figure 3, the equalization network function plays a similar role to the channel equalizer at the receiving end of the traditional SCMA transmission system. It is composed of two subnetworks, namely, the parameter estimation network $g_\varphi(\cdot)$ and the signal compensation network $g_\omega(\cdot)$. First, the phase offset φ generated by the fading channel is estimated through the parameter estimation network. Then, the received signal y and the estimated phase offset parameter φ are subjected to reversed-phase rotation processing through the signal compensation network to compensate for the signal. In this way, the output of the channel can be equalized, and the fading distortion of the signal can be overcome.

The parameter estimation network $g_\varphi(\cdot)\, z$ is a fully connected DNN whose input is the complex signal $y = [y_1, y_2, \cdots, y_K]^{\mathrm{T}}$ after passing through the channel, which is used to predict and process the Rayleigh fading channel parameter information and generate the output scalar $\tilde{\varphi}$. The network consists of two hidden layers and an output layer, and the number of neurons in the hidden layer is $2K$. The parameter estimation scalar obtained by the neural network is expressed as follows:

$$\begin{aligned}\tilde{\varphi} &= g_\varphi(\text{Re}(y), \text{Im}(y); \theta_1) \\ &= W_0 \tanh(W_2(\tanh(W_1(\text{Re}(y), \text{Im}(y)) + b_1))b_2) + b_0,\end{aligned} \tag{8}$$

where θ_1 represents the training parameters of the parameter estimation network, W_1, W_2 represent the weight matrix of the first layer and the second layer in the parameter estimation network, b_1, b_2 represent the bias vector of the first layer and the second layer in the parameter estimation network, and W_0, b_0 are the weight and bias of the output layer, respectively. The activation function in the hidden layer is the tanh activation function, which can be expressed as follows:

$$\tanh(W_l y_{l-1} + b_l) = \frac{\sinh(W_l y_{l-1} + b_l)}{\cosh(W_l y_{l-1} + b_l)} = \frac{e^{W_l y_{l-1} + b_l} - e^{-W_l y_{l-1} + b_l}}{e^{W_l y_{l-1} + b_l} + e^{-W_l y_{l-1} + b_l}}, \tag{9}$$

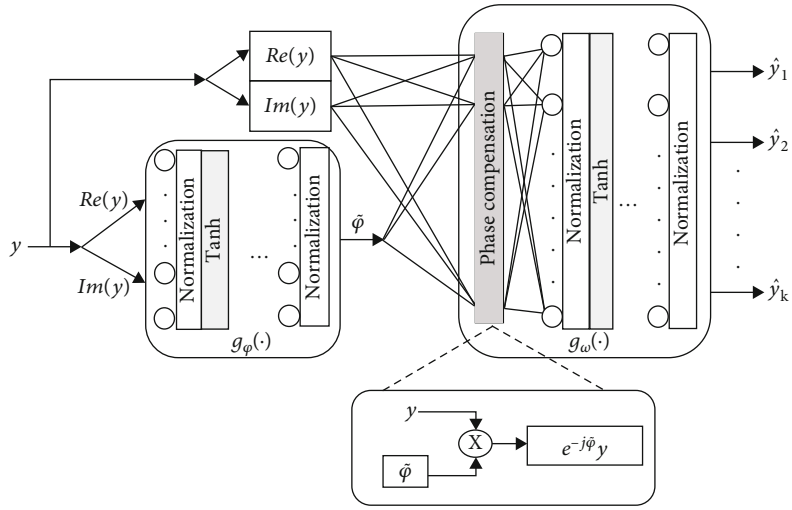

Figure 3: Equalization network.

where W_l and b_l represent the weight and bias of the l-th hidden layer, respectively, and y_{l-1} is the previous layer output.

The original received signal y and the output scalar $\tilde{\varphi}$ of the parameter estimation network $g_\varphi(\cdot)$ are sent to the input end of the signal compensation network $g_\omega(\cdot)$. A reversed-phase rotation operation is performed on the signal superimposed on each physical resource block and the output of the parameter estimation network; that is, the received signal is multiplied by the inverse transformation of the channel impulse response. The transformed signal μ is expressed as follows:

$$\mu = \begin{bmatrix} \cos(\tilde{\varphi})\,\mathrm{Re}(y) + \sin(\tilde{\varphi})\,\mathrm{Im}(y) \\ \cos(\tilde{\varphi})\,\mathrm{Im}(y) - \sin(\tilde{\varphi})\,\mathrm{Re}(y) \end{bmatrix} = e^{-j\tilde{\varphi}}y. \tag{10}$$

The transformed signal μ is further optimized through a DNN, and the output of the entire signal compensation network is the signal $\hat{y} = [\hat{y}_1, \hat{y}_2, \cdots, \hat{y}_K]^{\mathrm{T}}$ superimposed on each resource block to simplify the task of the multiuser detection network. The output $\hat{y}$ obtained after optimization by the signal compensation network $g_\omega(\cdot)$ is expressed as follows:

$$\hat{y} = g_\omega(\mu;\theta_2) = Q_0\mathrm{Tanh}(Q_L(\cdots\mathrm{Tanh}(Q_1(\mu)+a_1)\cdots)+a_L)+a_0, \tag{11}$$

where θ_2 is the weight and bias of the network, Q_l represents the weight matrix of the l-th layer in the signal compensation network, and a_l represents the bias vector of the l-th layer and the second layer in the signal compensation network. The activation function used in the hidden layer of the network is the tanh activation function, the number of hidden layers for the network is set to 3, and each hidden layer has 64 hidden nodes. Therefore, the channel output is equalized by an equalizing network to reduce the fading distortion problem in the fading channel.

Finally, we use a multiuser detection network instead of the MPA based on factor graphs in traditional algorithms to detect user information. The multiuser detection network $g_d(\hat{y};\theta_3)$ decodes the received output signal $\hat{y} = [\hat{y}_1, \hat{y}_2, \cdots, \hat{y}_K]^{\mathrm{T}}$ of the signal compensation network $g_\omega(\mu;\theta_2)$ and distinguishes the user data loaded in K resource blocks. θ_3 is the weight and bias of the network. The number of hidden layers of the network is set to 4, and the number of nodes in each hidden layer is 256. As shown in Figure 4, the rectified linear unit (ReLU) and tanh are the activation function of the hidden layer and the activation function of the output layer, respectively. Therefore, it is more appropriate to combine the mean squared error function since the value range of the tanh activation function is $[-1, 1]$.

The decoded data of the multiuser network can be expressed as follows:

$$\hat{s} = [\hat{s}_1, \hat{s}_2, \cdots, \hat{s}_6]^{\mathrm{T}} = g_d(\hat{y};\theta_3) = \sum_{k=1}^{K} g_d\left(\hat{y}_k;\theta_3^k\right). \tag{12}$$

3.3. Neural Network Training. The EN-DAE-SCMA system uses an end-to-end training method to update the weights and biases of all neural networks in the system and to establish an end-to-end mean squared error loss function:

$$\begin{aligned} L(s,\hat{s};\theta_f,\theta_1,\theta_2,\theta_3;\varepsilon) &= L\left(s, g\left(Hf(s;\theta_f;\varepsilon)+n;\theta_1,\theta_2,\theta_3\right)\right) \\ &= \frac{1}{N}\sum_{i=1}^{N}\left(s(i) - g\left(Hf(s(i);\theta_f;\varepsilon)+n;\theta_1,\theta_2,\theta_3\right)\right)^2. \end{aligned} \tag{13}$$

The mean squared error loss function averages the sum of the squared errors of the target value and the estimated value to reduce the sensitivity of sample data that deviate greatly. Here, $H = \sum_{k=1}^{K}\sum_{j=1}^{J} h_{kj}$ is the channel vector, and n is the channel noise vector.

Based on the characteristics of the EN-DAE-SCMA system, we use the adaptive moment estimation (ADAM)

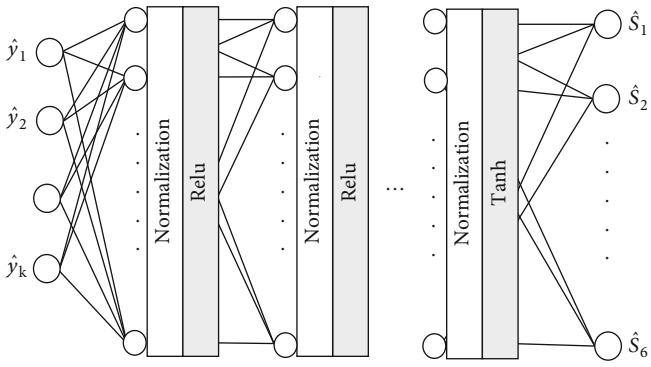

Figure 4: Multiuser detection network.

optimizer to update the network. The basic calculation expression is as follows:

$$\theta_t = \theta_{t-1} - \alpha \cdot \frac{\widehat{m}_t}{\sqrt{\widehat{\nu}_t} + \psi}, \tag{14}$$

where t is the momentum time step, $\widehat{m}_t$ is the deviation correction of the gradient mean, $\widehat{\nu}_t$ is the deviation correction of the square gradient, $\psi = 10^{-8}$ prevents the divisor from being 0, and the parameters are optimized by continuously updating m_t and ν_t.

In the training process, user data are randomly generated, and one-hot encoding is performed on the data, s, as the input data of the encoder, and is also the target value for the prediction of the entire neural network. Similarly, $\hat{s} = g(Hf(s(i); \theta_f; \varepsilon) + n; \theta_1, \theta_2, \theta_3)$, as the decoded data of the decoder, are also the estimated value of the entire neural network. At the same time, the training noise selected during neural network training has a greater impact on the BER performance of the system. The variance in the channel noise power is expressed as $\beta = E[|x|^2]/(\eta E_b/N_0)$, where $E[|x|^2]$ is the transmission signal power, E_b/N_0 represents the bit signal-to-noise ratio, and η represents the spectral efficiency. In the following text, we use enumeration to select the appropriate training noise.

4. Simulation Results

In this section, the performance of our proposed deep learning SCMA codec scheme is analyzed and verified through simulation experiments. The experimental environment of this paper uses TensorFlow, KERAS, and other deep learning libraries to conduct simulation experiments based on Python 3.7.6. The SCMA system carries out simulation experiments with 6 users occupying 4 resource blocks, and the codebook size is set as 4. In addition, each user data point takes 2 bits as a group for single thermal coding and codebook mapping. Since we use deep learning methods to adoptively learn the codebooks, the codebook design of each user does not follow a certain modulation mode, and the codebooks between users have great differences. The total dataset includes 300,000 random data points for training, and the data size of each batch is 400. The ADAM optimizer with an initial learning rate of 0.00001 is used to update the loss value of each sample with a gradient, and then, the weight and bias of the neural network are updated.

First, we study the influence of the number of encoder neural network hidden layers on the BER performance of the EN-DAE-SCMA codec scheme to seek a balance between BER performance and complexity. Figure 5 describes the influence of the number of layers of the encoder on the BER performance of the system under the channel environment of $E_b/N_0 = 8$ dB, $E_b/N_0 = 12$ dB, and $E_b/N_0 = 16$ dB. As the number of encoder layers increases, the BER performance improves, but it tends to converge after increasing to a certain number of layers. When the number of encoder layers reaches 3, the algorithm performance almost converges. Therefore, after the performance comparison of each algorithm, we set the number of encoder layers of the EN-DAE-SCMA system to 3.

Second, we aim to determine the impact of the input noise layer in the encoder on the BER performance of EN-DAE-SCMA. We use the standard deviation σ of the noise to represent the amount of noise added to the noise layer and carry out experiments under different E_b/N_0 values. As shown in Figure 6, the noise introduced by the input layer will have an impact on the performance of the system. When the noise standard deviation is $\sigma = 0$, which means no noise layer is added at the input, the BER performance is lower than the noise standard deviation $\sigma = 0.1$. However, as the noise increases, the BER performance begins to show a decreasing trend. If the neural network is trained by using noise-polluted data to learn some features of Gaussian noise, it can reduce the influence of Gaussian noise on the system to a certain extent. For the high noise in the low E_b/N_0 environment, the influence of the denoising network is very small, while the advantage of the denoising network is relatively obvious and shows better robustness for the low noise in the high E_b/N_0 environment. After many experiments and simulations, the optimal noise standard deviation σ of the noise layer added in the proposed EN-DAE-SCMA codec scheme proposed is 0.1.

To study the influence of neural networks trained under different channel noise levels on the BER performance of EN-DAE-SCMA, keeping the input noise layer of the encoder unchanged, we select different channel noise levels E_b/N_0 to train the system. As shown in Figure 7, regardless of the E_b/N_0 values chosen for training, the BER performance of EN-DAE-SCMA is similar in low testing E_b/N_0 environments. In high E_b/N_0 environments, when the values of training E_b/N_0 are set to 4 dB, 6 dB, and 8 dB, the BER performance is poor. When the values of training E_b/N_0 are set to 10 dB and 12 dB, the BER performance is obviously advanced, especially for the high E_b/N_0 regime. The experimental results show that the training channel noise level E_b/N_0 greatly affects the BER performance of EN-DAE-SCMA and that the proper value of training E_b/N_0 should be carefully selected in the training phase. Through many experiments, the suitable value of training E_b/N_0 is 10 dB, and the system trained in this E_b/N_0 environment has better generalization ability, as shown in Figure 7. However, we

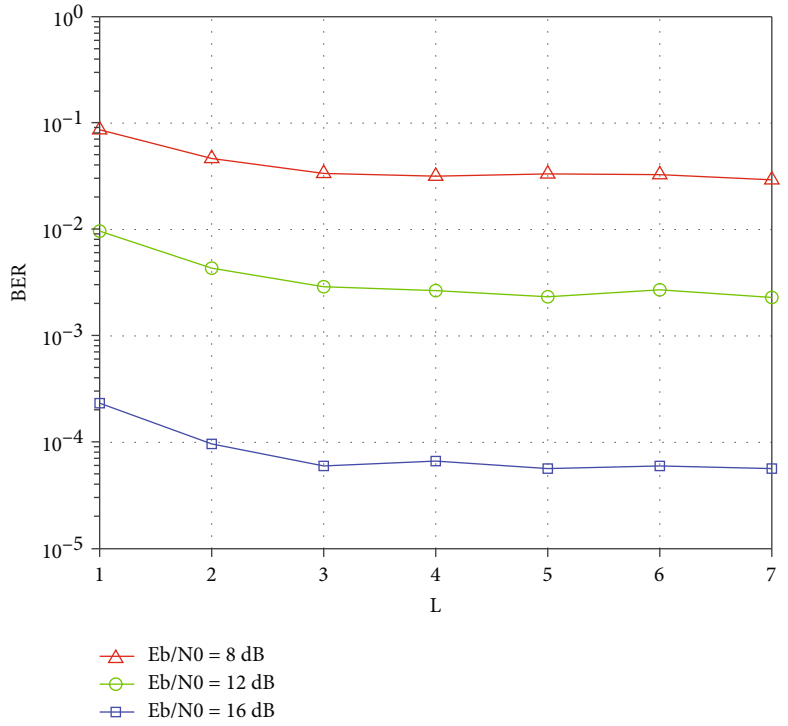

Figure 5: BER performance under different numbers of encoder network layers.

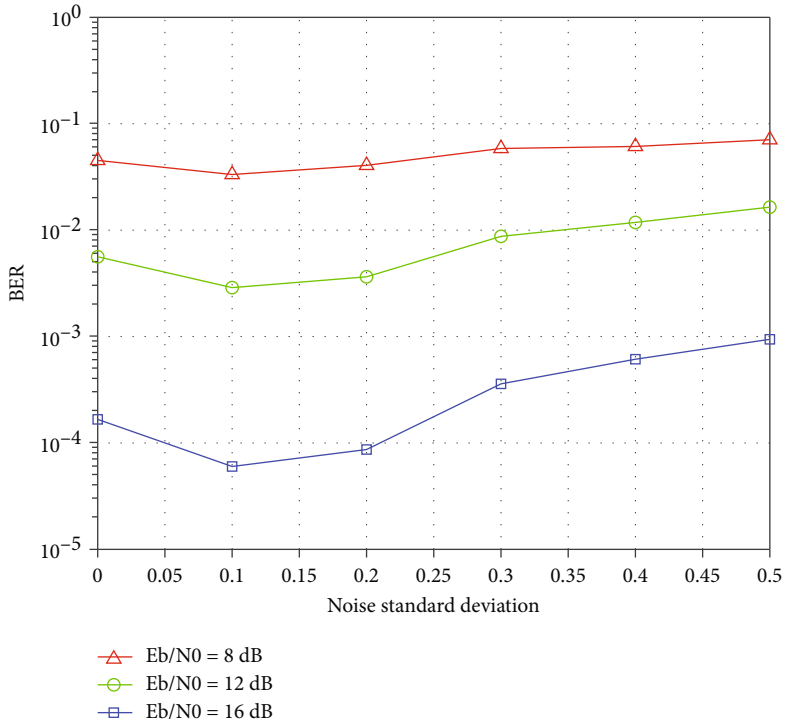

Figure 6: BER performance under different noise standard deviations.

also note that the optimal value of training E_b/N_0 may need to be revised according to the E_b/N_0 level of the actual communication channel.

In Figure 8, we compare the EN-DAE-SCMA codec scheme with the traditional 6-iteration MPA decoding algorithm, the traditional scheme with an optimal codebook design method [15], the deep learning-based codec scheme of D-SCMA [31], and the DAE-SCMA scheme without the equalization network of EN-DAE-SCMA. We set the number of nodes in the hidden layer of the multiuser detection

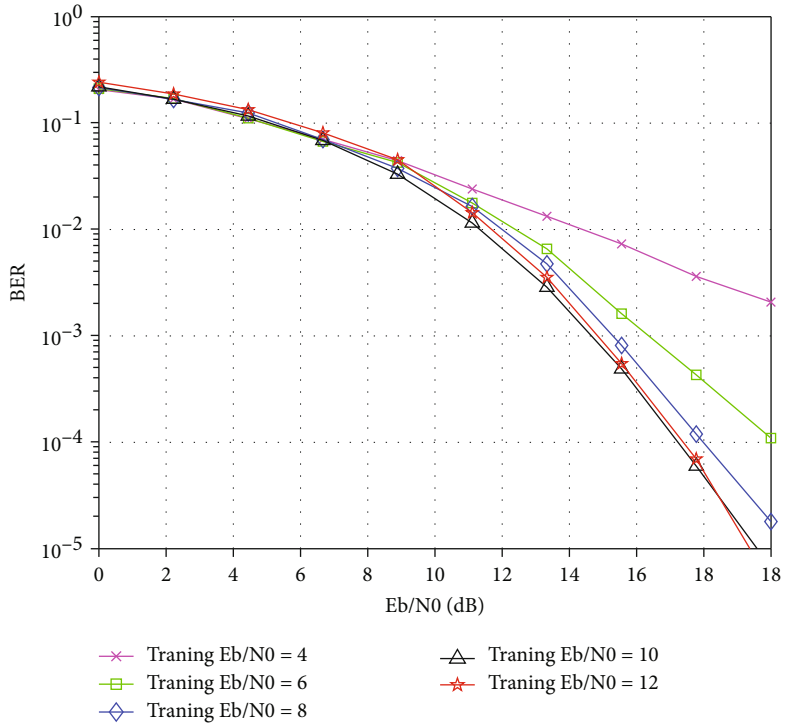

Figure 7: BER performance of EN-DAE-SCMA trained under various E_b/N_0.

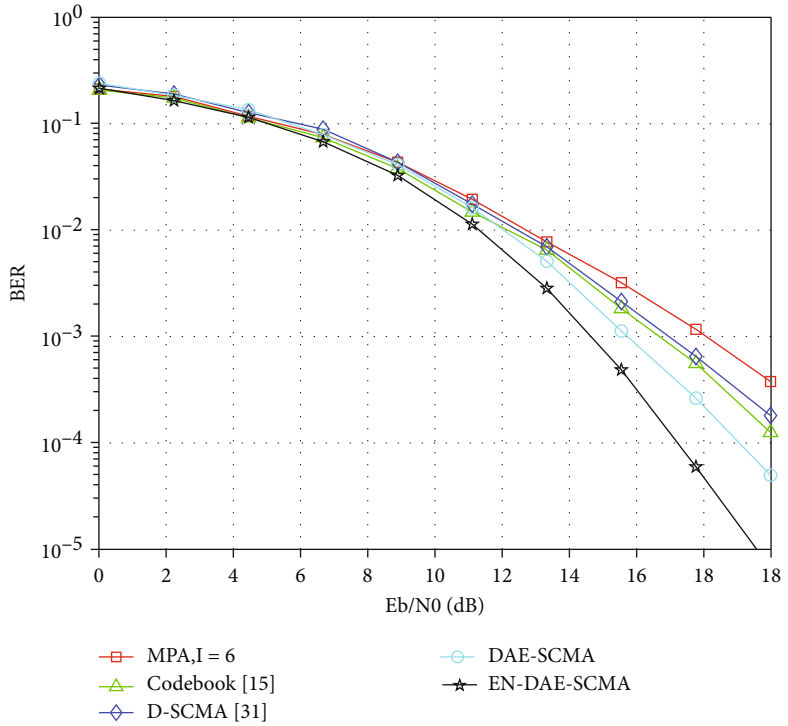

Figure 8: Comparison of the BER performances of different algorithms.

Table 1: MAC operations of SCMA decoders.

	D-SCMA [31]	EN-DAE-SCMA
MAC	794,694	214,208

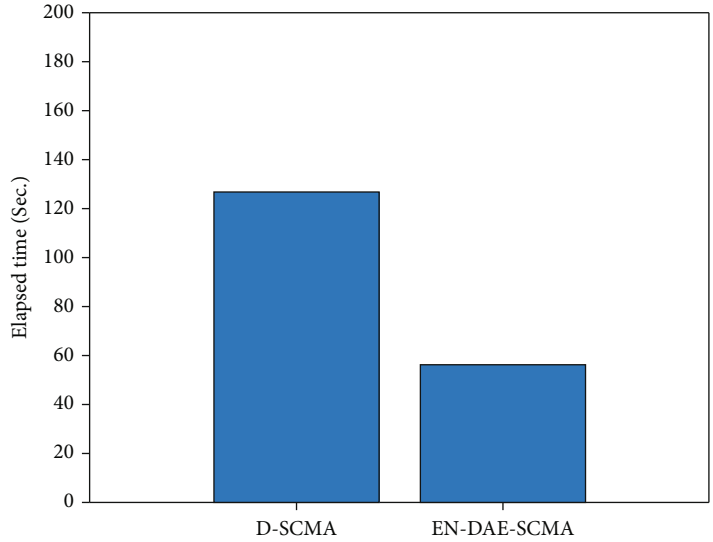

Figure 9: Comparison of elapsed time for different algorithms.

network to 512 to achieve its better decoding performance in DAE-SCMA. The BER performance is shown in Figure 8. Figure 8 shows that the three deep learning-based SCMA codec schemes outperform the traditional SCMA schemes. These deep learning-based schemes have better encoders than the traditional handcrafted codebook. The BER performance of the proposed EN-DAE-SCMA codec scheme is significantly better than that of the traditional MPA scheme, the traditional codebook optimal design scheme [15], and the codec scheme of the D-SCMA system [31]. Because the system has joined the equalization network, it can reduce the fading distortion caused by the influence of the transmission channel, and it is more practical than other solutions when applied to Rayleigh fading channels that are closer to the real environment. It is worth noting that the DAE-SCMA scheme without the equalization network also outperforms the D-SCMA scheme. This is because the DAE-SCMA scheme artificially introduces a noise layer to make the training of the system more robust, so the encoder learns a better codebook than D-SCMA.

Finally, we analyze the algorithm complexity of the proposed EN-DAE-SCMA scheme. The multiply accumulated (MAC) operations of the EN-DAE-SCMA decoder are as follows:

$$\begin{aligned}\mathrm{MAC} = {} & 2KN_{P,1} + \sum_{n=1}^{L_P-1}\left(N_{p,n}N_{p,n+1}\right) + 2KN_{S,1} + \sum_{n=1}^{L_S-1}\left(N_{S,n}N_{S,n+1}\right) \\ & + N_{S,L_S}N_{D,1} + \sum_{n=1}^{L_D-1}\left(N_{D,n}N_{D,n+1}\right) + N_{D,L_D},\end{aligned} \tag{15}$$

where K represents the number of resource blocks and L_P, L_S, and L_D represent the number of hidden layers of the parameter estimation network, signal compensation network, and multiuser detection network, respectively. Similarly, $N_{p,n}$, $N_{p,n}$, and $N_{D,n}$ represent the number of nodes of the nth hidden layer of each network.

For the sake of fairness, we choose to compare various algorithms that all use deep learning and the same experimental platform and simulation machine, where the CPU processor is an i7-6700 and has 8 GB of running memory and where the elapsed time of the program is exploited to represent the complexity. Table 1 shows the number of MAC operations of deep learning- (DL-) based SCMA decoders. The obtained results in Figure 9 show that the computing time of the proposed scheme is lower than that of the D-SCMA scheme. Consequently, the proposed EN-DAE-SCMA scheme has a lower computational complexity.

5. Conclusions

In this paper, we proposed a novel DL-based SCMA codec scheme for the uplink Rayleigh fading channel. On the one hand, we designed a decoding network based on DL. Compared with other conventional decoders, an equalization network composed of two DNN units was added to the decoder. Obtaining the parameter characteristics of the Rayleigh fading channel and compensating for the phase shifts of the received signals are executed by this equalization network. The decoder combined with the equalization network and multiuser detection network can achieve better BER performance. On the other hand, we make changes on the basis of the D-SCMA encoder and introduce an extra noise layer at the input in the training phase. It enhances the robustness of the encoder. Moreover, by adjusting the structure and scale of the neural network, the whole encoding and decoding network convergence speed was accelerated. Simulation and analysis results show that our proposed SCMA codec scheme requires significantly less training data and that the decoding complexity is reduced compared with that of D-SCMA, which also adopts DL schemes. Finally, unlike traditional codebooks based on handcrafted designs, our scheme can autonomously learn ideal codebooks with robustness

through denoising autoencoder technology, which can improve the applicability of the system in actual engineering. At present, our proposed scheme has achieved a significant performance improvement compared with the traditional SCMA scheme and D-SCMA scheme when the channel state information remains unchanged. In the future, we will study the use of a generative adversarial network to simulate the influence of Rayleigh fading channels or try to introduce transfer learning methods so that the system can still obtain performance advantages compared to traditional communication systems when the channel state information changes rapidly.

Data Availability

The data used to support the findings of this study are included within the article.

Conflicts of Interest

The authors declare that there are no conflicts of interest.

References

[1] C. Bockelmann, N. Pratas, H. Nikopour et al., "Massive machine-type communications in 5g: physical and MAC-layer solutions," *IEEE Communications Magazine*, vol. 54, no. 9, pp. 59–65, 2016.

[2] J. Xia, L. Fan, W. Xu et al., "Secure cache-aided multi-relay networks in the presence of multiple eavesdroppers," *IEEE Transactions on Communications*, vol. 67, no. 11, pp. 7672–7685, 2019.

[3] H. Ye, L. Liang, G. Y. Li, and B. H. Juang, "Deep learning-based end-to-end wireless communication systems with conditional GANs as unknown channels," *IEEE Transactions on Wireless Communications*, vol. 19, no. 5, pp. 3133–3143, 2020.

[4] Y. Saito, Y. Kishiyama, A. Benjebbour, T. Nakamura, A. Li, and K. Higuchi, "Non-orthogonal multiple access (NOMA) for cellular future radio access," in *2013 IEEE 77th Vehicular Technology Conference (VTC Spring)*, pp. 1–5, Dresden, Germany, 2013.

[5] H. Nikopour and H. Baligh, "Sparse code multiple access," in *2013 IEEE 24th Annual International Symposium on Personal, Indoor, and Mobile Radio Communications (PIMRC)*, pp. 332–336, London, UK, 2013.

[6] S. Hara and R. Prasad, "Overview of multicarrier CDMA," *IEEE Communications Magazine*, vol. 35, no. 12, pp. 126–133, 1997.

[7] R. Hoshyar, F. P. Wathan, and R. Tafazolli, "Novel low-density signature for synchronous CDMA systems over AWGN channel," *IEEE Transactions on Signal Processing*, vol. 56, no. 4, pp. 1616–1626, 2008.

[8] J. Liu, G. Wu, S. Li, and O. Tirkkonen, "On fixed-point implementation of log-MPA for SCMA signals," *IEEE Wireless Communications Letters*, vol. 5, no. 3, pp. 324–327, 2016.

[9] H. Mu, Z. Ma, M. Alhaji, P. Fan, and D. Chen, "A fixed low complexity message pass algorithm detector for UpLink SCMA system," *IEEE Wireless Communications Letters*, vol. 4, no. 6, pp. 585–588, 2015.

[10] Y. Du, B. Dong, Z. Chen, J. Fang, and L. Yang, "Shuffled multiuser detection schemes for uplink sparse code multiple access systems," *IEEE Communications Letters*, vol. 20, no. 6, pp. 1231–1234, 2016.

[11] F. Wei and W. Chen, "Low complexity iterative receiver design for sparse code multiple access," *IEEE Transactions on Communications*, vol. 65, no. 2, pp. 621–634, 2017.

[12] C. Zhang, C. Yang, X. Pang et al., "Efficient sparse code multiple access decoder based on deterministic message passing algorithm," *IEEE Transactions on Vehicular Technology*, vol. 69, no. 4, pp. 3562–3574, 2020.

[13] C. Husmann, C. Jayawardena, A. Maaref, P. Xiao, and K. Nikitopoulos, "Low-complexity SCMA detection for unsupervised user access," *IEEE Communications Letters*, vol. 25, no. 3, pp. 1019–1023, 2021.

[14] J. Bao, Z. Ma, G. K. Karagiannidis, M. Xiao, and Z. Zhu, "Joint multiuser detection of multidimensional constellations over fading channels," *IEEE Transactions on Communications*, vol. 65, no. 1, pp. 161–172, 2017.

[15] L. Tian, J. Zhong, M. Zhao, and L. Wen, "A suboptimal algorithm for SCMA codebook design over uplink Rayleigh fading channels," in *2018 IEEE 87th Vehicular Technology Conference (VTC Spring)*, pp. 1–5, Porto, Portugal, 2018.

[16] J. Bao, Z. Ma, Z. Ding, G. K. Karagiannidis, and Z. Zhu, "On the design of multiuser codebooks for uplink SCMA systems," *IEEE Communications Letters*, vol. 20, no. 10, pp. 1920–1923, 2016.

[17] L. Yu, P. Fan, D. Cai, and Z. Ma, "Design and analysis of SCMA codebook based on Star-QAM signaling constellations," *IEEE Transactions on Vehicular Technology*, vol. 67, no. 11, pp. 10543–10553, 2018.

[18] X. Li, F. Dong, S. Zhang, and W. Guo, "A survey on deep learning techniques in wireless signal recognition," *Wireless Communications and Mobile Computing*, vol. 2019, Article ID 5629572, 12 pages, 2019.

[19] H. Ye, G. Y. Li, and B. Juang, "Power of deep learning for channel estimation and signal detection in OFDM systems," *IEEE Wireless Communications Letters*, vol. 7, no. 1, pp. 114–117, 2018.

[20] G. Gui, H. Huang, Y. Song, and H. Sari, "Deep learning for an effective nonorthogonal multiple access scheme," *IEEE Transactions on Vehicular Technology*, vol. 67, no. 9, pp. 8440–8450, 2018.

[21] Y. Wang, M. Liu, J. Yang, and G. Gui, "Data-driven deep learning for automatic modulation recognition in cognitive radios," *IEEE Transactions on Vehicular Technology*, vol. 68, no. 4, pp. 4074–4077, 2019.

[22] J. Xia, D. Deng, and D. Fan, "A note on implementation methodologies of deep learning-based signal detection for conventional MIMO transmitters," *IEEE Transactions on Broadcasting*, vol. 66, no. 3, pp. 744-745, 2020.

[23] K. He, Z. Wang, D. Li, F. Zhu, and L. Fan, "Ultra-reliable MU-MIMO detector based on deep learning for 5G/B5G-enabled IoT," *Physical Communication*, vol. 43, pp. 101181–101187, 2020.

[24] L. He, K. He, L. Fan, X. Lei, A. Nallanathan, and G. K. Karagiannidis, "Towards optimally efficient search with deep learning for large-scale MIMO systems," *IEEE Transactions on Communications*, pp. 1–12, 2022.

[25] S. Tang, "Battery-constrained federated edge learning in UAV enabled IoT for B5G/6G networks," *Physical Communication*, vol. 47, article 101381, 2021.

[26] W. Zhou, "PSO based offloading strategy for cache-enabled mobile edge computing UAV networks," *Cluster Computing*, no. 24, pp. 1–13, 2021.

[27] L. Chen, "Intelligent ubiquitous computing for future UAV-enabled MEC network systems," *Cluster Computing*, no. 25, pp. 1–10, 2021.

[28] S. Tang and L. Chen, "SNIFF: a scalable network inference framework for measuring end-to-end performance," *IEEE Trans. Network Science and Engineering*, pp. 1–12, 2022.

[29] L. Chen, "Physical-layer security on mobile edge computing for emerging cyber physical systems," *Computer Communications*, pp. 1–10, 2022.

[30] T. O'Shea and J. Hoydis, "An introduction to deep learning for the physical layer," *IEEE Transactions on Cognitive Communications and Networking*, vol. 3, no. 4, pp. 563–575, 2017.

[31] M. Kim, N. Kim, W. Lee, and D. H. Cho, "Deep learning-aided SCMA," *IEEE Communications Letters*, vol. 22, no. 4, pp. 720–723, 2018.

[32] Y. Han, Z. Wang, Q. Guo, and W. Xiang, "Deep learning-based detection for moderate-density code multiple access in IoT networks," *IEEE Communications Letters*, vol. 24, no. 1, pp. 122–125, 2020.

[33] J. Lin, S. Feng, Y. Zhang, Z. Yang, and Y. Zhang, "A novel deep neural network based approach for sparse code multiple access," *Neurocomputing*, vol. 382, pp. 52–63, 2020.

[34] C. P. Wei, H. Yang, C. P. Li, and Y. M. Chen, "SCMA decoding via deep learning," *IEEE Wireless Communications Letters*, vol. 10, no. 4, pp. 878–881, 2021.

Hindawi
Wireless Communications and Mobile Computing
Volume 2022, Article ID 5721917, 12 pages
https://doi.org/10.1155/2022/5721917

Research Article

Efficient Data Integrity Auditing Supporting Provable Data Update for Secure Cloud Storage

Changsong Yang[1,2] **Bowen Song**[1] **Yong Ding**[1,3] **Jiangtao Ou**[4] **and Chengyuan Fan**[4]

[1]*Guangxi Key Laboratory of Cryptography and Information Security, Guilin University of Electronic Technology, Guilin 541004, China*
[2]*Guangxi Cooperative Innovation Center of Cloud Computing and Big Data, Guilin University of Electronic Technology, Guilin 541004, China*
[3]*Cyberspace Security Research Center, Peng Cheng Laboratory, Shenzhen 518000, China*
[4]*AI Sensing Technology, Chancheng District, Foshan 528000, China*

Correspondence should be addressed to Changsong Yang; csyang@guet.edu.cn

Received 13 January 2022; Revised 14 February 2022; Accepted 15 March 2022; Published 26 March 2022

Academic Editor: Junjuan Xia

Cloud storage, an economically attractive service offered by cloud service providers (CSPs), has attracted a large number of tenants. However, because the ownership and management of outsourced data are separated, outsourced data faces a lot of security challenges, for instance, data security, data integrity, data update, and so on. In this article, we primarily investigate the problem of efficient data integrity auditing supporting provable data update in cloud computing environment. Subsequently, on the basis of the Merkel sum hash tree (MSHT), we introduce an efficient outsourced data integrity auditing scheme. Our designed scheme could synchronously meet the requirements of provable data update and data confidentiality without dependency on a third authority. At the same time, the numerical analysis shows that the computing complexity logarithmically grows with the number of outsourced subfiles. Finally, a prototype implementation is developed to simulate our designed scheme and measure its performance. The consequences of experiments present that compared with some previous solutions, our designed scheme has much more attractive practicality and higher efficiency in practical applications.

1. Introduction

With the fast development of computer and network technology, the total volume of digital data shows an exponential growth tendency [1]. The investigation report shows that there were 5200 GB digital data for everyone on average in 2020 [2]. However, the storage resources of tenants are so limited that cannot preserve such large-scale data. Therefore, massive data storage would become a challenging problem for resource-constrained tenants. Fortunately, cloud storage offers a potential solution to handle the issue of massive data storage and management. By embracing cloud storage services, tenants could upload their data to the cloud data center, thus efficaciously reducing the local memory space and computational cost [3]. Because of these attractive advantages, a growing number of tenants prefer to employ cloud storage services. According to the report of Cisco, there were 3.6 billion Internet consumers at the beginning of 2020. At the same time, about 55% of Internet consumers embraced cloud storage [4].

In cloud storage, the management of outsourced data is separated from its ownership [5]. Therefore, tenants would lose the physical management of their outsourced data, thus cannot directly perform any operations over the outsourced data [6]. In other words, the cloud data center performs all operations over the outsourced data. Nevertheless, the cloud data center is not fully reliable, and it might not honestly perform these operations according to the tenant's commands. As a result, although cloud storage has huge advantages, it inevitably faces plenty of serious problems [7], for instance, data confidentiality, data integrity, data update, etc. If these problems, especially data integrity, are not solved well, it will greatly prevent the public from accepting and employing cloud storage services [8].

To guarantee outsourced data integrity and availability, plenty of solutions have been presented [9–11]. However, there still exist some problems which need to be solved solidly. First, most of the previous solutions are based on proof of retrievability (PoR) technology or provable data possession (PDP) technology, whose computing complexity grows approximatively linearly with the scale of outsourced files. Hence, the efficiency is not attractive if the scale of outsourced file keeps growing [12]. Second, lots of the previous works require to depend on a third authority (TA), whose security and stability are particularly troubling. On the one hand, because of the expensive overhead, the third authority would refuse to provide services, which will cause service interruption. On the other hand, the third authority might be attacked by the adversary, and it cannot resist the commands of the government, which both would trigger privacy leakage. Last but not least, although some of the previous solutions concurrently accomplish data confidentiality, data integrity, and data update in some special scenarios, the practicability and universality are so limited that they cannot be applied to large-scale data outsourcing scenarios.

From the above analysis, we can easily discover that there are still some issues in the previous solutions. Further, there are few solutions that can simultaneously achieve data integrity auditing and dynamic data update efficiently without dependency on a third authority. As a consequence, the main motivation of this paper is to design a novel scheme to simultaneously solve the above problems. Specifically, we aim to make use of Merkle sum hash tree (MSHT) to design an efficient outsourced data integrity auditing scheme supporting provable data update without interacting with a third authority. As a consequence, the main contributions of this article are the two folds as below.

(i) We use MSHT to establish a high-performance outsourced data integrity verification scheme, which simultaneously supports provable outsourced data update. Specifically, the designed scheme can not only ensure the data integrity and usability but also meet the requirement of block-based data update, by which tenants can efficaciously update the outsourced data and check the update result without retrieving the data. At the same time, the designed scheme can realize the confidentiality of outsourced data, thus preventing the leakage of privacy information

(ii) Our designed scheme could achieve the anticipant functionality objectives without dependency on a third authority. In the meantime, under the random oracle model, we conduct a detailed security analysis to prove that the designed scheme is secure. Finally, a prototype implementation is developed to simulate the proposed scheme and perform the efficiency evaluation, which directly presents the practicability of the designed scheme

1.1. Related Works. Data integrity auditing has already been investigated in the past several decades both in academic and industrial, resulting in a rich body of literature [13–16]. In 2007, Ateniese et al. [17] first designed a PDP model, in which they utilized random sampling to realize data integrity auditing efficiently. In the meantime, they put forward two detailed PDP schemes which were provable secure and efficient. In order to achieve remote data possession checking (RDPC), Chen [18] utilized algebraic signatures to design a possession auditing scheme for remote data. In her designed scheme, the communication overhead was constant in challenge and response protocols, which could improve efficiency. However, Yu et al. [19] found that the previous protocol [18] was not able to prevent replay attacks and deletion attacks. At the same time, they proposed a novel remote cloud data possession auditing scheme, which could effectively resist deletion attack and replay attack. Li et al. [20] studied the challenge of multiple copies of data integrity auditing, in which multiple copies of data were maintained by multiple cloud data centers. After that, they presented a novel data integrity auditing protocol, which could improve efficiency by checking all copies at one time. Wang [21] designed a novel model called identity-based distributed PDP (ID-DPDP). At the same time, he utilized bilinear pairings to present a concrete ID-DPDP protocol for multicloud storage scenario. His proposed scheme could support private validation, delegated validation, and public validation. In order to improve the efficiency, Chang et al. [22] designed an identity-based PDP protocol, in which they adopted a novel hash function to save the communication overhead.

In 2019, Fan et al. [23] designed an identity-based aggregate signature (SIBAS) and took it as the secure integrity validation protocol over cloud data, which could synchronously realize reliable key management through Shamir's threshold protocol. In 2021, Shen et al. [24] presented a novel concept named data integrity reliable without private key storage and designed a concrete solution, in which they utilized the advantages of biometric data to remove the hardware token. Lu et al. [25] utilized hyperledger fabric to build a secure data integrity validation protocol with scalability. Zhang et al. [26] put forward a blockchain-based cloud data integrity verification protocol, which could support public verifiability. In their scheme, all the verification results would be recorded into a transaction that was time-sensitive. Li and Zhang [27] designed a certificate-based integrity auditing protocol, which was provable secure under the random oracle model. Moreover, their scheme required constant computational overhead to generate a verification tag for a data block. Nevertheless, the above solutions could not realize data dynamic operations, such as data update.

In order to simultaneously achieve data integrity auditing and data dynamic update, Liu et al. [28] presented an improved dynamic PDP (DPDP) protocol, which, respectively, utilized tags and hash values to guarantee data integrity and tag integrity. Chen and Curtmola [29] designed a remote DPDP scheme, which could achieve data integrity auditing and data update with constant storage overhead for client. Barsoum and Hasan [30] presented a PDP protocol for multi-backup dynamic cloud data, which was able to support full data dynamics. In 2015, Esiner et al. [31] utilized

flexlist to design an optimized DPDP scheme, which was able to hand plenty of updates simultaneously, thus improving efficiency. Yuan et al. [32] studied the integrity auditing for dynamic multi-replica data that was maintained by multiple cloud data centers, and they presented a solution to hand this problem. In their protocol, the modular exponentiation was replaced by the vector dot products, thus effectively saving computational resources. In 2021, Yu et al. [33] used indexed Merkle hash tree (IMHT) to design an efficient dynamic data auditing protocol, which could support fully dynamic operations. To achieve batch verification, Guo et al. [34] utilized implicitly indexed balanced Merkle tree (IBMT) to put forward a dynamic proof of data possession and replication (DPDPR) protocol. Their proposed solution greatly saved computational and communication resources. However, their solution required introducing a TPA to complete cloud data integrity verification.

Besides PDP, plenty of authentication data structures also can achieve integrity auditing and support data dynamic operations. He et al. [35] utilized permission-based signature and blockless Merkle tree to present a dynamic group-oriented PDP protocol, and they claimed that their protocol was an important phase in establishing efficient multi-writer cloud storage systems. Chen et al. [36] designed a novel PDP model based on blockchain, which might be utilized to achieve distributed cloud storage framework. Subsequently, they designed a concrete decentralized PDP scheme by utilizing multi-replica storage tricks, which supported dynamic operations over outsourced data. Recently, Guo et al. [37] connected multi-leaf-authenticated and rank-based Merkle tree to realize integrity checking and batch update over outsourced data in secure cloud storage. Chen et al. [38] utilized vector commitment (VC) to build a novel verifiable database (VDB) model supporting replacement update, which could resist forward automatic update attack. Chen et al. [39] provided an improved VDB scheme, which utilized committed invertible Bloom filter to realize full dynamic operations. Nevertheless, their schemes required to perform plenty of bilinear pairing computations, resulting in expensive computational overhead.

1.2. Organization. We organize the rest of this paper as below. Section 2 describes the preliminary of MSHT, which will be used to establish our novel scheme. In Section 3, we introduce the problem statements and then introduce the proposed scheme in Section 4. After that, the scheme analysis, including security analysis, functionality contrast, and computational complexity analysis is introduced in Section 5. Next, we implement our designed scheme and evaluate its efficiency in Section 6. At last, Section 7 simply concludes this paper.

2. Preliminaries

MSHT was originally designed by Miao et al. in 2018 [40], which could be regarded as a development of the traditional MHT [41]. Similar to MHT, MSHT can also verify the data integrity of any subset [42]. However, there are two differences between MHT and MSHT. On the one hand, all leaves of MSHT could manage many data blocks, but each leaf of MHT could merely save one data block. On the other hand, the amount of data blocks managed by the leaf is used as input to generate the hash value, as demonstrated in Figure 1. Subsequently, the Merkle root node H_R contains all of the data blocks in the given set, and a signature Sig_R can be generated on the hash value H_R through a provable secure signature protocol.

Similar to MHT, MSHT also relies on the auxiliary validation information φ to achieve data integrity auditing. Auxiliary validation information φ contains the hash values and the data block numbers of the sibling nodes on the path from the verified leaf node to the Merkle root node [43]. For example, to verify the integrity of data block $f_{3,1}$, the auxiliary validation information is $\varphi_3 = ((h_{14}, 1), (h_{21}, 2))$. Then, the verifier can recompute a novel Merkle root node H_R' by utilizing the auxiliary validation information φ_3 and compare H_R' with H_R. At the same time, the verifier, audits the correctness of signature Sig_R. If and only if H_R is equal to H_R' and Sig_R is a correct signature on Merkle root node H_R', will the verifier believe that $f_{3,1}$ is intact.

3. Problem Statements

We present the problem statements (i.e., system framework, technology challenges, and design goals) in this section.

3.1. System Framework. We study the problem of high efficiency data integrity checking supporting provable data update for secure cloud storage, whose system framework consists of two participants: a tenant and a cloud data center, as demonstrated in Figure 2.

3.1.1. Tenant. The tenant is equipped with restricted storage capacities, so he/she could not save and manage massive data by himself/herself in local storage mediums. Therefore, the tenant prefers to upload his/her massive data to the remote cloud data center. Later, the tenant wants to utilize a few novel data blocks to replace some old data blocks for efficiently updating the outsourced data set. Since the tenant lacks trust in the cloud data center, the tenant would want to audit the integrity of the outsourced data and the result of the data update operation.

3.1.2. Cloud Data Center. The cloud data center connects plenty of dispersive physical disks, network resources, and computational devices by the Internet and establishes a sharing resource pool, thus providing the tenant with convenient and efficient storage services. Meanwhile, since the ownership outsourced data is separated from its management, the cloud data center executes outsourced data update operations for the tenant and returns related proofs to convince the tenant that the outsourced data blocks have been correctly updated according to the tenant's commands.

3.2. Security Challenges. The following three security challenges must be seriously considered and solidly solved in our proposal.

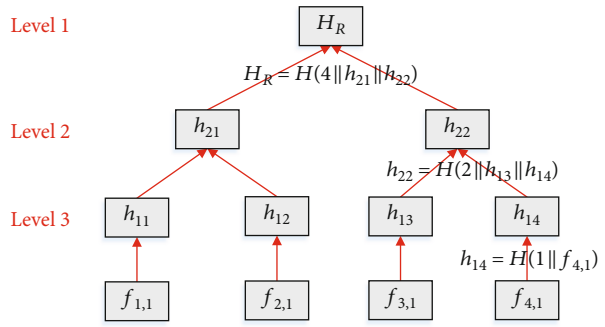

Figure 1: Basic structure of MSHT.

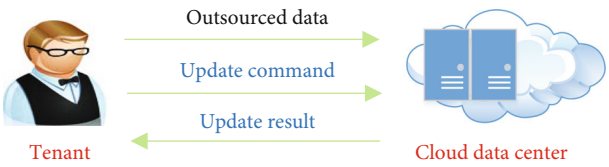

Figure 2: System framework of the designed scheme.

3.2.1. Privacy Leakage. Outsourced data usually contains some privacy information of tenant. In cloud storage, the cloud manager is so curious that peeps at the outsourced data for finding some privacy information of the tenant. Meanwhile, external attackers (such as hackers) might illegally access the outsourced data to dig the privacy information. As a consequence, privacy leakage is a severe challenge that should be seriously considered.

3.2.2. Data Pollution. Because of the following three reasons, outsourced data might be polluted. First, data loss would be caused by software failure, hardware breakdown, and erroneous operations of the cloud manager. Second, the cloud data center may maliciously remove a few outsourced data blocks which are seldom utilized in order to save storage overhead. Third, hacker might maliciously target the cloud data center, causing damage to the outsourced data.

3.2.3. Dishonest Data Update. The cloud data center must run some complex protocols or calculations in order to achieve outsourced data update. In consequence, the cloud data center has to cost some expensive computational overhead and some additional storage capacities, which is undesired for the cloud data center. Therefore, the cloud data center may not honestly execute the tenant's command to update the outsourced data.

3.3. Security Goals. In the designed scheme, we require to meet three requirements as follows, including data confidentiality, data integrity auditing, and provable data update.

3.3.1. Data Confidentiality. Data confidentiality refers to keeping the tenant's privacy information included in the outsourced data secret. In consequence, to avoid the leakage of privacy information, the tenant should encrypt the outsourced file by utilizing a secure encryption protocol before uploading.

3.3.2. Data Integrity Auditing. Data integrity is defined that the cloud data center saves and manages the outsourced data integrally. If malicious data pollution has occurred in outsourced data blocks, the tenant can effectively discover the data pollution through periodically performing a data integrity auditing operation.

3.3.3. Provable Data Update. Provable data update refers to that the cloud data center must sincerely perform the tenant's outsourced data update command and honestly return related evidence. The tenant can check the returned evidence to detect malicious acts if the cloud data center did not honestly update the outsourced data.

4. Our Scheme

We establish a high-efficiency data integrity auditing scheme, which can also realize data confidentiality and verifiable data update in secure cloud storage environment. Specifically, the proposed scheme contains five main phases: initialization, data preprocessing, data outsourcing, data integrity auditing, and data update.

4.1. Initialization. In this phase, the tenant achieves registration on the cloud data center. Meanwhile, some related public parameters and public/privacy key pairs are generated.

4.1.1. Tenant Registration. Before employing the cloud data center's data storage services, the tenant must become a legitimate customer of the cloud service providers. Hence, the tenant has to register and complete the identity authentication on the cloud data center. Then, the tenant becomes a legitimate customer of the cloud data center and obtains a unique identity number ID. As a consequence, the tenant can employ the cloud data center's data storage services directly.

4.1.2. Parameter/Key Generation. Firstly, the public/private key pair (PK_C, SK_C) for the elliptic curve digital signature algorithm (ECDSA) is generated by the cloud data center. Then, the cloud data center publishes the public key PK_C and keeps the privacy SK_C so confidential that nobody else can obtain it. Similarly, the tenant computes public/privacy key pair (PK_T, SK_T). Subsequently, the tenant publishes the public key PK_T and keeps the privacy SK_T confidential. At the same time, the tenant picks an identifier n_f for the file F.

4.2. Data Preprocessing. This phase mainly achieves data encryption and ciphertext segmentation. The detailed process of data preprocessing is below.

4.2.1. Data Encryption. Generally, the outsourced file involves some privacy information which has to be kept confidential. Hence, before uploading the outsourced data to the cloud data center, the tenant should encrypt it to protect the privacy data. To be more specific, the tenant first computes a key $K = H(ID \| n_f \| SK_T)$, in which $H(\cdot)$ is a secure hash algorithm. After that, the tenant executes data encryption operation $f = Enc_K(F)$, in which Enc is a symmetric encryption scheme, and it is indistinguishable under chosen-plaintext attack (IND-CPA), and f is the corresponding ciphertext.

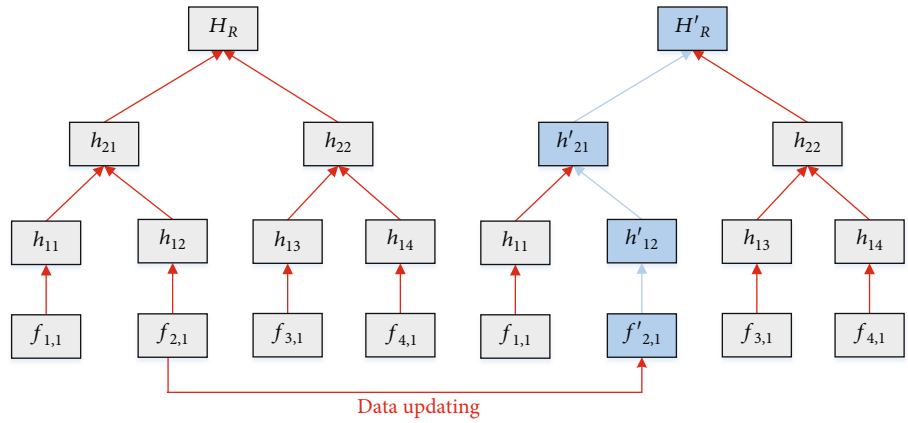

Figure 3: An illustration of data updating.

4.2.2. Ciphertext Segmentation. The tenant firstly divides the related ciphertext f into n subfiles $f = (f_1, f_2, \cdots, f_n)$. Subsequently, the tenant further splits each subfile into S data blocks $f_{i1}, f_{i2}, \cdots, f_{is}$, where $i = 1, 2, \cdots, n$. As a consequence, the tenant can obtain the outsourced data set $f = (f_1, f_2, \cdots, f_n) = \{f_{i,j}\}_{1 \le i \le n, 1 \le j \le S}$.

4.3. Data Outsourcing. In this phase, the outsourced data set is maintained through building an MSHT, and then, the whole tree is outsourced to the cloud data center. The details of data outsourcing are described as below.

4.3.1. Tree Building. The tenant uses the received data blocks to construct a Merkle sum hash tree *MSHT* that contains n leaf nodes $N_1, N_2, \cdots, N_n$. In *MSHT*, every leaf saves a subfile, i.e., leaf N_i saves subfile f_i. Subsequently, the tenant could acquire a Merkle root H_R. Meanwhile, the tenant computes a signature Sig_R for hash value H_R, where $Sig_R = Sign_{SK_T}(H_R)$, and *Sign* is the signature computation algorithm of ECDSA. Next, the tenant uploads the whole Merkle sum hash tree *MSHT* to the cloud data center, along with the Merkle root's signature Sig_R.

4.3.2. File Storage. On receipt of the outsourced data set f, the tree *MSHT*, and the signature Sig_R, the cloud data center audits the correctness of *MSHT*. To be more precise, the cloud data center rebuilds the tree by utilizing outsourced data set f and then acquires a novel hash value of the Merkle root H'_R. Subsequently, the cloud data center checks if equality $H_R = H'_R$ holds, meanwhile, confirms the correctness of the signature Sig_R. If and only if equality $H_R = H'_R$ holds and signature Sig_R is correct, will the cloud data center think the received tree *MSHT* is correct and then manage the outsourced file for the tenant by saving the tree *MSHT*. At last, the cloud data center returns success to the tenant to indicate the data storage result.

4.3.3. Data Deletion. After the outsourced file is successfully stored by the cloud data center, the tenant deletes all copies of outsourced file F and outsourced data set f for saving local storage capacities. Subsequently, the tenant merely stores the Merkle root H_R in local physical disks.

Table 1: Functionality contrast.

Scheme	Scheme [16]	Scheme [33]	Our scheme
Confidentiality	✓	✓	✓
Data integrity	✓	✓	✓
Data update	☒	✓	✓
Without TA	✓	☒	✓

4.4. Integrity Auditing. After the tenant uploads the outsourced data to the cloud data center, the data integrity auditing is periodically executed to ensure the integrity of outsourced data. Then, the details of data integrity auditing are below.

4.4.1. Information Retrieval. The tenant firstly discretionarily picks an integer i, where $1 \le i \le n$. Subsequently, the tenant gets the subfile $f_i = (f_{i,1}, f_{i,2}, \cdots, f_{is})$ and its related auxiliary validation information φ_i back from the cloud data center.

4.4.2. Merkle Root Rebuilding. The tenant utilizes the auxiliary validation information φ_i and the subfile $f_i = (f_{i,1}, f_{i,2}, \cdots, f_{is})$ to rebuild the Merkle root. Subsequently, the tenant can obtain a novel hash value H^*_R of Merkle root for contrasting with H_R. If equality $H_R = H^*_R$ does not hold, the tenant believes that the subfile $f_i = (f_{i,1}, f_{i,2}, \cdots, f_{is})$ has been polluted; Otherwise, if equality $H_R = H^*_R$ holds, the tenant can believe the subfile $f_i = (f_{i,1}, f_{i,2}, \cdots, f_{is})$ is intact.

4.5. Data Update. The tenant wants to utilize a few novel data blocks to replace some old outsourced data blocks, thus efficiently updating the outsourced file. Subsequently, the detailed steps of data update are below.

4.5.1. Command Generation. For simplicity, assume that the tenant hopes to update the outsourced data block $f_{k,p}$, which is stored by leaf node N_k, where $1 \le k \le n$ and $1 \le p \le S$. Subsequently, the tenant retrieves the subfile $f_k = (f_{k,1}, f_{k,2}, \cdots,$

Table 2: Computational complexity contrast.

Scheme	Scheme [16]	Scheme [33]	Our scheme
Data preprocessing	$nE + 2nH$	–	$1E + 1H$
Data outsourcing	$n(Exp + M)$	$n(Exp + H)$	$4nH + 1S + 1V$
Integrity auditing	$2P + nExp$	$2P + sExp + sH$	$k \log_2 nH$
Data updating	–	$\log_2 nH + sExp + 1S$	$2(S + V + q \log_2 nH)$

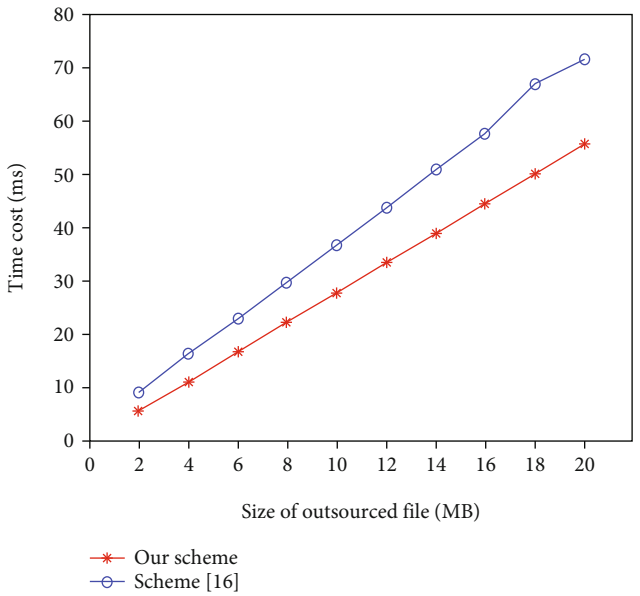

Figure 4: Time cost of data preprocessing.

$f_{k,S}$) from the cloud data center, as well as its auxiliary validation information φ_k. Meanwhile, the tenant generates a signature $Sig_T = \text{Sign}_{SK_T}(\text{update} \| k \| p \| T)$, where T represents the timestamp. Next, the tenant can further generate a data update command $UC = (\text{update}, k, p, T, Sig_T)$. Finally, the tenant transmits the data update order UC to the cloud data center, along with the novel data block $f'_{k,p}$.

4.5.2. Data Updating. When the cloud data center receives a data update command UC and a new data block $f'_{k,p}$, the cloud data center firstly audits the correctness of the data update command UC by signature checking. To be more specific, the cloud data center validates the signature Sig_T. If Sig_T is an invalid signature, the cloud data center returns failure; otherwise, if signature Sig_T is correct, the cloud data center replaces the old data block $f_{k,p}$ with the new data block $f'_{k,p}$. Meanwhile, the cloud data center obtains a new Merkle sum hash tree $MSHT'$, as presented in Figure 3. Subsequently, the cloud data center transmits the new Merkle root H_r, along with its corresponding signature Sig_r to the tenant, where $Sig_r = \text{Sign}_{SK_C}(H_r)$.

4.5.3. Result Checking. Upon receiving H_r and Sig_r from the cloud data center, the tenant could audit the data update result. Specifically, the tenant firstly utilizes the auxiliary validation information φ_k and the new subfile $f'_k = (f_{k,1}, \cdots, f_{k,p}', \cdots, f_{k,S})$ to acquire a novel hash value H'_r of the Merkle root for contrast with H_r, where H_r is returned by the cloud data center. Meanwhile, the tenant validates the validity of the signature Sig_r. If and only if the equality $H_r = H'_r$ holds and signature Sig_r is correct, will the tenant think that the cloud data center has honestly executed the data update command.

5. Scheme Analysis

5.1. Security Proof. We would formally demonstrate that the novel designed scheme could achieve the anticipant design goals, including data confidentiality, data integrity, and provable data update.

5.1.1. Theorem 1: The Designed Scheme Could Achieve Data Confidentiality. Data confidentiality refers to that the privacy information included in outsourced data should not be disclosed. Generally, outsourced data should be encrypted with a safe encryption protocol to avoid the leakage of sensitive information. As a consequence, the encryption protocol directly determines the security of outsourced data. In our designed scheme, before storing the outsourced file on the cloud data center, the tenant encrypts the outsourced file with an IND-CPA secure symmetric encryption protocol, such as *AES*. Thus, the corresponding ciphertext IND-CPA is secure too. As a result, if the attacker is unable to obtain the corresponding decryption key, he/she will be unable to extract any plaintext information from the ciphertext with a nonzero probability in polynomial time [44, 45]. That is, in our designed scheme, no attacker can get any plaintext data from the ciphertext if the tenant keeps the encryption/decryption keys secret.

5.1.2. Theorem 2: The Designed Scheme Could Ensure Data Integrity. Data integrity is defined that the cloud data center has to save and manage the outsourced data honestly and prevent it from being polluted. Otherwise, the tenant could discover the malicious outsourced data destruction with an overwhelming probability. In our designed scheme, the tenant randomly chooses an integer i from Z_n. After that, the tenant retrieves the subfile $f_i = (f_{i,1}, f_{i,2}, \cdots, f_{i,S})$ from the cloud data center, as well as its auxiliary validation information φ_i. As a result, the tenant can recompute a novel hash value H_R^* of Merkle root for contrast with H_R. Note that in data outsourcing scenario, the scale of outsourced subfiles

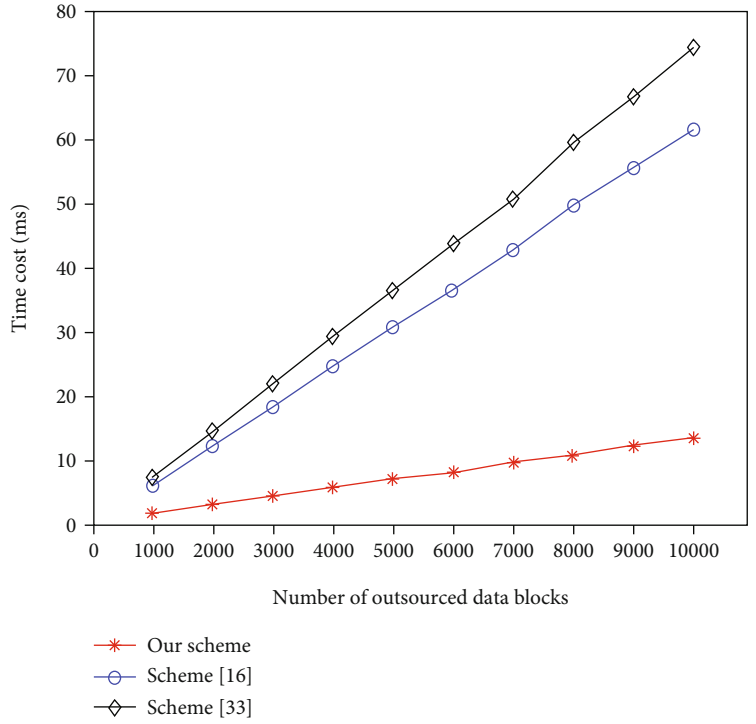

Figure 5: Time cost of data outsourcing.

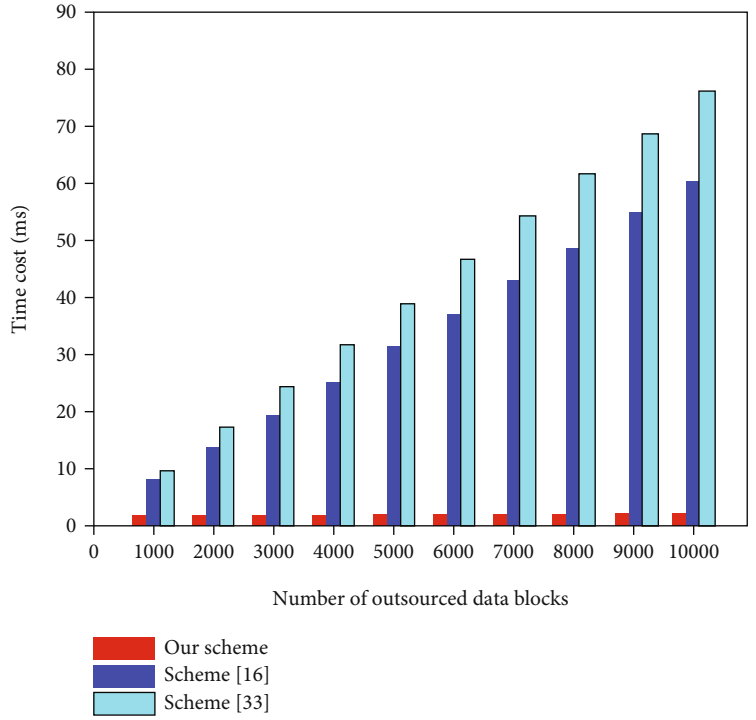

Figure 6: Time cost of integrity auditing.

is so large that the cloud data center could not correctly guess the chosen number i with nonnegligible probability in advance. Meanwhile, the hash function is collision-resistant and one-way. Therefore, if the outsourced data is polluted, in polynomial time, the cloud data center could not successfully forge a new data block to make equality $H_R^* = H_R$ hold with a nonnegligible probability. In other words, if and only if the outsourced data is intact, will

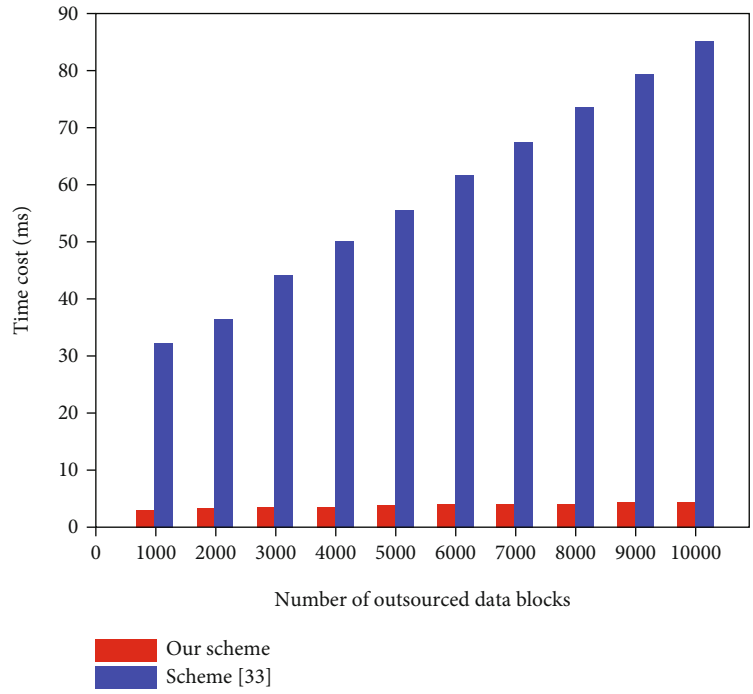

Figure 7: Time cost of data updating.

equality $H_R^* = H_R$ hold. That is, if and only if equality $H_R^* = H_R$ holds, will the tenant believe that the outsourced data is intact.

5.1.3. Theorem 3: The Designed Scheme Could Achieve Provable Data Update. Provable data update means the cloud data center sincerely updates the outsourced data under the tenant's permission. To guarantee the data update operation is executed under the tenant's permission, the cloud data center verifies whether the data update command DC is correct and valid by signature verification. Note that the data update command DC contains a digital signature Sig_T, which is generated by the tenant with the privacy key SK_T. As we know, the privacy key SK_T is kept so secret by the tenant that nobody else can obtain it. Further, only the tenant can compute the signature SK_T and generate the data update command DC. Therefore, the signature SK_T can be seen as evidence which proves that the tenant prefers to update the outsourced data set. In other words, if signature SK_T is valid, it can mean that the data update command is indeed generated by the tenant. Then, the data update operation is executed by the cloud data center under the tenant's permission.

Moreover, since the tenant lacks trust in the cloud data center, he/she would want to authenticate the result of data update to guarantee the data update command is honestly carried out by the cloud data center. Specifically, the tenant firstly checks the correctness of signature Sig_r. When signature Sig_r is correct, the tenant thinks that the Merkle root H_r is returned by the cloud data center without being tampering. Subsequently, the tenant utilizes the new subfile $f_k' = (f_{k,1}, \cdots, f_{k,p}', \cdots, f_{k,S})$ and the auxiliary validation information φ_k to recompute a novel Merkle root H_r'. Then, the tenant contrasts the new Merkle root H_r' with the Merkle root H_r that is returned by the cloud data center. Note that the chosen hash function is collision-resistant and one-way. Therefore, if the cloud data center did not update the outsourced data set honestly, in polynomial time, it is unable to efficiently forge the Merkle root H_r to make equality $H_r' = H_r$ hold with a nonnegligible probability. As a consequence, if equality $H_r' = H_r$ holds and signature Sig_r is correct, the tenant can believe that the data update command has been honestly performed by the cloud data center.

5.2. Functionality Contrast. We would compare the functionality of our designed scheme and two previous schemes [16, 33], as demonstrated in Table 1.

From Table 1, we can obviously get three findings as below. First, the three solutions all can ensure data integrity, which enables the cloud data center to maintain the outsourced file honestly. Meanwhile, they all utilize secure encryption algorithms to prevent privacy information from leakage, thus ensuring data confidentiality. Second, our designed scheme and the previous scheme [33] can achieve block-based data update, but the previous scheme [16] cannot support data update. Finally, the previous scheme [33] requires relying on a TA to realize data integrity checking and provable data update, while the other two solutions do not need to interact with a TA. Therefore, we can trust that the overall functionalities of our designed scheme are more appealing than the other two previous solutions [16, 33].

5.3. Numeric Analysis. We present the numeric analysis through computational complexity contrast. We first

introduce some symbols which would be utilized for the contrast. To be more specific, we adopt symbols E, H, Exp, and M to, respectively, represent encryption computation, hash calculation, modular exponentiation computation, and multiplication operation. Meanwhile, we utilize symbol S and symbol V to, respectively, represent signature computation and signature auditing. Moreover, symbol n represents the number of outsourced subfiles, symbol P represents bilinear pairings computation, symbol k denotes the number of audited data blocks, and symbol q denotes the number of updated data blocks. In scheme [33], we assume each data block would be further split into s sectors.

From Table 2, we obviously discover our designed scheme which merely requires to compute/audit some signatures and compute some hash values. However, the other two solutions [16, 33] need to perform some modular exponentiation calculations or bilinear pairing computations. Therefore, we can consider that our designed scheme has higher efficiency than the other two previous solutions [16, 33].

6. Experimental Results

We carry out a prototype system to simulate our designed solution. Meanwhile, we evaluate the computational performance of executing the primary computations in each process. All the experiments are carried out on a desktop with Unix system, Intel(R) Core(TM) i7-7700 CPU running at 8 GB random access memory and 3.6 GHz.

In the simulation experiments, the pairing-based cryptography library and the open secure socket layer library are used to simulate the related cryptographic algorithms. To be more specific, $SHA-1$ is chosen as the secure hash function and AES is chosen as the secure encryption algorithm. Moreover, we choose ECDSA as the signature algorithm. For simplicity, we ignore the communication cost and assume that in our designed solution, each subfile is divided into a data block. That is, we treat a subfile as a data block in the experiments.

6.1. Time Overhead of Data Preprocessing. This data preprocessing phase aims to complement data encryption and ciphertext segmentation. As a consequence, the running time overhead of data preprocessing is concerned with the scale of outsourced file and the quantity of outsourced subfiles. In the experiment, the number of outsourced subfiles is set to $n = 3000$ and the scale of outsourced file is increased from 2 MB to 20 MB. Subsequently, we measure the time overhead of data preprocessing, as presented in Figure 4.

Figure 4 clearly demonstrates that the time overhead of data preprocessing linearly increases with the scale of outsourced data approximatively. At the same time, our designed solution's growth rate is a little lower compared with that of the previous solution [16]. Moreover, we are able to discover that our designed solution requires less time than the previous solution [16] under the same size of outsourced file. For example, if the scale of outsourced data reaches 20 MB, our designed solution requires nearly 55.6 milliseconds, while the previous solution [16] costs about 71.5 milliseconds. As a result, although the data preprocessing phase is performed by the tenant, the data preprocessing is a single-use for a given outsourced file; meanwhile, it can be executed off-line. In consequence, we could trust that our designed solution is quite high-efficiency in the step of data preprocessing.

6.2. Time Overhead of Data Outsourcing. This data outsourcing phase aims to build a data structure for managing the outsourced file and upload the outsourced file to the cloud data center. Therefore, the running time overhead of data outsourcing is connected to the quantity of data blocks. For convenience, the quantity s is set to 500. At the same time, the quantity of data blocks is increased from 1000 to 10000. Subsequently, we provide the running time overhead, as presented in Figure 5.

Figure 5 shows that in data outsourcing phase, all the running time overhead of the three solutions roughly grows with the quantity of data blocks. In the meantime, our designed solution's growth rate is the lowest among the three solutions. Moreover, the other two solutions [16, 33] both require significantly more time than our designed solution. For instance, when the quantity of data blocks is 5000, the time overhead of our designed solution is nearly 7.0 milliseconds, but the time of the previous solution [16] is 30.8 milliseconds, and the time overhead of the previous solution [33] is approximately 36.3 milliseconds. Foreseeably, our designed solution would require the least time overhead to outsource the same quantity of data blocks. As a consequence, we could directly consider our designed solution is more efficient than the other two solutions [16, 33] in data outsourcing phase.

6.3. Time Overhead of Integrity Auditing. The data integrity checking process aims to check the integrity and availability to ensure the cloud data center sincerely saves and manages the outsourced data. Hence, the running time overhead of integrity auditing is connected to the quantity of outsourced data blocks. As a consequence, we let $k = 100$ and $s = n$ for convenience. Meanwhile, the quantity of outsourced data blocks is increased from 1000 to 10000. Subsequently, the running time cost of data integrity auditing is presented in Figure 6.

From Figure 6, we would directly discover that all the time cost of the three solutions grows with the quantity of outsourced data blocks, while our designed solution's growth rate is the lowest. This is because the time cost of our designed solution logarithmically increases with the quantity of outsourced data blocks, while the running time cost of the other two previous solutions [16, 33] linearly grows with the quantity of outsourced data blocks approximatively. Furthermore, our designed solution requires the least time cost, and the previous solution [33] requires the most time cost. For instance, if the quantity of outsourced data blocks is 5000, the running time cost of our designed solution is nearly 1.7 milliseconds, while the time overhead of the previous solution [16] is approximately 31.1 milliseconds, and the time of the previous solution [33] is about 38.9 milliseconds. Therefore, we could trust that the efficiency of our designed solution is higher than these of the other two previous solutions [16, 33].

6.4. Time Overhead of Data Updating. This data updating phase aims to utilize a few novel data blocks to replace the old data blocks, thus updating the outsourced data. Hence, the running time overhead of data updating is concerned with the quantity of outsourced subfiles. We let $q = 100$ and $s = n$ for convenience. Meanwhile, we grow the quantity of outsourced subfiles from 1000 to 10000. Subsequently, we measure the running time overhead, as presented in Figure 7.

From Figure 7, we can clearly discover that in data updating phase, the running time cost of both our designed solution and the previous solution [33] grows with the quantity of outsourced data blocks. At the same time, the time overhead of our designed solution shows a much lower growth rate compared with that of the previous solution [33]. Specifically, the running time cost of our designed solution shows a logarithmic growth tendency, while the time overhead of the previous solution [33] presents a linear growth tendency. Furthermore, our proposed solution requires a substantially less time overhead than the previous solution [33]. For instance, when the quantity of outsourced subfiles is 5000, the time overhead of our proposed solution is nearly 3.5 milliseconds. Nevertheless, the running time overhead of the previous solution [33] is 55.3 milliseconds. Therefore, we can trust that in data updating phase, our designed solution is equipped with much higher efficiency than the previous solution [33].

7. Conclusions

In this paper, we study the issue of outsourced data integrity checking with provable data update in cloud computing environment. In the meantime, we utilized MSHT to present an efficient integrity auditing scheme over outsourced data, which could also achieve block-based dynamic data update. Specifically, the tenant could permanently delete the local backups from the physical medium after the file was stored on the cloud data center. Meanwhile, the tenant could periodically perform data integrity and availability auditing to ensure the cloud data center sincerely stored and managed the outsourced data. Subsequently, the tenant was able to utilize a few novel data blocks to replace the old outsourced data blocks to achieve data update. Because the tenant lacks trust in the cloud data center, he/she could audit the result of data update. The security analysis formally proved that our proposed scheme could realize anticipant design goal without dependency on a third authority. Finally, the performance comparison and experiment results showed that our designed scheme was much more high-efficient.

In our designed scheme, we solved the problem of efficient data integrity auditing with provable data replacement update. However, in some specific scenarios, tenants not only want to audit the data integrity and update the data but also want to add a few novel data blocks and remove some old data blocks. Therefore, in the future, we aim to study the design of efficient data auditing scheme supporting all dynamic operations, thus simultaneously achieving data integrity checking, dynamic data insertion, verifiable data update, and secure data deletion.

Data Availability

The data utilized to sustain the contributions of this research are all contained in the paper. Thence, there is no need of more data collection.

Conflicts of Interest

The authors declare that they have no conflicts of interest.

Acknowledgments

The authors would like to sincerely thank the anonymous referees for their very valuable time. Meanwhile, this work is supported by the Science and Technology Program of Guangxi (AD20297028), the Natural Science Foundation of Guangxi (2020GXNSFBA297132), the National Key R&D Program of China (2020YFB1006003), the Guangdong Key R&D Program (2020B0101090002), the National Natural Science Foundation of China (61772150), and the Innovation Project of GUET Graduate Education (no. 2021YCXS063).

References

[1] C. Yang, F. Zhao, X. Tao, and Y. Wang, "Publicly verifiable outsourced data migration scheme supporting efficient integrity checking," *Journal of Network and Computer Applications*, vol. 192, 2021.

[2] T. Wang, J. Zhou, X. Chen, G. Wang, A. Liu, and Y. Liu, "A three-layer privacy preserving cloud storage scheme based on computational intelligence in fog computing," *IEEE Transactions on Emerging Topics in Computational Intelligence*, vol. 2, no. 1, pp. 3–12, 2018.

[3] K. Xue, W. Chen, W. Li, J. Hong, and P. Hong, "Combining data owner-side and cloud-side access control for encrypted cloud storage," *IEEE Transactions on Information Forensics and Security*, vol. 13, no. 8, pp. 2062–2074, 2018.

[4] C. Yang, X. Tao, F. Zhao, and Y. Wang, "Secure data transfer and deletion from counting bloom filter in cloud computing," *Chinese Journal of Electronics*, vol. 29, no. 2, pp. 273–280, 2020.

[5] J. Li, J. Wu, and L. Chen, "Block-secure: blockchain based scheme for secure P2P cloud storage," *Information Sciences*, vol. 465, pp. 219–231, 2018.

[6] C. Yang, X. Chen, and X. Yang, "Blockchain-based publicly verifiable data deletion scheme for cloud storage," *Journal of Network and Computer Applications*, vol. 103, pp. 185–193, 2018.

[7] S. Subashini and V. Kavitha, "A survey on security issues in service delivery models of cloud computing," *Journal of Network and Computer Applications*, vol. 34, no. 1, pp. 1–11, 2011.

[8] C. Yang, Y. Liu, F. Zhao, and S. Zhang, "Provable data deletion from efficient data integrity auditing and insertion in cloud storage," *Computer Standards & Interfaces*, vol. 82, 2022.

[9] P. Wei, D. Wang, Y. Zhao, S. K. S. Tyagi, and N. Kumar, "Blockchain data-based cloud data integrity protection mechanism," *Future Generation Computer Systems*, vol. 102, pp. 902–911, 2020.

[10] B. Li, Q. He, F. Chen, H. Jin, Y. Xiang, and Y. Yang, "Auditing cache data integrity in the edge computing environment," *IEEE Transactions on Parallel and Distributed Systems*, vol. 32, no. 5, pp. 1210–1223, 2021.

[11] Y. Yu, Y. Li, B. Yang, W. Susilo, G. Yang, and J. Bai, "Attribute-based cloud data integrity auditing for secure outsourced storage," *IEEE Transactions on Emerging Topics in Computing*, vol. 8, no. 2, pp. 377–390, 2020.

[12] C. Yang, X. Tao, S. Wang, and F. Zhao, "Data integrity checking supporting reliable data migration in cloud storage," in *International Conference on Wireless Algorithms, Systems, and Applications*, pp. 615–626, Springer, 2020.

[13] Y. Li, Y. Yu, G. Min, W. Susilo, J. Ni, and K. K. R. Choo, "Fuzzy identity-based data integrity auditing for reliable cloud storage systems," *IEEE Transactions on Dependable and Secure Computing*, vol. 16, no. 1, pp. 72–83, 2019.

[14] G. Cui, Q. He, B. Li et al., "Efficient verification of edge data integrity in edge computing environment," *IEEE Transactions on Services Computing*, 2022.

[15] J. Lin, W. Yu, N. Zhang, X. Yang, and L. Ge, "Data integrity attacks against dynamic route guidance in transportation-based cyber-physical systems: modeling, analysis, and defense," *IEEE Transactions on Vehicular Technology*, vol. 67, no. 9, pp. 8738–8753, 2018.

[16] C. Yang, J. Wang, X. Tao, and X. Chen, "Publicly verifiable data transfer and deletion scheme for cloud storage," *International Journal of Distributed Sensor Networks*, vol. 15, 458 pages, 2019.

[17] G. Ateniese, R. Burns, R. Curtmola et al., "Provable data possession at untrusted stores," in *in the 14th ACM conference on Computer and communications security*, pp. 598–609, Alexandria, Virginia, USA, 2007.

[18] L. Chen, "Using algebraic signatures to check data possession in cloud storage," *Future Generation Computer Systems*, vol. 29, no. 7, pp. 1709–1715, 2013.

[19] Y. Yu, Y. Zhang, J. Ni, M. H. Au, L. Chen, and H. Liu, "Remote data possession checking with enhanced security for cloud storage," *Future Generation Computer Systems*, vol. 52, pp. 77–85, 2015.

[20] J. Li, H. Yan, and Y. Zhang, "Efficient identity-based provable multi-copy data possession in multi-cloud storage," *IEEE Transactions on Cloud Computing*, vol. 10, 2022.

[21] H. Wang, "Identity-based distributed provable data possession in multicloud storage," *IEEE Transactions on Services Computing*, vol. 8, no. 2, pp. 328–340, 2015.

[22] J. Chang, B. Shao, Y. Ji, and G. Bian, "Efficient identity-based provable multi-copy data possession in multi-cloud storage, revisited," *IEEE Communications Letters*, vol. 24, no. 12, pp. 2723–2727, 2020.

[23] Y. Fan, X. Lin, G. Tan, Y. Zhang, W. Dong, and J. Lui, "One secure data integrity verification scheme for cloud storage," *Future Generation Computer Systems*, vol. 96, pp. 376–385, 2019.

[24] W. Shen, J. Qin, J. Yu, R. Hao, J. Hu, and J. Ma, "Data integrity auditing without private key storage for secure cloud storage," *IEEE Transactions on Cloud Computing*, vol. 9, no. 4, pp. 1408–1421, 2021.

[25] N. Lu, Y. Zhang, W. Shi, S. Kumari, and K.-K. R. Choo, "A secure and scalable data integrity auditing scheme based on hyperledger fabric," *Computers & Security*, vol. 92, 2020.

[26] Y. Zhang, C. Xu, X. Lin, and X. Shen, "Blockchain-based public integrity verification for cloud storage against procrastinating auditors," *IEEE Transactions on Cloud Computing*, vol. 9, no. 3, pp. 923–937, 2021.

[27] Y. Li and F. Zhang, "An efficient certificate-based data integrity auditing protocol for cloud-assisted WBANs," *IEEE Internet of Things Journal*, 2021.

[28] F. Liu, D. Gu, and H. Lu, "An improved dynamic provable data possession model," in *in 2011 IEEE International Conference on Cloud Computing and Intelligence Systems*, pp. 290–295, Beijing, China, 2011.

[29] B. Chen and R. Curtmola, "Robust dynamic provable data possession," in *in 2012 32nd International Conference on Distributed Computing Systems Workshops*, pp. 515–525, Macau, China, 2012.

[30] F. Barsoum and M. A. Hasan, "Provable multicopy dynamic data possession in cloud computing systems," *IEEE Transactions on Information Forensics and Security*, vol. 10, no. 3, pp. 485–497, 2015.

[31] E. Esiner, A. Kachkeev, S. Braunfeld, A. Küpçü, and Ö. Özkasap, "FlexDPDP," *ACM Transactions on Storage*, vol. 12, no. 4, pp. 1–44, 2016.

[32] Y. Yuan, J. Zhang, and W. Xu, "Dynamic multiple-replica provable data possession in cloud storage system," *IEEE Access*, vol. 8, pp. 120778–120784, 2020.

[33] H. Yu, Z. Yang, M. Waqas et al., "Efficient dynamic multi-replica auditing for the cloud with geographic location," *Future Generation Computer Systems*, vol. 125, pp. 285–298, 2021.

[34] W. Guo, S. Qin, F. Gao et al., "Dynamic proof of data possession and replication with tree sharing and batch verification in the cloud," *IEEE Transactions on Services Computing*, 2020.

[35] K. He, J. Chen, Q. Yuan, S. Ji, D. He, and R. Du, "Dynamic group-oriented provable data possession in the cloud," *IEEE Transactions on Dependable and Secure Computing*, vol. 18, no. 3, p. 1, 2021.

[36] R. Chen, Y. Li, Y. Yu, H. Li, X. Chen, and W. Susilo, "Blockchain-based dynamic provable data possession for smart cities," *IEEE Internet of Things Journal*, vol. 7, no. 5, pp. 4143–4154, 2020.

[37] W. Guo, H. Zhang, S. Qin et al., "Outsourced dynamic provable data possession with batch update for secure cloud storage," *Future Generation Computer Systems*, vol. 95, pp. 309–322, 2019.

[38] X. Chen, J. Li, X. Huang, J. Ma, and W. Lou, "New publicly verifiable databases with efficient updates," *IEEE Transactions on Dependable and Secure Computing*, vol. 12, no. 5, pp. 546–556, 2015.

[39] X. Chen, H. Li, J. Li et al., "Publicly verifiable databases with all efficient updating operations," *IEEE Transactions on Knowledge and Data Engineering*, vol. 33, no. 12, pp. 3729–3740, 2021.

[40] M. Miao, J. Ma, X. Huang, and Q. Wang, "Efficient verifiable databases with insertion/deletion operations from delegating polynomial functions," *IEEE Transactions on Information Forensics and Security*, vol. 13, no. 2, pp. 511–520, 2018.

[41] L. Rao, H. Zhang, and T. Tu, "Dynamic outsourced auditing services for cloud storage based on batch-leaves-authenticated Merkle hash tree," *IEEE Transactions on Services Computing*, vol. 13, no. 3, pp. 451–463, 2020.

[42] C. Yang, Y. Liu, and X. Tao, "Assure deletion supporting dynamic insertion for outsourced data in cloud computing," *International Journal of Distributed Sensor Networks*, vol. 16, no. 9, 2020.

[43] J. Mao, Y. Zhang, P. Li, T. Li, Q. Wu, and J. Liu, "A position-aware Merkle tree for dynamic cloud data integrity verification," *Soft Computing*, vol. 21, no. 8, pp. 2151–2164, 2017.

[44] Y. Yu, L. Xue, Y. Li, X. Du, M. Guizani, and B. Yang, "Assured data deletion with fine-grained access control for fog-based industrial applications," *IEEE Transactions on Industrial Informatics*, vol. 14, no. 10, pp. 4538–4547, 2018.

[45] C. Yang, Y. Liu, X. Tao, and F. Zhao, "Publicly verifiable and efficient fine-grained data deletion scheme in cloud computing," *IEEE Access*, vol. 8, pp. 99393–99403, 2020.

Hindawi
Wireless Communications and Mobile Computing
Volume 2022, Article ID 6185482, 12 pages
https://doi.org/10.1155/2022/6185482

Research Article

Specific Emitter Identification with Limited Labelled Signals Based on Variational Autoencoder Embedded in Information-Maximising Generative Adversarial Network and Gradient Penalty

CunXiang Xie,[1] **LiMin Zhang**,[1] **and ZhaoGen Zhong**[2]

[1]*Department of Information Fusion, Naval Aviation University, Yantai 264001, China*
[2]*The School of Aviation Basis, Naval Aviation University, Yantai 264001, China*

Correspondence should be addressed to ZhaoGen Zhong; zhongzhaogen@163.com

Received 28 January 2022; Accepted 24 February 2022; Published 12 March 2022

Academic Editor: Zhao Junhui

The lack of labelled signal datasets in noncooperative scenarios limits the performance of specific emitter identification (SEI). To address this limitation, a method for SEI with limited labelled signals is proposed. The bispectrum of the received signal is estimated to enhance individual discriminability. An information-maximising generative adversarial network (InfoGAN) is then developed to perform SEI with limited labelled signals. To prevent nonconvergence and mode collapse due to the complexity of the radiofrequency signals, we improve the InfoGAN, respectively, from the generator and discriminator perspective. For the former, an encoder is combined with the InfoGAN generator to form a variational autoencoder that reduces the difficulty of convergence during training. For the latter, a gradient penalty algorithm is applied during the training of the InfoGAN discriminator, which enables its training loss function to obey the 1-Lipschitz constraint, thereby avoiding gradient disappearance. The design of the objective function for the training of each subnetwork and the training procedure are provided. The proposed network is trained with limited labelled and abundant unlabelled data, and an auxiliary classifier categorizes the emitters after training. Numerical results indicate that our method outperforms state-of-the-art algorithms for SEI with limited labelled signal samples in terms of effectiveness, convergence, accuracy, and robustness against noise.

1. Introduction

With the advent of the 5G era, the demand for radio spectrum has increased significantly. Due to this, technologies that enable the usage of spectrum resources to be monitored and regulated have become complex but important tools for its successful exploitation [1–3]. Specific emitter identification (SEI), as one of such key technologies, enables the identification of individual sources of radiofrequency (RF) signals based on the RF fingerprints (RFFs) that result from the nonideal hardware tolerances of the emitters [4]. The RFFs extracted from the RF signals produced by a particular emitter contain unique characteristics that enable SEI to be implemented [5, 6].

In recent years, various methods for performing SEI have been proposed. For instance, Bihl et al. [7] developed a method to extract RFFs through a dimensional reduction analysis (DRA) based on feature selection and designed a multiple discriminant analysis classifier to recognize individual emitters based on DRA feature subsets. The method shows an excellent performance in terms of classification accuracy and robustness when applied for SEI of Zigbee devices. Padilla et al. [8] successfully identified 28 Wi-Fi devices with an accuracy of more than 95% by analysing the preamble information in the communication. However, this method is limited to signals with a communication preamble. A method for SEI based on the bispectrum-Radon transform was proposed in [9]. The method first estimates

the bispectrum of the RF signal to preliminarily represent the RFFs and then compresses it via the Radon transform to obtain the bispectrum projection vector, which is used as the input of a hybrid network model to extract deep RFFs and conduct individual emitter identification. The method was able to classify six emitter individuals with an identification accuracy higher than 90%. However, the bispectrum analysis-based method can easily lose some important subtle features, resulting in a negative impact on the SEI performance. Yuan et al. [10] applied the Hilbert–Huang transform (HHT) to transient RF signals, extracted RFFs based on the estimated time–frequency energy distribution, and finally used a support vector machine (SVM) for emitter identification. The method was able to successfully identify eight mobile phones but is only applicable to transient RF signals. Satija et al. [11] proposed the use of variational mode decomposition (VMD) to derive the temporal and spectral modes of RF signals. Various spectral features were then selected as RFFs to identify the received signals. The VMD spectral feature-based method is highly adaptable to various scenarios, including single hop and relaying, and considerably robust against noise in both additive white Gaussian noise (AWGN) and flat-fading channels. However, the performance of the method was verified using simulated rather than real-world signal data; thus, its practicality requires further research.

The abovementioned traditional RFF extraction schemes have achieved certain advancements in individual emitter identification, but some drawbacks remain. Owing to their complexity, RFFs cannot be represented by a unified mathematical model, which makes it necessary to blindly attempt multiple RFF extraction schemes and find a relatively optimal method for a specific SEI task. As a result, significant subjectivity is involved and successful identification is dependent on the cognitive level of the researcher. In other words, conventional methods mainly rely on measurements to extract the RFFs defined by specialists and cannot completely scan the representative characteristics of each emitter's RFFs.

With the progress in artificial intelligence technology, researchers have applied deep learning (DL) [12–14] to many fields. Various DL-based methods have been developed and have demonstrated considerable potential in applications such as computer vision (CV) and natural language processing (NLP). Furthermore, these advanced technologies have already achieved great success in emerging fields, such as the Internet of Vehicles [15–17], wireless radio processing [18–20], radar waveform recognition [21, 22], and edge computing [23–25]. Motivated by these developments, works on SEI have found in DL a new research direction. Wu et al. [26] proposed an RFF extraction scheme based on a long short-term memory (LSTM) network to learn the high-order correlation of the received signal and identify its emitter. Considering the advantages of convolutional neural networks (CNNs) in image processing, Wang et al. [27] used pulse waveform images and a CNN to identify specific radar emitters. Recently, considering the characteristics of SEI application, scholars have proposed some new network models and algorithms for SEI using basic network models, such as CNNs and LSTM networks. Qian et al. [28] proposed an automatic SEI system based on a CNN with multilevel sparse representation. The SEI system splices the shallow and deep RFF features extracted by the CNN and then performs SEI based on the sparse representation identification. With limited signal samples, this approach can identify nine emitter devices with an accuracy of more than 90%. Wang et al. [29] proposed a novel DL-based model comprising a complex-valued neural network (CVNN) for SEI. Just as CNNs were designed to process two-dimensional (2D) images, CVNNs were developed to process complex-valued data. Therefore, the CVNN model is suitable for directly processing complex baseband RF signals.

Overall, the existing SEI approaches based on DL mainly focus on supervised learning, where all training data are assumed to be labelled. However, in noncooperative scenarios, it is difficult to obtain labelled training data for SEI, which limits the performance of the DL methods used. To address this limitation, Yang et al. [30] applied a few-shot learning method based on model-agnostic meta-learning (MAML) to SEI with limited availability of labelled signal data. Similarly, to solve the problems of SEI in noncooperative scenarios, in this study, we propose a novel network model for SEI, referred to as VAE-InfoGAN-GP, which comprises a variational autoencoder (VAE) embedded in an information-maximising generative adversarial network (InfoGAN), and a gradient penalty algorithm. Unlike the method in [30], our method can make full use of a large number of easily accessible unlabelled signal data to perform SEI. Accordingly, the system can learn RFFs in a more comprehensive and deeper way, thereby achieving better performance in the identification process. We conducted bispectrum analysis on the received signals as a preprocessing step. The InfoGAN model [32], which is a DL algorithm based on a generative adversarial network (GAN) [31], was used because of its excellent performance in unsupervised learning and was improved by embedding a VAE into it and applying a gradient penalty algorithm during the discriminator training. Additionally, a new latent vector was used as the generator input.

The main contributions of this study can be summarised as follows:

(1) The RF signals are preprocessed using a bispectrum analysis to enhance the discriminability of different emitter individuals

(2) Considering the fact that the complexity of RFFs may pose certain difficulties during the execution of the InfoGAN, especially mode collapse and nonconvergence, we incorporate some innovations in both generators and discriminators. An encoder is added before the generator to compress the RF signal bispectrum into a low-dimensional hidden variable that is then decoded by the generator to recover real RFF representation data. This provides the prior RFF representation data to the generator, thereby facilitating the generator training. Additionally, we propose a gradient penalty algorithm to train the discriminator, enabling its loss function to obey the

1-Lipschitz constraint, which can avoid gradient disappearance and further optimise the network

(3) To improve the practicability of the proposed network, the loss function of each subnetwork training is analysed and designed; moreover, the training flow of the whole network is analysed and provided

(4) Numerous experiments are carried out to evaluate the convergence and identification performance of our method. Simulation results show that our method can perform SEI tasks well in noncooperative scenarios

The remainder of this paper is organised as follows. In Section 2, the proposed method for semisupervised SEI is provided. We first introduce the signal preprocessing method based on bispectrum analysis, then describe the design of the VAE-InfoGAN model and the details of the gradient penalty algorithm, and lastly explain a novel latent vector used as the generator input. The results of the experiments conducted on a real-world RF dataset generated through the software-defined radio (SDR) platform are presented in Section 3. Finally, Section 4 presents the conclusions of the paper.

2. Proposed Method for SEI with Limited Labelled Signals

2.1. Signal Preprocessing. A bispectrum analysis is an effective method for signal preprocessing, which can retain the amplitude and phase of the signal and measure its degree of nonlinearity and asymmetry [33, 34]. The estimated bispectrum of the RF signals forms the basis for RFF extraction. The estimated bispectrum can be obtained as follows:

$$B(\omega_1, \omega_2) = \sum_{\tau_1} \sum_{\tau_2} c_{3x}(\tau_1, \tau_2) e^{-j(\omega_1 \tau_1 + \omega_2 \tau_2)}, \tag{1}$$

where ω_1 and ω_2 represent the 2D frequencies, and the third-order cumulant $c_{3x}(\tau_1, \tau_2)$ can be expressed as

$$c_{3x}(\tau_1, \tau_2) = E[x^*(t)x(t+\tau_1)x(t+\tau_2)]. \tag{2}$$

To form some intuition, we perform a bispectrum analysis on two RF signals, $x_1(t)$ and $x_2(t)$, recorded from two emitter individuals of the same device type, obtaining the bispectral energy distributions shown in Figure 1. It is observed that the energy side lobe distribution in Figure 1(a) is smoother than that in Figure 1(b), whereas the main lobe distribution in Figure 1(b) is more concentrated than that in Figure 1(a). To visualise the differences more intuitively, the corresponding bispectral contour maps, which are the bispectra of the signals, are obtained in Figure 2 as the RFF representation data that are used as the input of the proposed network model.

As shown in Figure 2, there are visible differences between the two bispectrums, demonstrating the effectiveness of the bispectrum analysis for signal preprocessing, which can enhance individual discriminability.

2.2. VAE-InfoGAN. The basic architecture of the InfoGAN consists of a generator (G), a discriminator (D), and an auxiliary classifier (Q). The generator output data $G(\mathbf{z}, \mathbf{c})$ after being fed with the latent vector $\mathbf{z}$ and latent code $\mathbf{c}$, which is an interpretable constraint variable such as the real data category. The discriminator aims to distinguish the generated data from the real data, thereby facilitating the generator to output data that is as close to the real data as possible. Lastly, the auxiliary classifier decodes $G(\mathbf{z}, \mathbf{c})$ to maximise the mutual information between the generated data and the latent code $\mathbf{c}$, thereby enabling the generator output to have a higher correlation with said code. When InfoGAN converges, the auxiliary classifier can effectively identify generated data, $G(\mathbf{z}, \mathbf{c})$, that is similar to the real data. Therefore, the auxiliary classifier can also be used for the unsupervised classification of the real data.

In this study, we used InfoGAN as the initial structure of the algorithm and extended it by including a VAE. Figure 3 shows the resulting architecture of the proposed VAE-InfoGAN model, where $\mathbf{x} = \{\mathbf{x}_l, \mathbf{x}_u\}$ represents the bispectrum of the RF signals, that is, the RFF representation data, and includes both labelled data $\mathbf{x}_l$ and unlabelled data $\mathbf{x}_u$. The labels of $\mathbf{x}_l$ can be denoted as $\mathbf{y}_l = \{y_{l1}, y_{l2}, \cdots, y_{lM}\}$. Additionally, the latent code $\mathbf{c}$ is sampled from a categorical distribution, $\mathrm{Cat}(K, p = 1/K)$, where K represents the emitter classes.

To further optimise the network, instead of an original Gaussian distribution, the latent vector $\mathbf{z}$ is taken from a Gaussian mixture distribution [35], which can be expressed as follows:

$$P_z(\mathbf{z}) = \sum_{k=1}^{K} w_k \cdot \frac{1}{\sqrt{2\pi\sigma_k}} \exp\left\{\frac{(\mathbf{z}-\mu_k)^T(\mathbf{z}-\mu_k)}{2\sigma_k^2}\right\}, \tag{3}$$

where K represents the emitter classes, μ_k and σ_k are, respectively, the mean and covariance of the k-th emitter, and w_k represents a categorical random variable such that $w_k \geq 0$ and $\sum_{k=1}^{K} w_k = 1$.

Finally, we feed $\mathbf{z}$ and $\mathbf{c}$ into the generator to produce fake representation data G_f.

The InfoGAN model has a number of inherent failure modes that can occur during training. Of particular interest in this case are the problems of modal collapse and nonconvergence, which can be further exacerbated due to the complexity of the RF signals. To address this limitation, we introduce a VAE into the InfoGAN (which is referred to as VAE-InfoGAN). The VAE consists of an encoder (E) and a decoder (corresponding to generator G). The former encodes the RFF representation data to obtain bottleneck vectors, which include the mean vector $\boldsymbol{\mu}$ and covariance vector $\boldsymbol{\sigma}$. The bottleneck vector space is then constructed as follows [36].

$$\begin{aligned} \mathbf{Z} &= \boldsymbol{\mu} + \varepsilon \odot \exp(\boldsymbol{\sigma}), \\ \varepsilon &\sim N(0, I), \end{aligned} \tag{4}$$

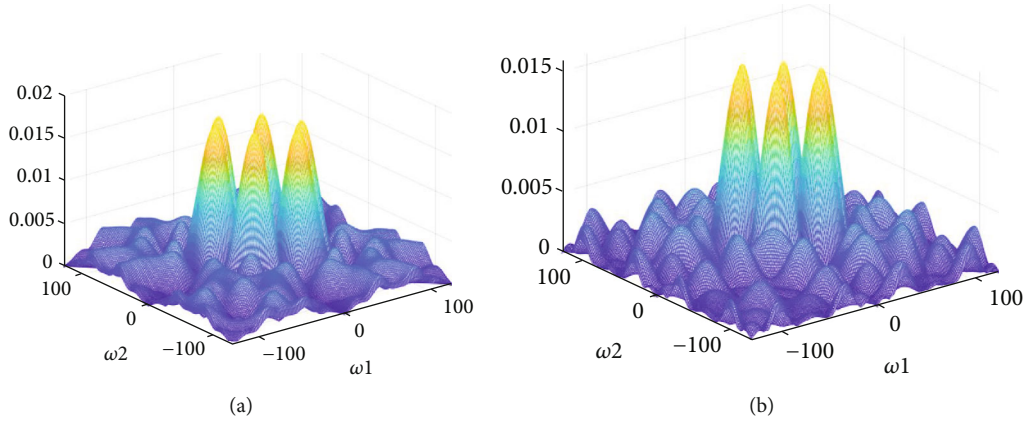

Figure 1: Bispectral energy distributions. (a) $x_1(t)$; (b) $x_2(t)$.

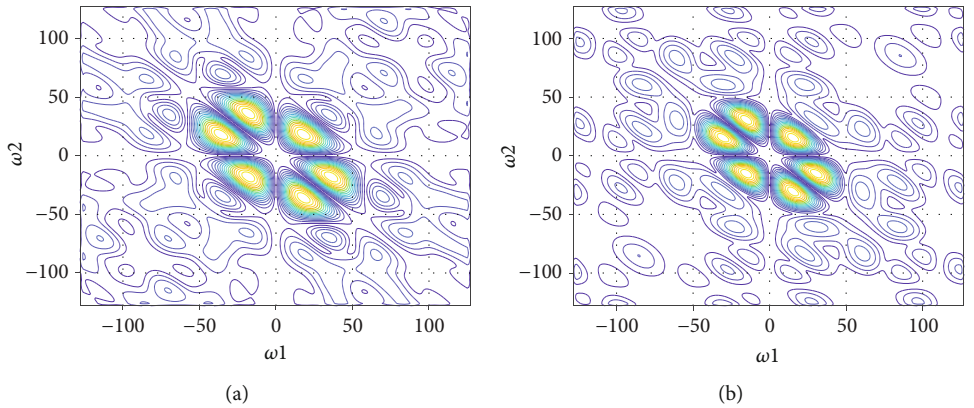

Figure 2: Two-dimensional-bispectral contour map. (a) $x_1(t)$; (b) $x_2(t)$.

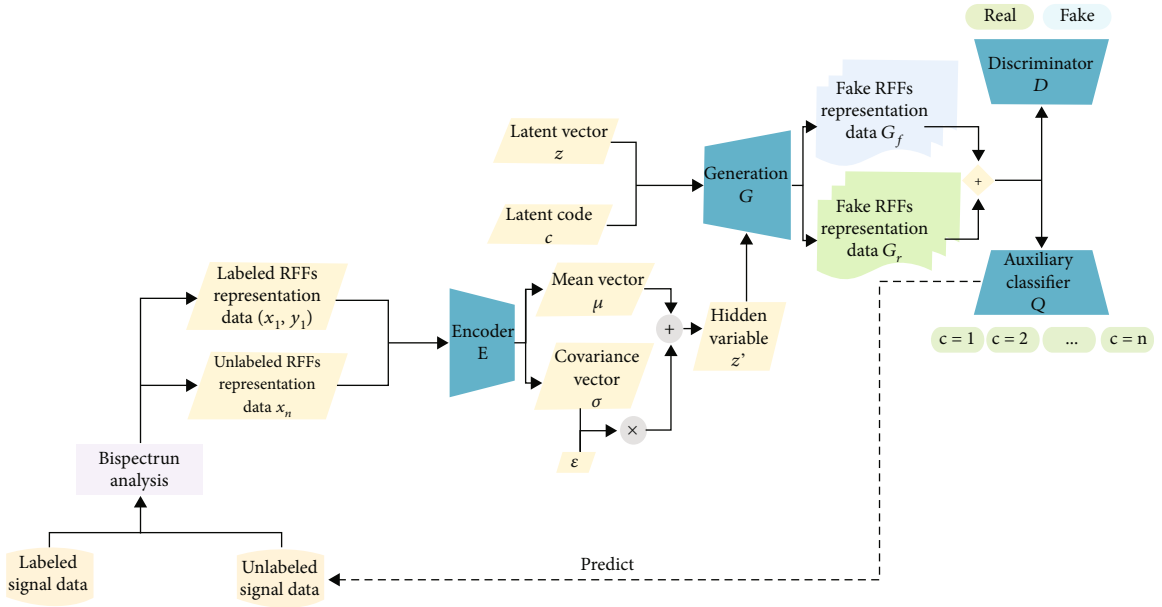

Figure 3: Architecture of the proposed VAE-InfoGAN.

where ε represents a random vector that follows a standard normal distribution.

By sampling from $\mathbf{Z}$, we obtain the hidden variable $\mathbf{z}'$ which is subsequently decoded by the generator to reconstruct the real RFF representation data G_r, aiming for it to be as close as possible to the RFF representation data $\mathbf{x}$. In the original InfoGAN, the training may become unstable because of the difficulty in balancing the capabilities of both the generator and discriminator. This results from the fact that the generator has no prior knowledge of the complex-featured RFF representation data and simply generates fake sets from random noise. Therefore, during training, the generator is significantly less powerful than the discriminator, and an effective confrontation cannot be achieved. In this case, the network will have a poor training effect, and mode collapse or nonconvergence problems may appear. However, when the VAE is embedded in the original InfoGAN, we can provide the generator with a loss value between the real RFF representation data G_r and RFF representation data $\mathbf{x}$, so that it obtains prior knowledge about the RFF representation data. With the help of this information, the generator can converge faster, thereby simplifying the training of the whole network.

Based on [36], the encoder training process can be expressed as follows:

$$E_{\text{opt}} = \min_{E} V'(E, G) = \min_{E} \left[V(E, G) - V_{\text{prior}}(E) \right], \tag{5}$$

where $V(E, G)$ is the function used to make the real RFF representation data G_r as close as possible to the RFF representation data $\mathbf{x}$ and $V_{\text{prior}}(E)$ is used to guide the encoded hidden variable $\mathbf{z}'$ into following the normal distribution. This can be expressed as follows:

$$V(E, G) = \mathbb{E}_{x \sim P_{\text{data}}} \| G(E(\mathbf{x})) - \mathbf{x} \|_2^2, \tag{6}$$

$$V_{\text{prior}}(E) = \frac{1}{2} \left[\boldsymbol{\mu}^T \boldsymbol{\mu} + \sum (e^{\boldsymbol{\sigma}} - \boldsymbol{\sigma} - 1) \right], \tag{7}$$

where P_{data} represents the real data distribution.

The discriminator is used to classify data as "real/fake," and its training process can be expressed as follows:

$$D_{\text{opt}} = \max_{D} V(D, G, E) = \max_{D} [V_{\text{real}}(D, G, E) - V_{\text{fake}}(D, G)], \tag{8}$$

where $V_{\text{real}}(D, G, E)$ is used to maximise the output value of the real RFF representation data G_r produced by the generator, which can be expressed as follows:

$$V_{\text{real}}(D, G, E) = \mathbb{E}_{x \sim P_{\text{data}}} [\log (D(G(E(\mathbf{x}))))]. \tag{9}$$

In contrast, $V_{\text{fake}}(D, G)$ is used to minimise the output value of the fake RFF representation data G_f produced by the generator, which can be expressed as follows:

$$V_{\text{fake}}(D, G) = \mathbb{E}_{z \sim P_z \, c \sim P_c} [\log (D(G(\mathbf{z}, \mathbf{c})))]. \tag{10}$$

The auxiliary classifier is used to maximise the mutual information between the latent code $\boldsymbol{c}$ and the generated data $G_f = G(\mathbf{z}, \mathbf{c})$; its training process can be expressed as follows:

$$Q_{\text{opt}} = \max_{Q} L_{ul}(G, Q) = \max_{Q} \left[\mathbb{E}_{z \sim p_z \quad c \sim p_c} \mathbf{c} \cdot \log (Q(G(\mathbf{z}, \mathbf{c}))) \right]. \tag{11}$$

When labelled training data are present, the training process can be extended as follows:

$$Q_{\text{opt}} = \max_{Q} V(G, Q, E) = \max_{Q} [L_{ul}(G, Q) + L_l(G, Q, E)], \tag{12}$$

where $L_l(G, Q, E)$ denotes the mutual information between the labelled RFF representation data $\mathbf{x}_l$ and the corresponding labels $\mathbf{y}_l$, which can be expressed as follows:

$$V(G, Q, E) = \mathbb{E}_{x_l \sim p_{\text{data}} \quad y_l \sim p_{\text{data}}} \mathbf{y}_l \cdot \log (Q(G(E(\mathbf{x}_l)))). \tag{13}$$

Acting as the link between the different subnetworks, the generator training process can be expressed as follows:

$$\begin{aligned} G_{\text{opt}} &= \min_{G} \max_{D} V(G, E, D, Q) \\ &= \min_{G} \max_{D} [V(E, G) + V(D, G, E) - V(G, Q, E)], \end{aligned} \tag{14}$$

where $V(E, G)$, $V(D, G, E)$, and $V(G, Q, E)$ are equivalent to those in Equations (5), (8), and (13), respectively.

2.3. Gradient Penalty for Discriminator. In the previous section, we introduced a VAE to reduce the training difficulty of the generator. However, this measure only improves the network from the perspective of the generator, so that it can effectively play an adversarial game with the discriminator. The defects of discriminator training are also an important factor hindering the training effect of the network. If the discriminator is too weakly trained, it will not be indicative enough for the generator to obtain good results. On the contrary, if the discriminator is too well trained, the generator will not obtain enough gradient information for further optimisation. As a result, discriminator training is very difficult to control. The mathematical proof in [37] shows that the above problem is caused by the use of JS divergence to measure the distance between the real and generated data distribution, which can cause gradient disappearance during training. In this regard, Arjovsky et al. [38] proposed a novel measurement method for calculating the distance between the real and generated data distribution, called the earth mover's distance (EMD), which can be expressed as

$$W(P_{\text{data}}, P_g) = \inf_{\gamma \in \Pi(P_{\text{data}}, P_g)} \mathbb{E}_{(x,y) \sim \gamma} [\| x - y \|], \tag{15}$$

where P_{data} and P_g represent the real and generated data distributions, respectively.

To apply the EMD to neural networks, Equation (15) needs to be transformed using the Kantorovich–Rubinstein duality [39] theory; the transformation result can be expressed as

$$W\left(P_{\text{data}}, P_g\right) = \sup_{\|f\|_L \le 1} \mathbb{E}_{x\sim P_{\text{data}}}[f(x)] - \mathbb{E}_{x\sim P_g}[f(x)], \quad (16)$$

where $f(\cdot)$ denotes a neural network function that obeys the 1-Lipschitz constraint, i.e., $|f(x_1) - f(x_2)| \le |x_1 - x_2|$.

Therefore, to apply the EMD to the GAN-based model, the mathematical model of the discriminator in (8) should be changed, which can be expressed as

$$D_{\text{opt}} = \max_{D\in 1-\text{Lipschitz}} [V_{\text{real}}(D,G,E) - V_{\text{fake}}(D,G)] = \max_{D\in 1-\text{Lipschitz}} \cdot \left\{\mathbb{E}_{x\sim P_{\text{data}}}[\log(D(G(E(\mathbf{x}))))] - \mathbb{E}_{z\sim P_z \quad c\sim P_c}[\log(D(G(\mathbf{z},\mathbf{c})))]\right\}. \quad (17)$$

Directly implementing a discriminator function subject to the 1-Lipschitz constraint is difficult, and this problem can be solved through a mathematically equivalent method, which can be expressed as

$$D \in 1-\text{Lipschitz} \Longleftrightarrow \|\nabla_x D(x)\| \le 1. \quad (18)$$

This essentially requires that $\nabla_x D(x)$ corresponding to all inputs x is less than 1. However, traversing the entire input data distribution is impossible. In this regard, we define a penalty data distribution,P_{penalty}, that only meets the requirement that the data sampled from P_{penalty} correspond to a gradient less than 1. Therefore, the mathematical model of the discriminator in (17) should be changed, which can be expressed as follows:

$$D_{\text{opt}} = \max_D [V_{\text{real}}(D,G,E) - V_{\text{fake}}(D,G)] = \max_D \cdot \left\{\mathbb{E}_{x\sim P_{\text{data}}}[\log(D(G(E(\mathbf{x}))))] - \mathbb{E}_{z\sim P_z \quad c\sim P_c}[\log(D(G(\mathbf{z},\mathbf{c})))] - \lambda \mathbb{E}_{x\sim P_{penalty}}[(\|\nabla_x D(x)\| - 1]^2\right\}, \quad (19)$$

where $\mathbb{E}_{x\sim P_{\text{penalty}}}[\|\nabla_x D(x)\| - 1]^2$ acts as a regular term that penalises the behaviour of gradient $\|\nabla_x D(x)\|$ larger than 1 when the discriminator weight parameters are updated.

In terms of the definition of the penalty data distribution, we define the data distribution space between the real RFF representation data distribution space P_{G_r} and the fake RFF representation data distribution space P_{G_f} as P_{penalty}, as intuitively shown in Figure 4.

The implementation details can be denoted as follows:

$$G_{\text{penalty1}} = G_{r1} + \zeta_1 \cdot \left(G_{f1} - G_{r1}\right) \quad 0 < \zeta_1 < 1,$$
$$G_{\text{penalty2}} = G_{r2} + \zeta_2 \cdot \left(G_{f2} - G_{r2}\right) \quad 0 < \zeta_2 < 1, \quad (20)$$

where G_{r1} and G_{r2} represent real RFF representation data samples sampled from P_{G_r}, G_{f1} and G_{f2} represent fake RFF representation data samples sampled from P_{G_f}, G_{penalty1} and G_{penalty2} denote penalty data samples sampled from P_{penalty}, and ζ_1 and ζ_2 denote random parameters.

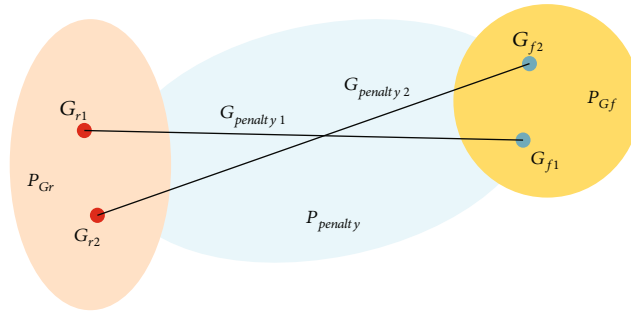

Figure 4: Penalty data distribution.

2.4. Method Procedure. The training process of the proposed method is described in Algorithm 1.

3. Results and Discussion

3.1. RF Signal Data Collection and Experimental Setup. We collected real-world RF signal data to evaluate the performance of our method based on an SDR system implementing GNU radio and containing seven USRP (B210) devices. We used seven USRP devices as transmitters at an RF of 2.4 GHz, with each device connected to a laptop running the Linux Ubuntu 18.04 operating system. The remaining USRP device was connected to the same laptop and served as a receiver to collect the seven classes of RF signals generated by the other devices. The SDR platform is shown in Figure 5.

For each of the seven classes of RF signals generated, we obtained 20,000 segments of RF signal data, and the modulation method is QPSK. Next, using MATLAB, we added different levels of AWGN to adjust the SNR to 0, 2, 4, …, and 20 dB. Bispectrum analysis was then applied to the RF signal data to obtain the RFF representation data, which have a uniform size of 256×256. At each SNR level, 20,000 RFF representation data were obtained per class. Of all the RFF representation data, 80% were used for training, 10% for validation, and the remaining 10% was used for testing. For the training sets, 20% were set as training data with category labels, and 80% were set as training data without category labels. Figure 6 shows the dataset structure.

We evaluated the performance of our method based on Python 3.6 in TensorFlow. The DL PC was equipped with an NVIDIA GeForce GTX 3090 Ti GPU, and the details of the network structure and training hyperparameters are presented in Table 1.

3.2. Convergence Performance. We compared the convergence performance of the VAE-InfoGAN performing gradient penalty algorithm (VAE-InfoGAN-GP) with other two network frameworks: VAE-InfoGAN and InfoGAN. Figure 7 shows the training loss value curves in 400 epochs.

Input:
$(\boldsymbol{s}_l, \boldsymbol{s}_{ul})$: Raw RF signal data;
$\boldsymbol{c}$: Latent code;
$\boldsymbol{z}$: Latent vector;
Output:
$\theta_E, \theta_G, \theta_D, \theta_Q$: Parameters of sub-networks E, G, D, Q
1. Perform bispectrum analysis on RF signal data $(\boldsymbol{s}_l, \boldsymbol{s}_{ul})$ and obtain bispectrum as RFFs representation data $(\boldsymbol{x}_l, \boldsymbol{x}_{ul})$;
2. Initialize network parameters of encoder, generator, discriminator and auxiliary classifier;
3. Fix the network parameters of encoder and generator, generate real and fake RFFs representation data based on the RFFs representation data $(\boldsymbol{x}_l, \boldsymbol{x}_{ul})$, latent code $\boldsymbol{c}$ and latent vector $\boldsymbol{z}$:
$\boldsymbol{z}' \longleftarrow E(\boldsymbol{x}) \quad G_r \longleftarrow G(\boldsymbol{z}')$
$G_f \longleftarrow G(\boldsymbol{z}, \boldsymbol{c})$
4. Calculate the loss function of discriminator:
$L_D = \mathbb{E}_{G_r \sim p_G(z')}[\log(D(G_r))] - \mathbb{E}_{G_f \sim p_G(z,c)}[\log(D(G_f))]$
$-\lambda \mathbb{E}_{x \sim P_{penalty}}[(\|\nabla_x D(x)\| - 1]^2$
5. Network parameters of discriminator are updated according to the loss function:
$\theta_D^{i+1} \longleftarrow \theta_D^i - \eta_D \nabla_\theta L_D(\theta)$
6. Calculate the loss function of auxiliary classifier:
$L_Q = \mathbb{E}_{\substack{G_f \sim p_G(z,c) \\ c \sim p_c}} \boldsymbol{c} \log(Q(G_f)) + \lambda_Q \mathbb{E}_{G_r \sim p_G(z')} \boldsymbol{y}_l \log(Q(G_r))$
7. Network parameters of auxiliary classifier are updated according to the loss function:
$\theta_Q^{i+1} \longleftarrow \theta_Q^i - \eta_Q \nabla_\theta L_Q(\theta)$
8. Fix network parameters of discriminator and auxiliary classifier, and train encoder and generator;
9. Calculate the loss function of generator:
$L_G = \lambda_{G1} L_D - \lambda_{G2} L_Q + \lambda_{G3} \|G_r - \boldsymbol{x}\|_2^2$
10. Network parameters of generator are updated according to the loss function:
$\theta_G^{i+1} \longleftarrow \theta_G^i - \eta_G \nabla_\theta L_G(\theta)$
11. Calculate the loss function of encoder:
$L_E = \|G_r - \boldsymbol{x}\|_2^2 - 1/2[\boldsymbol{\mu}^T \boldsymbol{\mu} + \sum(e^{\boldsymbol{\sigma}} - \boldsymbol{\sigma} - 1)]$
12. Network parameters of encoder are updated according to the loss function:
$\theta_E^{i+1} \longleftarrow \theta_E^i - \eta_E \nabla_\theta L_E(\theta)$
13. Repeat steps (2)-(12) until the network converges, and then auxiliary classifier is used to conduct semi-supervised SEI;

Algorithm 1: Training procedure of VAE-InfoGAN-GP.

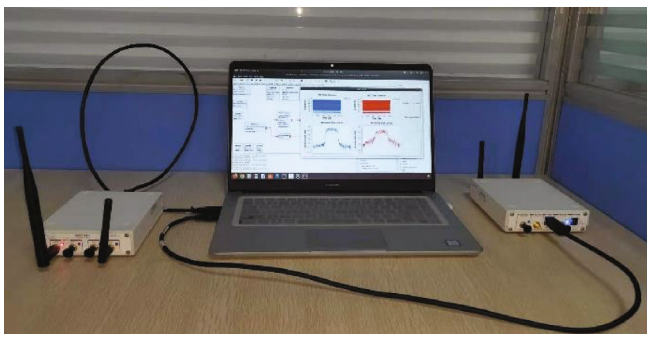

Figure 5: SDR platform.

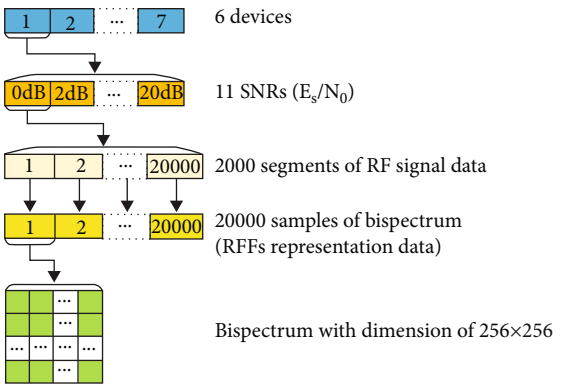

Figure 6: Dataset structure.

As shown in Figure 7, VAE-InfoGAN-GP achieves the fastest convergence speed and reaches the best convergence plane. In contrast, the loss value of VAE-InfoGAN is maintained at a higher level because the traditional discriminator adopts JS divergence to calculate the distance between the real and fake data distribution, resulting in gradient disappearance. In this case, the further optimisation of network parameters will be affected, so that the training loss value cannot be further decreased. This comparison demonstrates the effectiveness of the gradient penalty algorithm in avoiding disappearance and improving the network training effect. Additionally, the loss value curve of InfoGAN shows significant fluctuations, which are the manifestation of

Table 1: Network structure and hyperparameters.

Encoder E			
Conv 2D	Kernel_size = 4 × 8, Filters = 80, Tanh, batch norm		
Conv 2D	Kernel_size = 2 × 4, Filters = 32, Tanh, batch norm		
Dense	Units = 100, ReLU, batch norm		
Generator G			
Dense	Units = 8192, LeakyReLU, batch norm		
Reshape	32 × 256 × 1		
Conv 2D	Kernel_size = 4 × 8, Filters = 256, Tanh, batch norm		
Conv 2D	Kernel_size = 4 × 12, Filters = 80, Tanh, batch norm		
Conv 2D	Kernel_size = 4 × 16, Filters = 1, Tanh, batch norm		
Discriminator D & auxiliary classifier Q			
Conv 2D	Kernel_size = 4 × 16, Filters = 32, ReLU, batch norm, Maxpooling		
Conv 2D	Kernel_size = 4 × 12, Filters = 32, ReLU, batch norm, Maxpooling		
Conv 2D	Kernel_size = 4 × 8, Filters = 8, ReLU, batch norm		
Discriminator D		Auxiliary classifier Q	
Dense	Units = 128, ReLU	Dense	Units = 256, ReLU
Dense	Units = 1, sigmoid	Dense	Units = 64, ReLU
		Dense	Units = 6, softmax
Hyperparameters			Value
Optimiser			Adam
Learning rate			0.0001
Epochs			400
Minibatch			64
Dropout rate			0.5

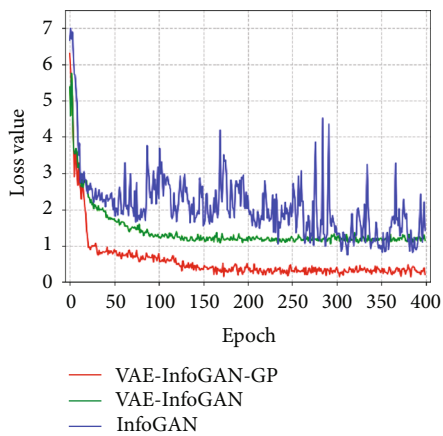

Figure 7: Training loss curves of VAE-InfoGAN-GP, VAE-InfoGAN, and InfoGAN.

network nonconvergence. However, the loss value curve of VAE-InfoGAN tends to flatten out with the progress of network training, showing a superior convergence performance. The reason for this significant difference is that VAE-InfoGAN can provide the generator for the prior information of the real data, thereby reducing the training difficulty of the generator and facilitating convergence of the whole network model. This comparison demonstrates that the VAE embedded original InfoGAN can effectively prevent mode collapse and nonconvergence, which is of considerable benefit to the improvement of the convergence performance.

3.3. Identification Performance vs. SNRs. We tested the identification performance of the proposed method according to the SNR. Furthermore, we compare it with that of the original InfoGAN and existing methods, including MAML [30] and virtual adversarial training (VAT) [40].

Figure 8 shows the identification accuracy as a function of the SNRs of the evaluated methods under AWGN and Rayleigh noise.

As shown in Figure 8(a), our method has an average identification accuracy of 7–10% higher than the original InfoGAN, which further demonstrates that the embedded VAE and gradient penalty algorithm can improve the training effect of InfoGAN, thereby enhancing the identification performance of the SEI system. Additionally, our proposed method achieves an approximate accuracy of 90% at 6 dB and 95% at 10 dB. Compared with the existing methods of VAT and MAML, the identification performance of our method is improved to different degrees. Especially at low SNRs, our method shows superior noise robustness, and the maximum accuracy gap between our method and MAML and VAT can, respectively, reach up to approximately 12% and 21%.

As is shown in Figure 8(b), our proposed method achieves an approximate accuracy of 84% at 6 dB and 90% at 10 dB, whereas the MAML method achieves the same accuracy at 10 dB and 14 dB, respectively. The VAT method deteriorates significantly in this scenario such that it is no longer considered. The results show that our method achieves the same excellent identification performance and noise robustness in the Rayleigh propagation channel, which further proves its practicability and superiority.

3.4. Visualised Analysis. To evaluate the excellent identification performance of our method in an intuitive way, the algorithm of t-SNE [41] was used to visualise the high-dimensional feature vectors, which were extracted from the MAML and VAE-InfoGAN-GP methods. Figure 9 displays the t-SNE dimensionality reduction distribution of two methods with SNR = 6 dB.

As shown in Figure 9, there are seven clusters in the 2D scatter diagram, representing seven different emitter individuals. Figure 9(a) shows that seven different clusters show stronger intraclass aggregation and larger interclass differentiation. In Figure 9(b), however, seven clusters show higher intraclass dispersion. The results show that our method can extract more discriminative feature parameters, partly due to the improvement of the network structure and the training algorithm and partly because of making full use of a large number of easily accessible unlabelled signal data, which can enhance the generalisation ability of the network to a certain extent. As a result, our method can identify different emitter individuals with a higher accuracy.

3.5. Identification Performance vs. Ratios of Labelled to Total Signal Data Samples. In this section, the identification

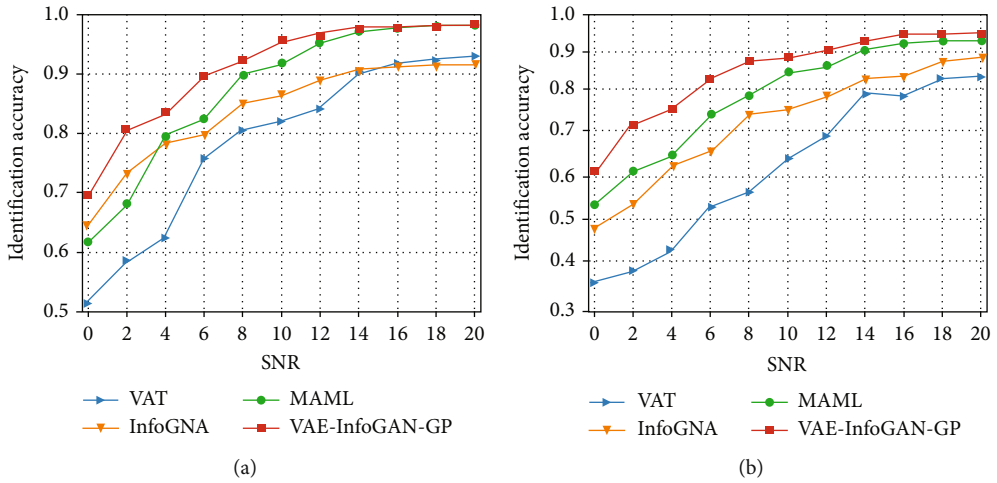

Figure 8: Identification accuracy as a function of the SNR. (a) AWGN. (b) Rayleigh noise.

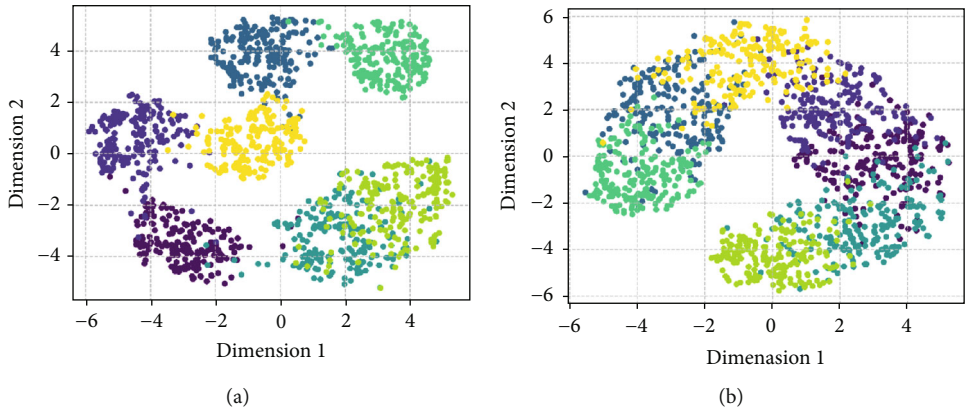

Figure 9: t-SNE dimensionality reduction distribution. (a) Feature visualisation with VAE-InfoGAN-GP. (b) Feature visualisation with MAML.

performance depending on different ratios of labelled to total signal data samples is considered. The ratios of labelled to total signal data samples are important factors affecting the classification performance of the algorithm. For the training samples of each class of signal, the ratios are set as 0%, 2%, …, 10%, and then, the identification accuracy is tested at different ratios. The experimental results are shown in Figure 10.

Figure 10 shows that the identification performance of our method remains relatively stable after reaching a ratio of 4%, which indicates that our method is still effective for the task of SEI with very limited labelled signal data. In particular, when the ratio decreases to 0%, that is, the training samples are all unlabelled signal data, the identification performance deteriorates but not seriously, and the accuracy can reach 90% at 12 dB. This result further proves the excellent performance of the proposed method in solving the few-shot problem in SEI.

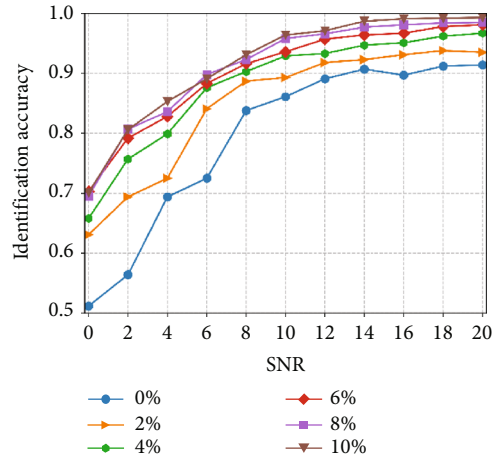

Figure 10: Identification performance according to the ratios of labelled to total signal data samples.

3.6. Other Evaluation Metrics for Identification Performance. The accuracy, which is the most common evaluation metric for classification problems, was used to evaluate the identification performance in the above experiments. However, it can only count the proportion of samples that are correctly predicted, which can reflect only the overall

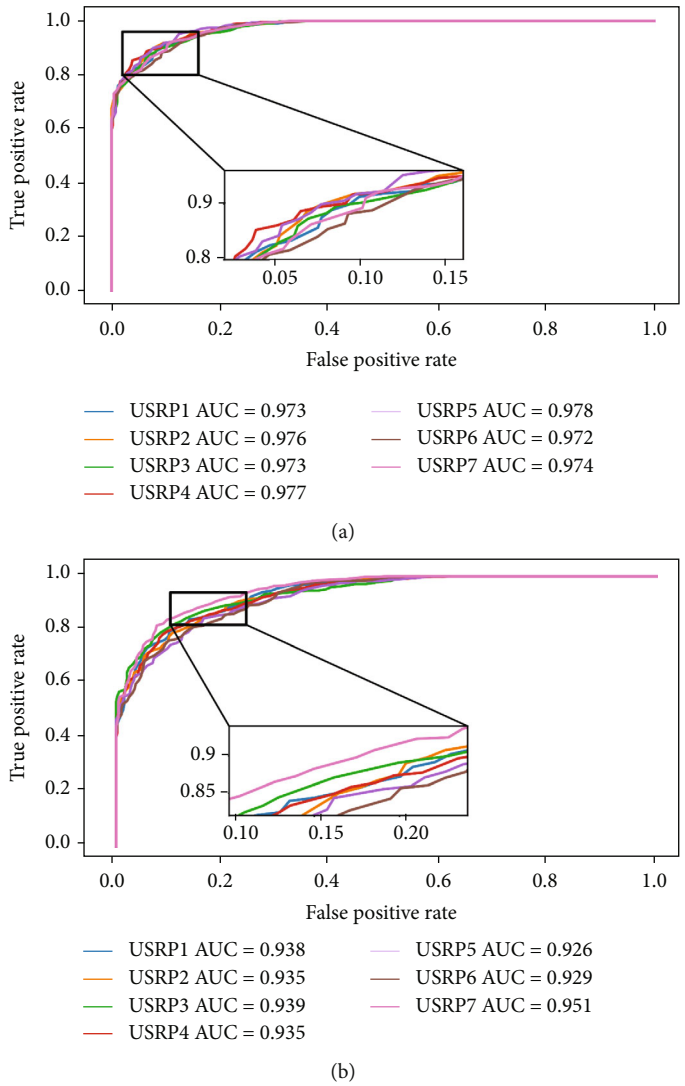

Figure 11: (a) ROC curves of proposed method. (b) ROC curves of MAML.

identification performance. For multicategory identification, each class is in a minority with respect to the rest of the RF signals, and it is difficult to evaluate whether one single class of RF signals is correctly identified through the evaluation metric of accuracy.

In this section, we use the metric of receiver operating characteristic (ROC) to further evaluate the identification performance. To avoid class imbalance, we select one USRP as a positive class with a weight of six and the other six USRPs as a negative class with a weight of one. Figure 11 shows the ROC curves of our method and MAML with the SNR set at 20 dB.

As shown in Figure 11, the ROC curves of our method are distributed in the upper left of the figure, while those of MAML are relatively offset to the lower right. This indicates that our method can achieve a higher true-positive rate with a lower false-positive rate, thereby intuitively illustrating that our method can efficiently identify each USRP device. The area under the curve (AUC) is also calculated for each USRP device. Figure 11 shows that the AUC for each device with our method is higher than 0.97, whereas the AUC for each device with MAML is between 0.926 and 0.951. Additionally, Table 2 provides the mean ROC AUC of the two methods at SNRs of 0–20 dB, and our method achieves a higher AUC than MAML at all SNRs. As expected, the results further demonstrate that our proposed method is superior to state-of-the-art methods in terms of identification performance and noise robustness.

Table 2: Mean ROC AUC at different SNRs.

SNR	Our method	MAML
0 dB	0.924	0.871
4 dB	0.939	0.898
8 dB	0.947	0.911
12 dB	0.958	0.928
16 dB	0.961	0.935
20 dB	0.972	0.941

4. Conclusion

In this paper, we proposed a method for SEI with limited labelled signals. Bispectrum analysis was performed as a preprocessing method on labelled and unlabelled RF signal data to obtain RFF representation data, which was then fed to the network model InfoGAN for semisupervised training and emitter identification. Considering the mode collapse and nonconvergence in InfoGAN and the fact that the complexity of RFFs may lead to difficulties, the network model InfoGAN was improved, and a VAE was introduced to compress the labelled and unlabelled RFF representation data into a hidden variable, which was then restored into real RFF representation data by the generator. In this way, the VAE can provide the prior information of RFF representation data for the generator, thereby facilitating generator training. Additionally, we proposed a gradient penalty algorithm to train the discriminator, enabling its loss function to obey the 1-Lipschitz constraint, which prevents gradient disappearance and further optimises the network.

The experimental results demonstrate the effectiveness of our proposed VAE-InfoGAN-GP method in improving the convergence performance. Furthermore, the identification accuracy of our method is higher than that of the state-of-the-art MAML and VAT methods and the baseline InfoGAN network model. Additionally, our method can maintain a high identification accuracy when only a few labelled data are available. Moreover, we used the metric of ROC AUC to further evaluate the identification performance. The results further demonstrate that our proposed method outperforms the state-of-the-art MAML method in terms of identification performance and noise robustness.

Data Availability

The data used to support the findings of this study are available from the corresponding author upon request.

Conflicts of Interest

The authors declare no conflicts of interest.

Acknowledgments

This work was supported in part by the National Natural Science Foundation of China under Grant 91538201, in part by the Taishan Scholar Project of Shandong Province under Grant ts201511020, and in part by the Project supported by the Chinese National Key Laboratory of Science and Technology on Information System Security under Grant 6142111190404.

References

[1] S. Ni, L. Yang, Z. Zhang, Y. Gong, and X. Yu, "Multiband cooperation for 5G HetNets: a promising network paradigm," *IEEE Vehicular Technology Magazine*, vol. 14, no. 4, pp. 85–93, 2019.

[2] J. Liu, L. Yang, B. Ai, and S. Ni, "Future 5G-oriented system for urban rail transit: opportunities and challenges," *China Communications*, vol. 18, no. 9, pp. 1–10, 2021.

[3] L. Yang, M. Xia, and M. Motani, "Unified analysis of coordinated multi-point transmissions in mmWave cellular networks," *IEEE Internet of Things Journal*, pp. 1–10, 2021.

[4] K. I. Talbot, P. R. Duley, and M. H. Hyatt, "Specific emitter identification and verification," *Technology Review Journal*, vol. 11, no. 1, pp. 203–209, 2003.

[5] A. E. Spezio, "Electronic warfare systems," *IEEE Transactions on Microwave Theory and Techniques*, vol. 50, no. 3, pp. 633–644, 2002.

[6] O. Ureten and N. Serinken, "Wireless security through RF fingerprinting," *Canadian Journal of Electrical and Computer Engineering*, vol. 32, no. 1, pp. 27–33, 2007.

[7] T. J. Bihl, K. W. Bauer, and M. A. Temple, "Feature selection for RF fingerprinting with multiple discriminant analysis and using ZigBee device emissions," *IEEE Transactions on Information Forensics and Security*, vol. 11, no. 8, pp. 1862–1874, 2016.

[8] P. Padilla, J. L. Padilla, and J. F. Valenzuela-Valdés, "Radiofrequency identification of wireless devices based on RF fingerprinting," *Electronics Letters*, vol. 49, no. 22, pp. 1409-1410, 2013.

[9] Y. P. Zhou, X. Wang, Y. Chen, and Y. Tian, "Specific emitter identification via bispectrum-radon transform and hybrid deep model," *Mathematical Problems in Engineering*, vol. 2020, Article ID 7646527, 17 pages, 2020.

[10] Y. J. Yuan, Z. T. Huang, H. Wu, and X. Wang, "Specific emitter identification based on Hilbert–Huang transform-based time–frequency–energy distribution features," *IET Communications*, vol. 8, no. 13, pp. 2404–2412, 2014.

[11] U. Satija, N. Trivedi, G. Biswal, and B. Ramkumar, "Specific emitter identification based on variational mode decomposition and spectral features in single hop and relaying scenarios," *IEEE Transactions on Information Forensics and Security*, vol. 14, no. 3, pp. 581–591, 2019.

[12] L. Fan and X. Lei, "Learning-based MIMO detection with dynamic spatial modulation," *SCIENCE CHINA Information Sciences*, vol. 2022, no. 1, pp. 185–199, 2022.

[13] T. O'Shea and J. Hoydis, "An introduction to deep learning for the physical layer," *IEEE Transactions on Cognitive Communications and Networking*, vol. 3, no. 4, pp. 563–575, 2017.

[14] L. Han, J. Z. Sun, and W. Zhang, "Convolutional neural network for convective storm nowcasting using 3-D Doppler weather radar data," *IEEE Transactions on Geoscience and Remote Sensing*, vol. 58, no. 2, pp. 1487–1495, 2019.

[15] L. Zhang and F. Zhu, "DQN based mobile edge computing for smart internet of vehicle," *EURASIP Journal on Advances in Signal Processing*, vol. 2022, no. 1, 2022.

[16] J. Lu and M. Tang, "Analytical offloading design for mobile edge computing based smart internet of vehicle," *EURASIP Journal on Advances in Signal Processing*, vol. 2022, no. 3, 2022.

[17] J. Zhao, X. Sun, Q. Li, and X. Ma, "Edge caching and computation management for real-time internet of vehicles: an online and distributed approach," *IEEE Transactions on Intelligent Transportation Systems*, vol. 22, no. 4, pp. 2183–2197, 2021.

[18] T. J. O'Shea, T. Roy, and T. C. Clancy, "Over-the-air deep learning based radio signal classification," *IEEE Journal of*

Selected Topics in Signal Processing, vol. 12, no. 1, pp. 168–179, 2018.

[19] M. Kulin, T. Kazaz, I. Moerman, and E. De Poorter, "End-to-end learning from spectrum data: a deep learning approach for wireless signal identification in spectrum monitoring applications," *IEEE Access*, vol. 6, pp. 18484–18501, 2018.

[20] Q. Mao, F. Hu, and Q. Hao, "Deep learning for intelligent wireless networks: a comprehensive survey," *IEEE Commun Surveys Tuts*, vol. 20, no. 4, pp. 2595–2621, 2018.

[21] C. Wang, J. Wang, and X. Zhang, "Automatic radar waveform recognition based on time-frequency analysis and convolutional neural network," in *2017 IEEE International Conference on Acoustics, Speech and Signal Processing (ICASSP)*, pp. 2437–2441, New Orleans, LA, USA, 2017.

[22] Z. Zhou, G. Huang, H. Chen, and J. Gao, "Automatic radar waveform recognition based on deep convolutional denoising auto-encoders," *Circuits, Systems, and Signal Processing*, vol. 37, no. 9, pp. 4034–4048, 2018.

[23] L. Chen and S. Tang, "Physical-layer security on mobile edge computing for emerging cyber physical systems," *Computer Communications*, vol. 2022, no. 1, pp. 101–112, 2022.

[24] X. Lai and L. Fan, "Outdated access point selection for mobile edge computing with cochannel interference," *IEEE Transactions on Vehicular Technology*, vol. 70, no. 3, pp. 185–196, 2022.

[25] Q. Li, Y. Gong, and K. Zhang, "Computation offloading and resource allocation for cloud assisted mobile edge computing in vehicular networks," *IEEE Transactions on Vehicular Technology*, vol. 68, no. 8, pp. 7944–7956, 2019.

[26] Q. Y. Wu, C. Feres, D. Kuzmenko et al., "Deep learning based RF fingerprinting for device identification and wireless security," *Electronics Letters*, vol. 54, no. 24, pp. 1405–1407, 2018.

[27] X. B. Wang, G. M. Huang, C. S. Ma, W. Tian, and J. Gao, "Convolutional neural network applied to specific emitter identification based on pulse waveform images," *IET Radar, Sonar & Navigation*, vol. 14, no. 5, pp. 728–735, 2020.

[28] Y. H. Qian, J. Qi, X. Y. Kuai, G. Han, H. Sun, and S. Hong, "Specific emitter identification based on multi-level sparse representation in automatic identification system," *IEEE Transactions on Information Forensics and Security*, vol. 16, pp. 2872–2884, 2021.

[29] Y. Wang, G. Gui, H. Gacanin, T. Ohtsuki, O. A. Dobre, and H. V. Poor, "An efficient specific emitter identification method based on complex-valued neural networks and network compression," *IEEE Journal on Selected Areas in Communications*, vol. 39, no. 8, pp. 2305–2317, 2021.

[30] N. Yang, B. Zhang, G. Ding et al., "Specific emitter identification with limited samples: a model-agnostic meta-learning approach," *IEEE Communications Letters*, vol. 26, 2022.

[31] I. Goodfellow, "Generative adversarial nets," in *in Proc. Advances in Neural Information Processing Systems*, pp. 2672–2680, Montreal, Canada, 2014.

[32] X. Chen, Y. Duan, and R. Houthooft, "InfoGAN: interpretable representation learning by information maximizing generative adversarial nets," in *in Proc. Advances in Neural Information Processing Systems*, pp. 2172–2180, Barcelona, Spain, 2016.

[33] D. Zhang and W. B. Wu, "Asymptotic theory for estimators of high-order statistics of stationary processes," *IEEE Transactions on Information Theory*, vol. 64, no. 7, pp. 4907–4922, 2017.

[34] L. Saidi, J. Ben Ali, and F. Fnaiech, "Application of higher order spectral features and support vector machines for bearing faults classification," *ISA Transactions*, vol. 54, pp. 193–206, 2015.

[35] M. Ben-Yosef and D. Weinshall, *Gaussian mixture generative adversarial networks for diverse datasets, and the unsupervised clustering of images*, 2018, http://arxiv.org/abs/1808.10356.

[36] D. P. Kingma and M. Welling, "Auto-encoding variational Bayes for inferring topics and visualization," in *Proceedings of the 28th International Conference on Computational Linguistics*, Barcelona, Spain, 2014.

[37] M. Arjovsky and L. Bottou, *Towards principled methods for training generative adversarial networks*, 2017, http://arxiv.org/abs/1701.04862.

[38] M. Arjovsky, S. Chintala, and L. Bottou, *Wasserstein GAN*, 2017, http://arxiv.org/abs/1701.07875.

[39] D. A. Edwards, "On the Kantorovich–Rubinstein theorem," *Expositiones Mathematicae*, vol. 29, no. 4, pp. 387–398, 2011.

[40] T. Miyato, S. I. Maeda, M. Koyama, and S. Ishii, "Virtual adversarial training: a regularization method for supervised and semi-supervised learning," *IEEE Transactions on Pattern Analysis and Machine Intelligence*, vol. 41, no. 8, pp. 1979–1993, 2019.

[41] L. V. Der Maaten and G. E. Hinton, "Visualizing data using t-SNE," *Journal of Machine Learning Research*, vol. 9, pp. 2579–2605, 2008.

Hindawi
Wireless Communications and Mobile Computing
Volume 2022, Article ID 1177544, 18 pages
https://doi.org/10.1155/2022/1177544

Research Article

Deep Reinforcement Learning-Based Joint Satellite Scheduling and Resource Allocation in Satellite-Terrestrial Integrated Networks

Yabo Yin,[1,2] **Chuanhe Huang**,[1,2] **Dong-Fang Wu**,[1,2] **Shidong Huang**,[1,2] **M. Wasim Abbas Ashraf**,[1,2] **Qianqian Guo**,[3] **and Lin Zhang**[4]

[1]*School of Computer Science, Wuhan University, Wuhan 430072, China*
[2]*Hubei LuoJia Laboratory, Wuhan 430072, China*
[3]*School of Information Engineering, Zhengzhou Institute of Finance and Economics, Zhengzhou 450053, China*
[4]*Wuhan Maritime Communication Research Institute, Wuhan 430072, China*

Correspondence should be addressed to Chuanhe Huang; huangch@whu.edu.cn

Received 21 December 2021; Revised 6 January 2022; Accepted 31 January 2022; Published 24 February 2022

Academic Editor: Junjuan Xia

Satellite-terrestrial integrated networks (STINs) are considered to be a new paradigm for the next generation of global communication because of its distinctive merits, such as wide coverage, high reliability, and flexibility. When the satellite associates with different base stations (BSs) and adopts different channels for communication, the utility of offloading data to BSs is different. In our work, we study how to jointly associate satellites with appropriate BSs and allocate channels to satellites. Our purpose is to maximize the utility of the data offloaded from satellites to BSs while considering the load balance of BSs. However, some satellites are often unable to connect to BSs because of their periodic flight characteristic, which makes the joint satellite-BS association and channel allocation more challenging. To solve the problem that satellites sometimes cannot connect to BSs, we abstract the communication model between satellites and BSs into a bipartite graph and add a virtual BS to ensure that all satellites can connect to at least one BS. Then, in the constructed joint optimization problem, we solve the assignment of satellites and channels simultaneously. Considering that the joint optimization problem is nonconvex, we use double deep Q-Network (DDQN) for achieving the optimal strategy of satellite association and channel allocation. Furthermore, the reward value in most state transition information generated by satellites is 0, which leads to the low learning efficiency of DDQN. Aiming at enhancing the learning efficiency of DDQN, the priority sampling-based DDQN (PSDDQN) algorithm is proposed. Experimental results demonstrate that PSDDQN gets better utility and achieves the load balance of BSs compared with other algorithms.

1. Introduction

Recently, 5G technology has developed rapidly, and many 5G base stations have been deployed at the same time. Therefore, 5G network communication services can be provided in many places, such as urban and metropolitan areas. However, for those remote areas without communication facilities, such as deserts, oceans, and other places, it is difficult to provide people with communication services. LEO satellite network has attracted researchers' attention due to its characteristics of wide coverage, low delay, and high bandwidth, and it can provide communication services for those places which are not covered by base stations [1]. Therefore, the STINs become a new paradigm for providing seamless communication. Meanwhile, people's demands for high quality video, voice, and other multimedia services grow explosively. Therefore, how to efficiently manage resources in STINs for providing people with better Internet services has become a new challenge [2, 3].

Resource allocation is a key technology that affects the performance of STINs. But most of researches focus on radio spectrum allocation [4, 5], power allocation [6, 7],

and other issues. And there is little research that studies the joint satellite association and channel allocation. Hu et al. [8] proposed a competitive market scheme to solve user association issue of satellite-drone networks. To address the user association issue of heterogeneous networks, a distributed belief propagation method was proposed [9]. Khalili et al. [10] investigated user association of the uplinks in heterogeneous networks and used maximization-minimization theory and augmented Lagrange method to guarantee users' data transmission rate. Zhao et al. [11] used multiagent RL approach for achieving the optimal user association strategy while considering the service requirements of users in heterogeneous cellular networks. However, these approaches are not suitable in STINs. The main reasons are as follows: (1) In the network scenarios mentioned above, when optimizing user association problem, users are within the communication range of BSs. That is, users are covered by at least one BS at any time. However, in STINs, many satellites cannot connect to BSs because satellites communicate with BSs by the Line-of-Sight (LoS) way. (2) Because of the periodic movement of satellites, the communication process between satellites and BSs is discontinuous rather than continuous. (3) The load balance of BSs seriously affect the performance of STINs. If the load balance of BSs is not considered, the capacity of some BSs will be exhausted in advance. And this degrades the performance of STINs. However, the above literature ignores the load balance of BSs.

In our research, the joint satellite scheduling and resource allocation in STINs are investigated. When satellites communicate with BSs, allocating appropriate BSs and channels to satellites for transmitting data has a great impact on the utility of STINs. Because the problem of joint satellite association and channel allocation is coupled and nonconvex, conventional methods cannot effectively obtain the optimal satellite association and channel allocation strategy.

Fortunately, in recent years, artificial intelligence algorithm such as reinforcement learning (RL) has developed rapidly and applied to many fields. RL has been used to solve system control problems [12]. Moreover, it has been applied in combinatorial optimization [13, 14], capacity management [15], resource management [16, 17], etc., especially in games and chess. Furthermore, RL also has good performance in dynamic network environment. Inspired by this, we try to use RL approach to achieve the optimal strategy in STINs.

This paper mainly studies the joint satellite scheduling and resource allocation in STINs. Our purpose is to maximize the utility of data offloaded from satellites to BSs as much as possible while considering the load balance of BSs. The joint optimization problem of the satellites and channel assignments is constructed. Then, a priority sampling-based double DQN (PSDDQN) method is used to address the aforementioned problem. We give the main contributions in the following:

(1) We focus on the joint satellite association and channel allocation while considering the load balance of BSs in STINs. We formulate the problem of joint satellite association and channel allocation as a joint optimization problem. And, we use RL approach to solve it

(2) We propose a bipartite graph with virtual BS to describe the communication model between satellites and BSs. By adding a virtual BS, we ensure that the action space of all satellites is the same. So we can easily determine the action space of our proposed RL model

(3) Considering that the reward value in most state transition information is 0, we propose a priority sampling-based DDQN (PSDDQN) to enhance the performance of DDQN. Moreover, to reduce the consumption of computing resources caused by sorting state transition information, we use SumTree structure to store state transition information. Experimental results demonstrate that PSDDQN can converge quickly and get better performance than the selected baseline approaches

The rest of our paper unfolds below. The recent research developments are summarized in Section 2. In Section 3, the system framework and problem formulation are illustrated. Section 4 describes our PSDDQN method. Section 5 evaluates our PSDDQN method and discusses the experimental results. We conclude this article and give the future research in Section 6.

2. Related Work

Many works investigated user association in wireless networks. Feng et al. [18] proposed a repeated game-based user association scheme while considering spectrum allocation to maximize users' data transmission rate of the MIMO system. Liu et al. [19] used Lagrange dual decomposition approach to address the user association issue in two different access schemes. Liu et al. [20] jointly optimized user association and power control and designed a semidistributed solution to obtain the optimal results. Considering that users' mobility affects the performance of heterogeneous networks, Cheng et al. [21] introduced the users' mobility and proposed a multiagent RL approach to maximize the system capacity. Based on users' preferences information, Zalghout et al. [22] proposed a priority-based user association approach to maximize user's QoS in heterogeneous wireless networks.

There are many works on the resource allocation of satellite networks. Zhu et al. [23] used multidimensional knapsack theory to minimize energy consumption while considering user's delay constraint. To improve the spectrum utilization of satellites, Zuo et al. [24] jointly optimized allocation of time, spectrum, power, and beam and solved it by heuristic algorithm. Mai et al. [25] used Stackelberg game method to reduce the transmission delay of remote sensing data. Deng et al. [26] jointly optimized virtual machine assignment and power allocation to minimize energy consumption in cloud-based satellite communication networks. Shahid et al. [27] used radio utilization as load metric and

proposed a load balancing-based resource management method for improving STINs' performance. Ji et al. [28] presented a data offloading method for solving the energy overhead issue in multicell STINs. Deng et al. [29] designed a satellite constellation deployment solution with minimum number of satellites while meeting backhaul requirements of users in STINs. However, none of them paid attention to the joint satellite association and channel allocation.

In recent years, researchers have used artificial intelligence algorithms to solve network problems. He et al. applied deep learning algorithm to memory optimal detection [30] and optimal strategy search [31] in MIMO system. Lai [32] used federated learning to select outdated access point in MEC networks. Tang and Chen [33] designed a federated edge learning framework to reduce the computational latency of tasks in IoT networks. RL has been applied to ubiquitous computing [34], network security [35], and resource allocation. For reducing the task execution time, the Q-learning approach was adopted to manage computing resources in IoT [36]. The Q-learning-based task offloading scheme was used to maximize the utility of system [37]. The designed deep RL-based radio resource management method was used to improve the radio utilization [38]. Zhang et al. [39] adopted deep RL approach to allocate resource while meeting users' reliability requirements. The multiagent RL-based hierarchical task management strategy can satisfy users' communication requirements [40]. Luong et al. [41] jointly optimized UAV position and transmitted beamforming and UAV-UE association in UAV-assisted wireless networks. Considering that this optimization problem was nonconvex, a method based on deep Q-learning was proposed for allocating resources.

3. System Model and Problem Formulation

3.1. Network Model. Figure 1 shows the structure of STINs. The STINs consist of N satellites and L BSs. For the terrestrial networks, it can connect to LEO satellite networks through BSs with satellite gateways. Because the LEO satellite network topology changes dynamically over time, we use snapshot method to discretize the satellite network topology according to reference [42]. During a snapshot, the network topology is fixed. The whole operation time is T, and the number of snapshots is N_T; then, we can easily get

$$\sum_{t=1}^{N_T} T_t = T. \tag{1}$$

The more snapshots, the higher the precision of the representation of satellite network topology. But extensive storage resources and computing resources are needed to deal with these snapshots. To ensure the precision of satellite network topology and reduce the consumption of storage resources, the duration of the snapshot should be less than the communication time between satellites and BSs. We define it as

$$T_t \le \min\left\{t_{i,j}\right\}, \forall i \in \{1, 2, 3, \cdots, N\}, j \in \{1, 2, 3, \cdots, L\}, \tag{2}$$

where variable $t_{i,j}$ expresses the communication time between ith satellite and jth BS. The structure of STINs is expressed by $G = (V, E)$. And graph G is undirected graph. The node set in STINs is denoted by V. And E represents the communication links between satellites and BSs.

3.2. Communication Model. When BSs are not within the coverage of satellites, satellites cannot communicate with BSs. Moreover, each satellite may cover many BSs sometimes. Therefore, the communication model between satellites and BSs can be abstracted into a bipartite graph. We show the structure of bipartite graph.

In Figure 2, grey nodes represent satellites, and orange nodes represent BSs. The grey lines indicate the communication links between satellites and BSs. From Figure 2, we observe that only four satellites can connect to BSs, and other satellites of the satellite networks cannot connect to any BSs. Considering the BSs covered by different satellites are different, the action space of different satellites is different. Therefore, the RL method cannot be directly applied to STINs. To solve this problem, we introduce the virtual BS. By adding a virtual BS, each satellite can be connected to a BS, and the action space of each satellite is same. We show the bipartite graph with virtual BS.

In Figure 3, the blue node is the added virtual BS. When a satellite cannot connect to any BS, we connect this satellite to the added virtual BS. Then, each satellite in STINs can be connected to at least one BS at any snapshot. Hence, the satellite can select one BS from $L + 1$ BSs to establish a communication link at any time. This operation ensures that the action space of each satellite is same, which is convenient for the definition of action space of RL in subsequent section.

3.3. Channel Model. Considering that we have added a virtual BS to STINs, we use set $\mathscr{L} = \{0, 1, 2, 3, \cdots, L\}$ to represent the BSs of STINs. And the index of the added virtual BS is 0. Only when the satellite is associated with one BS and occupies one channel of this BS can the satellite communicate with this BS. We use binary decision variable $s_{i,l}(t)$ that indicates whether satellite i associate with BS l at time t. If satellite i is assigned to BS l, then $s_{i,l}(t) = 1$; otherwise, $s_{i,l}(t) = 0$. For convenience, the satellite can only connect to one BS during one snapshot. So we can get

$$\sum_{l=0}^{L} s_{i,l}(t) \le 1, \forall i \in \{1, 2, 3, \cdots, N\}. \tag{3}$$

Moreover, we assume that each BS has M channels, and each channel can only be assigned to one satellite at any time. Therefore, each BS can connect at most M satellites simultaneously; we can get

$$\sum_{i=1}^{N} s_{i,l}(t) \le M, \forall l \in \{1, 2, 3, \cdots, L\}. \tag{4}$$

Here, we assume that the number of satellites connected to the virtual BS is not limited. So the added virtual BS can

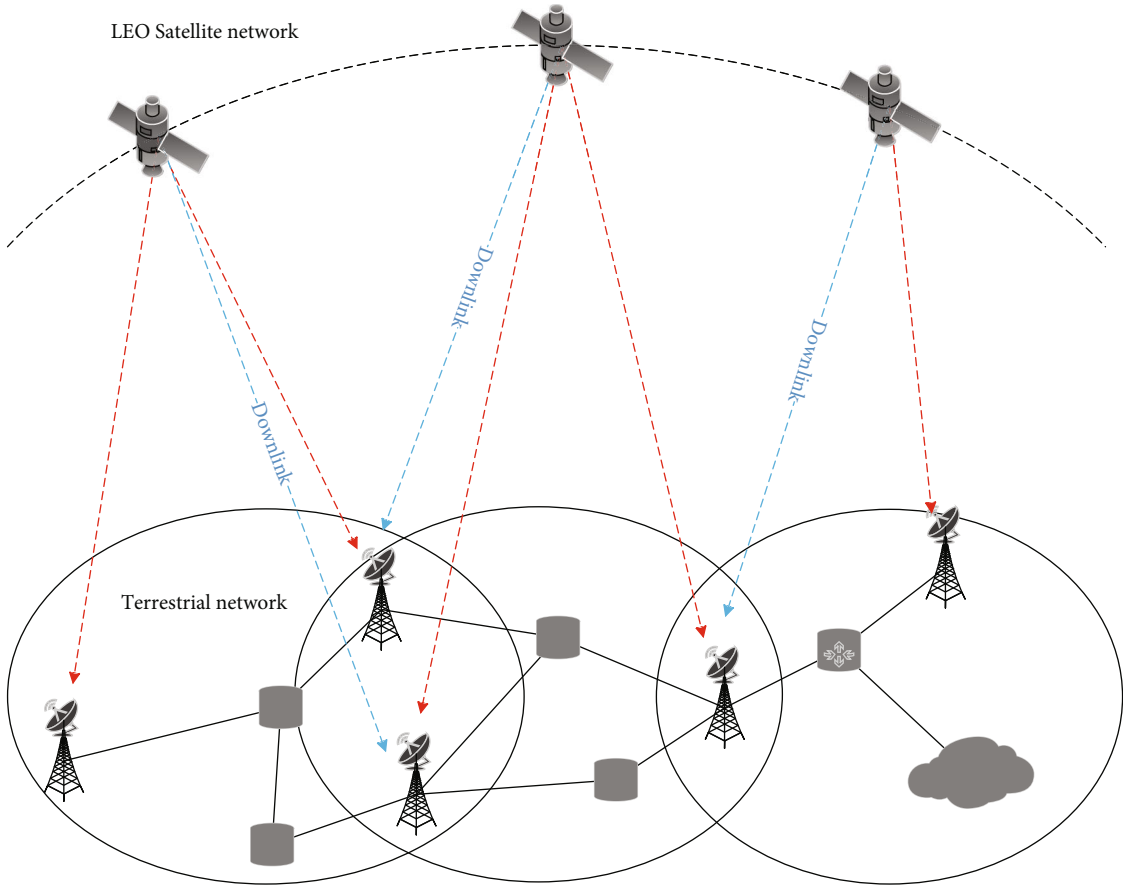

Figure 1: The structure of STINs. The dotted lines (including red and blue) indicate that the satellite is capable of connecting to the BSs under its coverage. The blue dotted line means the communication link established between the satellite and the BS. And each satellite is able to associate with one BS for communication in a time slice.

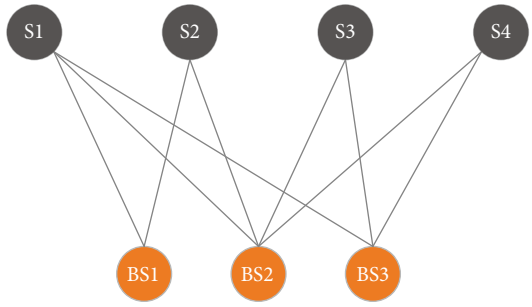

Figure 2: Structure of bipartite graph.

connect to all satellites. Considering that the index of the virtual BS is 0, we can get

$$\sum_{i=1}^{N} s_{i,0}(t) \le N. \tag{5}$$

Assigning different channels to satellites has an important impact on the data transmission rate between satellites and BSs. Assumed that different channels of the BS are orthogonal. Here, we use binary channel-allocation variable $c_{i,m}(t)$ that indicates whether satellite i communicate with BS on channel m. If satellite i uses channel m for communication at time t, $c_{i,m}(t) = 1$; otherwise, $c_{i,m}(t) = 0$. Here, one channel can only be allocated to one satellite. We can easily get

$$\sum_{m=1}^{M} c_{i,m}(t) \le 1, \forall i \in \{1, 2, 3, \cdots, N\}. \tag{6}$$

Considering that the satellite may cover many BSs, when satellite i communicates with BS l, other BSs will also interfere with the communication process. Therefore, the cochannel influence of other BSs should be considered. We obtain the SINR by

$$\mathrm{SINR}_{i,l,m}(t) = \frac{p_{i,l,m}(t) g_{i,l,m}(t) s_{i,l}(t) c_{i,m}(t)}{\sum_{b \in L \setminus \{0,l\}}^{L} p_{i,b,m}(t) g_{i,b,m}(t) s_{i,b}(t) c_{i,m}(t) + BN_0}. \tag{7}$$

The virtual BS does not interfere with the communication process of other BSs. Variable $p_{i,l,m}$ represents the transmit power operating on channel m between satellite i and BS

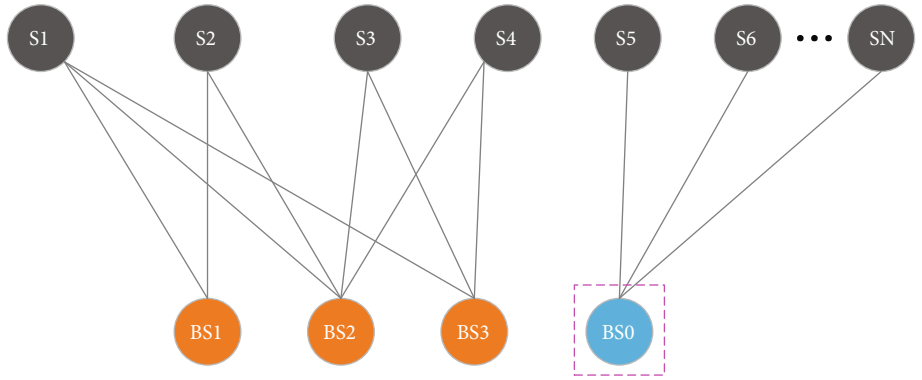

Figure 3: Bipartite graph with virtual BS.

l, and variable $g_{i,l,m}$ indicates the channel gain of channel m. The channel m is between ith satellite and lth BS. The variable N_0 indicates Gaussian white noise. B expresses the channel bandwidth.

Let the longitude and latitude of BS l be λ_l and φ_l, respectively. And λ_i and φ_i represent the longitude and latitude of satellite i. The height of satellite orbit is h, so the distance between satellite i and BS l is given by

$$d_{i,l} = (R_E + h)\sqrt{1 + \left(\frac{R_E}{R_E + h}\right)^2 - 2\frac{R_E}{R_E + h}(\cos(\lambda_l - \lambda_i)\cos\varphi_i \cos\varphi_l + \sin\varphi_i \sin\varphi_l)}, \tag{8}$$

where variable R_E denotes the earth's radius. Thus, we can get the path loss of the signal in the atmosphere

$$L_{i,l}(t) = 32.44 + 20\log d_{i,l} + 20\log f, \tag{9}$$

where variable f represents the carrier frequency. Thus, we can get the channel gain of satellite i

$$p_{i,l,m}(t) = A_{i,m} - L_{i,l}(t), \tag{10}$$

where variable $A_{i,m}$ represents the antenna gain operating on channel m of satellite i. Based on the computed SINR, we can get the data transmission rate by

$$r_{i,l,m}(t) = B\log_2(1 + \mathrm{SINR}_{i,l,m}(t)). \tag{11}$$

Variable B represents the channel bandwidth. Considering that the communication time between satellite i and BS l is different in a time slice, we can obtain the valid communication time between satellite i and BS l

$$\tau_{i,l} = \min(T_t, t_{i,l}). \tag{12}$$

3.4. Problem Formulation. Each satellite wants to get its maximum utility. Our object is to obtain the maximum utility of the data offloaded from satellites to BSs while considering the load balance of BSs. The utility of the data offloaded by satellite i is u_i. And it consists of the utility generated by the offloaded data and the cost of the BS storing these offloaded data. We define it as

$$u_i(t) = (\omega p_i - \xi f_l) r_{i,l,m}(t)\tau_{i,l}, \tag{13}$$

where variables ω and ξ are weight coefficients. Variable f_l represents the cost of storing unit data in BS l. As the storage capacity of BSs is consumed, the storage cost will gradually increase. Here, we define it as

$$f_l = \frac{1}{C_l - \sum_{i=1}^{N} r_{i,l,m}\tau_{i,l} + Q}, \tag{14}$$

where variable C_l represents the remaining capacity of BS l and variable Q is a constant. Based on the abovementioned, we can get the utility generated by the data offloaded from all satellites to BSs in a time slice,

$$\Gamma(t) = \sum_{i=1}^{N}\sum_{l=0}^{L}\sum_{m=1}^{M} u_i(t). \tag{15}$$

The running time T of satellites is composed of a series of time slices. Therefore, we can get the utility generated by the data offloaded from all satellites to BSs during the whole operation time T. We define it as

$$\begin{aligned} \Upsilon &= \max\left(\sum_{t=1}^{N_T}\Gamma(t)\right), \\ s.t. &\sum_{l=0}^{L} s_{i,l}(t) \le 1, \forall i \in \{1, 2, 3, \cdots, N\}, \\ &\sum_{i=1}^{N} s_{i,l}(t) \le M, \forall l \in \{1, 2, 3, \cdots, L\}, \\ &\sum_{i=1}^{N} s_{i,l}(t) \le N, l = 0, \\ &\sum_{m=1}^{M} c_{i,m}(t) \le 1, \forall i \in \{1, 2, 3, \cdots, N\}, \end{aligned} \tag{16}$$

where variable N_T denotes the number of snapshots. Considering that this problem is nonconvex, traditional approaches cannot be directly used to obtain the optimal results. Therefore, we adopt deep RL for achieving the optimal satellite association and channel allocation strategy.

4. Priority Sampling-Based DDQN Algorithm for Joint Satellite Scheduling and Resource Allocation

4.1. Reinforcement Learning Model

4.1.1. State Space. The state space mainly includes the real-time status of all satellites and the status of BSs. For the satellite, the status information includes its position at time t and valid communication time with different BSs. For the BS, the status information includes its remaining storage capacity and channel allocation state. We get the state space of satellite i by

$$S_i = \left\{ \begin{matrix} \lambda_i, \varphi_i, \tau_{i,0}, \tau_{i,1}, \tau_{i,2}, \cdots, \tau_{i,L}, s_{i,0}, s_{i,1}, s_{i,2}, \cdots, s_{i,L}, c_{i,1}, c_{i,2}, \cdots, c_{i,M}, \\ C_0, C_1, C_2, \cdots, C_L \end{matrix} \right\}, \forall i \in \{1, 2, 3, \cdots, N\}, \tag{17}$$

where variables λ_i and φ_i are introduced in Equation (8). Variable C_l represents the remaining capacity of BS l. Variable $s_{i,l}$ indicates whether satellite i is associated with BS l. Variable $c_{i,m}$ indicates whether satellite i adopts channel m for communication.

4.1.2. Action space. When the satellite communicates with the BS, the satellite must be associated with one BS and occupy one channel of this BS. Therefore, the action of satellite mainly includes two parts: satellite association and channel allocation. We define the action space of satellite i as

$$A_i = \left\{ s_{i,0}, s_{i,1}, s_{i,2}, \cdots, s_{i,L}, c_{i,0}, c_{i,1}, c_{i,2}, \cdots, c_{i,M} \right\}, \forall i \in \{1, 2, 3, \cdots, N\}. \tag{18}$$

From Equation (18), we can see that satellite association and channel allocation are coupled. For convenience, we use matrix **E** that represents the action space of the satellite

$$E = \begin{bmatrix} e_{0,1}, e_{0,2}, & e_{0,3}, \cdots, & e_{0,M} \\ e_{1,1}, e_{1,2}, & e_{1,3}, \cdots, & e_{1,M} \\ \vdots & \vdots & \vdots \\ e_{L,1}, e_{L,2}, & e_{L,3}, \cdots, & e_{L,M} \end{bmatrix}, \forall l \in \{0, 1, 2, 3, \cdots, L\}, m \in \{1, 2, \cdots, M\}. \tag{19}$$

We use binary variable $e_{l,m}$ that represents the joint satellite association and channel allocation of the satellite. For a satellite, when BS l and its channel m are assigned to this satellite simultaneously, $e_{l,m} = 1$; otherwise, $e_{l,m} = 0$.

4.1.3. Reward value. Reward value seriously affects the performance of RL, and the agent use it to obtain the optimal strategy. When satellites are associated with different BSs and adopt different channels for communication, the utility of data offloaded from satellites to BSs is different. Moreover, the storage cost of the BS also changes with the consumption of its capacity. In our research, our purpose is to obtain the maximum utility of offloaded data while considering the load balance of BSs. The reward value consists of the utility generated by the offloaded data and the cost of BS for storing these data. We define it as

$$r_i = (\omega p - \xi f_l) r_{i,l,m}(t) \tau_{i,l}, \tag{20}$$

where variables ω and ξ are the weight coefficients, which are initialized by analytic hierarchy process method. And variable $r_{i,l,m}(t)$ denotes the downlink data transmission rate between satellite i and BS l operating on channel m. Variable $\tau_{i,l}$ denotes the communication time between satellite i and BS l. Furthermore, we also normalize the utility of offloaded data and the cost of BSs.

4.2. Double Deep Q-Network (DDQN) Method. DQN is used widely in discrete scenarios. Meanwhile, the Q value is approximated by deep neural network. After the iterative training process, the obtained Q value is close to the true Q value

$$Q^*(s, a) \approx Q(s, a; \theta). \tag{21}$$

Moreover, the experience relay buffer scheme and gradient descent method are used for updating the parameter θ of neural network

$$L(\theta) = (y_i - Q(s, a; \theta))^2, \tag{22}$$

$$\nabla_\theta L(\theta) = (y_i - Q(s, a; \theta)) \nabla_\theta Q(s, a; \theta), \tag{23}$$

where variable y_i represents the Q value obtained by DQN; we can get it by

$$y_i = \begin{cases} r_i & , \text{is\_end}_i \text{ is true} \\ r_i + \gamma \max_{a'} Q\left(s', a'; \theta\right), & \text{is\_end}_i \text{ is false} \end{cases}. \tag{24}$$

Because greedy strategy is adopted for selecting action in DQN, the Q value obtained by DQN is over estimated. To solve this problem, double DQN (DDQN) selects actions and calculates the target Q value by two independent network structures. These two independent network structures are online Q-Network and target Q-Network, respectively, and they have the same network structure. The target Q-Network is used to decouple the action selection and the Q value estimation, which can solve the over estimation problem of Q value in DQN. When updating the parameters of DDQN, we select the action with the largest Q value by

$$a^{\max}\left(s'; \theta\right) = \arg \max_{a'} Q\left(s', a; \theta\right). \tag{25}$$

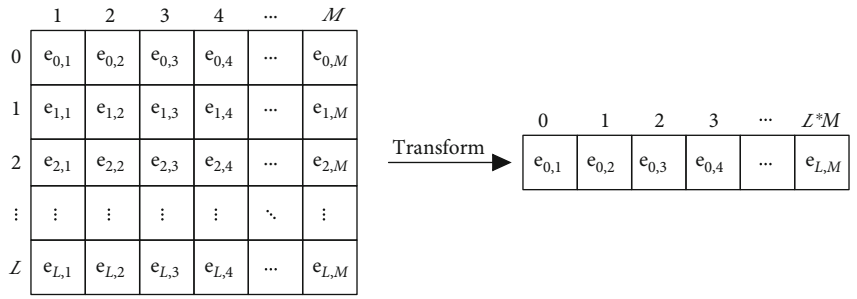

Figure 4: Action space transformation process.

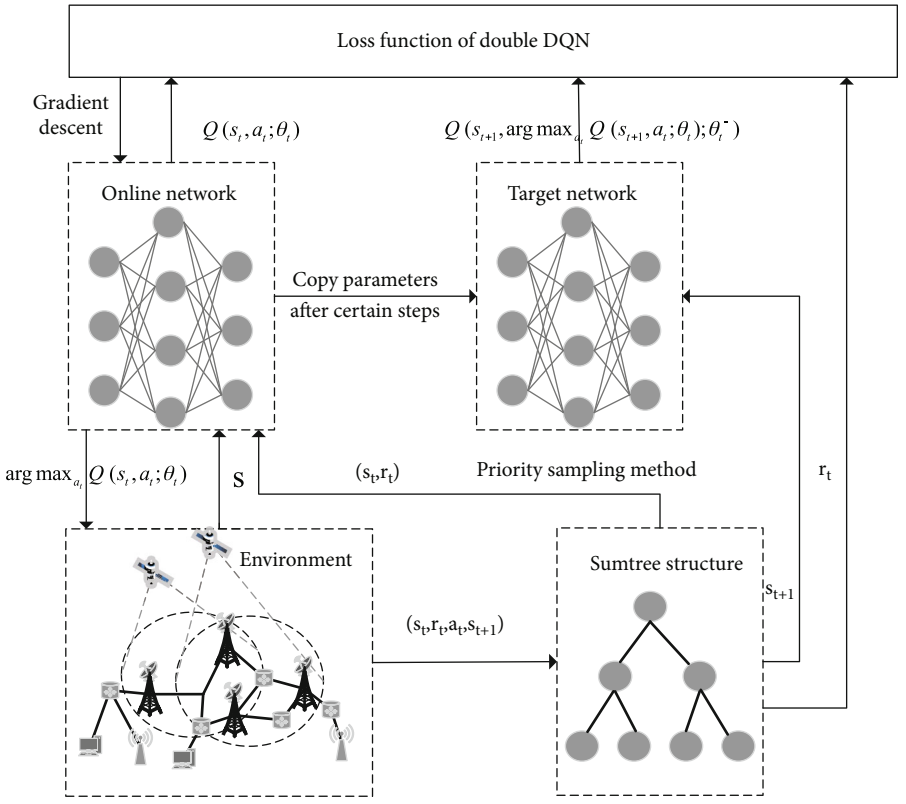

Figure 5: Structure of PSDDQN.

Then, the target Q value in DDQN is calculated by target Q-Network

$$y_i^{\mathrm{DDQN}} = \begin{cases} r_i & , \text{is\_end}_i \text{ is true} \\ r_i + \gamma Q'\left(s', a^{\max}\left(s'; \theta\right); \theta'\right), & \text{is\_end}_i \text{ is false} \end{cases}, \tag{26}$$

where r_i is the instant reward value. Variable γ denotes the discount rate. And the discount rate indicates the importance of instant reward and future reward. $\gamma = 0$ indicates that the agent is myopic, and the agent only considers the instant reward. When the discount rate is 1, the agent is farsighted and only considers the future reward. In practice, the value of γ is generally between 0 and 1.

Then, we use the target Q value to calculate the TD-error. Finally, we calculate the gradients according to the obtained TD-error and update the weights of online Q-Network. In the process of training, online Q-Network assigns its weights to target Q-Network every certain number of training steps to update the parameters of target Q-Network.

The last layer of DDQN is a fully connected layer. However, the action space of the satellite is a two-dimensional matrix. In order to train DDQN, we transform the action space of the satellite into a one-dimensional vector with size $(L + 1) * M$. The specific transformation process is shown in Figure 4.

Input: number of episodes, *Num_Episodes*; number of time slices, *Num_Timeslices*; number of leaves of Sumtree structure, B; exploration rate, ε; update frequency, F; learning rate, α ; number of satellites, N;
Output: the weight of online Q-Network, θ;
1. Initialize the state of STINs, including the capacity C of BSs, antenna model, channel model, satellite orbit parameters, and the initial positions of satellites;
2. Randomly initialize the weight θ of online Q-Network; for the weight in target Q-Network, $\theta'=\theta$;
3.For *episode* =1 to *Num_Episodes* do
4. For *time* =1 to *Num_Timeslices* do
5. For i =1 to N do
6. Get the state information of satellite i from the ground control centre at time t, s_i;
7. End for
8. Get the sate information of BSs from the ground control centre at time t, H;
9. Obtain the state information of STINs at time t, $S=(s_1,s_2,s_3,\ldots,s_N , H)$;
10. Get the next state of STINs S' from the ground control centre at t+1 and its termination *flag*;
11. For i =1 to N do
12. Use ε-greedy strategy to select an action, a_i;
13. The agent execute action a_i and obtain the instant reward r_i by Equation (20);
14. Store state transition information (s_i, a_i, r_i, s_i') in the Sumtree structure;
15. End for
16. $S= S'$;
17. The BSs and satellites send their state information to the ground control centre for updating the state information of STINs;
18. Sample samples from the Sumtree structure, and compute the loss of Q-value of each sample according to Equation (29);
19. Compute the gradient of each sample according to Equation (30);
20. Update the weight of online Q-Network according to the back propagation algorithm;
21. Compute the *TD-error* value of each sample according Equation (32) and update its priority by Equation (33);
22. Update the parameters of target Q-Network every frequency F, let $\theta'=\theta$;
23. End for
24.End for

Algorithm 1: PSDDQN for joint satellite association and channel allocation.

Table 1: Parameters of simulation.

Parameters	Value
Channel bandwidth B	41.67 kHz
Transmitter EIRP p	51.6 dBW
Antenna gain g	53.7 dBi
Antenna diameter of BS D	3.5 m
Carrier frequency f	20 GHz
Path loss model Loss	$32.44 + 20 \log d + 20 \log f$ (f:MHz)
Noise power N_0	-174 dBm/Hz
Number of satellites N	120
Number of BSs L	6
Number of channels M	4
Number of time slices *Num_timeslices*	30
Weight of utility ω	0.7
Weight of storage cost ξ	0.3

We assume the index of action $e_{l,m}$ is index$(e_{l,m})$, and we can get the location of $e_{l,m}$ in the last layer of DDQN

$$\text{index}(e_{l,m}) = l * M + m, \forall i \in \{1, 2, 3, \cdots, L\}, m \in \{1, 2, 3, \cdots, M\}. \tag{27}$$

By transforming the action space into a one-dimensional vector, we can use the state transition information to train DDQN.

4.3. Priority Sampling-Based DDQN Algorithm for Joint Satellite Scheduling and Resource Allocation. In DDQN, the

Table 2: Parameters of PSDDQN algorithm.

Parameters	Value
Batch size	32
Learning rate α	0.005
Number of leaves of SumTree structure	2000
Number of neurons in input layer	156
Number of neurons in hidden layers	64, 32
Number of neurons in output layer	24
Discount rate γ	0.9
Activation function	ReLU
Optimizer	Gradient descent optimizer

uniform sampling method is used to select samples when calculating the gradient and updating the model's parameters. If samples in experience replay buffer are evenly distributed, uniform sampling method is effective. However, because satellites communicate with BSs by LoS, few satellites can communicate with BSs at any time. Moreover, most satellites are connected to virtual BS. Therefore, most of state transition information generated by satellites is from virtual BS to virtual BS because the communication time between satellites and BSs is short. At this time, the reward received by the satellite is 0. Thus, the reward of most state transition information in experience replay buffer is 0. If these samples are uniformly sampled, the learning performance of DDQN model will be degraded. Therefore, we use priority sampling method to enhance the performance of DDQN.

For a sample, the greater its priority, the greater the probability of being sampled. We define the sampling probability of the sample as

$$P(j) = \frac{p(j)}{\sum_i p(i)}, \tag{28}$$

where $p(j)$ and $P(j)$ are the priority and sampling probability of sample j, respectively. Considering that sorting these samples wastes extensive computing resources, we use SumTree structure to store these samples. The specific structure of PSDDQN is shown in Figure 5.

When training PSDDQN model, we firstly select M samples from SumTree structure and compute their loss functions and gradients,

$$\mathrm{Loss}(\theta) = \sum_{j=1}^{M} w_j \left(y_j^{\mathrm{DDQN}} - Q(s_j, a_j; \theta) \right)^2, \tag{29}$$

$$\nabla_\theta \mathrm{Loss}(\theta) = w_j \left(y_j^{\mathrm{DDQN}} - Q(s_j, a_j; \theta) \right) \nabla Q(s_j, a_j; \theta), \tag{30}$$

$$w_j = \frac{(N * P(j))^{-\beta}}{\max_i(w_i)} = \frac{(N * P(j))^{-\beta}}{\max_i (N * P(i))^{-\beta}} = \frac{(P(j))^{-\beta}}{\max_i (P(i))^{-\beta}}, \tag{31}$$

where w_j represents the weight of priority of sample j for calculating the loss value. And variable β represents the hyperparameter, which is determined by empirical value.

Then, the weights of DDQN are updated according to the calculated gradients. Moreover, we also need to update the priorities of samples in the SumTree structure. For the sample, the greater the TD-error, the better the effect of training the DDQN model. Here, we use TD-error value to represent the priority of the sample. We get the TD-error value of the sample and update its priority by

$$\mathrm{TD-error}_j = y_j - Q(s_j, a_j; \theta), \tag{32}$$

$$p(j) = \mathrm{TD\text{-}error}_j. \tag{33}$$

The ground control centre has rich computing resources and can directly obtain the real-time state information of BSs and satellites. In the process of communication, BSs and satellites send their real-time state information to the ground control centre for updating their state information. The agent is able to obtain the latest state information of STINs from the ground control centre in real time. In our research, we deploy PSDDQN algorithm in the ground control centre. The specific details of PSDDQN is described in the following:

5. Experimental Results and Analysis

We firstly introduce the experimental environment. Then, we validate PSDDQN algorithm in the simulation data and analysis the experimental results.

5.1. Experimental Environment. The communication system of STINs in this paper is mainly composed of 120 LEO satellites and 6 BSs with satellite gateways. The index of virtual BS is 0. And we use Walker delta model to construct satellite constellation by satellite tool kit (STK). The satellite constellation has 12 orbits, and each orbit has 10 satellites. The inclination and height of each orbit are 45 degrees and 550 km, respectively. Moreover, every satellite is equipped with same antenna. The specific parameters of simulation are described by Table 1.

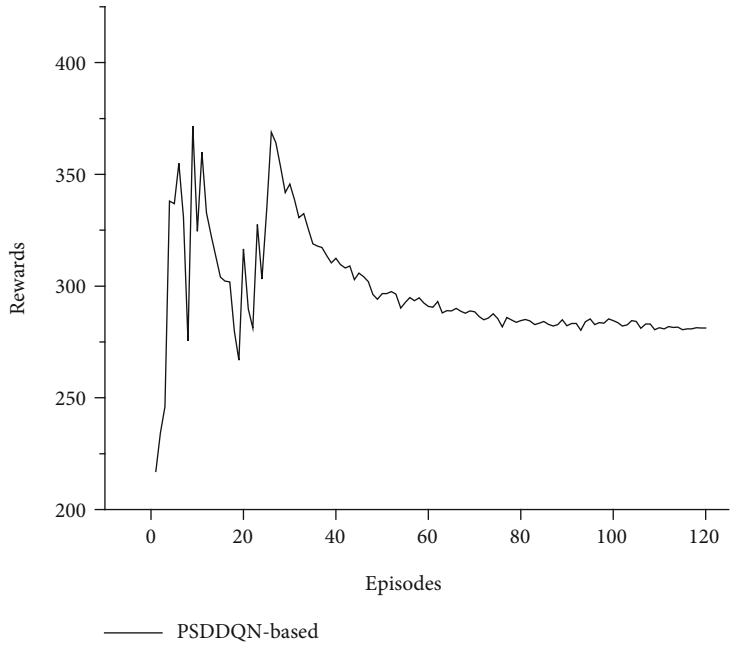

Figure 6: Rewards of PSDDQN with different episodes.

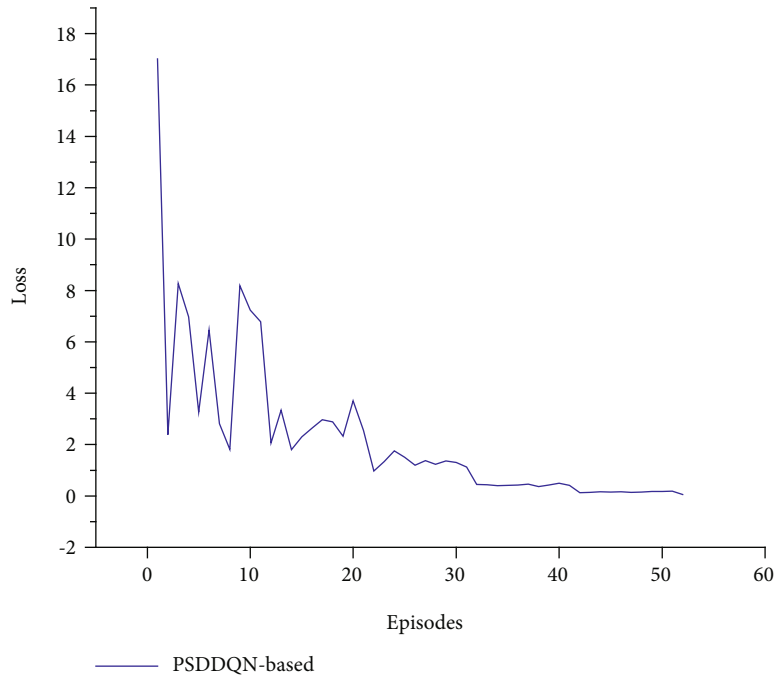

Figure 7: Loss value of PSDDQN with different episodes.

Considering that the estimated CSI is inaccurate and there is feedback propagation delay during the information transmission, the CSI information obtained by BSs is imperfect. Therefore, it is inaccurate to use the obtained CSI information to calculate the data transmission rate between satellites and BSs. To solve this problem, in practice, we use the estimated CSI value and the error value which follows circular symmetric complex Gaussian distribution to approximate the CSI value.

We conduct experiments on a computer with Win 10 OS, 16G RAM, and 3.2 GHz CPU. The programming language used is Python, and we select TensorFlow framework to construct PSDDQN model. Additionally, each BS contains 4 channels in this paper. Therefore, each BS can connect to 4 satellites simultaneously. Considering that the number of BSs is 6, the fully connected layer of PSDDQN has 24 neurons. Moreover, the two independent network structures of PSDDQN are same. And each neural network

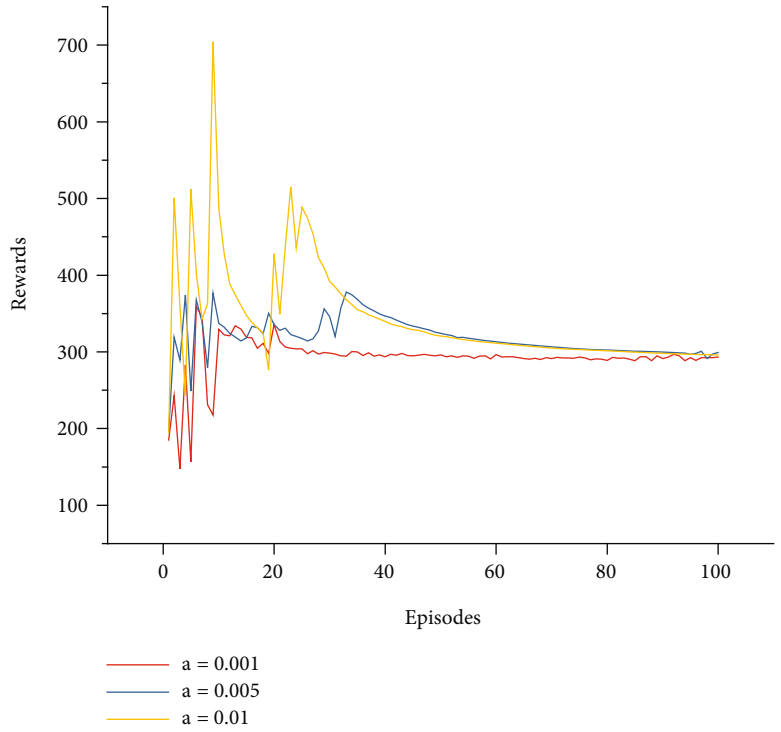

Figure 8: Rewards of PSDDQN with different learning rates.

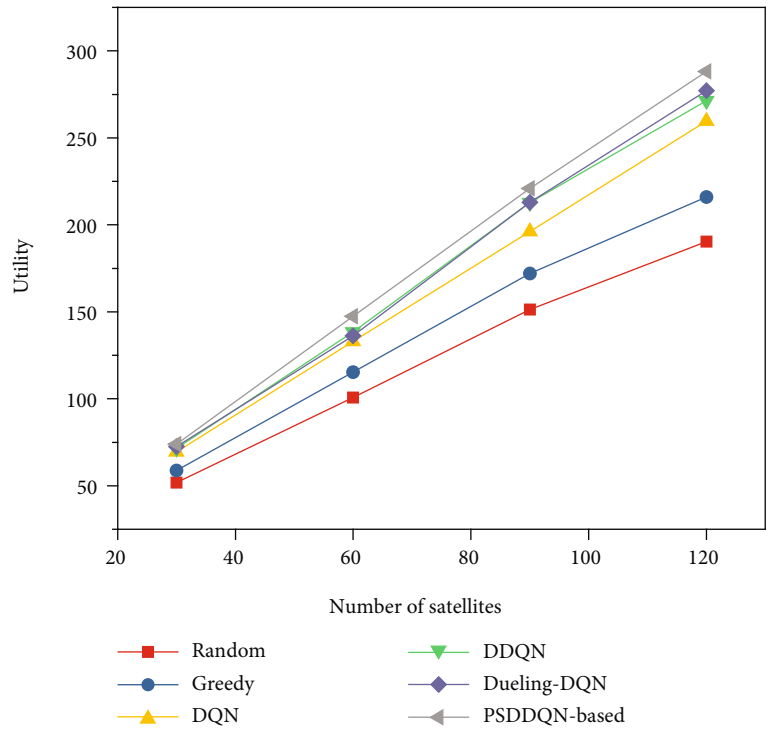

Figure 9: System utility with different number of satellites.

structure consists of the input layer, two hidden layers, and the output layer. In addition, the number of neurons in the input layer, hidden layer, and output layer is 156, 64 and 32, and 24, respectively. The specific parameters of PSDDQN are given by Table 2.

Considering that most operations in PSDDQN are dot product operations, we use FLOPS to represent its computation time. Because we use the full connection way to build the neural network, the FLOPs in the first layer, the second layer, and the third layer are $(2*156\text{-}1) * 64$, $(2 * 64\text{-}1) *$

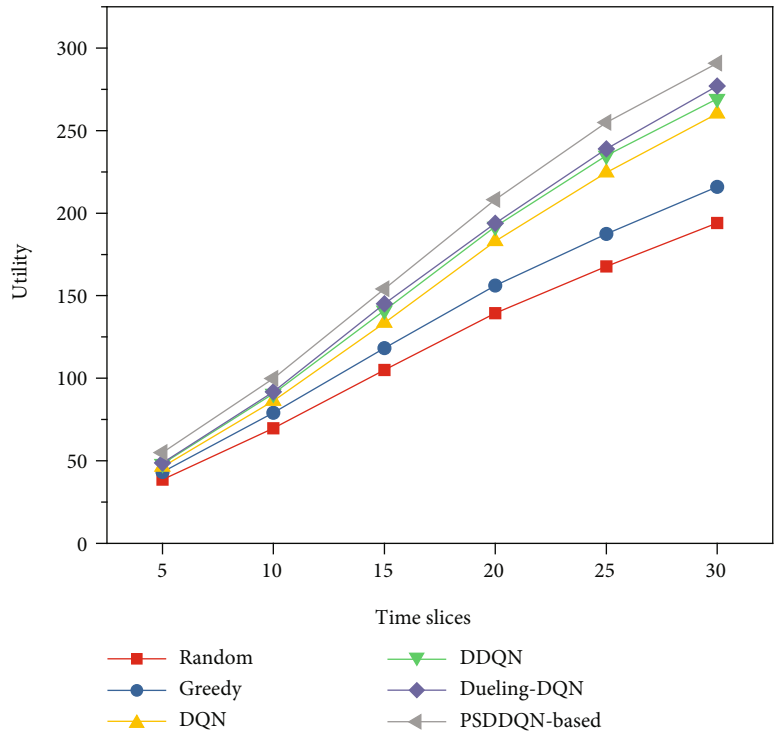

Figure 10: System utility with different time slices.

32, and (2 ∗ 32-1) ∗ 24, respectively. In addition, the activation function used in the first and second layers is ReLU; the required FLOPS of ReLU in these two layers are 64 and 32. The activation function used in the third layer is Softmax; the required FLOPS of Softmax in the third layer is 24 ∗ 4. Therefore, the total required FLOPs to execute one sample is 25672. Considering that the batch size we used is 32, the total FLOPS of PSDDQN is 25672 ∗ 32. For the parameters of PSDDQN, the parameters required in the first layer, the second layer, and the third layer are 156 ∗ 64+64, 64 ∗ 32+32, and 32 ∗ 24+24. Therefore, the total number of parameters in PSDDQN is 12920.

The weight of utility ω and storage cost ξ in Equation (20) is set to 0.7 and 0.3, respectively. The utility of unit data offloaded by the satellite is 1. Moreover, the duration of each time slice is 3.5 minutes, and there are 30 time slices in total.

5.2. Experimental Result Analysis. We firstly verify the convergence of PSDDQN. Then, we compare PSDDQN algorithm with random allocation algorithm, greedy allocation algorithm, DQN [37], DDQN [43], and Dueling-DQN [44], respectively. Finally, we show the experimental results and give the discussion.

Random allocation algorithm: for the satellite, one BS is randomly selected from the BSs within its coverage. Then, the satellite is associated with the selected BS, and a channel is randomly selected from the selected BS and assigned to the satellite.

Greedy allocation algorithm: for the satellite, the BS with the largest amount of offloaded data is selected from the BSs within its coverage and associated with the satellite. If the BS has no free channels, the suboptimal BS is selected.

5.2.1. Evaluation of Reinforcement Learning Model. Figure 6 shows the rewards of PSDDQN algorithm with different episodes. We note from Figure 6 that in the beginning, the rewards obtained by PSDDQN algorithm fluctuate sharply. The reason is that the parameters of PSDDQN algorithm are initialized randomly. As the number of episodes increases, the fluctuation of rewards obtained decreases gradually and finally tends to be stable. It is obvious from Figure 6 that PSDDQN algorithm converges at about 50 episodes.

Figure 7 plots the loss value of PSDDQN algorithm with different episodes. We observe that the loss value of PSDDQN is large in the beginning. With the increasing of episodes, the loss value of PSDDQN decreases gradually. Finally, the loss value tends to be stable. In addition, from Figure 7, we know that PSDDQN algorithm learns useful knowledge from state transition information.

From Figures 6 and 7, we can see that PSDDQN algorithm converges at about 50 episodes. The convergence speed of PSDDQN in STINs is relatively fast. In the training process, the satellite selects one BS from the BSs within its coverage as an action. Because the communication time between satellites and BSs is very short, most of state transition information is from virtual BS to virtual BS. Therefore, when state transition is from virtual BS to virtual BS, the satellite can only select virtual BS as an effective action. In PSDDQN, we directly set that the satellite at this time can only connect to virtual BS, which effectively reduces the convergence time of PSDDQN. This explains why PSDDQN converges fast.

When training PSDDQN algorithm, we use gradient descent method to update its parameters. If the learning rate

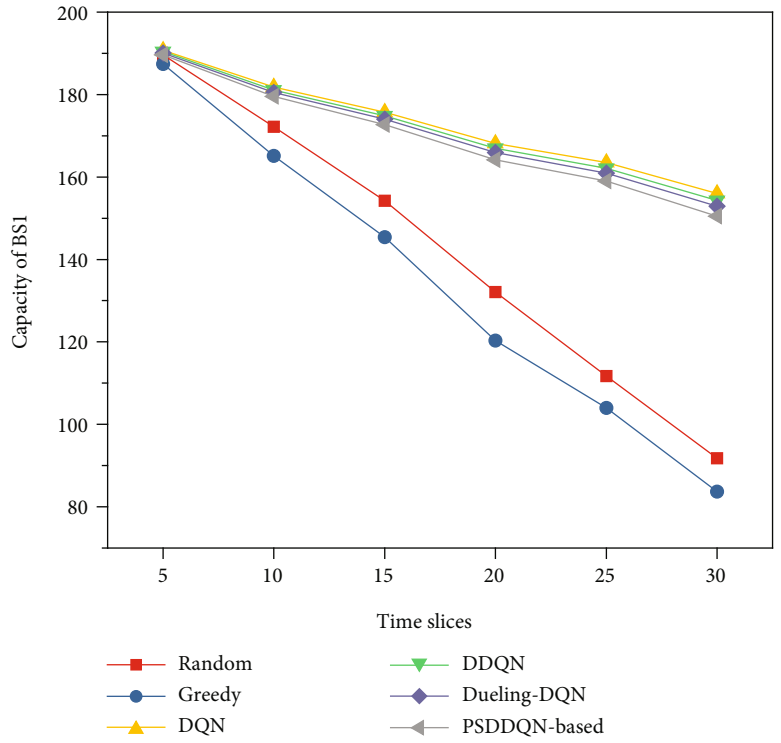

Figure 11: Capacity change of BS1.

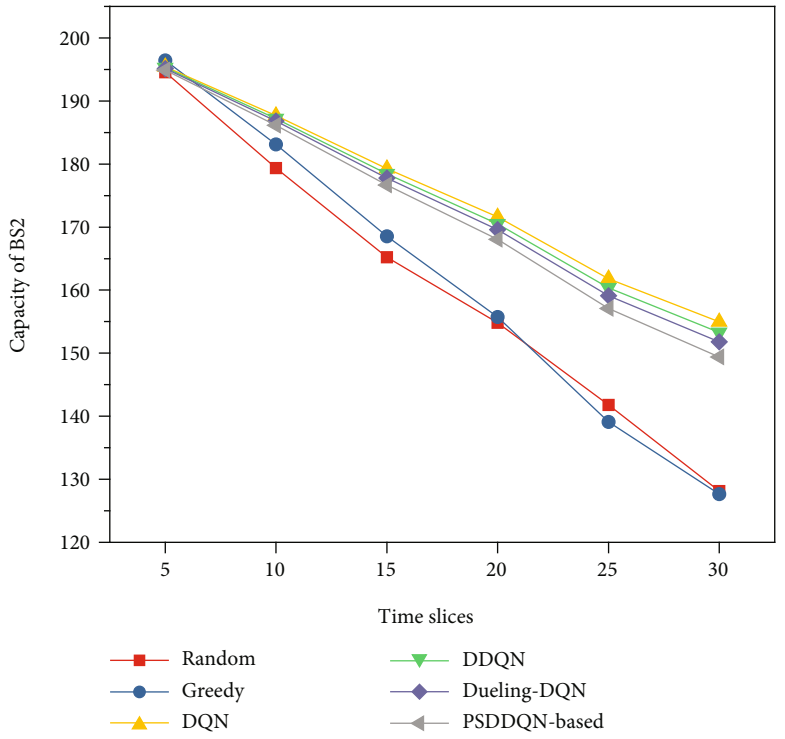

Figure 12: Capacity change of BS2.

is large, the step of parameter update is large. The convergence speed of PSDDQN is fast, but its performance fluctuates sharply in the convergence process. In addition, PSDDQN often cannot find the optimal solution. If the learning rate is small, the step of parameter update is small. And the convergence speed of PSDDQN is slow. Therefore, setting an appropriate learning rate in the experiment is very important for the convergence of PSDDQN.

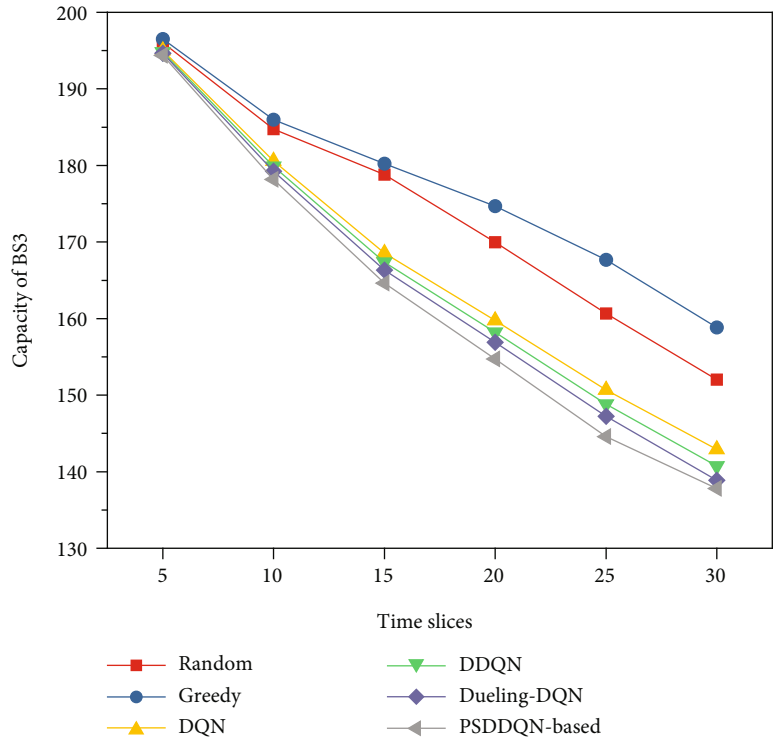

Figure 13: Capacity change of BS3.

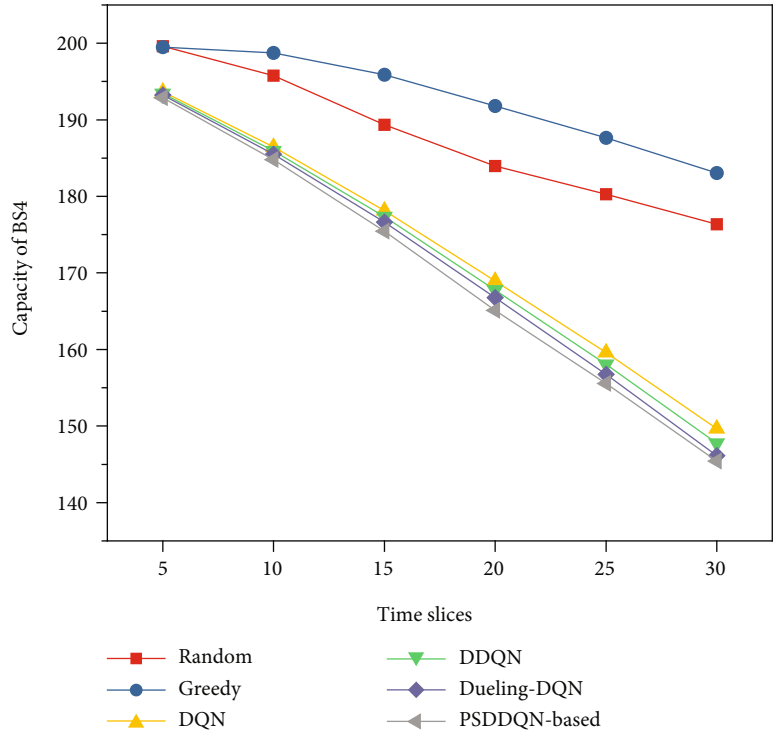

Figure 14: Capacity change of BS4.

Figure 8 depicts the rewards obtained by PSDDQN with different learning rates. With the increasing of episodes, PSDDQN algorithm with different learning rates can converge to a steady state. In addition, we also find that when $\alpha = 0.01$, the fluctuation of rewards obtained by PSDDQN is relatively large. However, if the value of α is too large, the agent often obtains the local optimal result rather than the optimal solution. When $\alpha = 0.001$, the convergence

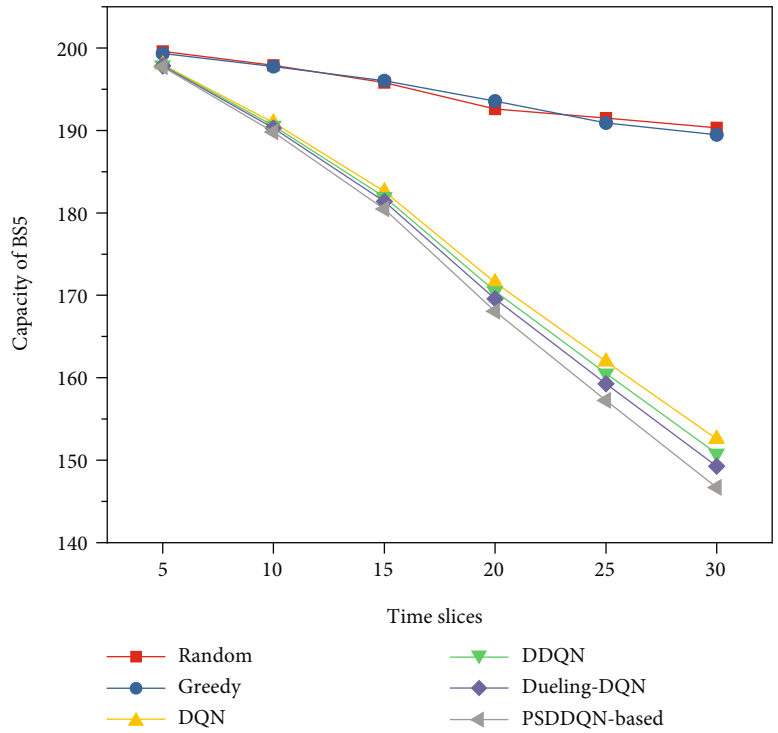

Figure 15: Capacity change of BS5.

speed of PSDDQN is slower than that of $\alpha = 0.005$. Therefore, in this paper, we set α to be 0.005 to train PSDDQN.

5.2.2. Evaluation of System Utility and Capacity Performance of BSs. We compare the system utility obtained by different algorithms with different number satellites in Figure 9. The increases of satellites number lead to the gradually increases of utility for all algorithms. This is because that the more satellites exist, the more connections between satellites and BSs in a time slice. Therefore, the amount of data offloaded from satellites to BSs increases, which increases the system utility. Moreover, we also find that the utility obtained by random allocation algorithm is the least, and the utility obtained by PSDDQN is the largest. For random allocation algorithm, it randomly assigns BSs and channels to satellites without considering the channel state and their communication time. As a result, the utility obtained by random allocation algorithm is the least. For greedy allocation algorithm, satellites prefer to associate with BSs that can offload more data. Therefore, greedy allocation algorithm achieves better performance than random allocation algorithm.

Furthermore, the performance of RL-based methods (e.g., DQN, DDQN, and Dueling-DQN) is similar. The reasons are as follows. First, RL-based algorithms consider the load of BSs in joint satellite association and channel allocation, so BSs can store offloaded data at a lower cost. Second, when offloading data, they not only consider the utility generated by satellites in the current time slice but also consider the utility generated by satellites in the subsequent time slices. Therefore, RL-based algorithms obtain more utility than random allocation algorithm and greedy allocation algorithm. In addition, DQN, DDQN, and Dueling-DQN algorithms use uniform sampling method to train their models. And PSDDQN adopts priority sampling method to train its model, which enhance the learning efficiency of uniform sampling. This explains why PSDDQN obtains the best performance.

In Figure 10, we compare the system utility obtained by all algorithms. We from Figure 10 note that with the increasing of time slices, the utility of all algorithms shows a gradual upward trend. And PSDDQN algorithm has the greatest utility, and random allocation algorithm has the least utility. Moreover, we also find that in the beginning, each algorithm obtains almost the same utility. However, with the increasing of time slices, the utility obtained by different algorithms is different. The main reason is that in satellite scheduling and resource allocation, RL-based algorithms pay more attention to the expected cumulative utility rather than the immediate utility. Therefore, they get better performance. In contrast, random allocation algorithm and greedy allocation algorithm only consider the utility generated by satellites in the current time slice and ignore the utility generated by satellites in the subsequent time slices.

Moreover, we can also see that for RL-based algorithms, the performance of PSDDQN is the best and that of DQN is the worst. The reason is that DQN is trained by a neural network structure, leading to the over estimation of the Q value. In addition, the training process of DQN is unstable, while DDQN adopts two independent network structures to select the action and calculate the Q value, which alleviate the over estimation problem. This explains why DDQN performs better than DQN. When calculating the Q value, Dueling-DQN pays more attention to the action with large advantage value. Thus, it achieves better results than DDQN. For

PSDDQN, it not only adopts two independent network structures to calculate the Q value but also uses priority sampling method to sample samples with larger TD-error value for training model. Therefore, compared with DQN, DDQN, and Dueling-DQN algorithms, PSDDQN algorithm gets better performance.

Here, we show the capacity change of BSs. In STINs, BS0 is virtual BS, and its capacity does not change at any time. So we do not show the change of its capacity.

Figures 11–15 show the capacity of BSs of different algorithms with different time slices. When the time slices increase, the remaining capacity of BSs decreases gradually. The reason is that with the increasing of time slices, more satellites can offload data to BSs. In addition, we find that the remaining capacity of different BSs is different. Particularly, we observe from Figures 11 and 12 that random allocation algorithm and greedy allocation algorithm offload most of data to BS1 and BS2, leading to the significant reduction in the capacity of BS1 and BS2. The remaining capacities of BS1 and BS2 are 90 and 128, respectively. From Figures 13–15, we also note that random allocation algorithm and greedy allocation algorithm offload less data to BS3, BS4, and BS5. The remaining capacities of BS3, BS4, and BS5 are 158, 185, and 195, respectively. Therefore, we know that random allocation algorithm and greedy allocation algorithm cause the capacities of BSs to be used unevenly.

Furthermore, we find that when RL-based algorithms are adopted, the remaining capacities of BS1, BS2, BS3, BS4, and BS5 are 160, 155, 140, 145, and 150, respectively. These algorithms basically ensure that the capacity of each BS is used evenly. When satellite association and channel allocation are performed, greedy allocation algorithm only considers the amount of offload data and ignores the load of BSs, which causes the capacity of some BSs to be overused and the storage cost of some BSs becomes larger. In contrast, RL-based algorithms consider not only the amount of offloaded data but also the capacity of BSs. Therefore, the results obtained by RL-based algorithms are better than those of greedy allocation algorithm and random allocation algorithm. In addition, considering that PSDDQN offloads more data to BSs, it consumes more capacity compared with other RL algorithms.

6. Conclusion

In our research, we investigated the joint satellite scheduling and resource allocation in STINs. We added a virtual BS to solve the problem that satellites cannot connect to BSs and reconstructed the communication model between satellites and BSs. Then, we formulated the joint satellite association and channel allocation as a joint optimization problem about utility and proposed PSDDQN algorithm to obtain the optimal strategy. When assigning appropriate BSs and channels to satellites, PSDDQN algorithm also considers the load balance of BSs. The simulation results demonstrate that PSDDQN obtains the maximum utility generated by offloaded data and achieves the load balance of BSs.

For some applications, data generated by satellites need to be transmitted to the terrestrial networks in real time. However, most satellites cannot communicate with BSs during the time of a snapshot. Therefore, it is a challenge to transmit the real-time data generated by satellites to the terrestrial networks. Considering that the satellites connected to BSs can be used as gateways, in the future work, we mainly study the traffic scheduling of satellites and try to design a traffic scheduling scheme for reasonably and dynamically transmitting the data of satellites to these gateways. Finally, these gateways are used to transmit these data to the terrestrial networks.

Data Availability

The simulation data used to support the findings of this study are available from the corresponding author upon request.

Conflicts of Interest

The authors declare that there is no conflict of interest regarding the publication of this paper.

Acknowledgments

This work is supported by the National Science Foundation of China (No. 61772385).

References

[1] S. Cioni, R. D. Gaudenzi, O. D. R. Herrero, and N. Girault, "On the satellite role in the era of 5G massive machine type communications," *IEEE Network*, vol. 32, no. 5, pp. 54–61, 2018.

[2] M. Shaat, E. Lagunas, A. I. Perez-Neira, and S. Chatzinotas, "Integrated terrestrial-satellite wireless backhauling: resource management and benefits for 5G," *IEEE Vehicular Technology Magazine*, vol. 13, no. 3, pp. 39–47, 2018.

[3] B. Di, H. Zhang, L. Song, Y. Li, and G. Y. Li, "Ultra-dense LEO: integrating terrestrial-satellite networks into 5G and beyond for data offloading," *IEEE Transactions on Wireless Communications*, vol. 18, no. 1, pp. 47–62, 2019.

[4] L. Kuang, X. Chen, C. Jiang, H. Zhang, and S. Wu, "Radio resource management in future terrestrial-satellite communication networks," *IEEE Wireless Communications*, vol. 24, no. 5, pp. 81–87, 2017.

[5] W. Wang, S. Zhao, Y. Zheng, and Y. Li, "Resource allocation method of cognitive satellite terrestrial networks under non-ideal spectrum sensing," *IEEE Access*, vol. 7, pp. 7957–7964, 2019.

[6] W. Wang, J. Wei, S. Zhao, Y. Li, and Y. Zheng, "Energy efficiency resource allocation based on spectrum-power tradeoff in distributed satellite cluster network," *Wireless Networks*, vol. 26, no. 6, pp. 4389–4402, 2020.

[7] C. C. Lin, N. W. Su, D. J. Deng, and I. Tsai, "Resource allocation of simultaneous wireless information and power transmission of multi-beam solar power satellites in space-terrestrial integrated networks for 6G wireless systems," *Wireless Networks*, vol. 26, no. 6, pp. 4095–4107, 2020.

[8] Y. Hu, M. Chen, and W. Saad, "Joint access and backhaul resource management in satellite-drone networks: a

competitive market approach," *IEEE Transactions on Wireless Communications*, vol. 19, no. 6, pp. 3908–3923, 2020.

[9] Y. Chen, J. Li, W. Chen, Z. Lin, and B. Vucetic, "Joint user association and resource allocation in the downlink of heterogeneous networks," *IEEE Transactions on Vehicular Technology*, vol. 65, no. 7, pp. 5701–5706, 2016.

[10] A. Khalili, S. Akhlaghi, H. Tabassum, and D. W. K. Ng, "Joint user association and resource allocation in the uplink of heterogeneous networks," *IEEE Wireless Communications Letters*, vol. 9, no. 6, pp. 804–808, 2020.

[11] N. Zhao, Y.-C. Liang, D. Niyato, Y. Pei, M. Wu, and Y. Jiang, "Deep reinforcement learning for user association and resource allocation in heterogeneous cellular networks," *IEEE Transactions on Wireless Communications*, vol. 18, no. 11, pp. 5141–5152, 2019.

[12] V. Mnih, K. Kavukcuoglu, D. Silver et al., "Human-level control through deep reinforcement learning," *Nature*, vol. 518, no. 7540, pp. 529–533, 2015.

[13] J. Qiu, J. Lyu, and L. Fu, "Placement optimization of aerial base stations with deep reinforcement learning," in *ICC 2020-2020 IEEE International Conference on Communications (ICC),*, pp. 1–6, Dublin, Ireland, 2020.

[14] J. Pei, P. Hong, M. Pan, J. Liu, and J. Zhou, "Optimal VNF placement via deep reinforcement learning in SDN/NFV-enabled networks," *IEEE Journal on Selected Areas in Communications*, vol. 38, no. 2, pp. 263–278, 2020.

[15] C. Jiang and X. Zhu, "Reinforcement learning based capacity management in multi-layer satellite networks," *IEEE Transactions on Wireless Communications*, vol. 19, no. 7, pp. 4685–4699, 2020.

[16] H.-X. Peng and X. Shen, "Multi-agent reinforcement learning based resource management in MEC- and UAV-assisted vehicular networks," *IEEE Journal on Selected Areas in Communications*, vol. 39, no. 1, pp. 131–141, 2021.

[17] N. Naderializadeh, J. J. Sydir, M. Simsek, and H. Nikopour, "Resource management in wireless networks via multi-agent deep reinforcement learning," *IEEE Transactions on Wireless Communications*, vol. 20, no. 6, pp. 3507–3523, 2021.

[18] M. Feng, S. Mao, and T. Jiang, "Joint frame design, resource allocation and user association for massive MIMO heterogeneous networks with wireless backhaul," *IEEE Transactions on Wireless Communications*, vol. 17, no. 3, pp. 1937–1950, 2018.

[19] R. Liu, Q. Chen, G. Yu, and G. Y. Li, "Joint user association and resource allocation for multi-band millimeter-wave heterogeneous networks," *IEEE Transactions on Communications*, vol. 67, no. 12, pp. 8502–8516, 2019.

[20] J. S. Liu, C. H. R. Lin, and Y. C. Hu, "Joint resource allocation, user association, and power control for 5G LTE-based heterogeneous networks," *IEEE Access*, vol. 8, pp. 122654–122672, 2020.

[21] Z. Cheng, N. Chen, B. Liu et al., "Joint user association and resource allocation in HetNets based on user mobility prediction," *Computer Networks*, vol. 177, p. 107312, 2020.

[22] M. Zalghout, A. Khalil, M. Crussiére, S. Abdul-Nabi, and J.-F. Hélard, "Context-aware and priority-based user association and resource allocation in heterogeneous wireless networks," *Computer Networks*, vol. 149, pp. 76–92, 2019.

[23] X. Zhu, C. Jiang, L. Kuang, N. Ge, and J. Lu, "Energy efficient resource allocation in cloud based integrated terrestrial-satellite networks," in *2018 IEEE International Conference on Communications (ICC)*, pp. 1–6, Kansas City, MO, USA, 2018.

[24] P. Zuo, T. Peng, W. Linghu, and W. Wang, "Resource allocation for cognitive satellite communications downlink," *IEEE Access*, vol. 6, pp. 75192–75205, 2018.

[25] T. Mai, H. Yao, F. Li, X. Xu, Y. Jing, and Z. Ji, "Computing resource allocation in LEO satellites system: a Stackelberg game approach," in *2019 15th International Wireless Communications & Mobile Computing Conference (IWCMC)*, pp. 919–924, Tangier, Morocco, 2019.

[26] B. Deng, C. Jiang, and S. Guo, "Energy minimization of resource allocation in cloud-based satellite communication networks," *IEEE Communications Letters*, vol. 23, no. 12, pp. 2353–2356, 2019.

[27] S. M. Shahid, Y. T. Seyoum, S. H. Won, and S. Kwon, "Load balancing for 5G integrated satellite-terrestrial networks," *IEEE Access*, vol. 8, pp. 132144–132156, 2020.

[28] Z. Ji, S. Wu, C. Jiang, D. Hu, and W. Wang, "Energy-efficient data offloading for multi-cell satellite-terrestrial networks," *IEEE Communications Letters*, vol. 24, no. 10, pp. 2265–2269, 2020.

[29] R. Deng, B. Di, H. Zhang, and L. Song, "Ultra-dense LEO satellite constellation design for global coverage in terrestrial-satellite networks," in *GLOBECOM 2020-2020 IEEE Global Communications Conference*, pp. 1–6, Taipei, Taiwan, 2020.

[30] L. He and K. He, "Efficient memory-bounded optimal detection for GSM-MIMO systems," *IEEE Transactions on Communications*, vol. PP, no. 99, pp. 1–12, 2022.

[31] L. He and K. He, "Towards optimally efficient search with deep learning for large-scale MIMO systems," *IEEE Transactions on Communications*, vol. PP, no. 99, pp. 1–14, 2022.

[32] X. Lai, "Outdated access point selection for mobile edge computing with cochannel interference," *IEEE Transactions on Vehicular Technology*, vol. PP, no. 99, pp. 1–10, 2022.

[33] S. Tang and L. Chen, "Computational intelligence and deep learning for next-generation edge-enabled industrial IoT," *IEEE Transactions on Network Science and Engineering*, vol. -PP, no. 99, pp. 1–15, 2022.

[34] L. Chen, R. Zhao, K. He, Z. Zhao, and L. Fan, "Intelligent ubiquitous computing for future UAV-enabled MEC network systems," *Cluster Computing*, vol. 2021, no. 25, pp. 1–10, 2021.

[35] L. Chen, "Physical-layer security on mobile edge computing for emerging cyber physical systems," *Computer Communications*, vol. PP, no. 99, pp. 1–9, 2022.

[36] X. Liu, Z. Qin, and Y. Gao, "Resource allocation for edge computing in IoT networks via reinforcement learning," in *ICC 2019-2019 IEEE International Conference on Communications (ICC)*, pp. 1–6, Shanghai, China, 2019.

[37] Y. Liu, H. Yu, S. Xie, and Y. Zhang, "Deep reinforcement learning for offloading and resource allocation in vehicle edge computing and networks," *IEEE Transactions on Vehicular Technology*, vol. 68, no. 11, pp. 11158–11168, 2019.

[38] F. Tang, Y. Zhou, and N. Kato, "Deep reinforcement learning for dynamic uplink/downlink resource allocation in high mobility 5G HetNet," *IEEE Journal on Selected Areas in Communications*, vol. 38, no. 12, pp. 2773–2782, 2020.

[39] X. Zhang, M. Peng, S. Yan, and Y. Sun, "Deep-reinforcement-learning-based mode selection and resource allocation for cellular V2X communications," *IEEE Internet of Things Journal*, vol. 7, no. 7, pp. 6380–6391, 2020.

[40] W. Hou, H. Wen, H. Song, W. Lei, and W. Zhang, "Multiagent deep reinforcement learning for task offloading and resource

allocation in Cybertwin-based networks," *IEEE Internet of Things Journal*, vol. 8, no. 22, pp. 16256–16268, 2021.

[41] P. Luong, F. Gagnon, L. N. Tran, and F. Labeau, "Deep reinforcement learning-based resource allocation in cooperative UAV-assisted wireless networks," *IEEE Transactions on Wireless Communications*, vol. 20, no. 11, pp. 7610–7625, 2021.

[42] R. Fdhila, T. M. Hamdani, and A. M. Alimi, "A multi objective particles swarm optimization algorithm for solving the routing pico-satellites problem," in *2012 IEEE International Conference on Systems, Man, and Cybernetics (SMC)*, pp. 1402–1407, Seoul, Korea (South), 2012.

[43] X. Chen, H. Zhang, C. Wu, S. Mao, Y. Ji, and M. Bennis, "Optimized computation offloading performance in virtual edge computing systems via deep reinforcement learning," *IEEE Internet of Things Journal*, vol. 6, no. 3, pp. 4005–4018, 2019.

[44] Z. Liu, X. Chen, Y. Chen, and Z. Li, "Deep reinforcement learning based dynamic resource allocation in 5G ultra-dense networks," in *2019 IEEE International Conference on Smart Internet of Things (SmartIoT)*, pp. 168–174, Tianjin, China, 2019.

Hindawi
Wireless Communications and Mobile Computing
Volume 2022, Article ID 3951376, 8 pages
https://doi.org/10.1155/2022/3951376

Research Article

Machine Learning-Aided Energy Efficiency Strategy for Multiuser Cooperative Networks

Lin Shan, Ou Zhao, Katsuhiro Temma, Fumihide Kojima, Fumiyuki Adachi, and Takeshi Matsumura

National Institute of Information and Communications Technology (NICT), 4-2-1, Nukui-Kitamachi, Koganei, Tokyo 184–8795, Japan

Correspondence should be addressed to Lin Shan; shanlin@nict.go.jp

Received 16 November 2021; Revised 17 December 2021; Accepted 22 December 2021; Published 17 January 2022

Academic Editor: Junjuan Xia

Cooperative communication is widely seen as a promising key technology for improving the energy efficiency of battery-driven multiple mobile terminals (MTs). In this study, we investigate the use of machine learning (ML) in multiuser cooperative access networks. Because MT cooperation and bandwidth allocation are considered two main issues in such networks, we design an ML-aided method to solve the bandwidth issues so that the proposed method can maximize the network's energy efficiency. Specifically, we use machine learning with artificial neural network (ANN) trained at base station (BS) (a) to decide whether MTs in the heterogeneous access network should cooperatively communicate and (b) to determine the optimal bandwidth allocation for this communication by distributing the trained ANN to all MTs. The computer simulation results show that under the described communication environment in this paper, the proposed method can provide 99.8% correct prediction for MT cooperation and output the optimal bandwidth allocation with at least 88% accuracy, which demonstrates the effectiveness of the proposed method. Besides, the simulations also show that the proposed method can provide about 14%–25% power consumption reduction, which validates the EE performance of the proposed method.

1. Introduction

In recent years, as mobile terminal (MT) applications are growing dramatically, the traffic loading on networks and the power consumption of each MT become very important issues in modern wireless networks. For reducing traffic loading and saving the power consumption for each MT, forwarding transmission via MTs using cooperative wireless methods, which are also called user cooperation, is widely considered a promising approach [1]. Recently, lots of studies have investigated power consumption of user cooperation in cellular systems [2–4]. For example, in [2], the authors studied MT cooperation-based traffic downloading for distributing content to MTs. In [3], the authors proposed a method to increase the energy efficiency (EE) of two-MT cooperative cognitive wireless networks with network coding. In [4], the tradeoff between throughput and energy consumption in cooperative cognitive radio networks was theoretically analyzed.

Due to the limited transmission power of battery-driven MTs, an appropriate access scheme for improving EE performance is necessary in uplink cellular systems. Besides, such low energy consumption scheme will offer the opportunity to accommodate more battery-driven MTs because the total energy consumption of the whole cooperative system can be reduced. In our previous work [5], we investigated user cooperation traffic loading and proposed a method for optimizing the bandwidth allocation strategy to save power in MTs. Theoretical analysis and experiments of evaluating the proposed method in [5] show that up to 70% of single MT's power can be saved via the method. However, this user cooperation-aided forwarding approach selects a proxy terminal to meet the total communication demands of other MTs, and thus, the proxy terminal (i.e., one of the MTs)

tends to be allocated more bandwidth (or spectrum resources) and may suffer from frequency selective fading. As a result, the transmission performance of the proxy terminal is occasionally worse than expected.

Although the method in [5] can substantially improve performance, the decision on whether MTs should cooperate for transmissions and the optimal allocation of bandwidth for these cooperative transmissions still remain as essential problems in cooperative transmission systems. According to the analysis results for the bandwidth allocation proportion (called ν in [5]) which is used for deciding the bandwidth allocated for cooperative communication, there exists an optimal proportion value called ν_{op} that can minimize system power consumption in the considered cooperative heterogeneous access networks. To determine this optimal value ν_{op}, the base station (BS) needs to collect the channel state information (CSI) and traffic demand of each MT and perform a series of tasks, which causes delay and thus reduces communication efficiency such as throughput. Past experience and available data can be used to perform such tasks, which are complex and computationally expensive, but traditional approaches based on explicit rules and instructions are not necessary. In particular, the best power-saving performance can be obtained by cooperative communication among MTs with an exhaustive search for the optimal bandwidth allocation, while it costs a lot of computation. If the bandwidth allocation can be determined in a less costly way, the method in [5] would be more feasible.

Owing to the rapid growth of machine learning (ML), many difficult research issues have been solved by ML-based methods, especially in future communication systems [6]. Thus, various ML-based approaches for wireless communication have been proposed in recent years [7–23]. For example, in [8], the authors used an ML-aided method to predict trajectory and detect conflict for aerial vehicles. In [9], the authors proposed an ML-based method to solve the resource allocation problem in cognitive radio systems. In [11], an ML-based method was used to solve the iterative decoding issue for ultra-dense small cell networks with cooperative transmission. In [16], the authors proposed an ML-based method to process transmission antenna selection task in multiple-input-multiple-output (MIMO) systems. ML-based methods also have a potential to further improve energy efficiency in cooperative heterogeneous networks. Meanwhile, it is important to prioritize the key performance indices (KPIs) that include intelligence, connectivity, spectrum efficiency, and energy efficiency as described in [24] because considering all the KPIs consumes a lot of computational resources to construct an optimal solution for a wireless system. In summary, in recent years, various ML-based methods were proposed to solve difficult problems in wireless communications. However, for the EE optimization problem in cooperative heterogeneous networks in the next-generation communications, we still need intelligent solutions, which motivate our work in this paper.

From the literature about EE problem, it can be known that how to achieve optimal EE performance in cooperative system is a difficult optimization problem of resource allocation so that optimal solution may not be found with limited computing resources. However, with the aid of ML technologies, it becomes less complicated and more feasible. Therefore in this study, we propose an effective bandwidth allocation strategy with ML-based methods using artificial neural networks (ANNs) for user-cooperative traffic forwarding. In our previous study [5], by averaging the effects of small-scale fading, each MT uploads its position and traffic demand to the BS. The BS then uses conventional methods to determine if cooperative communication would be more efficient and calculate ν_{op} with the help of this uploaded information. The results, noncooperative or cooperative communication (i.e., the communication mode) along with the value of ν_{op}, are returned to each MT and the BS performs follow-up operations. In ML-based approaches, the BS can further utilize the forementioned information to train or update ANNs, which are then used to predict the best communication mode and the value of ν_{op} without the existing algorithms. Once ANNs have been trained on the BS side, the trained ANN can be distributed to each MT by operator updates. Then, the MTs can use these trained or updated networks to determine whether they should use cooperative transmissions and further predict the value of ν_{op} (within an allowed error, of course) for the cooperative communication case. Finally, it is not necessary to upload the MT's information to the BS, and this reduces the system complexity and improves EE. It should be noted that, to apply it in a realistic transmission environment, here, we consider a generalized channel attenuation model with frequency selective fading and spatially correlated shadowing, in which the effect of small-scale fading is averaged for focusing on averaged transmission quality.

The main contributions of this paper are as follows:

(i) We introduce an ML-aided method in cooperative communications based on the validated evaluation results in [5], in which an effective energy efficiency optimization method is provided

(ii) The proposed ML-aided method predicts transmission performance parameters such as the optimal bandwidth proportion coefficient ν_{op} by using MT deployments and their communication demands. Henceforth, the proposed ML-aided methods can improve the computational cost and EE

(iii) A more realistic environment with the frequency selective fading channel and effect of spatially correlated shadowing is applied to the evaluation in this paper. To the best of our knowledge, there has been no previous work which dealt with the issue of bandwidth allocation under frequency selective channel in cooperative communications, although this issue is very important and may affect the system performance substantially

The rest of this paper is organized as follows. Section 2 describes the system model and formulates the problem in this study. Section 3 introduces the proposed method.

Section 4 provides simulation results. Finally, Section 5 concludes our work.

2. System Model and Problem Formulation

In this study, we consider an existing heterogeneous network that includes a set of MTs denoted as $\mathcal{U} = \{1, \cdots, U\}$ and indexed with $u = 1, \cdots, U$ together with a BS deployed in the network. The noncooperative and cooperative transmission scenarios considered in this study are illustrated in Figure 1. The MTs are in close proximity to each other and are able to communicate with the BS. Each MT is equipped with single antenna whereas the BS is equipped with M centralized antennas. The communications among the BS and MTs utilize an allocated bandwidth resource B for the uplink data transmissions. To make the proxy receive the traffic from other MTs and transmit the total traffic to the BS simultaneously, each MT is with two types of transmission modules: one can be operated as cellular link for sending data to the BS, and the other one can perform device-to-device (D2D) link for local data exchange with other MTs. In this type of network, all of the MTs are uniformly distributed in a circular communication area of radius R_{coop} that is R_{cell} away from the BS. Here, the radius of the cooperative-communication area depends on the capability of the D2D link.

In the conventional noncooperative transmission scenario, each MT directly sends its communication demand $C(u)$ to the BS using the equally allocated nonoverlapping bandwidths B/U. In the cooperative transmission scenario [5], the available bandwidth is divided into two parts: νB and $(1-\nu)B$. The MTs, which are also known as clients, equally occupy the partial nonoverlapping bandwidth resource of νB to communicate with a proxy using multiple D2D links. In other words, the allocated bandwidth for each MT is $\nu B/(U-1)$. The corresponding bandwidth allocations is shown in Figure 2. The proxy, which is selected from the MT set $\mathcal{U}$, works as a data aggregator and sends the total traffic demands $C_{\text{all}} = \sum_{u=1}^{U} C(u)$ to the BS using the remaining bandwidth $(1-\nu)B$.

Because ν is a coefficient indicating proportion in our bandwidth allocation strategy, it can range from 0 to 1. The analysis in our previous work [5] shows that the transmit power at the clients or proxy is mathematically infinity in the two extreme cases of $\nu = 0$ and $\nu = 1$ because one of the clients or proxy is allocated without any bandwidth. Therefore, there exists an optimal value ν_{op} that minimizes the power consumed by the whole system, and ν_{op} indirectly varies with respect to the MT deployments, the selected proxy, and the uplink CSI. This is the key finding in [5], and the existence of ν_{op} enables ML-based approaches to simplify the system and hence improves energy efficiency.

3. Proposed ML-Aided Methods for Cooperative Communications

In our previous study [5], we proposed an effective method for heterogeneous cooperative networks that can save up to

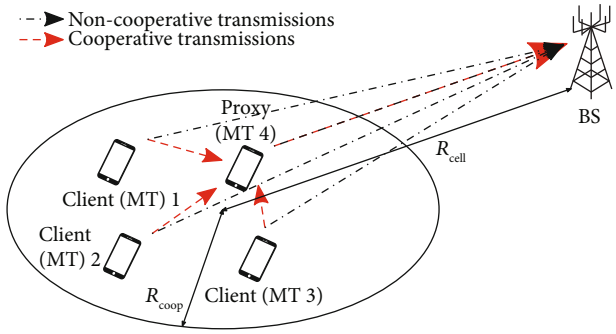

Figure 1: Noncooperative and cooperative transmissions with $U = 4$.

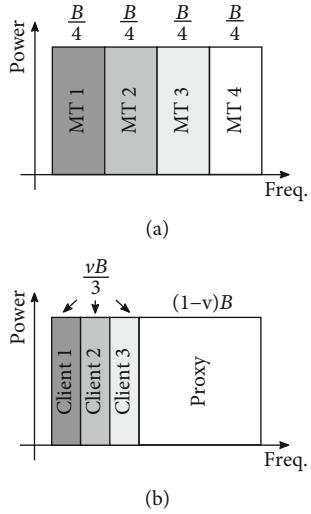

Figure 2: Bandwidth allocation strategy for the non-cooperative and cooperative transmissions with $U = 4$.

70% of MT transmit power. However, two major issues still remain in this method: One is how to decide if MTs should cooperate, and the other one is the proportion of bandwidth allocation to each MT. Therefore, in this study, for a given MT deployment and their communication demands, our goal is to use ML methods to resolve the following two issues: (a) deciding cooperative or noncooperative communication among MTs and (b) if cooperative, how the optimal value of ν_{op} is effectively determined. For this purpose, we first collect some data and generate a database $\mathcal{B}$ to train the ML algorithms. Database $\mathcal{B}$ consists of an input space $\mathcal{V}$ and two output spaces $\mathcal{T}_1$ and $\mathcal{T}_2$. The input–output pairs of $\mathcal{V}$ and $\mathcal{T}_1$ are used to train an ANN to determine the communication mode, and the input-output pair of $\mathcal{V}$ and $\mathcal{T}_2$ is used to train another ANN to predict the optimal value of ν_{op}. The generation of the database and the training of ANNs are performed in the offline phase, as shown in Figure 3.

In the input space $\mathcal{V}$, there are N possible feature vectors. Since large-scale fading is highly dependent on the geometrical locations and small-scale fading has been averaged, we consider each feature vector $\mathcal{V}(n), n = 1, \cdots, N$, which consists of MT deployments and their communication

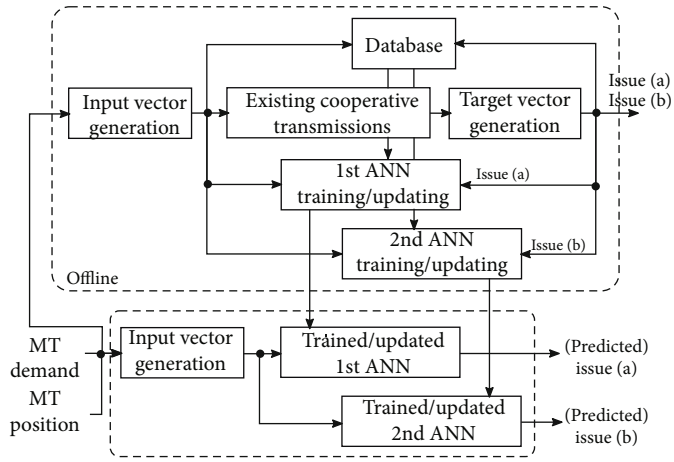

Figure 3: Functional block diagram of the proposed ML-aided bandwidth allocation strategy for the considered cooperative transmissions.

demands. The n-th feature vector for the input space $\mathscr{V} = \{\mathscr{V}(n)\}_{n=1}^{N}$ is written as

$$\mathscr{V}(n) = \left\{\left\{C(u,n), X(u,n), Y(u,n)\right\}_{u=1}^{U}\right\}^{T}, \tag{1}$$

where $X(u,n)$ and $Y(u,n)$ denote the n-th horizontal and vertical coordinates of MT u, respectively, and $C(u,n)$ is the communication demand of MT u at the n-th position. Certainly, in our future work, we can consider more parameters such as small-scale fading and mobility, to extend our study for more complicated scenarios.

Both output space $\mathscr{T}_1$ and $\mathscr{T}_2$ have N target values, and the n-th element in $\mathscr{T}_1 = \{\mathscr{T}_1(n)\}_{n=1}^{N}$ and $\mathscr{T}_2 = \{\mathscr{T}_2(n)\}_{n=1}^{N}$ is formulated as

$$\mathscr{T}_1(n) = \begin{cases} \{1,0\}^{\mathrm{T}}, & \text{for noncooperative communication,} \\ \{0,1\}^{\mathrm{T}}, & \text{for cooperative communication,} \end{cases} \tag{2}$$

$$\mathscr{T}_2(n) = \nu_{\mathrm{op}}(n), \tag{3}$$

where "1" and "0" in (2) represent the corresponding logical variables of "true" and "false," respectively. The values of $\mathscr{T}_1(n)$ and $\mathscr{T}_2(n)$ for all n are obtained from our previous study [5]. More specifically, for arbitrary n, we first exhaustively search for the optimal $\nu_{\mathrm{op}}(n)$ and record it in $\mathscr{T}_2$ and then further calculate the total consumed power with the corresponding $\nu_{\mathrm{op}}(n)$ for both communication modes (the calculations for noncooperative and cooperative $\nu_{\mathrm{op}}(n)$ follow equations (21) and (22) in [5]). In the last step, we compare the transmit power to determine the best communication mode and record the results in $\mathscr{T}_1$.

Once the database $\mathscr{B}$ is generated, two ANNs (i.e., models or functions) $\mathbb{M}_1^*$ and $\mathbb{M}_2^*$ are trained by substituting $\mathscr{V}$, $\mathscr{T}_1$, and $\mathscr{T}_2$ into the given network structures and training them. Generally, $\mathbb{M}_1^*$ and $\mathbb{M}_2^*$ can be written as

$$\mathbb{M}_i^* = \arg \min_{\mathbb{M}_i} \mathscr{L}_i(\mathscr{T}_i, \mathbb{M}_i(\mathscr{V})), \tag{4}$$

where $i = 1$ and $i = 2$ denote the first and second ANNs, respectively, and $\mathscr{L}_i$ is the loss function used for network training. After both ANNs have been trained, $\mathbb{M}_1^*$ and $\mathbb{M}_2^*$ can be used to predict the answers to communication mode determination and bandwidth allocation. Here, this process is called "Online Phase," which is also shown in Figure 3 with gray frames. Note that the "Existing Cooperative Transmissions" block in Figure 3 can be realized with any existing cooperative transmission method such as the one provided in [5]. The proposed method is summarized in Algorithm 1.

4. Simulation Results

In the simulations, we collected N sets of data for training $\mathbb{M}_1^*$ and $\mathbb{M}_2^*$ and N_{pred} sets of data for testing these trained ANNs. To evaluate the accuracy of the proposed ML-based prediction methods, we defined a parameter $\rho(n')$, where $n' = 1, \cdots, N_{\mathrm{pred}}$, to represent the predicted accuracy of the n'th ν_{op}. It is expressed as

$$\rho\left(n'\right) = 1 - \frac{\left|\tilde{\nu}_{\mathrm{op}}\left(n'\right) - \nu_{\mathrm{op}}\left(n'\right)\right|}{\nu_{\mathrm{op}}\left(n'\right)}, \tag{5}$$

where $\tilde{\nu}_{\mathrm{op}}(n')$ is the predicted optimal proportion of bandwidth for cooperative communication, which is mainly dominated by the MT deployments and communication demands. $\tilde{\nu}_{\mathrm{op}}(n')$ can be calculated by

$$\tilde{\nu}_{\mathrm{op}}\left(n'\right) = \mathbb{M}_2^*\left(\mathscr{V}\left(n'\right)\right). \tag{6}$$

Finally, the output of $\mathbb{M}_1^*(n')$ and the complementary cumulative distribution function (CCDF) of $\rho(n')$ for all of $n' = 1, \cdots, N_{\mathrm{pred}}$ are used to evaluate the proposal.

The main simulation configurations and settings for the ANN training in this study are listed in Tables 1 and 2, respectively. Here, the parameters of ANN such as maximum number of epochs or number of layers are chosen by

Input: $C(u,n)$, $X(u,n)$, $Y(u,n)$, $u = 1, \cdots, U$, $n = 1, \cdots, N$
Output: $\mathbb{M}_i^*$, $i = 1, 2$
Initialization: $\mathscr{V} = \varnothing$, $\mathscr{T}_1 = \varnothing$, $\mathscr{T}_2 = \varnothing$, Create ANNs $\mathbb{M}_i$ for $i = 1, 2$
%Generation of input space in database $\mathscr{B}$
for $n = 1, \cdots, N$ **do**
    $\mathscr{V}_{temp} = \varnothing$
    for $u = 1, \cdots, U$ **do**
        $\mathscr{V}_{temp} = \mathscr{V}_{temp} \bigcup C(u,n) \bigcup X(u,n) \bigcup Y(u,n)$;
    end
    $\mathscr{V} = \mathscr{V} \bigcup \mathscr{V}_{temp}^T$
end
%Generation of output space in database $\mathscr{B}$
for $n = 1, \cdots, N$ **do**
    Calculate $\nu_{op}(n)$ by substituting $\mathscr{V}(n)$ and using exhaustive searching based on [5];
    $\mathscr{T}_2 = \mathscr{T}_2 \bigcup \nu_{op}(n)$;
    Calculate the total power consumption of non- cooperative and cooperative communications according to [5];
    if Non-cooperative power ≤ Cooperative power **then**
        $\mathscr{T}_1 = \mathscr{T}_1 \bigcup \{1, 0\}^T$;
    else
        $\mathscr{T}_1 = \mathscr{T}_1 \bigcup \{0, 1\}^T$
    end
end
%Training all of ANNs
for each $i = 1, 2$ **do**
    $\mathbb{M}_i^* = \arg \min_{\mathbb{M}_i} \mathscr{L}_i(\mathscr{T}_i, \mathbb{M}_i(\mathscr{V}))$
end

Algorithm 1: The proposed ML-based energy efficiency method.

doing numbers of simulations and select the values which can result in good learning performance. Note that because the area of cooperative communication is not large, the shadowing loss variations can be viewed as completely correlated for all MTs. Furthermore, according to [5, 26], a frequency selective channel model with L (indexed with $l = 1, \cdots, L$) subchannels (or paths) is adopted, and a intertap correlation coefficient matrix Θ_{ISI} for simulation of intersymbol interference (ISI) is also considered. The detailed parameters can be found in our previous study in [5]. With the consideration of current computational complexity and computer resources, we adopt one hidden layer with 10 nodes for the ANNs.

Table 3 shows the prediction results of the 1st ANN for communication mode. As indicated in the first row, there are 921 cases that should use cooperative communication and were correctly predicted (true positive cases), whereas there is no case that should be non-cooperative but was falsely predicted to be cooperative (false positive cases). Therefore, in the cases that cooperative communication was predicted, the correct rate is 100%. Similarly, as indicated in the second row, there are 77 cases that should use noncooperative communication and were correctly predicted (true negative cases), whereas there are 2 cases that should use cooperative communication but were falsely predicted to be noncooperative (false negative cases). Therefore, in the cases that noncooperative communication was predicted, the correct rate is 97.5%. In summary, among all 1,000 test cases, 998 cases were correctly predicted and 2 cases were incorrectly predicted. Therefore, the first ANN

Table 1: Main configurations.

Parameter	Value
Number of BS antennas, M	8
Number of MTs, U	4
Position of BS	(0, 0)
BS antenna deployment	Centralized
Distance between BS and center of communication area, R_{cell}	$\leq 10^3$ m
Radius of communication area, R_{coop}	20 m
MT deployment in communication area	Uniform
Proxy selection	Best channel condition
Bandwidth, B	20 MHz
Channel model	Frequency selective
Path loss exponent	-4
Shadowing correlation	Completely correlated
Shadowing standard deviation [25]	9.6
Fading model	Rayleigh
Number of subchannels, L	4
Intertap correlation coefficient matrix for ISI	$\Theta_{\text{ISI}} = 0.95^{\lvert l-l' \rvert}/L$
Number of data for training, N	10^4
Number of data for testing, N_{pred}	10^3

Table 2: Parameters for the ANN training.

Parameters	Values
Number of hidden layers	1
Number of hidden layer nodes	10
Maximum number of epochs	10^3
Activation functions	Sigmoid
Validation data percentage	15%
Loss function for the 1st ANN	Cross entropy
Loss function for the 2nd ANN	MSE
Training algorithm for the 1st ANN	Scaled conjugate gradient
Training algorithm for the 2nd ANN	Levenberg–Marquardt

Table 3: Prediction results of 1st ANN.

Prediction result	Correct	Incorrect	Correct rate
Cooperative	921	0	100%
Noncooperative	77	2	97.5%
Total	998	2	99.8%

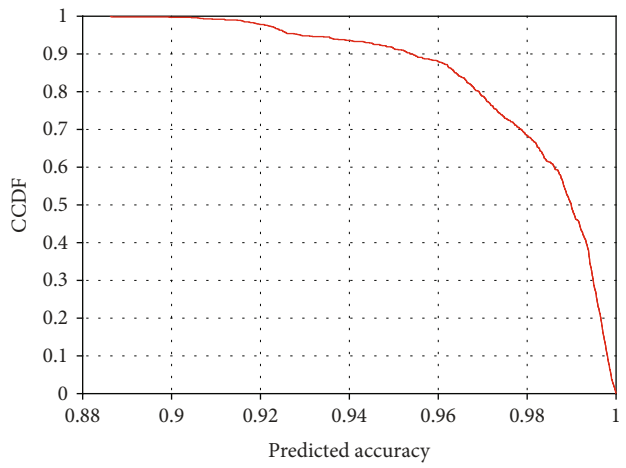

Figure 4: CCDF of the prediction accuracy of the second trained ANN $\mathbb{M}_2^*$.

of the proposed method predicted the communication mode with an accuracy of 99.8%.

Figure 4 shows the CCDF of the predicted accuracy for the second trained ANN $\mathbb{M}_2^*$. It can be seen that about 50% cases reach 99% prediction accuracy. Moreover, all the cases reach at least 88% prediction accuracy, which indicates the optimality of the output ν_{op} and means that bandwidth allocation is effectively optimized by the second ANN of the proposed method shown in Figure 3. This fact further verifies that when system is working with the proposed method, approximately 70% power consumption can be saved via cooperative communications as the experiment results in [5]. Consequently, from the results in Table 3 and Figure 4, it is obvious that the communication mode decision and bandwidth allocation mentioned in Section 3 can be effectively and accurately performed via the proposed

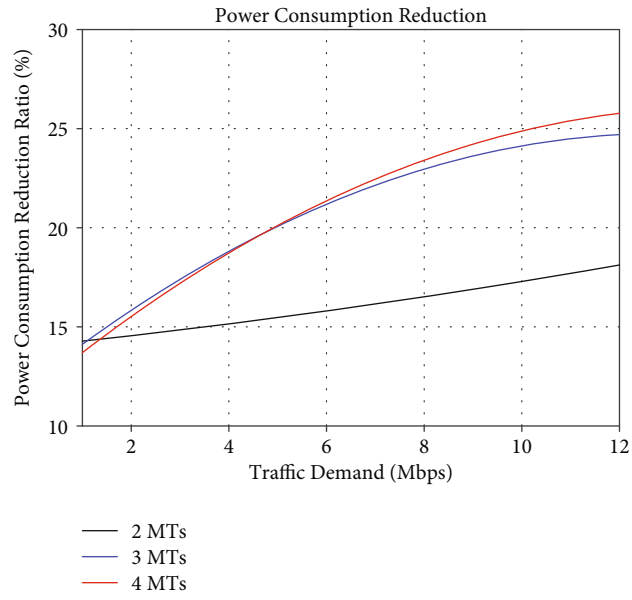

Figure 5: Power consumption reduction performance.

ML-based method with two ANNs. Specifically, after the training process of the two ANNs is finished, the first ANN can accurately predict whether the system should cooperate or not, and the second ANN can provide the optimal ν_{op} for optimizing EE performance, which makes the whole system always utilize energy in an optimal way.

Besides, since optimal bandwidth proportion $\tilde{\nu}_{\text{op}}(n')$ for cooperative communication can be predicted to reach optimal EE by using the proposed ML-aided method, here, we conduct simulations of cooperative communication with multiple MTs to validate the EE performance of the proposed method.

In the simulations, we evaluate the total power consumption of all MTs with and without proposed cooperative scheme under different traffic demands and check how much power consumption reduction can be obtained by using the proposed method. The simulation results are shown in Figure 5. The results shown here include the power consumption reduction results between systems using noncooperative and proposed cooperative communication schemes with 2 MTs, 3 MTs, and 4 MTs. From the results, it can be observed that, although the power consumption reduction performance is only about 14%–16% for system with small number of MTs, i.e., 2 MTs, for all traffic demands, it becomes much better which reaches maximally about 25% when MT number and traffic demand are getting larger. Besides the trend that larger MT number and traffic demand can result in better EE performance, there are also some points needed to be noted. Firstly, because of the physical constraints applied on the proxy, for example, maximum transmit power, we cannot increase the total communication demand without any limitation. Secondly, the results in Figure 5 are evaluated with consideration of the worst channel attenuation case. In other words, all MTs are affected by the shadowing, and hence, the large-scale fading is approximately identical. In real cases,

however, shadowing on each MT may be quite different because of the surrounding obstacles. As a result, the benefits of user cooperation aided transmission forwarding can be further improved. Therefore, from these simulation results, it can be known that the proposed method can effectively reduce system power consumption in cooperative communications with large number of MTs.

In summary, the method proposed in this study provides an effective way to optimize the EE performance using the approach in [5], which showed that the proposed cooperative communication scheme can offer optimal EE performance with optimal bandwidth allocation ν_{op}. However, in [5] the optimal ν_{op} was found by exhaustive search, which is very computationally consuming and difficult to be implemented. With the ML-based approach proposed in this study, the optimal ν_{op} can be determined effectively and the cooperative communication scheme becomes much more feasible. Moreover, in practical applications, because the ML training can be performed offline, the system can work online after ML training with very limited computational resources. In addition, although some suboptimization algorithms in [27] can also be used to find ν_{op} with reduced complexity, they need large amount of feedback information from MTs to obtain high search performance. Comparing to these traditional suboptimization methods, some feedback information such as CSI could be reduced by using the proposed ML-based approach, which can also improve communication efficiency such as throughput.

Besides, here, we also provide simulation results of power consumption reduction by using proposed cooperative scheme. From the results, it can be observed that maximally 25% power consumption reduction can be obtained for larger number of MTs. Instead of the best case of 25% reduction, it can be seen that the proposed can provide at least about 14% power consumption reduction, which validates the EE performance of the proposed method.

5. Conclusion

In this study, we investigated the cooperative transmission strategy of MTs in heterogeneous network and proposed an ML-aided method to determine MT communication mode and bandwidth allocation. For the networks considered in this study, there are two essential issues: (a) whether the MTs should perform cooperative or noncooperative communication and (b) how the optimal bandwidth allocation is determined. To solve these problems, we adopted two ANNs to predict the correct answers. The simulation results show that the first ANN of the proposed method predicted the communication mode with an accuracy of 99.8% and the second ANN can output bandwidth allocation parameter ν_{op} with at least 88% accuracy, which demonstrates the effectiveness of the proposed method. Besides, we also provide simulation results of power consumption reduction by using the proposed cooperative scheme. The results show that 14%–25% can be obtained, which verifies the EE performance of the proposed method. Certainly, in practice, the effectiveness of the proposed ML-aided method needs to be further verified with consideration of small-scale fading based channel variation, and discussion about computational cost for the proposed ML-aided method is also necessary, which are left as our future works.

Data Availability

The data including simulation configurations, parameters, and results used to support the findings of this study are included within the article.

Conflicts of Interest

The authors declare no conflict of interest.

Acknowledgments

This work was supported in part by the Secom Science and Technology Foundation, Japan.

References

[1] Federico Boccardi, Robert W. Heath, Angel Lozano, Thomas L. Marzetta, and Petar Popovski, "Five disruptive technology directions for 5G," *IEEE Communications Magazine*, vol. 52, no. 2, pp. 74–80, 2014.

[2] Y. Wu, J. C. Chen, L. P. Qian, J. W. Huang, and X. M. S. Shen, "Energy-aware cooperative traffic offloading via device-to-device cooperations: an analytical approach," *IEEE Transactions on Mobile Computing*, vol. 16, no. 1, pp. 97–114, 2017.

[3] R. Bordon, S. Montejo Sanchez, S. Baraldi Mafra, R. Demo Souza, J. L. Rebelatto, and E. M. G. Fernandez, "Energy efficient power allocation schemes for a two-user network-coded cooperative cognitive radio network," *IEEE Transactions on Signal Processing*, vol. 64, no. 7, pp. 1654–1667, 2016.

[4] M. Costa and A. Ephremides, "Energy efficiency versus performance in cognitive wireless networks," *IEEE Journal on Selected Areas in Communications*, vol. 34, no. 5, pp. 1336–1347, 2016.

[5] L. Shan, O. Zhao, K. Temma, K. Hattori, F. Kojima, and F. Adachi, "Evaluation of machine learnable bandwidth allocation strategy for user cooperative traffic forwarding," *IEEE Access*, vol. 7, pp. 85213–85225, 2019.

[6] F. Tang, B. Mao, N. Kato, and G. Gui, "Comprehensive survey on machine learning in vehicular network: technology, applications and challenges," *IEEE Communications Surveys & Tutorials*, vol. 23, no. 3, pp. 2027–2057, 2021.

[7] L. Shan, R. Miura, T. Kagawa, F. Ono, H.-B. Li, and F. Kojima, "Machine learning-based field data analysis and modeling for drone communications," *IEEE Access*, vol. 7, pp. 79127–79135, 2019.

[8] C. Cheng, L. Guo, T. Wu et al., "Machine Learning-Aided Trajectory Prediction and Conflict Detection for Internet of Aerial Vehicles," *IEEE Internet of Things Journal*, 2021.

[9] M. Liu, T. Song, J. Hu, J. Yang, and G. Gui, "Deep learning-inspired message passing algorithm for efficient resource allocation in cognitive radio networks," *IEEE Transactions on Vehicular Technology*, vol. 68, no. 1, pp. 641–653, 2019.

[10] M. Liu, T. Song, G. Gui, J. Hu, and H. Sari, "Deep cognitive perspective: resource allocation for NOMA-based heterogeneous

IoT with imperfect SIC," *IEEE Internet of Things Journal*, vol. 6, no. 2, pp. 2885–2894, 2019.

[11] W.-S. Liao, O. Zhao, M. G. Kibria, G. P. Villardi, K. Ishizu, and F. Kojima, "Machine learning-based signal detection for CoMP downlink in ultra-dense small cell networks," *IEEE Access*, vol. 8, pp. 17454–17463, 2020.

[12] J. Zhao, M. Kong, Q. Li, and X. Sun, "Contract-based computing resource management via deep reinforcement learning in vehicular fog computing," *IEEE Access*, vol. 8, pp. 3319–3329, 2020.

[13] X. Ma, J. Zhao, and Y. Gong, "Joint scheduling and resource allocation for efficiency-oriented distributed learning over vehicle platooning networks," *IEEE Transactions on Vehicular Technology*, vol. 70, no. 10, pp. 10894–10908, 2021.

[14] Y. Xu, G. Gui, H. Gacanin, and F. Adachi, "A survey on resource allocation for 5G heterogeneous networks: current research, future trends and challenges," *IEEE Communications Surveys & Tutorials*, vol. 23, no. 2, pp. 668–695, 2021.

[15] H. Ye, G. Y. Li, and B.-H. Juang, "Power of deep learning for channel estimation and signal detection in OFDM systems," *IEEE Wireless Communications Letters*, vol. 7, no. 1, pp. 114–117, 2018.

[16] D. He, C. Liu, T. Q. S. Quek, and H. Wang, "Transmit antenna selection in MIMO wiretap channels: a machine learning approach," *IEEE Wireless Communications Letters*, vol. 7, no. 4, pp. 634–637, 2018.

[17] B. Shang and L. Liu, "Machine learning meets point process: spatial spectrum sensing in user-centric networks," *IEEE Wireless Communications Letters*, vol. 9, no. 1, pp. 34–37, 2020.

[18] W. Ma, C. Qi, and G. Y. Li, "Machine learning for beam alignment in millimeter wave massive MIMO," *IEEE Wireless Communications Letters*, vol. 9, no. 6, pp. 875–878, 2020.

[19] L. He and K. He, "Towards optimally efficient search with deep learning for large-scale MIMO systems," *IEEE Transactions on Communications*, vol. 76, pp. 1-2, 2022.

[20] L. Chen, "Intelligent ubiquitous computing for future UAV-enabled MEC network systems," *Cluster Computing*, vol. 2021, no. 25, pp. 1–10, 2021.

[21] L. He and K. He, "Efficient memory-bounded optimal detection for GSM-MIMO systems," *IEEE Transactions on Communications*, vol. 69, no. 1, pp. 101–112, 2022.

[22] S. Tang and L. Chen, "Computational intelligence and deep learning for next-generation edge-enabled industrial IoT," *IEEE Trans. Network Science and Engineering*, vol. 8, no. 1, pp. 114–125, 2021.

[23] S. K. Sood and K. S. Rawat, "A fog assisted intelligent framework based on cyber physical system for safe evacuation in panic situations," *Computer Communications*, vol. 178, no. 1, pp. 297–306, 2021.

[24] G. Gui, M. Liu, F. Tang, N. Kato, and F. Adachi, "6G: opening new horizons for integration of comfort, security, and intelligence," *IEEE Wireless Communications*, vol. 27, no. 5, pp. 126–132, 2020.

[25] O. Zhao, W.-S. Liao, K. Ishizu, and F. Kojima, "Dynamic and non-centric networking approach using virtual gateway platforms for low power wide area systems," *IEEE Access*, vol. 7, pp. 186078–186090, 2019.

[26] C. Xiao, J. Wu, S. Y. Leong, Y. R. Zheng, and K. B. Letaief, "A discrete-time model for triply selective MIMO Rayleigh fading channels," *IEEE Transactions on Wireless Communications*, vol. 3, no. 5, pp. 1678–1688, 2004.

[27] Y. Nesterov, *Lectures on Convex Optimization*, Springer, 2nd Edition edition, 2018.

Hindawi
Wireless Communications and Mobile Computing
Volume 2022, Article ID 6309958, 14 pages
https://doi.org/10.1155/2022/6309958

Research Article

Virtual Adversarial Training-Based Semisupervised Specific Emitter Identification

CunXiang Xie,[1] **LiMin Zhang**,[1] **and ZhaoGen Zhong**[2]

[1]*Department of Information Fusion, Naval Aviation University, Yantai 264001, China*
[2]*The School of Aviation Basis, Naval Aviation University, Yantai 264001, China*

Correspondence should be addressed to ZhaoGen Zhong; zhongzhaogen@163.com

Received 21 November 2021; Revised 15 December 2021; Accepted 17 December 2021; Published 7 January 2022

Academic Editor: Junjuan Xia

Deep learning is a new direction of research for specific emitter identification (SEI). Radio frequency (RF) fingerprints of the emitter signal are small and sensitive to noise. It is difficult to assign labels containing category information in noncooperative communication scenarios. This makes network models obtained by conventional supervised learning methods perform unsatisfactorily, leading to poor identification performance. To address this limitation, this paper proposes a semisupervised SEI algorithm based on bispectrum analysis and virtual adversarial training (VAT). Bispectrum analysis is performed on RF signals to enhance individual discriminability. A convolutional neural network (CNN) is used for RF fingerprint extraction. We used a small amount of labelled data to train the CNN in an adversarial manner to improve the antinoise performance of the network in a supervised model. Virtual adversarial samples were calculated for VAT, which made full use of labelled and large unlabelled training data to further improve the generalization capability of the network. Results of numerical experiments on a set of six universal software radio peripheral (USRP; model B210) devices demonstrated the stable and fast convergence performance of the proposed method, which exhibited approximately 90% classification accuracy at 10 dB. Finally, the classification performance of our method was verified using other evaluation metrics including receiver operating characteristic and precision-recall.

1. Introduction

Specific emitter identification (SEI) refers to the technology used to identify individual emitters using distinctive external features of the signal called the radio frequency (RF) fingerprints [1]. This is obtained from the differences between the hardware characteristics of individual emitters and is hard to reproduce and/or eliminate. Moreover, the RF fingerprints of an emitter have unique characteristics that are independent of the content of the signal and may show consistency in different parts of the signal from the same emitter. Even for emitters produced by the same manufacturer and batch of equipment, the RF fingerprints are still different from each other. Therefore, the RF fingerprints can be used as a unique identification measure that enables SEI technology to be employed in military and civilian applications [2, 3].

In recent years, researchers have proposed various approaches for RF fingerprint extraction, which is a method to obtain the hardware characteristics of the emitter. For example, Padilla et al. [4] proposed methods for extracting parameters (transient waveform, instantaneous phase, and amplitude of the signal) of the RF signals, which are used as RF fingerprints, by means of the preamble in the communication. The method can identify 28 different Wi-Fi devices with an accuracy higher than 95%. However, because this method can only be applied to communication signals with preamble, its application scope is limited. Lopez-Risueno et al. [5] proposed using short-time Fourier transform to obtain the time-frequency energy spectrum of the signal, where the fingerprint features of the emitter signal are extracted based on the differences in the time-frequency energy spectrum. However, this method is based on a linear transformation, which is not suitable for nonlinear radiation source signals. Zhou et al. [6] proposed a feature extraction method based on the bispectrum-radon transform, which used bispectrum analysis to characterize the RF fingerprints

and completed feature compression through radon transform. The method identified 6 ADS-B emitters with an accuracy of 90.25%. The high-order spectrum analysis method, however, is only able to extract some of the features of the emitter signal while losing some of the important subtle features, which results in a lower identification performance. Yuan et al. [7] extracted 13 types of feature parameters of emitter transient characteristics through empirical mode decomposition (EMD) and Hilbert transform to form RF fingerprints and effectively identified 8 mobile phones. Moreover, the method can theoretically be used with any type of emitters as it does not require prior information for the RF signal. However, the method only applies to the transient signal of an emitter, which is challenging to capture in practical applications. Satija et al. [8] proposed an SEI approach based on variational mode decomposition and spectral features (VMD-SF). The advantage of the method lies in its adaptability to both single hop and relaying scenarios under both AWGN and flat-fading channels. Further, the method has a low computational cost and satisfactory real-time performance. However, the performance of this method must be verified using simulation signal data, so its practicability requires further research.

Although the conventional feature extraction scheme can reflect and amplify the individual differences of emitters, it needs to blindly try all the previous manually predefined RF fingerprint features to find an effective feature extraction method for a specific task. However, the complexity of the emitter signal renders it impossible to represent the signals using a unified mathematical model. Therefore, for the target signal of interest, the choice of the feature extraction method can only depend on the subjective judgment and cognitive level of the researchers, which cannot fully reflect the differences between individual emitters.

With advancements in artificial intelligence, techniques such as machine learning (ML), deep learning (DL), and reinforcement learning (RL) have been widely used in many fields [9]. In addition to the applications in traditional computer vision (CV), natural language processing (NLP), etc., deep learning technologies have gained great success in emerging fields, such as the Internet of Things (IoT) [9], physical layer communication [10, 11], and edge intelligence [12–14]. Furthermore, deep learning is now used in SEI, which is a new research direction that can comprehensively and deeply extract the fingerprint features of the emitter signal through neural networks to improve recognition performance. Wong et al. [15] used a convolutional neural network (CNN) to estimate the gain and phase deviations of the in-phase and quadrature components of an emitter signal, achieving SEI based on the estimated gain deviation and phase deviation. Their method does not require preprocessing, such as signal synchronization and carrier frequency tracking, and can be applied to signals of multiple modulation types. He et al. [16] used a long short-term memory (LSTM) network to learn RFFs from preprocessed RF signals. Compared with CNN, LSTM is more suitable for processing time series such as one-dimensional signals. This implies that it can achieve better identification performance. However, LSTM also introduces significant computational costs and training difficulties, resulting in poor real-time performance. Based on network models such as CNN and LSTM, some new deep learning-based network models and algorithms for SEI have been proposed recently. Qian et al. [17] proposed an approach of multilevel sparse representation-based identification for SEI, which comprehensively used the CNN for RF fingerprint extraction and principal component analysis for sparse representation. The method can classify nine transmitters with a classification accuracy of over 90% using a small number of training samples. A complex-valued neural network (CVNN) proposed in [18] was used to process complex baseband signals to perform SEI. In addition, a network compression algorithm was proposed to reduce the model size and decrease the training complexity. The CVNN-based SEI method can achieve nearly 100% recognition accuracy at high SNRs. Furthermore, the network size can be compressed by nearly 70%–90%, and the training complexity decreases at different SNR levels. The fixed neural network structure typically has the problem of poor flexibility when processing complex RF signals at different scenarios. Hence, a balanced network architecture search (NAS) mechanism proposed in [19] was applied to conduct SEI. The framework uses a recurrent neural network (RNN) as the controller and cooperates with a balance function to search for the optimal network structure, thereby providing a suitable scheme for processing RF signals at current SEI tasks.

SEI based on deep learning has been extensively studied; however, most studies focus on supervised learning models, which assume that all training samples have label information. SEI is used in noncooperative scenarios in most cases, and a typical application is radio surveillance, which is the application scenario for the SEI system considered in this study. SEI can be used to distinguish between legal and illegal radio stations, identify different types of illegal radio stations (which can be targeted to eliminate their interferences), and effectively control the utilization of spectrum resources. It is difficult for illegal radio stations to be assigned label information representing the signal category. Thus, only a few signal samples contain label information. Using a large number of unlabelled signal samples combined with a few labelled signal samples to conduct semisupervised SEI-based deep learning is a worthwhile research area. To address this problem, we propose a semisupervised SEI scheme based on bispectrum analysis and virtual adversarial training (VAT). Bispectrum analysis, a signal preprocessing method, is used as the representation of RF fingerprints. On this basis, we used the CNN to extract the RF fingerprints, and VAT is performed to fully utilize the labelled and large amount of unlabelled signal samples to conduct semisupervised SEI. Compared with other existing supervised learning-based SEI methods, our research focuses on semisupervised learning-based SEI. On the one hand, our method improves the antinoise performance of the SEI system by changing the traditional network training mode. On the other hand, more importantly, our method makes full use of many of unlabelled signal samples to carry out semisupervised training through VAT, thus applying to SEI in noncooperative scenarios.

The main contributions of this work are summarized as follows:

(1) To enhance the individual discriminability of different emitters, the bispectrum distribution is used as a characteristic representation of the RF signal, which lays the foundation for RF fingerprint extraction based on the CNN

(2) Considering that RF fingerprints are susceptible to noise, we perform adversarial training [20, 21] on the CNN to improve the antinoise performance of the network. In addition, we propose an algorithm for calculating the minimum number of adversarial samples for use during adversarial training to maximize the antinoise performance of the network

(3) After improving the antinoise performance of the network through adversarial training, we further propose a VAT method to train the CNN using labelled and large amounts of unlabelled signal samples collected in noncooperative scenarios, which can greatly enhance the generalization capacity of the network and improve the identification performance of the system

(4) Various experimental results are presented. We first evaluate the convergence proposed method. Then, we measure the classification accuracy of the proposed framework along several factors, including SNRs, ratio of labelled to unlabelled samples, communication propagation channel, and number of emitters. Simulation results show that our method performs well for SEI in noncooperative scenarios

The remainder of this paper is organized as follows. In Materials and Methods, we introduce the signal preprocessing method based on bispectrum analysis and the basic concepts of CNNs, adversarial training, and VAT. Our proposed method of VAT-based semisupervised SEI is also introduced in this section, together with the experiments conducted on a real-world RF dataset generated through a software-defined radio (SDR) platform. Results and Discussion present and discuss the experimental results. Finally, we conclude the paper.

2. Materials and Methods

2.1. Bispectrum Distribution of RF Signal. Bispectrum analysis is a special case of higher-order spectral analysis, which has demonstrated its superiority in processing non-Gaussian and nonstationary signals [22, 23]. The bispectrum distribution of the signal can be obtained by calculating the two-dimensional Fourier transform of the third-order cumulant of the signal:

$$B(\omega_1, \omega_2) = \sum_{\tau_1} \sum_{\tau_2} c_{3x}(\tau_1, \tau_2) e^{-j(\omega_1 \tau_1 + \omega_2 \tau_2)}, \quad (1)$$

where ω_1 and ω_2 represent the two-dimensional frequency and the third-order cumulant $c_{3x}(\tau_1, \tau_2)$ can be expressed as

$$c_{3x}(\tau_1, \tau_2) = E[x^*(t)x(t+\tau_1)x(t+\tau_2)]. \quad (2)$$

Figure 1 shows the bispectrum distributions of two different RF signals $x_1(t)$ and $x_2(t)$. It shows the visible differences in bispectrum distribution features, which demonstrate that the bispectrum analysis is an effective method of signal preprocessing to enhance individual discriminability.

2.2. Convolutional Neural Network. It is difficult to fully extract RF fingerprints using the methods mentioned earlier. In this study, we employed neural networks which have shown excellent performance in processing large quantities of data and extracting deep features [24, 25]. We used a CNN for RF fingerprint feature extraction and signal classification. A CNN is mainly composed of three structures: a convolution layer, an activation function, and a pooling layer. The function of the convolution layer is mainly to extract the features of the signals. In the convolution process, multiple convolution cores are used to convolve the respective feature maps of the previous layer to realize feature extraction and mapping. Each convolution layer includes many convolution cores, thus realizing multifeature extraction of signals. In a CNN, each feature map uses the same weight parameter, which is called weight sharing. Weight sharing reduces the number of parameters in the model and maintains displacement invariance for the position and size of the input. The activation function is used to introduce nonlinear factors into the convolutional layer for it to avoid becoming a linear combination of input vectors which helps in extracting complex and deep-level features [26]. The pooling layer is used for subsampling, whose main goal is to reduce the resolution of feature maps and thus facilitate the extraction of deep-level features.

When using a CNN to achieve signal classification, the feature space output by the CNN is used as the input of the fully connected neural network (FCN). The features extracted from the convolution layer are vectorized through the fully connected layer, thus mapping the distributed feature representation to the label space of samples. Finally, the output probability is mapped through the SoftMax function, and the maximum output probability corresponds to the recognized signal category.

2.3. Adversarial Training. Adversarial training is an important method to enhance the robustness of neural networks. The training samples mixed with some minor disturbances, which are subtle but can cause misidentification, are fed to the neural network to enable it to adapt to changes and be robust to interference. This method is widely used to defend against adversarial samples [27], which is one of the most effective means of adversarial defence. In contrast, adversarial training can be used for adversarial attacks [28]. The attacker constructs the adversarial input vector based on the adversarial sample so that the machine learning model misjudges, which is called an adversarial attack. Adversarial training can also be extended as VAT for semisupervised learning based on unlabelled data [29].

The RF fingerprints of the emitter signal caused by the subtle hardware differences of emitters are not generally evident and can be easily interfered by noise and be misidentified. To solve this problem, we used the adversarial training

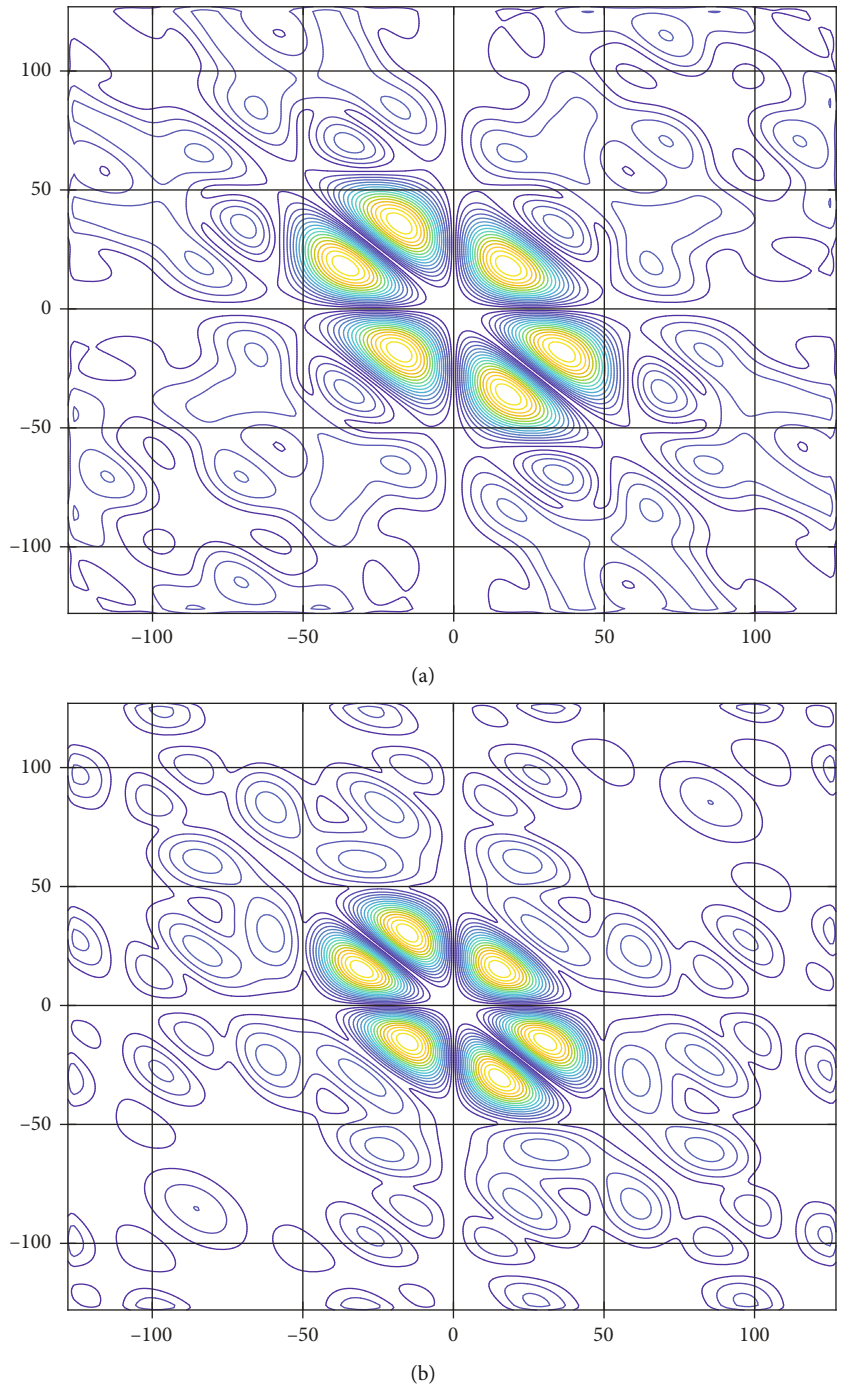

Figure 1: Bispectrum distributions of two different signals.

method to train the CNN by adding adversarial samples to the training data, which improves the network's recognition of adversarial samples and improves the robustness of the network. The key to adversarial training is the generation of adversarial samples. For a trained CNN, a subtle perturbation Δx is added to the input vector x. When the network loss reaches its maximum value, the corresponding $x + \Delta x$ becomes the adversarial sample [27]. The subtle perturbation Δx most likely results in the misjudgment of the original neural network. Therefore, the CNN needs to be trained with the input vector $x + \Delta x$ and the real label y_{true} to improve its recognition performance for adversarial samples, which will result in enhanced network robustness [28].

Let x_l, y_l, and x_{ul} represent the labelled training samples, their corresponding labels, and unlabelled training samples, respectively. We also assumed that x_l and x_{ul} are uniformly represented by x. The loss function of the adversarial training is defined as [28]

$$L_{\text{adv}}(x_l, y_l; \theta) = D[q(y_l \mid x_l), p(y_l \mid x_l + r_{\text{adv}}, \theta)], \quad (3)$$

Required:
$\boldsymbol{x}$: signal data, including labelled data $\boldsymbol{x}_l$ and unlabelled data $\boldsymbol{x}_u$
$\boldsymbol{y}_l$: labels corresponding to the labelled signal data
iter: number of training iterations
$\lambda_{\text{adv}}, \lambda_{\text{vadv}}$: regularization coefficients of (virtual) adversarial training
$L(\cdot)$: supervised loss function of network model
$L_{\text{adv}}(\cdot)$: loss function of adversarial training
$LDS_{\text{adv}}(\cdot)$: full loss function of adversarial training
$L_{\text{vadv}}(\cdot)$: loss function of virtual adversarial training
$LDS_{\text{vadv}}(\cdot)$: full loss function of virtual adversarial training
θ: parameters of network model
η: learning rate
$\varepsilon_{\text{max}}^{(0)}$: the upper limit of the perturbation weighting coefficient
$\varepsilon_{\text{min}}^{(0)}$: the lower limit of the perturbation weighting coefficient
$t = 0$: number of iterations of the perturbation weighting coefficient
1. for $i = 1$ to iter **do**
2. $r_{\text{adv}} \longleftarrow \underset{r:\|r\|\le\varepsilon}{\arg\max} D[q(y|x_l), p(y|x_l + r, \theta^i)]$
3. do
4. $\varepsilon_{\text{ave}}^{(t)} = (\varepsilon_{\text{max}}^{(t)} + \varepsilon_{\text{min}}^{(t)})/2$
5. $x_l^{(t)} \longleftarrow x_l + \varepsilon_{\text{ave}}^{(t)} r_{\text{adv}}$
6.
$$\begin{cases} \varepsilon_{\text{min}}^{(t+1)} = \varepsilon_{\text{ave}}^{(t)}, & y_{\text{pre}}(x_l^{(t)}) = y_l \\ \varepsilon_{\text{max}}^{(t+1)} = \varepsilon_{\text{ave}}^{(t)}, & y_{\text{pre}}(x_l^{(t)}) \neq y_l \end{cases}$$
7. $t \longleftarrow t + 1$
8. while $\varepsilon_{\text{max}}^{(t)} - \varepsilon_{\text{min}}^{(t)} \ge \varepsilon_{\text{acc}}$.
9. end while
10. $\varepsilon^* \longleftarrow \varepsilon_{\text{max}}^{(t)}$, $r_{\text{adv}} \longleftarrow \varepsilon^* \cdot r_{\text{adv}}$.
11. Initialize $\varepsilon_{\text{max}}^{(0)}$, $\varepsilon_{\text{min}}^{(0)}$, and t
12. $L_{\text{adv}}(x_l, y_l; \theta) = D[q(y_l|x_l), p(y_l|x_l + r_{\text{adv}}, \theta)]$
13. $LDS_{\text{adv}}(\theta) = L(x_l, y_l; \theta) + \lambda_{\text{adv}} L_{\text{adv}}(x_l, y_l; \theta)$
14. $\theta^{i+1} \longleftarrow \theta^i - \eta \nabla_\theta LDS_{\text{adv}}(\theta)$
15. end for
16. for j = iter + 1 to 2iter **do**
17. $r_{\text{vadv}} = \underset{r:\|r\|\le\varepsilon}{\arg\max} D[p(y|x, \theta^j), p(y|x + r, \theta^j)]$
18. $L_{\text{vadv}}(x, \theta) = D[p(y \mid x, \theta^j), p(y \mid x + r_{\text{vadv}}, \theta^j)]$
19. $LDS_{\text{vadv}}(\theta) = L(x_l, y; \theta) + \lambda_{\text{vadv}} L_{\text{vadv}}(x, \theta)$
20. $\theta^{j+1} \longleftarrow \theta^j - \eta \nabla_\theta LDS_{\text{vadv}}(\theta)$
21. end for

Algorithm 1: Semisupervised SEI based on VAT.

where $D[q, p]$ is used to measure the divergence between two distributions p and q; $q(y_l \mid x_l)$ is the true distribution of the output label, which can be approximated by a one-hot vector; $p(y_l \mid x_l + r_{\text{adv}}, \theta)$ is the data distribution predicted by the CNN; and r_{adv} represents an adversarial sample, which is equivalent to Δx and can be expressed as follows:

$$r_{\text{adv}} = \underset{r:\|r\|\le\varepsilon}{\arg\max} D[q(y_l \mid x_l), p(y_l \mid x_l + r, \theta)]. \tag{4}$$

After obtaining the adversarial samples of all signal types, we regarded the loss value generated by the adversarial sample as part of the original loss value and added it to the original loss function in the form of regularization, which is expressed as

$$LDS_{\text{adv}}(x_l, y_l; \theta) = \sum_{(x_l, y_l) \in D_l} L(x_l, y_l, \theta) + \lambda_{\text{adv}} \sum_{(x_l, y_l) \in D_l} L_{\text{adv}}(x_l, y_l; \theta), \tag{5}$$

where D_l represents the labelled training sets, λ_{adv} represents the weighting coefficient of regularization, and $L(x_l, y_l; \theta)$ represents the supervised loss function for the CNN, which can be calculated through the cross-entropy function.

$$L(x_l, y_l; \theta) = -y_l \log y_{\text{pre}}(x_l; \theta). \tag{6}$$

The parameter θ of the CNN is tuned using the backpropagation algorithm:

$$\theta^{i+1} \longleftarrow \theta^{i} - \eta \nabla_{\theta} LDS_{\text{adv}}(\theta), \tag{7}$$

where η represents the learning rate.

2.4. Virtual Adversarial Training (VAT). The adversarial training algorithm trains a CNN in a supervised learning model, where all the training samples must be labelled. However, in noncooperative communication scenarios, only a small number of signal samples are labelled. Using a small number of labelled samples to train the CNN through adversarial training results in poor generalization capacity.

To exploit the information in the unlabelled signals, we adopted VAT [30] to employ the labelled and unlabelled training data and to smoothen the output space of the neural network. This minimized the change in the output of the neural network where its input was locally perturbed. Therefore, VAT proved effective for semisupervised learning [31].

However, in the semisupervised learning model, there are many unlabelled training samples such as $q(y \mid x_{\text{ul}})$. Therefore, unlabelled training samples cannot be used to train the CNN through adversarial training algorithms. Note that, for a large amount of labelled training samples, $p(y \mid x, \theta)$ approaches $q(y \mid x)$. We can use "virtual" labels that are probabilistically generated from $p(y \mid x, \theta)$ rather than labels unknown to the user. We then compute the adversarial direction based on these virtual labels [32, 33]. The loss function for VAT can be expressed as

$$L_{\text{vadv}}(x, \theta) = D[p(y \mid x, \theta), p(y \mid x + r_{\text{vadv}}, \theta)], \tag{8}$$

where θ represents the weight parameters of the neural network in the current training state and r_{vadv} represents the virtual adversarial sample:

$$r_{\text{vadv}} = \underset{r:\|r\| \le \varepsilon}{\arg\max} D[p(y \mid x, \theta), p(y \mid x + r, \theta)]. \tag{9}$$

After obtaining the virtual adversarial samples, the full loss function is given by

$$LDS_{\text{vadv}}(x, \theta) = \sum_{(x_l, y_l) \in D_l} L(x_l, y_l, \theta) + \lambda_{\text{vadv}} \sum_{x \in D_l, D_{\text{ul}}} L_{\text{vadv}}(x, \theta), \tag{10}$$

where D_l and D_{ul} represent the labelled and unlabelled training sets, respectively; $\lambda_{\text{vadv}} > 0$ represents the regularization coefficient that needs to be set in advance. $L(x_l, y_l; \theta)$ represents the supervised loss function of the CNN, which is equivalent to Equation (6).

Equation (10) shows that both labelled data and a large amount of unlabelled data are used to carry out semisupervised training. The labelled data was combined with the unlabelled data to conduct virtual adversarial training. Supervised learning can use labelled data to guide network training. The loss function of VAT $L_{\text{vadv}}(x, \theta)$ can be regarded as a measure of the local smoothness of the current network, and its optimization can smooth the network output space. λ_{vadv}, as the regularization coefficient, is used to control the relative balance between supervised learning and virtual adversarial training, ensuring the effect of semisupervised training.

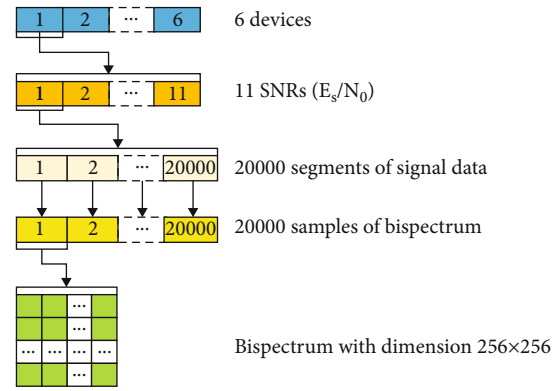

Figure 2: Dataset structure.

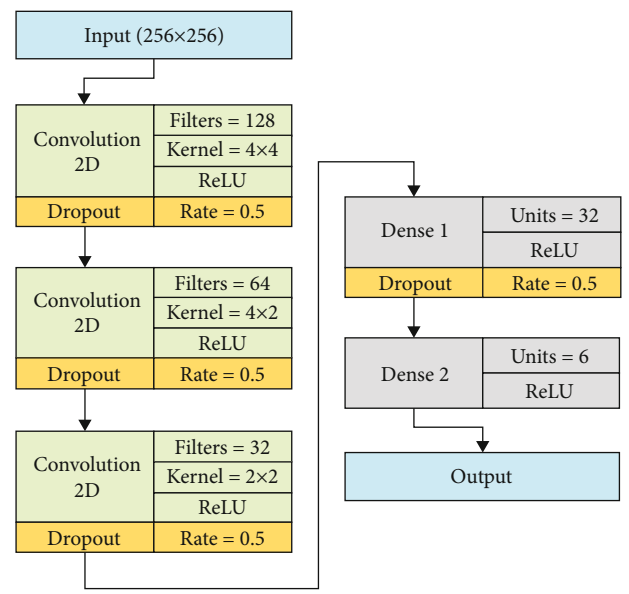

Figure 3: Architecture details of the network model.

Finally, the parameter θ of the CNN is tuned according to the backpropagation algorithm.

$$\theta^{j+1} \longleftarrow \theta^{j} - \eta \nabla_{\theta} LDS_{\text{vadv}}(\theta). \tag{11}$$

2.5. Semisupervised SEI Based on VAT. VAT is a semisupervised learning model that can be applied to SEI in noncommunication scenarios. However, networks trained with a considerably small amount of labelled signal data have poor generalization capability; these networks then probably assign the wrong virtual label for the unlabelled signal data, which can cause severely harmful effects for the subsequent classification. To solve this problem, we first trained the network model with labelled signal data via adversarial training, which improves the generalization capability of the network. Furthermore, we calculated a specific value ε^{*} for the

Table 1: Architecture details of the CNN on different depths.

Depth	Conv-1	Conv-2	Conv-3	Conv-4	Conv-5
1	Filters = 128 Size = 4 × 4				
2	Filters = 128 Size = 4 × 4	Filters = 64 Size = 4 × 2			
3	Filters = 128 Size = 4 × 4	Filters = 64 Size = 4 × 2	Filters = 32 Size = 2 × 2		
4	Filters = 128 Size = 4 × 4	Filters = 64 Size = 4 × 2	Filters = 32 Size = 2 × 2	Filters = 32 Size = 2 × 2	
5	Filters = 128 Size = 4 × 4	Filters = 64 Size = 4 × 2	Filters = 32 Size = 2 × 2	Filters = 32 Size = 2 × 2	Filters = 16 Size = 2 × 2

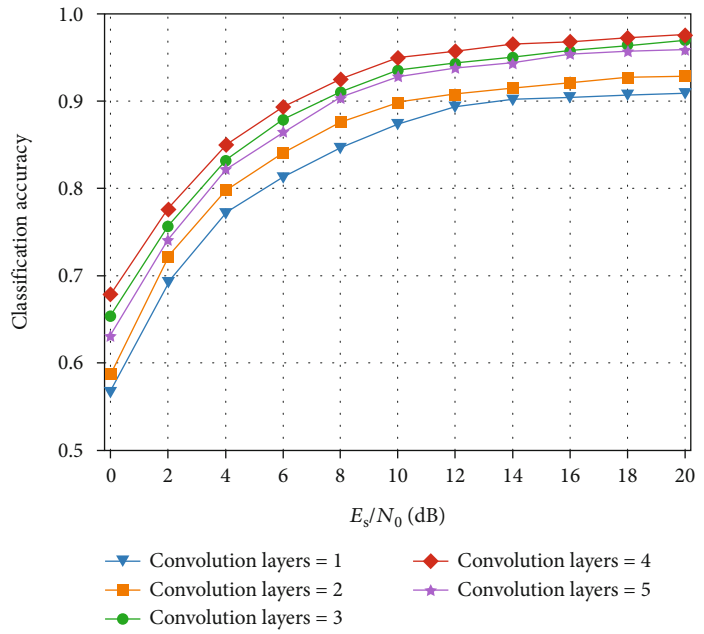

Figure 4: Classification accuracy on different network depths.

perturbation weighting coefficient ε of the adversarial sample, which is the minimum value of ε that causes misidentification. At this time, the corresponding r_{adv} is the smallest perturbation that can lead to misidentification. Using this as an adversarial sample for adversarial training maximizes the antinoise performance of the neural network. The network parameters obtained through adversarial training will be directly used in VAT to conduct semisupervised SEI. Therefore, the procedure of semisupervised SEI based on VAT is concluded in Algorithm 1.

2.6. Implementation Details. The calculation of (virtual) adversarial samples is essential for the (virtual) adversarial training algorithm. However, in practice, we cannot obtain a closed form of r_{adv} or r_{vadv} calculated in Equation (4) or Equation (8). Therefore, in this section, we provide the core implementation details of the proposed algorithm: calculating (virtual) adversarial samples in an approximate manner.

The calculation of r_{adv} in this study can be approximated with a linear approximation of D with respect to r in Equation (4), which can be expressed as

$$r_{\text{adv}} \approx \frac{\nabla_{x_l} L(x_l, y_l; \theta)}{\left\| \nabla_{x_l} L(x_l, y_l; \theta) \right\|_2}. \tag{12}$$

For a neural network model, the calculation of $\nabla_{x_l} L(x_l, y_l; \theta)$ can be computed through forward- and backpropagation.

Furthermore, the calculation of r_{vadv} is performed in an approximate manner, which can be described as follows: for an input training sample x, a random unit vector d of the same size that obeys the standard Gaussian distribution is generated. Then, r_{vadv} is obtained by taking the gradient of D with respect to r on $r = \xi d$ for x.

$$r_{\text{vadv}} \approx \frac{\nabla_r D[p(y \mid x, \theta), p(y \mid x + r, \theta)]|_{r=\xi d}}{\left\| \nabla_r D[p(y \mid x, \theta), p(y \mid x + r, \theta)]|_{r=\xi d} \right\|_2}. \quad (13)$$

For the neural network model, the calculation of $\nabla_r D$ can be computed through forward- and backpropagation.

2.7. Signal Data Collection and Experimental Setup. We demonstrate our network model based on a software-defined radio platform composed of GNU Radio and seven USRP model B210 devices. By combining GNU Radio with the USRP, we then define the transceiver of radio signals through the PC to form a complete communication system composed of software and hardware. This platform realizes communication functions, and signal modulation and demodulation can be done at the software level.

A computer, running on Ubuntu 18.04, was connected to USRP to build a communication system. We used six USRPs as the transmitters and one USRP as the receiver, and then, we collected six types of RF signals through six USRPs, which operated at a 2.4 GHz centre frequency, and the received signals were sampled at a rate of 16 MHz. The signal modulation mode was QPSK, and the bandwidth was 1.2 MHz.

For each emitter, 20,000 segments of RF signals were collected from the lab environment; thus, the signal to noise ratio (SNR) of the signals was high. After the preliminary measurement, the SNR was found to be more than 50 dB. Therefore, we assumed that the signal was not affected by noise. For each class sampled signal, we calculated the average symbol energy within the input frame as E_s and used MATLAB to add different levels of simulated additive white Gaussian noise (AWGN) to set the ratio of symbol energy to noise density (E_s/N_0) as 0 dB, 2 dB, …, 20 dB, respectively. The signal data polluted by noise were processed by bispectrum analysis to obtain bispectrum distributions, which have a uniform size of 256 × 256. Figure 2 shows the dataset structure of our experiments. The dataset contains six classes of sampled signal data. Each class signal includes 20,000 segments at a specific SNR (E_s/N_0), each of which is transformed to a bispectrum distribution with the dimension of 256 × 256.

For 20,000 bispectrum distributions of each class signal at a specific SNR, 80%, 10%, and 10% were allocated to training, validation, and testing, respectively. For the training and validation datasets, we set the ratio of labelled data to unlabelled data at 10%.

The proposed semisupervised SEI network architecture was built on the Keras framework based on TensorFlow, and the network was trained on a Windows 10, Intel (R) core (TM) i9-10900 CPU, 16 GB RAM, and NVIDIA GeForce RTX 3090 system.

The structure and the detailed architecture parameters of the CNN are shown in Figure 3. Three convolutional layers are utilized, and the ReLU function is used as the activation function of the convolutional layer, which has stable output and no vanishing gradient problem. The features extracted from the convolution layer are vectorized through the fully connected layer (Dense I), thus mapping the distributed feature representation to the label space of samples. Finally, the output probability is mapped through the SoftMax function of the last fully connected layer (Dense II). Dense II contains K neurons, corresponding to K transmitters. By comparing the output probabilities of K neurons, the maximum probability corresponds to the recognized emitter category.

Table 2: Hyperparameters of the network model.

Hyperparameters	Value
Optimizer	Adam
Learning rate	0.0004
Epochs	500
Batch size	1024
Dropout rate	0.5

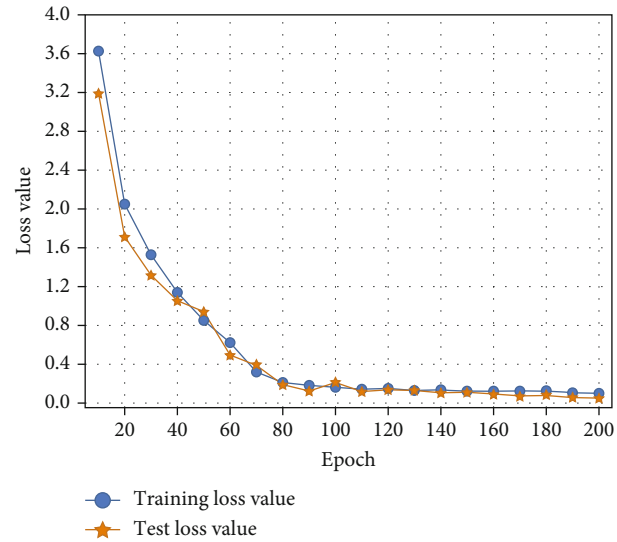

Figure 5: Training times and loss function graph of VAT.

In practice, the network depth (the number of convolution layers) is determined through simulations. Table 1 summarizes the architecture details of the CNN for different depths.

We evaluated the classification accuracy for different network depths based on the RF signal dataset mentioned above. Figure 4 shows that the classification accuracy improved with the increase in the number of convolution layers, and it remained at a high level when the number of convolution layers was 3. However, when the number of convolution layers reached 5, the network was too deep to fit the input signal data, and the classification accuracy slightly decreased. Considering classification accuracy and network complexity, the optimal network depth is 3 convolutional layers.

We also list the hyperparameters used to train the network model as summarized in Table 2.

We used the validation dataset for hyperparameter tuning. Learning rate is the most significant hyperparameter, which directly controls the magnitude of the network gradient update during training and affects the effective tolerance

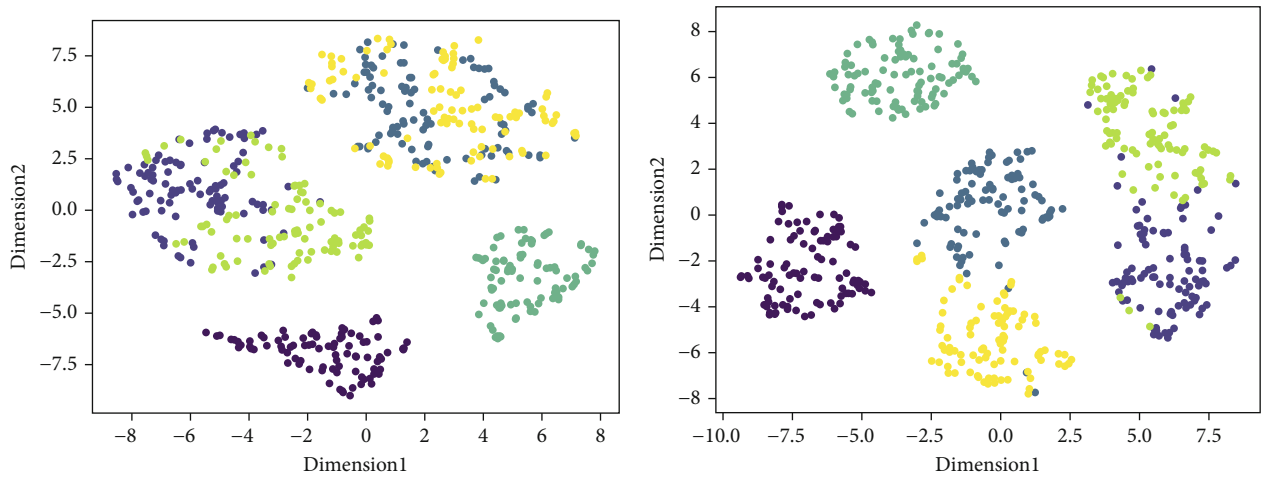

(a) Algorithm using only labelled data to train the CNN (b) Proposed method

Figure 6: t-SNE dimensionality reduction distribution diagram.

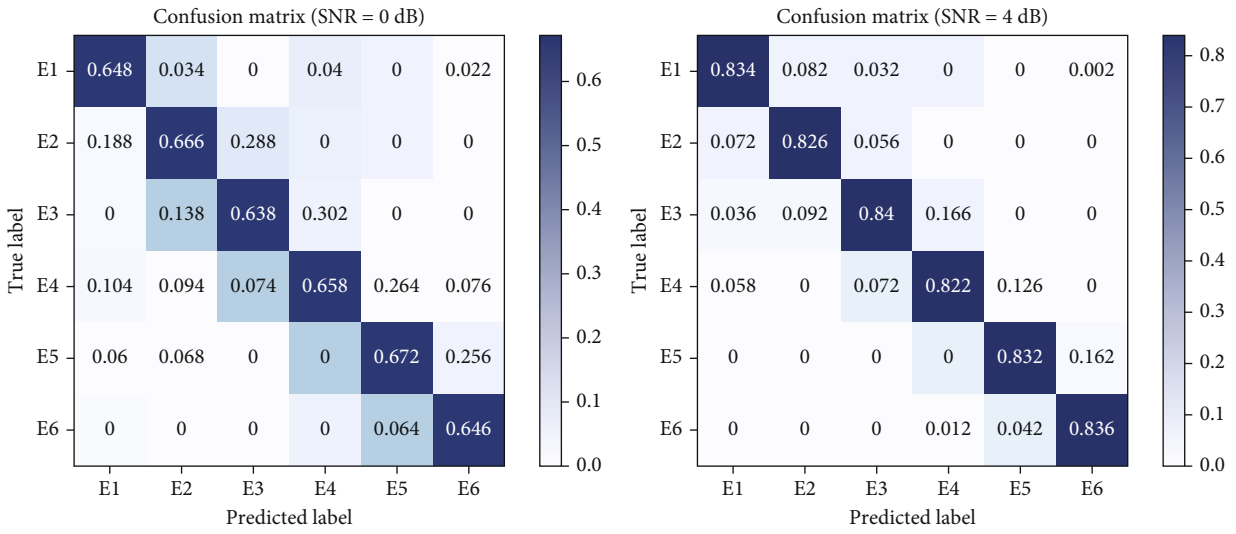

(a) SNR = 0 dB (b) SNR = 4 dB

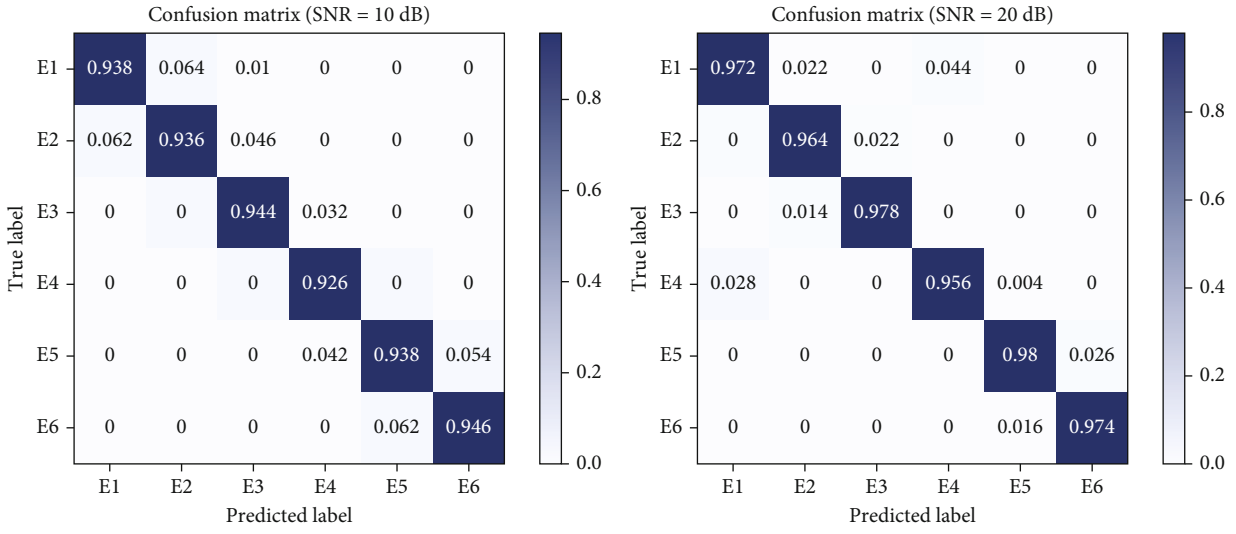

(c) SNR = 10 dB (d) SNR = 20 dB

Figure 7: Confusion matrix for the classification at different SNRs.

capability of the model. For tuning the learning rate, we first used a small amount of data to train the network to determine the magnitude of the learning rate. We then chose a specific value within this magnitude range as the initial learning rate. During the training process, as the number of training datasets increased, the learning rate decayed exponentially until the verification loss value converged, and the learning rate at this point was optimal. Batch size is a relatively independent hyperparameter that determines the direction in which the gradient decreases. Regarding the choice of the batch size, we determined several candidate values of 128, 256, 512, 1024, and 2048, and then evaluated how the classification accuracy in the validation dataset changed over time, and finally selected the batch size corresponding to the fastest improvement in classification performance over time. An epoch represents the training time. After each training epoch, the classification performance of the model on the validation dataset was evaluated, and the training was stopped when the classification performance stopped increasing. Therefore, generally, a large value was assigned to the epoch. The dropout rate was generally set to 0.5, which was used to prevent overfitting. By tuning hyperparameters, the network model can achieve better performance.

3. Results and Discussion

3.1. Convergence Performance. We evaluated the convergence performance of the neural networks trained using the proposed approach. We first collected RF signal data with an SNR of 10 dB from six USRPs, with each device representing a class of signal. The maximum epoch of network training was set at 200. Moreover, we chose the training loss value and test loss value as metrics to evaluate the convergence performance.

Figure 5 shows that the loss function of the network tended to be stable after approximately 80 training epochs, which means our approach has a relatively fast convergence speed. Moreover, the training loss function curve and the test loss function curve are relatively smooth with no noticeable fluctuation. This indicates that the training process was stable. The loss value of training and test procedure decreased as the number of iterations increased, i.e., the two curves exhibit a downward trend, which indicates that the network model performs well in both the training dataset and the test dataset and that no overfitting or underfitting problem occurred. The results show that our approach can be used for semisupervised training of neural networks.

3.2. Classification Accuracy. We first proved the superiority of the proposed method compared with that of the method using only labelled data to train CNN. The algorithm of t-distributed stochastic neighbour embedding (t-SNE), [34] one of the best dimensional reduction methods, was used to visually display the feature parameters extracted from the neural network model. Figure 6 shows the t-SNE dimension reduction distribution diagram of feature parameters extracted through two different methods.

As shown in Figure 6, compared with the algorithm using only labelled data to train the CNN, the feature parameters of

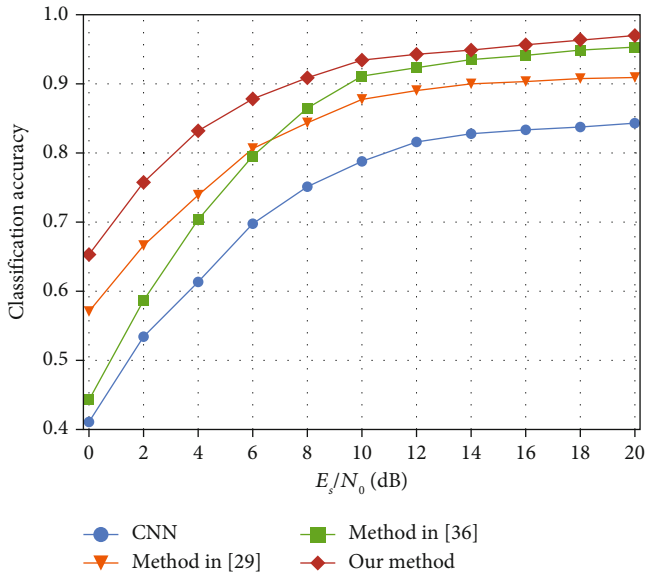

Figure 8: Classification accuracy under different SNRs.

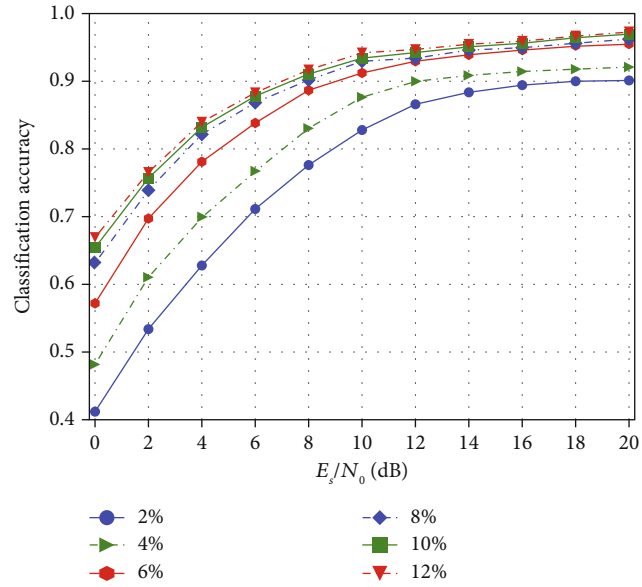

Figure 9: Classification accuracy under different ratios.

the RF fingerprints extracted by the proposed algorithm have stronger clustering within classes and greater differentiation between classes. This proves that the proposed VAT algorithm, which uses a large amount of unlabelled signal samples for training, can improve the neural network's generalization ability. This allows the network to extract the characteristic parameters of an individual emitter more comprehensively, thus improving the classification of RF signals.

We then considered four factors that significantly affect classification accuracy: (1) SNR, (2) ratio of labelled to unlabelled samples, (3) communication propagation channel, and (4) number of emitters.

Classification accuracy vs. SNR: first, we tested the classification accuracy on different SNRs. Both the labelled and

Table 3: Classification accuracy at different ratios.

Method	2%	4%	6%
Method in [29]	78.9%	82.2%	88.3%
Method in [35]	84.1%	87.5%	89.6%
Our proposed method	90.3%	91.8%	94.6%

unlabelled data were used to conduct semisupervised training on CNN based on the proposed method. Figure 7 shows the confusion matrix of classification at different SNRs.

As shown in Figure 7, all emitters maintain a relatively average classification accuracy, and no serious confusion occurs in the classification between individual emitters. This shows that our method can fully extract RF fingerprints and effectively distinguish between individual emitters, thus proving the effectiveness of the deep learning-based SEI. In addition, our method can classify six emitters with an average accuracy of more than 83% at 4 dB and 93% at 10 dB, which demonstrates that our proposed VAT-based semisupervised SEI is robust to noise interference.

Then, we compared the classification accuracy of the proposed method with that of the method using only labelled data to train CNN and those previously proposed methods in [29, 35]. The experimental results are shown in Figure 8.

Figure 8 shows that our approach achieves the highest classification accuracy compared to other SEI schemes. Compared to the method using only labelled data to train the CNN, our method can improve classification accuracy by 15%–20% on average. This is because VAT can smoothen the output space of the network to enhancing its generalization ability. This effectively overcomes noise interference and improves classification accuracy. Compared to the method proposed in [29], our method improves classification accuracy by 5%–10% on average. This is because our improved VAT method augments the antinoise performance and generalization capability of the network through adversarial training in the pretraining process. This results in the assignment of accurate virtual labels for the unlabelled signal data, thus contributing to the effectives of VAT. Compared to the method based on metalearning proposed in [35], our method shows an advantage in terms of classification accuracy at low SNRs, although both methods a have similar classification accuracy only when SNR > 10 dB. Therefore, the experimental result shows that our method can adapt well to the task of SEI at low SNRs.

Classification accuracy vs. ratio of labelled to unlabelled samples: we evaluated classification accuracy on different labelled to unlabelled ratios. Similarly, we fixed the unlabelled data sample at 10,000 for each class signal and the labelled data sample from 200 to 1200, which means that the ratio of labelled samples to unlabelled samples was 2 to 12%. These labelled and unlabelled training samples with SNRs from 0 dB to 20 dB were used to train the CNN through the method of VAT.

Figure 9 shows that the classification accuracy improved when ratio of labelled to unlabelled samples increased from 2% to 6%, but stabilized when the ratio reached approximately 8%. Furthermore, even in the worst case of 2%, the classification performance did not deteriorate significantly. The classification accuracy was more than 80% at 10 dB and approximately 90% at 20 dB. According to these results, our approach needs only a small amount of labelled data samples to achieve a high and stable classification accuracy, giving it the ability to handle practical situations.

We further evaluated the classification performance of our method compared with that in [29, 35] at a ratio of 2%, 4%, and 6%, respectively. To eliminate the factor of noise interference, the SNR for the signal dataset was set to 20 dB. The experimental results are shown in Table 3. For all the ratios, our proposed method outperformed the existing

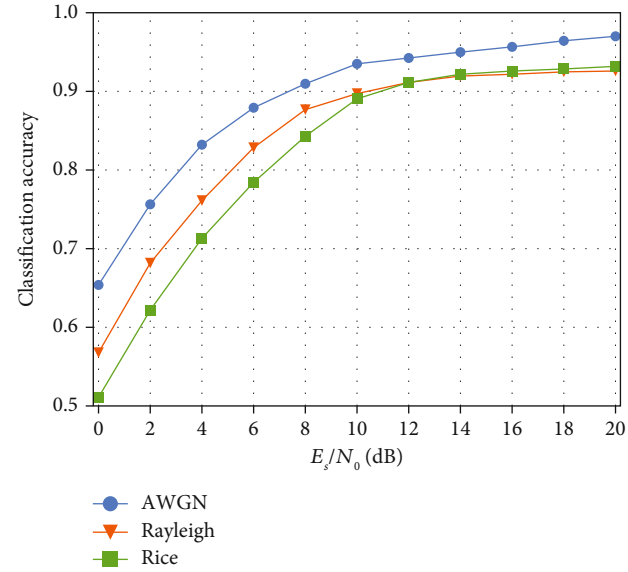

Figure 10: Classification accuracy on different propagation channels.

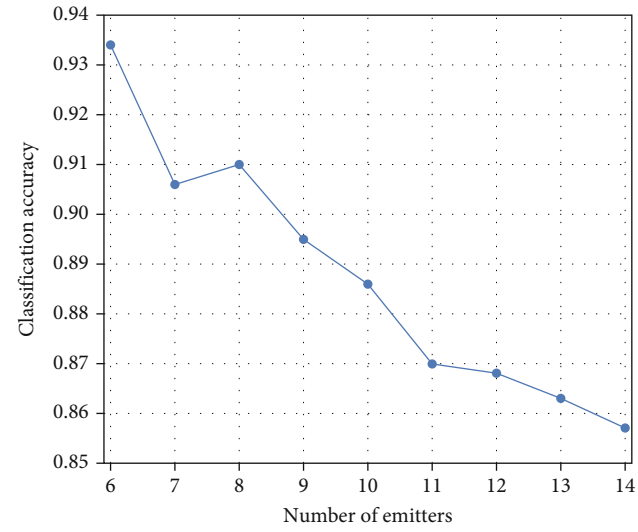

Figure 11: Classification accuracy under different number of emitters.

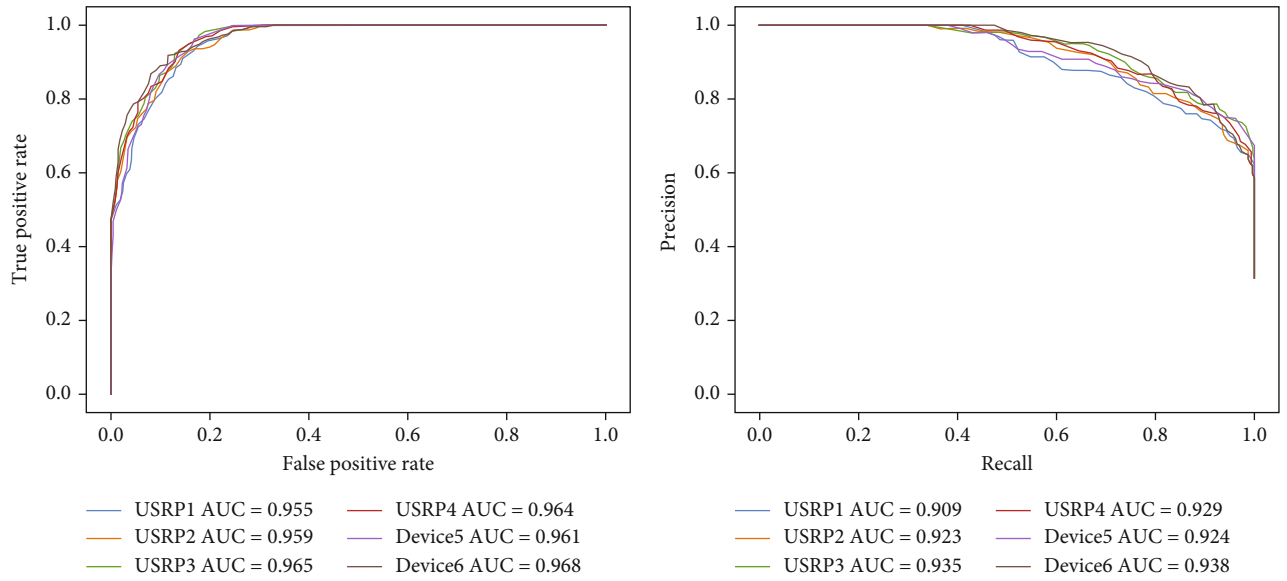

(a) ROC curves for each of the six devices

(b) Precision-recall curves for each of the six devices

Figure 12: ROC and precision-recall curves for each of the six devices.

methods, which further proves that the proposed method is adaptable and advanced in noncooperative scenarios.

Classification accuracy vs. communication propagation channel: we evaluated the classification accuracy of the proposed algorithm in different propagation channels. The collected RF signals were transmitted over an AWGN channel, Rayleigh channel, and Rice channel. Figure 10 shows the classification accuracy of different channels as a function of the SNR. With the Rayleigh and Rice channels, the classification accuracy was lower than with the AWGN channel; this is because the RF fingerprints of the signal emitted by the emitters were not apparent, and it was more difficult to distinguish after being affected by multiplicative noise. The proposed method essentially constructs (virtual) adversarial samples against additive noise, but not multiplicative noise, limiting the adaptiveness of the SEI system in terms of Rayleigh and Rice channels. However, the decline in classification accuracy, which is 5%–10% on average, is not significant. This demonstrates that the proposed approach can still calculate approximate and relatively effective (virtual) adversarial samples for signal samples according to the current network model under interference from multiplicative noise, which can improve the antinoise performance and generalization ability of the network to some extent. The experimental result further demonstrates the excellent classification performance of the proposed method.

Classification accuracy vs. number of emitters: we evaluated the classification accuracy on a different number of emitters. We collected RF signals from up to 14 different individual emitters and evaluated the classification performance of the network on different number of emitters, which varied from 6 to 14 and needed to be classified. The experiment was conducted based on an AWGN channel with SNR = 10 dB.

Figure 11 shows how the classification accuracy changes with the number of emitters. The experimental result indicates that although classification performance deteriorates as the number of emitters increases, the network can classify up to 14 emitters with an accuracy of more than 85%. In general, with the increase in the number of emitters to be identified, the network scale should be increased also, resulting in a higher computation cost. Nevertheless, our method can classify more emitter individuals at a high classification accuracy, maintaining the existing network scale, which benefits from the elaborate training algorithm based on VAT and indicates that the proposed method has good scalability for large emitter populations.

3.3. Other Evaluation Metrics for Classification Performance. Classification accuracy is the ratio of the number of correctly classified samples to the total number of test samples, which can reflect only the overall classification performance. However, it is difficult to determine whether each class of RF signals is correctly classified, particularly when each class is in a minority with respect to the rest of the RF signals, leading to the class imbalance problem. In this case, classification accuracy is not a comprehensive evaluation measure of classification performance.

We used the receiver operating characteristic (ROC) and the precision-recall as metrics to further evaluate the classification performance of the proposed approach. To identify six USRPs, we chose one device as the positive class with a weight of five and the remaining five devices as a single negative class with a weight of one. The six classes of RF signals were collected with SNR of 10 dB, which were used for training and identification. The ROC and precision-recall curves for each of the six devices are shown in Figure 12.

As shown in Figure 12(a), the ROC curve for each device is distributed in the upper left of the figure. This implies that the system achieves a high true-positive rate with a low false-positive rate. Furthermore, precision and recall are two evaluation indices that balance each other. Figure 12(b) shows

Table 4: Mean ROC AUC and mean precision-recall AUC at different SNRs.

SNR	ROC-AUC	Precision-recall AUC
0 dB	0.924	0.811
4 dB	0.939	0.878
8 dB	0.957	0.907
12 dB	0.978	0.928
16 dB	0.981	0.935
20 dB	0.981	0.937

that the precision-recall curve for each device is distributed in the upper right of the figure, indicating that precision occupies a larger proportion. We also calculated the area under the curve (AUC) for each device. The ROC AUC and precision-recall AUC for each device is more than 90%, which further proves the excellent classification performance of the proposed method. Table 4 summarizes the mean ROC AUC and mean precision-recall AUC at SNRs of 0 to 20 dB. As expected, our proposed framework achieves a better mean AUC on higher SNRs and has a drop-off at lower SNRs, which is not significant.

4. Conclusion

To address the shortcomings of traditional SEI based on deep learning, this paper proposes an SEI method based on bispectrum analysis and VAT. First, bispectrum analysis is performed on the RF signals as a way of signal preprocessing. Noting that the emitter signal is susceptible to noise interference and only a small number of labelled training samples are available with many of the samples being unlabelled in a noncooperative communication scenario, we calculated the virtual adversarial samples for both labelled and unlabelled signal samples, using which we then calculated the corresponding loss functions. Loss functions based on the labelled samples were also calculated. Using the two loss functions and the preset harmonic parameters, the objective function of the neural network was calculated. Through iterative tuning, the neural network model corresponding to the minimum loss function value of the verification dataset was obtained as the optimal output. Finally, the neural network model could be used for SEI.

Numerical experiments were conducted to evaluate the performance of the proposed method. First, convergence experiments showed that our approach has stable and fast convergence. Second, we considered four factors that impact the classification accuracy of our method. The classification accuracy vs. SNR experiment showed that our method is significantly robust to noise. The classification accuracy vs. ratio of labelled to unlabelled sample experiment showed that our method can handle weak labelling problems in practical situations. The classification accuracy vs. propagation channel experiment showed that our method can also resist the interference of nonlinear multiplicative noise to RF signals and maintain a relatively high classification accuracy. The classification accuracy vs. number of emitter experiment showed that our method exhibits good scalability for large emitter populations. Moreover, we used two other methods including ROC and precision-recall to further evaluate the classification performance of our method. The AUC for ROC and precision-recall curves were calculated to represent the correct recognition rate of each device, and experimental results demonstrated the excellent classification performance of our method more comprehensively.

Future research will consider the following two aspects. (1) Various emitter devices, in addition to USRP, will be used to collect more types of RF signals to avoid using one type of signal data for experimentation and verify the scalability of the proposed method for RF signals emitted by different types of devices. Furthermore, these devices work in an outdoor environment to obtain more realistic signal data to verify the practicability of our method. (2) Our method is essentially for closed-set identification. The RF signal class to be identified is the same as that in the database used for training. However, our method cannot address anomalous emitters it was not previously trained on, which is common in real-world applications. Therefore, future work will focus on detecting anomalous emitters and classifying known emitters.

Data Availability

The data used to support the findings of this study are available from the corresponding author upon request.

Conflicts of Interest

The authors declare no conflicts of interest.

Acknowledgments

This work was supported in part by the National Natural Science Foundation of China under Grant 91538201, in part by Taishan Scholar Project of Shandong Province under Grant ts201511020, and in part by project supported by Chinese National Key Laboratory of Science and Technology on Information System Security under Grant 6142111190404.

References

[1] L. Li, H. B. Ji, and L. Jiang, "Quadratic time–frequency analysis and sequential recognition for specific emitter identification," *IET Signal Process*, vol. 5, no. 6, pp. 568–574, 2011.

[2] H. J. Liu, Z. Liu, W. L. Jiang, and Y. Y. Zhou, "Incremental learning approach based on vector neural network for emitter identification," *IET Signal Process*, vol. 4, no. 1, pp. 45–54, 2010.

[3] H. J. Liu, Z. Liu, W. L. Jiang, and Y. Y. Zhou, "Approach based on combination of vector neural networks for emitter identification," *IET Signal Process*, vol. 4, no. 2, pp. 137–148, 2010.

[4] P. Padilla, J. F. Valenzuela-Valdes, and J. L. Padilla, "Radiofrequency identification of wireless devices based on RF fingerprinting," *Electronics letters*, vol. 49, no. 22, pp. 1409-1410, 2013.

[5] G. Lopez-Risueno, J. Grajal, and A. Sanz-Osorio, "Digital channelized receiver based on time-frequency analysis for signal interception," *IEEE Transactions on Aerospace and Electronic Systems*, vol. 41, no. 3, pp. 879–898, 2005.

[6] Y. P. Zhou, X. Wang, Y. Chen, and Y. Tian, "Specific emitter identification via bispectrum-radon transform and hybrid deep model," *Mathematical Problems in Engineering*, vol. 2020, no. 2020, Article ID 7646527, 17 pages, 2020.

[7] Y. J. Yuan, Z. T. Huang, W. Hao, and X. Wang, "Specific emitter identification based on Hilbert–Huang transform-based time–frequency–energy distribution features," *IET Communications*, vol. 8, no. 13, pp. 2404–2412, 2014.

[8] U. Satija, N. Trivedi, G. Biswal, and B. Ramkumar, "Specific emitter identification based on variational mode decomposition and spectral features in single hop and relaying scenarios," *IEEE Transactions on Information Forensics and Security*, vol. 14, no. 3, pp. 581–591, 2019.

[9] S. Tang, L. Chen, K. H. J. Xia, L. Fan, and A. Nallanathan, "Computational intelligence and deep learning for next-generation edge-enabled industrial IoT," *IEEE Transactions on Network Science and Engineering*, vol. 8, no. 1, pp. 114–125, 2021.

[10] L. He and K. He, "Efficient memory-bounded optimal detection for GSM-MIMO systems. Accepted by," *IEEE Transactions on Communications*, pp. 1–12, 2021.

[11] K. He, L. F. Le He, Y. Deng, G. K. Karagiannidis, and A. Nallanathan, "Learning-based signal detection for MIMO systems with unknown noise statistics," *IEEE Transactions on Communications*, vol. 69, no. 5, pp. 3025–3038, 2021.

[12] M. Chen, T. Wang, S. Zhang, and A. Liu, "Deep reinforcement learning for computation offloading in mobile edge computing environment," *Computer Communications*, vol. 175, pp. 1–12, 2021.

[13] X. Lai, L. Fan, and A. Nallanathan, "Outdated access point selection for mobile edge computing with cochannel interference," *IEEE Transactions on Vehicular Technology*, 2021.

[14] L. Y. Chen, R. Zhao, K. He, Z. Zhao, and L. Fan, "Intelligent ubiquitous computing for future UAV-enabled MEC network systems," *Cluster Computing*, vol. 2021, no. 25, pp. 1–10, 2021.

[15] L. J. Wong, W. C. Headley, and A. J. Michaels, "Specific emitter identification using convolutional neural network-based IQ imbalance estimators," *IEEE Access*, vol. 7, pp. 33544–33555, 2019.

[16] B. X. He and F. G. Wang, "Cooperative specific emitter identification via multiple distorted receivers," *IEEE Transactions on Information Forensics and Security*, vol. 15, pp. 3791–3806, 2020.

[17] Y. H. Qian, J. Qi, X. Y. Kuai, G. Han, H. Sun, and S. Hong, "Specific emitter identification based on multi-level sparse representation in automatic identification system," *IEEE Transactions on Information Forensics and Security*, vol. 16, pp. 2872–2884, 2021.

[18] Y. Wang, G. Gui, H. Gacanin, T. Ohtsuki, O. A. Dobre, and H. V. Poor, "An efficient specific emitter identification method based on complex-valued neural networks and network compression," *IEEE Journal on Selected Areas in Communications*, vol. 39, no. 8, pp. 2305–2317, 2021.

[19] M. Du, X. He, X. Cai, and D. Bi, "Balanced neural architecture search and its application in specific emitter identification," *IEEE Transactions on Signal Processing*, vol. 69, pp. 5051–5065, 2021.

[20] K. Lee, H. M. Yang, and S. Y. Oh, "Adversarial training on joint energy based model for robust classification and out-of-distribution detection," in *2020 20th International Conference on Control, Automation and Systems (ICCAS)*, pp. 17–21, Busan, Korea, 2020.

[21] Z. J. Wang, W. Zhang, X. W. Rong, and Y. B. Li, "Salient object detection with adversarial training," *IET Image Processing*, vol. 13, no. 14, pp. 2859–2865, 2019.

[22] D. Zhang and W. B. Wu, "Asymptotic theory for estimators of high-order statistics of stationary processes," *IEEE Transactions on Information Theory*, vol. 64, no. 7, pp. 4907–4922, 2018.

[23] L. Saidi, J. Ben, and F. Fnaiech, "Application of higher order spectral features and support vector machines for bearing faults classification," *ISA Transactions*, vol. 54, pp. 193–206, 2015.

[24] T. O'Shea and J. Hoydis, "An introduction to deep learning for the physical layer," *IEEE Transactions on Cognitive Communications and Networking*, vol. 3, no. 4, pp. 563–575, 2017.

[25] L. Han, J. Z. Sun, and W. Zhang, "Convolutional neural network for convective storm nowcasting using 3-D doppler weather radar data," *IEEE Transactions on Geoscience and Remote Sensing*, vol. 58, no. 2, pp. 1487–1495, 2020.

[26] P. Giampaolo, M. Ludovico, and Z. Pietro, "Segmentation and semantic labelling of RGBD data with convolutional neural networks and surface fitting," *IET Computer Vision*, vol. 11, no. 8, pp. 633–642, 2017.

[27] S. Kokalj-Filipovic, R. Miller, and G. Vanhoy, "Adversarial examples in RF deep learning: detection of the attack and its physical robustness," in *Proceedings 2019 IEEE Global Conference on Signal and Information Processing (GlobalSIP)*, pp. 1–6, Shaw Centre, Ottawa, Canada, 2019.

[28] M. Sadeghi and E. G. Larsson, "Adversarial attacks on deep-learning based radio signal classification," *IEEE Wireless Communications Letters*, vol. 8, no. 1, pp. 213–216, 2019.

[29] T. Miyato, S. I. Maeda, M. Koyama, and S. Ishii, "Virtual adversarial training: a regularization method for supervised and semi-supervised learning," *IEEE Transactions on Pattern Analysis and Machine Intelligence*, vol. 41, no. 8, pp. 1979–1993, 2019.

[30] H.-K. Poon, W.-S. Yap, Y.-K. Tee, W.-K. Lee, and B.-M. Goi, "Hierarchical gated recurrent neural network with adversarial and virtual adversarial training on text classification," *Neural Networks*, vol. 119, pp. 299–312, 2019.

[31] A. Oliver, A. Odena, C. Raffel, E. D. Cubuk, and J. Ian, "Realistic evaluation of deep semi-supervised learning algorithms," in *Proceedings 32nd Conference on Neural Information Processing Systems (NIPS)*, pp. 1–19, Montréal, Canada, December 2018.

[32] T. Miyato, A. M. Dai, and I. Goodfellow, "Virtual adversarial training for semi-supervised text classification," in *Proceedings 2017 International Conference on Learning Representations(ICLR)*, pp. 1–11, Toulon, France, 2017.

[33] T. Miyato, S. I. Maeda, M. Koyama, K. Nakae, and S. Ishii, "Distributional smoothing with virtual adversarial training," in *ICLR 2016: 4th International Conference on Learning Representations, ICLR 2016*, pp. 1–12, San Juan, Puerto Rico, 2016.

[34] L. V. Der Maaten and G. E. Hinton, "Visualizing data using t-SNE," *Journal of Machine Learning Research*, vol. 9, pp. 2579–2605, 2008.

[35] N. Yang, B. Zhang, G. Ding et al., "Specific emitter identification with limited samples: a model-agnostic meta-learning approach," *IEEE Communications Letters*, 2021.

Hindawi
Wireless Communications and Mobile Computing
Volume 2022, Article ID 3580376, 12 pages
https://doi.org/10.1155/2022/3580376

Research Article

Application of Multiparameter Kalman Filter in Ultrasonic Water Meter

Fuqiang Zuo[1,2,3] **and Yu Liu**[1,2]

[1]*Research and Development Center of Healthcare Electronics, Institute of Microelectronics of Chinese Academy of Sciences, Beijing 100029, China*
[2]*School of Microelectronics, University of Chinese Academy of Sciences, Beijing 100049, China*
[3]*Research and Development Department, Sanchuan Wisdom Technology Co., Ltd., Yingtan 335200, China*

Correspondence should be addressed to Fuqiang Zuo; zuofuqiang@ime.ac.cn and Yu Liu; liuyu5@ime.ac.cn

Received 14 October 2021; Revised 8 November 2021; Accepted 19 November 2021; Published 6 January 2022

Academic Editor: Junjuan Xia

With the gradual development of the superior performance of the ultrasonic water meter, the use of the water meter gradually occupies most of the market due to its unique advantages. Through the analysis of the influencing factors of the ultrasonic water meter, the Kalman filter is used to analyze the influencing factors, and the differences are obtained. In this paper, combined with the application scope of the Kalman filter, it is introduced. Combined with the method of data fusion, the influencing factors of the ultrasonic water meter are analyzed. They are the flow rate, temperature, speed of sound, time difference, etc. The appropriate sensor is selected through the sensor selection method, and the corresponding data is obtained by the method of the corresponding sensor. We combine the data fusion method and use Kalman's method to filter the data. By comparing the data before and after the processing, it is found that the data before and after the filtering of different influencing factors are small. Among them, the flow speed factor has the greatest impact on the accuracy of the ultrasonic water meter; temperature and sound velocity have little effect on the performance of the ultrasonic water meter. When designing an ultrasonic water meter, it is mainly necessary to consider the impact of flow rate and time difference on the performance of the ultrasonic water meter.

1. Introduction

The ultrasonic water meter is a new type of water meter that detects the time difference caused by the speed change when the ultrasonic sound beam propagates in the water upstream and downstream and analyzes and processes the water velocity to further calculate the water flow rate. It is characterized by a low starting flow rate, wide range ratio, high measurement accuracy, and stable work. There are no moving parts inside and no flow-blocking elements, and it is not affected by impurities in the water and has a long service life. The output communication function is complete, meeting all kinds of communication and wireless networking requirements. It has excellent small flow detection capabilities, can solve many traditional water meter problems, is more suitable for water fee gradient charging, is more suitable for water resource saving and rational use, and has broad market and application prospects. The ultrasonic water meter is a fully electronic water meter manufactured with industrial-grade electronic components using the principle of ultrasonic time difference. Compared with mechanical water meters, it has the characteristics of high accuracy, good reliability, wide range ratio, long service life, no moving parts, no need to set parameters, and installation at any angle.

The Kalman filter is an algorithm that uses linear system state equations and system input and output observation data to optimally estimate the system state [1–4]. Since the observation data contains the influence of noise and interference in the system, the optimal estimation can also be regarded as a filtering process [5]. Data filtering is a data processing technique that removes noise and restores real

data [6]. When the measurement variance is known, the Kalman filter can estimate the state of the dynamic system from a series of data containing measurement noise [7–10]. Kalman filtering is currently the most widely used filtering method because it is convenient for computer programming and can update and process the data collected on site in real time [11–13]. It has a wide range of applications in the fields of communication, navigation, guidance, and control [14–16]. In the process of Kalman filtering, the data is selected by sensors, combined with the data collected by the sensors and related algorithms; the Kalman filtering results are fused; and finally, data about four factors originating from the flow rate, temperature, sound velocity, and time difference are obtained [17–19].

2. Method

2.1. Kalman Principle. Kalman filtering is a recursive filtering method that does not need to save past historical information. The new data combines the estimated value obtained at the previous moment and the state equation of the system itself to obtain a new estimated value in a certain way. Kalman filtering does not require that the signal and noise are the assumptions of a stationary process. It is realized by computer programming and can update and process the data collected on the spot in real time. For the system disturbances and observation errors at each moment, some appropriate assumptions are made about their statistical properties. By processing the observation signal with noise, the estimated value of the real signal with the smallest error is obtained.

2.1.1. Linear Kalman. Assuming that the state of the linear system is k, Kalman's principle can be expressed by the following five formulas:

$$X(k \mid k-1) = A\,X(k-1 \mid k-1) + B\,U(k), \tag{1}$$

$$P(k \mid k-1) = A\,P(k-1 \mid k-1)\,A' + Q, \tag{2}$$

$$X(k \mid k) = X(k \mid k-1) + \mathrm{Kg}(k)\,(Z(k) - H\,X(k \mid k-1)), \tag{3}$$

$$\mathrm{Kg}(k) = \frac{P(k \mid k-1)\,H'}{H\,P(k \mid k-1)\,H' + R}, \tag{4}$$

$$P(k \mid k) = (I - \mathrm{Kg}(k)\,H)P(k \mid k-1). \tag{5}$$

In formula (1),$X(k \mid k-1)$is the result of the previous state prediction,$X(k-1 \mid k-1)$is the optimal result of the previous state, and$U(k)$is the current state control quantity; in formula (2), $P(k \mid k-1)$is the covariance corresponding to$X(k \mid k-1)$and$P(k-1 \mid k-1)$is$X(k-1 \mid k-1)$). The corresponding covariance,A', represents the transposition matrix of$A$, and$Q$is the covariance of the system process; the optimal estimation value of the current state (k) is$X(k \mid k)$;Kgis the Kalman gain.

2.1.2. Extended Kalman. Actual systems always have different degrees of nonlinearity. For nonlinear system filtering problems, the commonly used method is to use linearization techniques to transform them into an approximate linear filtering problem. This is the extended Kalman filter method (extended Kalman filter, EKF). The extended Kalman filter is based on the linear Kalman filter. Its core is to expand the filter value nonlinear functions f $(*)$ and $h(*)$ into a Taylor series for general nonlinear systems and omit the second-order and above terms. An approximate linearized model is obtained, and then, Kalman filtering is applied to complete the filtering and estimation of the target.

2.1.3. Unscented Kalman. Extended Kalman filtering is to perform Taylor expansion on nonlinear system equations or observation equations and retain its first-order approximation terms, which inevitably introduces linearization errors. If the linearization assumption is not true, the use of this algorithm will cause the filter performance to degrade and cause divergence. Unscented Kalman filter (unscented Kalman filter, UKF) abandons the traditional approach of linearizing nonlinear functions, adopts the Kalman linear filter framework, and uses Unscented Transform (UT) to process the mean and covariance for prediction equations.

2.2. Data Fusion

2.2.1. Sensor Selection. The sensor is the main design of the system. The quality of the sensor directly affects the subsequent data processing and whether the source of this data processing is correct. This is the most fundamental basis of a system, which is the acquisition of raw data. However, the sensor is the most important link in the acquisition of raw data. The sensor needs to convert the acquired signal into a transmittable electrical signal. The accuracy of this signal is related to the quality of the entire data.

In the selection of sensors, there are a few basic requirements that need to be paid attention to.

(1) Types of Sensors. We select the sensor type and select the correct sensor according to the types and functions of various sensors. Many sensors involved in this article are selected using this method. These sensors include pressure sensors and temperature changes mentioned in the influencing factors. These sensors include pressure sensors and temperature changes mentioned in the influencing factors, and temperature sensors affect pressure, etc.

(2) The Number of Sensors. The selection of the number of sensors is mainly determined by the number of sensors needed, and the key position of the ultrasonic water meter is generally used as the criterion.

(3) Selection of Range. The measurement range of the sensor is determined by the measurement range of the sensor when the measurement is finally required. The measured value is generally a value close to the range. The closer the value is, the higher the range obtained will be. Under normal circumstances, the working range of the sensor is within the working range to prevent damage or damage to the sensor.

Table 1: Influencing factors of ultrasonic flow data and sensor data collection.

Flow rate v (m/s)	10	10.2	10.1	9.8	10.2	10.1	10.2	10.1	10
Temperature T (°C)	25	25.3	25.5	24.9	25.3	25.1	25.3	25.2	25
Speed of sound C (m/s)	1494.463	1495.234	1495.744	1494.204	1495.234	1494.720	1495.234	1494.977	1494.463
Time difference Δt (ns)	895.4884	912.4562	902.8941	877.8824	912.4562	904.1313	912.4562	903.8204	895.4884

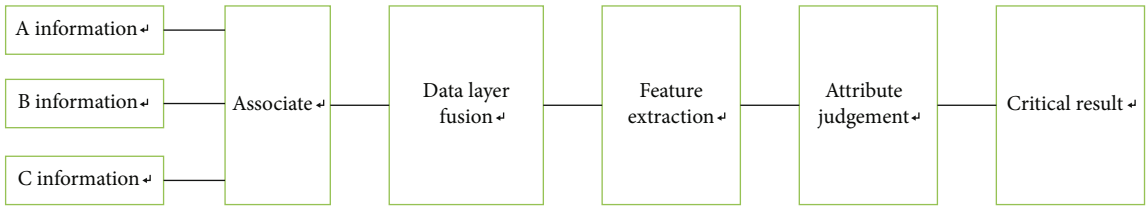

Figure 1: Data layer fusion.

(4) Precision Selection. The selection of sensor measurement accuracy is a very important aspect of the measured data. Generally, it is sufficient to consider meeting the requirements of dynamic weight measurement. It is not appropriate to choose a sensor that is too large or too small. A sensor that is too large will increase the error, and a sensor that is too small may not be able to measure the required data. It may also cause damage to the sensor.

(5) The Scope of Application of the Sensor. The scope of application of the sensor is mainly related to the size of the sensor and the size of the sensor installation location. To ensure that the sensor can work safely is the prerequisite for sensor installation. Combined with the environment in which the sensor is used, we ensure that the sensor will not be affected by the problem of the installation location.

2.2.2. Data Collection. Ultrasonic flow measurement is not only a simple data filter but also a complex nonlinear conversion process. Only the basic Kalman filter algorithm cannot solve the nonlinear problem, so this article also tries to use the extended EKF filter algorithm for derivation. Regarding the coefficients determined in the model analysis, the state of the system, and the observation equations and their corresponding correlation coefficients, I will not repeat them. The data to be filtered and the initial state used are the same as those in the previous section. Due to the addition of the observed state variables, the data are shown in the following Table 1.

2.2.3. Data Fusion Method. Multisource information fusion is to analyze the factors that affect the results of the target, obtain the data in a certain way, obtain the description and interpretation process of the required target, and achieve the mapping between the fused data and the target. According to the fusion level, the fusion model is usually divided into three levels: data, features, and decision-making for information fusion and processing. Then, according to the structure of information fusion, the data is fused in centralized, distributed, and hybrid fusion methods, and finally, combined with the data characteristics in the mapping relationship, the combination method is selected for data fusion, and the optimal fusion plan is obtained through error analysis.

Information fusion is to simulate the real situation, ignore the less influential factors, determine the more influential factors, and combine the law of time and space to establish a mathematical model, describe and classify the information data, and use the subset data contained in it. We form a better information fusion system.

(1) Information Fusion Level. Information fusion is usually divided into 4 stages, which are the information source collection and arrangement stage, the information source processing stage, the analysis and decision-making stage, and the fusion conclusion output stage. Information data is collected by sensors and then processed by algorithms after model conversion to determine the data fusion target at the decision-making level. After studying each level, the following analysis can be obtained.

(1) Data layer fusion refers to the direct fusion of the original data. The source of the data is obtained through factor analysis using the corresponding sensor, and after correlation through the data model, data layer fusion is gradually carried out, and the data is extracted before the data processing result is judged. The advantage of data layer fusion is that the details of data extraction can be reduced through the fusion layer. When there are deficiencies, there are more calculation data and poor real-time calculation. The data layer fusion block diagram is shown in Figure 1.

Feature layer fusion refers to the feature analysis of data and the extraction of the same type of data. Then, we analyze and process through algorithms, retain the main component data, and provide support for the final result. The advantage of feature layer fusion is to reduce the amount of data processing and facilitate real-time data processing. The block diagram of feature layer fusion is shown in Figure 2.

Decision-making fusion refers to high-level fusion, which is summarized and flexible in the data processing

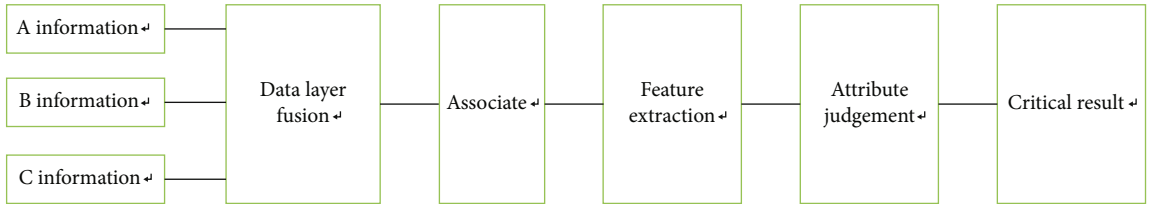

Figure 2: Feature layer fusion.

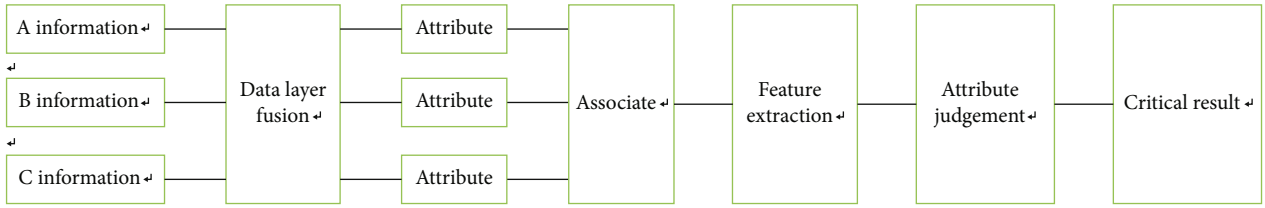

Figure 3: Decision-making.

process. After preprocessing the data, a decision plan is obtained, and then, the plans are combined and compared to determine the final combination plan. The fusion block diagram of the decision-making layer is shown in Figure 3.

Through the introduction of information fusion levels, we can see that different information fusions have different characteristics and scope of application. When sensor data can be used in various information fusions, information fusion technology can be used directly. When the sensors do not match, the data needs to be fused by a specific method, and the enumeration method is selected to use various methods to fuse the data to determine the final data selection method.

(2) Information Fusion Structure. The system structure of information fusion technology can generally be divided into centralized fusion, distributed fusion, and hybrid fusion architecture. We make the following discussions during the research:

(1) Centralized fusion refers to sending the observation data of each sensor to the database, through the database to make preliminary judgments on the data fusion and determine the structural accuracy and information loss rate. In the transmission process, a good network speed is required to ensure the integrity of data transmission

(2) Distributed fusion refers to preprocessing the observed data through a specific mathematical model design algorithm through each sensor and then sending the partial processing results to the database after the initial conclusion is obtained. Compared with the centralized fusion structure, the processed data has a smaller data size, lower bandwidth requirements, and higher feasibility in actual operation

(3) Hybrid fusion is a combination of the advantages of centralized fusion and distributed fusion. But it has higher economic requirements and is generally used in dealing with more complex models

(3) Information Fusion Algorithm. The information fusion algorithm is the basis and important content of fusion processing. The algorithm obtains the relationship between the data or the relationship between the data and the target through the actual situation by establishing a data analysis model and then combines the established model with the existing data processing model and achieves the purpose of data fusion through the computer. The algorithms that can be fused at this stage usually include fuzzy theory, D-S evidence theory, Bayes reasoning, and neural network algorithms. The analysis of different algorithms is as follows.

Fuzzy theoretical value refers to determining the key factors of data fusion through the fusion process, gradually expanding through the key factors, and finally deriving the fuzzy method of target extraction gradually.

D-S evidence theory adopts the method of probability theory. This theory can effectively solve the probability of position influencing factors and then integrate the data through the full probability formula to obtain the overall target result. Therefore, it is widely used.

Bayes reasoning refers to the establishment of the relationship between the prior probability and the posterior probability through the Bayes rule, the overall probability analysis is carried out, the probability law of different factors is determined, and the overall probability analysis is obtained through the data. Due to the unknown probability, the error of this method is relatively large.

Neural networks are essentially the process of simulating the human brain through deep learning, through the process of repeated repetition, to gain cognition of things and perform temporary human brain functions. Deep learning

combines the data of multiple sensors on multisensor data fusion, and comprehensive deep learning acquires the data of each sensor for mapping and obtains the mapping relationship between the sensors. Then, according to repeated training, the error of the obtained prediction data is getting smaller and smaller. When the error reaches a certain accuracy, it can meet practicability.

The corresponding initial state and coefficients are as follows:

$$x^{(0)} = \begin{pmatrix} 25 \\ 10 \end{pmatrix}, \quad P^{(0)} = \begin{pmatrix} 1 & 0 \\ 0 & 1 \end{pmatrix}, \quad L = 0.1\,\text{m}. \tag{6}$$

For the noise of the prediction process and the measurement process, there are adjustments for different variables, as follows:

$$Q = \begin{pmatrix} 0.05 & 0 \\ 0 & 0.5 \end{pmatrix}, \quad R = \begin{pmatrix} 20 & 0 \\ 0 & 10 \end{pmatrix}. \tag{7}$$

Due to the extended EKF filtering algorithm, the calculation and iteration of the Jacobian partial derivative matrix is added during the calculation process, which is the measurement matrix of the observation equation, as follows:

$$\begin{aligned} H &= \begin{pmatrix} \dfrac{\partial h_1}{\partial T} & \dfrac{\partial h_1}{\partial v} \\ \dfrac{\partial h_2}{\partial T} & \dfrac{\partial h_2}{\partial v} \end{pmatrix} \\ &= \begin{pmatrix} 0.0006 \cdot T^2 - 0.1058 \cdot T + 4.852 & 0 \\ -4LvC^{-3}10^9 \cdot \left(0.0006 \cdot T^2 - 0.1058 \cdot T + 4.852\right) & \dfrac{2L}{C^2}10^9 \end{pmatrix}. \end{aligned} \tag{8}$$

According to the above measurement matrix and assuming other initial states, the initial value of the matrix can be obtained, as follows:

$$H^{(0)} = \begin{pmatrix} 2.5820 & 0 \\ -3.0943 & 89.5488 \end{pmatrix}. \tag{9}$$

The iterative calculation process of the algorithm is detailed. Only when each step is carefully calculated can the calculation amount and complexity of the extended EKF filter algorithm be understood more deeply; the calculation is performed according to the following iterative process.

$$\hat{x}_k^- = A\hat{x}_{k-1} = \begin{pmatrix} 1 & 0 \\ 0 & 1 \end{pmatrix}\begin{pmatrix} 25 \\ 10 \end{pmatrix} = \begin{pmatrix} 25 \\ 10 \end{pmatrix}, \quad Z_k = \begin{pmatrix} 1495.234 \\ 912.456 \end{pmatrix},$$

$$\begin{aligned} P_k^- &= AP_{k-1}A^T + Q = \begin{pmatrix} 1 & 0 \\ 0 & 1 \end{pmatrix}\begin{pmatrix} 1 & 0 \\ 0 & 1 \end{pmatrix}\begin{pmatrix} 1 & 0 \\ 0 & 1 \end{pmatrix}^T \\ &\quad + \begin{pmatrix} 0.05 & 0 \\ 0 & 0.5 \end{pmatrix} = \begin{pmatrix} 1.05 & 0 \\ 0 & 1.5 \end{pmatrix} \end{aligned}$$

$$H^{(0)} = \begin{pmatrix} 2.5820 & 0 \\ -3.0943 & 89.5488 \end{pmatrix}$$

$$\begin{aligned} K &= P_k^- H^T \left(HP_k^- H^T + R\right)^{-1} \\ &= \begin{pmatrix} 1.05 & 0 \\ 0 & 1.5 \end{pmatrix}\begin{pmatrix} 2.5820 & 0 \\ -3.0943 & 89.5488 \end{pmatrix}^T \\ &\quad \cdot \left\{ \begin{pmatrix} 2.5820 & 0 \\ -3.0943 & 89.5488 \end{pmatrix}\begin{pmatrix} 1.05 & 0 \\ 0 & 1.5 \end{pmatrix}\begin{pmatrix} 2.5820 & 0 \\ -3.0943 & 89.5488 \end{pmatrix}^T \right. \\ &\quad \left. + \begin{pmatrix} 2.5820 & 0 \\ -3.0943 & 89.5488 \end{pmatrix}\begin{pmatrix} 20 & 0 \\ 0 & 10 \end{pmatrix}\begin{pmatrix} 2.5820 & 0 \\ -3.0943 & 89.5488 \end{pmatrix}^T \right\}^{-1} \\ &= \begin{pmatrix} 2.7111 & -3.2490 \\ 0 & 134.3232 \end{pmatrix}\left\{ \begin{pmatrix} 2.5820 & 0 \\ -3.0943 & 89.5488 \end{pmatrix}\begin{pmatrix} 21.05 & 0 \\ 0 & 11.5 \end{pmatrix} \right. \\ &\quad \left. \cdot \begin{pmatrix} 2.5820 & 0 \\ -3.0943 & 89.5488 \end{pmatrix}^T \right\}^{-1} \\ &\quad + \begin{pmatrix} 2.5820 & 0 \\ -3.0943 & 89.5488 \end{pmatrix}\begin{pmatrix} 20 & 0 \\ 0 & 10 \end{pmatrix}\begin{pmatrix} 2.5820 & 0 \\ -3.0943 & 89.5488 \end{pmatrix}^T \Bigg\}^{-1} \\ &= \begin{pmatrix} 2.7111 & -3.2490 \\ 0 & 134.3232 \end{pmatrix}\left\{ \begin{pmatrix} 2.5820 & 0 \\ -3.0943 & 89.5488 \end{pmatrix}\begin{pmatrix} 21.05 & 0 \\ 0 & 11.5 \end{pmatrix} \right. \\ &\quad \left. \cdot \begin{pmatrix} 2.5820 & 0 \\ -3.0943 & 89.5488 \end{pmatrix}^T \right\}^{-1} \\ &= \begin{pmatrix} 2.7111 & -3.2490 \\ 0 & 134.3232 \end{pmatrix}\begin{pmatrix} 140.3345 & -168.1786 \\ -168.1786 & 92419.90 \end{pmatrix}^{-1} \\ &= \begin{pmatrix} 2.7111 & -3.2490 \\ 0 & 134.3232 \end{pmatrix}\begin{pmatrix} 0.007141 & 0.000013 \\ 0.000013 & 0.000011 \end{pmatrix} \\ &= \begin{pmatrix} 0.019318 & 0 \\ 0.001746 & 0.001478 \end{pmatrix}, \end{aligned}$$

$$\begin{aligned} \hat{x}_k &= \hat{x}_k^- + K(Z_k - h(\hat{x}_k^-)) = \begin{pmatrix} 25 \\ 10 \end{pmatrix} + \begin{pmatrix} 0.019318 & 0 \\ 0.001746 & 0.001478 \end{pmatrix} \\ &\quad \cdot \left\{ \begin{pmatrix} 1495.234 \\ 912.456 \end{pmatrix} - \begin{pmatrix} 1494.4625 \\ 895.488 \end{pmatrix} \right\} \\ &= \begin{pmatrix} 25 \\ 10 \end{pmatrix} + \begin{pmatrix} 0.0149 \\ 0.0264 \end{pmatrix} = \begin{pmatrix} 25.0149 \\ 10.0264 \end{pmatrix}, \end{aligned}$$

$$\begin{aligned} P_k &= (I - KH)P_k^- = \left\{ \begin{pmatrix} 1 & 0 \\ 0 & 1 \end{pmatrix} - \begin{pmatrix} 0.019318 & 0 \\ 0.001746 & 0.001478 \end{pmatrix} \right. \\ &\quad \left. \cdot \begin{pmatrix} 2.5820 & 0 \\ -3.0943 & 89.5488 \end{pmatrix} \right\}\begin{pmatrix} 1.05 & 0 \\ 0 & 1.5 \end{pmatrix} = \begin{pmatrix} 0.997627 & 0 \\ 0.000071 & 1.301470 \end{pmatrix}. \end{aligned} \tag{10}$$

```
longitude_fil(1) = y(1);
p_fil(1) = 1;
for t = 2:n
longitude_pre(t) = a* longitude_fil(t-1);
p_pre(t) = a* p_fil(t-1) + a'*P;
K(t) = p_pre(t)*H'*inv(H*p_pre(t)*H' + Q);
longitude_fil(t) = longitude_pre(t) + K(t)*(longitude(t)-H*longitude_pre(t));
p_fil(t) = (1-K(t)*H)*p_pre(t);
end
for i =1:n
Err1(i) = RMS(y(i), longitude(i));
Err2(i) = RMS(y(i), longitude_fil(i));
end
```

Code 1

Table 2: Data collation and analysis before and after filtering.

Before filtering	Flow velocity (m/s)	10	10.2	10.1	9.8	10.2	10.1	10.2	10.1	10
	Temperature (°C)	25	25.3	25.5	24.9	25.3	25.1	25.3	25.2	25
	Speed of sound (m/s)	1494.463	1495.234	1495.744	1494.204	1495.234	1494.720	1495.234	1494.977	1494.463
	Time difference (ns)	895.4884	912.4562	902.8941	877.8824	912.4562	904.1313	912.4562	903.8204	895.4884
After filtering	Flow velocity (m/s)	10	10.0264	10.0348	9.9954	10.0322	10.0449	10.0579	10.0661	10.0531
	Temperature (°C)	25	25.0149	25.0377	25.0301	25.0435	25.0463	25.0491	25.0565	25.0537
	Speed of sound (m/s)	1494.463	1494.501	1494.560	1494.540	1494.575	1494.582	1494.589	1494.608	1494.601
	Time difference (ns)	895.4884	897.806	898.488	894.983	898.237	899.365	900.521	901.232	900.077

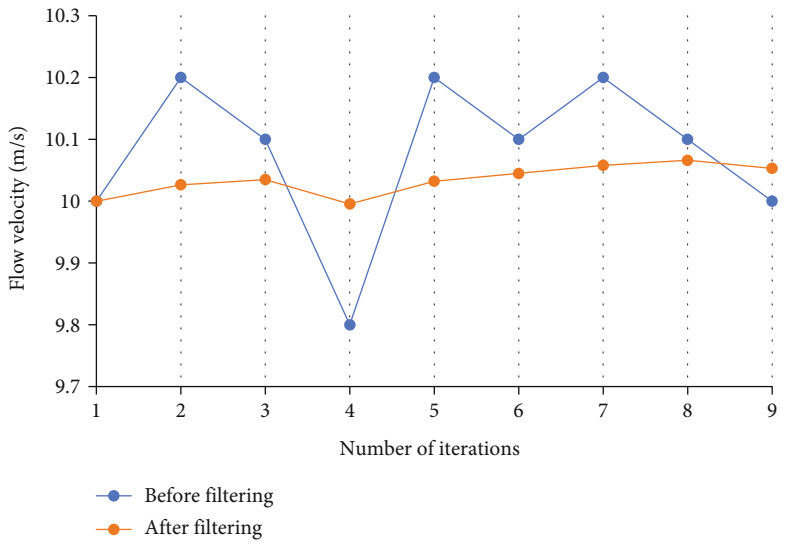

Figure 4: Comparison of flow rate data before and after filtering.

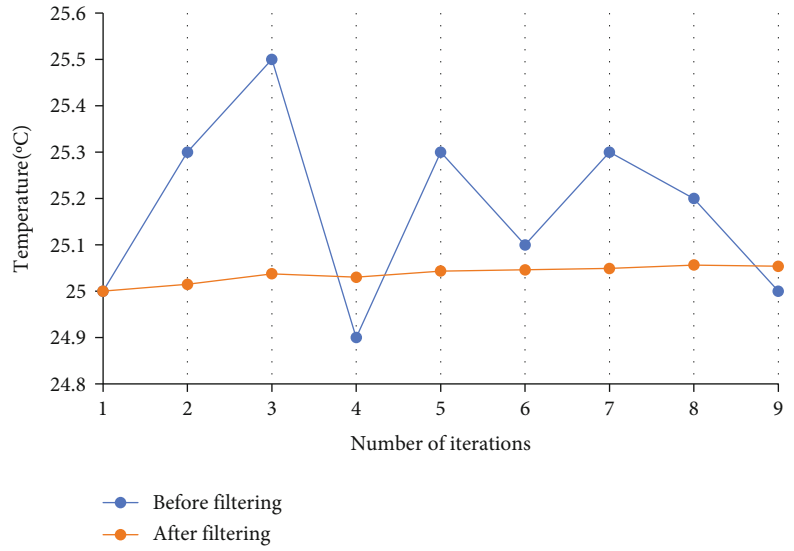

Figure 5: Comparison of temperature data before and after filtering.

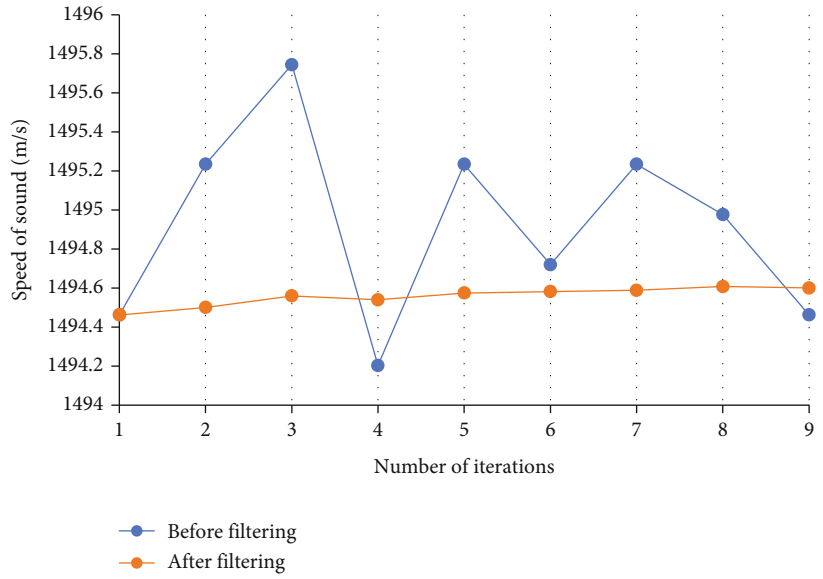

Figure 6: Comparison of sound velocity data before and after filtering.

The data is processed through the above algorithm combined with related software, and finally, the result after data fusion is obtained.

The Kalman MATLAB code is shown as follows.

2.3. Experimental Results and Analysis. From the above iterative calculation process, it can be seen that the extended EKF filtering algorithm is much more complicated than the basic KF filtering algorithm, the Jacobian matrix update is added in the calculation process, and the complexity of the vector is not a little bit higher than the scalar. If the variables are related and not independent, the amount of calculation will increase. In the above iterative calculation process, when initializing the covariance matrix, it is a diagonal matrix, and no cross-correlation is added; in the update process, it is also assumed that the noise covariance is a diagonal matrix and is not correlated. In the continuous iterative calculation, the variance value corresponding to the flow velocity in the covariance matrix is getting larger and larger, the discussion of its convergence should be strengthened in the follow-up, and programming calculation is easy to travel, which can be realized by MATLAB programming, which can be iterated more times and calculated. There is no error in the process; after the above filtering, it is found that the data filtering effect is good, with almost no fluctuations. The comparison table and analysis of the data before and after filtering are shown in the following Table 2.

From the table data, it is not very intuitive. The changes before and after the corresponding data filtering are drawn into graphs, and the filtering results of the four variables are compared. From Figures 4–7, it can be very intuitive to see that the filtering effect is better.

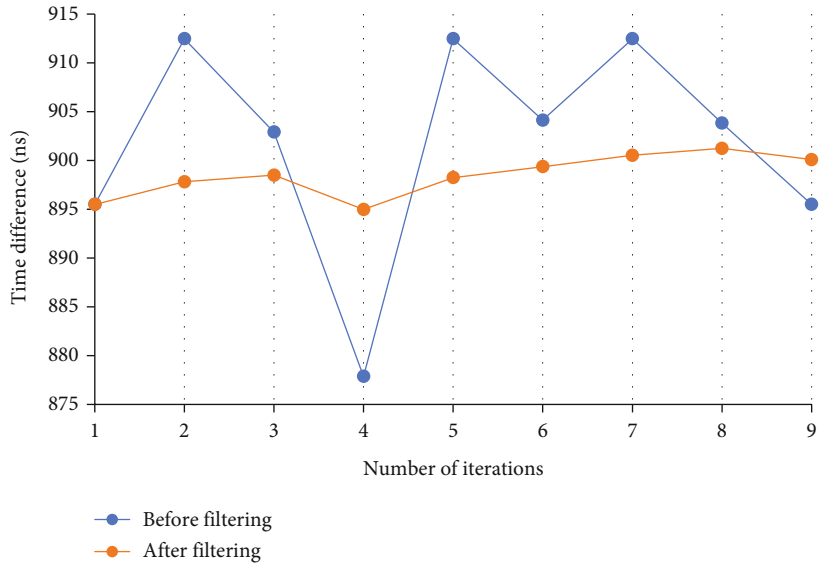

Figure 7: Comparison of time difference data before and after filtering.

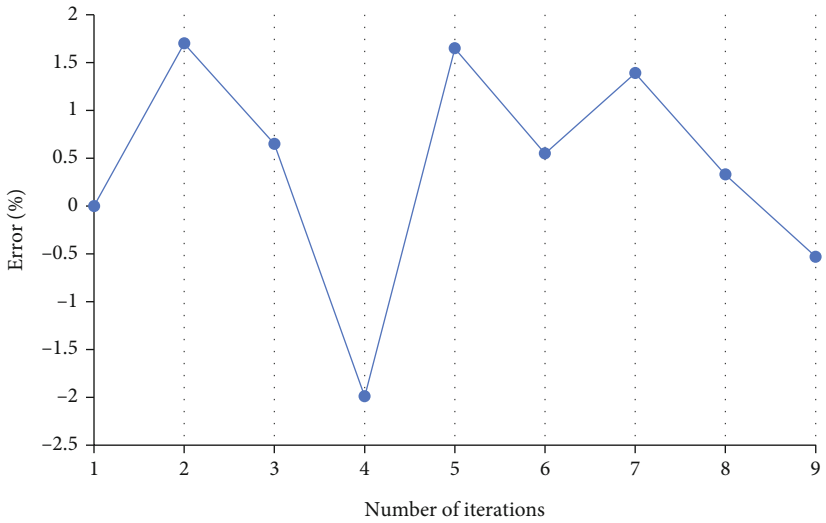

Figure 8: Flow velocity error analysis diagram.

It can also be seen from the above figure that the graphs in Figures 5 and 6 have the same changes, because the propagation speed of ultrasonic waves in water is a function of temperature, so the law of change is the same. It shows that the effects of the two on ultrasound are the same. The graphs in Figure 4 are similar to those in Figure 7, but the fluctuation of Figure 4 is greater than that of Figure 7, indicating that there are certain influencing factors between the two.

3. Conclusion

This article analyzes the influencing factors of the accuracy of the ultrasonic water meter and consults relevant information to find that the influencing factors are mainly the flow rate, temperature, speed of sound, and time difference. The corresponding sensor method is used to obtain the corresponding data, and the Kalman method is used to carry out the data. With regard to filter processing, by comparing the data before and after processing, it is found that the data before and after filtering is relatively small for different influencing factors. The errors in the comparison are shown in the following Figures 8–11. The comprehensive analysis of errors can be found in Figure 12. Flow speed factors have a greater impact on the accuracy of ultrasonic water meters. The speed of sound has a small influence on the ultrasonic water meter, so the data is in line with the actual situation, indicating that the accuracy of the data and the establishment of the data model are better.

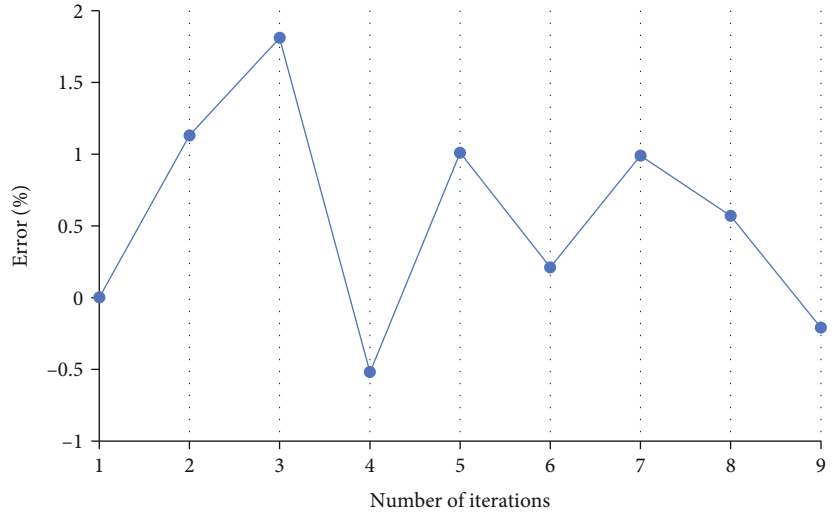

Figure 9: Temperature error analysis diagram.

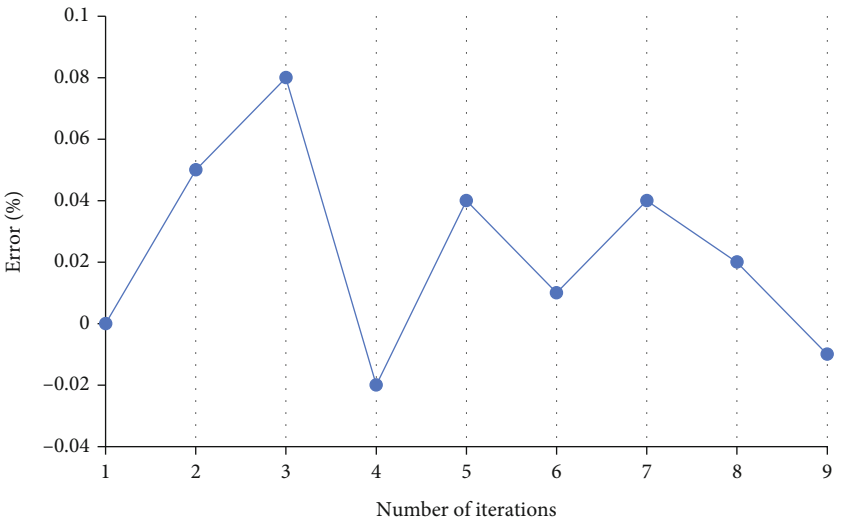

Figure 10: Sound velocity error analysis diagram.

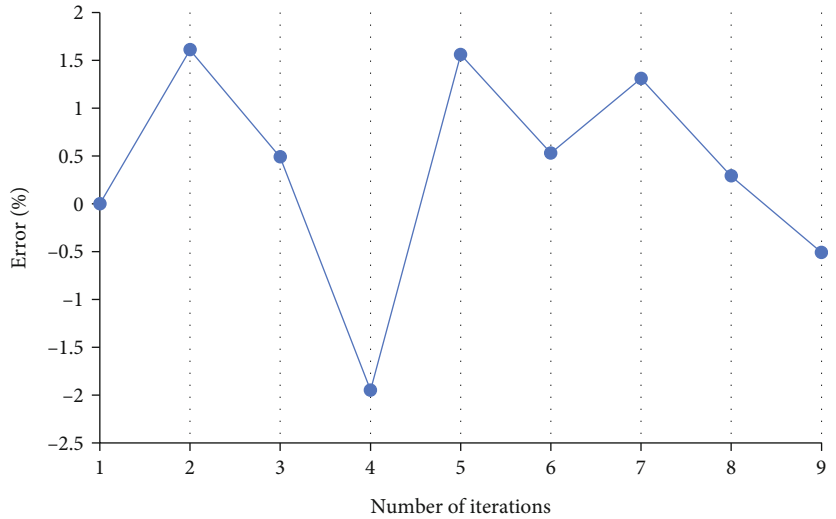

Figure 11: Time difference error analysis diagram.

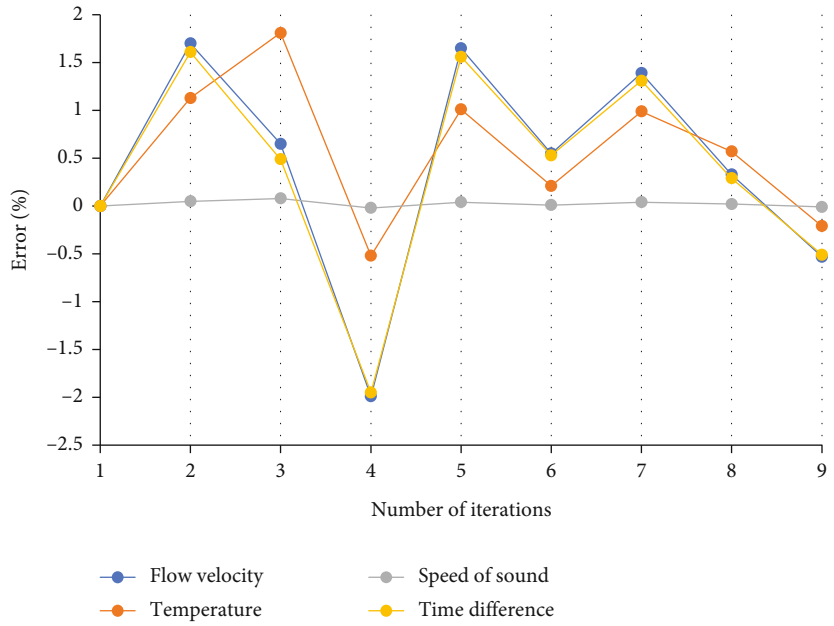

Figure 12: Overall analysis of flow velocity, temperature, sound velocity, and time difference error.

Table 3: Comparison of flow velocity and temperature before and after filtering and error analysis.

Flow velocity				Temperature			
Before filtering	After filtering	Error	Error analysis (%)	Before filtering	After filtering	Error	Error analysis (%)
10	10	0.00	0	25	25	0.00	0
10.2	10.0264	0.17	1.70	25.3	25.0149	0.29	1.13
10.1	10.0348	0.07	0.65	25.5	25.0377	0.46	1.81
9.8	9.9954	-0.20	-1.99	24.9	25.0301	-0.13	-0.52
10.2	10.0322	0.17	1.65	25.3	25.0435	0.26	1.01
10.1	10.0449	0.06	0.55	25.1	25.0463	0.05	0.21
10.2	10.0579	0.14	1.39	25.3	25.0491	0.25	0.99
10.1	10.0661	0.03	0.33	25.2	25.0565	0.14	0.57
10	10.0531	-0.05	-0.53	25	25.0537	-0.05	-0.21

Table 4: Comparison of flow velocity and temperature before and after filtering and error analysis.

Speed of sound				Time difference			
Before filtering	After filtering	Error	Error analysis (%)	Before filtering	After filtering	Error	Error analysis (%)
1494.463	1494.463	0.00	0	895.4884	895.4884	0.00	0
1495.234	1494.501	0.73	0.05	912.4562	897.806	14.65	1.61
1495.744	1494.56	1.18	0.08	902.8941	898.488	4.41	0.49
1494.204	1494.54	-0.34	-0.02	877.8824	894.983	-17.10	-1.95
1495.234	1494.575	0.66	0.04	912.4562	898.237	14.22	1.56
1494.72	1494.582	0.14	0.01	904.1313	899.365	4.77	0.53
1495.234	1494.589	0.64	0.04	912.4562	900.521	11.94	1.31
1494.977	1494.608	0.37	0.02	903.8204	901.232	2.59	0.29
1494.463	1494.601	-0.14	-0.01	895.4884	900.077	-4.59	-0.51

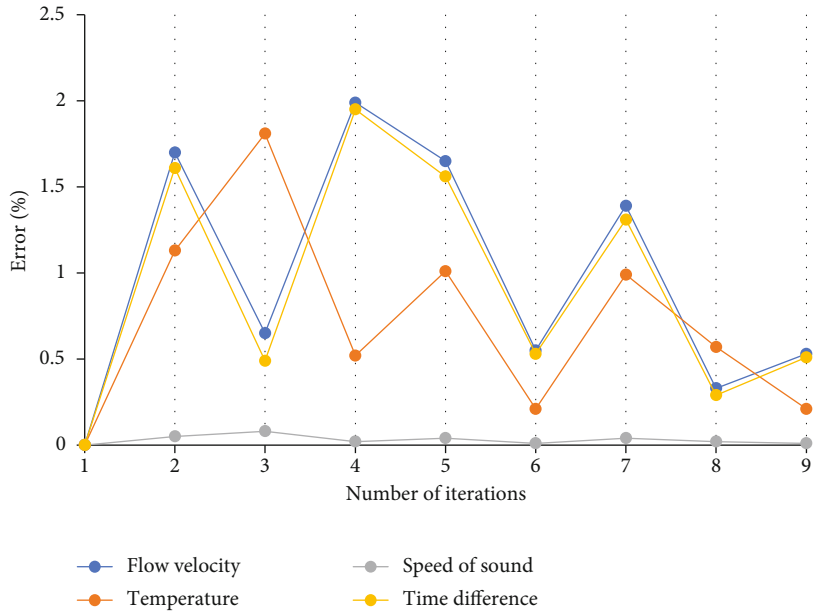

Figure 13: The corrected error analysis diagram.

3.1. Feasibility Verification of Proposed Algorithm. After processing the data in Table 2, the original data and error data in the following Tables 3 and 4 are obtained. From the data, it can be found that the absolute value of the error of the data is basically below 2%, and the error analysis of most of the data is around 1%. It shows that the error of the data satisfies the needs of the existing data analysis.

The Kalman method is used to filter the data. By comparing the data before and after the processing, it is found that the data before and after the filtering of different influencing factors are relatively small. The errors in the comparison are shown in the following Figures 8–11, and there is a comprehensive analysis of the error. It can be found that by analyzing the error trend of the flow velocity, the flow velocity error analysis diagram shown in Figure 8 is obtained.

Through the analysis of the temperature error trend, the temperature error analysis chart shown in Figure 9 is obtained.

By analyzing the error trend of sound velocity, the sound velocity error analysis diagram shown in Figure 10 is obtained.

By analyzing the error trend of the time difference, the time difference error analysis chart shown in Figure 11 is obtained.

It can be found from the data that the absolute value of the error of the data is basically below 2%, and the error analysis of most of the data is about 1%. It shows that the error of the data meets the needs of the existing data analysis.

3.2. Actual Experimental Results and Analysis. The Kalman method is used to filter the data. By comparing the data before and after the processing, it is found that the data before and after the filtering of different influencing factors are relatively small. The errors in the comparison are shown in the following Figures 9–12, and there is a comprehensive analysis of the error. It can be found that the flow speed factor has a greater impact on the accuracy of the ultrasonic water meter in Figure 12. The speed of sound has a small influence on the ultrasonic water meter, so the data is in line with the actual situation, indicating that the accuracy of the data and the establishment of the data model are better. During the application of the ultrasonic water meter, it is necessary to strengthen the control of the flow speed to prevent the change of the flow speed of the ultrasonic water meter from causing a large change in the performance of the ultrasonic water meter, which will affect the application of the water meter. Through the comparison of four factors, it can be found that the error analysis data of the speed of sound before and after filtering is about 0.04%, and the impact on the ultrasonic water meter can be neglected. If necessary, it can reduce the influence of factor propagation on the ultrasonic water meter to achieve the purpose of increasing the performance of the water meter.

By comparing the error before and after filtering the four factors of flow velocity, temperature, sound velocity, and time difference, it can be found that there are negative numbers among them. After correcting the data, the following Figure 13 is obtained.

It can be seen from Figure 13 that the main impact on the ultrasonic water meter is the difference in flow rate and time. Temperature and sound velocity have little effect on the performance of the ultrasonic water meter. When designing an ultrasonic water meter, it is mainly necessary to consider the impact of flow rate and time difference on the performance of the ultrasonic water meter. Secondly, we consider the influence of temperature on the performance of ultrasonic water meters. The effect of sound velocity on ultrasonic water meters can basically be ignored.

Data Availability

The labeled dataset used to support the findings of this study are available from the corresponding author upon request.

Conflicts of Interest

The authors declare no competing interests.

Authors' Contributions

Fuqiang Zuo and Yu Liu contributed equally to this work.

Acknowledgments

This research was funded by the special fund of the State Key Joint Laboratory of Environment Simulation and Pollution Control under grant number 18K07ESPCT.

References

[1] B. Dutra, A. Silveira, and A. Pereira, "Grasping force estimation using state-space model and Kalman filter," *Biomedical Signal Processing and Control*, vol. 70, article 103036, 2021.

[2] F. Rahmanian, M. H. Asemani, M. Dehghani, and S. Mobayen, "Robust dynamic output feedback control of blood glucose level in diabetic rat with robust descriptor Kalman filter," *Biomedical Signal Processing and Control*, vol. 71, no. 2, article 103088, 2022.

[3] H. Kong, M. Shan, S. Sukkarieh, W. X. Zheng, and T. Chen, "Kalman filtering under unknown inputs and norm constraints," *Automatica*, vol. 133, no. 6, article 109871, 2021.

[4] G. Veerasamy, R. Kannan, R. K. Siddharthan, G. Muralidharan, V. Sivanandam, and R. Amirtharajan, "Integration of genetic algorithm tuned adaptive fading memory Kalman filter with model predictive controller for active fault-tolerant control of cement kiln under sensor faults with inaccurate noise covariance," *Mathematics and Computers in Simulation*, vol. 191, pp. 256–277, 2022.

[5] T. Mukherjee, D. Varshney, K. K. Kottakki, and M. Bhushan, "Broyden's update based extended Kalman filter for nonlinear state estimation," *Journal of Process Control*, vol. 105, no. 1, pp. 267–282, 2021.

[6] H. O. Ilhan, M. Yuzkat, and N. Aydin, "Sperm motility analysis by using recursive Kalman filters with the smartphone based data acquisition and reporting approach," *Expert Systems with Applications*, vol. 186, no. 3, article 115774, 2021.

[7] Y. Cao, R. Wang, J. Peng et al., "Humidity enhanced N_2O photoacoustic sensor with a 4.53 μm quantum cascade laser and Kalman filter," *Photoacoustics*, vol. 24, article 100303, 2021.

[8] E. Hou, Y. Xu, X. Qiao, G. Liu, and Z. Wang, "State of power estimation of echelon-use battery based on adaptive dual extended Kalman filter," *Energies*, vol. 14, no. 17, 2021.

[9] C. Urrea and R. Agramonte, "Kalman filter: historical overview and review of its use in robotics 60 years after its creation," *Journal of Sensors*, vol. 2021, no. 5, Article ID 9674015, 21 pages, 2021.

[10] F. Tomizawa and Y. Sawada, "Combining ensemble Kalman filter and reservoir computing to predict spatiotemporal chaotic systems from imperfect observations and models," *Geoscientific Model Development*, vol. 14, no. 9, pp. 5623–5635, 2021.

[11] F. Lamyae, B. Siham, and M. Hicham, "Mathematical model and attitude estimation using extended colored Kalman filter for transmission lines inspection's unmanned aerial vehicle," *IIETA*, vol. 54, no. 4, pp. 529–537, 2021.

[12] A. Samia, L. Yahia, C. Kheireddine, and S. Salah, "Position and speed estimation of PMSM based on extended Kalman filter tuned by biogeography-based-optimization," *IIETA*, vol. 54, no. 4, pp. 559–568, 2021.

[13] S. Ito, M. Furukawa, K. Yamada, and K. Manabe, "Applying ensemble Kalman filter to transonic flows through a two-dimensional turbine cascade," *Journal of Fluids Engineering*, vol. 143, no. 12, article 121113, 2021.

[14] J. Wang and O. R. Barry, "Real-time identification of wrist kinematics via sparsity-promoting extended Kalman filter based on ellipsoidal joint formulation," *IEEE transactions on bio-medical engineering*, vol. 99, 2021.

[15] Q. Wang, X. Sun, and C. Wen, "Design method for a higher order extended Kalman filter based on maximum correlation entropy and a Taylor network system," *Sensors*, vol. 21, no. 17, 2021.

[16] K. V. Parag, "Improved estimation of time-varying reproduction numbers at low case incidence and between epidemic waves," *PLoS Computational Biology*, vol. 17, no. 9, pp. 1–26, 2021.

[17] P. J. G. Teunissen, A. Khodabandeh, and D. Psychas, "A generalized Kalman filter with its precision in recursive form when the stochastic model is misspecified," *Journal of Geodesy*, vol. 95, no. 9, 2021.

[18] V. Mahboub and S. Ebrahimzadeh, "Non-linear block least-squares adjustment for a large number of observations," *Survey Review*, vol. 53, no. 9, pp. 1–11, 2021.

[19] B. Yurii, "Implementation of an adaptive bias-aware extended Kalman filter for sea-ice data assimilation in the HARMONIE-AROME numerical weather prediction system," *Journal of Advances in Modeling Earth Systems*, vol. 13, no. 9, pp. 1–26, 2021.

Hindawi
Wireless Communications and Mobile Computing
Volume 2021, Article ID 8000869, 6 pages
https://doi.org/10.1155/2021/8000869

Research Article

Denial-of-Service Attack Detection over IPv6 Network Based on KNN Algorithm

Yasser Alharbi,[1] Ali Alferaidi,[1] Kusum Yadav,[1] Gaurav Dhiman,[2] and Sandeep Kautish[3]

[1]*College of Computer Science and Engineering, University of Ha'il, Ha'il, Saudi Arabia*
[2]*Department of Computer Science, Government Bikram College of Commerce, -147001, Patiala, Punjab, India*
[3]*LBEF Campus, Kathmandu, Nepal*

Correspondence should be addressed to Sandeep Kautish; dr.skautish@gmail.com

Received 19 October 2021; Revised 29 November 2021; Accepted 8 December 2021; Published 24 December 2021

Academic Editor: Junjuan Xia

With the rapid increase and complexity of IPv6 network traffic, the traditional intrusion detection system Snort detects DoS attacks based on specific rules, which reduces the detection performance of IDS. To solve the DoS intrusion detection problem in the IPv6 network environment, the lightweight KNN optimization algorithm in machine learning is adopted. First, the double dimensionality reduction of features is achieved through the information gain rate, and discrete features with more subfeatures are selected and aggregated to further dimensionality reduction and feature dimension of the actual operation. Secondly, the information gain rate is used as the weight to optimize the sample Euclidean distance measurement. Based on the proposed measure of the reverse distance influence, the classification decision algorithm of the KNN algorithm is optimized to make the detection technology better. The effect is further improved. The experimental results show that the traditional TAD-KNN algorithm based on average distance and the GR-KNN algorithm that only optimizes the distance definition, the GR-AD-KNN algorithm can not only improve the overall detection performance in the detection of IPv6 network traffic characteristics but also for small groups of samples. As a result, classification has better detection results.

1. Introduction

With the rapid development of computer networks, traditional IPv4 network addresses have gradually been exhausted. To alleviate this problem, the birth of NAT technology has delayed the exhaustion of IPv4 addresses but still has not fundamentally solved the problem of insufficient addresses. Next, the generation of the Internet network protocol IPv6 [1–3] has radically solved this problem, significantly increasing the number of IP addresses that can be used and providing many IP addresses for networks such as the Internet of Things, as shown in Figure 1.

The difference between IPv6 and IPv4 is not only in the number of available addresses. There are significant differences, and the IP datagram headers of the two protocol versions are also different. At the same time, protocols such as ARP have been cancelled in the IPv6 network and replaced by the NDP protocol. Therefore, to a certain extent, the two versions are still differences in the IP protocol. In terms of security, with the rapid development of IPv6 technology, there are more and more DoS attacks related to it, and the emergence of IPv6 does not wholly eliminate DoS attacks [4–6].

For DoS attacks in the network, the network intrusion detection system (IDS) can detect such hidden network security risks [7]. IDS can find the changes in the data transmitted on the web to find the abnormal situation in the network in time. However, currently in the network, the amount and type of traffic are increasing rapidly. Therefore, IDS based on specific rules may have poor adaptability and more extended rule matching time when detecting DoS attacks in IPv6 networks [8].

Aiming at DoS attacks in IPv6 networks, this paper studies intrusion detection technology and realizes the function of DoS intrusion detection based on IPv6 networks [9]. The specific contributions are as follows:

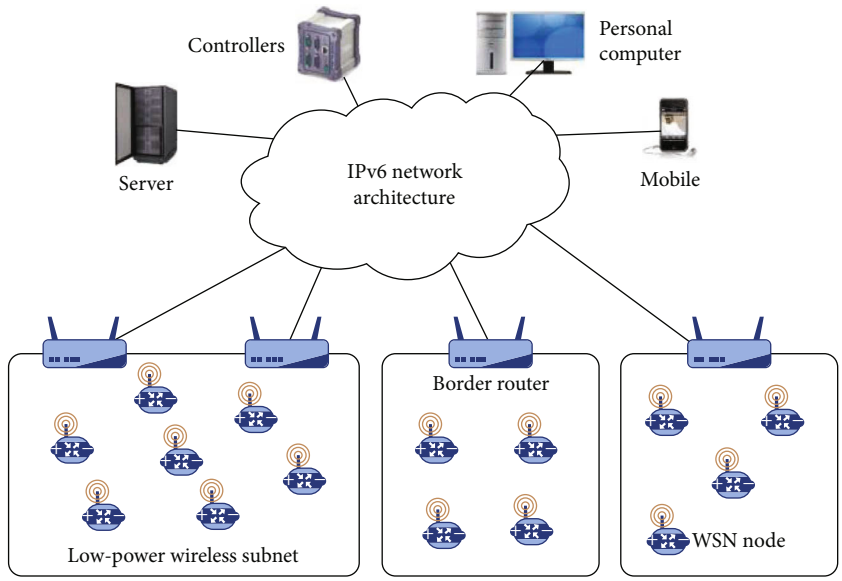

Figure 1: IPv6 network architecture.

(1) Due to the rapid increase of IPv6 traffic, this paper reduces the dimensionality of network traffic characteristics to improve the detection efficiency based on the information gain rate. As a result, it achieves the effect of "dual dimensionality reduction" for discrete features [10, 11]. Furthermore, once the realization of feature selection, discrete type features are partially aggregated, which can further reduce the feature dimension in actual calculations and improve the detection efficiency of DoS attacks in IPv6 networks

(2) Use the information gain rate as the weight of the feature, and use the idea of offset increment average distance to optimize the decision-making method of the KNN algorithm to improve the stability of the KNN algorithm. For example, the GR-AD-KNN (Information Gain Ratio Average Distance KNN) algorithm is used for IPv6 DoS intrusion detection, which optimizes detection performance and reduces the negative impact of "small group classification disadvantages"

2. DoS Attack on IPv6

With the rapid development of the network scale, the number of devices connected to the Internet has skyrocketed, and the original IPv4 network addresses have gradually dried up [12]. Therefore, the birth of the IPv6 network has solved the problem of insufficient addresses [13], and it is also for the Internet of Things. Moreover, it has laid the foundation for developing other industries that require many network addresses. In recent years, the scale of IPv6 networks has continued to expand [14]. The original purpose was to solve the problem of insufficient addresses. Therefore, IPv6 networks have not fundamentally prevented network attacks from occurring. For example, in IPv6 networks, DoS attacks are still a relatively common network intrusion attack [15–17].

Traditional network intrusion detection the software Snort can detect DoS attacks. The detection rules in the literature [18] can be supplemented with honeypot technology logs. However, using many specific rules to detect DoS attacks in network traffic will reduce Snort and execution efficiency of intrusion detection software. To solve the problem of feature selection, literature [19] proposed a feature selection framework, using support vector machine (SVM) and particle swarm optimization (PSO), determined the best detection feature, and realized the effect of DoS attack detection on IPv6 networks. In the new IPv6 environment, network traffic is increasing rapidly, and DoS attacks have not disappeared. The amount of IPv6 network traffic is more significant than traditional IPv4, and it is necessary to detect DoS attacks. The time and amount of calculation will also increase. Therefore, detecting DoS attacks in the IPv6 network should pay attention to the detection performance. It is necessary to select essential features to reduce the feature dimension in the detection process as much as possible. Features can be used for attack detection, but the impact of different features in the actual detection process is also high or low. This article should use machine learning methods to detect DoS attacks on IPv6 networks and use a double dimensionality reduction method. Features are selected, and discrete types of subfeatures are filtered and aggregated. At the same time, the weight of different features is reflected through the information gain rate, which is used in DoS attack detection to improve the adaptability and detection efficiency of the detection system [20, 21].

3. Information Gain

The information gain rate originated from c4.5 algorithms is used in the decision tree splitting process [4]. The decision tree algorithm uses the id3 algorithm based on information

gain, but this will make it easier to choose attributes with more values [5]. Therefore, in some cases, it is not appropriate to use information gain as a reference indicator for feature weights. In a decision tree, in general, the attribute with the more significant information gain rate is closer to the root node, and the impact of such characteristics in the classification process is also more critical [22, 23]. Therefore, this paper uses the information gain rate as an essential evaluation index for feature "dual dimensionality reduction" and uses the information gain rate as the weight to improve the distance to improve the effectiveness of the classification algorithm. The information gain rate is based on the original information gain.

4. KNN Algorithm

The KNN algorithm is one of the commonly used algorithms in machine learning. This algorithm has the characteristics of lightweight classification. SVM algorithm and random forest algorithm need to be trained based on samples first. In the network intrusion detection system to detect DoS attacks, this often requires high timeliness. The KNN algorithm with fast response capability does not need to train the classifier before use, so that this algorithm can be better used for DoS intrusion detection. The implementation process of the traditional KNN algorithm is as follows: First, calculate the distance between the point to be measured and all known types of sample points; second, sort according to the space; finally, based on the nearest k sample points, count the number of sample points in each category, and select one. The class with the most significant number is used as the classification result of the topics to be tested. However, for small group sample points, the classification decision-making disadvantages may occur due to the change of k value during the classification process. At the same time, the traditional KNN algorithm has the same number of reasons for the problem of bias in classification decisions [6].

On the other hand, the use of ordinary Euclidean distance to measure the distance between two points cannot reflect the importance of different features to a certain extent. In literature [10], the analytic hierarchy process is used to assign the feature weights, but the analytical hierarchy process may be subject to a certain degree of subjectivity. Literature [11], based on the information gain rate, gives weighting the Euclidean distance feature in the KNN algorithm thought. Therefore, in this research, this paper improves the deficiencies of the KNN algorithm so that the improved algorithm can be better used for DoS intrusion detection in IPv6 networks.

5. Intrusion Detection Algorithm

5.1. Feature Selection and Dimensionality Reduction. Based on IPv6 network traffic, traffic characteristics can be extracted from it and used to describe changes in network traffic. Network traffic characteristics can be divided into discrete features and continuous features according to types. Among them, discrete features can be divided into discrete digital features and type discrete features. However, if only the original features are selected for feature selection, this is still far from enough. The number of feature dimensions involved in the calculation may also show explosive growth in the actual calculation process. In the execution process of the classification algorithm, the types of discrete features are all. Therefore, it needs to be converted into 0-1 features, which will cause the overall number of dimensions of features to grow rapidly, which will affect the performance of classification and detection to a certain extent. As mentioned before, the traffic in IPv6 networks is growing rapidly, and it should be as accurate as possible to the final. As a result, the actual number of features involved in the calculation is reduced. Therefore, based on IPv6 network traffic characteristics, it is necessary to reduce the original first-level features and reduce the dimensionality of the second-level "type subfeatures" in the type discrete features and thus improve the execution efficiency of later classification.

In this paper, the information gain rate is used as the evaluation index of feature importance. Based on the information gain rate, the function of "double dimension reduction" is realized for the feature. For discrete digital features, the information gain rate of the feature can be directly calculated. However, in the continuous type, in calculating the information gain rate of the feature, it is necessary to discredit the continuous feature first and then calculate the information gain rate of the feature [5]. The following process is the discretization method of the continuous feature.

5.2. GR-AD-KNN Algorithm. In-network DoS intrusion attacks, because some attacks occur less frequently, fewer data can be used for training or detection. On the other hand, to improve the performance of IPv6 network traffic DoS intrusion detection, when detecting, a lightweight classification algorithm should be selected to reduce the time and space costs caused by training. Therefore, a lightweight KNN algorithm that does not need to be trained in advance meets the above requirements.

The traditional KNN algorithm has the problem of "small group classification disadvantage." When the k value is not selected correctly, the algorithm has high sensitivity and poor stability, leading to misjudgments when classifying data of small group types. Therefore, this shortcoming needs to be optimized if you use the KNN algorithm for DoS intrusion detection in an IPv6 network. The original KNN algorithm used the core evaluation indicators to classify samples based on quantity. Although this has a faster detection speed, it brings the problem of "small group classification disadvantage." In the original KNN algorithm classification process, the classification algorithm believes that all sample points have the same value among the most recent k sample points. Therefore, a large sample size group will negatively impact a small sample size group during classification decision-making. In fact, in the classification process, points with different distances from the sample to be tested should have different values in decision-making. Therefore, this article adopts. The idea of offsetting the average length of the increment optimizes the algorithm of the KNN decision-making part.

On the other hand, in the traditional KNN algorithm, Euclidean distance is usually used as an index to measure the distance between two points. Using the idea of the literature, the information gain rate is used to optimize the Euclidean distance calculation of the algorithm ways to improve the influence of essential features and their subfeatures in classification decision-making.

In brief, under the condition that the distance between the point to be measured and the sample point increases at an equal length, the change in the increment of the reverse influence is no longer a similar increase; the farther the distance from the point to be measured is caused by the distance interval, the more significant the growth of the reverse influence. Therefore, the farther the distance of the sample point is, the greater the increased speed of the reverse influence. This requires the overall consistency of the "behavior" of the sample points involved in the classification decision-making process, because issues with a longer distance will have a more "serious" reverse influence on the classification of this category due to a more significant negative impact. Compared with the traditional ordinary average distance algorithm, the above decision method adds each type of sample point and set the idea of "holistic decision-making." Researchers are proposing various protocol schemes [24–28] to maintain integrity, confidentiality, and security of the information shared among users and servers.

6. Experiments and Results

The experimental data set selected for DoS intrusion detection in the IPv6 network is derived from the 10% test set, a training set of the KDDCUP99 [29] data set; the normal type samples and the attack type samples related to DoS attacks are selected. The data specified in this data set features can be divided into TCP basic features, TCP content features, and time-based and host-based network traffic features; therefore, this paper uses this data set to test the algorithm's performance. In addition, through analysis, the number of discrete features in the data set is 9; the number of continuous features is 32. Because the number of samples of some types of attacks in the network is small, in the experiment process, this paper retains all small sample groups; based on the approximate percentage, the approximate ratio is fine-tuned; from different numbers of samples are randomly selected from the large sample group as the data set for this experiment. To verify the classification effect of the algorithm, during the formation of the test set, the sample types that did not exist in the original training set were deleted.

The experiment is mainly divided into two parts. The first part is to realize the double dimensionality reduction of features and calculate the information gain rate of the first-level and second-level features. When calculating the information gain rate of the first-level feature to achieve the dimensionality reduction function, this paper adopts the continuous type. The average value of each feature and discrete feature is used as the filtering threshold. In the secondary non-0-1 discrete subfeature dimensionality reduction and threshold calculation process, only features with many subfeatures are subjected to dimensionality reduction and aggregation operations. For example, in the above data concentrated, features Service and Flag belong to the category of discrete features, and their subfeatures are both 70 and 11, respectively. Therefore, only Service and Flag are considered.

The dimensionality reduction process of Flag's subfeatures; and the feature Protocol type only has three sub-features, so it does not need to participate in the second dimensionality reduction process. The second part of the experiment is to evaluate the performance of the GR-AD-KNN algorithm. In the classification algorithm, in terms of experimental control settings, this article will only compare the GR-KNN algorithm with the weighted optimization of the Euclidean distance and the GR-AD-KNN algorithm. Ten experiments are performed, respectively, and the average F1-Score of the ten experiments is recorded for judgment of the optimization of the algorithm. In terms of the selection of k value, six sets of horizontal control experiments are set up. Finally, to test the overall improvement effect of selecting sample points on the overall improvement of the experimental classification results by comparing the traditional TAD-KNN based on average distance decision-making.

The classification capabilities of the Traditional Average Distance-KNN algorithm and the GR-AD-KNN algorithm are used to count the detection results of attack types with weak detection capabilities to evaluate the improvement and stability of the classification performance of the algorithm. In terms of evaluation indicators, we use the F1-Score indicator to measure the detection performance of the algorithm comprehensively. Among them, the calculation method of the F1-Score indicator is as follows:

$$\mathrm{F1-score} = \frac{\mathrm{Precision} * \mathrm{Recall}}{\mathrm{Precision} + \mathrm{Recall}}. \tag{1}$$

The experiment designed in Section 1 first preprocessed the experimental data set, thereby transforming 41-dimensional traffic features into 122-dimensional features. By implementing one-level dimensionality reduction, the dimensionality of the features is reduced to 106. Then, we reduce the dimensionality of the subfeatures of Service and Flag. Next, we set the size of the parameter bound_number in the secondary dimensionality reduction process to 5. Finally, the dimension of the feature that participates in the classification calculation can be determined to 36. Information obtained by analysis, the gain rate can be used as the weight of different features. Based on Algorithm 1, the secondary dimensionality reduction of Service and Flag features will generate other aggregated subfeatures of their respective categories, namely, subfeatures service_others and subfeature flag_ohters. These two features are in Europe. The calculated weight in the distance is obtained by calculating the average value of the information gain rate of the subfeatures whose class is not selected and the information gain rate is nonzero.

This paper conducts a control experiment on the GR-KNN algorithm and the GR-AD-KNN algorithm. It sets up

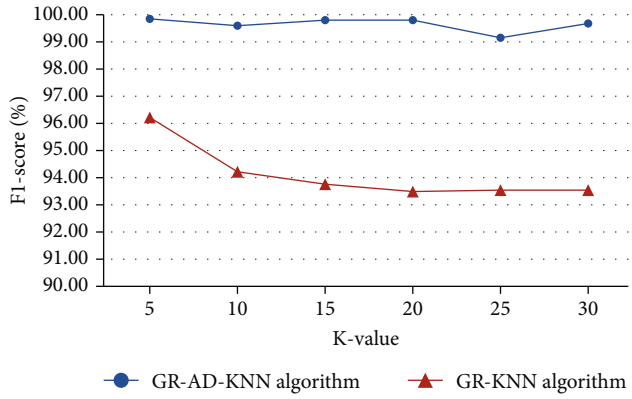

Figure 2: GR-KNN algorithm and GR-AD-KNN algorithm detection.

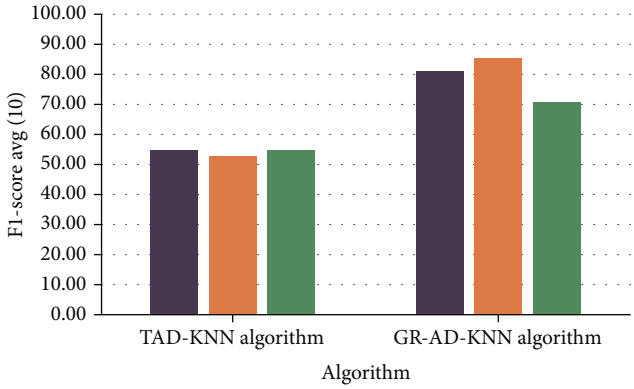

Figure 3: Ten average F1-Score detection results of Teardrop attack.

six horizontal control experiments with k, respectively [6, 8, 15, 28, 30, 31], and records the experimental results. At the same time, before the algorithm performance comparison experiment starts, the data in the two data sets are normalized, respectively. The specific experimental comparison results are shown in Figure 2.

It can be seen from Figure 2 that the experimental classification results of the GR-AD-KNN algorithm are better. At the same time, the GR-AD-KNN algorithm is less sensitive to the value of k, thereby reducing the algorithm's strictness of selecting the value of k and reducing the factor the negative impact of excessive sensitivity caused by model parameter adjustment. On the other hand, this paper compares the detection performance of the traditional TAD-KNN algorithm based on the average Euclidean distance and the GR-AD-KNN algorithm. For example, when k is 5, we conducted three rounds of experiments independently, and each round of experiments included ten detection experiments. Finally, the average value of 10 detection results of F1-Score with Teardrop's attack type in each game was counted, as shown in Figure 3.

Through experiments, it can be found that when comparing the performance of the two algorithms to detect the Teardrop attack type, the GR-AD-KNN algorithm has a better detection effect for the Teardrop attack type, which can show that the optimized algorithm can improve the original detection ability. Therefore, the optimized KNN algorithm for DoS intrusion detection in the IPv6 network has better classification results and detection performance.

7. Conclusion

This article uses the IPv6 network DoS intrusion attack technology as the research background and the information gain rate. To evaluate the quality of network features, the double dimensionality reduction method is used to achieve the effect of feature dimensionality reduction and improve the classification execution efficiency of the later classification algorithm. In terms of classification algorithms, this article will improve the KNN algorithm GR-AD-KNN. The algorithm is used in the field of DoS attack detection. Based on the weight provided by the information gain rate, making different characteristics have different degrees of influence is realized. Based on the idea of the offset increment average distance, the point to be measured is improved. It is recognized that the effect of different long and short distance sample points on decision-making is different, and the algorithm's stability is improved. The problem of "small group classification disadvantages" is alleviated. Therefore, the above research has a better effect on realizing DoS intrusion detection in IPv6 network strong theoretical significance.

Data Availability

The data used to support the findings of this study are available from the author upon request (kusumasyadav0@gmail.com).

Conflicts of Interest

The authors declare that they have no conflicts of interest.

References

[1] A. Altaher, S. Ramadass, and A. Ali, "A dual stack IPv4/IPv6 testbed for malware detection in IPv6 networks," in *2011 IEEE International Conference on Control System, Computing and Engineering*, pp. 168–170, Penang, Malaysia, 2011.

[2] D. Gu, Y. Xue, D. Wang, Z. Luo, and B. Yan, "Improving IPv6 transition management with IPv6 network virtualization," in *2017 9th International Conference on Advanced Infocomm Technology (ICAIT)*, pp. 95–104, Chengdu, 2017.

[3] S. Praptodiyono, R. K. Murugesan, R. Budiarto, and S. Ramadass, "Handling transmission error for IPv6 packets over high speed networks," *First International Conference on Distributed Framework and Applications*, vol. 2008, pp. 159–163, 2008.

[4] R. Kumar and G. Dhiman, "A comparative study of fuzzy optimization through fuzzy number," *International Journal of Modern Research*, vol. 1, 2021.

[5] I. Chatterjee, "Artificial intelligence and patentability: review and discussions," *International Journal of Modern Research*, vol. 1, pp. 15–21, 2021.

[6] P. K. Vaishnav, S. Sharma, and P. Sharma, "Analytical review analysis for screening COVID-19," *International Journal of Modern Research*, vol. 1, pp. 22–29, 2021.

[7] C. -W. Tseng, L. -F. Wu, S. -C. Hsu, and S. -W. Yu, "IPv6 DoS attacks detection using machine learning enhanced IDS in SDN/NFV environment," in *2020 21st Asia-Pacific Network Operations and Management Symposium (APNOMS)*, pp. 263–266, Daegu, Korea (South), 2020.

[8] A. K. Al-Ani, M. Anbar, A. Al-Ani, and D. R. Ibrahim, "Match-prevention technique against denial-of-service attack on address resolution and duplicate address detection processes in IPv6 link-local network," *IEEE Access*, vol. 8, pp. 27122–27138, 2020.

[9] J. N. Goel and B. M. Mehtre, "Dynamic IPv6 activation based defense for IPv6 router advertisement flooding (DoS) attack," *IEEE International Conference on Computational Intelligence and Computing Research*, vol. 2014, pp. 1–5, 2014.

[10] G. Dhiman and V. Kumar, "Spotted hyena optimizer: a novel bio-inspired based metaheuristic technique for engineering applications," *Advances in Engineering Software*, vol. 114, pp. 48–70, 2017.

[11] G. Dhiman and V. Kumar, "Emperor penguin optimizer: a bio-inspired algorithm for engineering problems," *Knowledge-Based Systems*, vol. 159, pp. 20–50, 2018.

[12] N. R. Samineni, F. A. Barbhuiya, and S. Nandi, "Stealth and semi-stealth MITM attacks, detection and defense in IPv4 networks," in *2012 2nd IEEE International Conference on Parallel, Distributed and Grid Computing*, pp. 364–367, Solan, India, 2012.

[13] R. K. Murugesan, S. Ramadass, and R. Budiarto, "Increased performance of IPv6 packet transmission over ethernet," in *2009 2nd IEEE International Conference on Computer Science and Information Technology*, pp. 171–175, Beijing, China, 2009.

[14] R. K. Murugesan and S. Ramadass, "IPv6 address distribution: an alternative approach," in *2010 3rd IEEE International Conference on Broadband Network and Multimedia Technology (IC-BNMT)*, pp. 252–257, Beijing, China, 2010.

[15] M. Huang, J. Liu, and Y. Zhou, "An improved SEND protocol against DoS attacks in mobile IPv6 environment," *IEEE International Conference on Network Infrastructure and Digital Content*, vol. 2009, pp. 232–235, 2009.

[16] L. He and K. He, "Efficient memory-bounded optimal detection for GSM-MIMO systems," *IEEE Transactions on Communications*, vol. 69, no. 1, pp. 101–112, 2021.

[17] L. He and K. He, "Learning-based signal detection for MIMO systems with unknown noise statistics," *IEEE Transactions on Communications*, vol. 69, no. 5, pp. 3025–3038, 2021.

[18] K. Kishimoto, K. Ohira, Y. Yamaguchi, H. Yamaki, and H. Takakura, "An adaptive honeypot system to capture IPv6 address scans," *International Conference on Cyber Security*, vol. 2012, pp. 165–172, 2012.

[19] M. Yang and T. Li, "A RDO-PSO algorithm for anycast routing with multi-QoS constraints," in *2009 4th International Conference on Computer Science & Education*, pp. 376–379, Nanning, 2009.

[20] L. Chen, "Intelligent ubiquitous computing for future UAV-enabled MEC network systems," *Cluster Computing*, 2021.

[21] L. Chen, "A fog assisted intelligent framework based on cyber physical system for safe evacuation in panic situations," *Computer Communications*, vol. 178, no. 1, pp. 297–306, 2021.

[22] W. Zhou, "PSO based offloading strategy for cache-enabled mobile edge computing UAV networks," *Cluster Computing*, vol. 2021, no. 24, 2021.

[23] S. Tang and L. Chen, "Computational intelligence and deep learning for next-generation edge-enabled industrial IoT," *IEEE Trans Network Science and Engineering*, vol. 8, no. 1, pp. 114–125, 2021.

[24] S. Du and J. Li, "Parallel processing of improved KNN text classification algorithm based on Hadoop," in *2019 7th international conference on information, Communication and Networks (ICICN)*, pp. 167–170, Macao, Macao, 2019.

[25] H. Song, E. Zhu, and L. Ma, "Design of embedded real-time target tracking system based on KNN algorithm," in *2020 IEEE 9th Joint International Information Technology and Artificial Intelligence Conference (ITAIC)*, pp. 443–446, Chongqing, China, 2020.

[26] A. A. Bahashwan, M. Anbar, I. H. Hasbullah, Z. R. Alashhab, and A. Bin-Salem, "Flow-based approach to detect abnormal behavior in neighbor discovery protocol (NDP)," *IEEE Access*, vol. 9, pp. 45512–45526, 2021.

[27] M. A. Lawal, R. A. Shaikh, and S. R. Hassan, "A DDoS attack mitigation framework for IoT networks using fog computing," *Procedia Computer Science*, vol. 182, pp. 13–20, 2021.

[28] P. Kushwaha, H. Buckchash, and B. Raman, "Anomaly based intrusion detection using filter based feature selection on KDD-CUP 99," in *TENCON 2017 - 2017 IEEE Region 10 Conference*, pp. 839–844, 2017.

[29] V. Alieksieiev and B. Andrii, "Information analysis and knowledge gain within graph data model," in *2019 IEEE 14th International Conference on Computer Sciences and Information Technologies (CSIT)*, pp. 268–271, 2019.

[30] H. Sukarman, F. Y. Rizkiyana, and M. F. A. F. Apriyanto, "The design of information system and technology strategy for improving performance of healthcare service with EA3 framework: (case study: summit)," in *2020 International Conference on Information Management and Technology (ICIMTech)*, pp. 788–793, Bandung, Indonesia, 2020.

[31] M. Soni, G. Dhiman, B. S. Rajput, R. Patel, and N. K. Tejra, "Energy-effective and secure data transfer scheme for mobile nodes in smart city applications," *Wireless Personal Communications*, 2021.

Hindawi
Wireless Communications and Mobile Computing
Volume 2021, Article ID 3834550, 10 pages
https://doi.org/10.1155/2021/3834550

Research Article

Interior Design Scheme Recommendation Method Based on Improved Collaborative Filtering Algorithm

Wei He

School of Design and Art, Xijing University, Xi'an, Shaanxi 710123, China

Correspondence should be addressed to Wei He; 20070044@xijing.edu.cn

Received 20 October 2021; Revised 8 November 2021; Accepted 17 November 2021; Published 23 December 2021

Academic Editor: Junjuan Xia

The recommendation engine is similar to the function of the product recommender in our real life, which provides great convenience for people to choose the appropriate decoration scheme in the process of interior design and decoration. A home improvement website or company can design a suitable recommendation algorithm to provide home improvement program recommendation services for users with decoration needs. After understanding the user behavior of the home decoration website, this paper proposes an interior design scheme recommendation method based on an improved collaborative filtering algorithm. The method designs a collaborative filtering algorithm that combines multilayer hybrid similarity and trust mechanisms. Fuzzy set membership function is introduced to correct users' rating similarity, and users' interest vector is extracted to calculate users' preference for different types of items. The algorithm dynamically fuses those two aspects to obtain the mixed similarity of users; meanwhile, the user's hybrid similarity and trust are fused in an adaptive model. Then, the user neighbor data set generated based on the overall similarity of users is used as a training set, taking the item scores and features into consideration. On the one hand, the users and the projects are taken into account as well. The final prediction score is more accurate, and the recommendation effect is better. The experimental results show that this method can recommend interior design schemes with high performance, and its performance is better than other methods.

1. Introduction

With the sustained and rapid growth of China's national economy and the increasing per capita income, coupled with the strong promotion of China's real estate industry, the demand of our interior design and decoration industry has remained strong. The rapid development of the Internet has also promoted people's participation and demand on the Internet. The number of Internet users has increased to a considerable degree. Online shopping has penetrated into every aspect of our daily life. Amazon, Taobao, Jingdong and many other websites are relatively successful and mature e-commerce platforms, while home decoration e-commerce has not yet become mature. As the online shopping experience of home decoration is not high, users' purchasing desire is not strong. While the consumption of home decoration is increasingly hot in recent years, it is relatively backward in e-commerce [1].

The domestic decoration market economy scale has exceeded 4 trillion yuan. The number of home decoration consumers is huge, but the proportion of online shopping in the total consumption of the home decoration market is relatively small. Home decoration websites record behavior logs of hundreds of millions of users [2]. However, the main task of this paper is how to automatically locate and push the home decoration scheme that users are interested in from the massive information.

A home outfit plan covers the design idea of the stylist. When it is accepted and adopted by decoration users, the plan will involve the interests of users themselves, furniture companies, decoration companies, designers, home decoration websites, and other aspects [3]. The server can record user behavior logs when users browse, click, or download home decoration solutions. If their favorite home decoration scheme from the growing user behavior log can be dug out and recommended to users, the decoration needs of users

will be met and a good reputation be established, with more value being brought to home decoration websites and related enterprise chains.

The online behavior of the home outfit industry is moving towards scale gradually. Literatures [4, 5] have begun to design home decoration products based on user perception. Literature [6] proposes a new method to extract and retrieve furniture items from image databases and online websites containing multiple furniture items. This method supports finding similar items from the database. Consumers usually pay the most attention to the pictures, prices, and brand reputation evaluation of home improvement programs when shopping online for home improvement [7]. Poor user experience and the fact of not being able to find a satisfactory home improvement plan within a certain period of time are major weaknesses of domestic home improvement online consumption, which bring huge economic loss to home outfit network shopping. The recommendation system is a good solution. However, the problems of massive log processing efficiency and recommendation accuracy brought by the rapidly increasing number of users are important factors restricting the application of the recommendation system.

The concept of the recommendation system, which was gradually applied to the commercial field after a period of time, was first formally proposed by Varian and Resnick. Nowadays, recommendation has developed into a very popular research field [8]. Collaborative filtering algorithm is widely used in the research of recommendation system algorithm [9]. However, it is found that the traditional collaborative filtering algorithm still has many problems to be improved with the deepening of research [10]. Researchers have studied the improved algorithm. The key to the improved algorithm in Ref. [11] was the calculation of semantic similarity and the acquisition of similarity word frequency weight. Reference [12] proposed an improved metric. The method considers the ratio between the absolute score value and the number of common scoring items. Literature [13] proposed that the recommendation results could be more reliable by mining the potential relationship between rating users. By comprehensively analyzing the user's historical behavior and item label information, literature [14] realized the recommendation of label probability without relying on the user's item score. Literature [15] used genetic algorithm to find the best item list for users. Most of the objects studied by these recommendation algorithms are for music, movies and digital products, etc., but there are few recommendation system algorithms specifically for the consumption behavior of home decoration websites. And it is even rarer to apply the recommendation algorithm to practical applications. Literature [16] mentioned interior design recommendation technology based on collaborative filtering algorithm. The literature only gives a framework, but does not give the actual recommendation algorithm and application.

Aiming at the above problems, this paper applies the improved collaborative filtering algorithm to the design of interior design recommendation technology. This method provides accurate interior design recommendation service for users by integrating user behavior and project behavior. Interior design recommendation technology has low operational requirements for users and plays an important role in enhancing user experience. The results show that the proposed method solves the limitations of the current interior design project recommendation method, and it is a project recommendation method with high precision and high speed.

2. Related Research

The collaborative filtering (CF) algorithm uses past behavior or the opinions of existing user groups to predict data and also uses neighborhood data similar to the current user or project to generate recommendations. The basic steps include data collection and processing, generation of a user-item score matrix, calculation of similarity, generation of the nearest neighbor, prediction of score, and generation of a top N recommendation.

2.1. User-Based Collaborative Filtering Algorithm (UserCF). Firstly, the score data set and the current user ID are entered to find other users with similar preferences to the current user. These users are called nearest neighbors. Then, the ratings of all items are ranked from highest to lowest using the ratings of the neighbor user-predicted items. Finally, the top N items are recommended to the current user. The algorithm flow in this paper is shown in Figure 1.

Similarity measurement is the core of the collaborative filtering algorithm, including cosine similarity, modified cosine similarity, and Pearson similarity. Pearson correlation coefficient is used to calculate the linear correlation between two variables, and the formula is as follows:

$$\text{correlation}(m,n)=\frac{\sum_{k\in I_{mn}}(s_{mk}-\bar{s}_m)\times(s_{nk}-\bar{s}_n)}{\sqrt{\sum_{k\in I_{mn}}(s_{mk}-\bar{s}_m)^2}\times\sqrt{\sum_{k\in I_{mn}}(s_{nk}-\bar{s}_n)^2}}, \tag{1}$$

where $\text{correlation}(m,n)$ represents the similarity between users m and n. I_{mn} represents the set of goods jointly rated by users m and n, while s_{mk} and s_{nk} represent the scores on goods k. $\bar{s}_m$ and $\bar{s}_n$ represent the average rating of the product by users m and n, respectively.

The scoring prediction formula is defined as follows:

$$P_{mk}=\bar{s}_m+\frac{\sum_{n\in I_m}\text{sim}(m,n)\times(s_{nk}-\bar{s}_n)}{\sum_{n\in I_m}\text{sim}(m,n)}, \tag{2}$$

where $\bar{s}_m$ represents the average score of all rated products by target user m. I_m indicates the neighbor set of the target user. s_{nk} represents the neighbor user's rating of item k. $\bar{s}_n$ represents the average value of ratings of the items rated by the neighbor users. $\text{sim}(m,n)$ indicates the similarity between the target user and the neighbor user.

Although the UserCF algorithm has been widely used in the field of recommendation, it also faces many challenges. For e-commerce websites, the number of projects is relatively stable, but the number of users is updated at a high

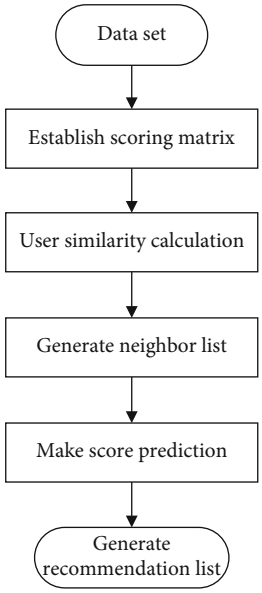

Figure 1: User-based collaborative filtering algorithm flow.

frequency. When the number of users is much larger than the number of items, computing similarities between users becomes increasingly time-consuming and takes up more memory. The recommendation results generated by UserCF algorithms are poorly interpretable.

2.2. Item-Based Collaborative Filtering Algorithm (ItemCF). Firstly, an item similarity matrix is constructed to describe the similarity between two items. k nearest neighbor projects similar to the current project are found. The user score for each item m not seen by the current user is then calculated based on k nearest neighbors. Finally, the user's ratings for all items are sorted from large to small, and the top N items with the highest scores are recommended to the current user.

The basic steps of the item-based collaborative filtering algorithm (ItemCF) are processing data, generating user-item score matrix, computing item similarity, generating nearest neighbor, predicting score, and generating top N recommendation.

Then, cosine similarity is used to calculate the similarity between the two items. In addition, based on the k nearest neighbor projects acquired, the current user's interest in the target project is predicted.

3. Interior Design Scheme Recommendation Based on Improved Collaborative Filtering Algorithm

The traditional collaborative filtering recommendation algorithm only generates recommendations based on the user's historical score data. CF only considers scoring data, which not only is incomplete but also leads to cold start problems. This makes new projects or new users unable to recommend according to the collaborative filtering recommendation algorithm. At the same time, it will also bring serious data sparsity problems and affect the accuracy of recommendation results. Therefore, this paper presents an interior design scheme recommendation method based on an improved collaborative filtering algorithm. This method considers multidimensional mixed similarity, trust mechanism, and item scoring, which make the final prediction score more accurate and the recommendation effect better.

3.1. User Feature Extraction. For users or interior design projects, they all have their own characteristics. In the design process of the indoor project design project recommendation method based on the improved collaborative filtering algorithm, the user characteristics have a certain stability. For two users with similar characteristics, the probability of selecting similar interior design projects is higher. Firstly, the characteristics of interior design users are described, and then, they are quantified.

For the gender characteristics of interior design users, "1" represents male and "-1" represents female, while the gender and age characteristics of interior design users are quantified by "0-4," where "0" represents under 30 years old, "1" represents 30-39, "2" represents 39-44, "3" represents 45-60, and "4" represents over 60 years old. The occupation and education level are also quantified by numbers, which will not be described in detail here.

3.2. Design of Multidimensional Similarity and Trust Measurement

3.2.1. Revise Score Similarity. In the recommendation system, the score of an item reflects the user's preference for the item to a certain extent. At this point, the measurement of preference degree is determined by the user rating value. But the ratings are not an accurate representation of how much users like them. For example, a movie is scored on a 5-point scale. User i gives a score of 4. At this time, the user's preference for the movie cannot be accurately quantified in numerical form. It can only roughly predict the probability that user i likes the movie with high probability. To solve the problem of measuring the degree of preference in this situation, this paper adopts the fuzzy logic method to enrich the single numerical score, so as to obtain the numerical quantification of user preference. The membership function definition of scoring triangle fuzzy set is shown in Figure 2.

$$\begin{aligned} \varphi_{\text{good}}(z) &= , \quad 1 \le z \le 5, \\ \varphi_{\text{bad}}(z) &= , \quad 1 \le z \le 5. \end{aligned} \tag{3}$$

The calculation of preference difference between any two users depends on the rating difference between them for the common rated items. The greater the difference in ratings, the greater the degree of preference difference between them. The preference difference can be calculated by formula (3). Based on this inference, the preference similarity of any two users calculated by using public

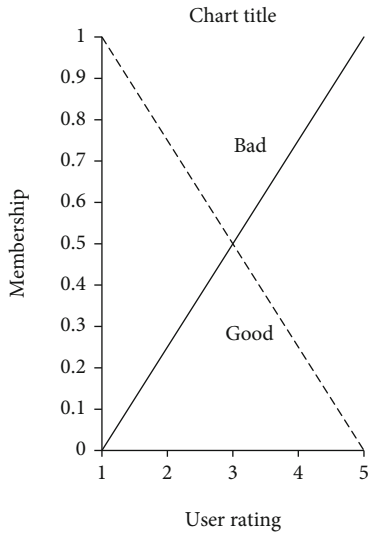

Figure 2: Membership function of scoring triangular fuzzy.

Table 1: MAE values under different interest vector weights.

ε	10	20	30	40	50	60
0	0.7550	0.7418	0.7338	0.7310	0.7249	0.7233
0.1	0.7540	0.7420	0.7351	0.7317	0.7256	0.7237
0.2	0.7549	0.7397	0.7346	0.7313	0.7243	0.7228
0.3	0.7559	0.7389	0.7349	0.7330	0.7257	0.7237
0.4	0.7549	0.7409	0.7349	0.7308	0.7260	0.7231
0.5	0.7570	0.7418	0.7349	0.7317	0.7244	0.7226
0.6	0.7539	0.7408	0.7358	0.7320	0.7239	0.7218
0.7	0.7559	0.7398	0.7366	0.7297	0.7249	0.7208
0.8	0.7569	0.7420	0.7367	0.7289	0.7259	0.7229
0.9	0.7598	0.7428	0.7397	0.7318	0.7290	0.7249
1	0.7605	0.7467	0.7427	0.7376	0.7347	0.7307

items is represented by $\mathrm{Ps}(m, n)$.

$$\begin{aligned} \mathrm{dis}(r_{m\mathrm{com}} - r_{n\mathrm{com}}) &= \sqrt{\sum_{k=1}^{K} \left(r_{m\mathrm{com}}^{k} - r_{n\mathrm{com}}^{k}\right)^2}, \\ \mathrm{diff}(\bar{m}, n) &= , \\ \mathrm{Ps}(m, n) &= \frac{1}{\left(1 + \mathrm{diff}(\bar{m}, n)\right)}, \end{aligned} \tag{4}$$

where $r_{m\mathrm{com}}$ and $r_{n\mathrm{com}}$ represent the fuzzy preferences of any two users m and n. k represents the kth element of vector $r_{m\mathrm{com}}^{k}$. K represents the dimension of the vector. $\mathrm{dis}(r_{m\mathrm{com}} - r_{n\mathrm{com}})$ represents the Euclidean distance between vectors. $\mathrm{diff}(\bar{m}, n)$ is used to represent the mean difference degree of the scoring preference.

In the calculation of the user rating similarity $\mathrm{sim}_a(m, n)$, user preference modified by introducing fuzzy mapping is combined with the Jaccard similarity of modified rating. This balances the dimensions of the user to the item and the proportion of items in the common rating among users. Finally, the user's score similarity is calculated based on the user's modified cosine similarity.

Table 2: MAE values under different dynamic weights.

ω	10	20	30	40	50	60
0	0.7797	0.7597	0.7500	0.7444	0.7409	0.7387
0.1	0.7771	0.7580	0.7484	0.7432	0.7399	0.7371
0.2	0.7731	0.7578	0.7479	0.7416	0.7390	0.7369
0.3	0.7710	0.7548	0.7459	0.7416	0.7372	0.7348
0.4	0.7720	0.7537	0.7436	0.7390	0.7356	0.7336
0.5	0.7699	0.7528	0.7428	0.7386	0.7342	0.7325
0.6	0.7659	0.7488	0.7417	0.7375	0.7327	0.7295
0.7	0.7636	0.7459	0.7375	0.7351	0.7318	0.7281
0.8	0.7566	0.7467	0.7363	0.7321	0.7295	0.7258
0.9	0.7599	0.7469	0.7366	0.7316	0.7288	0.7248
1	0.7608	0.7479	0.7399	0.7368	0.7343	0.7284

$$\mathrm{sim}_a(m, n) = \mathrm{sim}(m, n)^{\mathrm{Adcos}} \times \mathrm{Ps}(m, n) \times \mathrm{Jaccard}, \tag{5}$$

where $\mathrm{Jaccard} = |I_m \cap I_n| / |I_m \cup I_n|$. I_m and I_n represent the set of rated items for users m and n.

3.2.2. User Interest Similarity. The traditional collaborative filtering algorithm only considers the user's project score value and ignores the similarity of the user's interest to different project types. However, users' interest similarity affects the recommendation accuracy of projects to a great extent. In the case of sparse data, there are few common scoring items among users, or even zero. At this point, user interest similarity evaluated based on project type can compensate for the impact of data sparsity to a large extent.

The calculation of the user's interest degree is affected by the scoring value of different item types and the proportion of quantity. For example, it is known that the user is interested in comedy and romance movies by analyzing and calculating a user's movie viewing history. Then, when a movie of a related type appears, it can be inferred that the user has a greater possibility to like the movie. The user interest vector $\mathrm{interest}_{m,n}$ is defined as the user's preference degree for different types of items based on the above deduction. The composition of the interest vector includes the proportion of the scoring value and the proportion of the scoring quantity of each item type.

$$\begin{aligned} \mathrm{avg}_m(q) &= \frac{\sum_{m \in I_q} R_{m,c}}{|I_q|}, \\ \mathrm{interest}_{m,n} &= \varepsilon \frac{\mathrm{avg}_m(q)}{\sum_{z \in Q} \mathrm{avg}_m(z)} + (1 - \varepsilon) \frac{N_q}{N}, \end{aligned} \tag{6}$$

where $\mathrm{avg}_m(q)$ represents the average score of a certain type of item. $R_{m,c}$ represents the score of a certain type of item. I_q represents the number of scoring for this type of item. Q represents the collection of all types of items. z represents a certain type of items. N_q represents the number of scoring

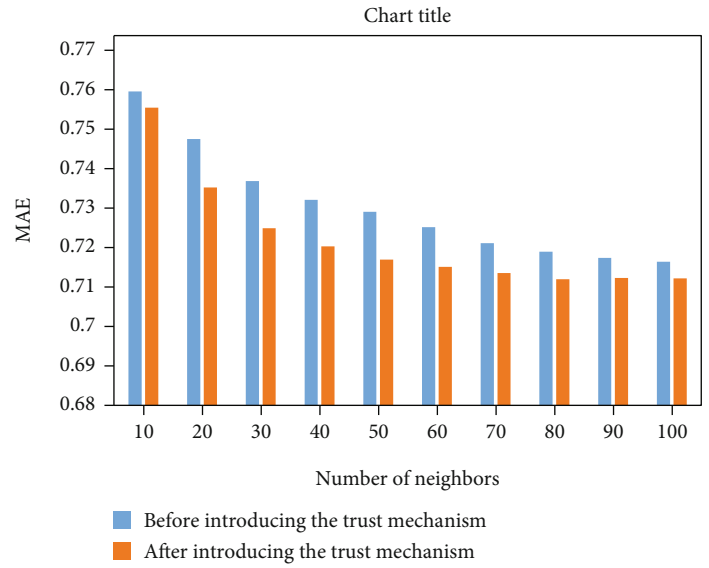

Figure 3: Comparison of MAE before and after introducing trust mechanism.

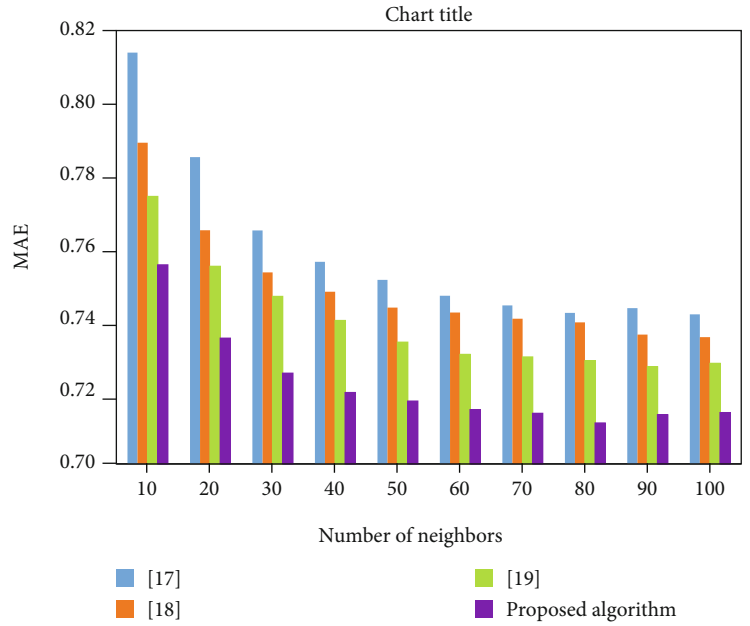

Figure 4: Comparison of MAE values of different algorithms.

statistics for q-type items. N represents the number of all scores. ε represents the weight of interest.

At the same time, using the user's interest vector combined with the cosine similarity calculation formula, the user interest similarity can be calculated for any two users m and n.

$$\mathrm{sim}_b(m,n) = \frac{\sum_{q\in Q} \mathrm{interest}_{m,q} \times \mathrm{interest}_{n,q}}{\sqrt{\sum_{q\in Q} \mathrm{interest}_{m,q}^2} \times \sqrt{\sum_{q\in Q} \mathrm{interest}_{n,q}^2}}, \quad (7)$$

where Q represents the set of all item types.

3.2.3. Users' Mixed Similarity. In summary, the similarity obtained by the two is merged to obtain the user mixed similarity. The calculation of the two similarities is affected by the sparsity of the data in different degrees: when the number of public ratings is small, the measurement of the rating scale is susceptible to the impact of the peak of the rating, resulting in large errors in the calculation results. The interest similarity obtained based on the item type is less affected by the peak score, so the weight of the latter should be increased at this time. When the number of public scoring items is large, the accuracy of the recommendation results calculated based on user scoring is higher, so the proportion of scoring similarity should be increased at this time.

Therefore, the threshold $d1$ of the number of public scores is set. According to the $d1$ size, the balanced distribution weight of the two in the case of different data sparsity is adjusted to ensure the accuracy and flexibility of the algorithm.

$$\mathrm{sim}_{\mathrm{mix}}(m,n)=\begin{cases}\omega\dfrac{N_u}{d1}\mathrm{sim}_a(m,n)+\left(1-\omega\dfrac{N_u}{d1}\right)\mathrm{sim}_b(m,n),\\ N_u<d1,\\ \omega\mathrm{sim}_a(m,n)+(1-\omega)\mathrm{sim}_b(m,n),\\ N_u\geq d1,\end{cases}\tag{8}$$

where $\mathrm{sim}_{\mathrm{mix}}(m,n)$ represents the user mixed similarity. N_u represents the number of user scores. ω is the fusion factor. $\mathrm{sim}_a(m,n)$ represents corrected score similarity. $\mathrm{sim}_b(m,n)$ represents user interest similarity.

3.2.4. The Degree of Trust between Users. The analysis indicates that the trust relationship between users plays a vital role in daily life, involving all aspects. However, the description of trust is a relatively vague concept, whose cognition includes subjectivity, asymmetry, and dynamics. Traditional recommendation algorithms only consider from the point of view of scoring. But in real life, the recommendation accuracy obtained only by this method is difficult to guarantee. For example, some merchants falsify rating data to get more recommendations for their products. To reduce the impact of recommendation results on the accuracy of the scoring data, this paper introduces the trust mechanism between users. The higher the reliability between users, the higher the reliability of the recommendation data generated by them.

The trust degree between two users in the recommendation system is influenced by the interactive relationship between users. The more shared historical behavior users experience, the more trust they accumulate between each other. It is considered that there has been an interaction whenever the scoring behavior of the same item occurs between users. The interaction relationship between users can be obtained according to the proportion between the interaction times and their own historical scoring times.

$$\mathrm{IT}(m,n)=,\tag{9}$$

where I_m and I_n represent the set of scoring items of users m and n, respectively. $|I_m|$ and $|I_n|$ represent the potential of the set.

The trust degree between users is affected by the interaction relationship and the interaction state. A successful interaction state is bound to strengthen trust between users. Similarly, the failed interaction state will also weaken the trust between users. This section takes the user satisfaction status as the standard to measure the success of interaction. If two users show satisfaction or dissatisfaction with a project at the same time, their interaction state will be considered to be successful. If two users have different satisfactions with the jointly evaluated items, their interaction state will be considered to be a failure. Satisfaction is calculated by comparing the scores of two users' common items with their respective average scores. If the score is higher than their own average score, it means satisfaction; otherwise, it means dissatisfaction.

The interaction states between users are as follows.

$$S(m,n)=\begin{cases}\mathrm{sus},\ (r_{m\mathrm{com}}-\bar{r}_m)(r_{n\mathrm{com}}-\bar{r}_n)\geq 0,\\ \mathrm{fal},\ (r_{m\mathrm{com}}-\bar{r}_m)(r_{n\mathrm{com}}-\bar{r}_n)<0,\end{cases}\tag{10}$$

where sus represents the statistical times of successful interaction. sus + 1 is recorded for each successful interaction. fal indicates the statistical number of failed interactions. We record fal + 1 for each interaction failure. The interaction relationship between users is calculated in combination with formula (11) to obtain the user.

$$\mathrm{ITP}(m,n)=\mathrm{IT}(m,n)\times\frac{\mathrm{sus}}{\mathrm{sus}+\mathrm{fal}}.\tag{11}$$

In the above formula, the success or failure of the interaction is considered to have the same degree of influence on trust, yet the actual situation is different. In the case of interaction failure, the difference between the two users' scores is much larger than that in the case of interaction success, which indicates that there is a great difference between the two users' satisfaction with the common score item. Therefore, it can be argued that the negative effects of failed interactions are greater. In the revision of trust degree, the score difference is added as the penalty weight affecting the interaction balance to strengthen the negative impact of failed interaction. The improved trust between users is as follows.

$$\mathrm{IDP}(m,n)=\mathrm{IT}(m,n)\times\sum_{e\in I_{\mathrm{sus}}}\mathrm{sus}|r_{me}-r_{ne}|,\\ \sum_{e\in I_{\mathrm{sus}}}\mathrm{sus}|r_{me}-r_{ne}|+\sum_{e\in I_{\mathrm{fal}}}\mathrm{fal}|r_{me}-r_{ne}|,\tag{12}$$

where $\mathrm{IDP}(m,n)$ represents the trust degree of user m to user n. I_{sus} represents the set of successful interactions. I_{fal} represents the set of interaction failures. r_{me} and r_{ne} represent the scores of user m and user n on item e, respectively. Formula (9) satisfies the asymmetric principle of trust, that is, $\mathrm{IDP}(m,n)\neq\mathrm{IDP}(n,m)$.

If the hybrid similarity between target user m and target user n is higher, and m feels that n is trustworthy, then m is more likely to adopt n's suggestion. Therefore, when establishing the neighbor user set U_s, the hybrid similarity and trust degree are arranged in reverse order according to the value, and the top k users with the highest comprehensive value are selected to establish the neighbor user set. The prediction score $P_{m,e}$ is generated.

$$P_{m,e}=\bar{r}_m+\frac{\sum_{n\in U_s}\theta\mathrm{sim}_{\mathrm{mix}}(m,n)+(1-\theta)\mathrm{IDP}(m,n)(r_{n,e}-\bar{r}_n)}{\sum_{n\in U_s}|\mathrm{sim}_{\mathrm{mix}}(m,n)+(1-\theta)\mathrm{IDP}(m,n)|}.\tag{13}$$

In the formula, the value of θ is determined by the adaptive model, and the value range of θ is [0,1].

$$\theta = \frac{\text{sim}_{\text{mix}}^2(m,n)}{\text{sim}_{\text{mix}}^2(m,n) + \text{IDP}(m,n)^2(m,n)}. \tag{14}$$

3.3. Improved Algorithm Based on the Item and Its Characteristics. Section 3.2 generates neighbor data according to multidimensional user scores and user characteristic data. However, the similarity of project features is not taken into account; besides, the recommendation accuracy is not very good. In this section, multidimensional user similarity and trust are used to generate user neighbor data sets as training sets, and item scores and features are taken into account to improve the traditional slope one algorithm. Users and items are taken into account, which make the final prediction score more accurate and the recommendation effect better. The calculation method of item feature similarity is similar to that of user feature similarity.

$$\begin{aligned} \text{Dis}(m,n) &= \sqrt{\sum_{l=1}^{L}(m_l - n_l)^2}, \\ \text{SimItem}(m,n) &= \frac{1}{1+\text{Dis}(m,n)}. \end{aligned} \tag{15}$$

In the formula above, L represents the number of attribute features of the item. m_l represents the lth attribute of item m. n_l represents the lth attribute value of item n. The similarity of item features is calculated as the method of calculating the similarity of similar user features.

Item similarity is also calculated by the Pearson formula.

$$\text{SimItem}(m,n) = \frac{\sum_{v=1}^{V}(R_{v,m} - A_m) \times (R_{v,n} - A_n)}{\sqrt{\sum_{v=1}^{V}(R_{v,m} - A_m)^2 \times \sum_{v=1}^{V}(R_{v,n} - A_n)^2}}. \tag{16}$$

In the formula, A_m refers to the average score of all users' nearest neighbors of user v on item m. V is the number of recent neighbors for all items of project m. $R_{v,n}$ refers to the score of user v on item n. $\text{SimItem}(m,n)$ refers to the score similarity of item m and item n.

Based on the recommendation set of the user's nearest neighbor set, the item's nearest neighbor set is calculated, and the recommendation is finally generated.

$$p(v)_n = \frac{\sum_{m=1}^{V}(1/\text{card}(R_n))\sum_{m\in R_n}(\text{dev}_{m,n} + v_m) \times \text{SimItem}(m,n)}{\sum_{m=1}^{V}\text{SimItem}(m,n)}, \tag{17}$$

where $\text{card}(R_n)$ represents the number of elements in R_n. $\text{dev}_{m,n}$ represents the average deviation between items m and n. v_m represents user v's rating of item m.

3.4. Recommended Steps for Interior Design Schemes to Improve Collaborative Filtering Algorithm. Step 1: collect the relevant historical data of indoor project design and process it to remove some wrong data.

Step 2: extract the user features and project features of interior project design, which form the corresponding feature set. Then, mark all users and scoring data in the matrix.

Step 3: by introducing the fuzzy logic method, the user's fuzzy preference is obtained by enriching the score difference between users. Then, the score similarity is modified based on fuzzy preference differences. The user modified score similarity $\text{sim}_a(m,n)$ is obtained by combining the Jaccard similarity coefficient.

Step 4: calculate the proportion between the mean scores of various types of items and the sum of the mean scores of all items, as well as the ratio between the scoring times of various items and the total scoring times of items. The sum of the two is calculated to obtain the user's interest vector. Combined with cosine similarity, $\text{sim}_b(i,j)$ of user interest similarity is calculated.

Step 5: calculate the similarity between Step 3 and Step 4 based on different factors. The weight fusion is carried out by combining formula (8) to obtain the mixed similarity $\text{sim}_{\text{mix}}(m,n)$. Considering that only using the predicted score generated by $\text{sim}_{\text{mix}}(m,n)$ for project recommendation may lead to the problem of single recommendation factor and poor recommendation accuracy, the trust relationship between users is introduced on this basis. The first k users with the highest comprehensive value are obtained to establish the neighbor user set.

Step 6: use multidimensional user similarity and trust to generate user neighbor data set as the training set. Formula (17) is used to score items.

Step 7: arrange the predicted scores in descending order and recommend the top N interior items with the highest predicted scores to the target users for the projects not scored by the target users.

4. Experimental Results

4.1. Experimental Data and Experimental Environment. Some interior design item data sets are used as test objects to test the performance of collaborative filtering technology in the interior design project recommendation method proposed in this paper.

In the researches on the collaborative filtering algorithm, most of them use the MovieLens website data set maintained by the GroupLens laboratory. This data set contains more comprehensive user rating information of movies covering all time points. And it is still being maintained at present. In this paper, the historical behavior data of users are processed into the same format with reference to the MovieLens data set. The data set of user rating on the design scheme, which is recorded by the icolor server of the company's project background home decoration website for one month, is selected as the experimental data. The data set contains 12,829,401 scoring information of 16,427 home decoration design schemes by 13,512 website users, ranging from 1 to 5 points.

The experimental environment settings are as follows: (1) hardware environment: Intel 7 core CPU @ 2.69 GHz,

12 GB memory; (2) software environment: Win10 operating system with Java programming language.

4.2. Experimental Indicators. In most studies, the commonly used indicators are as follows, which are applied to measure the effect of the collaborative filtering algorithm conveniently.

The mean absolute error (MAE) is the average of the absolute values of errors. It uses the deviation between the item score predicted by the recommendation algorithm and the user's actual score value to measure the accuracy of the recommendation. The range of this value is [0,1]. The smaller the MAE value, the higher the accuracy of the recommendation algorithm and the better the recommendation quality.

$$\mathrm{MAE} = \frac{1}{\mathrm{num}(R)} \sum_{m \in R} (p_{vm} - r_{vm}). \tag{18}$$

4.3. Analysis of Experimental Results

4.3.1. Determination of Interest Vector Weight ε. Interest vector weight α is mainly used to adjust the ratio between different types of items and the total score value and adjust the ratio between the number of different types of items and the total score items. By adjusting the proportion of the two, different interest vectors $\mathrm{interest}_{m,n}$ can be obtained. Then, interest similarity between users is calculated according to interest vector $\mathrm{sim}_b(m, n)$. During the experiment, ε increases with a step size of 0.1, and the value range is [0,1]. The neighbor set $\mathrm{Nei}_{\mathrm{col}}$ takes 10 steps and ranges from 10 to 60. Multiple groups of predicted scores are generated according to the calculation, and the MAE of the corresponding real score and predicted score is obtained. The statistical results are shown in Table 1.

It can be seen from Table 1 that MAE decreases with the increase of the number of neighbor sets, indicating that the recommendation accuracy is significantly affected by data sparsity. As can be seen from Table 2, when $k = 60$ and $\varepsilon = 0.7$, the average absolute error between the predicted score and the real score is minimum and reaches the optimal value. Therefore, the unknown parameter ε is 0.7.

4.3.2. Determination of Fusion Factor ω. The function of dynamic fusion factor ω is to dynamically adjust the proportion of two similarity algorithms in mixed similarity according to the difference of data sparsity. In the experiment, the number of neighbor sets k and fusion factor ω is uniformly changed by step size, and the change curves of multiple sets of prediction scores and MAE are calculated. The experimental results are shown in Table 2.

It can be seen from Table 2 that as the number of neighbor sets increases, the MAE difference decreases gradually. When the set number k is 60 and the dynamic factor ω is 0.9, MAE obtains the optimal value, so $\omega = 0.9$ in this paper.

4.3.3. Comparison of Algorithm Performance before and after Introducing Trust Mechanism. The smaller the MAE value obtained by the two algorithms before and after the introduction of trust mechanism, the higher the accuracy of the algorithm. According to the optimal values $\varepsilon = 0.7$ and $\omega = 0.9$ obtained in experiment 1, the neighbor user sets before and after the introduction of trust mechanism are obtained. The neighbor set number k is incremented with the step size of 10, and two MAE groups corresponding to the two algorithms are calculated. The experimental results are shown in Figure 3.

It can be seen from the analysis in Figure 3 that with the increase of the number of neighbor users, the MAE change trend obtained by the algorithm after the introduction of trust mechanism shows a downward trend from sharp to slow compared with the algorithm before the introduction. It can be seen that this algorithm has higher recommendation accuracy when the data sparsity is high. With the increase of the number k of neighbor users, the accuracy of the algorithm with trust mechanism is improved to a certain extent compared with the algorithm without the trust mechanism. This verifies that the trust mechanism is introduced to optimize the performance of the algorithm.

4.3.4. Comparison of Accuracy between the Proposed Algorithm and Other Algorithms. The accuracy comparison of several algorithms also adopts the method of comparative experiment. The comparative algorithms include the collaborative filtering recommendation algorithm with cosine similarity correction score in literature [17], the collaborative filtering algorithm based on improved time function and user similarity proposed in literature [18], and the collaborative filtering recommendation algorithm based on heuristic similarity measurement in literature [19]. MAE corresponding to each algorithm was calculated. The experimental results are shown in Figure 4.

The MAE of the proposed algorithm is smaller than that of the other three algorithms. The experimental results are analyzed as follows.

By introducing user interest, trust mechanism and item score, the algorithm in this paper has obvious advantages in the case of data sparsity compared with other algorithms. When $k = 10$, MAE of this algorithm is 0.7551. Compared with literature [17–19], MAE of the proposed algorithm is reduced by 7.23%, 4.30%, and 2.45%, respectively. When the number of neighbor users increase, the recommendation accuracy of each algorithm is improved to varying degrees. When the number of neighbor sets $k = 80$, MAE of this algorithm gets the minimum value, reaching 0.7113. Compared with literature [17–19], MAE of the proposed algorithm is reduced by 4.12%, 3.78%, and 2.37%, respectively. In conclusion, compared with other collaborative filtering algorithms, the recommendation accuracy of the proposed algorithm is significantly improved, and the performance improvement of recommendation accuracy is more obvious in the case of data sparsity.

5. Conclusion

Interior design, the quality of which is critical, is the current hot spot. Therefore, the recommendation method of the interior design item has become a highly concerned issue.

Due to the shortcomings of current interior design recommendation methods such as large errors and long time consumption, an interior design project recommendation method based on an improved collaborative filtering algorithm was designed to obtain ideal interior design project recommendation results. The following conclusions can be drawn from the experimental data. (1) Due to the fusion of multilayer hybrid similarity, trust mechanism, and extraction of interior design item features, the algorithm in this paper can achieve an accurate recommendation of interior design projects, and its performance is better than that of other algorithms. This algorithm controls the error rate of interior design project recommendation within the scope of practical application, solving the problem of high error rate in current interior design project recommendation methods. (2) The interior design item recommendation method based on improved collaborative filtering technology can be applied to solving problems with similar characteristics in other fields, which has very wide application value. In the future research work, it is necessary to focus on the problem of starting the algorithm. Moreover, we will incorporate some intelligent algorithms such as deep learning, federated learning, and mobile edge computing techniques into the considered system [20–27], in order to further enhance the system performance.

Data Availability

The labeled data set used to support the findings of this study is available from the corresponding author upon request.

Conflicts of Interest

The author declares no competing interests.

Acknowledgments

This study was supported by the Scientific Research Program of Shaanxi Provincial Department of Education: Research on the Innovative Application of Chinese Traditional Decorative Elements in Urban Public Space—Taking Xi'an as an Example (No. 19jk0896).

References

[1] Y. Yu, X. Wang, R. Y. Zhong, and G. Q. Huang, "E-commerce logistics in supply chain management," *Industrial Management & Data Systems*, vol. 117, no. 10, pp. 2263–2286, 2017.

[2] L. Haibing and K. Yuyue, "Business model innovation of Qingdao Youzhu Decoration Company," *EDP Sciences*, vol. 214, article 02046, 2020.

[3] Y. S. Chang, K. J. Hu, C. W. Chiang, and A. Lugmayr, "Applying mobile augmented reality (AR) to teach interior design students in layout plans: evaluation of learning effectiveness based on the ARCS model of learning motivation theory," *Sensors*, vol. 20, no. 1, pp. 105–130, 2020.

[4] S. Zhong, P. Tan, T. Fu, and Y. Ji, "Product design model for E-commerce Cantonese porcelain based on user perceptual image in China," in *Human-Computer Interaction. Human Values and Quality of Life. HCII 2020*, Lecture Notes in Computer Science, M. Kurosu, Ed., pp. 350–364, Springer, Cham, 2020.

[5] J. Zhang, X. Hu, Z. Ning et al., "Energy-latency tradeoff for energy-aware offloading in mobile edge computing networks," *IEEE Internet of Things Journal*, vol. 5, no. 4, pp. 2633–2645, 2018.

[6] S. R. Pardhi and K. H. Wanjale, "Extraction and retrieval of furniture from designing decoration and furniture database," in *2017 International Conference on Computer Communication and Informatics (ICCCI)*, pp. 1–6, IEEE, Coimbatore, India, 2017.

[7] X. Xu, "Home decoration comprehensive application web design and analysis," *International Journal of Science*, vol. 6, no. 4, pp. 36–41, 2019.

[8] Z. Cui, X. Xu, F. Xue et al., "Personalized recommendation system based on collaborative filtering for IoT scenarios," *IEEE Transactions on Services Computing*, vol. 13, no. 4, pp. 685–695, 2020.

[9] X. Chen, S. Li, H. Li, S. Jiang, Y. Qi, and L. Song, "Generative adversarial user model for reinforcement learning based recommendation system," in *International Conference on Machine Learning*, pp. 1052–1061, Long Beach, California, USA, 2019.

[10] L. Jiang, Y. Cheng, L. Yang, J. Li, H. Yan, and X. Wang, "A trust-based collaborative filtering algorithm for E-commerce recommendation system," *Journal of Ambient Intelligence and Humanized Computing*, vol. 10, no. 8, pp. 3023–3034, 2019.

[11] B. Hong and M. Yu, "A collaborative filtering algorithm based on correlation coefficient," *Neural Computing and Applications*, vol. 31, no. 12, pp. 8317–8326, 2019.

[12] M. Ayub, M. A. Ghazanfar, T. Khan, and A. Saleem, "An effective model for Jaccard coefficient to increase the performance of collaborative filtering," *Arabian Journal for Science and Engineering*, vol. 45, no. 12, pp. 9997–10017, 2020.

[13] S. Jiang, S. C. Fang, Q. An, and J. E. Lavery, "A sub-one quasi-norm-based similarity measure for collaborative filtering in recommender systems," *Information Sciences*, vol. 487, pp. 142–155, 2019.

[14] Z. Ning, X. Hu, Z. Chen et al., "A cooperative quality-aware service access system for social Internet of vehicles," *IEEE Internet of Things Journal*, vol. 5, no. 4, pp. 2506–2517, 2017.

[15] B. Alhijawi and Y. Kilani, "A collaborative filtering recommender system using genetic algorithm," *Information Processing & Management*, vol. 57, no. 6, article 102310, 2020.

[16] Z. Li, "Interior design recommendation technology based on collaborative filtering algorithm," *Modern Electronics Technique.*, vol. 43, no. 13, pp. 176–179, 2020.

[17] R. Zhang and X. Qian, "A collaborative filtering recommendation algorithm with revised rating by cosine similarity," *Computer Engineering and Science.*, vol. 42, no. 6, pp. 1096–1105, 2020.

[18] W. Zhang, X. Zhou, and W. Yuan, "Collaborative filtering algorithm based on improved time function and user similarity," *Journal of physics: conference series*, vol. 1757, no. 1, article 012080, 2021.

[19] R. Shaw, D. K. Agrawal, and B. K. Patra, "An effective similarity measure for improving performance of user based collaborative filtering," in *IEEE EUROCON 2021-19th International Conference on Smart Technologies*, pp. 209–215, Lviv, Ukraine, 2021.

[20] J. Xia and D. Deng, "A note on implementation methodologies of deep learning-based signal detection for conventional MIMO transmitters," *IEEE Transactions on Broadcasting*, vol. 66, no. 3, pp. 744-745, 2020.

[21] L. He and K. He, "Efficient Memory-Bounded Optimal Detection for GSM-MIMO Systems," *IEEE Transactions on Communications*, vol. 69, no. 1, pp. 101–112, 2021.

[22] H. Xiping, J. Cheng, M. Zhou et al., "Emotion-aware cognitive system in multi-channel cognitive radio ad hoc networks," *IEEE Communications Magazine*, vol. 56, no. 4, pp. 180–187, 2018.

[23] W. Zhou, "PSO based offloading strategy for cache-enabled mobile edge computing UAV networks," *Cluster Computing*, vol. 2021, no. 24, pp. 1–13, 2021.

[24] L. Chen, "Intelligent ubiquitous computing for future UAV-enabled MEC network systems," *Cluster Computing*, vol. 2021, no. 25, pp. 1–10, 2021.

[25] L. He and K. He, "Towards optimally efficient search with deep learning for large-scale MIMO systems," *IEEE Transactions on Communications*, no. 99, pp. 1–12, 2022.

[26] S. Tang and L. Chen, "Computational intelligence and deep learning for next-generation edge-enabled industrial IoT," *IEEE Transactions on Network Science and Engineering*, no. 99, pp. 1–12, 2022.

[27] L. Chen, "Physical-layer security on mobile edge computing for emerging cyber physical systems," *Computer Communications*, no. 99, pp. 1–10, 2022.

Hindawi
Wireless Communications and Mobile Computing
Volume 2021, Article ID 5344890, 14 pages
https://doi.org/10.1155/2021/5344890

Research Article

Human Detection via Image Denoising for 5G-Enabled Intelligent Applications

Hui Li,[1] **Hang Zhou**,[1] **Xiaoguo Liang**,[1] **Fen Cai**,[2] **Lingwei Xu**,[1,2,3] **Wei Kong**,[1] **and Ying Guo**[1]

[1]*School of Information Science and Technology, Qingdao University of Science and Technology, Qingdao 266000, China*
[2]*Fujian Provincial Key Laboratory of Data Intensive Computing, Quanzhou, 362000 Fujian, China*
[3]*Key Laboratory of Computer Network and Information Integration (Southeast University), Ministry of Education, Nanjing, 211189 Jiangsu, China*

Correspondence should be addressed to Lingwei Xu; xulw@qust.edu.cn

Received 9 September 2021; Revised 6 October 2021; Accepted 28 October 2021; Published 23 November 2021

Academic Editor: Junjuan Xia

5G technology strongly supports the development of various intelligent applications, such as intelligent video surveillance and autonomous driving. And the human detection technology in intelligent video surveillance has also ushered in new challenges. A number of video images will be compressed for efficient transmission; the resulting incomplete feature representation of images will drop the human detection performance. Therefore, in this work, we propose a new human detection method based on compressed denoising. We exploit the quality factor in the compressed image and incorporate the pixel_shuffle inverse transform based on FFDNet to effectively improve the performance of image compression denoising, then HRNet and HRFPN are used to extract and fuse high-resolution features of denoised images, respectively, to obtain high-quality feature representation, and finally, a cascaded object detector is used for classification and bounding box regression to further improve object detection performance. At last, the experimental results on PASCAL VOC show that the proposed method effectively removes the compression noise and further detects human objects with multiple scales and different postures. Compared with the state-of-the-art methods, our method achieved better detection performance and is, therefore, more suited for human detection tasks.

1. Introduction

With the emergence and development of 5G technology [1], it is widely used for data transmission, wireless communication, and other intelligent applications such as intelligent video surveillance and industrial Internet of Things [2–4]. Therefore, some researchers attempt to exploit deep learning technology to solve some problems in wireless communication [5] and industrial Internet of Things [6–8]. Besides, there are still many serious challenges in terms of human detection for intelligent video surveillance, a large number of images are processed by the JPEG compression algorithm for efficient transmission and storage, and the compression noise generated by this process causes image distortion, feature loss, and decrease in human detection performance. Although traditional denoising methods such as BM3D [9] and BM4D [10] and deep neural network denoising methods such as UDNet [11] and CBDNet [12] have achieved effective denoising to a certain extent, the denoising performance still needs to be improved. Besides, though the method based on deep learning for human detection can achieve more robust detection results than traditional methods like HOG [13] +SVM [14], and DPM [15], it still needs to further improve its detection accuracy for objects with small objects and variable scales [16, 17]. To solve the above problems, we propose a new human detection method based on image compression denoising. What is more, our method is evaluated and demonstrated on the PASCAL VOC benchmark datasets. Compared with the state-of-the-art methods, our method can achieve better detection performance after denoising and is, therefore, more suited for human detection tasks. The code will be released.

2. Related Work

Recently, in the field of denoising, the traditional methods based on manual design rules have limited capabilities; however, the deep learning technology based on the convolutional neural network (CNN) has made significant progress in the problem of image denoising [18]. For blind noise, DnCNN [19] is inspired by the idea of learning the residual of the mapping in the residual network instead of mapping itself to generate a noise map instead of the image after denoising, which can be widely applied to various noises. And for nonblind noise, FFDNet [20] adopts the noise level as a feature map and forwards it to the network together with the noise image after pixel_shuffle [21] inverse transformation, making full use of the noise level information. What is more, some scholars attempt to employ the Generative Adversarial Networks (GANs) proposed by Goodfellow and Pouget-Abadie [22] for the remarkable results in the field of image generation to denoise an image [23–26]. The core idea is to exploit MAE or MSE to retain the low-frequency part of the image, and then, it exploits GAN to restore the high frequency part of the image, but GAN is difficult to train and easily crashes during the training process. Yu et al. [27] attempt to incorporate reinforcement learning, resulting in a restoration algorithm RL-restore for a variety of degradation situations of universal images. Lehtinen et al. [28] investigated that for noise with expectation 0, it is possible to train a denoising network containing only dirty data noise to obtain clean images, using these images as an example.

In the object detection algorithm, the object detection method based on deep learning can obtain more robust detection results than traditional methods [29]. What is more, it has gradually formed a two-stage detection method based on the candidate region and a one-stage detection method based on regression. The two-stage object detection method based on the candidate region is mainly represented by the R-CNN series of algorithms. In R-CNN [30], selective search is first used to obtain the proposal region on the original image, then the original image is cropped according to the proposal region, then it is scaled to a fixed size to forward it into the convolutional neural network for extracting features, and finally, the support vector machine (SVM) is used for classification and bounding box prediction. Fast R-CNN [31] convolves the entire image to obtain a feature map and then performs other operations. Faster R-CNN [32] has changed the selective search to the region proposal network, which became an end-to-end training framework. Cascade R-CNN [33] is aimed at the problem that Faster RCNN only has single object detector, which leads to its poor detection performance. Therefore, the object detector is cascaded to improve the quality of prediction. On the other hand, although the one-stage detection method based on regression has lower accuracy than the two-stage detection method, it has a significant increase in speed. The one-stage detection method is represented by the YOLO [34, 35] and SSD [36] algorithms. It exploits only single CNN to directly predict the category and locate different objects in an end-to-end manner. However, if the object scale has changed, the detection results will have poor robustness. Therefore, Lin et al. propose Feature Pyramid Networks (FPN) [37], by fusing different levels of the feature map, so that a low-level feature map has strong semantic information and high-resolution characteristics to achieve high-quality detection of small object and multiscale object. In addition, HRNet [38] and HRFPN [39] improve on the common problem that an image's feature is first extracted and then restored to ensure feature extraction always maintains a high-resolution feature map.

Furthermore, Carion et al. [40] regard object detection as a direct set prediction problem and propose an end-to-end detection framework based on the encoder-decoder of transformer; Shen et al. [41] exploit residual structure and spatial sensitive entropy to reduce the negative impact of web images with noisy labels to a certain extent; Dai et al. [42] propose a dynamic detection head framework by unifying attention and object detection head; Wang et al. [43] propose a prediction-aware one-to-one label assignment to replace nonmaximum suppression postprocessing and achieve performance comparable to NMS.

However, each of the existing techniques in the literature has its limitations when used to include image denoising and human detection in complex scenes. Our approach here is to alleviate these difficulties. The contributions of our work are twofold.

Firstly, we establish a new denoising framework, which exploits the improved ResNet18 to extract the quality factor in the compressed image and then combines the pixel_shuffle inverse transform based on the FFDNet to effectively execute compression denoising.

Secondly, we introduce HRNet and HRFPN to extract and fuse high-resolution features of the denoised image, respectively, to obtain a high-quality feature representation of the object. And then, we exploit the cascaded object detector to classification and bounding box regression to make the inferred object box more accurate and further improve the object detection performance.

3. Method

Based on the characteristics of compressed noise and the existing problems of human detection, we deeply research the human detection algorithm with compressed noise images. In this paper, firstly, we obtain the denoised image based on deep learning technology; we establish a joint optimization solution for image noise removal and human detection by combining the extraction and fusion of high-quality features and gradually improving the human object estimation. It not only improves the subjective feeling of the image and the quantifiable performance index but also improves the performance of human detection (including the accuracy of classification and bounding box). A flowchart of the proposed framework is shown in Figure 1.

3.1. Human Image Compression Denoising. The image compression denoising method based on the convolutional neural network mainly consists of three steps, that is, noisy

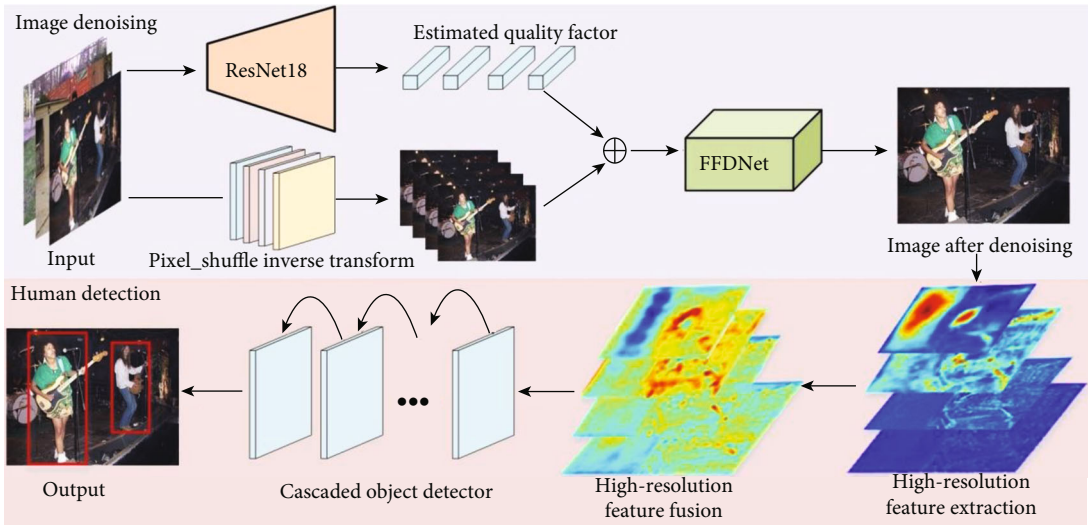

Figure 1: Flowchart of the proposed framework.

images are generated by lossy compression, quality factor estimation, and image denoising. Firstly, the JPEG compression algorithm is used to generate the training data with noise, then the value of the quality factor is estimated from the noisy image by the quality factor estimation network, and finally, original image containing noise and estimated quality factor values are used to form a set of feature maps as input to get the final image after denoising. And a flowchart of human image compression denoising is shown in Figure 2.

3.1.1. Image Lossy Compression. JPEG [44] (Joint Photographic Experts Group) compression algorithm is the most commonly used image compression algorithm on the Internet. It contains both lossy and lossless compression. What is more, lossy compression can be roughly divided into three processes: discrete cosine transform (DCT), quantization, and entropy coding. Discrete cosine transform is a process of transforming the image signal in the frequency domain to separate high-frequency and low-frequency information. The one-dimensional discrete cosine transform formula is as follows:

$$F(u) = c(u)\sum_{i=0}^{N-1} f(i)\cos\left[\frac{(i+0.5)\pi}{N}u\right],$$
$$c(u)\begin{cases}\sqrt{\frac{1}{N}}, & u=0,\\ \sqrt{\frac{2}{N}}, & u\neq 0,\end{cases} \tag{1}$$

where $f(i)$ is the vector to be converted, N is the vector length, and $c(u)$ is the coefficient of change. And the discrete cosine transform formula of a two-dimensional image is as follows:

$$F(u,v) = c(u)c(v)\sum_{i=0}^{N-1}\sum_{j=0}^{N-1} s(i,j)\cos\left[\frac{(i+0.5)\pi}{N}u\right]\cos\left[\frac{(j+0.5)\pi}{N}v\right], \tag{2}$$

where $f(i,j)$ is the pixel value of point (i,j) and $c(u)$ and $c(v)$ are transformation coefficients. To speed up calculation, the restrictions are the same as formula (1). For the discrete cosine transform in an image, N is usually set to 80. Similarly, the calculation in formula (2) is usually completed in the form of a matrix to speed up the calculation:

$$A(i,j) = c(i)\cos\left[\frac{(j+0.5)\pi}{N}i\right], \tag{3}$$

where $c(i)$ is the inverse discrete cosine transform coefficient, and iterative traversal operation is turned into a parallel matrix operation through the calculated matrix $A(i,j)$. The corresponding inverse transformation formula is as follows:

$$f(i,j) = \sum_{i=0}^{N-1}\sum_{j=0}^{N-1} c(u)c(v)F(u,v)\cos\left[\frac{(i+0.5)\pi}{N}u\right]\cos\left[\frac{(j+0.5)\pi}{N}v\right], \tag{4}$$

where $c(u)$ and $c(v)$ are the inverse discrete cosine transform coefficients and $F(u,v)$ is the frequency value of point (u,v). Since $A(i,j)$ is orthogonal, the matrix operation of the inverse discrete cosine transform is as follows:

$$f = A^{-1}F\left(A^{T}\right)^{-1} = A^{T}FA, \tag{5}$$

where A is the transformation matrix. Because inverse discrete cosine transform is lossless, therefore, it can restore

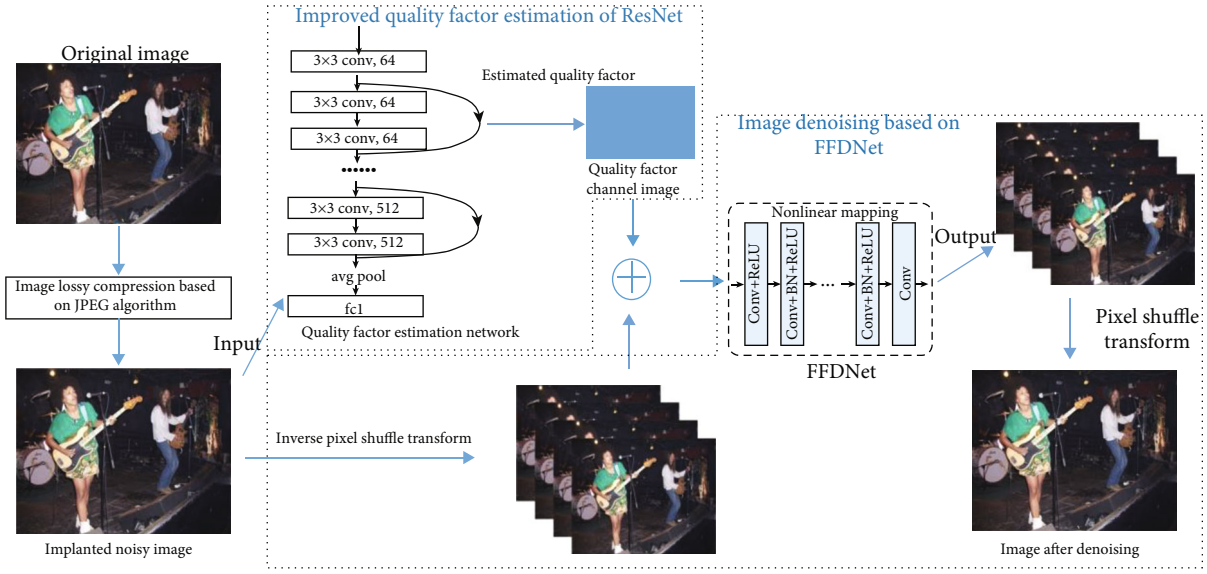

Figure 2: Flowchart of human image compression denoising.

the representation of the frequency domain to the pixel domain without loss.

Quantization is the only process that causes information loss in the JPEG algorithm. Since JPEG compresses the high-frequency part of image (i.e., image details) to reduce data, the image data are quantized and rounded to approximate values, which are different from the original image data, resulting in a permanent loss of information. Discrete cosine transform and quantization are both prepared for encoding. After the encoding is completed, the image compression is truly realized.

3.1.2. Quality Factor Estimation. In addition to standard R, G, and B channels, FFDNet can also receive noise channel N. Therefore, when the JPEG algorithm compresses an image to provide data for the noise channel, we exploit ResNet [45, 46] to learn the quality factor parameters; the quality factor is a key parameter that determines the degree of image distortion. However, estimating the quality factor from the noisy image is the task of regression; it is impossible to employ ResNet for classification directly. Therefore, we utilize the improved ResNet18 as the quality factor estimation network. The comparison diagram of the ResNet18 structure before and after the improvement is shown in Figure 3. The input is an image with compression noise, and the output is the estimated quality factor of each image. It contains a total of 17 convolutional layers and 1 fully connected layer. It uses a 3×3 convolution kernel and a convolution operation with a step size of 1. The number of convolution kernels for the first time is 64, and then, the step size becomes 3 at the 6, 10, and 14 layers; the number of convolution kernels is doubled. The last layer is a fully connected layer, which changes the number of neurons to 1, and there is an average pooling operation between the convolutional layer and the fully connected layer. The activation function of all activation layers in the improved ResNet18 is a ReLU function, and the improved function is shown in the following formula:

$$\mathrm{ReLU} = \begin{cases} x, & x > 0, \\ 0, & x \le 0. \end{cases} \tag{6}$$

(1) Loss Function. It is a regression problem to estimate the quality factor of the compressed image with an unknown quality factor during compression. Therefore, the most common square loss is used as the loss function. The square loss function is expressed as follows:

$$L(Y, f(X)) = \sum_{i=1}^{N} (Y - f(X))^2, \tag{7}$$

where X is the image with noise, f is the noise estimation network, $f(X)$ is the noise estimation value, and Y is the true value of the noise.

3.1.3. Image Denoising Network. Image denoising is mainly twofold: noise image preprocessing, and FFDNet denoising and generating an image postprocessing.

(1) Noise Image Preprocessing. To improve the denoising performance of the FFDNet, the noise image needs to be preprocessed. Firstly, the pixel_shuffle inverse conversion operation is executed, then the length and width of the original image P (C, W, H) is halved, and the number of channels becomes four times the original, i.e., the original image P is transformed into a tensor T1 with the shape $(4 * C, W/2, H/2)$, where C is the number of original image channels (the number of RGB color image channels is 3, and the gray image is 1), W is the width of the image, and H is the height of the image. Then, the quality factor estimated by the improved ResNet18 is used as a channel, and the shape of the tensor T2 forming the channel is $(1, W/2, H/2)$, and each value in it is a quality factor. Combining the

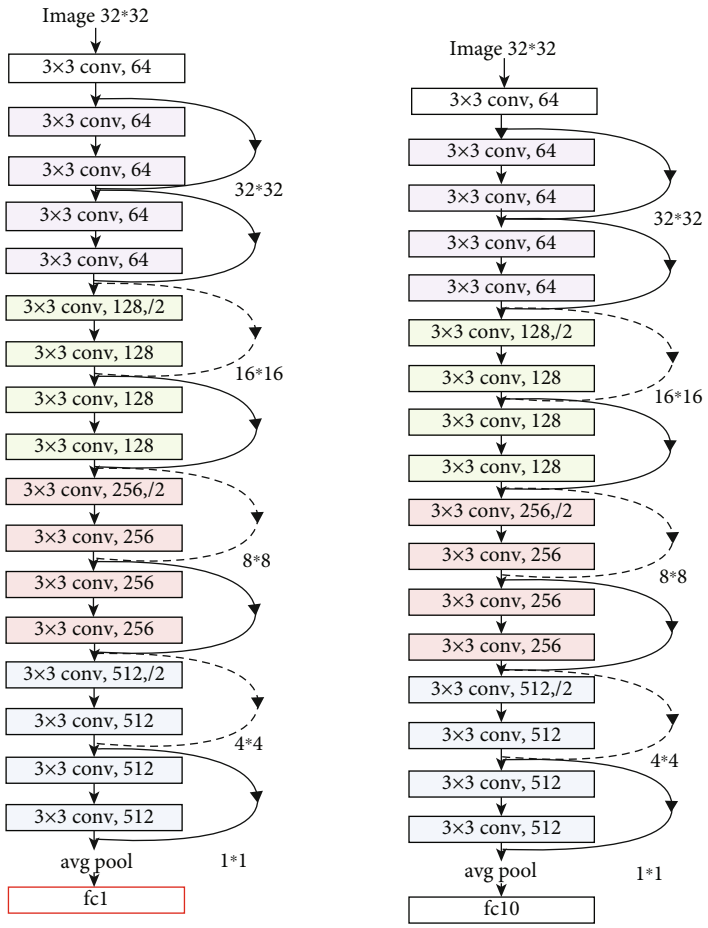

Figure 3: Comparison of ResNet18 network structure before and after improvement.

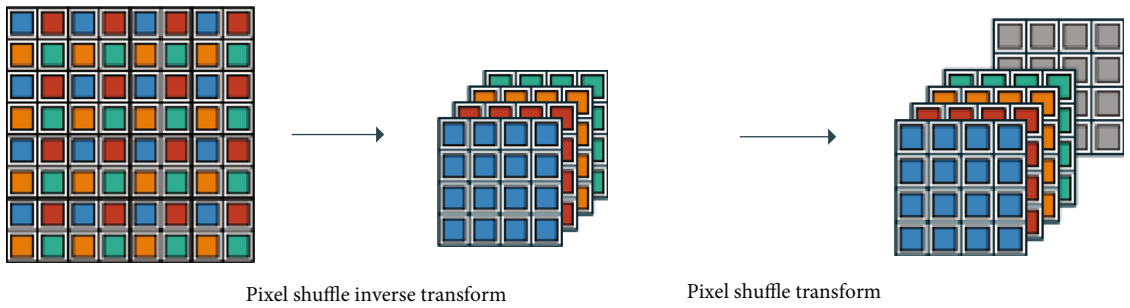

Figure 4: Flowchart of noise image preprocessing.

image pixel_shuffle inverse transformation, the $C * 4$ channel tensor and the tensor formed by the quality factor are concated, and the final tensor is $(C * 4 + 1, W/2, H/2)$. The schematic diagram of this process is shown in Figure 4.

(2) FFDNet Denoising and Image Postprocessing. The preprocessed noisy image is sent to the FFDNet. FFDNet is a fully convolutional network [47], which can generate clean images through end-to-end training. Its structure is shown in Figure 5. The network consists of $N + 2$ convolutional layers: the first convolutional layer uses ReLU as the activation function; each of the middle N layers has a convolutional layer, a BatchNormal layer, and a ReLU activation function. The last layer has only one convolutional layer without the BatchNormal layer and any activation function and directly outputs the denoised tensor. The direct result of the FFDNet output is a tensor of $(4C, W/2, H/2)$, not an image. In order to restore the tensor back to an image, a pixel_shuffle transformation is needed to restore $(C * 4, W/2, H/2)$ to (C, W, H), and this is the final denoised image.

(3) Loss Function. In the denoising stage of FFDNet, the absolute value loss is used as the loss function. The reason is that the square loss will blur the generated image for the

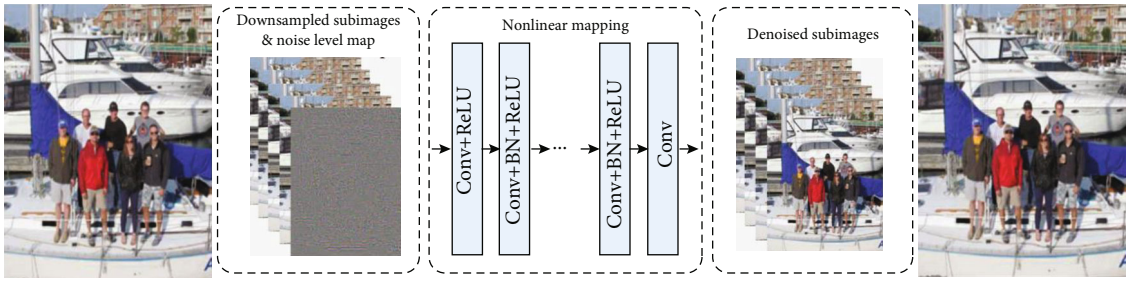

Figure 5: FFDNet structure diagram.

task of image denoising. The absolute value loss function is as follows:

$$L(Y, f(X)) = |Y - f(X)|, \tag{8}$$

where X is a tensor composed of a noisy RGB channel image and noise channel N, f is the denoising network, $f(X)$ is the image after denoising, and Y is the original image.

3.2. Human Detection. After image denoising, in order to further improve the performance of human detection, a human detection method based on high-resolution feature fusion is proposed in this paper. Firstly, HRNet is performed to extract high-resolution features, combined with HRFPN fusion multiscale features to obtain high-quality feature representation of the object, and then, the number of positive and negative anchors is balanced, and interest pooling is carried out in RPN to get the same size feature map. Finally, the cascaded object detector is used to execute multiobject detection. The technical route of this detection method is shown in Figure 6.

3.2.1. High-Resolution Feature Extraction and Fusion. In this paper, HRNet (High-Resolution Network) and HRFPN (High-Resolution Feature Pyramid Networks) are utilized to extract and fuse features in the image; these two operations yield a high-quality representation of features. Since HRNet can maintain a high-resolution representation of features during runtime, and the final feature maps contain both high-level semantic information and low-level cosmetic information about the object, so the final target features are more robust and rich. Its structure is shown in Figure 7. Firstly, it designs a path to obtain a high-resolution representation of the object; in this path, the resolution of the object feature map remains constant. And then, two parallel low-resolution paths are introduced in turn; meanwhile, the resolution of the feature map on the two parallel paths will remain constant; high-resolution features flow into the low-resolution layer after passing through several convolution layers, and finally, information is exchanged repeatedly between different resolution layers. In this way, the HRNet can extract richer information of the corresponding feature maps of human objects.

In addition, in order to improve the detection accuracy of a small object and variable object size, the HRFPN is performed to further integrate features obtained by HRNet; at last, we obtain a higher-quality feature representation of the image. Different from the Feature Pyramid Network (FPN) proposed specifically for multiscale object detection, HRFPN fuses all features from the beginning, and then, it scales layer by layer to fuse the information of each layer effectively so that higher quality features can be obtained. The comparison between FPN and HRFPN is shown in Figure 8. HRFPN first upsamples the feature maps of each layer with bilinear upsampling to a scale consistent with the largest feature map, stitches them together to form a new feature map, and then pools the feature maps in turn into feature maps of different scales. Since the proposed detection method is predicted at four scales, three pooling layers are also needed to obtain feature maps at different scales. And the pooling layer convolution kernel sizes are [2, 4, 8] in order; the pooling layer step size corresponds to the pooling layer convolution kernel size, which is also [2, 4, 8] in order.

3.2.2. RPN Extract ROIs. We are based on the Faster R-CNN framework, and then, we combine HRFPN based on backbone network HRNet with two stages of Faster R-CNN, and finally, multiscale RoIs and the multiscale object region are obtained according to multiscale RPN and the multiscale human object detector, respectively. The feature map obtained by HRFPN is fed into the RPN network. In each level, we employ the sliding to generate the region of interest. According to the region score and regression position, the multiscale region of interest (ROI) is obtained by clipping. The loss function at this stage is shown in the following formula:

$$L(\{p_i\}, \{t_i\}) = \frac{1}{N_{\text{cls}}} \sum_i L_{\text{cls1}}(p_i, p_i^*) + \lambda \frac{1}{N_{\text{reg}}} \sum_i p_i^* L_{\text{reg1}}(t_i, t_i^*), \tag{9}$$

where i represents the serial number of anchors in a small training batch, p_i is the probability of predicting the i-th anchor as the object, p_i^* is used to distinguish between positive and negative anchor points, t_i represents the bounding box predicted in the RPN stage, t_i^* represents the true bounding box position of the object, N_{cls} is the size of a small batch of training, N_{reg} is the number of anchors, and λ is the balance parameter and is used to balance classification loss and regression loss. The N_{cls1} classification loss function employs the exponential loss, and the N_{reg1} regression loss function exploits the smooth L_1 loss, as shown in the

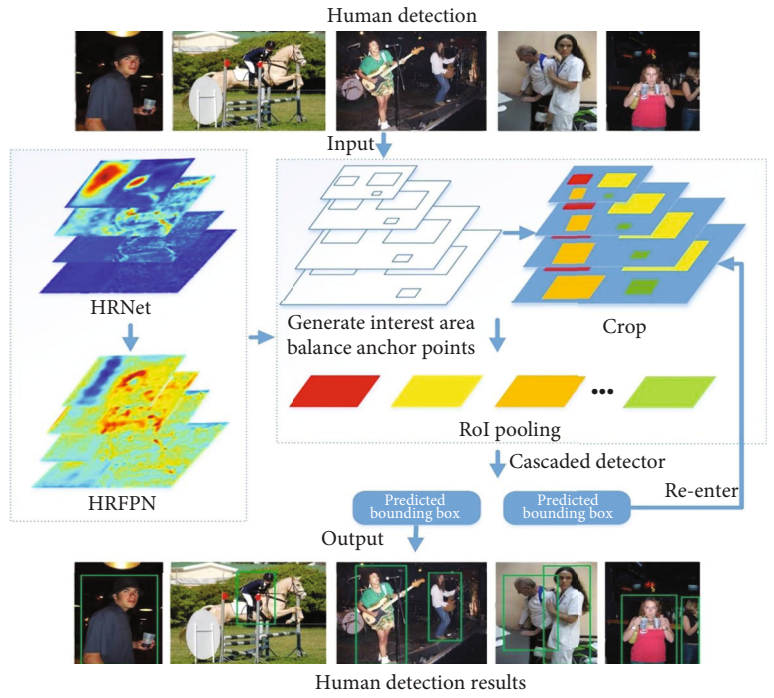

Figure 6: Technical flowchart of human detection method.

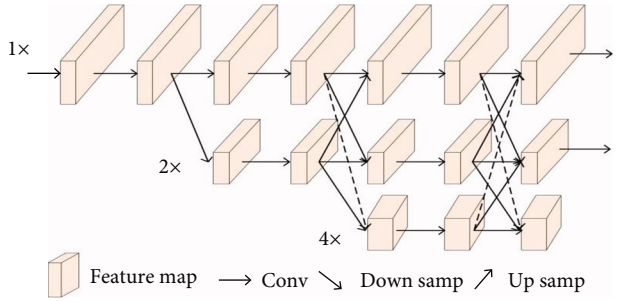

Figure 7: HRNet structure diagram.

following formula:

$$\text{smooth}_{L1}(x) = \begin{cases} 0.5x^2, & \text{if } |x| < 1, \\ x| - 0.5, & \text{otherwise.} \end{cases} \tag{10}$$

In the formula, the parameter x is the difference between the predicted result and the true value.

In the RPN network, we divide the anchor regions into positive anchors and negative anchors according to the Intersection over Union (IoU) of the anchor region and the object ground truth. When the input image contains small objects, the number of negative anchors is far more than that of positive anchors; it will cause the problem of extracting too much background semantic information and ignoring the foreground object information; we adopt the method of randomly removing some negative anchors so that their number does not exceed three times that of positive anchors; the ratio of positive and negative anchors generated in the RPN stage is balanced, which can effectively improve the performance of the object detection network.

3.2.3. Cascaded Human Detector. In the human detection stage, the FPN is also utilized to extract human object features. We employ regions of interest from RPN, and we then matched them to their respective levels of the Feature Pyramid Network based on their size (length and width), and finally, we get the features of the object. Because the FPN stage has extracted enough deep feature maps, we only exploit ROI pooling to extract fixed-size object feature maps, and the final feature maps are fed into the Fast R-CNN object detector. Before the object detector, two fully connected layers are set up to get the confidence and region of the object. The loss function at this stage is shown in the following formula:

$$L(p, u, t^u, v) = L_{\text{cls}}(p, u) + \delta[u \geq 1]L_{\text{loc}}(t^u, v), \tag{11}$$

where L is the total loss function of the second stage object detection; p is the confidence of the predicted object; u is the true object category; t^u represents the predicted bounding box corresponding to the u category; v represents the true bounding box corresponding to the u category at the location; L_{cls} is the classification loss, which is the log loss corresponding to the real category u; δ is the balance parameter; and L_{loc} is the smooth L1 regression loss function, which is the level indicator function. When $u \geq 1$, the level indicator function value is 1; otherwise, the value of the function is 0, so that the bounding box loss can be calculated only for the foreground object, and the regression loss of the background cannot be calculated.

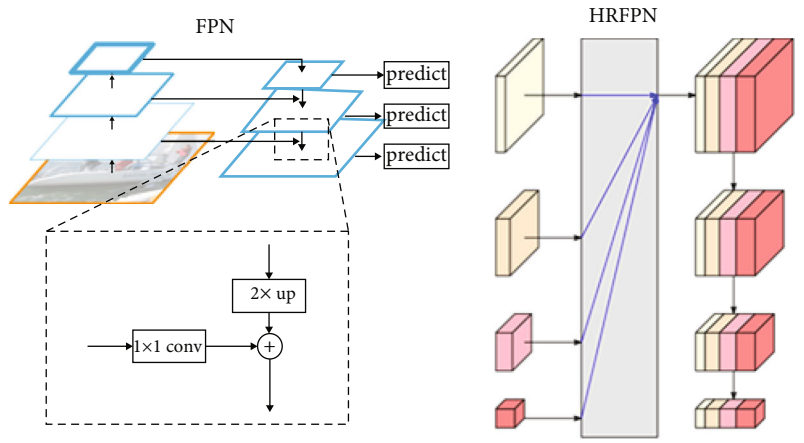

Figure 8: FPN and HRFPN process comparison diagram.

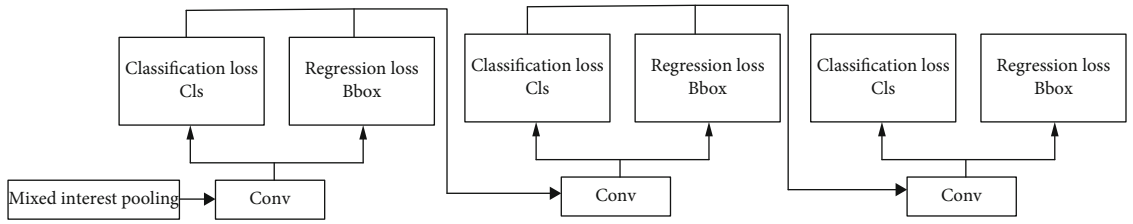

Figure 9: Cascaded human detector.

Table 1: Test results.

Iteration	50	100	150	200	250	300	350	400	450	…	1000
MSE	0.209	0.157	0.132	0.099	0.092	0.081	0.087	0.074	0.065	…	0.057

For the feature map after RoI pooling, classification and bounding box regression is performed on the cascaded object detector. Thus, the accuracy and robustness of object detection can be improved, and the categories of the predicted object and the positions of the corresponding bounding box can be obtained. The cascade operation is to exploit three object detectors with the same structure but different parameters, and it exploits the bounding box prediction results of the previous object detector as the new RPN proposal region, which is performed to crop the feature map. Finally, the cropped feature maps are fed into the next level of object detectors. The cascaded operation accumulates the loss of each object detector during training, where each object detector is composed as shown in Figure 9.

4. Experiment

4.1. Experiment Environment. We implement our network using the PyTorch framework. Furthermore, we utilize Ubuntu 16.04 and python 3.6 in our experiments, and the server CPU is Intel® Xeon® CPU E5-2678 V3 @ 2.50 GHz ∗ 2. Training is performed on NVIDIA GeForce GTX 1080 Ti GPU, which has 12 GB of memory. CUDA8.0 and CUDN6.0 were used to improve GPU utilization. Meanwhile, since we exploit two GPUs for training, we employ NCCL V2 to enable the GPU to communicate. At last, we use OpenCV for image processing.

Table 2: Test results of the network model.

Quality factor	PSNR (dB)		SSIM	
	Before denoising	After denoising	Before denoising	After denoising
35	30.89	32.71	0.910	0.928
45	31.70	33.54	0.921	0.938
65	33.23	35.20	0.933	0.947
75	34.40	36.20	0.946	0.958

4.2. Implementation Details. Our experimental dataset is the human body data from PASCAL VOC [48] with more than 6,000 pieces, divided by the original training and test sets of VOC; new human body images are selected to be trained with the training set and then tested with the test set in each round. In the human image denoising stage, we use the ADAM optimizer, and the training epoch is 10, the learning rate of the first 7 epochs is 1e-3, the learning rate of 8 and 9 is 1e-4, and the last epoch is 1e-6; a mini batch size is 128. In the stage of human target detection, we utilize stochastic gradient descent optimization algorithm, a learning rate of

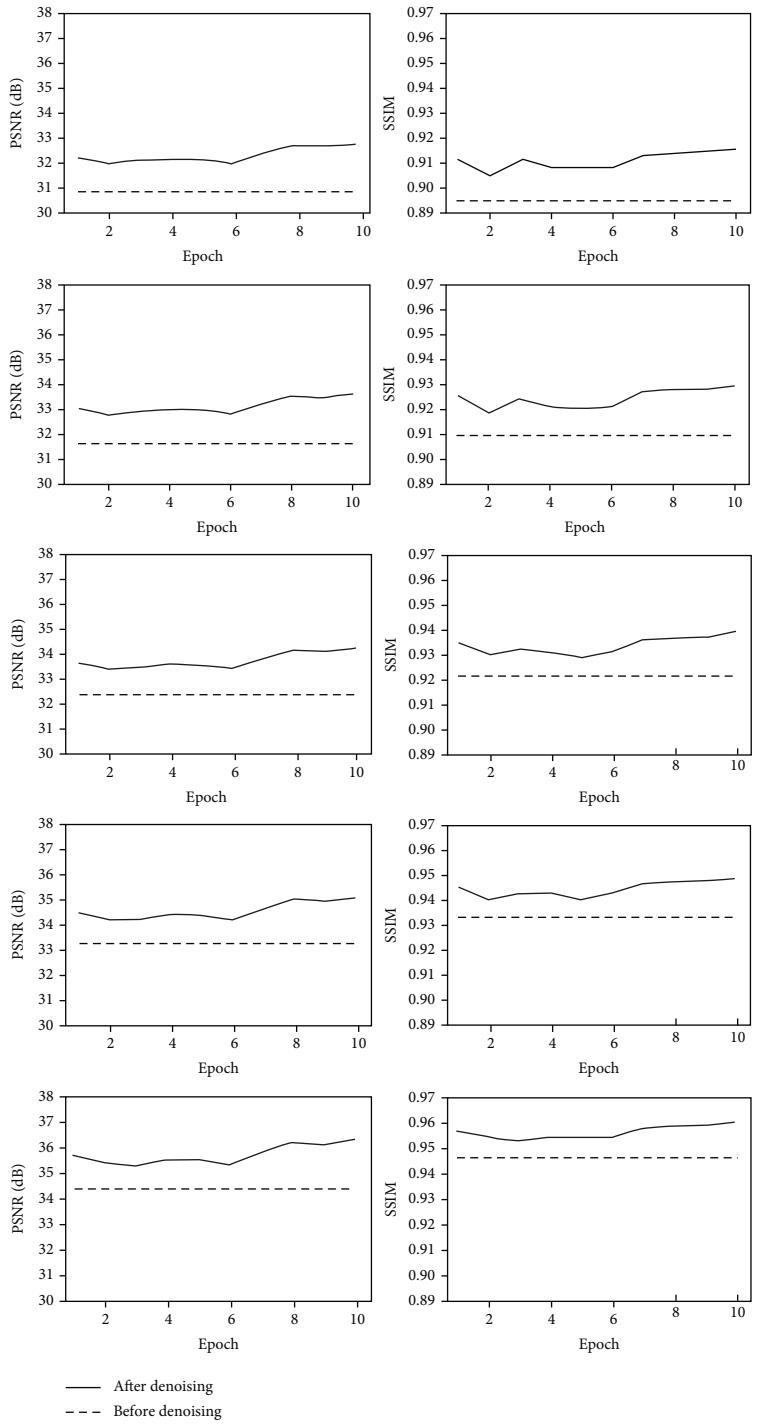

Figure 10: PSNR and SSIM value change curve before and after denoising.

0.02, the momentum is 0.9, the weight decay is 0.0001, and the training epoch is 75. In the above two stages, preprocessing operations are performed on the input images in order to increase the amount of data as well as to keep the training stable.

4.3. Evaluation Index. In our experimental, Peak Signal-to-Noise Ratio (PSNR) [49] and Structural Similarity (SSIM) [50] are used as judging metrics in the image compression denoising phase. PSNR is usually defined by mean square error (MSE). Firstly, given a pair of clean image I and noisy image K with the same size $m * n$, MSE is defined as follows:

$$\mathrm{MSE}(I, K) = \frac{1}{mn} \sum_{i=1}^{m} \sum_{j=1}^{n} \left(I_{i,j} - K_{i,j}\right)^2. \tag{12}$$

Then, PSNR is calculated as follows:

$$\mathrm{PSNR}(I,K)=10\cdot\log_{10}\left[\frac{\mathrm{MAX}_I^2}{\mathrm{MSE}(I,K)}\right], \tag{13}$$

where MAX_I is the maximum pixel value of the image in the color space. Since MAX_K comes from the same color space, the maximum value of the two is equal, that is, $\mathrm{MAX}_I=\mathrm{MAX}_K$.

$$\begin{aligned} l(x,y)&=\frac{2\mu_x\mu_y+c_1}{\mu_x^2+\mu_y^2+c_1},\\ c(x,y)&=\frac{2\sigma_x\sigma_y+c_2}{\sigma_x^2+\sigma_y^2+c_2},\\ s(x,y)&=\frac{\sigma_{xy}+c_3}{\sigma_x\sigma_y+c_3}, \end{aligned} \tag{14}$$

where μ_x and μ_y are the mean values of x and y, respectively. The σ_x and σ_x are the variances of x and y, respectively. σ_x is the covariance of x and y.

The AP value is mainly used in the object detection phase to evaluate the detection algorithm proposed in this paper and also to measure the strengths and weaknesses of the algorithm by comparing it with other detection algorithms.

4.4. Results and Analysis

4.4.1. Denoising Results. To verify whether the improved ResNet18 can accurately estimate the value of the quality factor in the compressed image, Table 1 shows the mean square error between the value of the quality factor estimated using our method and its corresponding true value at different iterations; it can be seen that the mean square error between the estimated and true values of the compression quality factor is 0.099 at the number of iterations of 200, which is less than 0.1, then the improved ResNet18 network can be considered to be able to estimate the compression quality factor accurately.

In the training process based on FFDNet denoising, the L1 loss function (also known as the Mean Absolute Error) is used for training, and its formula is shown in 15 where x denotes a set of input values, y denotes the corresponding object value, n denotes the number of input values, x_i denotes the input value of the i^{th} sample, y_i denotes the object value of the i^{th} sample, and $f(x_i)$ denotes the estimate of the target value of the i^{th} sample.

$$\mathrm{MAE}(x,y)=\frac{1}{n}\sum_{i=1}^{n}|y_i-f(x_i)|. \tag{15}$$

Table 2 shows the results obtained by using the final trained network to test the image with compressed noise. It can be seen that for different quality factors between 35 and 75, the peak signal-to-noise is improved by about 2 dB after denoising, while the structural similarity is improved by about 0.15.

The before and after denoising results for images with compressed noise are shown Figure 10, where the dashed lines denote the PSNR and SSIM values of the images containing compression noise, the solid lines denote the PSNR and SSIM values after denoising, and the first to fifth rows of the figure show the PSNR and SSIM values before and after denoising obtained by the compression algorithm with quality factors of 35, 45, 55, 65, and 75, and it can be seen in the figure that both have improved with the increase in the number of training sessions, and it can be assumed that the performance of the network in removing the compressed noise is also increasing.

In Figure 11, the left column is the images with compressed noise, and then, the middle column represents the denoised images; at last, the right column represents the difference before and after image denoising. We observe the images of the left and right columns, it can be clearly seen that the distribution of noise is related to the content of the input, and its distribution is square with locality. Its change is obvious when the compression noise in the high frequency region of the image is removed. This is consistent with the JPEG compression process; it shows that the designed denoising network can indeed identify and remove JPEG compression noise.

Figure 11: Image comparison result display.

Table 3: Detection accuracy of human.

Detection method	AP
Baseline model	0.829
Baseline model+HRNet	0.849
Ours	0.861

Note: the results in the table are AP values, and the AP used is calculated according to the PASCAL VOC object detection standard.

Figure 12: Qualitative human detection results on PASCAL VOC.

4.4.2. Object Detection Results. To verify the object detection method proposed in this paper, Faster R-CNN+ResNet is used as the baseline model. Based on the baseline model, the backbone network is first replaced with HRNet, then the cascaded object detector is introduced, and the two are finally combined. Table 3 shows the accuracy results of human detection. The experiment first chooses Faster R-CNN+ResNet as the baseline model to determine a baseline for human detection, and its AP value is 0.829. Then, replacing the backbone network of the baseline model with HRNet, the AP value is 0.849, and the AP accuracy value is improved by 2% compared to the baseline model, indicating that HRNet can indeed extract high-resolution features to bring accuracy improvements. After that, when the backbone network uses ResNet, the single object detector is replaced with a cascaded object detector, and the AP value is 0.861. The accuracy of AP has been increased by about 1.2%, which is an increase of 3.2% compared to that of the baseline model. Therefore, it can be shown that the detection performance can be gradually improved by cascading object detectors and complement each other with HRNet to achieve high-performance human detection. Figure 12 shows part of the detection results of human objects. It can be seen that the detection method in this paper has better detection performance for human objects of different scales and poses in different complex scenarios.

To further illustrate that the performance of the human detection algorithm proposed in this paper is better than the current mainstream object detection algorithm, we exploit SSD, YOLO, Fast R-CNN, and other current mainstream object detection algorithms to conduct an experimental comparison with the algorithm in this paper. Various performance evaluation indicators are shown in Table 4. Comparative experiment results show that the AP value of the algorithm in this paper is significantly higher than that of other mainstream object detection algorithms, which also confirms the practicability of the algorithm in this paper.

Table 4: Comparison of the results of mainstream object detection algorithms on the PASCAL VOC dataset.

Detection method	AP
SSD	0.635
YOLO	0.794
Fast RCNN	0.825
Faster RCNN	0.829
Mask RCNN	0.833
Cascade RCNN	0.843
Ours	0.861

Table 5: Comparison of detection results before and after denoising.

Detection method	Before denoising	After denoising
Baseline model	0.780	0.801
Baseline model+HRNET	0.795	0.807
Ours	0.803	0.832

4.4.3. Detection Results before and after Denoising. The above experiments are only carried out on the original PASCAL VOC test set. In order to show that the denoising algorithm can improve the performance of human detection, the quality factor of the JPEG compression algorithm is set to 40 and then applied to the test set, that is, the compression noise is implanted to imitate the distortion caused by the actual JPEG, thereby verifying the correctness of the algorithm. The experimental results are shown in Table 5. It can be seen

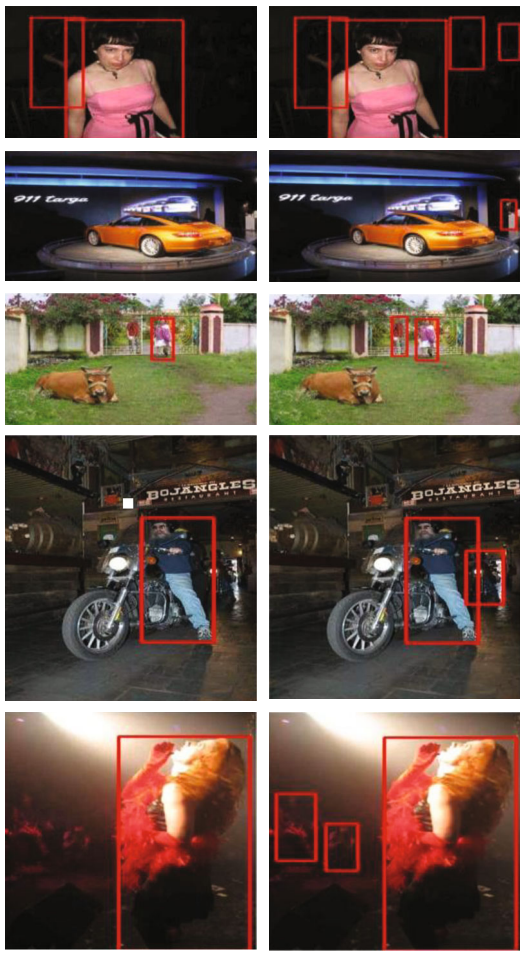

Figure 13: Comparison of visualization results before and after denoising.

from the table that the accuracy of human detection is about 2-3 percentage points higher than that before denoising, which shows that the information loss caused by the JPEG compression process not only produces visual artifacts but also interferes with the determination of target detection, and the feature distribution of the image after denoising is closer to that of the original image, thus improving the detection accuracy. The visualization results are shown in Figure 13.

5. Conclusion

In this paper, we present a human detection method based on image compression denoising. We exploit the improved ResNet to accurately estimate the quality factor in the image with compression noise and then combine the pixel_shuffle inverse transform based on FFDNet to effectively denoise; after that, we utilize cascaded object detectors for classification and bounding box regression based on high-quality feature representations obtained by HRNet and HRFPN. Finally, compared with the state-of-the-art methods, our method can achieve better detection performance after denoising and is, therefore, more suited for human object detection of intelligent video surveillance in 5G-enabled intelligent applications. In the future, we hope that the method proposed in this paper can make some contribution to the rapid development of 5G-enabled intelligent applications.

Data Availability

The data used to support the findings of this study are available from the corresponding author upon request.

Conflicts of Interest

The authors declare that they have no conflicts of interest.

Acknowledgments

The work is supported by the Opening Foundation of Fujian Provincial Key Laboratory of Data Intensive Computing under Grant BD202001 and Opening Foundation of Key Laboratory of Computer Network and Information Integration (Southeast University), Ministry of Education under Grant K93-9-2021-09.

References

[1] S. Tang, W. Zhou, L. Chen, L. Lai, J. Xia, and L. Fan, "Battery-constrained federated edge learning in UAV-enabled IoT for B5G/6G networks," *Physical Communication*, vol. 47, pp. 101381–101389, 2021.

[2] J. Xia, D. Deng, and D. Fan, "A note on implementation methodologies of deep learning-based signal detection for conventional MIMO transmitters," *IEEE Transactions on Broadcasting*, vol. 66, no. 3, pp. 744-745, 2020.

[3] K. He, Z. Wang, D. Li, F. Zhu, and L. Fan, "Ultra-reliable MU-MIMO detector based on deep learning for 5G/B5G-enabled IoT," *Physical Communication*, vol. 47, pp. 1–7, 2020.

[4] S. Tang, L. Chen, K. H. Xia, L. Fan, and A. Nallanathan, "Computational intelligence and deep learning for next-generation edge-enabled industrial IoT," *IEEE Transactions on Network Science and Engineering*, pp. 1–12, 2021, http://arxiv.org/abs/2110.14937.

[5] L. He, Z. Wang, T. Q. S. Quek, S. Chen, and L. Hanzo, "Deep learning-assisted terahertz QPSK detection relying on single-bit quantization," *IEEE Transactions on Communications*, pp. 1–12, 2021.

[6] Y. Guo, Z. Zhao, K. He, S. Lai, J. Xia, and L. Fan, "Efficient and flexible management for industrial Internet of Things: a federated learning approach," *Computer Networks*, vol. 192, article 108122, 2021.

[7] J. Xia, L. Fan, W. Xu et al., "Secure cache-aided multi-relay networks in the presence of multiple eavesdroppers," *IEEE Transactions on Communications*, vol. 67, no. 11, pp. 7672–7685, 2019.

[8] H. Wang, L. Xu, Z. Yan, and T. A. Gulliver, "Low-complexity MIMO-FBMC sparse channel parameter estimation for industrial big data communications," *Transactions on Industrial Informatics*, vol. 17, no. 5, pp. 3422–3430, 2021.

[9] K. Dabov, A. Foi, V. Katkovnik, and K. Egiazarian, "Image denoising by sparse 3-d transform-domain collaborative

filtering," *IEEE Transactions on Image Processing*, vol. 16, no. 8, pp. 2080–2095, 2007.

[10] M. Maggioni, V. Katkovnik, K. Egiazarian, and A. Foi, "Nonlocal transform-domain filter for volumetric data denoising and reconstruction," *IEEE Transactions on Image Processing*, vol. 22, no. 1, pp. 119–133, 2013.

[11] S. Lefkimmiatis, "Universal denoising networks: a novel CNN architecture for image denoising," in *2018 IEEE/CVF Conference on Computer Vision and Pattern Recognition*, pp. 3204–3213, Salt Lake City, UT, USA, 2018.

[12] S. Guo, Z. Yan, K. Zhang, W. Zuo, and L. Zhang, "Toward convolutional blind denoising of real photographs," in *2019 IEEE/CVF Conference on Computer Vision and Pattern Recognition (CVPR)*, pp. 1712–1722, Long Beach, CA, USA, 2019.

[13] N. Dalal and B. Triggs, "Histograms of oriented gradients for human detection," *IEEE Computer Society Conference on Computer Vision & Pattern Recognition*, vol. 1, no. 12, pp. 886–893, 2005.

[14] J. A. K. Suykens and J. Vandewalle, "Least squares support vector machine classifiers," *Neural Processing Letters*, vol. 9, no. 3, pp. 293–300, 1999.

[15] D. Forsyth, "Object detection with discriminatively trained part-based models," *Computer*, vol. 47, no. 2, pp. 6-7, 2014.

[16] J.-Y. Zhu, T. Park, P. Isola, and A. A. Efros, "Unpaired image-to-image translation using cycle-consistent adversarial networks," in *2017 IEEE International Conference on Computer Vision (ICCV)*, pp. 2223–2232, Venice, Italy, 2017.

[17] Y. Lecun, L. Bottou, Y. Bengio, and P. Haffner, "Gradient-based learning applied to document recognition," *Proceedings of the IEEE*, vol. 86, no. 11, pp. 2278–2324, 1998.

[18] J. Deng, W. Dong, R. Socher, L.-J. Li, K. Li, and L. Fei-Fei, "ImageNet: a large-scale hierarchical image database," in *2009 IEEE Conference on Computer Vision and Pattern Recognition*, pp. 248–255, Miami, FL, USA, 2009.

[19] K. Zhang, W. Zuo, Y. Chen, D. Meng, and L. Zhang, "Beyond a Gaussian denoiser: residual learning of deep CNN for image denoising," *IEEE Transactions on Image Processing*, vol. 26, no. 7, pp. 3142–3155, 2017.

[20] K. Zhang, W. Zuo, and L. Zhang, "FFDNet: toward a fast and flexible solution for CNN-based image denoising," *IEEE Transactions on Image Processing*, vol. 27, no. 9, pp. 4608–4622, 2018.

[21] W. Shi, J. Caballero, F. Huszar et al., "Real-time single image and video super-resolution using an efficient sub-pixel convolutional neural network," in *Proceedings of the IEEE conference on computer vision and pattern recognition.*, pp. 1874–1883, Las Vegas, NV, USA, 2016.

[22] I. Goodfellow and J. Pouget-Abadie, "Generative adversarial nets," *Advances in Neural Information Processing Systems*, vol. 7, pp. 2672–2680, 2014.

[23] J. M. Wolterink, T. Leiner, M. A. Viergever, and I. Isgum, "Generative adversarial networks for noise reduction in low-dose CT," *Medical Imaging*, vol. 36, no. 12, pp. 2536–2545, 2017.

[24] N. Divakar and R. V. Babu, "Image denoising via CNNs: an adversarial approach," in *2017 IEEE Conference on Computer Vision and Pattern Recognition Workshops (CVPRW)*, pp. 1076–1083, Honolulu, HI, USA, 2017.

[25] Y. C. Li, N. F. Xiao, and W. L. Ouyang, "Improved boundary equilibrium generative adversarial networks," *IEEE access*, vol. 6, pp. 11342–11348, 2018.

[26] Q. Yang, P. Yan, and Y. Zhang, "Low-dose CT image denoising using a generative adversarial network with Wasserstein distance and perceptual loss," *IEEE Transactions on Medical Imaging*, vol. 37, no. 6, pp. 1348–1357, 2018.

[27] K. Yu, C. Dong, L. Lin, and C. C. Loy, "Crafting a toolchain for image restoration by deep reinforcement learning," in *2018 IEEE/CVF Conference on Computer Vision and Pattern Recognition*, pp. 2443–2452, Salt Lake City, UT, USA, 2018.

[28] J. Lehtinen, J. Munkberg, J. Hasselgren et al., "Noise2Noise: learning image restoration without clean data," *International Conference on Machine Learning*, pp. 2965–2974, 2018.

[29] D. T. Nguyen, W. Li, and P. O. Ogunbona, "Human detection from images and videos: a survey," *Pattern Recognition*, vol. 51, pp. 148–175, 2016.

[30] R. Girshick, J. Donahue, T. Darrell, and J. Malik, "Rich feature hierarchies for accurate object detection and semantic segmentation," in *2014 IEEE Conference on Computer Vision and Pattern Recognition*, pp. 23–28, Columbus, OH, USA, 2014.

[31] R. Girshick, "Fast R-CNN," in *2015 IEEE International Conference on Computer Vision (ICCV)*, pp. 1440–1448, IEEE Press, Santiago, Chile, 2015.

[32] Z. Cai and N. Vasconcelos, "Cascade R-CNN: delving into high quality object detection," in *2018 IEEE/CVF Conference on Computer Vision and Pattern Recognition*, pp. 6154–6162, Salt Lake City, UT, USA, 2018.

[33] S. Ren, K. He, R. Girshick, and J. Sun, "Faster R-CNN: towards real-time object detection with region proposal networks," *Advances in neural information processing systems*, vol. 28, pp. 91–99, 2015.

[34] J. Redmon, S. Divvala, R. Girshick, and A. Farhadi, "You only look once: unified, real-time object detection," in *2016 IEEE Conference on Computer Vision and Pattern Recognition (CVPR)*, pp. 779–788, Las Vegas, NV, USA, 2016.

[35] J. Redmon and A. Farhadi, "YOLO9000: better, faster, stronger," in *2017 IEEE Conference on Computer Vision and Pattern Recognition (CVPR)*, pp. 7263–7271, Honolulu, HI, USA, 2017.

[36] W. Liu, D. Anguelov, D. Erhan et al., "SSD: single shot multibox detector," in *Computer Vision – ECCV 2016*, pp. 21–37, Springer, Cham, 2016.

[37] T.-Y. Lin, P. Dollar, R. Girshick, K. He, B. Hariharan, and S. Belongie, "Feature pyramid networks for object detection," in *2017 IEEE Conference on Computer Vision and Pattern Recognition (CVPR)*, pp. 2117–2125, Honolulu, HI, USA, 2017.

[38] K. Sun, B. Xiao, D. Liu, and J. Wang, "Deep high-resolution representation learning for human pose estimation," in *Proceedings of the IEEE conference on computer vision and pattern recognition*, pp. 5693–5703, Long Beach, CA, USA, 2019.

[39] B. Cheng, B. Xiao, J. Wang, H. Shi, T. S. Huang, and L. Zhang, "HigherHRNet: scale-aware representation learning for bottom-up human pose estimation," in *2020 IEEE/CVF Conference on Computer Vision and Pattern Recognition (CVPR)*, pp. 5386–5395, Seattle, WA, USA, 2020.

[40] N. Carion, F. Massa, G. Synnaeve, N. Usunier, A. Kirillov, and S. Zagoruyko, "End-to-end object detection with transformers," *European Conference on Computer Vision*, vol. 12346, pp. 213–229, 2020.

[41] Y. Shen, R. Ji, Z. Chen et al., "Noise-aware fully Webly supervised object detection," in *2020 IEEE/CVF Conference on Computer Vision and Pattern Recognition (CVPR)*, pp. 11323–11332, Seattle, WA, USA, 2020.

[42] X. Dai, Y. Chen, B. Xiao et al., "Dynamic head: unifying object detection heads with attentions," in *Conference on Computer Vision and Pattern Recognition*, Nashville, TN, USA, 2021.

[43] J. Wang, L. Song, Z. Li, H. Sun, J. Sun, and N. Zheng, "End-to-end object detection with fully convolutional network," in *2021 IEEE/CVF Conference on Computer Vision and Pattern Recognition (CVPR)*, Nashville, TN, USA, 2021.

[44] G. Hudson, A. Léger, B. Niss, I. Sebestyén, and J. Vaaben, "JPEG-1 standard 25 years: past, present, and future reasons for a success," *Journal of Electronic Imaging*, vol. 27, no. 4, article 040901, 2018.

[45] K. He, X. Zhang, S. Ren, and J. Sun, "Deep residual learning for image recognition," in *2016 IEEE Conference on Computer Vision and Pattern Recognition (CVPR)*, pp. 770–778, Las Vegas, NV, USA, 2016.

[46] K. He, X. Zhang, S. Ren, and J. Sun, "Identity mappings in deep residual networks," in *Computer Vision – ECCV 2016*, pp. 630–645, Springer, Cham, 2016.

[47] J. Long, E. Shelhamer, and T. Darrell, "Fully convolutional networks for semantic segmentation," *IEEE Transactions on Pattern Analysis and Machine Intelligence*, vol. 39, no. 4, pp. 640–651, 2015.

[48] H. Xian-Hua, C. Yen-Wei, and R. Xiang, "Multi-class object recognition by fusion of image descriptors: classification evaluation of PASCAL VOC challenge database," *Ice Technical Report*, vol. 109, pp. 103–108, 2009.

[49] Q. Huynh-Thu and M. Ghanbari, "The accuracy of PSNR in predicting video quality for different video scenes and frame rates," *Telecommunication Systems*, vol. 49, no. 1, pp. 35–48, 2012.

[50] Z. Wang, A. C. Bovik, H. R. Sheikh, and E. P. Simoncelli, "Image quality assessment: from error visibility to structural similarity," *IEEE Transactions on Image Processing*, vol. 13, no. 4, pp. 600–612, 2004.

Hindawi
Wireless Communications and Mobile Computing
Volume 2021, Article ID 6013448, 15 pages
https://doi.org/10.1155/2021/6013448

Research Article

Diagnosis of Diabetic Retinopathy through Retinal Fundus Images and 3D Convolutional Neural Networks with Limited Number of Samples

Ahsan Bin Tufail,[1,2] **Inam Ullah**,[3] **Wali Ullah Khan**,[4] **Muhammad Asif**,[5] **Ijaz Ahmad**,[6] **Yong-Kui Ma**,[1] **Rahim Khan**,[1] **Kalimullah**,[7] **and Md. Sadek Ali**[8]

[1]*School of Electronics and Information, Harbin Institute of Technology, Harbin, Heilongjiang Province, China*
[2]*Department of Electrical and Computer Engineering, COMSATS University Islamabad, Sahiwal Campus, Sahiwal, Pakistan*
[3]*College of Internet of Things (IoT) Engineering, Hohai University (HHU), Changzhou Campus, Changzhou 213022, China*
[4]*Interdisciplinary Centre for Security, Reliability and Trust (SnT)/SigCom, University of Luxembourg, 1855 Luxembourg City, Luxembourg*
[5]*College of Electronics and Information Engineering, Shenzhen University, Shenzhen, Guangdong 518060, China*
[6]*School of Pattern Recognition and Intelligent System, Shenzhen Institute of Advance Technology (Chinese Academy of Sciences), Shenzhen, China*
[7]*Department of Electrical Engineering, University of Science and Technology Bannu, Khyber Pakhtunkhwa, Pakistan*
[8]*Communication Research Laboratory, Department of Information and Communication Technology, Islamic University, Kushtia-7003, Bangladesh*

Correspondence should be addressed to Md. Sadek Ali; sadek@ice.iu.ac.bd

Received 12 September 2021; Revised 24 October 2021; Accepted 2 November 2021; Published 17 November 2021

Academic Editor: Junjuan Xia

Diabetic retinopathy (DR) is a worldwide problem associated with the human retina. It leads to minor and major blindness and is more prevalent among adults. Automated screening saves time of medical care specialists. In this work, we have used different deep learning (DL) based 3D convolutional neural network (3D-CNN) architectures for binary and multiclass (5 classes) classification of DR. We have considered mild, moderate, no, proliferate, and severe DR categories. We have deployed two artificial data augmentation/enhancement methods: random weak Gaussian blurring and random shift along with their combination to accomplish these tasks in the spatial domain. In the binary classification case, we have found the performance of 3D-CNN architecture trained by deploying combined augmentation methods to be the best, while in the multiclass case, the performance of model trained without augmentation is the best. It is observed that the DL algorithms working with large volumes of data may achieve better performances as compared to the methods working with small volumes of data.

1. Introduction

Diabetes weakens the blood sugar regulation process inside the human body. In the year 2017, approximately 451 million peoples were suffering from this disease. A higher level of blood sugar severely cripples human body organs leading to risky complications such as coronary episode, vision loss, cataracts, glaucoma, retinopathy, and dementia. A growing population of peoples, irrespective of age, suffering from diabetes have problems in vision termed as diabetic retinopathy (DR) [1–4].

In clinical settings, four stages are generally involved in the assessment of DR, which are mild, moderate, severe, and proliferative retinopathy, respectively. In the earliest stage, microaneurysms, which are balloon-like structures, are formed in the small veins of the retina which are obstructed in the moderate stage. In the final stages, visual deficiency can occur [2].

Problems associated with DR can be treated in initial stages. The human eye is made up of optic nerves/discs, and the images of the eye can be segmented to get a good classification accuracy of different stages involved in DR [2]. Fundus images display the existence of exudates, hemorrhages, and other eye deficits and are graded manually by a limited number of ophthalmologists whose numbers are shrinking every year [3]. Microaneurysms, hemorrhages, hard exudates, cotton wool spots, neovascularization, and macular edema are some of the characteristics of DR [5, 6]. For the screening of DR, at the level of an image, "normal" category contains no lesion while "abnormal" category contains at least one lesion. A computer-aided diagnostic system can help health care specialists in alleviating variabilities. Deep learning (DL) is a popular method for analysing retinal fundus images [7, 8]. It captures high-level features throughout the learning process effectively adapting to any type of noise [9] thus forming a natural solution for identifying retinal diseases.

Various algorithms have been proposed for the examination of scan reports to diagnose DR [10–12]. Usually, researchers have focused on automatic recognition of lesions associated with DR [13–15]. In [16], the authors deployed convolutional neural networks (CNNs) to obtain a precision of 75% on the validation dataset for classifying DR images in the presence of artificial data augmentation/enhancement techniques. Shanthi and Sabeenian in [17] classified the fundus images employing a modified AlexNet architecture validated using Messidor database. The authors in [18] used transfer learning architectures, such as AlexNet, VGGNet, GoogleNet, and ResNet to reach a recognition rate of 95.68% exploiting publicly available Kaggle platform. A full patch-based CNN architecture is designed in [19] using only 28 retinal images achieving a sensitivity of 0.940. Authors in [2] constructed a 3D capsule network and validated their model on the Messidor dataset to achieve an accuracy of 98.64% on the stage 3 fundus images. In [4], a deep and densely connected network was designed to classify Messidor-2 and EyePACS datasets to attain a precision of 95% on Messidor-2 and 88% on the EyePACS dataset. Researchers in [20] used CNNs to achieve a sensitivity of 90% on the EyePACS dataset and a sensitivity of 87% on Messidor-2 dataset. Sayres et al. [21] deployed DL models achieving a sensitivity of 91% on Messidor-2 and a sensitivity of 94.5% on the EyePACS datasets. The work in [22] employed transfer learning-based VGG-19 architecture to classify 9 retinal diseases and one normal retina class with limited number of samples to obtain an accuracy of 30.5% when considering all the ten categories with the deployment of translation, rotation, and brightness change augmentation methods. The researcher used a deep CNN architecture [23] on the EyePACS dataset achieving a sensitivity of 98% deploying rotation, shearing, flipping, zooming, cropping, Krizhevsky augmentation, and translation as augmentation methods. Shankar et al. [24] proposed a DL model deploying histogram-based segmentation and a synergic network achieving an accuracy of 99.28% on the classification task for the Messidor dataset. Beede et al. [25] conducted a study on the clinical characterization of eye screening workflows for the detection of diabetic eye disease. They discovered factors such as gradability, Internet speed and connectivity, nursing workflows, and patient experience to be responsible for the model's performance. Khare et al. [26] proposed a firefly algorithm for dimensionality reduction, principal component analysis for feature extraction, and a deep neural network (DNN) model for the classification of DR to achieving an accuracy of 97%, precision and recall of 96%, specificity of 95%, and a sensitivity of 92% for the binary classification task. Qureshi et al. [27] proposed a DL architecture based on active learning for multiclass (e.g., 5 classes) classification of DR images from EyePACS benchmark for achieving a sensitivity of 92.2%, specificity of 95.1%, F-measure of 93%, and an accuracy of 98% on a wide range of fundus images. Das et al. [28] utilized maximal principal curvature, adaptive histogram equalization, morphological opening, and a CNN-based classifier to achieve an accuracy of 98.7% on DIARETDB1 dataset. Li et al. [29] presented a deep ensemble algorithm for the detection of DR using retinal fundus images. They exploited Inception-v4 architecture on Messidor-2 dataset to achieve an area under the curve of 0.994, sensitivity of 0.930, and a specificity of 0.971. Limwattanayingyong et al. [30] compared the screening of DR in a longitudinal setting via DL and human grading. They achieved a prevalence rate of 5.1% using DL while they observe a reduction in prevalence rate on a two-year follow-up. Tsiknakis et al. [31] provided an overview of DR detection based on fundus images discussing several aspects such as datasets, preprocessing techniques, and DL models for the characterization of important lesions. Karakaya and Hacisoftaoglu [32] compared different smart phone-based solutions such as iExaminer, D-Eye, Peek Retina, and iNview finding that field of view is the most important parameter for the detection of DR where iNview provides the largest and iExaminer provides the smallest value for this field.

Few-shot learning has been a topic of considerable interest where very few examples are used to categorize classes especially those classes that are not presented during training [33–35]. Fine-tuning is a common approach for few-shot learning. These systems require complex inference mechanisms due to the processing of complex inductive bias. Meta learning, augmentation/generative met-hods, transfer learning, and semisupervised methods are some of the typical approaches for this type of learning.

Besides health issues, researchers in academia and industry also investigated other problems in science, technology, and engineering using various DL-based approaches [36–50].

Although the reported studies offer competitive solutions to the binary and multiclass classification of DR, most of them are geared towards utilizing information in the 2D domain. Higher dimensions, such as 3D, offers rich scale and geometry information, which are challenging solutions for computer vision algorithms [51–53]. There is a need for studies to utilize the information offered by higher dimensions for these tasks. To take advantage of these representation learning methods on a limited number of samples [54] in the presence of data augmentation, we have used a 3D-CNN architecture [55] in the spatial domain for one

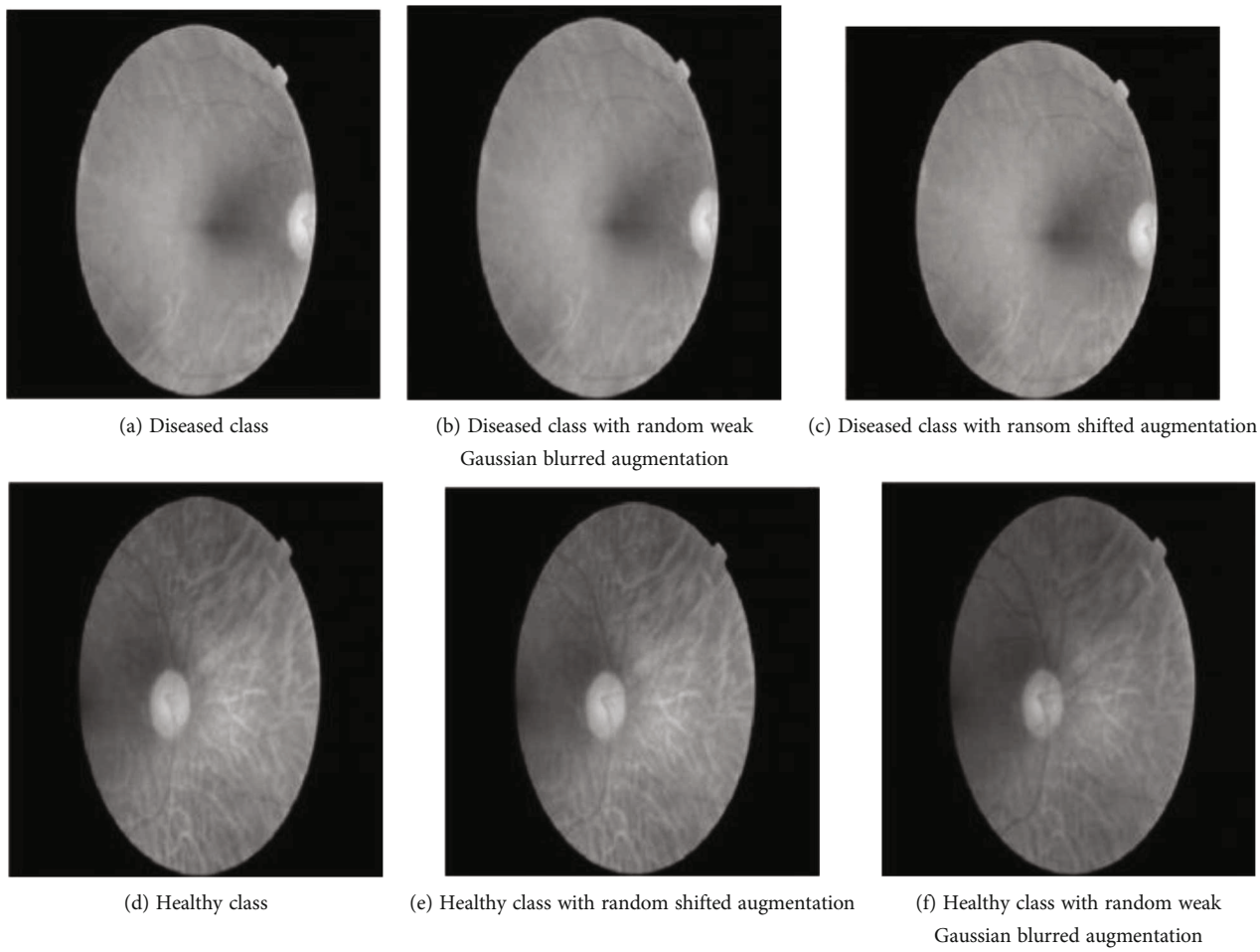

(a) Diseased class (b) Diseased class with random weak Gaussian blurred augmentation (c) Diseased class with ransom shifted augmentation

(d) Healthy class (e) Healthy class with random shifted augmentation (f) Healthy class with random weak Gaussian blurred augmentation

FIGURE 1: Sample images in the TeleOphta database with random shifted and random weak Gaussian blurred augmentation methods for the binary classification task.

binary and one multiclass classification task on the DR datasets. We have employed random weak Gaussian blurring and random shift as data augmentation/enhancement techniques along with their combination to study the impact of these methods on both classification tasks.

This work contributes to the existing literature on the classification of DR in the following ways. To the best of authors' knowledge, very few researches have been carried out in the literature to solve this problem in the 3D domain. This study is designed to achieve that which offers the advantage by considering both spatial and temporal dimensions simultaneously. Impact of different data augmentation schemes on the final classification performance is also worth investigating especially in the 3D domain. Few-shot learning is also a problem worth investigating as limited number of samples is a bottleneck in achieving good classification performances using DL methods.

The remaining sections of this paper are organized as follows. A brief description of the datasets is given in Section 2, while Section 3 provides the details of the methods used in this study. Section 4 presents the details of the conducted experiments. Section 5 provides results and a thorough discussion. Finally, conclusions are drawn in Section 6 from the work presented.

2. Dataset Description

We have used two datasets to carry out the experiments. The first one named TeleOphta [3] is a database of fundus images with exudates and microaneurysm lesions. Using this database, we have constructed 99 3D volumes of healthy subjects and 83 3D volumes of diseased class that show signs of exudates and microaneurysms, and these volumes are split at the subject level [56]. Random shifting and random weak Gaussian blurred augmentation techniques are deployed to enhance the dataset. Some samples of the images are shown in Figure 1. The volume size is $210 \times 210 \times 12$.

The second dataset has Gaussian filtered retina scan images to detect DR with five categories, which are no, mild, moderate, severe, and proliferate. The size of the 3D volumes is $512 \times 512 \times 2$. In this database, we have 262 3D volumes of each of these categories that are split at the subject level [56]. Some samples of the images that are present in the database are shown in Figures 2–4, respectively. We have implemented random shifting and random weak Gaussian blurred augmentation techniques to enhance the dataset. This dataset is taken from the Kaggle website. All the 3D volumes in both these databases are normalized to have intensity values in the range between 0 and 255.

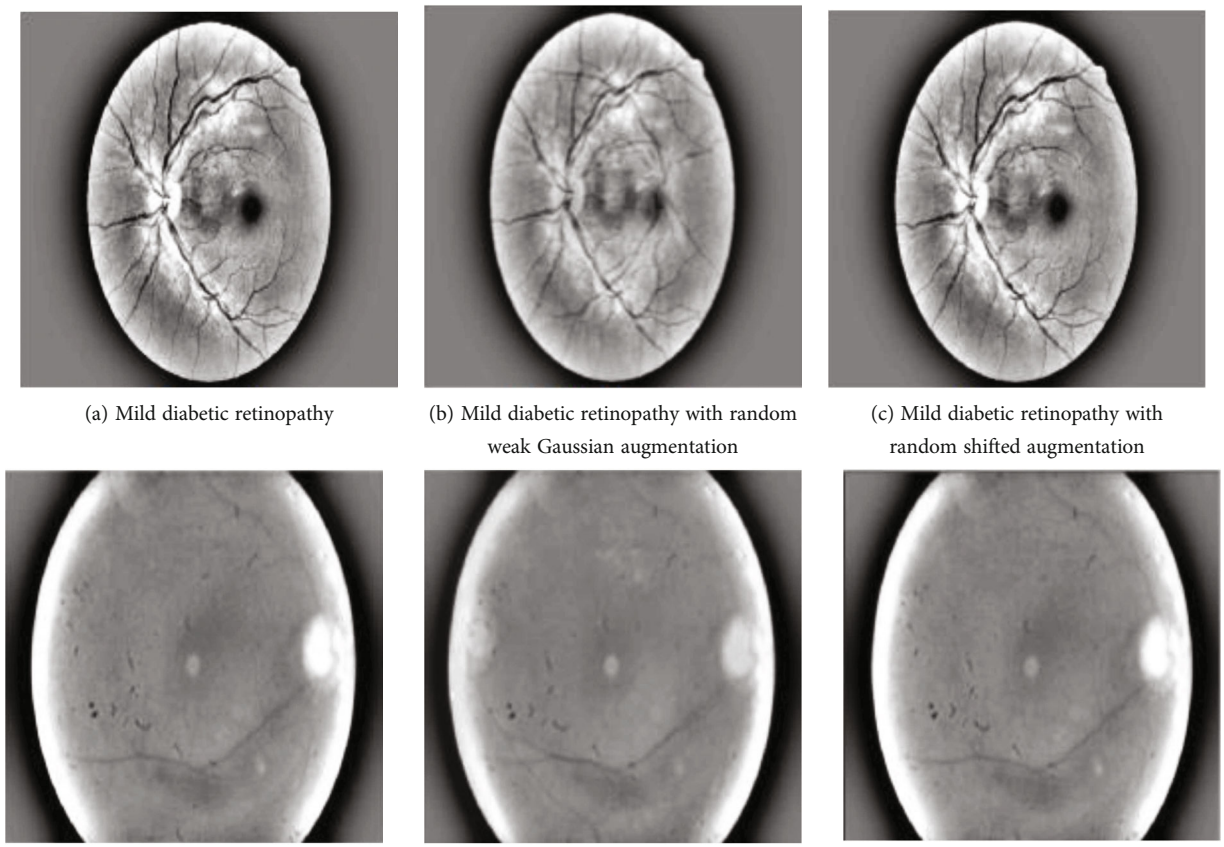

(a) Mild diabetic retinopathy
(b) Mild diabetic retinopathy with random weak Gaussian augmentation
(c) Mild diabetic retinopathy with random shifted augmentation
(d) Moderate diabetic retinopathy
(e) Moderate diabetic retinopathy with random weak Gaussian blurred augmentation
(f) Moderate diabetic retinopathy with random shifted augmentation

Figure 2: Sample images of mild and moderate classes in the Kaggle DR database with random shifted and random weak Gaussian blurred augmentation methods.

3. Methodology

In this work, we have considered both binary and multiclass classification tasks using different DL-based 3D-CNN architectures. These architectures are presented visually in Figures 5 and 6, respectively.

As given in Figure 5, there are small differences between the architectures deployed without augmentation, combined augmentation schemes, and with random weak Gaussian blurring and random shifted augmentation schemes. Feature maps in the convolutional layers are 10 for the combined augmentation scheme, 8 for no augmentation, and 9 for the classification tasks involving random weak Gaussian blurring and random shifted augmentation schemes. Rest of the architectures in Figure 5 are equivalent. An input layer accepts a volume of size $210 \times 210 \times 12$ with rescale-zero-one normalization method that scales the values of the incoming input between 0 and 1 according to the minimum and maximum values per channel. After that, a block that is repeated 5 times named block-A consists of a 3D convolutional layer, batch normalization layer, rectified linear nit (ReLU) activation layer, and a max pooling 3D layer which is used for the extraction, normalization, and downsizing of feature maps. Subsequently, there is a block which is repeated a single time named block-B consisting of 3 fully connected (FC) layers with number of neurons equal to 300, 150, and 2, one dropout layer with probability 0.1, and, finally, a softmax and a classification layer to culminate the binary classification task. ReLU is equivalent to max $(x, 0)$. Batch normalization [57] is another technique used for the improvement of training efficiency through a reduction in the statistical difference between the fundus volumes [58]. It contributes to a rapid convergence and a reduction in sensitivity during learning process [59]. Dropout [60] is effective in reducing the overfitting of models by omitting both hidden and visible units during the training process. It is a type of regularization method that prevents complex formation of adaptations on the training data. Weight and bias L2 factors are added to encourage smaller weights and biases by penalizing a network based on the size of weights and biases. Transformation of the input values of the softmax function can be interpreted as probabilities. Table 1 shows detailed 3D-CNN architecture hyperparameters for the binary classification task with 8 feature maps in the convolutional 3D layer.

As given in Figure 6, there are small architectural differences between the architectures deployed using no augmentation, combined augmentation schemes, and with random

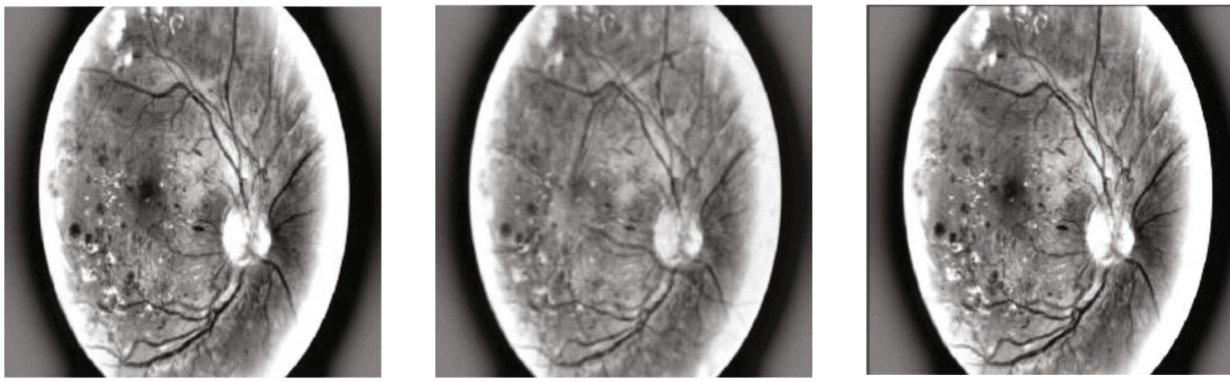

(a) Proliferative diabetic retinopathy (b) Proliferative diabetic retinopathy with random weak Gaussian blurred augmentation (c) Proliferative diabetic retinopathy with random shifted augmentation

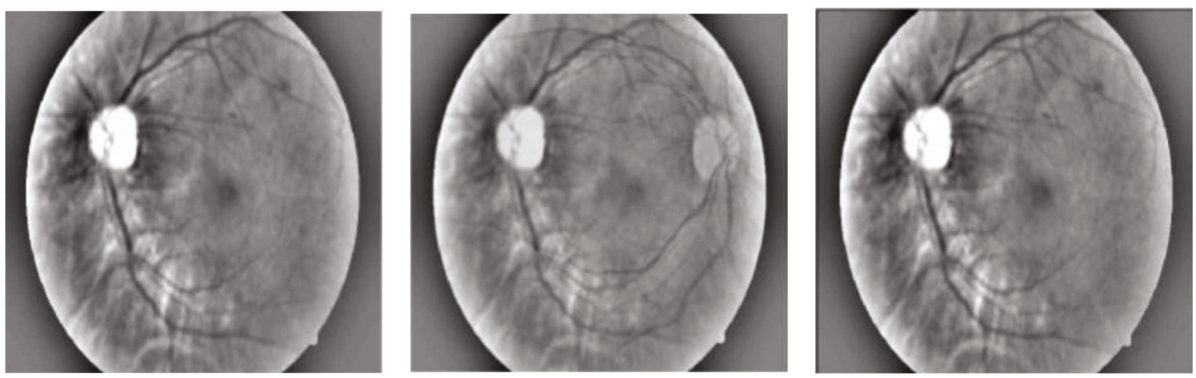

(d) Severe diabetic retinopathy (e) Severe diabetic retinopathy with random weak Gaussian blurred augmentation (f) Severe diabetic retinopathy with random shifted augmentation

Figure 3: Sample images of severe and proliferative classes in the Kaggle DR database with random shifted and random weak Gaussian blurred augmentation methods.

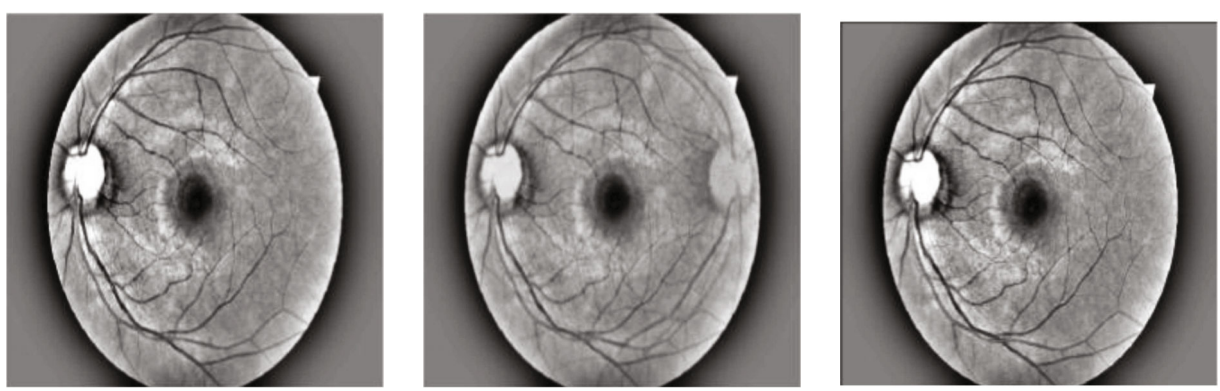

(a) No diabetic retinopathy (b) No diabetic retinopathy with random weak Gaussian blurred augmentation (c) No diabetic retinopathy random shifted augmentation

Figure 4: Sample images of no DR class in the Kaggle DR database with random shifted and random weak Gaussian blurred augmentation methods.

weak Gaussian blurring and random shifted augmentation schemes. The numbers of features maps in the convolutional layer are 12 for combined augmentations, 10 for no augmentation, and 11 for random weak Gaussian blurring and random shifted augmentation scheme-based classification tasks. The rest of the architectures are equivalent. An input layer accepts a volume of size $512 \times 512 \times 2$ with zero centre normalization applied to the 3D volume. After that, there comes a block that is repeated 6 times named block-A consisting of a feature extracting convolutional layer, batch normalization layer, exponential linear unit (ELU) activation layer, and a max pooling 3D layer that is used for the extraction,

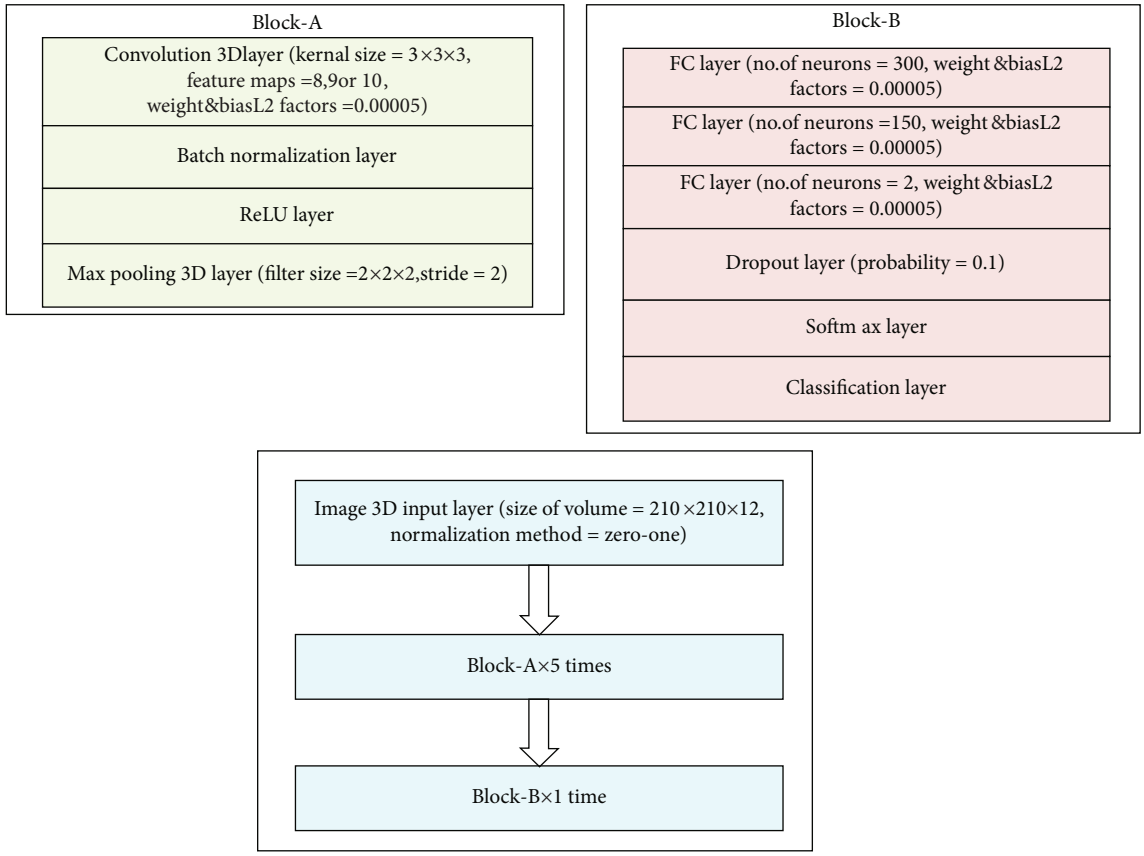

Figure 5: Architectures for binary classification (healthy/diseased) tasks without augmentation, with random shifted and random weak Gaussian blurred augmentation schemes, and by combined augmentation schemes. A tenfold cross-validation approach is used for hyperparameter selection.

normalization, and downsizing of feature maps. After that, there is another block that is repeated a single time named block-B consisting of 3 FC layers with 500, 300, and 5 neurons, one dropout layer with probability 0.1, and, finally, a softmax and a classification layer to culminate the multiclass (5 classes) classification task. ELUs [61] solve the vanishing gradient problem by having values in the negative region allowing them to push mean unit activations closer to zero but with lower computational complexity. Mathematically,

$$\mathrm{ELU}(\alpha > 0): \begin{cases} x, & x \geq 0, \\ \alpha(e^x - 1), & x < 0. \end{cases} \quad (1)$$

Table 2 shows detailed 3D-CNN architecture hyperparameters for the multiclass classification task with 10 feature maps in the convolutional 3D layer.

4. Experiments

We have performed experiments in the spatial domain for both binary and multiclass classification tasks to differentiate between the different categories of DR deploying two data augmentation methods: random weak Gaussian blurring and random shifting. We set the σ value to 1.5 for the random weak Gaussian blurring and shift value to 1 or 2 pixels for the random shifting augmentations. We have also combined the training samples of both these augmentation methods. We have carried out the experiments related to the following tasks: (1) binary classification of healthy/diseased classes without augmentation, (2) binary classification of healthy/diseased classes with random weak Gaussian blurring augmentation, (3) binary classification of healthy/diseased classes with random shifting augmentation, (4) binary classification of healthy/diseased classes with combined random shifting and random weak Gaussian blurring augmentation methods, (5) multiclass classification without augmentation, (6) multiclass classification with random weak Gaussian blurring augmentation, (7) multiclass classification with random shifting augmentation, and, finally, (8) multiclass classification with combined random shifting and random weak Gaussian blurring augmentation methods. A number of samples in the training and validation splits are 72 and 8 for each class, respectively, in the case of binary classification task. We have also created a test split and place 19 samples of healthy class and 3 samples of diseased class in this split. To run experiments on the test split, we have deployed complete dataset of 80 samples of each class in the training split and only samples of the test subset in the validation split.

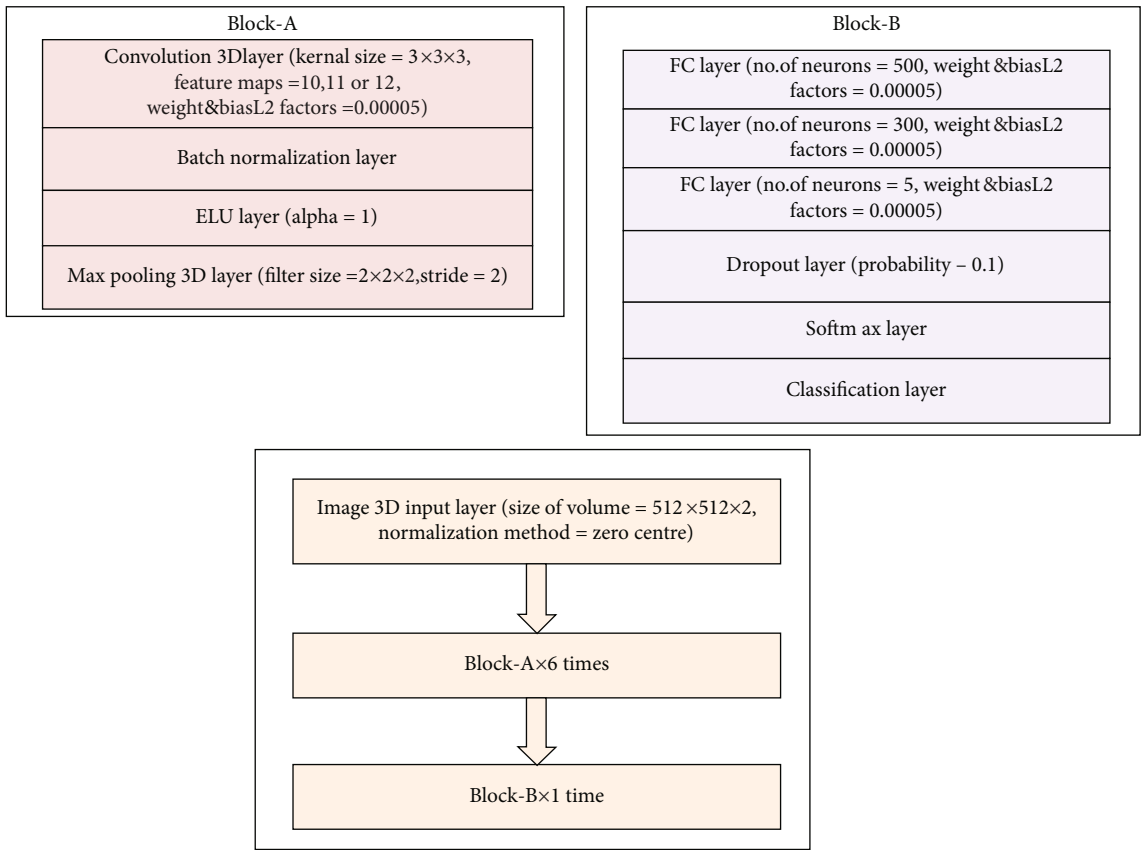

Figure 6: Architectures for multiclass classification tasks without augmentation, with random shifted and random weak Gaussian blurred augmentation schemes, and by combined augmentation schemes. A tenfold cross-validation approach is used for hyperparameter selection.

Table 1: Architecture hyperparameters for the proposed 3D-CNN model for binary classification task with 8 feature maps in the convolutional layer.

Layer	Filter size	Number of filters	Stride size	Dropout rate	Output size
Conv1+BN+ReLU	$3 \times 3 \times 3$	8	1	—	$8 \times 210 \times 210 \times 12$
MaxPool1	$2 \times 2 \times 2$	—	2	—	$8 \times 105 \times 105 \times 6$
Conv2+BN+ReLU	$3 \times 3 \times 3$	8	1	—	$8 \times 105 \times 105 \times 6$
MaxPool2	$2 \times 2 \times 2$	—	2	—	$8 \times 53 \times 53 \times 3$
Conv3+BN+ReLU	$3 \times 3 \times 3$	8	1	—	$8 \times 53 \times 53 \times 3$
MaxPool3	$2 \times 2 \times 2$	—	2	—	$8 \times 27 \times 27 \times 2$
Conv4+BN+ReLU	$3 \times 3 \times 3$	8	1	—	$8 \times 27 \times 27 \times 2$
MaxPool4	$2 \times 2 \times 2$	—	2	—	$8 \times 14 \times 14 \times 1$
Conv5+BN+ReLU	$3 \times 3 \times 3$	8	1	—	$8 \times 14 \times 14 \times 1$
MaxPool5	$2 \times 2 \times 2$	—	2	—	$8 \times 7 \times 7 \times 1$
FC 1	—	300	—	—	300
FC 2	—	150	—	—	150
FC 3	—	2	—	—	2
Dropout	—	—	—	0.1	2
Softmax	—	—	—	—	2

FC: fully connected; MaxPool: maximum pooling; BN: batch normalization; ReLU: rectified linear unit; Conv: convolutional.

Table 2: Architecture hyperparameters for the proposed 3D-CNN model for multiclass classification task with 10 feature maps in the convolutional layer.

Layer	Filter size	Number of filters	Stride size	Dropout rate	Output size
Conv1+BN+ELU	$3 \times 3 \times 3$	10	1	—	$10 \times 512 \times 512 \times 2$
MaxPool1	$2 \times 2 \times 2$	—	2	—	$10 \times 256 \times 256 \times 1$
Conv2+BN+ELU	$3 \times 3 \times 3$	10	1	—	$10 \times 256 \times 256 \times 1$
MaxPool2	$2 \times 2 \times 2$	—	2	—	$10 \times 128 \times 128 \times 1$
Conv3+BN+ELU	$3 \times 3 \times 3$	10	1	—	$10 \times 128 \times 128 \times 1$
MaxPool3	$2 \times 2 \times 2$	—	2	—	$10 \times 64 \times 64 \times 1$
Conv4+BN+ELU	$3 \times 3 \times 3$	10	1	—	$10 \times 64 \times 64 \times 1$
MaxPool4	$2 \times 2 \times 2$	—	2	—	$10 \times 32 \times 32 \times 1$
Conv5+BN+ELU	$3 \times 3 \times 3$	10	1	—	$10 \times 32 \times 32 \times 1$
MaxPool5	$2 \times 2 \times 2$	—	2	—	$10 \times 16 \times 16 \times 1$
Conv6+BN+ELU	$3 \times 3 \times 3$	10	1	—	$10 \times 16 \times 16 \times 1$
MaxPool6	$2 \times 2 \times 2$	—	2	—	$10 \times 8 \times 8 \times 1$
FC 1	—	500	—	—	500
FC 2	—	300	—	—	300
FC 3	—	5	—	—	5
Dropout	—	—	—	0.1	5
Softmax	—	—	—	—	5

FC: fully connected; MaxPool: maximum pooling; BN: batch normalization; ELU: exponential linear unit; Conv: convolutional.

A number of samples in the training and validation splits are 225 and 25 for each class, respectively, in the case of multiclass classification task. We have also created a test split and place 12 samples of each class in this split. To run experiments on the test split, we have employed complete dataset of 250 samples of each class in the training split and only samples of the test subset in the validation split.

For experiments on the binary classification tasks, we have used the following settings: minibatch size is set to 2, initial learning rate is set to 0.001, epochs are set to 50, learning rate schedule is set to piecewise, optimization algorithm is Adam [62], categorical cross-entropy is chosen as a loss function, total number of experiments equals 41, while time taken to perform these experiments is approximately 642 minutes or 10.7 hours.

For experiments on the multiclass classification tasks, we have considered the following settings: minibatch size is set to 2, initial learning rate is set to 0.001, epochs are set to 30, learning rate schedule is set to piecewise, optimization algorithm is Adam, loss function is categorical cross-entropy, total number of experiments equals 41, while time taken to perform these experiments is approximately 8448 minutes or 140 hours.

5. Results and Discussion

For binary classification between healthy and diseased classes, the experimental results are presented in Tables 3 and 4, respectively. As a visual aid, Figure 7 presents the results given in Table 3 while Figure 8 presents the results given in Table 4. We have used accuracy, F_1-score, Matthews

Table 3: Performance metrics for the binary classification tasks without augmentation, with random weak Gaussian blurred augmentation, with random shift augmentation, and with combined augmentations.

Task	Performance metrics
Without augmentation	Accuracy = 55.63% F_1 − score = 56.44% MCC = 0.1126 Sensitivity = 57.5% Specificity = 53.75% Precision = 55.42%
With random weak Gaussian blurred augmentation	Accuracy = 59.38% F_1 − score = 60.12% MCC = 0.1876 Sensitivity = 61.25% Specificity = 57.5% Precision = 59.04%
With random shifted augmentation	Accuracy = 57.5% F_1 − score = 58.54% MCC = 0.1502 Sensitivity = 60% Specificity = 55% Precision = 57.14%
With combined augmentations (along with test split)	Accuracy = 59.89% F_1 − score = 63.32% MCC = 0.1908 Sensitivity = 63.64% Specificity = 55.42% Precision = 63%

Table 4: Ranking of methods for the binary classification tasks based on performance metrics without augmentation, with random weak Gaussian blurred augmentation, with random shift augmentation, and with combined augmentations.

Performance metric	Ranking
Accuracy	(1) With combined augmentations (2) With random weak Gaussian blurred augmentation (3) With random shift augmentation (4) Without augmentation
F_1-score	(1) With combined augmentations (2) With random weak Gaussian blurred augmentation (3) With random shift augmentation (4) Without augmentation
MCC	(1) With combined augmentations (2) With random weak Gaussian blurred augmentation (3) With random shift augmentation (4) Without augmentation
Sensitivity	(1) With combined augmentations (2) With random weak Gaussian blurred augmentation (3) With random shift augmentation (4) Without augmentation
Specificity	(1) With random weak Gaussian blurred augmentation (2) With combined augmentations (3) With random shift augmentation (4) Without augmentation
Precision	(1) With combined augmentations (2) With random weak Gaussian blurred augmentation (3) With random shift augmentation (4) Without augmentation
Overall performance	(1) With combined augmentations (2) With random weak Gaussian blurred augmentation (3) With random shift augmentation (4) Without augmentation

correlation coefficient (MCC), sensitivity, specificity, and precision as performance metrics to assess the performance of different 3D-CNN architectures for this task which are trained from scratch. Mathematically,

$$\text{Accuracy} = \frac{\text{TP} + \text{TN}}{\text{TP} + \text{TN} + \text{FP} + \text{FN}}, \tag{2}$$

$$F_1\text{-score} = \frac{2\text{TP}}{2\text{TP} + \text{FP} + \text{FN}}, \tag{3}$$

$$\text{MCC} = \frac{\text{TP} \times \text{TN} - \text{FP} \times \text{FN}}{\sqrt{(\text{TP} + \text{FP})(\text{TP} + \text{FN})(\text{TN} + \text{FP})(\text{TN} + \text{FN})}}, \tag{4}$$

$$\text{Sensitivity} = \frac{\text{TP}}{\text{TP} + \text{FN}}, \tag{5}$$

$$\text{Specificity} = \frac{\text{TN}}{\text{TN} + \text{FP}}, \tag{6}$$

$$\text{Precision} = \frac{\text{TP}}{\text{TP} + \text{FP}}, \tag{7}$$

where TP, TN, FP, and FN stand for true positive, true negative, false positive, and false negative samples, respectively. Ranking of the methods for the binary classification tasks based on individual and collective performance metrics is given in Table 4.

As given in Tables 3 and 4, validation on test split is performed with the model trained using combined augmentation methods. The best performing model is the one that is trained using combined augmentation methods, then comes the model that is trained using random weak Gaussian blurred augmentation method, followed by the model trained using random shift augmentation scheme, and, finally, the model that does not use augmentation at all performed the worst. Here, combined augmentations mean combination of both random weak Gaussian blurred augmentation and random shifted augmentation schemes. Except for specificity metric, the rankings for all the methods remained the same which shows strong correlation between these performance metrics.

For the multiclass classification task, we have considered overall accuracy, relative classifier information (RCI), confusion entropy (CEN), index of balanced accuracy (IBA), geometric mean (GM), and MCC as performance metrics. Overall accuracy is the ratio of values that are correctly predicted to the sum of total values.

Tables 5–8 lists the complete statistics of the performance metrics for the multiclass classification tasks. In these tables, class-wise statistics for CEN, IBA, GM and MCC performance metrics as well as overall accuracy and RCI values for each of the four tasks, i.e., without augmentation, with random weak Gaussian blurred augmentation, with random shifted augmentation, and with combined augmentation schemes, are presented. Here, combined augmentations mean combination of both random weak Gaussian blurred augmentation and random shifted augmentation schemes. Finally, the statistics of the task involving test subset validated on the model trained without augmentation are also presented in these tables.

Table 9 lists the summary statistics of the performance metrics for the multiclass classification task, while Figure 9 visually presents the results given in Table 9. In this table, averages of CEN, IBA, GM, and MCC performance metrics are calculated by summing their class-wise values and dividing with 5. The RCI and overall accuracy values remain the same as in Table 5.

Table 10 presents a system of ranking based on the statistics given in Table 9 for the multiclass classification task. As a visual aid, Figure 10 visually presents the results given in Table 10. In this table, ranking based on individual performance metrics as well as an overall ranking obtained by considering the individual performance-based metrics is presented. Overall accuracy, RCI, IBA, GM, and MCC based ranking is obtained by considering the fact that higher values

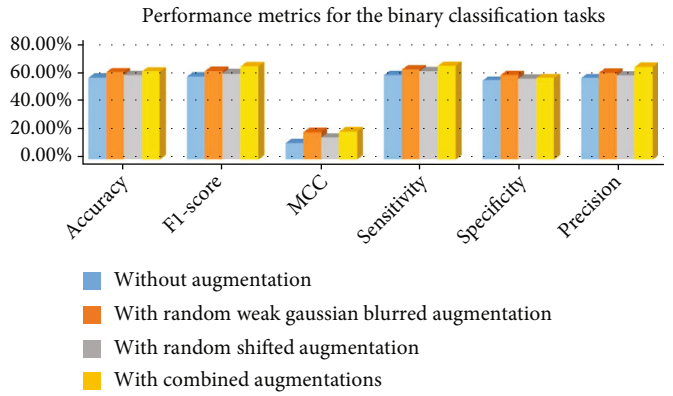

Figure 7: Visual presentation of the performance metrics for the binary classification tasks.

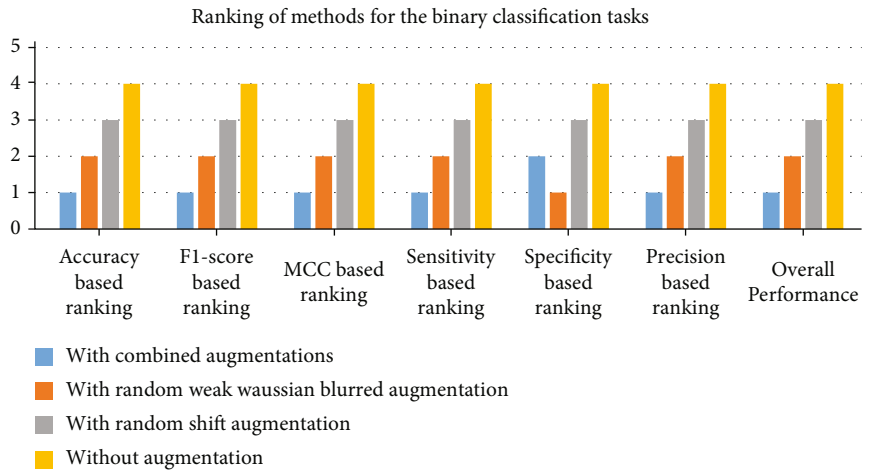

Figure 8: Visual presentation for ranking of methods for the binary classification tasks based on performance metrics.

Table 5: Overall accuracy, RCI, and class-wise CEN values for the multiclass classification tasks without augmentation, with random weak Gaussian blurred augmentation, with random shift augmentation, and with combined augmentations.

Method	Overall accuracy	RCI	CEN (mild)	CEN (moderate)	CEN (no)	CEN (proliferate)	CEN (severe)
Without augmentation	36.64%	0.0867	0.7752	0.8557	0.7734	0.5673	0.8015
With random weak Gaussian blurred augmentation	31.04%	0.038	0.8086	0.8458	0.8391	0.7008	0.8272
With random shifted augmentation	30.56%	0.0546	0.8259	0.8834	0.8242	0.6418	0.8165
With combined augmentations	33.12%	0.0647	0.793	0.8352	0.8085	0.6155	0.8341
Test set validated on the model trained without augmentation	26.66%	0.1522	0.6992	0.6274	0.9175	0.6904	0.7688

Table 6: Class-wise IBA values for the multiclass classification tasks without augmentation, with random weak Gaussian blurred augmentation, with random shift augmentation, and with combined augmentations.

Method	IBA (mild)	IBA (moderate)	IBA (no)	IBA (proliferate)	IBA (severe)
Without augmentation	0.1366	0.0649	0.1232	0.4747	0.1183
With random weak Gaussian blurred augmentation	0.1176	0.09	0.088	0.2458	0.1048
With random shifted augmentation	0.0967	0.0631	0.0833	0.3109	0.1095
With combined augmentations	0.1203	0.1	0.0997	0.3086	0.1031
Test set validated on the model trained without augmentation	0.1475	0.1974	0	0.073	0.1388

Table 7: Class-wise GM values for the multiclass classification tasks without augmentation, with random weak Gaussian blurred augmentation, with random shift augmentation, and with combined augmentations.

Method	GM (mild)	GM (moderate)	GM (no)	GM (proliferate)	GM (severe)
Without augmentation	0.5297	0.4162	0.5131	0.7558	0.5056
With random weak Gaussian blurred augmentation	0.4972	0.4523	0.4557	0.6307	0.4815
With random shifted augmentation	0.4635	0.3925	0.4513	0.6817	0.4889
With combined augmentations	0.5001	0.4639	0.4754	0.6891	0.476
Test set validated on the model trained without augmentation	0.4859	0.6038	0	0.4841	0.527

Table 8: Class-wise MCC values for the multiclass classification tasks without augmentation, with random weak Gaussian blurred augmentation, with random shift augmentation, and with combined augmentations.

Method	MCC (mild)	MCC (moderate)	MCC (no)	MCC (proliferate)	MCC (severe)
Without augmentation	0.1803	0.043	0.1599	0.4756	0.1484
With random weak Gaussian blurred augmentation	0.1238	0.0639	0.0773	0.3103	0.1093
With random shifted augmentation	0.077	-0.0176	0.0821	0.3933	0.1194
With combined augmentations	0.1264	0.0695	0.1051	0.4232	0.097
Test set validated on the model trained without augmentation	0.03636	0.3015	-0.2629	0.25	0.1666

Table 9: Summary statistics of performance metrics for the multiclass classification tasks without augmentation, with random weak Gaussian blurred augmentation, with random shift augmentation, and with combined augmentations.

Task	Performance metrics
Without augmentation	Overall accuracy = 36.64% RCI = 0.0867 Average CEN = 0.75462 Average IBA = 0.18354 Average GM = 0.54408 Average MCC = 0.20144
With random weak Gaussian blurred augmentation	Overall accuracy = 31.04% RCI = 0.038 Average CEN = 0.8043 Average IBA = 0.12924 Average GM = 0.50348 Average MCC = 0.13692
With random shift augmentation	Overall accuracy = 30.56% RCI = 0.0546 Average CEN = 0.79836 Average IBA = 0.1327 Average GM = 0.49558 Average MCC = 0.13084
With combined augmentations	Overall accuracy = 33.12% RCI = 0.0647 Average CEN = 0.77726 Average IBA = 0.14634 Average GM = 0.5209 Average MCC = 0.16424

of these metrics represent better classification while CEN-based ranking is obtained by considering that lower values are desirable as they represent better classification.

In Table 10, it can be observed that the model that performs the best is the one that is trained without augmentation followed by the model that is trained with combined augmentations, followed by the models that are trained with random weak Gaussian blurred and random shifted augmentation methods. Training without augmentation has the best performance considering individual and overall metric-based rankings, while combined augmentations have second best overall performance. Random shifted and random weak Gaussian blurred augmentation methods have equal performances. We can observe strong correlation among these performance metrics as depicted in their rankings where without augmentation and with combined augmentations can be completely specified by only a single performance metric alone. However, there is a clear difference between performances of methods employing random shift augmentation and random weak Gaussian blurred augmentation methods for the multiclass classification tasks when they are observed from individual metric-based performances alone. GM, MCC, and overall accuracy of methods employing random shifted augmentation are the worst while RCI, CEN, and IBA of methods employing random weak Gaussian blurred augmentation are the worst which signifies that these methods have disparities leading to difference in the opinion of these performance metrics. These differences could also be due to the way CNNs generalize to image transformations at a small scale [63].

For the multiclass classification task, we have found that the instances of proliferate DR class have the highest diagnostic performance. The performance of DL architectures is better in the case of binary classification than in the case of multiclass classification tasks, and this result is quite natural. Furthermore, architectures that combine different augmentation methods tend to perform better than those that do not. Furthermore, we have found the performance

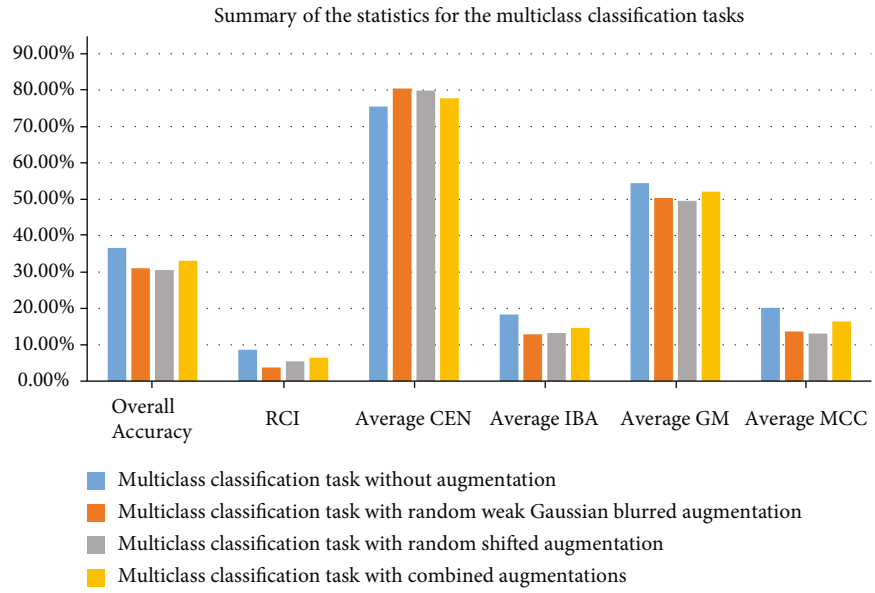

Figure 9: Visual presentation for summary statistics of performance metrics for the multiclass classification tasks.

Table 10: Ranking of methods based on performance metrics for the multiclass classification tasks without augmentation, with random weak Gaussian blurred augmentation, with random shift augmentation, and with combined augmentations.

Task	Ranking
Without augmentation	Overall accuracy – based ranking = 1 RCI – based ranking = 1 CEN – based ranking = 1 IBA – based ranking = 1 GM – based ranking = 1 MCC – based ranking = 1 Overall ranking = 1
With random weak Gaussian blurred augmentation	Overall accuracy – based ranking = 3 RCI – based ranking = 4 CEN – based ranking = 4 IBA – based ranking = 4 GM – based ranking = 3 MCC – based ranking = 3 Overall ranking = 3
With random shift augmentation	Overall accuracy – based ranking = 4 RCI – based ranking = 3 CEN – based ranking = 3 IBA – based ranking = 3 GM – based ranking = 4 MCC – based ranking = 4 Overall ranking = 3
With combined augmentations	Overall accuracy – based ranking = 2 RCI – based ranking = 2 CEN – based ranking = 2 IBA – based ranking = 2 GM – based ranking = 2 MCC – based ranking = 2 Overall ranking = 2

of architectures trained using random weak Gaussian blurring augmentation to be better than those that are trained using random shifted augmentation as the global sum of the feature maps will not be invariant to translation while performing the operation of convolution.

Architecture engineering has an impact on the performances of classification tasks. It can be observed that, for the binary classification tasks, large number of feature maps in the convolutional layer helps in getting better performances when compared with small number of feature maps in this layer. We can see that combined augmentation methods whose performances are better than other methods used large number of feature maps in the convolutional feature extracting layers. However, interesting observations can be seen for the multiclass classification tasks, where architectures with small number of feature maps help in getting the best performance overall. We can see architectures that did not employ any form of data augmentation performed better than those that employed data augmentation and these architectures employed less number of feature maps in the convolutional feature extracting layers. However, more feature maps in the convolutional layers help in getting better performances on the multiclass classification task as can be seen for the combined augmentations case that outperformed single augmentations for this task by using more complex architecture. In general, we can see the advantages brought by using deeper architectures in comparison with shallower ones when both these tasks (binary and multiclass classifications) are considered.

The suboptimal performance of DL architectures could be explained by the limited number of samples that we have used during training and validation processes [22]. Modern DL architectures require a lot of samples to train without experiencing overfitting issues. Another major limitation of our study is the lack of validation on a multicentre validation set which will prove beneficial in clinical practice. Finally, we

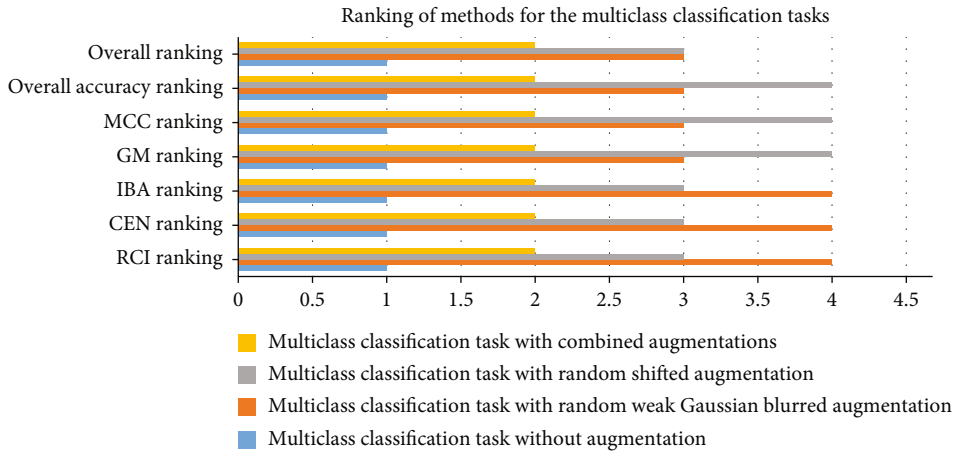

Figure 10: Visual presentation for ranking of methods based on performance metrics for the multiclass classification tasks.

hope that this pilot study deploying 3D CNN architectures with data augmentation schemes can be supportive to eye care specialists on the deployment of DL methods in terms of their clinical use.

6. Conclusions

In this research, we have utilized different DL methods to study both binary and multiclass classification problems to differentiate between different stages of DR. We have deployed 10-fold cross-validation approach to select optimal set of hyperparameters for the binary and multiclass classification tasks. For the binary classification task, we have found the performance of architecture trained using combined augmentation methods to be the best while the performance of model trained without any augmentation is found to be the worst. In contrast, in the multiclass case, we have observed the overall performance of model trained without augmentation to be the best while the performance of models trained with a single augmentation method whether random weak Gaussian blurring augmentation or random shifted augmentation to be the worst.

In the future, we will work on other retinal diseases such as retinal detachment using fundus images deploying data augmentation methods such as elastic/plastic deformations as well as other DL-based architectures such as graph convolutional networks. Eye diseases such as age-related macular degeneration, media haze, drusen, myopia, branch retinal vein occlusion, tessellation, epiretinal membrane, laser scars, macular scar, central serous retinopathy, optic disc cupping, central retinal vein occlusion, tortuous vessels, asteroid hyalosis, optic disc pallor, optic disc edema, optociliary shunt, anterior ischemic optic neuropathy, parafoveal telangiectasia, retinal traction, retinitis, chorioretinitis, exudation, retinal pigment epithelium changes, macular hole, retinitis pigmentosa, and many other eye diseases [64] are affecting a large number of people worldwide, and their accurate and early detection using DL-based methods may allow for palliative care procedures employed by clinicians and medical practitioners.

Data Availability

The data employed to support the findings of this research is publicly available from the Kaggle platform and TeleOphta database.

Conflicts of Interest

The authors declare that there are no conflicts of interest regarding the publication of this paper.

References

[1] X. Lin, Y. Xu, X. Pan et al., "Global, regional, and national burden and trend of diabetes in 195 countries and territories: an analysis from 1990 to 2025," *Scientific Reports*, vol. 10, no. 1, pp. 1–11, 2020.

[2] G. Kalyani, B. Janakiramaiah, A. Karuna, and L. V. N. Prasad, "Diabetic retinopathy detection and classification using capsule networks," *Complex & Intelligent Systems*, 2021.

[3] E. Decencière, G. Cazuguel, X. Zhang et al., "TeleOphta: machine learning and image processing methods for teleophthalmology," *IRBM*, vol. 34, no. 2, pp. 196–203, 2013.

[4] H. Riaz, J. Park, H. Choi, H. Kim, and J. Kim, "Deep and densely connected networks for classification of diabetic retinopathy," *Diagnostics*, vol. 10, no. 1, p. 24, 2020.

[5] S. Sooraj and M. Bedeeuzzaman, "Automatic classification of diabetic retinopathy based on deep learning - a review," in *2020 International Conference on Futuristic Technologies in Control Systems & Renewable Energy (ICFCR)*, pp. 1–5, Malappuram, India, 2020.

[6] M. R. K. Mookiah, U. R. Acharya, C. K. Chua, C. M. Lim, E. Y. K. Ng, and A. Laude, "Computer-aided diagnosis of diabetic retinopathy: a review," *Computers in Biology and Medicine*, vol. 43, no. 12, pp. 2136–2155, 2013.

[7] Y. LeCun, Y. Bengio, and G. Hinton, "Deep learning," *Nature*, vol. 521, no. 7553, pp. 436–444, 2015.

[8] I. Ahmad, I. Ullah, W. U. Khan et al., "Efficient algorithms for E-healthcare to solve multiobject fuse detection problem," *Journal of Healthcare Engineering*, vol. 2021, Article ID 9500304, 16 pages, 2021.

[9] C. You, W. Cong, G. Wang et al., "Structurally-sensitive multi-scale deep neural network for low-dose CT denoising," *IEEE Access*, vol. 6, pp. 41839–41855, 2018.

[10] A. Samanta, A. Saha, S. C. Satapathy, S. L. Fernandes, and Y. D. Zhang, "Automated detection of diabetic retinopathy using convolutional neural networks on a small dataset," *Pattern Recognition Letters*, vol. 135, pp. 293–298, 2020.

[11] S. R. Shiva, R. R. NilambarSethi, and M. Gadiraju, "Extensive analysis of machine learning algorithms to early detection of diabetic retinopathy," *Materials Today: Proceedings*, 2020.

[12] G. Saxena, D. K. Verma, A. Paraye, A. Rajan, and A. Rawat, "Improved and robust deep learning agent for preliminary detection of diabetic retinopathy using public datasets," *Intelligence-Based Medicine*, vol. 3-4, article 100022, 2020.

[13] M. M. Butt, G. Latif, D. N. F. A. Iskandar, J. Alghazo, and A. H. Khan, "Multi-channel convolutions neural network based diabetic retinopathy detection from fundus images," *Procedia Computer Science*, vol. 163, pp. 283–291, 2019.

[14] M. M. Islam, H.-C. Yang, T. N. Poly, W.-S. Jian, and Y. C. Li, "Deep learning algorithms for detection of diabetic retinopathy in retinal fundus photographs: a systematic review and meta-analysis," *Computer Methods and Programs in Biomedicine*, vol. 191, p. 105320, 2020.

[15] H. Safi, S. Safi, A. Hafezi-Moghadam, and H. Ahmadieh, "Early detection of diabetic retinopathy," *Survey of Ophthalmology*, vol. 63, no. 5, pp. 601–608, 2018.

[16] A. P. Bhatkar and G. U. Kharat, "Detection of diabetic retinopathy in retinal images using MLP classifier," in *2015 IEEE International Symposium on Nanoelectronic and Information Systems*, pp. 331–335, Indore, India, 2015.

[17] T. Shanthi and R. S. Sabeenian, "Modified Alexnet architecture for classification of diabetic retinopathy images," *Computers & Electrical Engineering*, vol. 76, pp. 56–64, 2019.

[18] S. Wan, Y. Liang, and Y. Zhang, "Deep convolutional neural networks for diabetic retinopathy detection by image classification," *Computers & Electrical Engineering*, vol. 72, pp. 274–282, 2018.

[19] G. T. Zago, R. V. Andreão, B. Dorizzi, and E. O. Teatini Salles, "Diabetic retinopathy detection using red lesion localization and convolutional neural networks," *Computers in Biology and Medicine*, vol. 116, p. 103537, 2020.

[20] V. Gulshan, L. Peng, M. Coram et al., "Development and validation of a deep learning algorithm for detection of diabetic retinopathy in retinal fundus photographs," *JAMA*, vol. 316, no. 22, pp. 2402–2410, 2016.

[21] R. Sayres, A. Taly, E. Rahimy et al., "Using a deep learning algorithm and integrated gradients explanation to assist grading for diabetic retinopathy," *Ophthalmology*, vol. 126, no. 4, pp. 552–564, 2019.

[22] J. Y. Choi, T. K. Yoo, J. G. Seo, J. Kwak, T. T. Um, and T. H. Rim, "Multi-categorical deep learning neural network to classify retinal images: a pilot study employing small database," *PLoS One*, vol. 12, no. 11, article e0187336, 2017.

[23] S. M. S. Islam, M. M. Hasan, and S. Abdullah, "Deep learning based early detection and grading of diabetic retinopathy using retinal fundus images," 2018, https://arxiv.org/abs/1812.10595.

[24] K. Shankar, A. R. W. Sait, D. Gupta, S. K. Lakshmanaprabu, A. Khanna, and H. M. Pandey, "Automated detection and classification of fundus diabetic retinopathy images using synergic deep learning model," *Pattern Recognition Letters*, vol. 133, pp. 210–216, 2020.

[25] E. Beede, E. Baylor, F. Hersch et al., "A human-centered evaluation of a deep learning system deployed in clinics for the detection of diabetic retinopathy," in *Proceedings of the 2020 CHI Conference on Human Factors in Computing Systems*, pp. 1–12, Honolulu, HI, USA, 2020.

[26] N. Khare, P. Devan, C. Chowdhary et al., "SMO-DNN: spider monkey optimization and deep neural network hybrid classifier model for intrusion detection," *Electronics*, vol. 9, no. 4, p. 692, 2020.

[27] I. Qureshi, J. Ma, and Q. Abbas, "Diabetic retinopathy detection and stage classification in eye fundus images using active deep learning," *Multimedia Tools and Applications*, vol. 80, no. 8, pp. 11691–11721, 2021.

[28] S. Das, K. Kharbanda, S. M, R. Raman, and E. D. D, "Deep learning architecture based on segmented fundus image features for classification of diabetic retinopathy," *Biomedical Signal Processing and Control*, vol. 68, article 102600, 2021.

[29] F. Li, Y. Wang, T. Xu et al., "Deep learning-based automated detection for diabetic retinopathy and diabetic macular oedema in retinal fundus photographs," *Eye*, 2021.

[30] J. Limwattanayingyong, V. Nganthavee, K. Seresirikachorn et al., "Longitudinal screening for diabetic retinopathy in a nationwide screening program: comparing deep learning and human graders," *Journal of Diabetes Research*, vol. 2020, Article ID 8839376, 8 pages, 2020.

[31] N. Tsiknakis, D. Theodoropoulos, G. Manikis et al., "Deep learning for diabetic retinopathy detection and classification based on fundus images: a review," *Computers in Biology and Medicine*, vol. 135, article 104599, 2021.

[32] M. Karakaya and R. E. Hacisoftaoglu, "Comparison of smartphone-based retinal imaging systems for diabetic retinopathy detection using deep learning," *BMC Bioinformatics*, vol. 21, no. S4, p. 259, 2020.

[33] O. Vinyals, C. Blundell, T. Lillicrap, K. Kavukcuoglu, and D. Wierstra, "Matching networks for one shot learning," in *Advances in Neural Information Processing Systems*, pp. 3630–3638, Curran Associates, Inc., 2016.

[34] J. Snell, K. Swersky, and R. Zemel, "Prototypical networks for few-shot learning," in *Advances in Neural Information Processing Systems*, pp. 4077–4087, Curran Associates, Inc., 2017.

[35] F. Sung, Y. Yang, L. Zhang, T. Xiang, P. H. S. Torr, and T. M. Hospedales, "Learning to compare: relation network for few-shot learning," in *2018 IEEE/CVF Conference on Computer Vision and Pattern Recognition*, pp. 1199–1208, Salt Lake City, UT, USA, 2018.

[36] J. Xia, D. Deng, and D. Fan, "A note on implementation methodologies of deep learning-based signal detection for conventional MIMO transmitters," *IEEE Transactions on Broadcasting*, vol. 66, no. 3, pp. 744-745, 2020.

[37] K. He, Z. Wang, D. Li, F. Zhu, and L. Fan, "Ultra-reliable MU-MIMO detector based on deep learning for 5G/B5G-enabled IoT," *Physical Communication*, vol. 43, pp. 101181–101187, 2020.

[38] B. K. Yousafzai, S. Afzal, T. Rahman et al., "Student-performulator: student academic performance using hybrid deep neural network," *Sustainability*, vol. 13, no. 17, p. 9775, 2021.

[39] W. U. Khan, M. A. Javed, T. N. Nguyen, S. Khan, and B. M. Elhalawany, "Energy-efficient resource allocation for 6G backscatter-enabled NOMA IoV networks," *IEEE Transactions on Intelligent Transportation Systems*, 2021.

[40] C. Li, J. Xia, F. Liu et al., "Dynamic offloading for multiuser Muti-CAP MEC networks: a deep reinforcement learning approach," *IEEE Transactions on Vehicular Technology*, vol. 70, no. 3, pp. 2922–2927, 2021.

[41] W. U. Khan, F. Jameel, X. Li, M. Bilal, and T. A. Tsiftsis, "Joint spectrum and energy optimization of NOMA-enabled small-cell networks with QoS guarantee," *IEEE Transactions on Vehicular Technology*, vol. 70, no. 8, pp. 8337–8342, 2021.

[42] Y. Guo, Z. Zhao, K. He, S. Lai, J. Xia, and L. Fan, "Efficient and flexible management for industrial Internet of Things: a federated learning approach," *Computer Networks*, vol. 192, pp. 108122–108129, 2021.

[43] W. U. Khan, X. Li, A. Ihsan, M. A. Khan, V. G. Menon, and M. Ahmed, "NOMA-enabled optimization framework for next-generation small-cell IoV networks under imperfect SIC decoding," *IEEE Transactions on Intelligent Transportation Systems*, 2021.

[44] X. Li, Y. Zheng, W. U. Khan et al., "Physical layer security of cognitive ambient backscatter communications for green Internet-of-Things," *IEEE Transactions on Green Communications and Networking*, vol. 5, no. 3, pp. 1066–1076, 2021.

[45] W. U. Khan, X. Li, M. Zeng, and O. A. Dobre, "Backscatter-enabled NOMA for future 6G systems: a new optimization framework under imperfect SIC," *IEEE Communications Letters*, vol. 25, no. 5, pp. 1669–1672, 2021.

[46] F. Jameel, W. U. Khan, N. Kumar, and R. Jantti, "Efficient power-splitting and resource allocation for cellular V2X communications," *IEEE Transactions on Intelligent Transportation Systems*, vol. 22, no. 6, pp. 3547–3556, 2021.

[47] W. U. Khan, F. Jameel, N. Kumar, R. Jantti, and M. Guizani, "Backscatter-enabled efficient V2X communication with non-orthogonal multiple access," *IEEE Transactions on Vehicular Technology*, vol. 70, no. 2, pp. 1724–1735, 2021.

[48] A. U. Khan, M. Tanveer, W. U. Khan et al., "An enhanced spectrum reservation framework for heterogeneous user in CR-enabled IoT networks, IEEE Wireless Communications Letters," *Early Access*, vol. 10, p. 1, 2021.

[49] A. B. Tufail, Y.-K. Ma, M. K. A. Kaabar et al., "Deep learning in cancer diagnosis and prognosis prediction: a minireview on challenges, recent trends, and future directions," *Computational and Mathematical Methods in Medicine*, vol. 2021, Article ID 9025470, 28 pages, 2021.

[50] A. B. Tufail, Y.-K. Ma, Q.-N. Zhang et al., "3D convolutional neural networks-based multiclass classification of Alzheimer's and Parkinson's diseases using PET and SPECT neuroimaging modalities," *Brain Informatics*, vol. 8, no. 1, p. 23, 2021.

[51] S. Ji, W. Xu, M. Yang, and K. Yu, "3D convolutional neural networks for human action recognition," *IEEE Transactions on Pattern Analysis and Machine Intelligence*, vol. 35, no. 1, pp. 221–231, 2013.

[52] S. Tang, W. Zhou, L. Chen, L. Lai, J. Xia, and L. Fan, "Battery-constrained federated edge learning in UAV-enabled IoT for B5G/6G networks," *Physical Communication*, vol. 47, pp. 101381–101389, 2021.

[53] J. Xia, L. Fan, W. Xu et al., "Secure cache-aided multi-relay networks in the presence of multiple eavesdroppers," *IEEE Transactions on Communications*, vol. 67, no. 11, pp. 7672–7685, 2019.

[54] V. Nair and G. E. Hinton, "Rectified linear units improve restricted Boltzmann machines," in *ICML*, pp. 807–814, Omnipress, 2010.

[55] R. Khan, Q. Yang, I. Ullah et al., "3D convolutional neural networks based automatic modulation classification in the presence of channel noise," *IET Communications*, 2021.

[56] R. Sayres, N. Hammel, and Y. Liu, "Artificial intelligence, machine learning and deep learning for eye care specialists," *Annals of Eye Science*, vol. 5, p. 18, 2020.

[57] S. Ioffe and C. Szegedy, "Batch normalization: accelerating deep network training by reducing internal covariate shift," in *Proceedings of the 32nd International Conference on Machine Learning, PMLR, JMLR*, pp. 448–456, France, 2015.

[58] X. Yin, J. L. Coatrieux, Q. Zhao et al., "Domain progressive 3D residual convolution network to improve low-dose CT imaging," *IEEE Transactions on Medical Imaging*, vol. 38, no. 12, pp. 2903–2913, 2019.

[59] J. Ming, B. S. Yi, and Y. G. Zhang, "Low-dose CT image denoising using classification densely connected residual network," *KSII Transactions on Internet and Information Systems*, vol. 14, no. 6, pp. 2480–2496, 2020.

[60] N. Srivastava, G. Hinton, A. Krizhevsky, I. Sutskever, and R. Salakhutdinov, "Dropout: a simple way to prevent neural networks from overfitting," *Journal of Machine Learning Research*, vol. 15, pp. 1929–1958, 2014.

[61] D.-A. Clevert, T. Unterthiner, and S. Hochreiter, "Fast and accurate deep network learning by exponential linear units (ELUs)," 2015, https://arxiv.org/abs/1511.07289.

[62] D. P. Kingma and J. Ba, "Adam: a method for stochastic optimization," 2014, https://arxiv.org/abs/1412.6980.

[63] A. Azulay and Y. Weiss, "Why do deep convolutional networks generalize so poorly to small image transformations?," *Journal of Machine Learning Research*, vol. 20, pp. 1–25, 2019.

[64] S. Pachade, P. Porwal, D. Thulkar et al., "Retinal fundus multi-disease image dataset (RFMiD): a dataset for multi-disease detection research," *Data*, vol. 6, no. 2, p. 14, 2021.

Hindawi
Wireless Communications and Mobile Computing
Volume 2021, Article ID 6043391, 12 pages
https://doi.org/10.1155/2021/6043391

Research Article

A General Order Reduction Method of Wideband Digital Predistortion Model Using Attention Mechanism

Zhijun Liu, Xin Hu, and Weidong Wang

School of Electronic Engineering, Beijing University of Posts and Telecommunications, Beijing 100876, China

Correspondence should be addressed to Weidong Wang; wangweidong@bupt.edu.cn

Received 9 September 2021; Revised 4 October 2021; Accepted 12 October 2021; Published 5 November 2021

Academic Editor: Junjuan Xia

In wireless networks, for the common in-phase and quadrature-phase (I/Q) imbalance in the transmitters, the I/Q branch models of digital predistortion (DPD) need to be identified separately, to improve the linearization effects. The existing order reduction methods of the predistorter are based on the contributions of the complex basis function terms, so as not to deal with the different contributions of I/Q components of the complex basis function terms caused by the separate identification of the I/Q branch models. The separate pruning of the I/Q branch models will increase the complexity. Aiming at this issue, this paper proposes a general order reduction method based on the attention mechanism for the predistortion of the power amplifiers (PAs). This method is suitable for pruning both the traditional models and neural network-based models. In this method, the attention mechanism is used to evaluate the contributions of the real basis function terms to the predistorted output's I/Q components through offline training, and the influence of the cross terms of the I/Q branch models is considered. The experimental results based on the comparison with other typical methods under 100 MHz Doherty PA and different I/Q imbalance levels show that this method has superior pruning performance and good linearization ability.

1. Introduction

With the rapid iteration of the fifth-generation (5G) wireless systems, wider signal bandwidth and more complex modulation modes are used, to satisfy the rapid growth of the requirement of the data service [1–3]. However, the wide signal bandwidth and efficient modulation make the transmitters, especially the power amplifiers (PAs), exhibit more complex nonlinear behavior characteristics [4], which leads to the difficulty of high-efficiency transmission in the transmitting system. To solve this problem, digital predistortion (DPD) is one of the most commonly used linearization techniques [5–7].

DPD techniques compensate for the nonlinear behaviors of the transmitter by constructing a nonlinear model that is opposite to the nonlinear characteristics of the transmitter [8]. At present, the most common and popular predistortion models are the full Volterra (FV) series models. Since these models' parameters are linear with respect to the output of the system, these models can be easily identified by the classical regression theory [9]. However, the complex nonlinear behaviors (including nonlinearity and memory effects [6]) caused by the increase of the signal bandwidth and complex modulation modes will lead to the curse of dimensionality of the FV models [9]. Therefore, the order reduction of the FV model has become an effective means to improve the availability of the model and reduce the cost [10, 11]. To this end, based on the general FV series model, various prior pruning models, such as the memory polynomial (MP) model [12] and the generalized MP (GMP) model [13], are proposed. These models are easy to be modeled in the field-programmable gate array (FPGA), such as through lookup table (LUT) [14–16], so they are commonly used engineering models at present. However, these models are pruned based on prior knowledge and are still general predistortion models [4]. For a specific PA, in order to meet the linearization requirements, these models still include many basic function terms with fewer contributions, leading to the complexity of the model.

For this reason, classical posterior pruning techniques are proposed to select the necessary terms based on the nonlinear behavior of the specific PA, to find the optimal

structure under a given PA [14, 17, 18]. The most typical method is the predistortion model pruning technique based on orthogonal matching pursuit (OMP) [11]. This method selects the term with the greatest correlation with the remaining output in each iteration [11] to determine the optimal predistortion structure. To solve the ill-condition of the equation system caused by the high correlation between the basis function terms, a doubly OMP (DOMP) algorithm uses Gram-Schmidt orthogonalization to eliminate the correlation between the selected and unselected basis function spaces after each iteration [17]. However, the pseudo inverse calculation and the Kronecker product calculation in the orthogonalization process lead to the high computational complexity of the algorithm [9]. To this end, the simplified sparse parameter identification DOMP (SSPI DOMP) algorithm is proposed to implement the pseudo inverse computation through the recursive process [19], which effectively reduces the computational complexity. Reference [9] also proposed to realize the pseudo inverse calculation by processing the covariance matrix by the orthogonal properties, to reduce the calculation cost further. In addition, a predistortion model pruning algorithm based on adaptive principal component analysis (PCA) was proposed in reference [14]. Reference [20] also proposed a pruning algorithm based on the projection of the residual vector. All the above pruning methods regard the complex basis function term as a whole and then achieve order reduction.

However, in real wireless communication systems, the nonideal behavior of the modulator will lead to the mismatch between the gain and the phase of the transmission signal and then cause the imbalance of in-phase and quadrature-phase (I/Q) components [21]. The modulator imperfections are interwoven with the nonlinear behavior of PA, which further reduces the transmission quality of the system [22, 23]. For this situation, the two branches (namely, I/Q components) of the transmitters can be compensated, respectively. In other words, the I/Q components of the compensator can be identified independently, to cope with the nonideal behavior of the modulator. For example, widely used artificial neural network (ANN) models, such as the neural network (NN) model [21] and convolutional NN (CNN) model [5], are predistortion models of I/Q separate identification. The traditional models can also be used for independent modeling of I/Q branches, which can be expressed as

$$\begin{cases} x_I(n) = \left[\bar{\mathbf{U}}_I(n) \quad \bar{\mathbf{U}}_Q(n)\right]\mathbf{w}_I', \\ x_Q(n) = \left[\bar{\mathbf{U}}_I(n) \quad \bar{\mathbf{U}}_Q(n)\right]\mathbf{w}_Q', \end{cases} \tag{1}$$

where $x_I(n)$ and $x_Q(n)$ represent the I/Q components of the predistorter and $\bar{\mathbf{U}}(n)$ is the predistortion model. Table 1 shows the comparison of the normalized mean square error (NMSE) performance between independent identification and combined identification of I/Q components of the predistorter under 100 MHz Doherty PA, which verifies the above idea. References [8, 23] also proposed the compensation models for I/Q imbalance, which are independent of the DPD model and resulting in the complexity of the design.

In this case, the I/Q components of the basis function terms have independent contributions to the linearization effects. If the I/Q branch models of the predistorter are pruned separately, such as using DOMP, the basis function terms of the I/Q branch models of the predistorter need to be constructed independently, which leads to the high design complexity in FPGA. It has become a difficult point to find the real basis function terms that are important to the I/Q components of the predistortion output.

To solve this issue, this paper proposes a general order reduction method of the predistortion model based on the attention mechanism. In reference [24], we have verified that this method can effectively prune the input items of the NN-based models. In this paper, we improve this method and apply it to the pruning of the traditional polynomial models, to prove its universality. This method firstly calculates the comprehensive contributions of the real basis function terms to the predistorted output's I/Q components using the attention mechanism through offline training, which considers the influence of the cross basis function terms of the I/Q branch models. Since the contributions of the real basis function terms to the predistorted output's I/Q components are calculated simultaneously, that is, the cross terms are evaluated, the I/Q branch models are consistent, which further reduces the design complexity of the model. The experimental results based on the comparison with other typical methods under 100 MHz Doherty PA and different I/Q imbalance levels show the effectiveness of the method.

The contributions of this paper are as follows:

(i) The traditional I/Q imbalance models are configured independently, which leads to high model complexity [8, 23]. In order to reduce the model complexity, the I/Q branch models of the predistorter are modeled separately, to compensate for the I /Q imbalance and PA's nonlinearity simultaneously

(ii) The existing order reduction methods are based on the contributions of the complex basis function terms, so as not to deal with the different contributions of I/Q components of the complex basis function terms [11, 17]. This paper distinguishes the different contributions of the I/Q components of the basis function terms to the I/Q branch models, to further reduce the complexity of the model

(iii) As a result of all the above contributions, this work achieves a good compromise between the model complexity and linearization effects to drive the 100 MHz Doherty PA. In addition, compared with the existing order reduction models, the proposed model has the lowest complexity of the model

The structure of the paper is organized as follows. In Section 2, the modeling and identification processes of the I/Q branch models of the predistorter are described, and the principle of the attention mechanism is analyzed. Section 3 describes in detail the proposed order reduction method of

Table 1: Performance comparison of I/Q independent identification and I/Q combined identification (GMP model).

	PA nonlinearity	PA nonlinear and I/Q imbalance
Combination identification of I/Q	NMSE = −32.67 dB	NMSE = −22.75 dB
Independent identification of I/Q	NMSE = -37.67 dB	NMSE = −34.47 dB

the predistortion model based on the attention mechanism and gives the specific training process. Section 4 introduces the test platform for validation of the proposed order reduction method. In Section 5, the measurement and validation results of the proposed method are described and analyzed. The conclusion is given in Section 6.

2. Digital Predistortion Based on I/Q Separate Identification

2.1. Predistortion Model of I/Q Separate Identification. Due to the nonideal behavior of the modulator, the nonlinear behaviors of PA are interleaved with the I/Q imbalance, which leads to more complex nonlinear characteristics of the transmitter [21]. Therefore, to improve the linearization effects, the compensators of the I/Q branches should be identified separately, to deal with the asymmetry of the I/Q branches of the transmitter. The predistortion structure of I/Q separate identification is shown in Figure 1. The I/Q branch models of the predistorter are modeled using the real basis function terms composed of the I/Q components of the traditional complex basis function terms and then identified separately. The indirect learning architecture (ILA) [7] is used to identify the predistorter. The I/Q branch models based on the GMP model can be expressed as follows [13]:

$$\begin{aligned} x_I(n) = & \sum_{k=0}^{Ka-1}\sum_{l=0}^{La-1} \alpha_{kl}^{II} y_I(n-l)|y(n-l)|^k \\ & + \sum_{k=1}^{Kb}\sum_{l=0}^{Lb-1}\sum_{m=1}^{Mb} \beta_{klm}^{II} y_I(n-l)|y(n-l-m)|^k \\ & + \sum_{k=1}^{Kc}\sum_{l=0}^{Lc-1}\sum_{m=1}^{Mc} \gamma_{klm}^{II} y_I(n-l)|y(n-l+m)|^k \\ & + \sum_{k=0}^{Ka-1}\sum_{l=0}^{La-1} \alpha_{kl}^{IQ} y_Q(n-l)|y(n-l)|^k \\ & + \sum_{k=1}^{Kb}\sum_{l=0}^{Lb-1}\sum_{m=1}^{Mb} \beta_{klm}^{IQ} y_Q(n-l)|y(n-l-m)|^k \\ & + \sum_{k=1}^{Kc}\sum_{l=0}^{Lc-1}\sum_{m=1}^{Mc} \gamma_{klm}^{IQ} y_Q(n-l)|y(n-l+m)|^k, \end{aligned} \tag{2}$$

where $y(n)$ is the output signal of the PA and $y_I(n)$ and $y_Q(n)$ represent the I/Q components of $y(n)$, respectively. $\{K_a, L_a, K_b, L_b, M_b, K_c, L_c, M_c\}$ are the parameters of the GMP model. $\{\alpha_{kl}^{II}, \beta_{klm}^{II}, \gamma_{klm}^{II}, \alpha_{kl}^{IQ}, \beta_{klm}^{IQ}, \gamma_{klm}^{IQ}\}$ are the model coefficients. $x_I(n)$ is the I component of the PA input. The Q component can be represented by the same model as Equation (2).

The input and output data of N groups of the predistortion model are collected, and then, the I/Q branch models of the predistortion can be written in matrix form.

$$\begin{cases} \mathbf{x}_I = \left[\bar{\mathbf{Y}}_I \quad \bar{\mathbf{Y}}_Q\right]\boldsymbol{\omega}_I, \\ \mathbf{x}_Q = \left[\bar{\mathbf{Y}}_I \quad \bar{\mathbf{Y}}_Q\right]\boldsymbol{\omega}_Q, \end{cases} \tag{3}$$

where $\mathbf{x}_I = [x_I(N), x_I(N-1), \cdots, x_I(1)]^T$,

$$\mathbf{x}_Q = \left[x_Q(N), x_Q(N-1), \cdots, x_Q(1)\right]^T, \tag{4}$$

$$\boldsymbol{\omega}_I = \left[\alpha_{00}^{II}, \alpha_{01}^{II}, \cdots, \gamma_{Kc(Lc-1)Mc}^{II}, \alpha_{00}^{IQ}, \cdots, \gamma_{Kc(Lc-1)Mc}^{IQ}\right]^T, \tag{5}$$

$$\boldsymbol{\omega}_Q = \left[\alpha_{00}^{QI}, \alpha_{01}^{QI}, \cdots, \gamma_{Kc(Lc-1)Mc}^{QI}, \alpha_{00}^{QQ}, \cdots, \gamma_{Kc(Lc-1)Mc}^{QQ}\right]^T, \tag{6}$$

$$\bar{\mathbf{Y}} = \left[\bar{\mathbf{Y}}(N), \bar{\mathbf{Y}}(N-1), \cdots, \bar{\mathbf{Y}}(1)\right]^T, \tag{7}$$

$$\bar{\mathbf{Y}}(n) = \left[\bar{y}_1(n), \bar{y}_2(n), \cdots, \bar{y}_S(n)\right]^T, \tag{8}$$

where $\bar{\mathbf{Y}}_I$ and $\bar{\mathbf{Y}}_Q$ are the I/Q component matrices of $\bar{\mathbf{Y}}$, respectively. $\bar{\mathbf{Y}}(n), (n = 1, 2, \cdots N)$ is a complex vector composed of the basis function terms corresponding to signal $y(n)$, and $S = K_aL_a + K_bL_bM_b + K_cL_cM_c$ is the number of complex basis function terms.

The I/Q branch models of the predistortion have the same structure but are identified separately, to cope with the I/Q imbalance. Equation (3) is solved by the least-squares (LS) algorithm [25, 26]; then, the coefficients of the I/Q branch models can be estimated.

$$\begin{cases} \widehat{\boldsymbol{\omega}}_I = \left(\left[\bar{\mathbf{Y}}_I \quad \bar{\mathbf{Y}}_Q\right]^H\left[\bar{\mathbf{Y}}_I \quad \bar{\mathbf{Y}}_Q\right]\right)^{-1}\left[\bar{\mathbf{Y}}_I \quad \bar{\mathbf{Y}}_Q\right]^H\mathbf{x}_I, \\ \widehat{\boldsymbol{\omega}}_Q = \left(\left[\bar{\mathbf{Y}}_I \quad \bar{\mathbf{Y}}_Q\right]^H\left[\bar{\mathbf{Y}}_I \quad \bar{\mathbf{Y}}_Q\right]\right)^{-1}\left[\bar{\mathbf{Y}}_I \quad \bar{\mathbf{Y}}_Q\right]^H\mathbf{x}_Q, \end{cases} \tag{9}$$

where $\widehat{\boldsymbol{\omega}}_I$ and $\widehat{\boldsymbol{\omega}}_Q$ are the estimations of $\boldsymbol{\omega}_I$ and $\boldsymbol{\omega}_Q$, respectively. In the calculation of the I/Q components of the predistortion in FPGA, the coefficients of the predistortion model are multiplied by the model in I/Q branches, respectively. Therefore, the different coefficients of the I/Q branch models do not complicate the predistortion process.

2.2. The Principle of the Attention Mechanism. The achievements of artificial intelligence in the field of communication provide us with ideas [27, 28]. The attention mechanism is an effective structure to focus on important features, which has been widely applied in the fields of speech recognition [29] and image processing [30]. Based on the importance of the input features to the generation of the output, the attention mechanism weights the input features, to

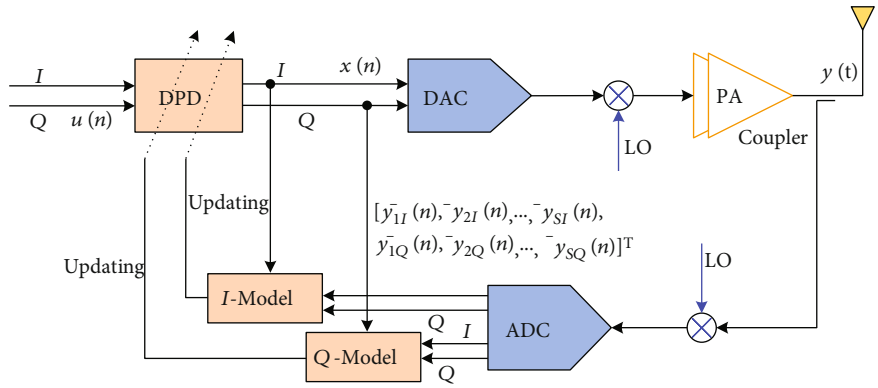

Figure 1: Digital predistortion structure based on I/Q separate identification.

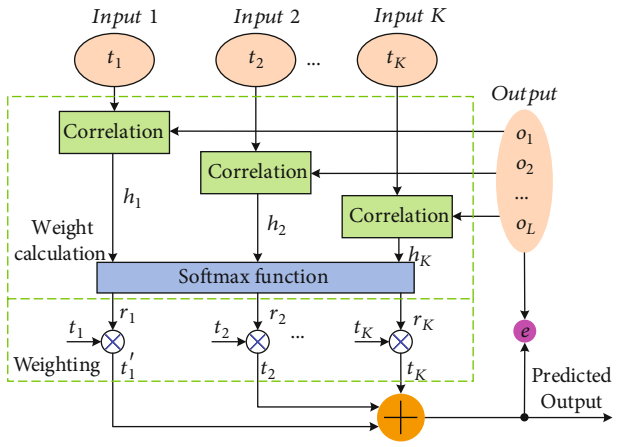

Figure 2: Implementation block diagram of the attention mechanism.

strengthen the important features and weaken the unimportant features, which can improve the fitting ability. The principle of the attention mechanism is shown in Figure 2. Let the input of the module be $\mathbf{t}$, which can be written as

$$\mathbf{t} = [t_1, t_2, \cdots, t_K]^T, \tag{10}$$

where K is the number of input nodes. The fitting output is $\mathbf{o}$, which can be written as

$$\mathbf{o} = [o_1, o_2, \cdots, o_L]^T, \tag{11}$$

where L is the number of output nodes.

First, the correlation between each input $t_i, (i = 1, 2, \cdots, K)$ and all outputs $\mathbf{o}$ is calculated. The commonly used method to calculate correlation is NN [28]. The correlation obtained can be written as

$$h_i = \mathrm{Cor}(t_i, \mathbf{o}), (i = 1, 2, \cdots, K), \tag{12}$$

where $\mathrm{Cor}(\cdot)$ is the function that calculates the correlation.

Then, the correlations are normalized and converted to the probability form through the Softmax function, to mean the weights of the input. The weights of the input can be written as

$$r_i = \frac{\exp(h_i)}{\sum_{j=1}^{K} \exp(h_j)}, (i = 1, 2, \cdots, K), \tag{13}$$

where $\exp(k)$ stands for e^k and $\sum(\cdot)$ represents the sum function.

Finally, the weights are used to weigh the corresponding input of the module. Using weighted inputs, the model outputs can be fitted. By weighting the inputs, the valid input features are emphasized, and the invalid ones are weakened, so as to improve the fitting performance. This paper does not use the attention mechanism to improve the modeling ability but embeds the attention mechanism into the predistortion model to obtain the weights of the basis function terms to evaluate the contributions of the basis function terms by weights.

3. The Proposed Order Reduction Method of the Predistortion Model

In this section, the structure of the proposed order reduction method of the predistortion model is given first, and each module is described in detail. Then, the training method and process of the proposed order reduction method are analyzed.

3.1. The Structure of the Proposed Order Reduction Method. In order to improve the linearization performance in the case of I/Q imbalance, the I/Q branch models of the predistorter are identified separately. At this point, the I/Q components of all complex basis function terms have separate model coefficients and independent contributions to the predistortion output, as shown in the analysis in Section 2, part 1. To further simplify the structure of the predistortion model, this paper proposes an order reduction method of the predistortion model based on the attention mechanism, as shown in Figure 3. In this method, all real basis function terms are distinguished, and their contributions to the predistortion output are given, so that I/Q branch models of the predistorter can be pruned. Meanwhile, to ensure the

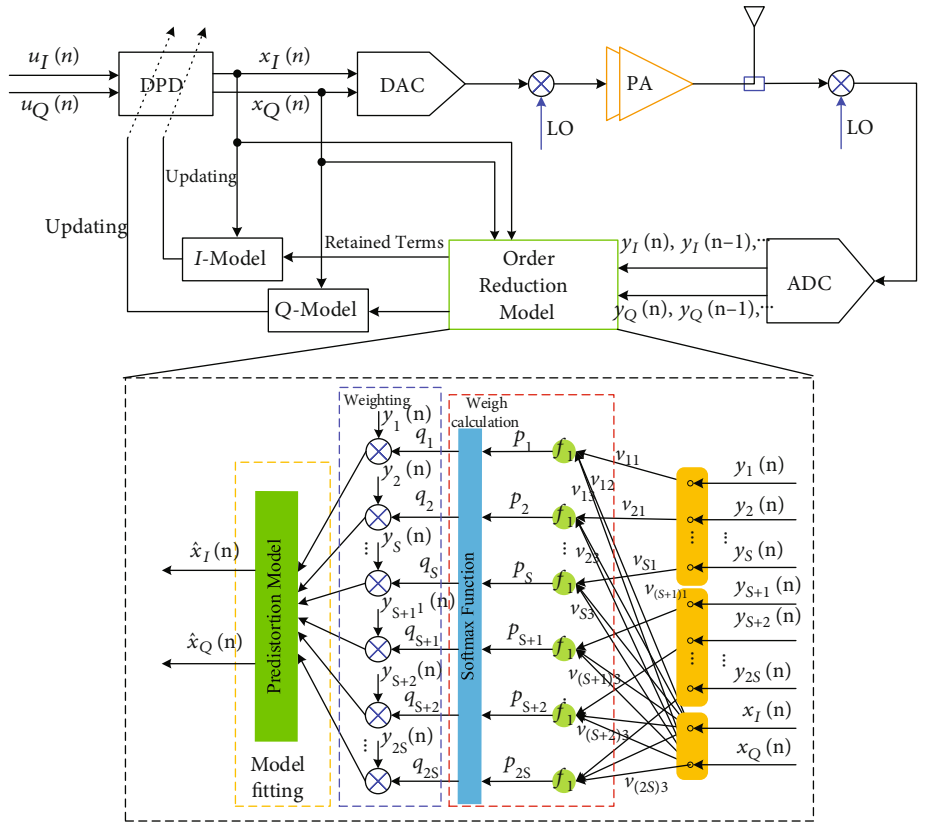

FIGURE 3: The structure of the proposed order reduction method of the predistortion model based on the attention mechanism.

consistency of the I/Q branch models of the predistorter, the contributions of the real basis function terms to the I/Q components of the predistortion output are calculated simultaneously, to reduce the predistortion model's design complexity in FPGA. The specific model structure is described as follows.

The input signal $x(n)$ is fed into PA after passing through the upconversion module and the digital-to-analog converter (DAC). In the feedback loop, the coupling output of the coupler passes through the downconversion module and the analog-to-digital converter (ADC) to obtain the digital baseband signal $y(n)$ of the PA output. We use the output signal $y(n)$ and input signal $x(n)$ of the PA to build the I/Q branch models of the predistorter based on the indirect learning architecture (ILA). Then, the proposed order reduction method is used to select important basis function terms in the I/Q branch models. Finally, the selected basis function terms are modeled on the main road using the lookup table (LUT) in the field-programmable gate array (FPGA), to achieve the PA's linearization.

The I/Q branch models can be constructed by the I/Q components of the traditional models or the ANN-based models. Let us take the GMP model as an example. The I/Q components of the complex basis function terms have independent contributions to the predistortion output, so the input data of the order reduction structure should contain all the real basis function terms, as shown in Equation (8), which can be written as

$$\begin{aligned}\bar{\mathbf{y}}(n) &= \left[\bar{y}_{1I}(n), \bar{y}_{2I}(n), \cdots, \bar{y}_{SI}(n), \bar{y}_{1Q}(n), \bar{y}_{2Q}(n), \cdots, \bar{y}_{SQ}(n)\right]^T \\ &= \left[y_1(n), y_2(n), \cdots, y_S(n), \cdots, y_{2S}(n)\right]^T,\end{aligned} \tag{14}$$

where $\bar{y}_{iI}(n)$ and $\bar{y}_{iQ}(n), (i = 1, 2, \cdots, S)$ are the I/Q components of the complex basis function term $\bar{y}_i(n)$, respectively. $\bar{\mathbf{y}}(n)$ is a vector with a dimension of $2S \times 1$, where $2S$ is the number of the real basis function terms. To facilitate numbering, $y_1(n), y_2(n), \cdots, y_{2S}(n)$ are used to represent these elements.

The output data of the structure contains the I/Q components of the output of the predistorter, which can be expressed as

$$\bar{\mathbf{x}}(n) = \left[x_I(n), x_Q(n)\right]^T, \tag{15}$$

where $x_I(n)$ and $x_Q(n)$ are the predistortion model output $x(n)$'s I/Q components.

To improve the fitting performance, a NN layer is used to calculate the correlation between each input and output data. Since each input needs to be calculated the correlation with all outputs, the i-th neuron in the NN layer is connected to the i-th input $y_i(n)$ and all outputs $\bar{\mathbf{x}}(n)$. The number of neurons is $2S$, corresponding to $2S$ inputs of the module. The NN layer's output can be written as

$$p_i = f_1(v_{i1}y_i(n) + [v_{i2}v_{i3}]\bar{\mathbf{x}}(n) + b_i), (i = 1, 2, \cdots, 2S), \quad (16)$$

where $\{v_{i1}, v_{i2}, v_{i3}\}$ are the weight coefficients of the i-th neuron and b_i is the bias coefficient of the i-th neuron. $f_1(\cdot)$ is the activation function, usually "tanh." The output p_i, $(i = 1, 2, \cdots, 2S)$ of the i-th neuron represents the correlation between the i-th input $y_i(n)$ and the output $\bar{\mathbf{x}}(n)$.

Then, the obtained correlation values p_i between the input and output data are converted numerically using the Softmax function. And the output of the Softmax function can be expressed as

$$q_i = \frac{\exp(p_i)}{\sum_{j=1}^{2S} \exp\left(p_j\right)}, (i = 1, 2, \cdots, 2S), \quad (17)$$

where $\sum_{i=1}^{2S} q_i = 1$. q_i, $(i = 1, 2, \cdots, 2S)$ is the form of probability, reflecting the spatial importance of the corresponding input $y_i(n)$ to the output, which is considered in this paper as the contribution of input (the basis function term) $y_i(n)$ to the generation of the output.

The inputs are weighted by the contributions of the inputs (the basis function terms), to emphasize the important inputs. The weighted inputs $y_i'(n)$ can be written as

$$y_i'(n) = q_i \times y_i(n), (i = 1, 2, \cdots, 2S). \quad (18)$$

By weighting the inputs (basis function terms) using the contributions, the important spatial details can be emphasized, and unimportant information can be weakened.

Finally, the weighted inputs $y_i'(n)$ are used to fit the output of the predistortion model. Since the I/Q branch models of the predistorter are identified separately, two coefficient vectors are used to fit the I/Q components of the predistorter. The predicted I/Q components of the predistorter can be expressed as

$$\begin{cases} \hat{x}_I(n) = \left[y_1'(n), y_2'(n), \cdots, y_{2S}'(n)\right]\mathbf{w}_I, \\ \hat{x}_Q(n) = \left[y_1'(n), y_2'(n), \cdots, y_{2S}'(n)\right]\mathbf{w}_Q, \end{cases} \quad (19)$$

where $\hat{x}_I(n)$ and $\hat{x}_Q(n)$ are the predicted I/Q components of the predistorter, respectively. $\mathbf{w}_I$ and $\mathbf{w}_Q$ are the coefficient vectors of the model, $\mathbf{w}_I = [w_{I1}, w_{I2}, \cdots, w_{\mathrm{IS}}, w_{I(S+1)}, \cdots, w_{I(2S)}]^T$, $\mathbf{w}_Q = [w_{Q1}, w_{Q2}, \cdots, w_{QS}, w_{Q(S+1)}, \cdots, w_{Q(2S)}]^T$.

The label data of the model training is output data $\bar{\mathbf{x}}(n)$ in Equation (15). By calculating the error between the predicted output and the label data, the order reduction structure can be trained. When the model converges, the contributions q_i of the inputs (the basis function terms) are obtained. Then, the real basis function terms can be sorted according to their contributions. Considering the trade-off between the model complexity and linearization effects, a contribution threshold q_0 is set. Then, the real basis terms with contributions greater than the threshold are retained, and the real basis terms with contributions less than the threshold are removed. According to the retained basis function terms, the I/Q branch models of the predistorter are modeled and identified.

3.2. Training of the Proposed Order Reduction Method. The input signal $y(n)$ and output signal $x(n)$ of the predistortion model are captured first. Then, the input data $\bar{\mathbf{y}}(n)$ of the order reduction structure is constructed according to Equation (14), and the output data $\bar{\mathbf{x}}(n)$ is obtained according to Equation (15). This paper uses 16,000 sets of input and output data to model the proposed method. The data is divided into training data and test data in a ratio of 1 : 1, which are used to train the method and test the method, respectively. The cost function of the training is set as the mean square error (MSE) function, which is written as

$$\mathrm{MSE} = \frac{1}{2N}\sum_{i=1}^{N}\left(\left(x\wedge_I(i) - x_I(i)\right)^2 + \left(x\wedge_Q(i) - x_Q(i)\right)^2\right), \quad (20)$$

where N is the number of data sets for training.

In this paper, the Adam optimization algorithm [31] is used to update the coefficients $\theta = \{v_{i1}, v_{i2}, v_{i3}, b_i, \mathbf{w}_I, \mathbf{w}_Q\}$ of the proposed structure. The updating process of coefficients can be expressed as

$$\begin{cases} \theta^{(k)} = \theta^{(k-1)} - \delta\dfrac{A^{(k)}/\left(1-\beta_1^k\right)}{\sqrt{B^{(k)}/\left(1-\beta_2^k\right)} + \varepsilon}, \\ \begin{cases} A^{(k)} = \beta_1 A^{(k-1)} + (1-\beta_1)\nabla, \\ B^{(k)} = \beta_2 B^{(k-1)} + (1-\beta_2)\nabla^2, \end{cases} \end{cases} \quad (21)$$

where ∇ is the gradient of the cost function to the coefficients and δ is the learning rate. β_1, β_2, and ε are constants.

The training process of the proposed order reduction method is shown in Algorithm 1. During the training, the attention module's output and the model output are calculated successively, and then, the cost function is calculated based on the model output and label data. According to the obtained cost function, the coefficients of the proposed method were updated using the Adam algorithm. In the next iteration, the attention module's output and the model output are calculated based on the updated model coefficients. Then, the cost function is calculated, and the coefficients are updated again. When the training times of the method reach the given iteration times, the training is finished.

When the model completes the training, the weight values q_i of the attention module output represent the contributions of the corresponding input. According to the contribution values of the basis function terms, the real basis function terms are filtered, and the retained basis function terms are obtained

$$\bar{\mathbf{y}}'(n) = \left[y_{d_1}(n), y_{d_2}(n), \cdots, y_{d_D}(n)\right]^T, \quad (22)$$

where D is the number of the retained basis function terms, and d_i, $(i = 1, 2, \cdots, D)$ satisfy $q_{d_i} \geq q_0$. Then, the

Definition:
1. Construct the structure of the order reduction method;
2. Obtain the training data, including the input and output data of the training;
3. Define MSE as the cost function of training.

Training of the method:
1. Initialization:
   1) Set the learning rate $\delta = 0.001$, and the training parameters $\beta_1 = 0.9$, $\beta_2 = 0.999$, $\varepsilon = 10^{-8}$;
   2) Initialize vector $A^{(0)} = 0$ and $B^{(0)} = 0$;
   3) Initialize coefficients $\theta^{(0)}$.
2. Training:

Loop: $k = 1, 2, \cdots$
   1) Calculate the output q_i of the attention module from Equation (17);
   2) Calculate model output from Equation (19);
   3) Calculate the cost function MSE from Equation (20);
   4) Calculate vector $A^{(k)} = \beta_1 A^{(k-1)} + (1-\beta_1)\nabla$ and $B^{(k)} = \beta_2 B^{(k-1)} + (1-\beta_2)\nabla^2$;
   5) Update coefficients $\theta^{(k)} = \theta^{(k-1)} - \delta(A^{(k)}/(1-\beta_1^k)/\sqrt{B^{(k)}/(1-\beta_2^k)} + \varepsilon)$.

End

Algorithm 1: Training of the order reduction method

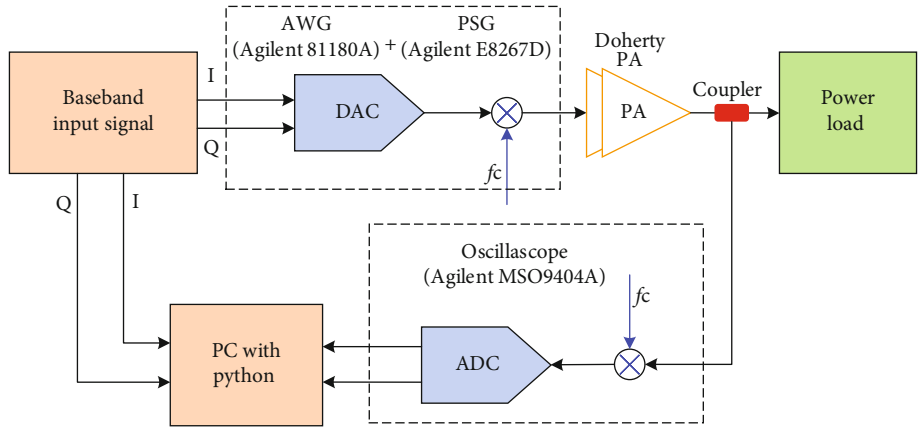

Figure 4: Experimental setup.

predistortion model is constructed using the retained basis function terms, and the predistorter coefficients are calculated by the LS algorithm.

$$\begin{cases} \widehat{\boldsymbol{\omega}}_I' = \left(\left(\bar{\mathbf{y}}'\right)^H \bar{\mathbf{y}}'\right)^{-1} \left(\bar{\mathbf{y}}'\right)^H \mathbf{x}_I, \\ \widehat{\boldsymbol{\omega}}_Q' = \left(\left(\bar{\mathbf{y}}'\right)^H \bar{\mathbf{y}}'\right)^{-1} \left(\bar{\mathbf{y}}'\right)^H \mathbf{x}_Q, \end{cases} \tag{23}$$

where $\bar{\mathbf{y}}' = [\bar{\mathbf{y}}'(N), \bar{\mathbf{y}}'(N-1), \cdots, \bar{\mathbf{y}}'(1)]^T$.

4. Experimental Setup

The experimental platform in Figure 4 is used to test the pruning effect of the order reduction method. The test signal used is an orthogonal frequency division multiplexing (OFDM) signal with a bandwidth of 100 MHz and a PAPR of 9.46 dB. In this OFDM signal, the symbol vector is modulated by 16 quadrature amplitude modulation (16-QAM). The OFDM signal is first transmitted to the Arbitrary Waveform Generator (AWG81180A), and then, the device is connected to the Performance Signal Generator (PSGE8267D) to transmit the generated baseband signal. PSG realizes digital to analog conversion and upconversion functions and then transmits the signal to Doherty PA. The PA has a center frequency of 2.14 GHz and a saturated power of 43 dBm, and the output backoff (OBO) is 6 dB. The output signal of PA is fed into the coupler.

In the feedback loop, the coupler's coupling output is connected to an oscilloscope (MSO9404A), to realize the sampling of the feedback signal. MSO9404A realizes the functions of downconversion and ADC. The sampling bandwidth is set to 500 MHz. Finally, the sampled digital baseband signal is downloaded to a personal computer (PC) to achieve predistortion design. The order reduction method of the predistortion model is constructed using the Python software's TensorFlow module on a PC. In order to verify the performance of the proposed method under different

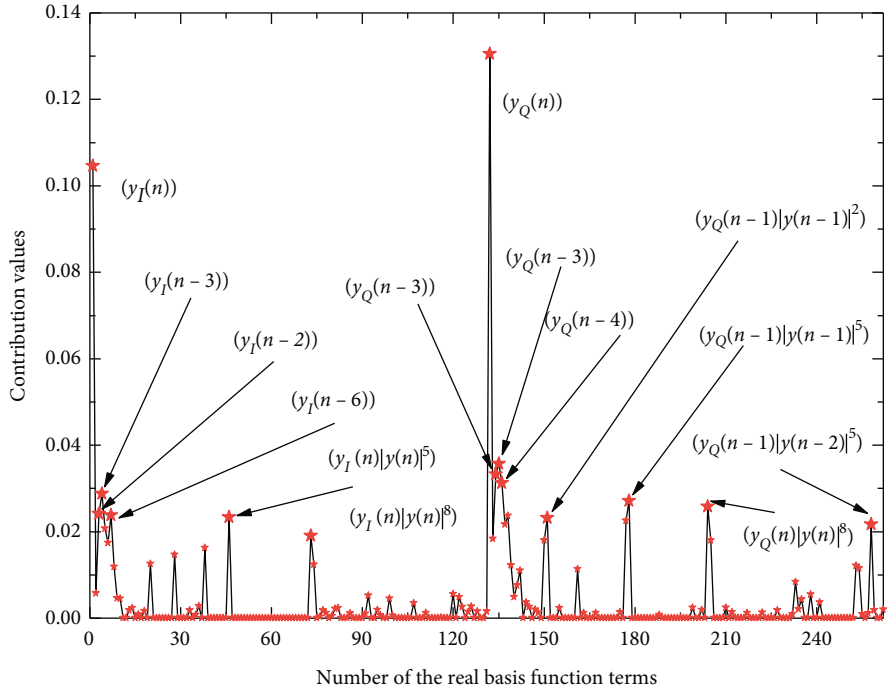

Figure 5: The contribution values of the real basis function terms.

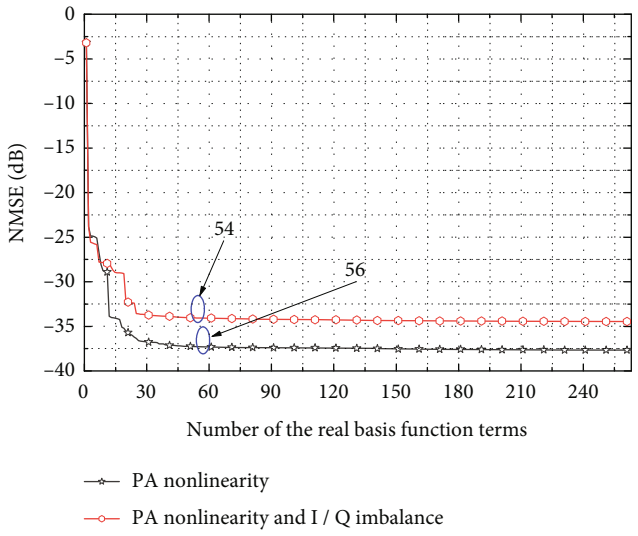

Figure 6: Comparison of NMSE performance between case A and case B at different order reduction levels.

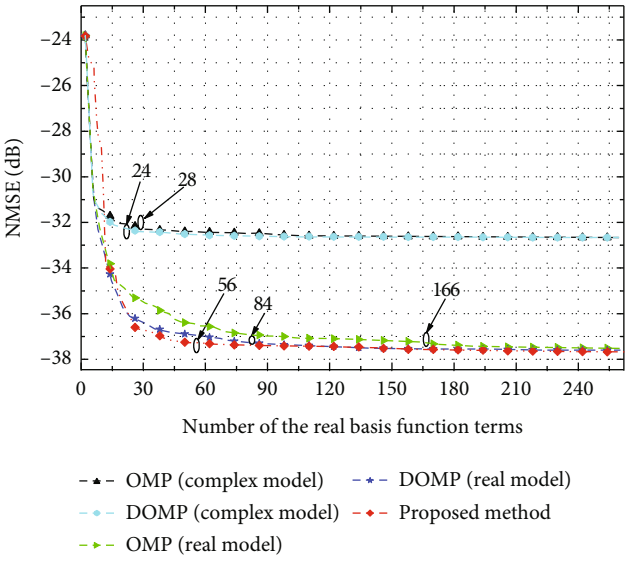

Figure 7: Comparison of NMSE performance between the proposed method and other typical methods at different order reduction levels.

conditions, we evaluate two cases of transmitter nonlinearity. Case A only contains PA's nonlinear distortion in the link, and case B contains nonlinear distortion of PA and I/Q imbalance in the link. In the I/Q imbalance, the amplitude imbalance is set to 1 dB, and the phase imbalance is set to 3 degrees.

5. Experimental Results

Figure 5 shows the contribution values of the real basis function terms to the generation of the predistortion output, where the predistortion model is modeled using the GMP model, and the model parameters $K_a = 9$, $L_a = 9$, $K_b = 5$, $L_b = 2$, $M_b = 5$, $K_c = 0$, $L_c = 0$, and $M_c = 0$. In Figure 5, the horizontal axis shows the number of the real basis function terms, in the order shown in Equation (10), and the vertical axis represents the corresponding contribution values of the real basis function terms. It can be seen from the figure that different basis function terms show different contribution values with a great difference, which is the basis of the effectiveness of the proposed method. Meanwhile, the I/Q components of some complex basis function terms all display

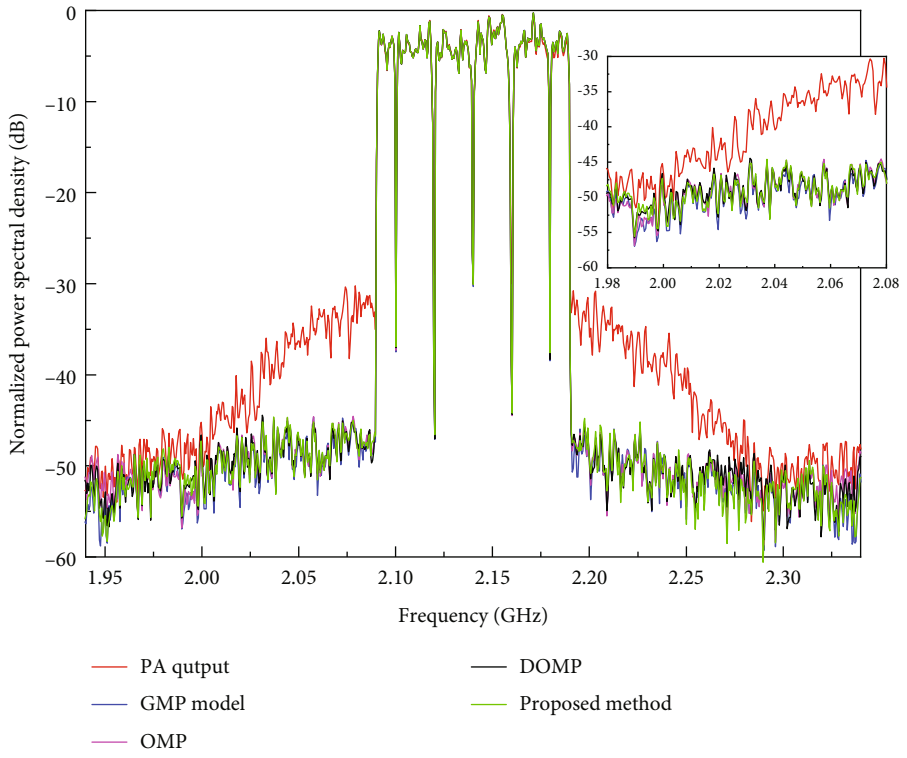

Figure 8: Comparison of the predistortion effects between the typical pruning models and the proposed pruning model.

Table 2: Comparison of linearization effects under different nonlinear conditions.

	PA nonlinearity			PA nonlinearity and I/Q imbalance		
	Num. of real basis function terms	NMSE (dB)	ACPR (±25 MHz) (dBc)	Num. Of real basis function terms	NMSE (dB)	ACPR (±25 MHz) (dBc)
No DPD	\	-8.68	-31.14/-33.24	\	-7.51	-29.75/-31.52
GMP (complex model)	262	-32.67	-44.63/-44.99	262	-22.75	-38.02/-39.94
OMP (complex model)	28	-32.30	-44.34/-44.95	8	-22.47	-38.14/-39.81
DOMP (complex model)	24	-32.30	-44.57/-44.87	6	-22.40	-38.07/-39.91
GMP (real model)	262	-37.67	-45.65/-46.97	262	-34.47	-41.29/-42.77
OMP (real model)	166	-37.28	-45.66/-46.74	188	-34.09	-41.20/-42.69
DOMP (real model)	84	-37.29	-45.53/-46.84	74	-34.09	-41.18/-42.75
Proposed pruning model	56	-37.28	-45.64/-46.81	54	-34.07	-41.21/-42.72

large contribution values, such as the I/Q components $y_I(n)$, $y_Q(n)$, $y_I(n-3)$, $y_Q(n-3)$, $y_I(n)|y(n)|^8$, $y_Q(n)|y(n)|^8$ of $y(n)$, $y(n-3)$, and $y(n)|y(n)|^8$. However, there are also some complex basis functions with only one component showing a larger contribution, such as $y_I(n-6)$, $y_I(n)|y(n)|^5$, and $y_Q(n-1)|y(n-1)|^5$, which suggests that distinguishing the contributions of the I/Q components of the complex basis function terms can further reduce model complexity.

Figure 6 compares the linearization performance of case A and case B at different order reduction levels. It can be found that in case A, the NMSE decreases rapidly with the increase of the number of the selected real basis function terms, when the number of the selected real basis function terms is less than 40. This is because the basis function terms with larger contributions are selected first and can generate most of the predistortion output. When the number of the selected real basis function terms is between 40 and 55, the NMSE decreases slowly. When the real basis function terms' number exceeds 56, the NMSE performance is barely improved. We select 56 real basis function terms, and the NMSE performance at this time can be maintained to -37.28 dB. Compared with 262 real basis terms of the GMP model, the number of the real function basis terms of the pruning method is reduced by 79%. The NMSE curve of case B shows the same trend as that of case A. However, the NMSE curve of case B has a faster decline rate as the number of the real basis function terms increases. According to the linearization performance, 54 real basis function terms with large contributions were selected to mitigate the PA's

nonlinearity and I/Q imbalance, and the NMSE at this time can be maintained to -34.07 dB. In case B, the number of the real basis function terms of the pruning model is reduced by 79%.

Figure 7 compares the NMSE of the proposed method with other methods at different order reduction levels. In OMP (real model) and DOMP (real model), the important real basis function terms for the I/Q branch models of the predistorter are calculated separately. It can be found that the linearization performance of the real model (the I/Q branch models of the predistorter) is obviously better than that of the complex model. In the real model, to achieve the same NMSE (-36.27 dB, which is 0.4 dB higher than the NMSE of the GMP model), the proposed method requires only 56 basis function terms and the basis function terms' number is reduced by 79%. However, OMP and DOMP require 166 and 84 basis function terms, respectively, which are 3 times and 1.5 times the number of the selected basis function terms of the proposed method, respectively. The reduced basis function terms represent the influence of the cross terms of the I/Q branch models.

Figure 8 compares the linearization effects of the typical pruning models and the proposed pruning model. The number of the real basis function terms selected for the proposed model is the abovementioned 56. It can be seen from the figure that the proposed pruning model reduces the adjacent channel power ratio (ACPR) of the PA output signal from -32 dBc to -46 dBc, which proves the superior pruning performance of this model. Compared with the full GMP model, the linearization effects of the proposed pruning model are almost no worse, which can be seen from the almost overlapping spectrum. Meanwhile, the linearization effects of the proposed model are almost the same as those of the OMP model and the DOMP model, but the complexity of the predistortion model is significantly reduced. The number of the real basis function terms of the proposed model is only 67% of the number of the real basis function terms of the OMP model and 34% of the number of the real basis function terms of the DOMP model.

Table 2 comprehensively compares the performance of the typical methods and the proposed pruning method in case A and case B. It can be found that in case A, the proposed pruning method achieved the NMSE of -36.28 dB (0.4 dB higher than the NMSE of the GMP model) with only 21% real basis function terms. The ACPR performance of the proposed pruning method is almost equal to that of the full GMP model. Meanwhile, the ACPR and NMSE of the proposed pruning method are almost the same as those of OMP and DOMP, using the least real basis function terms. In case B, the NMSE performance of the proposed pruning method reaches -34.07 dB (0.4 dB higher than the NMSE of the GMP model) using only 21% of the real basis function terms. Similarly, the proposed pruning method achieves nearly the same NMSE and ACPR performance as OMP and DOMP by using the least real basis function terms in case B.

Figure 9 shows the NMSE performance of the proposed order reduction model under different I/Q imbalance levels. It can be found that under different I/Q imbalance levels, the

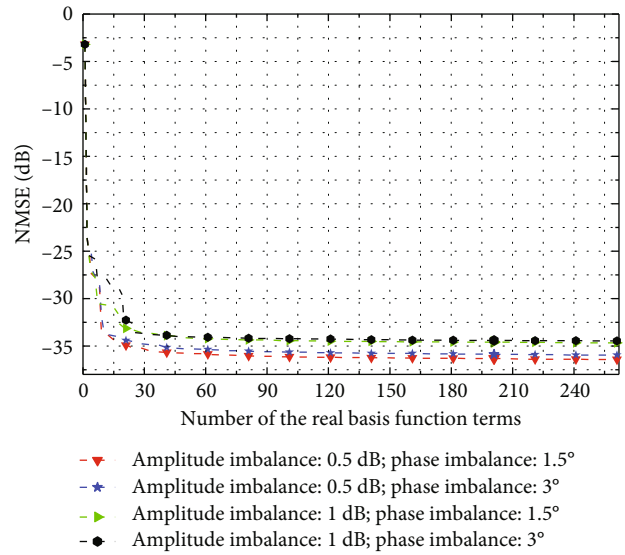

Figure 9: Comparison of NMSE performance under different I/Q imbalance levels.

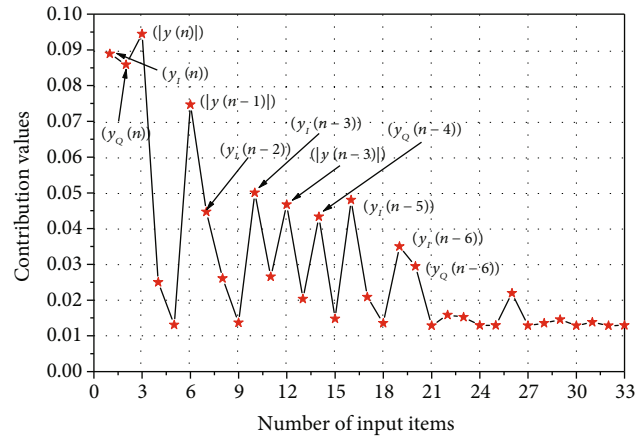

Figure 10: The contribution value of the input items in the NN-based predistortion model.

proposed order reduction model can quickly find the important real basis function terms, to construct the low-complexity predistortion model, which proves that the proposed order reduction model is suitable for different transmitter nonlinear conditions. The higher the level of the amplitude imbalance and phase imbalance, the worse the NMSE performance. However, the proposed order reduction model can almost achieve the optimal NMSE performance when the number of the selected real basis function terms is 30.

Figure 10 shows the contributions of the input items of the NN-based predistortion model, where the proposed method is used for the input term pruning of the NN-based predistortion model, and the pruning structure is described in literature [24]. It can be found that this method can get the contribution values of the input items. Then, the input items are sorted according to the contribution values. Figure 11 shows the NMSE performance under the different

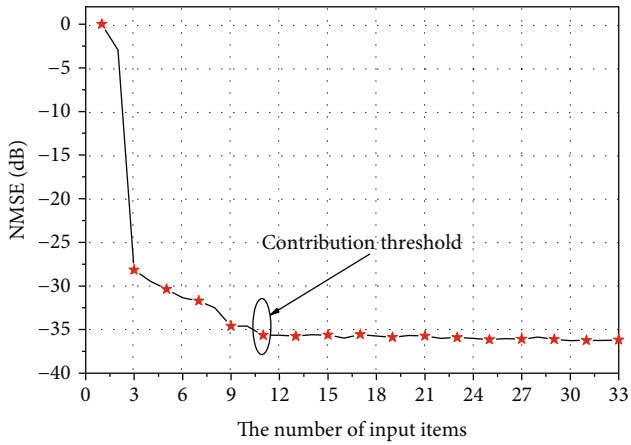

Figure 11: NMSE performance under the different number of the input items in the NN-based predistortion model.

number of input items. It can be found that with the increase of the input item's number, the NMSE performance improves rapidly. When the input item's number is 11, the NMSE performance is almost equal to that of the full model, which proves that this method is suitable for the pruning of the NN model-based model.

6. Conclusions

In this paper, an order reduction method of the predistortion model based on the attention mechanism is proposed. This method calculates the contributions of the real basis function terms to the I/Q components of the predistortion output using the attention mechanism, to select the important real basis function terms to build the I/Q branch models. The experimental results based on 100 MHz Doherty PA and I/Q imbalance verify the superior pruning performance of this method. In case A, the proposed method can prune the number of the real basis function terms to 21%, and the NMSE can be maintained to -36.3 dB. And in case B, the proposed method prunes the number of the real basis function terms to 21%, and the NMSE can be maintained to -34.1 dB. Meanwhile, to achieve almost the same ACPR and NMSE performance, the number of the basis function terms required by the proposed method is only 67% that of DOMP. In order to further reduce the complexity of the digital predistortion model in wideband systems, we will consider designing a fixed core suitable for most nonlinear transmitters and then pruning the I/Q branch models for the remaining basis function terms.

Data Availability

The data used to support the findings of this study are available from the corresponding author upon request.

Conflicts of Interest

The authors declare that they have no conflicts of interest.

Acknowledgments

This work was supported by the Low-orbit satellite undersampling broadband predistortion high-efficiency transmission technology (No. A2021023) and the BUPT Excellent Ph.D. Students Foundation (No. CX2020112).

References

[1] J. J. Xia, L. Fan, N. Yang et al., "Opportunistic access point selection for mobile edge computing networks," *IEEE Transactions on Wireless Communications*, vol. 20, no. 1, pp. 695–709, 2021.

[2] K. He, Z. Wang, D. Li, F. Zhu, and L. Fan, "Ultra-reliable MU-MIMO detector based on deep learning for 5G/B5G-enabled IoT," *Physical Communication*, vol. 43, no. 11, p. 101181, 2020.

[3] S. P. Tang, W. Zhou, L. Chen, L. Lai, J. Xia, and L. Fan, "Battery-constrained federated edge learning in UAV-enabled IoT for B5G/6G networks," *Physical Communication*, vol. 47, p. 101381, 2021.

[4] J. A. Becerra, M. J. Madero-Ayora, and C. Crespo-Cadenas, "Comparative analysis of greedy pursuits for the order reduction of wideband digital predistorters," *IEEE Transactions on Microwave Theory and Techniques*, vol. 67, no. 9, pp. 3575–3585, 2019.

[5] X. Hu, Z. Liu, X. Yu et al., "Convolutional neural network for behavioral modeling and predistortion of wideband power amplifiers," *IEEE Transactions on Neural Networks and Learning Systems*, pp. 1–15, 2021.

[6] X. Hu, Z. Liu, W. Wang, M. Helaoui, and F. M. Ghannouchi, "Low-feedback sampling rate digital predistortion using deep neural network for wideband wireless transmitters," *IEEE Transactions on Communications*, vol. 68, no. 4, pp. 2621–2633, 2020.

[7] Z. Wang, W. Chen, G. Su, F. M. Ghannouchi, Z. Feng, and Y. Liu, "Low feedback sampling rate digital predistortion for wideband wireless transmitters," *IEEE Transactions on Microwave Theory and Techniques*, vol. 64, no. 11, pp. 3528–3539, 2016.

[8] L. Anttila, P. Handel, and M. Valkama, "Joint mitigation of power amplifier and I/Q modulator impairments in broadband direct-conversion transmitters," *IEEE Transactions on Microwave Theory and Techniques*, vol. 58, no. 4, pp. 730–739, 2010.

[9] J. A. Becerra, M. J. M. Ayora, J. Reina-Tosina, and C. Crespo-Cadenas, "Sparse identification of Volterra models for power amplifiers without pseudoinverse computation," *IEEE Transactions on Microwave Theory and Techniques*, vol. 68, no. 11, pp. 4570–4578, 2020.

[10] A. Abdelhafiz, A. Kwan, O. Hammi, and F. M. Ghannouchi, "Digital predistortion of LTE-A power amplifiers using compressed-sampling-based unstructured pruning of Volterra series," *IEEE Transactions on Microwave Theory and Techniques*, vol. 62, no. 11, pp. 2583–2593, 2014.

[11] J. Reina-Tosina, M. Allegue-Martinez, C. Crespo-Cadenas, C. Yu, and S. Cruces, "Behavioral modeling and predistortion of power amplifiers under sparsity hypothesis," *IEEE Transactions on Microwave Theory and Techniques*, vol. 63, no. 2, pp. 745–753, 2015.

[12] J. Kim and K. Konstantinou, "Digital predistortion of wideband signals based on power amplifier model with memory," *Electronics Letters*, vol. 37, no. 23, pp. 1417-1418, 2001.

[13] D. R. Morgan, Z. Ma, J. Kim, M. G. Zierdt, and J. Pastalan, "A generalized memory polynomial model for digital predistortion of RF power amplifiers," *IEEE Transactions on Signal Processing*, vol. 54, no. 10, pp. 3852–3860, 2006.

[14] D. Lopez-Bueno, Q. A. Pham, G. Montoro, and P. L. Gilabert, "Independent digital predistortion parameters estimation using adaptive principal component analysis," *IEEE Transactions on Microwave Theory and Techniques*, vol. 66, no. 12, pp. 5771–5779, 2018.

[15] A. Molina, K. Rajamani, and K. Azadet, "Digital predistortion using lookup tables with linear interpolation and extrapolation: direct least squares coefficient adaptation," *IEEE Transactions on Microwave Theory and Techniques*, vol. 65, no. 3, pp. 980–987, 2017.

[16] P. L. Gilabert, A. Cesari, G. Montoro, E. Bertran, and J. M. Dilhac, "Multi-lookup table FPGA implementation of an adaptive digital predistorter for linearizing RF power amplifiers with memory effects," *IEEE Transactions on Microwave Theory and Techniques*, vol. 56, no. 2, pp. 372–384, 2008.

[17] J. A. Becerra, M. J. Madero-Ayora, J. Reina-Tosina, C. Crespo-Cadenas, J. Garcia-Frias, and G. Arce, "A doubly orthogonal matching pursuit algorithm for sparse predistortion of power amplifiers," *IEEE Microwave and Wireless Components Letters*, vol. 28, no. 8, pp. 726–728, 2018.

[18] W. Chen, S. Zhang, Y. J. Liu, F. M. Ghannouchi, Z. Feng, and Y. Liu, "Efficient pruning technique of memory polynomial models suitable for PA behavioral modeling and digital predistortion," *IEEE Transactions on Microwave Theory and Techniques*, vol. 62, no. 10, pp. 2290–2299, 2014.

[19] J. A. Becerra, M. J. Madero-Ayora, J. Reina-Tosina, C. Crespo-Cadenas, J. Garcia-Frias, and G. Arce, "A reduced-complexity doubly orthogonal matching pursuit algorithm for power amplifier sparse behavioral modeling," in *2019 IEEE Topical Conference on RF/Microwave Power Amplifiers for Radio and Wireless Applications (PAWR)*, pp. 1–3, Orlando, FL, USA, January 2019.

[20] J. Peng, S. He, Z. Dai, and B. Wang, "A simplified sparse parameter identification algorithm suitable for power amplifier behavioral modeling," *IEEE Microwave and Wireless Components Letters*, vol. 27, no. 3, pp. 290–292, 2017.

[21] D. Wang, M. Aziz, M. Helaoui, and F. M. Ghannouchi, "Augmented real-valued time-delay neural network for compensation of distortions and impairments in wireless transmitters," *IEEE Transactions on Neural Networks and Learning Systems*, vol. 30, no. 1, pp. 242–254, 2019.

[22] S. Lajnef, N. Boulejfen, A. Abdelhafiz, and F. M. Ghannouchi, "Two-dimensional Cartesian memory polynomial model for nonlinearity and I/Q imperfection compensation in concurrent dual-band transmitters," *IEEE Transactions on Circuits and Systems II: Express Briefs*, vol. 63, no. 1, pp. 14–18, 2016.

[23] H. Y. Cao, A. Soltani Tehrani, C. Fager, T. Eriksson, and H. Zirath, "I/Q imbalance compensation using a nonlinear modeling approach," *IEEE Transactions on Microwave Theory and Techniques*, vol. 57, no. 3, pp. 513–518, 2009.

[24] Z. Liu, X. Hu, T. Liu, X. Li, W. Wang, and F. M. Ghannouchi, "Attention-based deep neural network behavioral model for wideband wireless power amplifiers," *IEEE Microwave and Wireless Components Letters*, vol. 30, no. 1, pp. 82–85, 2020.

[25] L. Guan and A. Zhu, "Optimized low-complexity implementation of least squares based model extraction for digital predistortion of RF power amplifiers," *IEEE Transactions on Microwave Theory and Techniques*, vol. 60, no. 3, pp. 594–603, 2012.

[26] Lei Ding, Zhengxiang Ma, D. R. Morgan, M. Zierdt, and J. Pastalan, "A least-squares/Newton method for digital predistortion of wideband signals," *IEEE Transactions on Communications*, vol. 54, no. 5, pp. 833–840, 2006.

[27] J. J. Xia, D. Deng, and D. Fan, "A note on implementation methodologies of deep learning-based signal detection for conventional MIMO transmitters," *IEEE Transactions on Broadcasting*, vol. 66, no. 3, pp. 744-745, 2020.

[28] J. Xia, L. Fan, W. Xu et al., "Secure cache-aided multi-relay networks in the presence of multiple eavesdroppers," *IEEE Transactions on Communications*, vol. 67, no. 11, pp. 7672–7685, 2019.

[29] J. K. Chorowski, D. Bahdanau, D. Serdyuk, K. Cho, and Y. Bengio, "Attention-based models for speech recognition," in *Proc. Advances in Neural Information Processing Systems*, pp. 577–585, Cambridge, MA, USA, 2015.

[30] W. Xu, R. Chen, B. Huang, and Q. Zhou, "Enhanced context attention network for image super resolution," *IEEE Sensors Journal*, vol. 21, no. 10, pp. 11665–11673, 2021.

[31] D. P. Kingma and J. Ba, "Adam: a method for stochastic optimization," in *Proc. 3rd International Conference for Learning Representations (ICLR 2015)*, pp. 7–9, San Diego, USA, 2015.